

Advances in Civil Engineering

Dynamic Hazard Controls in Underground Mines

Lead Guest Editor: Jia Lin

Guest Editors: Zhao-hui Chong and Gong-Da Wang





Dynamic Hazard Controls in Underground Mines

Advances in Civil Engineering

Dynamic Hazard Controls in Underground Mines

Lead Guest Editor: Jia Lin

Guest Editors: Zhao-hui Chong and Gong-Da
Wang



Copyright © 2021 Hindawi Limited. All rights reserved.

This is a special issue published in "Advances in Civil Engineering." All articles are open access articles distributed under the Creative Commons Attribution License, which permits unrestricted use, distribution, and reproduction in any medium, provided the original work is properly cited.





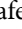
Chief Editor

Cumaraswamy Vipulanandan, USA













Associate Editors

Chiara Bedon , Italy
Constantin Chalioris , Greece
Ghassan Chehab , Lebanon
Ottavia Corbi, Italy
Mohamed ElGawady , USA
Husnain Haider , Saudi Arabia
Jian Ji , China
Jiang Jin , China
Shazim A. Memon , Kazakhstan
Hossein Moayedi , Vietnam
Sanjay Nimbalkar, Australia
Giuseppe Oliveto , Italy
Alessandro Palmeri , United Kingdom
Arnaud Perrot , France
Hugo Rodrigues , Portugal
Victor Yepes , Spain
Xianbo Zhao , Australia

Academic Editors

José A.F.O. Correia, Portugal
Glenda Abate, Italy
Khalid Abdel-Rahman , Germany
Ali Mardani Aghabaglou, Turkey
José Aguiar , Portugal
Afaq Ahmad , Pakistan
Muhammad Riaz Ahmad , Hong Kong
Hashim M.N. Al-Madani , Bahrain
Luigi Aldieri , Italy
Angelo Aloisio , Italy
Maria Cruz Alonso, Spain
Filipe Amarante dos Santos , Portugal
Serji N. Amirkhanean, USA
Eleftherios K. Anastasiou , Greece
Panagiotis Ch. Anastasopoulos , USA
Mohamed Moafak Arbili , Iraq
Farhad Aslani , Australia
Siva Avudaiappan , Chile
Ozgur BASKAN , Turkey
Adewumi Babafemi, Nigeria
Morteza Bagherpour, Turkey
Qingsheng Bai , Germany
Nicola Baldo , Italy
Daniele Baraldi , Italy

Eva Barreira , Portugal
Emilio Bastidas-Arteaga , France
Rita Bento, Portugal
Rafael Bergillos , Spain
Han-bing Bian , China
Xia Bian , China
Huseyin Bilgin , Albania
Giovanni Biondi , Italy
Hugo C. Biscaia , Portugal
Rahul Biswas , India
Edén Bojórquez , Mexico
Giosuè Boscato , Italy
Melina Bosco , Italy
Jorge Branco , Portugal
Bruno Briseghella , China
Brian M. Broderick, Ireland
Emanuele Brunesi , Italy
Quoc-Bao Bui , Vietnam
Tan-Trung Bui , France
Nicola Buratti, Italy
Gaochuang Cai, France
Gladis Camarini , Brazil
Alberto Campisano , Italy
Qi Cao, China
Qixin Cao, China
Iacopo Carnacina , Italy
Alessio Cascardi, Italy
Paolo Castaldo , Italy
Nicola Cavalagli , Italy
Liborio Cavaleri , Italy
Anush Chandrappa , United Kingdom
Wen-Shao Chang , United Kingdom
Muhammad Tariq Amin Chaudhary, Kuwait
Po-Han Chen , Taiwan
Qian Chen , China
Wei Tong Chen , Taiwan
Qixiu Cheng, Hong Kong
Zhanbo Cheng, United Kingdom
Nicholas Chileshe, Australia
Prinya Chindaprasirt , Thailand
Corrado Chisari , United Kingdom
Se Jin Choi , Republic of Korea
Heap-Yih Chong , Australia
S.H. Chu , USA
Ting-Xiang Chu , China


Zhaofei Chu , China
Wonseok Chung , Republic of Korea
Donato Ciampa , Italy
Gian Paolo Cimellaro, Italy
Francesco Colangelo, Italy
Romulus Costache , Romania
Liviu-Adrian Cotfas , Romania
Antonio Maria D'Altri, Italy
Bruno Dal Lago , Italy
Amos Darko , Hong Kong
Arka Jyoti Das , India
Dario De Domenico , Italy
Gianmarco De Felice , Italy
Stefano De Miranda , Italy
Maria T. De Risi , Italy
Tayfun Dede, Turkey
Sadik O. Degertekin , Turkey
Camelia Delcea , Romania
Cristoforo Demartino, China
Giuseppe Di Filippo , Italy
Luigi Di Sarno, Italy
Fabio Di Trapani , Italy
Aboelkasim Diab , Egypt
Thi My Dung Do, Vietnam
Giulio Dondi , Italy
Jiangfeng Dong , China
Chao Dou , China
Mario D'Aniello , Italy
Jingtao Du , China
Ahmed Elghazouli, United Kingdom
Francesco Fabbrocino , Italy
Flora Faleschini , Italy
Dingqiang Fan, Hong Kong
Xueping Fan, China
Qian Fang , China
Salar Farahmand-Tabar , Iran
Ilenia Farina, Italy
Roberto Fedele, Italy
Guang-Liang Feng , China
Luigi Fenu , Italy
Tiago Ferreira , Portugal
Marco Filippo Ferrotto, Italy
Antonio Formisano , Italy
Guoyang Fu, Australia
Stefano Galassi , Italy

Junfeng Gao , China
Meng Gao , China
Giovanni Garcea , Italy
Enrique García-Macías, Spain
Emilio García-Taengua , United Kingdom
DongDong Ge , USA
Khaled Ghaedi, Malaysia
Khaled Ghaedi , Malaysia
Gian Felice Giaccu, Italy
Agathoklis Giaralis , United Kingdom
Ravindran Gobinath, India
Rodrigo Gonçalves, Portugal
Peilin Gong , China
Belén González-Fonteboa , Spain
Salvatore Grasso , Italy
Fan Gu, USA
Erhan Güneyisi , Turkey
Esra Mete Güneyisi, Turkey
Pingye Guo , China
Ankit Gupta , India
Federico Gusella , Italy
Kemal Hacıefendioğlu, Turkey
Jianyong Han , China
Song Han , China
Asad Hanif , Macau
Hadi Hasanzadehshooiili , Canada
Mostafa Fahmi Hassanein, Egypt
Amir Ahmad Hedayat , Iran
Khandaker Hossain , Canada
Zahid Hossain , USA
Chao Hou, China
Biao Hu, China
Jiang Hu , China
Xiaodong Hu, China
Lei Huang , China
Cun Hui , China
Bon-Gang Hwang, Singapore
Jijo James , India
Abbas Fadhil Jasim , Iraq
Ahad Javanmardi , China
Krishnan Prabhakan Jaya, India
Dong-Sheng Jeng , Australia
Han-Yong Jeon, Republic of Korea
Pengjiao Jia, China
Shaohua Jiang , China

MOUSTAFA KASSEM , Malaysia
Mosbeh Kaloop , Egypt
Shankar Karuppannan , Ethiopia
John Kechagias , Greece
Mohammad Khajehzadeh , Iran
Afzal Husain Khan , Saudi Arabia
Mehran Khan , Hong Kong
Manoj Khandelwal, Australia
Jin Kook Kim , Republic of Korea
Woosuk Kim , Republic of Korea
Vaclav Koci , Czech Republic
Loke Kok Foong, Vietnam
Hailing Kong , China
Leonidas Alexandros Kouris , Greece
Kyriakos Kourousis , Ireland
Moacir Kripka , Brazil
Anupam Kumar, The Netherlands
Emma La Malfa Ribolla, Czech Republic
Ali Lakirouhani , Iran
Angus C. C. Lam, China
Thanh Quang Khai Lam , Vietnam
Luciano Lamberti, Italy
Andreas Lampropoulos , United Kingdom
Raffaele Landolfo, Italy
Massimo Latour , Italy
Bang Yeon Lee , Republic of Korea
Eul-Bum Lee , Republic of Korea
Zhen Lei , Canada
Leonardo Leonetti , Italy
Chun-Qing Li , Australia
Dongsheng Li , China
Gen Li, China
Jiale Li , China
Minghui Li, China
Qingchao Li , China
Shuang Yang Li , China
Sunwei Li , Hong Kong
Yajun Li , China
Shun Liang , China
Francesco Liguori , Italy
Jae-Han Lim , Republic of Korea
Jia-Rui Lin , China
Kun Lin , China
Shibin Lin, China

Tzu-Kang Lin , Taiwan
Yu-Cheng Lin , Taiwan
Hexu Liu, USA
Jian Lin Liu , China
Xiaoli Liu , China
Xuemei Liu , Australia
Zaobao Liu , China
Zhuang-Zhuang Liu, China
Diego Lopez-Garcia , Chile
Cristiano Loss , Canada
Lyan-Ywan Lu , Taiwan
Jin Luo , USA
Yanbin Luo , China
Jianjun Ma , China
Junwei Ma , China
Tian-Shou Ma, China
Zhongguo John Ma , USA
Maria Macchiaroli, Italy
Domenico Magisano, Italy
Reza Mahinroosta, Australia
Yann Malecot , France
Prabhat Kumar Mandal , India
John Mander, USA
Iman Mansouri, Iran
André Dias Martins, Portugal
Domagoj Matesan , Croatia
Jose Matos, Portugal
Vasant Matsagar , India
Claudio Mazzotti , Italy
Ahmed Mebarki , France
Gang Mei , China
Kasim Mermerdas, Turkey
Giovanni Minafò , Italy
Masoomah Mirrashid , Iran
Abbas Mohajerani , Australia
Fadzli Mohamed Nazri , Malaysia
Fabrizio Mollaioli , Italy
Rosario Montuori , Italy
H. Naderpour , Iran
Hassan Nasir , Pakistan
Hossein Nassiraei , Iran
Satheeskumar Navaratnam , Australia
Ignacio J. Navarro , Spain
Ashish Kumar Nayak , India
Behzad Nematollahi , Australia

Chayut Ngamkhanong , Thailand
Trung Ngo, Australia
Tengfei Nian, China
Mehdi Nikoo , Canada
Youjun Ning , China
Olugbenga Timo Oladinrin , United Kingdom
Oladimeji Benedict Olalusi, South Africa
Timothy O. Olawumi , Hong Kong
Alejandro Orfila , Spain
Maurizio Orlando , Italy
Siti Aminah Osman, Malaysia
Walid Oueslati , Tunisia
SUVASH PAUL , Bangladesh
John-Paris Pantouvakis , Greece
Fabrizio Paolacci , Italy
Giuseppina Pappalardo , Italy
Fulvio Parisi , Italy
Dimitrios G. Pavlou , Norway
Daniele Pellegrini , Italy
Gatheeshgar Perampalam , United Kingdom
Daniele Perrone , Italy
Giuseppe Piccardo , Italy
Vagelis Plevris , Qatar
Andrea Pranno , Italy
Adolfo Preciado , Mexico
Chongchong Qi , China
Yu Qian, USA
Ying Qin , China
Giuseppe Quaranta , Italy
Krishanu ROY , New Zealand
Vlastimir Radonjanin, Serbia
Carlo Rainieri , Italy
Rahul V. Ralegaonkar, India
Raizal Saifulnaz Muhammad Rashid, Malaysia
Alessandro Rasulo , Italy
Chonghong Ren , China
Qing-Xin Ren, China
Dimitris Rizos , USA
Geoffrey W. Rodgers , New Zealand
Pier Paolo Rossi, Italy
Nicola Ruggieri , Italy
JUNLONG SHANG, Singapore



Nikhil Saboo, India
Anna Saetta, Italy
Juan Sagaseta , United Kingdom
Timo Saksala, Finland
Mostafa Salari, Canada
Ginevra Salerno , Italy
Evangelos J. Sapountzakis , Greece
Vassilis Sarhosis , United Kingdom
Navaratnarajah Sathiparan , Sri Lanka
Fabrizio Scozzese , Italy
Halil Sezen , USA
Payam Shafigh , Malaysia
M. Shahria Alam, Canada
Yi Shan, China
Hussein Sharaf, Iraq
Mostafa Sharifzadeh, Australia
Sanjay Kumar Shukla, Australia
Amir Si Larbi , France
Okan Sirin , Qatar
Piotr Smarzewski , Poland
Francesca Sollecito , Italy
Rui Song , China
Tian-Yi Song, Australia
Flavio Stochino , Italy
Mayank Sukhija , USA
Piti Sukontasukkul , Thailand
Jianping Sun, Singapore
Xiao Sun , China
T. Tafsirojjaman , Australia
Fujiao Tang , China
Patrick W.C. Tang , Australia
Zhi Cheng Tang , China
Weerachart Tangchirapat , Thailand
Xiixin Tao, China
Piergiorgio Tataranni , Italy
Elisabete Teixeira , Portugal
Jorge Iván Tobón , Colombia
Jing-Zhong Tong, China
Francesco Trentadue , Italy
Antonello Troncone, Italy
Majbah Uddin , USA
Tariq Umar , United Kingdom
Muahmmad Usman, United Kingdom
Muhammad Usman , Pakistan
Mucteba Uysal , Turkey

Ilaria Venanzi , Italy
Castorina S. Vieira , Portugal
Valeria Vignali , Italy
Claudia Vitone , Italy
Liwei WEN , China
Chunfeng Wan , China
Hua-Ping Wan, China
Roman Wan-Wendner , Austria
Chaohui Wang , China
Hao Wang , USA
Shiming Wang , China
Wayne Yu Wang , United Kingdom
Wen-Da Wang, China
Xing Wang , China
Xiuling Wang , China
Zhenjun Wang , China
Xin-Jiang Wei , China
Tao Wen , China
Weiping Wen , China
Lei Weng , China
Chao Wu , United Kingdom
Jiangyu Wu, China
Wangjie Wu , China
Wenbing Wu , China
Zhixing Xiao, China
Gang Xu, China
Jian Xu , China
Panpan , China
Rongchao Xu , China
HE YONGLIANG, China
Michael Yam, Hong Kong
Hailu Yang , China
Xu-Xu Yang , China
Hui Yao , China
Xinyu Ye , China
Zhoujing Ye, China
Gürol Yildirim , Turkey
Dawei Yin , China
Doo-Yeol Yoo , Republic of Korea
Zhanping You , USA
Afshar A. Yousefi , Iran
Xinbao Yu , USA
Dongdong Yuan , China
Geun Y. Yun , Republic of Korea


Hyun-Do Yun , Republic of Korea
Cemal YİĞİT , Turkey
Paolo Zampieri, Italy
Giulio Zani , Italy
Mariano Angelo Zanini , Italy
Zhixiong Zeng , Hong Kong
Mustafa Zeybek, Turkey
Henglong Zhang , China
Jiupeng Zhang, China
Tingting Zhang , China
Zengping Zhang, China
Zetian Zhang , China
Zhigang Zhang , China
Zhipeng Zhao , Japan
Jun Zhao , China
Annan Zhou , Australia
Jia-wen Zhou , China
Hai-Tao Zhu , China
Peng Zhu , China
QuanJie Zhu , China
Wenjun Zhu , China
Marco Zucca, Italy
Haoran Zuo, Australia
Junqing Zuo , China
Robert Černý , Czech Republic
Süleyman İpek , Turkey

Contents


Experimental Study of Size Effects on the Deformation Strength and Failure Characteristics of Hard Rocks under True Triaxial Compression

Qiang Han , Yaohui Gao , and Yan Zhang
Research Article (15 pages), Article ID 6832775, Volume 2021 (2021)



Study on the Effect of Polysulfide Content on the Micromorphology and Spontaneous Combustion Characteristics of Coal

Hai-Fei Yao 
Research Article (10 pages), Article ID 7399808, Volume 2021 (2021)






Elimination of Coal and Gas Outburst Dynamic Disasters in Dengfeng Coalfield through Gas Extraction Based on Extremely Thin Protective Coal Seam Mining

Haibo Liu , Xucheng Xiao, and Zhihang Shu
Research Article (13 pages), Article ID 8675060, Volume 2021 (2021)


Deflection Laws of Gas Drainage Boreholes in Interbedded Soft and Hard Seams: A Case Study at Xinzheng Coal Mine, China

Xiaoyan Sun, Zhiheng Cheng , Liang Chen, Zhenhua Li , Hongbing Wang, and Shuaifeng Yin
Research Article (11 pages), Article ID 5533879, Volume 2021 (2021)


Similarity Model Test on the Spatiotemporal Evolution Law of Deformation and Failure of Surrounding Rock-Induced Caving in Multi-Mined-Out Areas

Fengyu Ren , Yanjun Zhou , Rongxing He , Jianli Cao , and Kaihua Zou 
Research Article (15 pages), Article ID 1224658, Volume 2021 (2021)

Study on the Key Technology of Controlling the Instability of Deep High-Stress Coal and Rock Mass and Relieving the Danger

Zhijing Zhang, Jianghong Zuo, and Dongji Lei 
Research Article (13 pages), Article ID 1290260, Volume 2021 (2021)

Analysis and Monitoring Technology of Upper Seam Mining in Multiunderlayer Goaf

Han Liang , Pengfei Li, and Chen Cao
Research Article (10 pages), Article ID 8485059, Volume 2021 (2021)

A Case Study of Optimization and Application of Soft-Rock Roadway Support in Xiaokang Coal Mine, China

Shuai Guo , Xun-Guo Zhu , Xun Liu , and Hong-Fei Duan 
Research Article (14 pages), Article ID 3731124, Volume 2021 (2021)

Width Design of Small Coal Pillar of Gob-Side Entry Driving in Soft Rock Working Face and Its Application of Zaoquan Coal Mine

Ai Chen 
Research Article (10 pages), Article ID 9999957, Volume 2021 (2021)

Characteristics of Pressure Relief Gas Extraction in the Protected Layer by Surface Drilling in Huainan

Xiaozhang Tong , Hu Wen , Xiaojiao Cheng , Shixing Fan , Chunhui Ye, Mingyang Liu, and Hu Wang 




Research Article (11 pages), Article ID 9966843, Volume 2021 (2021)

Distribution Characteristics and Formation Mechanism of Surface Crack Induced by Extrathick Near Horizontal Seam Mining: An Example from the Datong Coal Field, China

Yueguan Yan , Weitao Yan , Huayang Dai, and Junting Guo

Research Article (10 pages), Article ID 5545128, Volume 2021 (2021)

Experimental Study on Impermeability Law of Aquiclude Reconstructed by Mudstone of External Dump in Arid Zone

Li Ma , Chendong Liu , Yinli Bi, Suping Peng, Kaisheng Jiang, Hui Zhang, Qiang Luo , Fei Xue, Tianxin Xu, Tianxiang Li, Jing Wu, Jiahao Tian, and Dongxu Zhang



Research Article (14 pages), Article ID 5561794, Volume 2021 (2021)

Simulation Analysis and Experimental Study on the Working State of Sinking Headframe in the Large Underground Shaft

Yin Qixiang , Zhao Weiping , Xin Wen, Yang Hailin, and Zhang Linglei

Research Article (11 pages), Article ID 5513954, Volume 2021 (2021)

Mechanism and Classification of Coal and Gas Outbursts in China

Qi Zhang , Chun-li Yang, Xiang-chun Li , Zhong-bei Li, and Yi Li


Review Article (12 pages), Article ID 5519853, Volume 2021 (2021)

Study on Rock Burst Early Warning in the Working Face of Deep Coal Mines Based on the Law of Gas Emission

Qinghua Zhang  and Shudong He

Research Article (10 pages), Article ID 9940505, Volume 2021 (2021)

Presplit Blasting Technique in Treating Hard Overlying Strata: From Numerical Simulation to Field Practice

Baisheng Zhang , Zhiping Yang, Xuming Yang, and Shuai Zhang


Research Article (20 pages), Article ID 5558538, Volume 2021 (2021)

Distribution and Variation of Mining-Induced Stress in the Reverse Fault-Affected Coal Body

Rui Zhou, Yujin Qin , and Zhizhen Zhang 

Research Article (23 pages), Article ID 5527092, Volume 2021 (2021)







Effects of Cyclic Loading on the Pore Structure of Anthracite Coal

Dong Wang, Tie Li, Zhiheng Cheng , and Weihua Wang

Research Article (12 pages), Article ID 5549147, Volume 2021 (2021)

Contents

Experimental Study on Local Scour and Related Mechanical Effects at River-Crossing Underwater Oil and Gas Pipelines

Fan Cui , Yunfei Du , Xianjie Hao , Suping Peng , Zhuangzhuang Bao , and Shiqi Peng 
Research Article (15 pages), Article ID 6689212, Volume 2021 (2021)




Study on Change Rules of Factors Affecting Gas Loss during Coalbed Air Reverse Circulation Sampling

Demin Chen , Wei Long , Yanyan Li , and Rui Zhang 
Research Article (15 pages), Article ID 5550726, Volume 2021 (2021)

A Study on the Mechanical Properties and Bursting Liability of Coal-Rock Composites with Seam Partings

Dong Xu , Mingshi Gao , Yongliang He , and Xin Yu 
Research Article (13 pages), Article ID 9953241, Volume 2021 (2021)


The Influence of Confining Stresses on Rock Fragmentation, Thrust Force, and Penetration Energy in Sandstone Indentation Tests Using Disc Cutters

Gaofeng Wang , Ting Ren , and Gaolei Zhu 
Research Article (13 pages), Article ID 5541538, Volume 2021 (2021)

Theoretical Analysis of Mining Induced Overburden Subsidence Boundary with the Horizontal Coal Seam Mining

Weitao Yan , Junjie Chen , Yi Tan , Wenzhi Zhang, and Lailiang Cai
Research Article (7 pages), Article ID 6657738, Volume 2021 (2021)





Influencing Factors for the Instability and Collapse Mode of the Goaf Structure in a Gypsum Mine

Zhaowen Du , Zhihe Liu , Rui Liu, Sheng Wang, and Faxin Li
Research Article (12 pages), Article ID 5577287, Volume 2021 (2021)






Coupling Technology of Deep-Hole Presplitting Blasting and Hydraulic Fracturing Enhance Permeability Technology in Low-Permeability and Gas Outburst Coal Seam: A Case Study in the No. 8 Mine of Pingdingshan, China

Wei Wang, Yanzhao Wei, Minggong Guo , and Yanzhi Li
Research Article (12 pages), Article ID 5569678, Volume 2021 (2021)

Influence of Deformation and Instability of Borehole on Gas Extraction in Deep Mining Soft Coal Seam

Xue-Bo Zhang , Shuai-Shuai Shen, Xiao-Jun Feng , Yang Ming , and Jia-jia Liu 
Research Article (11 pages), Article ID 6689277, Volume 2021 (2021)

Three-Dimensional, Real-Time, and Intelligent Data Acquisition of Large Deformation in Deep Tunnels

Yue-Mao Zhao , Yong Han , Yong-Yuan Kou , Lin Li , and Jiu-Hua Du 
Research Article (11 pages), Article ID 6671118, Volume 2021 (2021)

Research Article

Experimental Study of Size Effects on the Deformation Strength and Failure Characteristics of Hard Rocks under True Triaxial Compression

Qiang Han , Yaohui Gao , and Yan Zhang

Key Laboratory of Ministry of Education on Safe Mining of Deep Metal Mines, Northeastern University, Shenyang, Liaoning 110819, China

Correspondence should be addressed to Qiang Han; hanqnu@163.com

Received 25 June 2021; Revised 4 September 2021; Accepted 17 September 2021; Published 4 October 2021

Academic Editor: Jia Lin

Copyright © 2021 Qiang Han et al. This is an open access article distributed under the Creative Commons Attribution License, which permits unrestricted use, distribution, and reproduction in any medium, provided the original work is properly cited.

Size effect has always been the focus of rock mechanics as a bridge between laboratory test and engineering site. Previously, the research conditions and objects of the rock size effect have mostly focused on cylindrical rock samples with different height-to-diameter ratios (H/D_s) under uniaxial or conventional triaxial compression, while there has been little research on the rock size effect under true triaxial compression (TTC), especially rectangular rock samples with different sizes and the same length-to-width-to-height ratio. Based on this, the deformation, strength, and failure characteristics of Beishan (BS) granite and Baihetan (BHT) basalt with different sample sizes under TTC were studied by a comparative analysis method. The size effect of deformation and failure characteristics under TTC are not obvious, including stress-strain curves, Young's modulus, peak strains, failure angles, and macrofailure mode. However, the damage stress (σ_{cd}) and peak strength (σ_p) have obvious size effect; that is, the smaller the sample size is, the higher the strength is. Additionally, the relationship among the peak strength, sample size, and intermediate principal stress (σ_2) is power function. In addition, by comparing the peak strength increment caused by the sample size of the two types of rocks, the σ_p of the fine-grained BHT basalt is more sensitive to sample size than that of the coarse-grained BS granite. Finally, by analyzing the relationship between the size of the mineral grains or clusters in the two types of hard rocks and the complexity of crack propagation in the fracture surface under TTC, it is suggested that the minimum side length of rock samples should not be less than 10 times the maximum mineral clusters (such as feldspar phenocrysts in BHT basalt). In addition, the method of estimating elastic strain is established by analyzing the relationship between the size of the rock sample σ_2 and the elastic strain under TTC.

1. Introduction

For a long time, how to combine the laboratory test results with the monitoring results of the project has been a major problem faced by rock mechanics. The size difference between indoor rock samples and engineering rock mass is the most direct obstacle to this problem, and research on the size effect is considered to be an important part of solving this problem. To date, three main theories on the size effect have been proposed: (a) the Weibull statistical theory of the size effect represented by [1], (b) the energy release-based theory of the size effect represented by [2], and (c) the fractal approach of the size effect represented in [3]. Previous

studies [4–8] have focused more on the size effect of cylindrical rock samples with different aspect ratios under uniaxial compression. Meanwhile, the reason why there were few studies on the size effect of rocks under conventional triaxial conditions was that most rocks have showed brittle ductile transition characteristics with the increase of confining pressure [9].

It is well known that the in situ stress in field engineering typically satisfies $\sigma_1 > \sigma_2 > \sigma_3$ (σ_1 : the maximum principal stress, σ_2 : the intermediate principal stress, and σ_3 : the minimum principal stress). After [10, 11] designed the first true triaxial testing machine for rock mechanics, the research on and application of TTC testing machines have

become popular in the field of rock mechanics because this type of machine can reflect σ_2 . However, due to different research needs and the differences in research technologies, the sample sizes are largely different. In the studies of [10, 11], the sample size was $15 \times 15 \times 30 \text{ mm}^3$; in [12], the sample size was $19 \times 19 \times 38 \text{ mm}^3$; in [13], the sample sizes were $57 \times 57 \times 25 \text{ mm}^3$ and $76 \times 76 \times 178 \text{ mm}^3$; in [14–18], the sample size was $50 \times 50 \times 100 \text{ mm}^3$; in [19], the sample size was $150 \times 60 \times 30 \text{ mm}^3$; and in [20], the sample size was $100 \times 100 \times 100 \text{ mm}^3$. The sample sizes used in the previously mentioned studies were quite different, and most studies only tested samples of one size. However, there have been few studies on rock samples with different sizes under TTC, and only the studies [21–23] have investigated the mechanical and failure characteristics of the same rock with different aspect ratios under true triaxial unloading conditions. Moreover, these studies did not provide the strength, deformation, and failure characteristics of rock samples with a fixed aspect ratio but different sizes under TTC. Meanwhile, the existing strength criterion does not consider the size effect of rock, and there have been few studies on certain important issues, for example, which sample size is more suitable for the study of crack propagation on fracture surfaces.

In this study, the deformation, strength, and failure of BS granite and BHT basalt with different sample sizes under TTC were analyzed. Moreover, by analyzing the relationship between the complexity of crack propagation and mineral particle size in the fracture surface with different sample sizes, the recommended sample sizes for analyzing crack propagation in the fracture surface are determined. The results of this study can help to understand the size effect under TTC.

2. Test Scheme and Process

2.1. Specimen Preparation. BS granite and BHT basalt are selected as the research objects. To prevent the dispersion of test results caused by the different rock samples, the samples of the same rock with different sizes are selected from the same parent rock, and the samples with large differences are eliminated, the rock samples with the same or similar P -wave velocity are selected for the test. The specimens were used the same processing technologies, and the length:width:height ratio of the specimens was strictly controlled to 1:1:2. The sizes of the samples were $25 \times 25 \times 50 \text{ mm}^3$ (SS), $35 \times 35 \times 70 \text{ mm}^3$ (SM), and $50 \times 50 \times 100 \text{ mm}^3$ (SL), and dimensional tolerance and perpendicularity tolerance were given as ± 0.01 and 0.02 mm for each side, respectively. The basic physical and mechanical parameters of these two types of rocks are shown in Table 1.

Figure 1 shows the size and photos of rock selected in this study. Figure 1(a) is the grayish-green BHT basalt with scattered white plagioclase on the surface, and Figure 1(b) is the BS granite. X-ray diffraction (XRD) analysis showed that the mineral composition of the BHT basalt was feldspar 41.96%, pyroxene 45.57%, clinoclone 6.25%, mica 4%, and quartz 2.22%, while the mineral composition of the BS granite was feldspar 51%, quartz 35%, biotite 8%, pyroxene

3%, and calcite 3%. Figure 2 shows the microstructures under cross-polarized illumination of the two types of rocks. Figure 2(a) is the microstructure of the BHT basalt; feldspar minerals with idiomorphic structures are filled by pyroxene minerals with allotriomorphic structures, with no clear boundaries between the two. According to the image scale, the grain size was $50\sim 150 \mu\text{m}$. Figure 2(b) is the microstructure of the BS granite. There is an alternating arrangement of feldspar minerals with idiomorphic or hypidiomorphic structures and irregular quartz. The grain size was $500\sim 1500 \mu\text{m}$.

2.2. Scheme and Process. True triaxial tests at the same stress level were carried out on each type of rock sample according to the sample size, in which σ_3 was constant ($\sigma_3 = 5 \text{ MPa}$) and the ratios of $\sigma_3:\sigma_2$ were 1:1, 1:6, 1:12 and 1:18. The specific stress levels are shown in Table 2. The experiment was completed on the high-pressure hard rock true triaxial test system [17] developed by Northeastern University.

The test process was carried out according to the stress path shown in Figure 3(a), and the stress path was divided into the following three stages: (a) under hydrostatic pressure, $\sigma_1 = \sigma_2 = \sigma_3$ was loaded simultaneously at a rate of 0.5 MPa/s until σ_3 reached the predetermined value; (b) σ_3 was kept constant, and σ_1 and σ_2 were loaded synchronously at a loading rate of 0.5 MPa/s until σ_2 reached the target value; (c) σ_2 and σ_3 were kept constant, the stress-controlled loading method was used to increase σ_1 to approximately 60~70% of the peak strength, and then the strain-controlled loading method was used until the rock sample was completely damaged. Figure 3(b) shows the strain measurement method, and Figure 3(c) shows the measurement method of failure angle of the rock sample.

Note that the focus of this study was size effect, so when the stress-controlled loading method is changed to the strain-controlled loading method, the strain rate should be the same ($2.67 \times 10^{-6} \text{ /s}$) for all the rock samples. According to the sample width (from largest to smallest), the controlled deformation rates were as follows: 0.008 mm/min , 0.0056 mm/min , and 0.004 mm/min . The detailed control variables of each stage of the stress path are shown in Table 3.

3. Test Results

3.1. Influence of Specimen Size on Deformation Behavior. Figure 4 shows the stress-strain curves of the BS granite (Figure 4(a)) and BHT basalt (Figure 4(b)) with different sample sizes under $\sigma_3 = 5 \text{ MPa}$ and $\sigma_2 = 30 \text{ MPa}$. The stress-strain curves of the BS granite show the elastic-plastic-brittle deformation and failure process, while that of the BHT basalt shows the elastic-brittle deformation and failure process. Meanwhile, changing the size of rocks did not significantly affect the overall deformation and failure processes (the stress-strain type) because the microfractures were dominant in rocks before their peak strength was reached. However, due to the heterogeneity and the randomness of the location of macro cracks in the sample, the postpeak stress-strain curve will show some differences, especially the BHT basalt with high brittleness [24], as shown in Figure 4(b).

TABLE 1: Basic physical and mechanical parameters of the BHT basalt and BS granite samples.

Rock type	Density (g/cm ³)	P-wave velocity (m/s)	Young's modulus (GPa)	Poisson's ratio (μ)	Tensile strength (MPa)	Grain size (μm)
BHT basalt	2.95	5650 \pm 150	55~60	0.22	18.4	50~150
BS granite	2.69	5100 \pm 120	50~54	0.27	5.06	500~1500

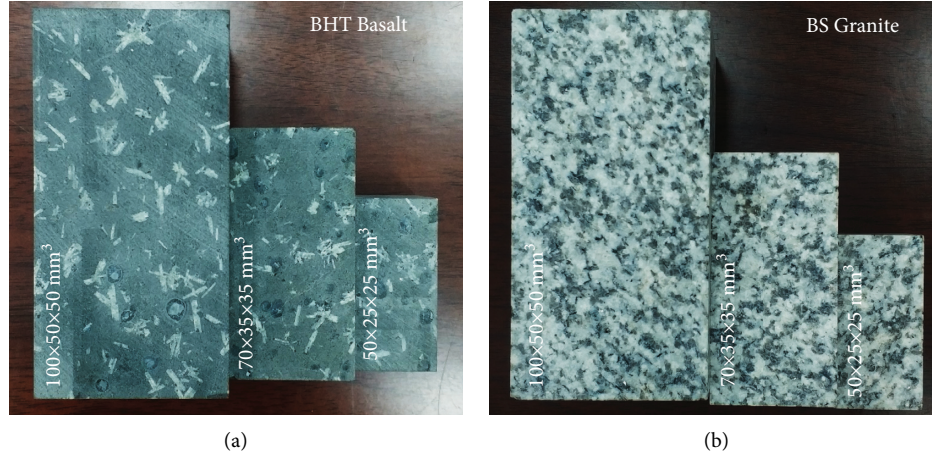


FIGURE 1: Photos of different sizes of two kinds of rocks. (a) BHT basalt and (b) BS granite.

Figure 5 shows Young's modulus under the influence of rock size under TTC for the two types of rocks (the calculation method of Young's modulus is based on [25]). When the rock size was constant, Young's modulus increased with increasing σ_2 , but there is not a strict positive correlation between Young's modulus and rock size. Under the same stress condition, when the sample size changed, the variation in Young's modulus of BS granite was within 5 GPa, while that of BHT basalt were basically within 3 GPa. When the sample size changed, Young's modulus always changed small within the rock size range of this study, as shown in the light blue area in Figures 5(a) and 5(b), indicating that Young's modulus of the two types of rocks was less affected by the sample size and the regularity was not obvious.

Figure 6 shows the influence of sample size on the peak strain (ϵ_{3p} and ϵ_{2p}) in the direction of σ_3 and σ_2 under TTC (for example, peak strain ϵ_{3p} refers to the strain when the stress in the direction of σ_3 reaches peak strength). For the BS granite and BHT basalt, when the rock size was constant, ϵ_{3p} decreased with increasing σ_2 , which showed the rock was always under tensile deformation in the direction of σ_3 during the loading process, while ϵ_{2p} increased under the same stress condition, which showed the deformation in the direction of σ_2 changed from tensile to compression. Figure 6(a) shows the peak strain of the BS granite of different sizes in the direction of σ_3 and σ_2 under TTC. It can be seen that, under the same stress condition, the peak strain ϵ_{2p} in the direction of σ_2 is very close and independent of the sample size. The relationship between ϵ_{2p} and sample size of BHT basalt under TTC was the same as that of the BS granite, as shown in Figure 6(b). Therefore, the rock size had no significant effect on ϵ_{2p} within the scope of this study. However, when $\sigma_2 = 30$ MPa, the ϵ_{3p} of BS granite under

different sizes was significantly different. The difference between the ϵ_{3p} for the size of SL and SS was 0.206% and was significantly higher than the changes in the peak strain under other stress states ($\sigma_2 = 5$ MPa, 60 MPa, and 90 MPa), as shown in Figure 6(a), while the ϵ_{3p} of the BHT basalt was hardly affected by the sample size, and the changes in ϵ_{3p} were always between 0.03% and 0.07%.

Under the stress condition in this paper, the peak strain ranges of the BS granite were $-0.46 < \epsilon_{2p} < 0.11$ and $-0.72 < \epsilon_{3p} < -0.42$, and those of the BHT basalt were $-0.17 < \epsilon_{2p} < 0.03$ and $-0.31 < \epsilon_{3p} < -0.11$. The analysis showed that the peak strain range of the BHT basalt was significantly smaller than that of the BS granite, which indicates that the BS granite is prone to a large yield deformation under the same stress. To sum up, the stress-strain curves, Young's modulus, and peak strains for the BS granite and BHT basalt were related to the stress state and rock properties, but these were not significantly affected by the rock size.

3.2. Influence of Rock Size on Characteristic Stress.

Figure 7 shows the characteristics of damage stress (σ_{cd}) under the influence of rock size. σ_{cd} is the stress point corresponding to the turning point of the volume strain curve, which is the maximum point of the volume strain curve before the peak and the calculation method refers to [25, 26]. Figure 7 shows that the σ_{cd} of the two types of rocks showed an increasing with decreasing sample size under the same stress level. However, for the BS granite, as shown in Figure 7(a), when $\sigma_2 = 90$ MPa, the σ_{cd} of SM was slightly lower than that $\sigma_2 = 60$ MPa, which may be caused by two reasons. On the one hand, when $\sigma_3 = 5$ MPa, $\sigma_2 = 90$ MPa

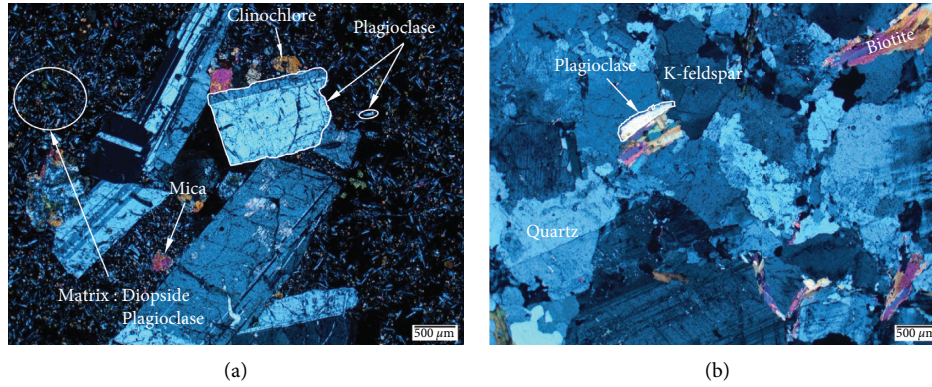


FIGURE 2: Microstructures under cross-polarized illumination of the two types of rocks. (a) BHT basalt and (b) BS granite.

TABLE 2: Test scheme and results of the size effect for two rocks under TTC.

Rock type	Size (mm ³)	σ_3 (MPa)	σ_2 (MPa)	σ_{cd} (MPa)	σ_p (MPa)	σ_{cd}/σ_p	ε_{3p} (%)	ε_{2p} (%)	θ (°)	A	Failure mode
BS granite	SL	5	5	144	202	0.71	-0.452	-0.452	74	201.82	Shear
			30	186	268	0.69	-0.512	-0.080	79	270.33	Shear
			60	193	295	0.65	-0.493	-0.006	80	294.79	Tension-shear
			90	197	308	0.64	-0.577	0.061	80	305.97	Tension-shear
	SM	5	5	150	203	0.74	-0.438	-0.438	73	201.82	Shear
			30	190	285	0.67	-0.602	-0.143	77	270.33	Shear
			60	205	300	0.68	-0.501	-0.006	81	294.79	Tension-shear
			90	204	313	0.65	-0.589	0.106	81	305.97	Tension-shear
	SS	5	5	151	205	0.74	-0.453	-0.453	72	201.82	Shear
			30	200	292	0.69	-0.718	-0.163	78	270.33	Shear
			60	212	311	0.68	-0.612	0.021	82	294.79	Tension-shear
			90	211	325	0.65	-0.608	0.052	81	305.97	Tension-shear
BHT basalt	SL	5	5	250	250	1.00	-0.168	-0.168	74	247.94	Tension-shear
			30	278	282	0.99	-0.185	-0.023	78	277.89	Tension-shear
			60	324	324	1.00	-0.186	0.010	78	318.65	Tension-shear
			90	341	350	0.97	-0.270	0.030	80	346.57	Tension-shear
	SM	5	5	261	261	1.00	-0.119	-0.119	75	265.25	Tension-shear
			30	286	296	0.97	-0.202	-0.100	79	277.89	Tension-shear
			60	339	339	1.00	-0.224	-0.019	79	318.65	Tension-shear
			90	353	358	0.99	-0.230	0.028	80	346.57	Tension-shear
	SS	5	5	274	284	0.96	-0.165	-0.165	75	265.25	Tension-shear
			30	329	334	0.99	-0.218	-0.073	78	277.89	Tension-shear
			60	362	366	0.99	-0.233	-0.032	80	318.65	Tension-shear
			90	367	386	0.95	-0.302	-0.029	88	346.57	Tension-shear

was just near the turning point where σ_p first increased and then decreased [27]. On the other hand, reference [26] pointed out that the σ_{cd} range of the BS granite is (0.64~0.74) σ_p under TTC, which is within a reasonable range. In comparison, the σ_{cd}/σ_p of the BHT basalt under TTC was relatively large, approximately 0.95~1.0 (Table 2), and the turning point for it, where σ_p first increases and then decreases, is higher than BS granite. Therefore, this result is rarely found in BHT basalt: σ_{cd} at $\sigma_2 = 90$ MPa is slightly lower than that of $\sigma_2 = 60$ MPa (Figure 7(b)).

References [28–30] showed that when σ_3 is constant, the σ_p increases first and then decreases with increasing σ_2 under TTC. Figure 8 shows the σ_p under the influence of sample size for the BS granite and BHT basalt. As seen from Figure 8, when $\sigma_3 = 5$ MPa, the σ_p of the two types of rocks with different sizes increased with increasing σ_2 (since the

preset σ_2 did not reach the decreasing stage of σ_p in the two types of rocks under this condition, σ_p did not decrease). Moreover, the smaller the sample size was, the higher the σ_p of the two types of rocks under the same stress, such as when $\sigma_2 = 30$ MPa.

Figure 8(a) shows the σ_p of the BS granite with different sizes under TTC. When $\sigma_2 = \sigma_3 = 5$ MPa, as the sample size decreased from SL to SM and SS, the σ_p increment was very small, approximately 1 MPa or 2 MPa, which indicated that the σ_p of the BS granite was almost unaffected by sample size. In contrast, when the conventional triaxial stress condition ($\sigma_2 = \sigma_3$) changed to the true triaxial stress condition ($\sigma_2 \neq \sigma_3$), the size effect on the σ_p of the BS granite was significant.

Compared with that of BHT basalt, changing the sample size (SL \rightarrow SM \rightarrow SS) of the BS granite will lead to the

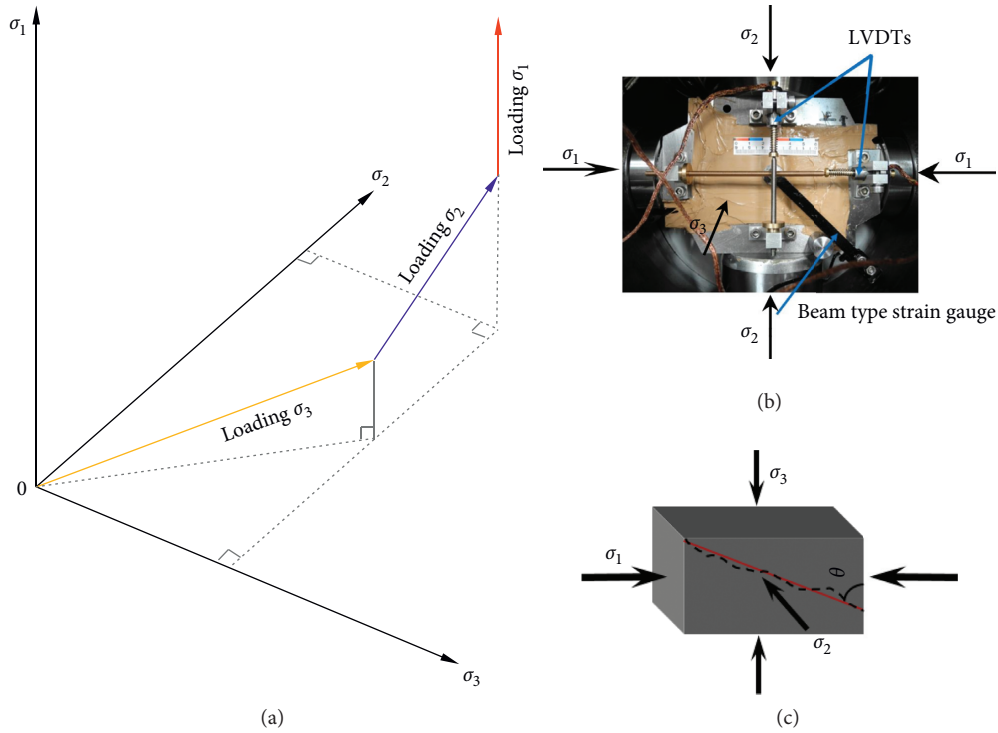


FIGURE 3: Stress path and strain measurement of rock under TTC. (a) Stress path, (b) strain measurement method [17], and (c) measurement method of failure angle.

TABLE 3: Controlling rates of each loading stage during the TTC test.

Rock size (mm ³)	Loading rate of σ_3 (MPa/s)	Loading rate of σ_2 (kN/s)	Loading rate of σ_1 (kN/s)	Deformation rate (mm/min)
50 × 50 × 100 (SL)	0.5	2500	1250	0.008
35 × 35 × 70 (SM)	0.5	1225	612.5	0.0056
25 × 25 × 50 (SS)	0.5	625	312.5	0.004

unstable change of the peak strength increment ($(\sigma_{pSM} - \sigma_{pSL})/\sigma_{pSL}$ or $(\sigma_{pSS} - \sigma_{pSM})/\sigma_{pSM}$). For example, the σ_p increment was 6.34% when the sample size of the BS granite decreased from SL to SM under the stress condition that $\sigma_3 = 5$ MPa and $\sigma_2 = 30$ MPa, which was significantly higher than the average 2.52% under other stress states. In contrast, when the sample size of BHT basalt decreased from SL to SM and from SM to SS, the percentages of the σ_p increment were always maintained at approximately 4.1% and 9.3%, respectively, which was obtained by comparing the width of the blue or yellow areas enclosed by the changes in the peak strength caused by the sample size under each stress in Figures 8(a) and 8(b). However, Figure 8(b) showed that the size effect on σ_p of BHT basalt was obvious in both the conventional triaxial and TTC. When the sample size decreased from SL to SM, change of the width of the blue strip area was consistent with the change of the width of the yellow strip area when the sample size decreased from SM to SS, and there were no abrupt changes in the σ_p increment under a certain stress, which was different from the results for the BS granite.

The previously mentioned analysis showed that the sensitivity of σ_p for BS granite and BHT basalt to sample size was different. When the sample size decreased from SL to SS,

the σ_p increment of the BS granite was approximately less than 10%, while that of the BHT basalt was approximately 20%. For BHT basalt, the σ_p increment caused by the reduction of sample size from SM to SS was almost twice that caused by the reduction of sample size from SL to SM. Meanwhile, the σ_p increment of the BS granite also increased as the sample size changed, but the changes were very small. The smaller the sample size of the BHT basalt, the higher the sensitivity of the peak strength to the size effect, indicating that the sensitivity of the peak strength of BHT basalt to the size effect was higher than that of BS granite under the same stress.

To clarify the relationship between the peak strength, the sample size, and the stress state under TTC, the statistical analysis of the test results was carried out, as shown in Figure 9. The volume of the SL sample was V , and the volumes of the SM and SS samples were normalized according to V , such as $V_{SM}' = 0.343 V$ and $V_{SS}' = 0.125 V$. In Figure 9, the normalized results are plotted as the horizontal axis, and the peak strength is the vertical axis. Figure 9(a) is the results of BS granite, and Figure 9(b) shows those of BHT basalt.

As can be seen from Figure 9, the peak strengths of both types of rocks decreased with increasing sample size under

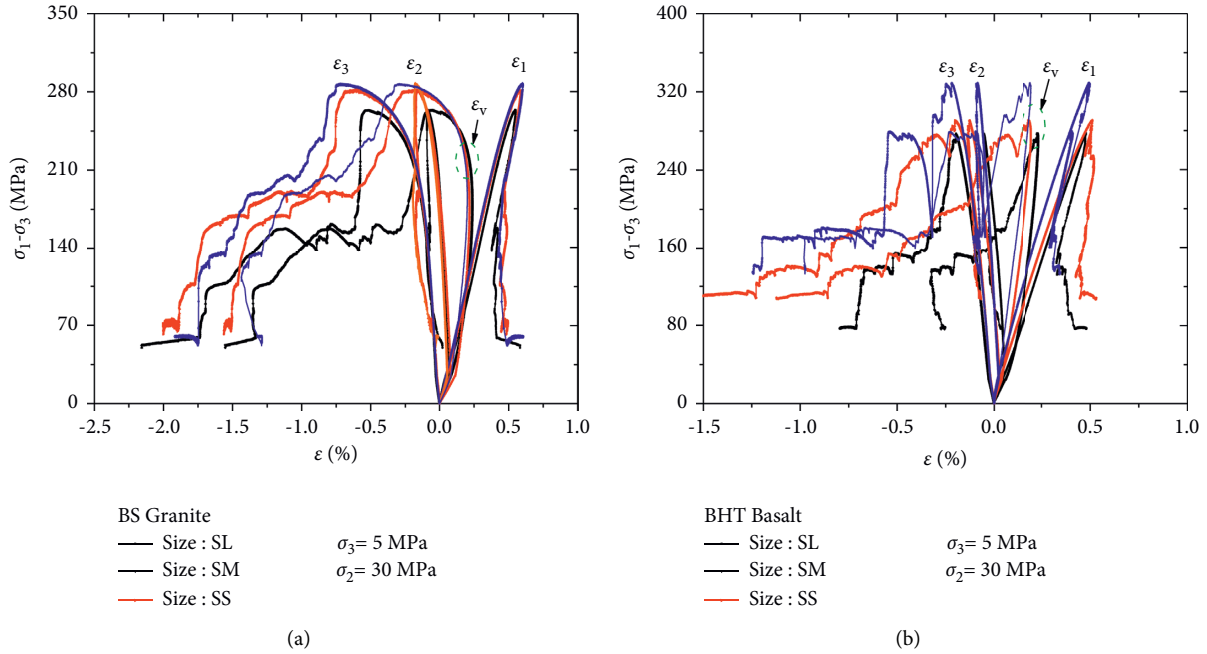


FIGURE 4: Full stress-strain curves of the BS granite and BHT basalt with different sample sizes under $\sigma_3 = 5 \text{ MPa}$ and $\sigma_2 = 30 \text{ MPa}$. (a) BS granite and (b) BHT basalt.

the same stress state. All test data were fitted by power function, and the fitting variance of data was greater than 0.9, indicating that the power function could well express the relationship between peak strength, sample size, and stress state. Note that multiple curves were used to fit the experimental data under TTC because of the variable of σ_2 , and the general equation of the fitting curve was determined to be

$$\sigma_p = A \times \left(\frac{V'}{V} \right)^B, \quad (1)$$

where B ($B < 0$) is a parameter related to the rock type and σ_2 and the units of V and V' are mm^3 . When $V' = V$,

$$\sigma_{pV} = A. \quad (2)$$

Substituting equation (2) into (1), we derive the following:

$$\sigma_p = \sigma_{pV} \times \left(\frac{V'}{V} \right)^B. \quad (3)$$

Because B is related to σ_2 , the fitting relationship between them is obtained (Figure 10), which shows that the fitting result is well ($R^2 = 1$). Thus, the relationship between B and σ_2 of the BS granite and BHT basalt can be expressed as follows:

$$B = a\sigma_2^2 + b\sigma_2 + c, \quad (4)$$

where a , b , and c are the fitting parameters related to lithology, as shown in Figure 10. The general expression of σ_p was obtained by substituting equation (4) into (3):

$$\sigma_p = \sigma_{pV} \times \left(\frac{V'}{V} \right)^{a\sigma_2^2 + b\sigma_2 + c}. \quad (5)$$

According to a , b , and c of the BS granite and BHT basalt obtained in Figure 10, the binomial expression of B and σ_2 can be expressed as follows:

$$B_{\text{Granite}} = -2.778 \times 10^{-6} \sigma_2^2 + 7.167 \times 10^{-4} \sigma_2 - 0.06, \quad (6)$$

$$R^2 = 1,$$

$$B_{\text{Basalt}} = -7.222 \times 10^{-6} \sigma_2^2 + 1.45 \times 10^{-3} \sigma_2 - 0.12, \quad (7)$$

$$R^2 = 1.$$

Equations (6) and (7) can be substituted into equation (5) to obtain an expression relating σ_p , V , and σ_2 for the BS granite and BHT basalt:

$$\sigma_{p\text{Granite}} = \sigma_{pV} \times \left(\frac{V'}{V} \right)^{-2.778 \times 10^{-6} \sigma_2^2 + 7.167 \times 10^{-4} \sigma_2 - 0.06}, \quad (8)$$

$$\sigma_{p\text{Basalt}} = \sigma_{pV} \times \left(\frac{V'}{V} \right)^{-7.222 \times 10^{-6} \sigma_2^2 + 1.45 \times 10^{-3} \sigma_2 - 0.12}.$$

The relationship of the peak strength and damage stress to the sample size of the BS granite and BHT basalt under TTC showed that the variation amplitude of the characteristic stress increment caused by the size effect in the fine-grained BHT basalt was obviously smaller than that of the medium- to coarse-grained BS granite, and the characteristic stress of the two types of rocks was

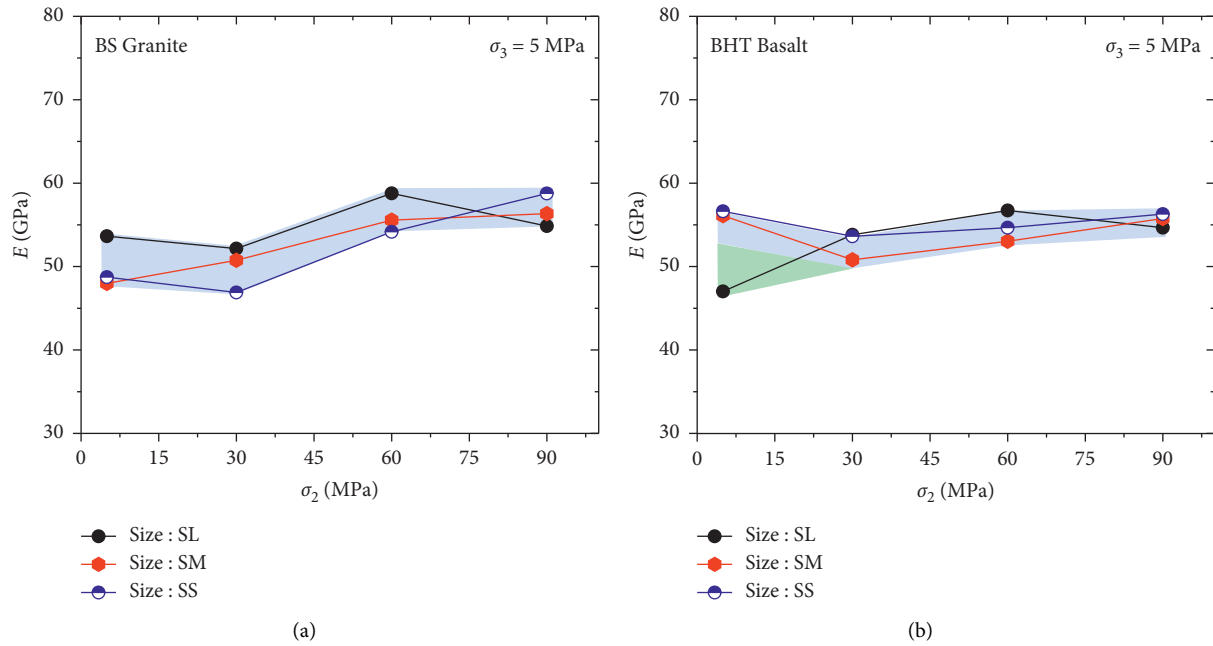


FIGURE 5: Young's modulus characteristics under the influence of rock sample size under TTC. (a) BS granite and (b) BHT basalt.

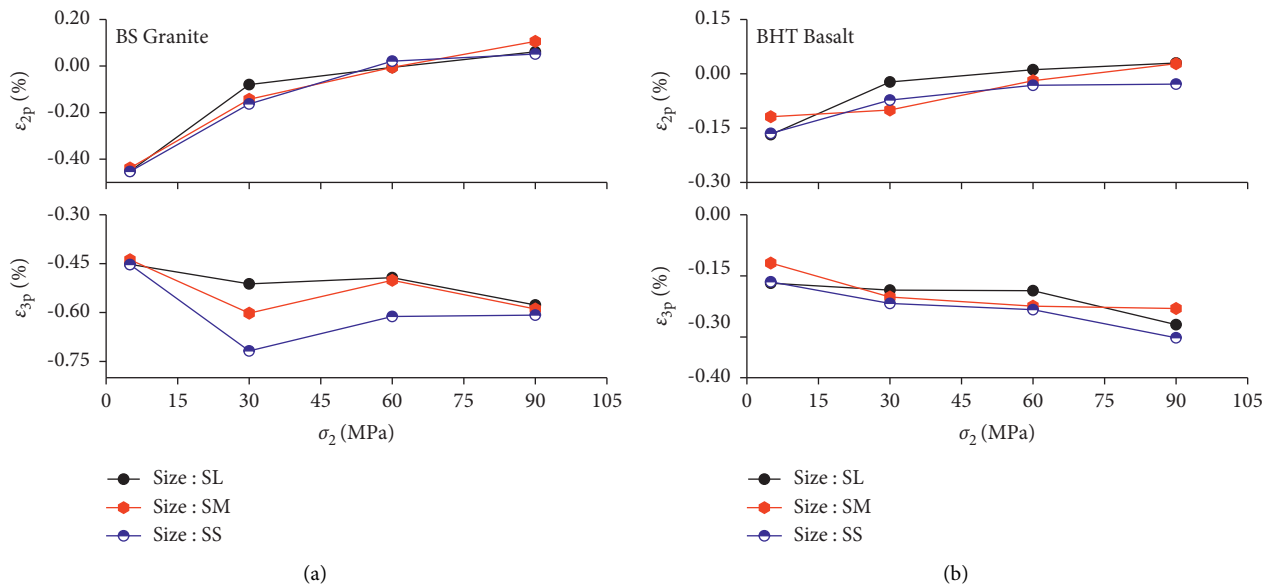


FIGURE 6: Influence of sample size on the peak strain in the direction of σ_3 and σ_2 under TTC. (a) BS granite and (b) BHT basalt.

obviously affected by the sample size. The relationships among the peak strength, rock sample size, and intermediate principal stress could be represented by a power function.

3.3. Influence of Sample Size on Failure Characteristics. To better compare the rock failure modes with different sizes, the failure pictures of the samples with different sizes were enlarged to the same size. Figure 11 shows the failure photos of BS granite and BHT basalt under different sizes at

$\sigma_2 = 30$ MPa and $\sigma_3 = 5$ MPa, and Table 2 shows the failure modes and fracture angles of the rocks under TTC. It can be seen from Figure 11 that both BS granite and BHT basalt show macroshear failure under the same stress condition $\sigma_3 = 5$ MPa and $\sigma_2 = 30$ MPa, which indicates that the sample size did not change the macroscopic failure mode for the two types of rocks under the same stress. However, reducing the sample size may lead to secondary cracks near the main crack near the center of the sample, which are nearly parallel to the direction of σ_1 , making the fracture surface more complex as shown in areas enclosed by red lines in

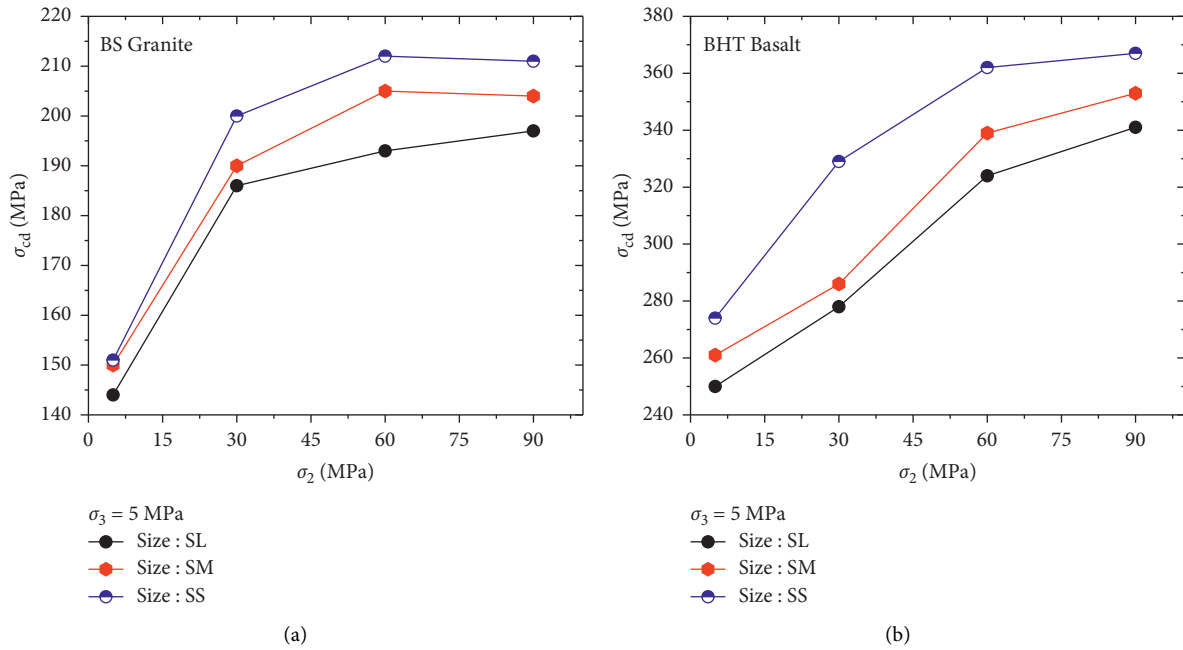


FIGURE 7: Damage stress characteristics under the influence of rock sample size. (a) BS granite and (b) BHT basalt.

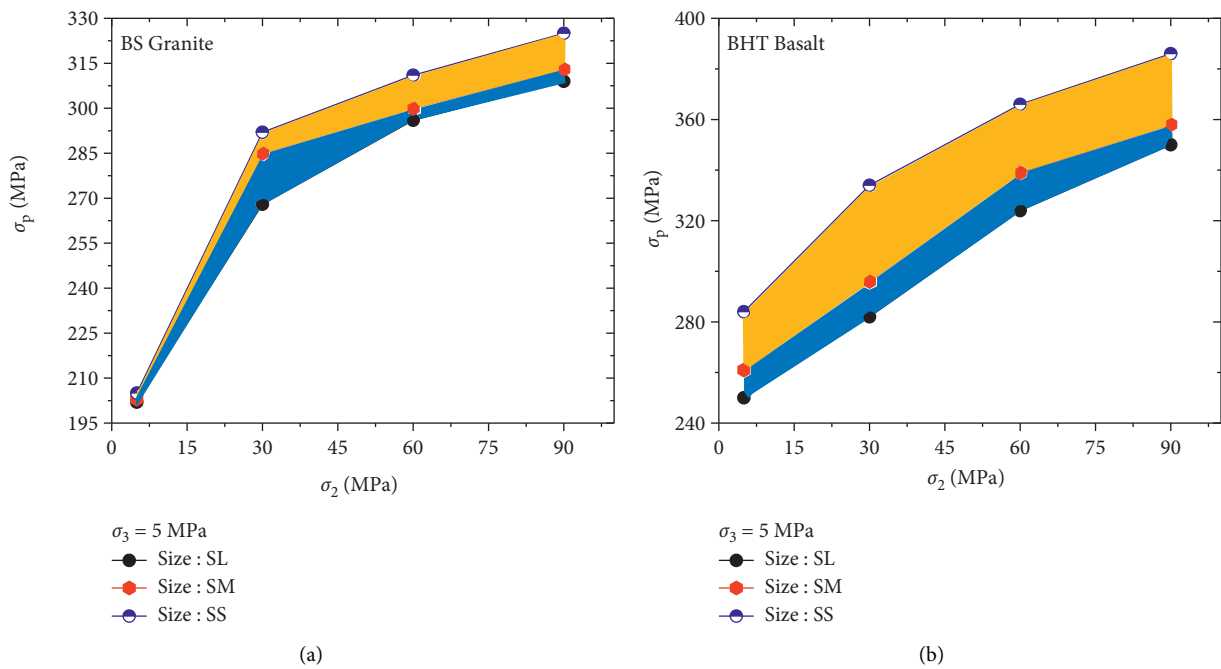


FIGURE 8: Peak strengths of the two types of rocks with different sizes under TTC. (a) BS granite and (b) BHT basalt.

Figures 11(c), 11(f), and 12(a). Additionally, for the BHT basalt with the size of SS, the cracks are easy to develop along the mineral cluster (feldspar phenocryst) during its propagation except for secondary cracks in the fracture surface, as shown in the areas enclosed by blue lines in Figures 11(e), 11(f), and 12(b), which is possibly because the size of the mineral clusters was of the same order of magnitude as the length of the shortest edge of rock samples. Therefore, the generation of secondary cracks and cracks along the mineral

clusters increased the complexity of the fracture surfaces of the small-sized rock samples.

Figure 13 shows the failure angles of the two types of rocks with different sizes under TTC, and the measurement of the failure angle refers to [17]. For the tortuous fracture surface, the near-linear measuring method was used, as shown in Figure 3(c). Figure 13 shows that when the sample size was constant and σ_2 increased, the failure angle θ increased. However, changing the sample size did not

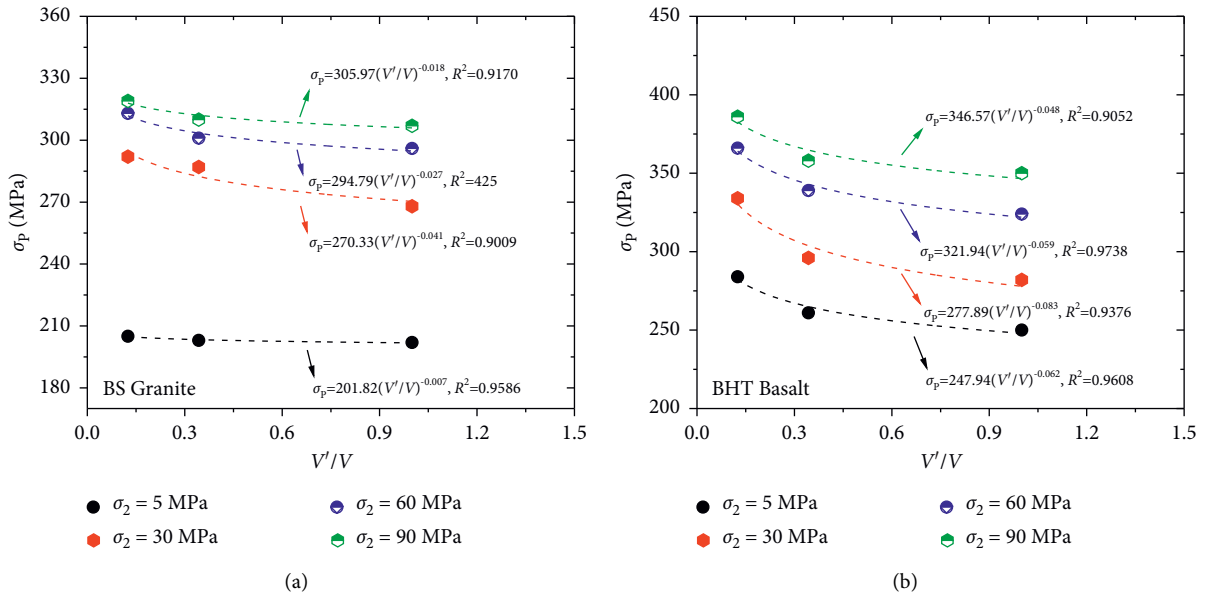


FIGURE 9: Relationship between the peak strength, sample size, and stress state of the two rocks under TTC (symbols of the same color represent the σ_p of different sizes under the same stress level). (a) BS granite and (b) BHT basalt.

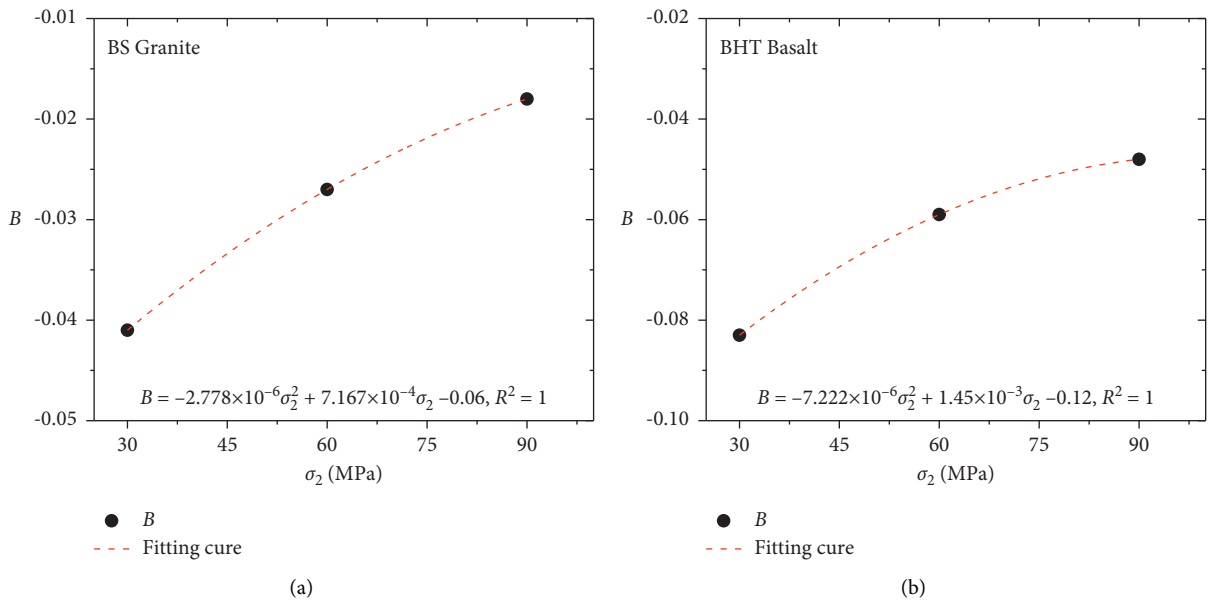


FIGURE 10: Fitting results between σ_2 and B . (a) BS granite and (b) BHT basalt.

significantly impact the angle of the fracture surface under the same stress. For example, in Figure 13(a), when the sample size of the BS granite decreased from SL to SS under the same stress, the fracture angle only varied by approximately 1~2°; in Figure 13(b), the variation in the fracture angle of the BHT basalt was basically the same as that of the BS granite under the same condition, approximately 0~3°. Thus, the small variation of the fracture angle in this paper further shows that the sample size do not significantly change the macroscopic failure mode of these two types of rocks, while the reduction of sample size will lead to more complex crack propagation on the fracture surface.

4. Discussion

4.1. Microscopic Interpretation of Complex Fracture Surfaces Caused by the Size Effect. Section 3.3 showed that changing the sample size does not significantly affect the macroscopic failure mode under the same stress. However, the crack propagation in the fracture surface became more complex when the sample size decreased to SM or SS, as shown in Figures 11(c), 11(e), 11(f), and 12. Under TTC, a macroscopic shear fracture plane with a “V” shape was easily generated [29, 31, 32]. On this type of fracture surface, especially near the center of the rock sample, almost no

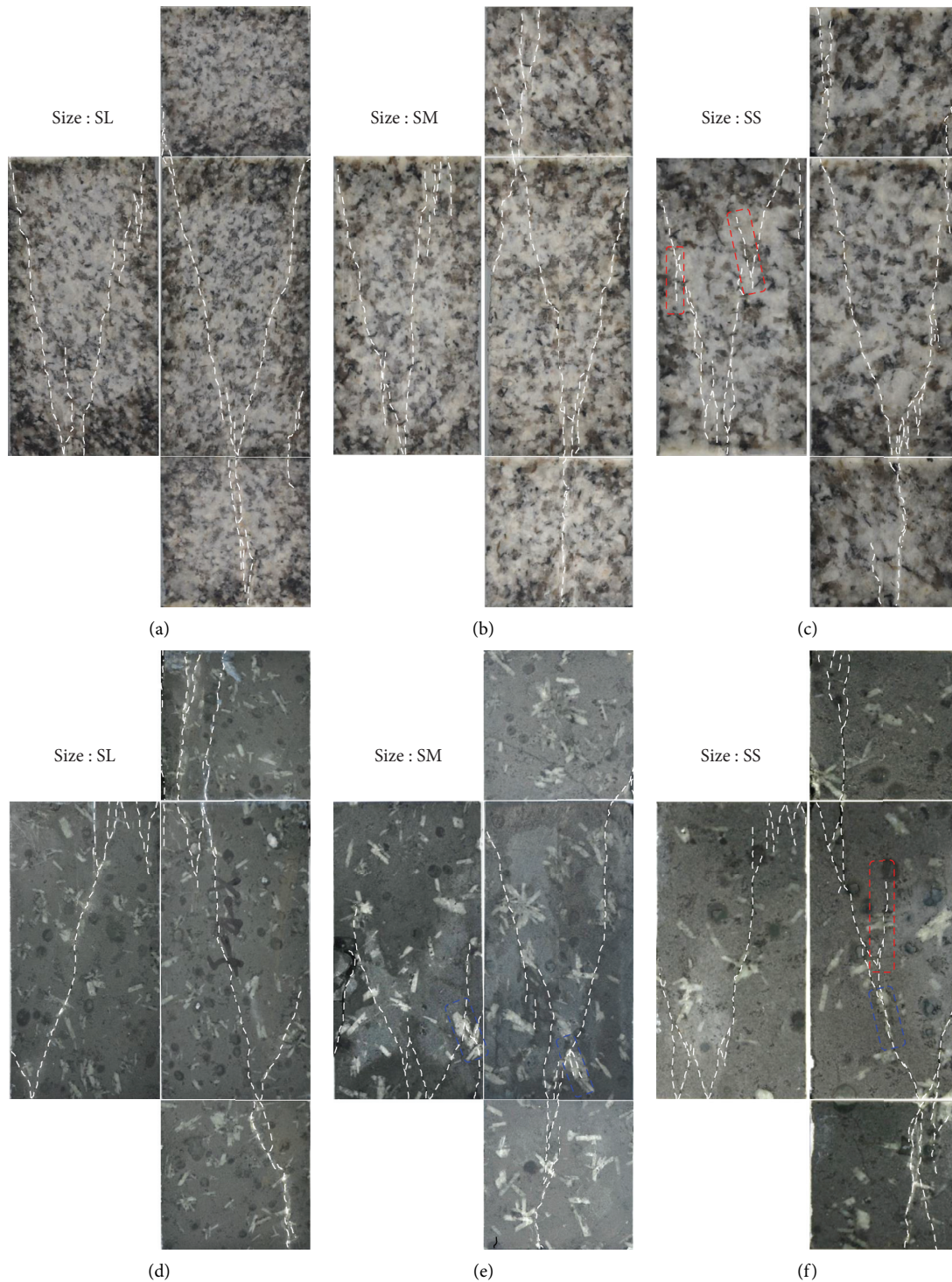


FIGURE 11: Failure modes of rock samples with different sizes under the same stress state of $\sigma_2 = 30$ MPa and $\sigma_3 = 5$ MPa. (a–c) BS granite; (d–f) BHT basalt.

obvious secondary cracks nearly parallel to the direction of σ_1 were generated during the propagation of the main cracks, as shown in Figures 11(a), 11(b), and 11(d). However, this situation is likely to occur when the sample size decreased from SL to SS under the same stress, as shown in Figures 11(c), 11(f), and 12(a).

The complex crack propagation on the failure surface of the small-sized samples may be related to the mineral grain size or the mineral grain aggregate size of the rocks. It is well known that grain size is one of the most important microstructure parameters of rock mechanical properties. Taking the BHT basalt as an example,

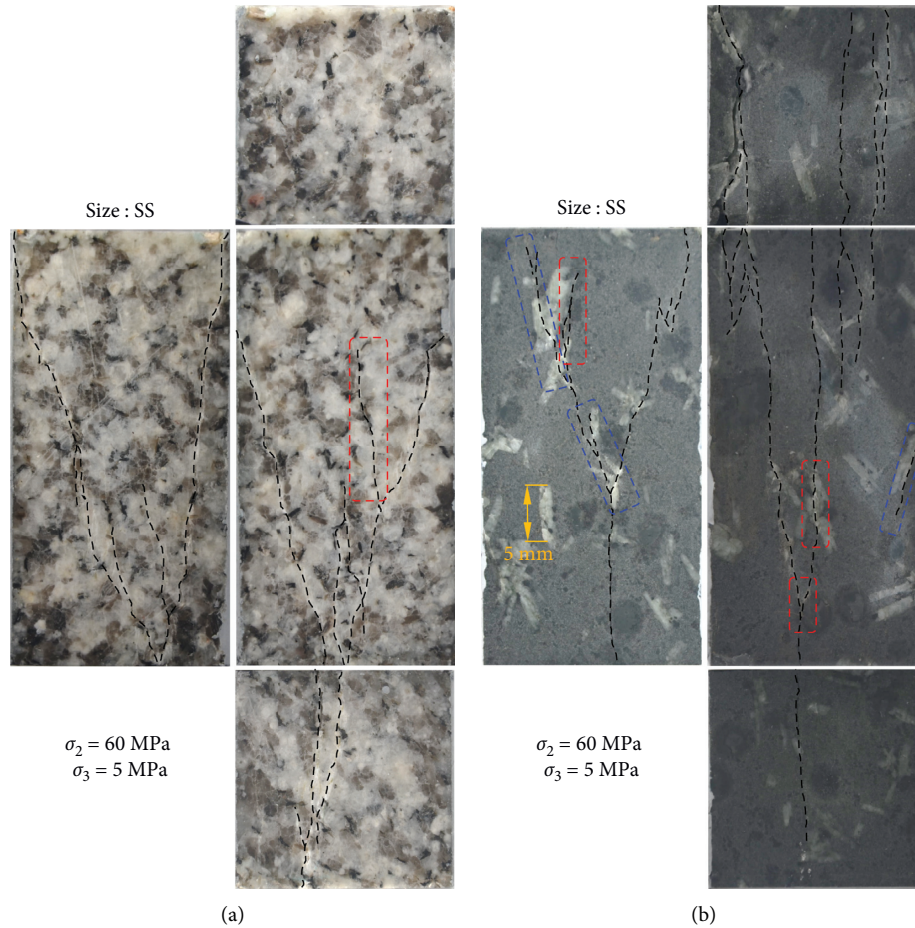


FIGURE 12: Failure mode of two rock samples of SS size at the same true triaxial stress state of $\sigma_2 = 60$ MPa and $\sigma_3 = 5$ MPa. (a) BS granite and (b) BHT basalt.

Figure 2(a) shows that pyroxene, feldspar, and other minerals were uniformly arranged in the matrix of the BHT basalt and the size of feldspar grain was $50\sim 150\ \mu\text{m}$. During the diagenetic process, a large number of feldspar grains aggregated to form lath-shaped white feldspar phenocrysts, with a length of 5 mm or larger, as shown in Figures 12(b), 14(a), and 14(b). Pyroxene is a silicate rock-forming mineral with a shear modulus of 64.9 GPa, and feldspar is a brittle rock-forming mineral with a shear modulus of 28.6 GPa. Section 2.1 showed that the total composition of pyroxene and feldspar minerals in the BHT basalt accounted for more than 87%, and the two constituted the basic framework. Pyroxene is a mineral with an allotriomorphic structure, while feldspar and others are minerals with idiomorphic structures, and the structural relationship between them is similar to the relationship between water and stone in a river. Basalt is igneous rock and pyroxene (like water) can fill the holes and gaps between minerals with an allotriomorphic structure (like stone) in the process of diagenesis with no clear boundaries between the two.

Reference [33] showed that, in the 6×6 stiffness matrix represented by the Voigt notation, the stiffness of single-crystal pyroxene in all directions is larger than that

of feldspar. Therefore, feldspar and other weaker minerals were more prone to brittle failure during the process of stress cracking, as demonstrated by the closed fractures on the surface of feldspar phenocrysts (Figures 2(a) and 14(c)), which may explain why the crack propagation on the fracture surface is more complex for small samples than for large samples (the complexity of the crack propagation of large rock samples was much lower).

In the samples with size SS in this study, the ratio of the size of the large feldspar phenocrysts to the length or width of the sample reached $1/5$ (Figure 12(b)), and the ratio was even larger when multiple phenocrysts were aggregated. Reference [34] pointed out that grain size plays an important role in crack propagation and used numerical modeling to show that the interactions of adjacent cracks can be used to inhibit crack propagation. Additionally, they also pointed out that this inhibitory effect can gradually disappear with the increase of grain size. For the BHT basalt, the size of the feldspar phenocrysts remained unchanged, but the decreased sample size was equivalent to indirectly increasing the size of the relatively weak feldspar phenocrysts (Figures 14(a) and 14(b)), and the role of feldspar phenocrysts in the structure could not be ignored. Therefore, the inhibition effect of the surrounding cracks could be

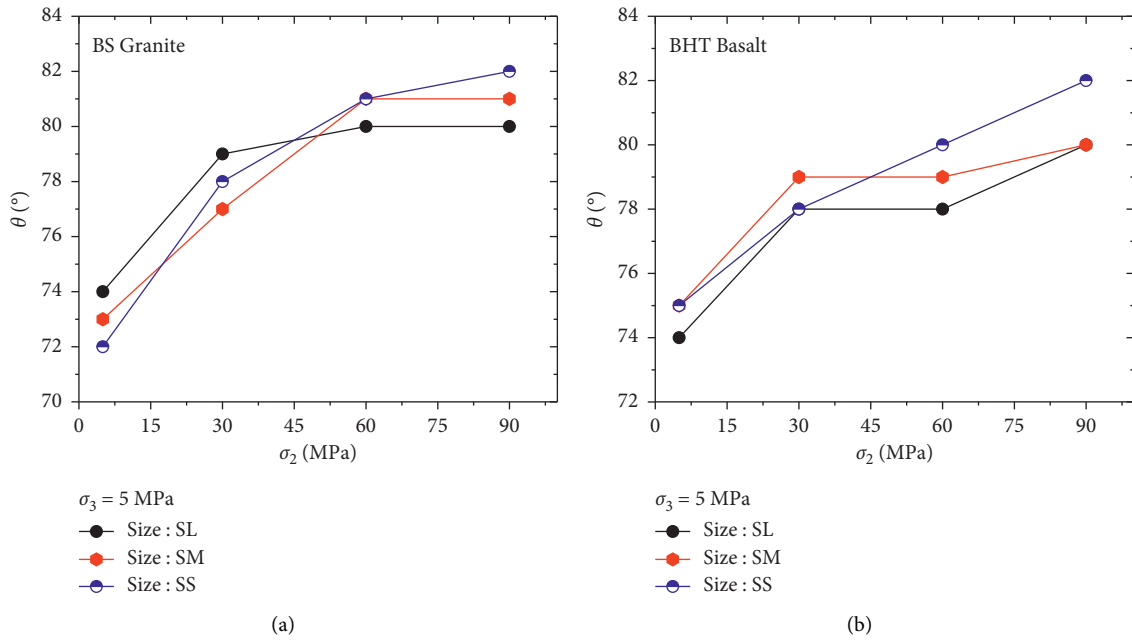


FIGURE 13: Failure angles of two types of rocks with different sizes under TTC. (a) BS granite and (b) BHT basalt.

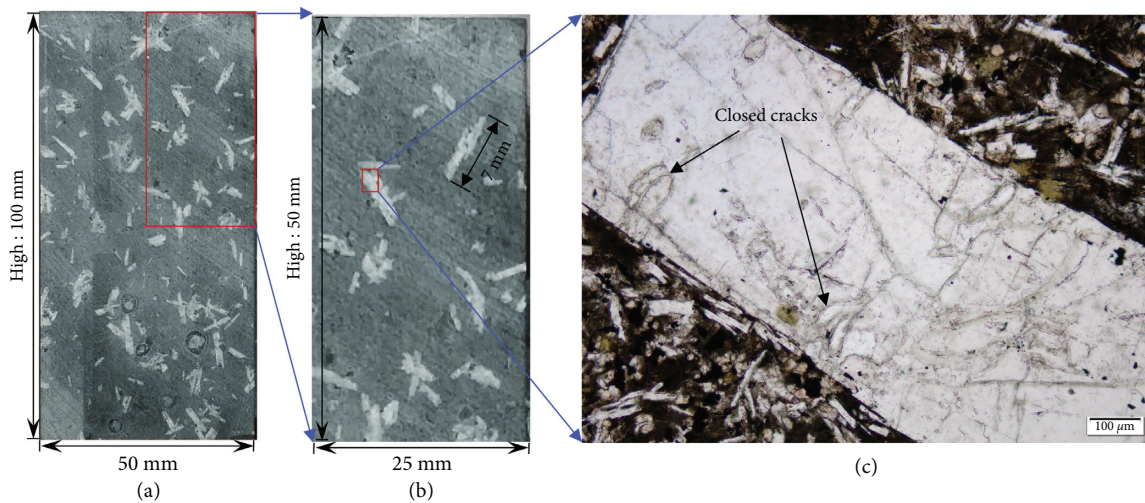


FIGURE 14: Pictures of BHT basalt and its microstructures under cross-polarized illumination. (a) BHT basalt specimen of SL size; (b) local magnification of the specimen in (a); (c) microstructures of (b) under cross-polarized illumination part.

weakened and the crack density could increase when the cracks propagated to the vicinity of feldspar phenocrysts with a relatively large size. References [35, 36] showed that, for fine-grained materials, an increase in crack density can be equivalent to an increase in the spatial heterogeneity of the local stress field. Therefore, when cracks occur, cracks are more likely to propagate along the weak feldspar phenocrysts, which results in a complex crack morphology on the fracture surface. For example, in the area enclosed by the blue dashed line in Figure 11(e), it is obvious that a crack developed along the axis of feldspar phenocrysts. In the small area enclosed by the blue dashed line in Figure 11(f), the main crack passed through the axis of the feldspar phenocrysts and produced secondary cracks nearly parallel

to the direction of σ_1 . In the left main fracture plane (Figure 12(b)), two groups of feldspar phenocrysts in the two areas enclosed by blue dashed lines led to the propagation direction of some cracks (all in the same direction), resulting in poor symmetry of the left and right fracture planes and a “Y” shaped fracture plane. The cracks that grew along the feldspar phenocrysts were also observed in the area enclosed by red dashed lines in the right main fracture surface. When the direction of the feldspar phenocrysts was close to the growth direction of cracks in the fracture surface, the cracks were more likely to grow along the feldspar phenocrysts. For the BS granite, the distribution of constituent minerals was relatively uniform, and the grain size reached 500~1500 μm or even larger. When the sample size was reduced to SS, the

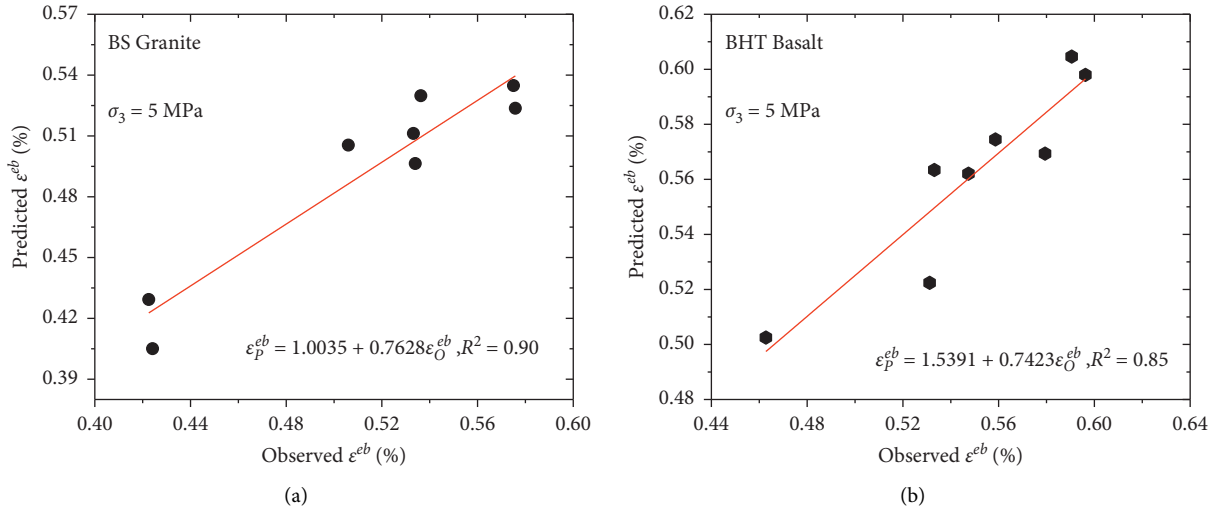


FIGURE 15: Prediction ability of equation (11) for total elastic strain in the direction of σ_1 for two types of samples. (a) BS granite and (b) BHT basalt.

fracture surface became complex, as shown in Figures 11(c) and 12(a). This may be one of the reasons why the International Society for Rock Mechanics (ISRM) recommends that the minimum side length of the sample should be more than 10 times the maximum grain size of minerals. Based on the previously mentioned analysis, it is better to choose a large rock sample when studying crack propagation on the fracture surface under TTC. The minimum side length of the sample should be at least 10 times larger than the maximum grain size of the mineral (ISRM) and the maximum grain size of the mineral aggregates with an idiomorphic structure (such as feldspar phenocrysts) to avoid a complex fracture surface.

4.2. Relationship between Elastic Strain and Sample Size. The test results in Section 3.2 showed that there was little relationship between Young's modulus and sample size. The maximum Young's modulus of the same samples with different sizes under the same stress state was fitted with σ_2 , and the relationship between them was obtained as follows:

$$E = d\sigma_2 + e, \quad (9)$$

where d and e are related to rock type.

According to the calculation method of elastic strain under TTC proposed in [24],

$$\epsilon^{eb} = \epsilon_1^{eb} + \frac{\sigma_p - \sigma_2}{E}, \quad (10)$$

where ϵ^{eb} is the total elastic strain in the direction of σ_1 and ϵ_1^{eb} is the elastic strain in the biaxial loading stage in the direction of σ_1 under TTC, that is, the elastic strain in the process of Section 2.2 stress path b .

Taking equation (5) into (10), the following can be obtained for calculating the total elastic strain in the direction of σ_1 related to the sample size under TTC:

$$\epsilon^{eb} = \epsilon_1^{eb} + \frac{\sigma_{pV} \times (V'/V)^{a\sigma_2^2 + b\sigma_2 + c} - \sigma_2}{f(\sigma_2)}. \quad (11)$$

As shown in Figure 15, the linear regression coefficients of the total elastic strain of the BS granite and BHT basalt with sizes of SM and SS predicted by formula (11) in the direction of σ_1 were $R^2 = 0.90$ and $R^2 = 0.85$, respectively, indicating that the prediction ability of formula (11) was reasonable.

5. Conclusion

In this study, BS granite and BHT basalt with the same length : width : height ratio and different sizes were used to study the size effect under TTC conditions. The following conclusions are drawn:

- (1) Regarding the deformation and failure characteristics within the range of rock size for this study, including the stress-strain curve, Young's modulus, peak strain in the directions of σ_3 and σ_2 , fracture angle, and macrofailure mode, there was almost no obvious size effect. However, the characteristics of deformation for the two types of rocks were related to the rock properties and external stress conditions.
- (2) The peak strength and damage stress of the BS granite and BHT basalt were significantly affected by the sample size and σ_2 under TTC. As the sample size decreased, the σ_p and σ_{cd} increased. For these two types of rocks, there was a power function relationship among the peak strength, sample size, and σ_2 under TTC. Under the same conditions, the sensitivity of the peak strength of the fine-grained BHT basalt to the sample size was higher than that of the medium- to coarse-grained BS granite.
- (3) The complex crack propagation on the fracture surface of smaller rock samples was due to indirectly

increasing the mineral grain size or mineral cluster size in the rocks. Moreover, this study suggests that the minimum side length of rock samples should be at least 10 times the maximum size of the mineral clusters when studying crack propagation on a fracture surface.

- (4) The estimation method of elastic strain in a certain range of sample sizes was established by analyzing the relationship among sample size, peak strength, intermediate principal stress, and elastic strain in the direction of σ_1 , and the prediction result was well.

Data Availability

The data used to support the findings of this study are available from the corresponding author upon request.

Conflicts of Interest

The authors declare that they have no conflicts of interest.

Acknowledgments

The authors sincerely acknowledge the financial support from the Liao Ning Revitalization Talents Program under Grant no. XLYC1801002, the National Natural Science Foundation of China under Grant no. 51839003, and the 111 Project under Grant no. B17009. The authors are grateful to Prof. Xiating Feng, Prof. Xiwei Zhang, Prof. Chengxiang Yang, Mr. Zhaofeng Wang, and Ms. Xinyue Wang for their great assistance.

References

- [1] W. Weibull, "A statistical distribution function of wide applicability," *Journal of Applied Mechanics*, vol. 18, no. 3, pp. 293–297, 1951.
- [2] Z. P. Bažant and J. Planas, *Fracture and Size Effect in concrete and Other Quasibrittle Materials*, CRC Press, Boca Raton, FL, USA, 1998.
- [3] A. Carpinteri, "Scaling laws and renormalization groups for strength and toughness of disordered materials," *International Journal of Solids and Structures*, vol. 31, no. 3, pp. 291–302, 1994.
- [4] H. R. Pratt, A. D. Black, W. S. Brown, and W. F. Brace, "The effect of specimen size on the mechanical properties of unjointed diorite," *International Journal of Rock Mechanics and Mining Science & Geomechanics Abstracts*, vol. 9, no. 4, pp. 513–516, 1972.
- [5] B. C. Liu, J. S. Zhang, Q. Z. Du, and J. F. Tu, "Size effect of compressive strength of rock," *Chinese Journal of Rock Mechanics and Engineering*, vol. 17, pp. 611–614, 1998, (in Chinese).
- [6] E. Tuncay, N. T. Özcan, and A. Kalender, "An approach to predict the length-to-diameter ratio of a rock core specimen for uniaxial compression tests," *Bulletin of Engineering Geology and the Environment*, vol. 78, no. 7, pp. 5467–5482, 2019.
- [7] J. Fládr and P. Bílý, "Specimen size effect on compressive and flexural strength of high-strength fibre-reinforced concrete containing coarse aggregate," *Composites Part B: Engineering*, vol. 138, pp. 77–86, 2018.
- [8] P. A. Cundall, M. E. Pierce, and D. M. Ivars, "Quantifying the size effect of rock mass strength," in *Proceedings of the Southern Hemisphere International Rock Mechanics Symposium*, Perth, Australia, January 2008.
- [9] D. D. Hunt, "The influence of confining pressure on size effect," *Master of Sciences in Civil Engineering*, Massachusetts Institute of Technology, Cambridge, MA, USA, 1973.
- [10] K. Mogi, "Effect of the triaxial stress system on rock failure," *Rock Mechanics Japan*, vol. 1, pp. 53–55, 1970.
- [11] K. Mogi, "Fracture and flow of rocks under high triaxial compression," *Journal of Geophysical Research*, vol. 76, no. 5, pp. 1255–1269, 1971.
- [12] B. Haimson and C. Chang, "A new true triaxial cell for testing mechanical properties of rock, and its use to determine rock strength and deformability of Westerly granite," *International Journal of Rock Mechanics and Mining Sciences*, vol. 37, no. 1–2, pp. 285–296, 2000.
- [13] W. R. Wawersik, L. W. Carlson, D. J. Holcomb, and R. J. Williams, "New method for true-triaxial rock testing," *International Journal of Rock Mechanics and Mining Sciences*, vol. 34, pp. 3–4, 1997.
- [14] P. Michelis, "A true triaxial cell for low and high pressure experiments," *International Journal of Rock Mechanics and Mining Science & Geomechanics Abstracts*, vol. 22, no. 3, pp. 183–188, 1985.
- [15] M. Takahashi and H. Koide, "Effect of the intermediate principal stress on strength and deformation behavior of sedimentary rocks at the depth shallower than 2000 m," *International Journal of Rock Mechanics and Mining Science & Geomechanics Abstracts*, vol. 27, pp. 19–26, 1989.
- [16] J. T. Chen and X. T. Feng, "True triaxial experimental study on rock with high geostress," *Chinese Journal of Rock Mechanics and Engineering*, vol. 25, pp. 1537–1543, 2006, (in Chinese).
- [17] X.-T. Feng, X. Zhang, R. Kong, and G. Wang, "A novel mogi type true triaxial testing apparatus and its use to obtain complete stress-strain curves of hard rocks," *Rock Mechanics and Rock Engineering*, vol. 49, no. 5, pp. 1649–1662, 2016.
- [18] L. Shi, X. B. Li, B. Bing, A. Wang, Z. Zeng, and H. He, "A mogi-type true triaxial testing apparatus for rocks with two moveable frames in horizontal layout for providing orthogonal loads," *Geotechnical Testing Journal*, vol. 40, pp. 542–558, 2017.
- [19] M. C. He, J. L. Miao, and J. L. Feng, "Rock burst process of limestone and its acoustic emission characteristics under true-triaxial unloading conditions," *International Journal of Rock Mechanics and Mining Sciences*, vol. 47, no. 2, pp. 286–298, 2010.
- [20] X. Li, K. Du, and D. Li, "True triaxial strength and failure modes of cubic rock specimens with unloading the minor principal stress," *Rock Mechanics and Rock Engineering*, vol. 48, no. 6, pp. 2185–2196, 2015.
- [21] X. G. Zhao and M. Cai, "Influence of specimen height-to-width ratio on the strainburst characteristics of Tianhu granite under true-triaxial unloading conditions," *Canadian Geotechnical Journal*, vol. 52, pp. 890–902, 2014.
- [22] F. Zhao and M. C. He, "Size effects on granite behavior under unloading rockburst test," *Bulletin of Engineering Geology and the Environment*, vol. 76, no. 3, pp. 1183–1197, 2016.
- [23] X. B. Li, F. Feng, D. Y. Li, K. Du, P. G. Ranjith, and J. Rostami, "Failure characteristics of granite influenced by sample height-to-width ratios and intermediate principal stress under true-triaxial unloading conditions," *Rock Mechanics and Rock Engineering*, vol. 51, pp. 1–25, 2018.

- [24] X. T. Feng, J. Zhao, Z. F. Wang, C. X. Yang, Q. Han, and Z. Zheng, "Effect of high differential stress and mineral properties on deformation and failure mechanism of hard rocks," *Canadian Geotechnical Journal*, vol. 58, 2020.
- [25] C. D. Martin, *The strength of massive Lac du Bonnet granite around underground openings*, Ph.d. thesis, Department of Civil Engineering, University of Manitoba, Winnipeg, Canada, 1993.
- [26] Y.-H. Gao, X.-T. Feng, X.-W. Zhang, G.-L. Feng, Q. Jiang, and S.-L. Qiu, "Characteristic stress levels and brittle fracturing of hard rocks subjected to true triaxial compression with low minimum principal stress," *Rock Mechanics and Rock Engineering*, vol. 51, no. 12, pp. 3681–3697, 2018.
- [27] Y. Zhang, *Energy evolution mechanism of failure process of hard rock in deep tunnel and discrimination of typical hazard types*, Ph.d thesis, Northeastern University, Shenyang, China, 2020.
- [28] B. Haimson and J. W. Rudnicki, "The effect of the intermediate principal stress on fault formation and fault angle in siltstone," *Journal of Structural Geology*, vol. 32, no. 11, pp. 1701–1711, 2010.
- [29] X. Ma, J. W. Rudnicki, and B. C. Haimson, "Failure characteristics of two porous sandstones subjected to true triaxial stresses: a," *Journal of Geophysical Research: Solid Earth*, vol. 122, no. 4, pp. 2525–2540, 2017.
- [30] R. Kong, X.-T. Feng, X. Zhang, and C. Yang, "Study on crack initiation and damage stress in sandstone under true triaxial compression," *International Journal of Rock Mechanics and Mining Sciences*, vol. 106, pp. 117–123, 2018.
- [31] J. Zhao, X.-T. Feng, X.-W. Zhang, Y. Zhang, Y.-Y. Zhou, and C.-X. Yang, "Brittle-ductile transition and failure mechanism of Jinping marble under true triaxial compression," *Engineering Geology*, vol. 232, pp. 160–170, 2018.
- [32] Y. Zhang, X. T. Feng, X. W. Zhang, Z. F. Wang, M. Sharifzadeh, and C. X. Yang, "A novel application of strain energy for fracturing process analysis of hard rock under true triaxial compression," *Rock Mechanics and Rock Engineering*, vol. 52, pp. 1–16, 2019.
- [33] J. D. Bass, "Elasticity of minerals, glasses, and melts," *American Geophysical Union*, vol. 2, pp. 45–63, 1995.
- [34] E. Eberhardt, D. Stead, B. Stimpson, and E. Z. Lajtai, "The effect of neighbouring cracks on elliptical crack initiation and propagation in uniaxial and triaxial stress fields," *Engineering Fracture Mechanics*, vol. 59, no. 2, pp. 103–115, 1998.
- [35] J. T. Fredrich, B. Evans, and T.-F. Wong, "Effect of grain size on brittle and semibrittle strength: implications for micro-mechanical modelling of failure in compression," *Journal of Geophysical Research*, vol. 95, no. B7, pp. 10907–10920, 1990.
- [36] J. Peng, L. N. Y. Wong, and C. I. Teh, "Influence of grain size heterogeneity on strength and microcracking behavior of crystalline rocks," *Journal of Geophysical Research: Solid Earth*, vol. 122, no. 2, pp. 1054–1073, 2017.

Research Article

Study on the Effect of Polysulfide Content on the Micromorphology and Spontaneous Combustion Characteristics of Coal

Hai-Fei Yao ^{1,2,3}

¹*School of Emergency Management and Safety Engineering, China University of Mining and Technology (Beijing), Beijing 100083, China*

²*Mine Safety Technology Branch, China Coal Research Institute, Beijing 100013, China*

³*National Key Laboratory of Coal Resources Highly Efficient Mining and Clean Utilization, China Coal Research Institute, Beijing 100013, China*

Correspondence should be addressed to Hai-Fei Yao; yhf8000@163.com

Received 4 June 2021; Accepted 6 September 2021; Published 29 September 2021

Academic Editor: Jia Lin

Copyright © 2021 Hai-Fei Yao. This is an open access article distributed under the Creative Commons Attribution License, which permits unrestricted use, distribution, and reproduction in any medium, provided the original work is properly cited.

This paper aimed to study the effect of the polysulfide content on the micromorphology and spontaneous combustion characteristics of coal, in order to develop more targeted prevention and treatment strategies. To this end, this study selected the method of mixing different sulfides with very low sulfur content raw coal to prepare the coal samples to be tested. Various parameters, such as true density, porosity, micromorphology, and oxygen uptake of the different sulfur samples, were tested. The results reveal that sulfide had a certain expansion effect on the coal body and improved the pore structure of coal, and the porosity increased with the increase of the sulfur content. After adding iron (II) disulfide (FeS_2) and iron (II) sulfide (FeS) powder to the original coal sample, the number of fine particles on the surface increased significantly. After increasing the oxidation temperature, the lamellar structure disintegrated, and the massive coal body was broken into several fine particles, which promoted the spontaneous combustion of coal. Polysulfide promotes the low-temperature oxygen absorption of coal and shortens the natural firing period of coal. FeS has a slightly greater effect on increasing the tendency of coal to spontaneously combust and shortening the shortest natural firing period of coal. Before the addition of FeS_2 and FeS to the coal samples, the coal production amount was not much different below 80–90°C, and then, the gap gradually widened. Under the same temperature condition of coal, carbon monoxide (CO) production basically occurred first as the sulfur content increased. When FeS_2 and FeS were added, the sulfur content of the coal samples was 3 and 4%, respectively, and the production of CO and ethene (C_2H_4) was the largest. Although the peak areas of aliphatic hydrocarbon, aromatic hydrocarbon, hydroxyl group, and carbonyl group in the coal samples with FeS were different, they all reached their maximum value when the sulfur content was 4%.

1. Introduction

The sulfur content in China's coal resources varies greatly, ranging from 0.04 to 9.62%. According to the sulfur content, coal resources can be divided into low sulfur coal (<1%), medium sulfur coal (between 1 and 2%), and high-sulfur coal (>2%). The content and distribution of sulfur in coal are closely related to the coal formation age and coal-forming environment [1, 2]. With the continuous expansion of underground mining, I-beams, anchor rods, nets, and other

iron-containing materials are widely used, and ferrous sulfide (FeS), which is a combustible product of the corrosion of sulfur and sulfide with iron and its oxides in coal [3–5], has gradually become a common sulfide present in mines. The oxidation of inorganic sulfur in coal produces a lot of heat, promotes the process of spontaneous combustion of coal, and significantly shortens the natural combustion period of coal [6, 7]. In addition, the original hydrogen sulfide (H_2S) gas in some coal is also flammable and produces a blue flame when burning [8–10].

The mutual conversion between different sulfur-containing substances is a very complex reaction system. Depending on different factors, such as temperature, oxygen concentration, and environmental pH, whether other substances are involved, different reactions will occur and different substances will be generated [11]. Under certain conditions, various substances can be converted into each other. However, usually, the underground environment of a coal mine is extremely complex, and the chemical composition of the coal body is diverse [12, 13]. Various factors work together to enable the presence of polysulfide in the underground coal body, which has a certain effect on the law of coal spontaneous combustion. The polysulfide complex reaction system has been preliminarily established. As shown in Figure 1, complex reactions of FeS_2 , FeS , and H_2S will occur under different conditions, and many complex intermediates, such as Fe , iron oxide, elemental S , and acid, will be formed [14–17].

Some Chinese high-sulfur coal mines (Shenhua Wulan Coal Mine, Laoshidan Coal Mine, etc.) once had blue flame and flue gas, but the concentration of carbon monoxide (CO) at the upper corner of the working face did not exceed the standard and was even 0, and the cause of ignition was not completely clear. Therefore, the study of the influence of multiple sulfides (mainly FeS_2 , FeS , and H_2S) on the physical structure and spontaneous combustion characteristics of coal has an important guiding significance for the analysis of the influence of multiple sulfides on the natural combustion law of coal and fire prevention and extinguishing work in the process of high-sulfur coal seam mining.

2. The Effect of Coal Porosity

As a kind of porous medium, there are a lot of pores in the coal body, and the proportion of the pore volume of the total volume of the coal body is the porosity of coal [18]. The porosity of coal has an important effect on the coal-oxygen composite reaction in the low-temperature oxidation stage. The larger the porosity of coal is, the larger the coal surface area involved in the coal-oxygen composite reaction will be, which is more conducive to the coal-oxygen composite reaction. The true density of coal refers to the ratio of the true weight to the true volume of the coal [19, 20]. For the same coal sample, the higher the true density is, the smaller the porosity is, and the two are inversely proportional [21–24].

Coal blocks were crushed and ground into coal samples smaller than 0.2 mm, which were divided into 9 groups with different sulfur contents according to the test scheme and two samples for each group. One part was left untreated, and the other was cooled after 8 hours of oxidation and heating in an air blast high-temperature chamber at 180°C . The true density of coal before and after oxidation was tested according to GB/T23561.2-2009 “Methods for the determination of physical and mechanical properties of coal and rock—Part 2: Methods for the determination of true density of coal and rock,” and the process setup is shown in Figure 2.

The experimental results of the true density test shown in Table 1 and Figure 2 reveal that the true density increases to

varying degrees when FeS_2 and FeS are added to the original coal samples before the increase of the oxidation temperature. With the increase of the sulfur content, the true density increases and the porosity decreases. The experimental results of the true density test shown in Table 1 and Figure 3 reveal that the true density increases to varying degrees when FeS_2 and FeS are added to the original coal samples before the increase of the oxidation temperature. With the increase of the sulfur content, the true density increases and the porosity decreases. With the same sulfur content, the true density of the coal samples with FeS is higher than that with FeS_2 . This is due to the high porosity of the coal, with many pores on its surface and inside, and also that the added sulfide is solid powder, so the addition of sulfide reduces the number of pores in the coal sample per unit mass, while the added FeS mass is greater than that of FeS_2 with the same sulfur content.

The results in Table 1 and Figure 2 also reveal that the change rule of the true density and porosity of coal samples after oxidation and heating is basically the same as that before heating. In the process of oxidation and heating of a coal sample, ferrite compounds react with oxygen and release heat. Ferric hydroxide ($\text{Fe}(\text{OH})_3$), one of the reaction products, will form a sol in the presence of water, with a particle radius of between $10^{-7}\sim 10^{-5}$ cm, and a pore radius of the coal macromolecule of 10^{-5} cm. Thus, the $\text{Fe}(\text{OH})_3$ sol will enter the pore of the coal macromolecule and gradually condense into $\text{Fe}(\text{OH})_3$ micelles to fill the pores, thereby reducing the effective pore volume of the coal particles, ultimately increasing its true density, and reducing its porosity. Also, the greater the sulfur content of coal is, the greater the plugging effect is, and with the increase of the temperature, this effect is more pronounced.

In this test, the coal sample was not humidified, and its water content was the natural water content. If the coal containing sulfur under the shaft is in a humid environment and there is a risk of natural combustion, the effect of sulfur compounds on the reduction of its porosity will be more obvious.

3. The Influence of the Microscopic Morphology of Coal

Scanning electron microscopy (SEM) is usually used to examine the microscopic morphology of substances. In this study, SEM was used to examine the microscopic morphology of coal samples with different sulfur contents before and after heating using a Hitachi S-3400N scanning electron microscope (Hitachi Ltd., Tokyo, Japan). The SEM images of raw coal samples and coal samples with FeS_2 and FeS added before and after the increase of the oxidation temperature (the increasing oxidation temperature conditions were the same as those for the true density test) were recorded at a magnification of 10,000x, and the images are displayed in Figures 4~6.

Through continuous observation with a moving lens, representative images with a magnification of 10,000x were selected for analysis.

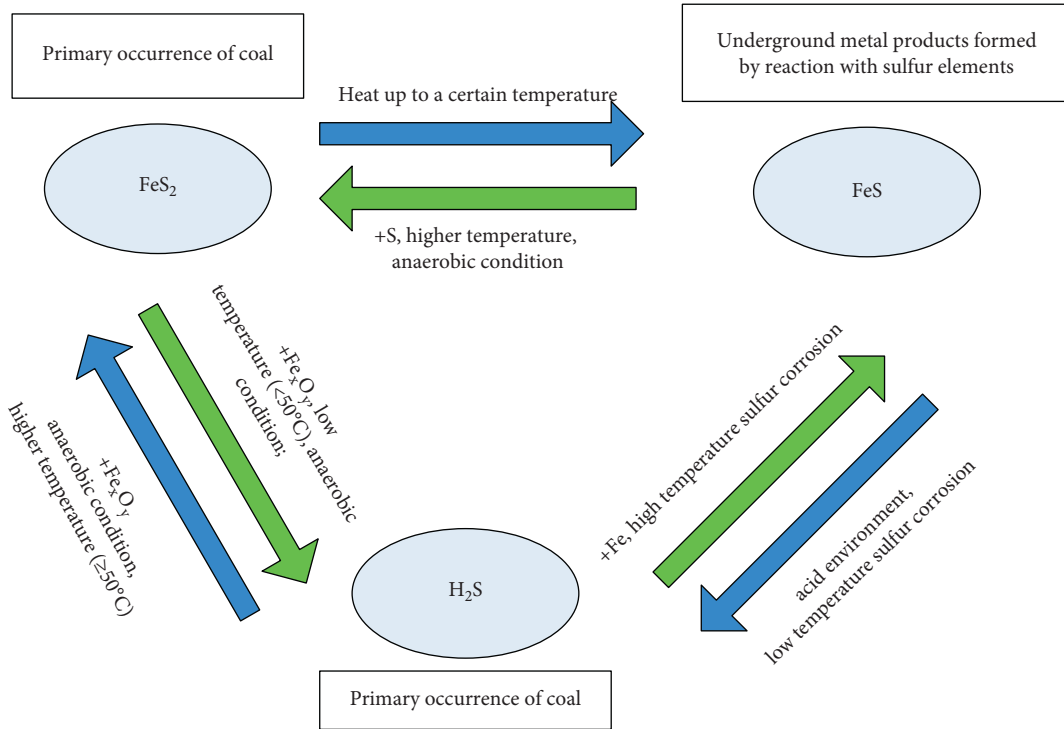


FIGURE 1: Downhole multisulfide complex reaction system.



FIGURE 2: True density test process setup of the coal samples with different sulfur contents before and after the increase of the oxidation temperature.

The images in Figure 4 reveal that the surface of the raw coal sample before and after the oxidation and heating exhibits a lamellar structure, and there is a small pore structure on the surface. After heating, the pore structure on the surface of the raw coal sample expands compared with that before heating, and the cracks increase. The surface of the coal sample is partially oxidized, and the surface of the coal sample is cracked as a whole.

The images in Figure 5 show that after adding FeS_2 powder to the raw coal sample, the microscopic morphology of the coal sample surface changes from that before adding FeS_2 . In particular, the number of fine particles on the coal surface increases significantly, and such increase in the number of fine particles increases the contact area between the coal and oxygen, which is conducive to natural combustion. After the oxidation temperature increases, the number of fine particles increases, and

TABLE 1: True density test results of coal samples with different sulfur contents before and after the increase of the oxidation temperature.

Oxidation temperature	Sulfur/sulfur content	0	2	3	4	5
Before	FeS_2	1.39	1.44	1.46	1.48	1.52
	FeS	1.39	1.45	1.47	1.5	1.58
After	FeS_2	1.64	1.65	1.67	1.68	1.73
	FeS	1.64	1.72	1.74	1.79	1.82

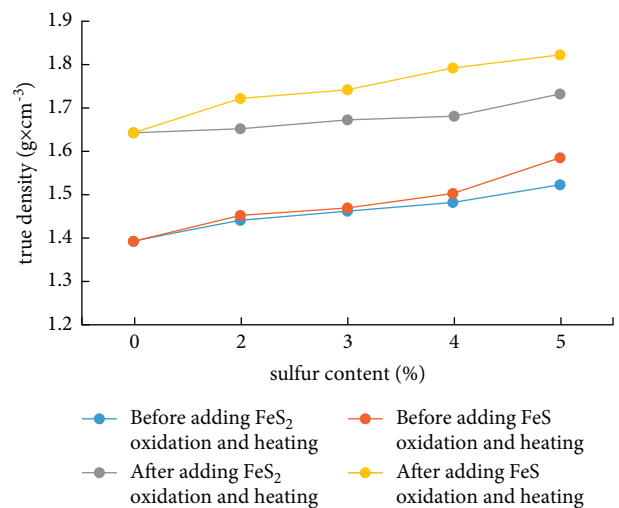


FIGURE 3: True density test results of coal samples with different sulfur contents before and after oxidation and heating.

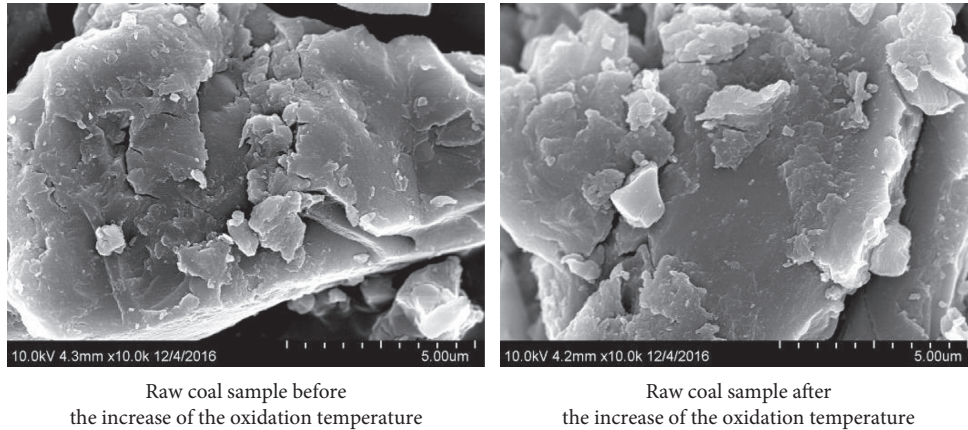


FIGURE 4: Microscopic morphology of raw coal sample (a) before and (b) after the increase of the oxidation temperature.

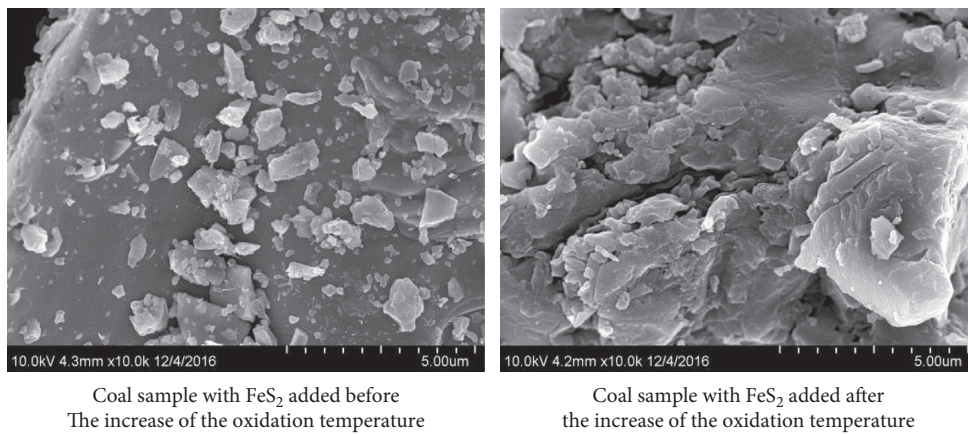


FIGURE 5: Microscopic morphology of the coal sample with FeS_2 added (a) before and (b) after the increase of the oxidation temperature.

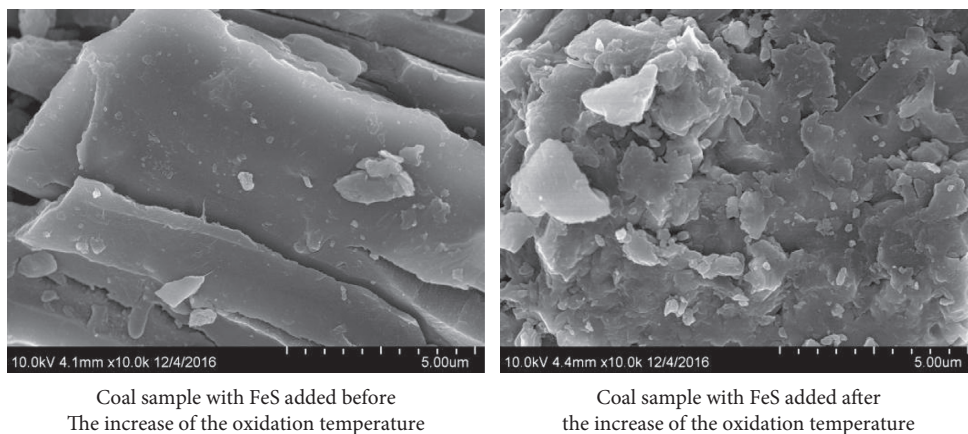


FIGURE 6: Microscopic morphology of coal sample with FeS added (a) before and (b) after the increase of the oxidation temperature.

the original massive area becomes loose. Cracks appear on the surface of both the massive coal and the particles, which sets up the conditions for further accelerated oxidation.

The images in Figure 6 reveal that after the addition of the FeS powder to the raw coal sample, the surface becomes smooth and exhibits an obvious lamellate distribution, and deep cracks are found between each

lamellate. After the oxidation temperature increases, the lamellar structure is clearly disintegrated, and the block of coal is broken into numerous fine particles. The thin layer of fine particles loosens the structure of the coal seam and increases the air leakage velocity and oxygen content in micropores, further promoting the spontaneous combustion of coal.

4. The Effect of the Tendency of Coal Spontaneous Combustion

The spontaneous combustion of coal is directly related to the adsorption of oxygen by coal. In this study, the ZRJ-1 briquette spontaneous combustion tester is used to test the influence of the sulfur content on the dynamic oxygen uptake of coal under different temperature conditions. During the experiment, fresh large coal samples were taken, and then, the coal core of 100–150 g was used. The coal was crushed to less than 0.2 mm particles within 20 min, and particles of 0.1–0.15 mm accounted for more than 70% [5–8]. Eight groups of coal samples with a sulfur content of 2, 3, 4, and 5% were prepared by adding FeS₂ and FeS, and the raw coal sample was considered to have approximately the sulfur content of 0%. There were 9 groups in total.

The oxygen intake levels of coal samples with different sulfur contents at 30°C shown in Table 2 reveal that with the addition of FeS₂ and FeS, the oxygen uptake level of coal at 30°C increases along with the increase of the sulfur content in the coal sample, indicating that the sulfur content promotes the physical oxygen uptake of coal, with a maximum increase of about 15.33 and 21.90%.

With the increase of the sulfur content of the coal sample, the oxygen absorption, as measured by chromatography, initially increases and then decreases. This finding indicates that within the usual sulfur content range of coal seam, there is a sulfur content value that has the strongest promoting effect on the oxygen absorption measured by chromatography of the coal sample, which has the greatest enhancing effect on the spontaneous combustion tendency of coal. With the same sulfur content, the chromatographic oxygen uptake at 30°C of the coal samples containing FeS is higher than that of coal samples containing FeS₂, indicating that the promoting effect of FeS on the spontaneous combustion tendency of coal is slightly greater than that of FeS₂ under the same experimental conditions. For the FeS coal sample, the peak value of oxygen absorption is about 4% of sulfur content, while for the FeS₂ coal sample it is about 3%.

5. The Effect of the Coal Spontaneous Combustion Mark Gas

The effect of sulfur compounds with different sulfur contents on the generation regularity of the symbol gas of coal spontaneous combustion was studied by a programmed temperature experiment. Fresh large-lump coal samples were shelled, cored, and crushed, and four kinds of coal particles with a particle size of 0–1 mm, 1–3 mm, 3–5 mm, and 5–10 mm were selected to prepare mixed coal samples required for the temperature-programmed characteristic experiment according to the mass ratio of 1:1:1:1. Then, the correct weight of the FeS₂ or FeS powder sample was evenly mixed with the coal sample according to the designed sulfur content. Each sample weighed 1,000 g [25, 26]. The prepared coal sample was slowly loaded into the coal sample tank and then placed into the programmed heating furnace. During the

TABLE 2: Chromatographic oxygen intake of coal samples with different sulfur contents at 30°C.

Sulfide species	Oxygen uptake under different sulfur content conditions (cm ³ ·g ⁻¹)				
	0%	2%	3%	4%	5%
FeS ₂	1.37	1.51	1.58	1.52	1.42
FeS	1.37	1.54	1.59	1.67	1.52

experiment, dry air was injected into the coal sample tank at a flow rate of 130 mL/min; then the gas was taken for every 10°C increase and analyzed by gas chromatography.

5.1. Rule of CO Production. CO is the earliest oxidized gas product in the process of coal spontaneous combustion and runs through the whole process. After adding FeS₂ and FeS, the change of CO production in coal samples with different sulfur contents with the coal temperature is shown in Figure 7.

The results in Figure 7(a) show that before the temperature of the coal samples with added FeS₂ and FeS reaches 80–90°C, there is little difference in the amount of CO produced in each coal sample. Above 80–90°C, the difference gradually increases. Under the same coal temperature condition, the amount of CO produced usually increases first and then decreases with the increase of the sulfur content. In the case of the two additives, when the sulfur content is 3 and 4%, respectively, the coal sample produces the largest amount of CO, the raw coal sample is the smallest, and the rest is between the two, with some staggered overlap, which is basically consistent with the change rule of oxygen intake. Compared with the CO production data with the same sulfur content with different sulfur compounds, when the sulfur content is 2 and 3%, the CO production in the coal sample with added FeS₂ is slightly higher than that in the coal sample with added FeS. When the sulfur content is 4 and 5%, the result is the opposite to that obtained when the sulfur content is 2 and 3%. The difference between the two is the largest when the sulfur content is 4%.

5.2. Rule of Ethylene (C₂H₄) Production. The appearance of C₂H₄ indicates that the coal spontaneous combustion has entered the accelerated oxidation stage, which is generally used as the index of coal spontaneous combustion. After adding FeS₂ and FeS, the C₂H₄ production of the coal samples with different sulfur contents varies with the coal temperature, as shown in Figure 8. When FeS₂ is added, the production of C₂H₄ is less regular, and the temperature at which C₂H₄ appears for the first time does not change in the process of programmed heating, which is at 80°C. The C₂H₄ production of each coal sample with sulfur content is clearly higher than that of the raw coal sample, but their curves overlap at many points. Therefore, under the condition of the same coal temperature, the variation rule of C₂H₄ production with sulfur content is not clear, but it can be seen that when the sulfur content is 3%, the C₂H₄ production is the maximum in the whole process.

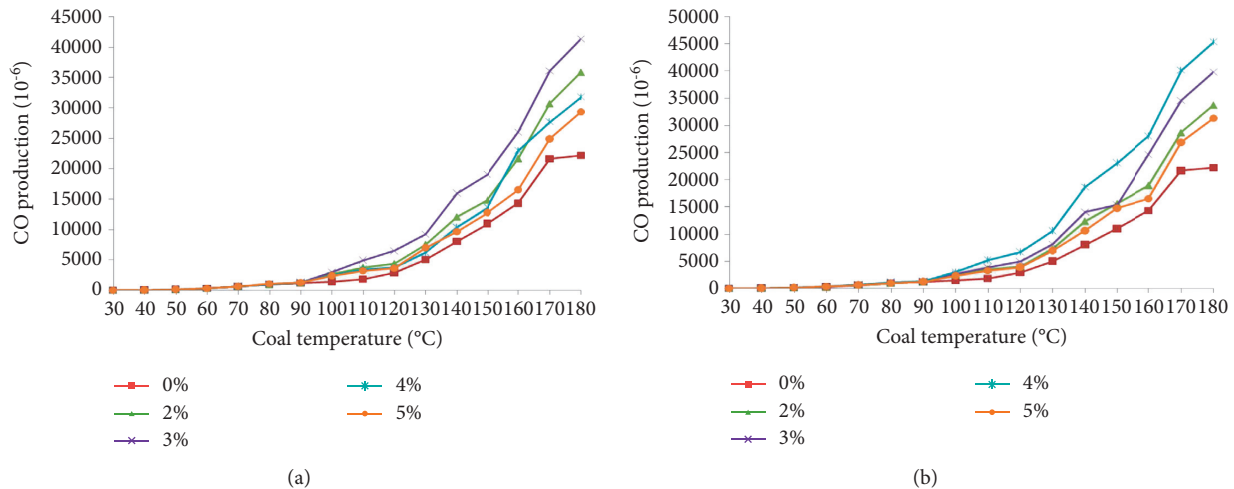


FIGURE 7: CO generation rules of coal samples with different sulfur contents in the process of programmed heating (a) with FeS_2 and (b) with FeS .

The regularity of C_2H_4 production of the coal samples with added FeS in the process of programmed heating is clearly better than that with added FeS_2 , and the overlapping of curves is significantly reduced. The temperature of C_2H_4 in the coal sample with a sulfur content of 4% was increased to 70°C for the first time, which indicated that it had a significant promoting effect on the spontaneous combustion of coal. At the same coal temperature, with the increase of the sulfur content, C_2H_4 production usually increases first and then decreases, and the C_2H_4 production reaches its maximum when the sulfur content is 4%.

6. The Effect of the Shortest Spontaneous Combustion Period of Coal

The shortest spontaneous combustion period in coal experiments refers to the time from coal exposure to air to coal spontaneous combustion, which can better characterize the risk of coal spontaneous combustion [27, 28]. The variation trend of the coal spontaneous combustion period with sulfur content is shown in Figure 9.

The data in Figure 8 show that with the increase of the sulfur content, the coal spontaneous ignition period generally exhibits a decreasing trend, indicating that sulfur plays a promoting role in the natural combustion of coal. In addition, for the coal samples with added FeS_2 , the minimum value is 14.23 when the sulfur content is 3%, and for the coal samples with added FeS , the minimum value is 13.24 d when the sulfur content is 4%. The promoting effect of the added FeS is greater than that of the added FeS_2 . Therefore, in the daily fire prevention work, it is necessary to detect the content and type of sulfur in the coal seam at any time to prevent the occurrence of the natural combustion of coal.

7. The Influence of Distribution of Main Active Groups in Coal

The distribution characteristics of coal samples with different contents of sulfide functional groups and the variation characteristics of each functional group during oxidation are analyzed by *in situ* Fourier transform infrared (FTIR) spectroscopy. Then, the real-time change rule of the groups in the reaction process of coal is obtained, which provides the basis of the microstructure distribution and change for the study of the effect of different sulfides on the distribution of the main active groups in coal [29, 30]. The *in situ* FTIR spectroscopy analysis was performed on a Nicolet 6700 FTIR spectrometer (Thermo Fisher Scientific Inc., Waltham, MA, USA) equipped with a smart diffuse reflectance accessory, sample reaction tank, temperature control device, gas supply device, and water cooling device, as shown in Figure 10.

The infrared spectra of the functional groups of coal samples with different sulfides in the coal oxidation process that change with time are shown in Figure 11.

The chemical activity of coal is determined by its composition and content of functional groups. The content of each functional group in coal can be determined by quantitative analysis of infrared spectra of coal samples. The quantitative analysis method of an infrared spectrum is mainly based on Lambert-Beer law, expressed as follows:

$$A(\nu) = \lg \frac{1}{T(\nu)} = K(\nu)bc, \quad (1)$$

where $A(\nu)$ is the absorbance of the sample spectrum at the wavenumber ν , $T(\nu)$ is the transmittance of the spectrum of the sample at the wavenumber ν , $K(\nu)$ is the absorbance coefficient of sample at the wavenumber ν , b is the thickness of the sample, and c is the concentration of the sample. There are two kinds of

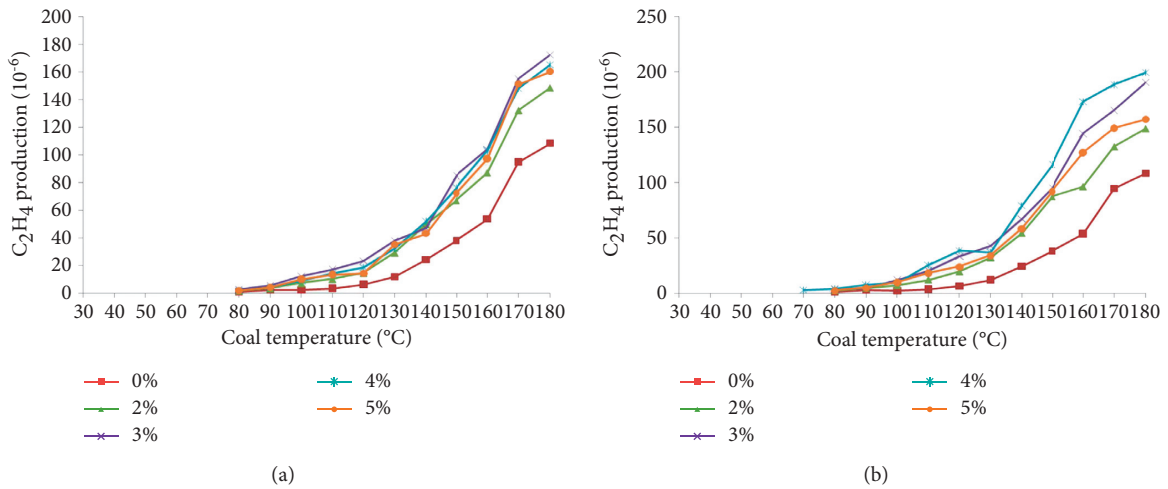


FIGURE 8: Ethylene (C_2H_4 generation) rules of coal samples with different sulfur contents in the process of programmed heating (a) with FeS_2 and (b) with FeS .

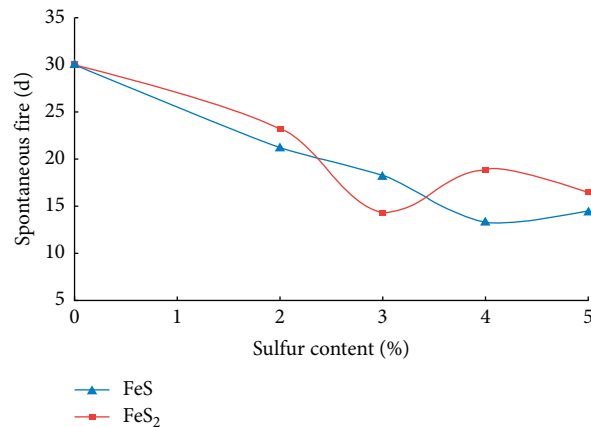


FIGURE 9: The variation trend of the shortest spontaneous combustion period of coal with the sulfur content.

quantitative analysis methods based on Lambert-Beer law: one is based on peak height; the other is based on peak area. The peak area value of the infrared absorption spectrum is less affected by the factors of sample and instrument than the peak height value. Therefore, in this study, the method of peak area is used to quantitatively analyze the content of each functional group in the coal samples.

The peak area values of the main functional groups of the coal samples with different sulfur contents at different temperatures were obtained by the fitting method. As shown in Table 3, the main functional groups in the coal structure include aromatic hydrocarbons, aliphatic

hydrocarbons, and various oxygen-containing functional groups (mainly hydroxyl and carbonyl groups).

The peak area of aliphatic hydrocarbon and aromatic hydrocarbon of the FeS coal samples generally increased first and then decreased with the sulfur content, while the peak area of the hydroxyl and carbonyl groups decreased first and then increased, reaching its maximum value when the sulfur content was 4%. With the addition of FeS_2 , the peak area of the aliphatic hydrocarbon increased first and then decreased with the sulfur content, the peak area of the aromatic hydrocarbon increased first and then decreased with the sulfur content, and the peak area of the hydroxyl



FIGURE 10: Fourier transform infrared spectroscopy *in situ* testing system equipped with a smart diffuse reflectance accessory.

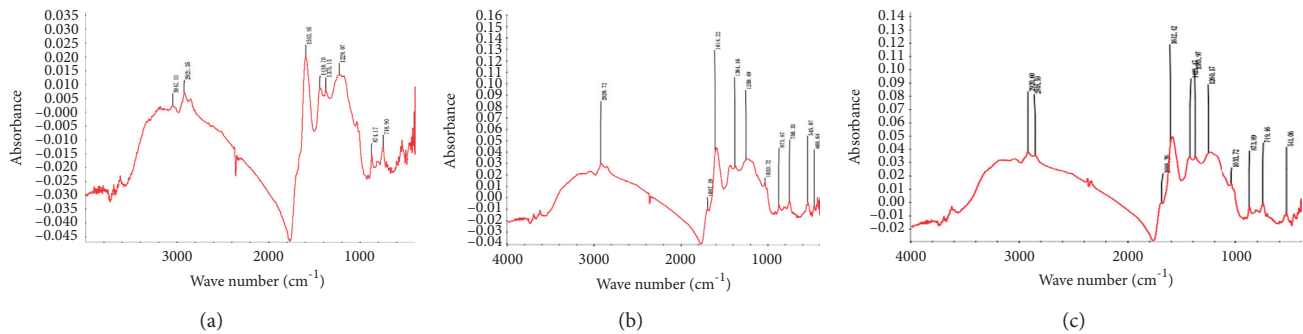


FIGURE 11: Infrared spectra of coal samples at 30°C: (a) raw coal sample; (b) coal sample with 2% FeS; (c) coal sample with 2% FeS₂.

TABLE 3: Infrared absorption peak area values of the main functional groups in each coal sample at 30°C.

Name of added sulfide	Sulfur content (%)	Aliphatic hydrocarbon-CH ₃ /-CH ₂ /-CH	Aromatic hydrocarbon C=C	Oxygen-containing functional group		
				-OH	C=O	C-O
Nothing	0	10.161	5.592	15.531	4.762	7.418
	2	12.452	2.409	17.108	4.762	7.581
	3	18.576	10.369	26.345	3.355	13.191
	4	20.850	12.553	41.493	4.762	14.316
	5	12.308	6.324	19.467	1.497	6.945
FeS ₂	2	13.432	7.579	21.908	2.244	7.780
	3	11.894	7.410	18.865	2.464	9.979
	4	12.999	9.518	20.578	3.412	12.897
	5	14.630	7.577	23.372	2.948	10.033

and carbonyl groups increased first and then decreased, reaching its maximum value when the sulfur content was 4%.

8. Conclusion

From the study of the effect of various sulfides on the physical structural properties of coal, such as porosity and microstructure, as well as its spontaneous combustion tendency, spontaneous combustion mark gas, and spontaneous combustion period, the following conclusions are drawn:

(1) Sulfide can expand coal and improve its pore structure. The true density decreases with the increase of the sulfur content, while the porosity

increases with the increase of the sulfur content. After adding FeS₂ and FeS powder to the raw coal sample, the number of fine particles on the surface increases significantly. After the oxidation and temperature increase, the lamellar structure is clearly disintegrated, and the block of coal is broken into several fine particles. The thin layer of fine particles loosens the structure of the coal seam, increases the air leakage velocity and oxygen content in micropores, and further promotes the spontaneous combustion of coal

(2) The addition of sulfur promotes the low-temperature oxygen absorption of coal. The promoting effect of FeS on the spontaneous combustion tendency of coal is slightly greater than that of FeS₂. With the increase

of the sulfur content, oxygen uptake increases first and then decreases, and there is a sulfur content level that enables the coal to have its maximum oxygen uptake value. It is preliminarily determined that the optimal sulfur content of the spontaneous combustion of coal samples with the addition of FeS₂ and FeS is 3 and 4%, respectively

- (3) Under the same coal temperature condition, the CO production of the coal samples increases first and then decreases with the increase of the sulfur content. When there are two kinds of additives with a sulfur content of 3 and 4%, respectively, the coal sample produces the largest amount of CO, and the law of CO generation is basically consistent with the change law of oxygen intake. The C₂H₄ production of the coal samples with various sulfur contents is greater than that of the raw coal samples, and there are many overlapping points. When the sulfur content of the coal samples with FeS₂ and FeS is 3% and 4%, respectively, the C₂H₄ production is the largest
- (4) Sulfur promotes the spontaneous combustion of coal, and the effect of adding FeS is greater than that of adding FeS₂
- (5) The peak area of the aliphatic hydrocarbon and aromatic hydrocarbon of FeS coal samples generally increased first and then decreased with the sulfur content, while the peak area of the hydroxyl group and carbonyl group decreased first and then increased and reached the maximum value when the sulfur content was 4%. With the addition of FeS₂, the peak area of the aliphatic hydrocarbon increased first and then decreased with the sulfur content, the peak area of the aromatic hydrocarbon increased first and then decreased with the sulfur content, and the peak area of the hydroxyl and carbonyl groups increased first and then decreased, reaching its maximum value when the sulfur content was 4%

Data Availability

The data used to support the findings of this study are available from the corresponding author upon request.

Conflicts of Interest

The author declares that there are no conflicts of interest.

References

- [1] B. Nie, X. Liu, L. Yang, J. Meng, and X. Li, "Pore structure characterization of different rank coals using gas adsorption and scanning electron microscopy," *Fuel*, vol. 158, pp. 908–917, 2015.
- [2] J. Xie, J. Xie, G. Ni, S. Rahman, Q. Sun, and H. Wang, "Effects of pulse wave on the variation of coal pore structure in pulsating hydraulic fracturing process of coal seam," *Fuel*, vol. 264, Article ID 116906, 2020.
- [3] Y. Tang, X. He, A. Cheng et al., "Occurrence and sedimentary control of sulfur in coals of China," *Journal of China Coal Society*, vol. 40, no. 9, pp. 1977–1988, 2015.
- [4] L. Zhang, *The Study Of Influence On Coal Spontaneous Combustion Characteristics By Organic Sulfide*, China University of Mining and Technology, Xuzhou, China, 2016.
- [5] J. Xu, H. Xue, J. Deng, W. Hu, and X. Zhang, "Investigation into the surface active groups of coal," *Journal of Coal Science & Engineering*, vol. 7, no. 1, pp. 88–96, 2001.
- [6] L. Ge, H. Xue, J. Deng, and X. Zhang, "Study on the oxidation mechanism of active groups of coal," *Coal conversion*, vol. 24, pp. 23–28, 2001.
- [7] X. Qi, D. Wang, H. Xin, and G. Qi, "In situ FTIR study of real-time changes of active groups during oxygen-free reaction of coal," *Energy & Fuels*, vol. 27, no. 6, pp. 3130–3136, 2013.
- [8] C. Xu, X. Zhang, and S. Zhang, "The summary of comprehensive prevention and control technology of spontaneous combustion in high-sulfur coal seam," *China Mining Magazine*, vol. 28, no. 08, pp. 165–169, 2019.
- [9] H. Jia, C. Zhai, X. Zhao, X. Yanwei, and Z. Minyuan, "Analysis on spontaneous combustion characteristics of coal adding associated sulfide," *Journal of Safety Science and Technology*, vol. 14, no. 10, pp. 106–111, 2018.
- [10] M. Yu, Z. Yuan, and T. Chu, "Experimental study on oxidation characteristics of coal with different spontaneous combustion tendency," *Fire Safety Science*, vol. 25, no. 3, pp. 119–126, 2016.
- [11] C. Wang, J. Deng, and Y. Zhang, "Effect of micro structure characteristics on coal spontaneous combustion," *Journal of Xi'an University of Science and Technology*, vol. 36, no. 01, pp. 8–12, 2016.
- [12] Z. Hongfen, G. Erxin, C. Xiaoguo, and S. Fang-fang, "Relation between quantity of coal absorbing oxygen and internal and external influence factors," *Coal Technology*, vol. 34, no. 10, pp. 196–198, 2015.
- [13] H. Zhu, L. Qu, and J. Shen, "Experimental study on effects of different factors on coal oxygen absorption and enthalpy," *China Safety Science Journal*, vol. 22, no. 10, pp. 30–35, 2012.
- [14] J. Li, Z. Li, Y. Yang, J. Niu, and Q. Meng, "Room temperature oxidation of active sites in coal under multi-factor conditions and corresponding reaction mechanism," *Fuel*, vol. 256, 2019.
- [15] S. Sharon, M. Maria, E. Mark et al., "Pore characteristics of Wilcox group coal, U.S. Gulf coast region: implications for the occurrence of coalbed gas," *International Journal of Coal Geology*, vol. 139, no. 1, pp. 80–94, 2015.
- [16] L. Wang, F. Sun, J. Gao, X. Pi, Z. Qu, and G. Zhao, "Adjusting the porosity of coal-based activated carbons based on a catalytic physical activation process for gas and liquid adsorption," *Energy & Fuels*, vol. 32, no. 2, pp. 1255–1264, 2018.
- [17] Y. Sun, Z. Cheng, J. Xu, Y. Cong, and Y. Zheng, "Experimental study on pore structure evolution of coal in macroscopic, mesoscopic, and microscopic scales during liquid nitrogen cyclic cold-shock fracturing," *Fuel*, vol. 291, pp. 120–150, 2021.
- [18] M. J. Mavor and W. D. Gunter, "Secondary porosity and permeability of coal vs. gas composition and pressure," *SPE Reservoir Evaluation and Engineering*, vol. 9, no. 2, pp. 114–125, 2007.
- [19] W. Lin and A. R. Kocscek, "Gas sorption and the consequent volumetric and permeability change of coal I: experimental," *Transport in Porous Media*, vol. 105, no. 2, pp. 371–389, 2014.
- [20] W. Zhao, K. Wang, L. Wang et al., "Influence of matrix size and pore damage path on the size dependence of gas adsorption capacity of coal," *Fuel*, vol. 283, Article ID 119289, 2021.

- [21] R. Qin, L. Zhou, Yu Gan, and Y. Huang, "Oxidation characteristic and active group evolution of oil-immersed coal," *Environmental Earth Sciences*, vol. 80, no. 12, p. 433, 2021.
- [22] X. Zhong, L. Kan, H. Xin, B. Qin, and G. Dou, "Thermal effects and active group differentiation of low-rank coal during low-temperature oxidation under vacuum drying after water immersion," *Fuel*, vol. 236, pp. 1204–1212, 2019.
- [23] W. Joe and D. Frank, "Origins and functions of microporosity in activated carbons from coal and wood precursors," *Fuel*, vol. 70, no. 5, pp. 655–661, 1991.
- [24] H. Fujitsu, I. Mochida, T. V. Verheyen, G. J. Perry, and D. J. Allardice, "The influence of modifications to the surface groups of brown coal chars on their flue gas cleaning ability," *Fuel*, vol. 72, no. 1, pp. 109–113, 1993.
- [25] M. C. Turrini, P. Visintainer, E. B. Khomyakova, M. V. petrova, and A. Nodenski, "Sorption and desorption of gases(CH₄, CO₂) on hard coal and active carbon at elevated pressures," *Fuel*, vol. 99, no. 11, pp. 1243–1246, 1998.
- [26] J. Han, H. Zhang, W. Song, Li. Sheng, and T. Lan, "Coal and gas outburst mechanism and risk analysis of tectonic concave," *Journal of China Coal Society*, vol. 36, no. 1, pp. 108–113, 2011.
- [27] H. Yao, H. Wang, Y. Li, and L. Jin, "Three-dimensional spatial and temporal distributions of dust in roadway tunneling," *International Journal of Coal Science & Technology*, vol. 7, no. 1, pp. 88–96, 2020.
- [28] P. Lu, G. X. Liao, J. H. Sun, and P. D. Li, "Experimental research on index gas of the coal spontaneous at low-temperature stage," *Journal of Loss Prevention in the Process Industries*, vol. 17, no. 3, pp. 243–247, 2004.
- [29] J. Li, Z. Li, Y. Yang, and C. Wang, "Study on oxidation and gas release of active sites after low-temperature pyrolysis of coal," *Fuel*, vol. 233, pp. 237–246, 2018.
- [30] L. Jinhu, L. Zenghua, Y. Yongliang, and W. Chaojie, "Study on oxidation and gas release of active sites after low-temperature pyrolysis of coal," *Fuel*, vol. 233, pp. 237–246, 2018.

Research Article

Elimination of Coal and Gas Outburst Dynamic Disasters in Dengfeng Coalfield through Gas Extraction Based on Extremely Thin Protective Coal Seam Mining

Haibo Liu , Xucheng Xiao, and Zhihang Shu

School of Safety Engineering, China University of Mining and Technology (CUMT), Xuzhou 221116, China

Correspondence should be addressed to Haibo Liu; liuhaibo-8888@163.com

Received 25 April 2021; Revised 18 June 2021; Accepted 31 August 2021; Published 16 September 2021

Academic Editor: Juan Sagaseta Sagaseta

Copyright © 2021 Haibo Liu et al. This is an open access article distributed under the Creative Commons Attribution License, which permits unrestricted use, distribution, and reproduction in any medium, provided the original work is properly cited.

No. 2₁ coal seam is a full-thickness structured soft coal in Dengfeng coalfield. The coal seam gas-bearing capacity is high, and the permeability is poor, thus resulting in serious coal and gas outburst dynamic disasters. According to the gas geological conditions of Baoyushan Mine, No. 1₇ coal seam without outburst danger, which is 0.5 m thick and 23.4 m under No. 2₁ coal seam, was mined in advance as the lower protective seam. At the same time, a gas extraction roadway was constructed in No. 2₁ coal seam floor. Cross-layer boreholes were constructed to extract the pressure relief gas of No. 2₁ coal seam for comprehensive treatment of mine gas. The mobile deformation of the overburden coal and rock mass after mining No. 1₇ coal seam, the fracture development characteristics of No. 2₁ coal seam, the pressure relief gas migration of the coal seam, the gas extraction, and the outburst danger elimination were studied. The research findings showed the following: (1) after mining No. 1₇ coal seam, the overburden hard and extremely thick limestone roof sagged slowly, albeit leading to no craving zone. (2) The permeability of No. 2₁ coal seam was increased by about 394 times, from 0.0012 mD to 0.4732 mD. (3) After the extraction of pressure relief gas through the gas extraction roadway on the floor through the cross-layer borehole, the gas pressure of No. 2₁ coal seam decreased from 1.17 MPa to 0.12 MPa, while the gas content decreased from 9.74 m³/t to 3.1 m³/t, which suggested that the coal and gas outburst dynamic danger of No. 2₁ coal seam was totally eliminated and the goal of safe and efficient mining in the mine was realized.

1. Introduction

Coal is the major energy of China, which accounts for more than 60% of the primary energy [1, 2]. With the rapid development of Chinese economy, the coal demand also increased dramatically. From 2001 to 2020, China's coal output soared from 1.106 billion tons to 3.7 billion tons. Limited by the conditions of coal resources, 90% of coal resources are obtained through underground mining. The mining depth of coal increases at an annual rate of 10~30 m. Currently, the average mining depth of the coal resources in China has exceeded 600 m, with the deepest one exceeding 1,500 m. With the intensification of coal mining, the mining depth keeps on increasing, resulting in growing ground stress on the working seam, increasing coal seam gas pressure and gas emission amount, and increasing complexity and danger of gas disasters [3]. Many low gas mines

have been turned into high gas ones, and the high gas ones have been turned into coal and gas outburst ones. In China, the coal mines had a tendency to increase gas grade and increase the number of outburst mines. In particular, the mines in central China are characterized by in-depth mining, high coal seam gas content, high gas pressure, complex geographical conditions, and soft and crushed coal seam structure, so the coal mines are faced with serious gas disasters [4–7].

Located in about 60 km southwest of Zhengzhou, Henan Province, Dengfeng coalfield is about 70 km long and 8~15 km wide and covers an area of about 1,000 km². The coalfield stratum can be divided into Permian System Shanxi Group and Taiyuan Group. No. 2₁ coal seam under the bottom of Shanxi Group is stable. It is the major minable coal seam of the coalfield. No. 2₁ coal seam features a thickness of about 0~26.73 m and an average thickness of

4.57 m. Thus, it is a medium-thickness coal seam. The coal rank is the meager coal. Affected by the extrusion, rubbing, and other tectonic movements, No. 2₁ coal seam is characterized by full-thickness constructed soft coal. Most coals are of types III~V. The coal strength and permeability are extremely low, the coal seam gas content is high, and the coal seam gas extraction effect is poor. Thus, the gas disasters are extremely serious. For a long time, the gas disasters of No. 2₁ coal seam in Dengfeng coalfield, especially the coal and gas outburst disasters, have greatly limited the development of the local coal mine enterprises and seriously threatened the safety of miners. In order to ensure the mining safety of No. 2₁ coal seam in the deep area of the mine, the regional outburst prevention measures should be adopted to eliminate the coal and gas outburst dynamic disasters of No. 2₁ coal seam.

Many mines in China have achieved remarkable results by adopting the measure of protective coal seam mining to prevent and control coal and gas outburst dynamic disasters [8–11]. Concerning the gas geological conditions of No. 2₁ coal seam of Dengfeng coalfield, the adoption of protective seam mining combined with stress-relief gas extraction technique is the most effective, simplest, and most economic measure to prevent the coal and gas outburst disasters [12–16]. The technique can eliminate the coal and gas outburst dynamic disasters and finally realize the goal of safe and efficient mining. However, mines adopting the measure must be equipped with the condition of coal seam group occurrence. In other words, within the effective protection vertical interval, there should be a coal seam free of outburst danger whose thickness is no smaller than 0.5 m acting as the protective seam. According to the geological data of Dengfeng coalfield, the gas content of No. 1₇ coal seam, which is 23.4 m below No. 2₁ coal seam and whose thickness averages 0.5 m, is extremely low, so it is the coal seam free of outburst danger and can be first mined as the lower protective seam. At the same time, the adoption of the gas extraction roadway during the construction in the chassis of No. 2₁ coal seam and the extraction of the pressure relief gas of No. 2₁ coal seam in the cross-layer boreholes can eliminate the coal and gas outburst dynamic disasters. However, there is a layer of 7.3 m thick hard limestone between No. 1₇ coal seam and No. 2₁ coal seam, which is unfavorable to the pressure relief and permeability increase effect of No. 2₁ coal seam. Therefore, under the condition, it is necessary to conduct an experiment and field study to see whether the technique of mining extremely thin No. 1₇ coal seam combined with the pressure relief gas extraction technique can eliminate the coal and gas outburst dynamic dangers of No. 2₁ coal seam. The Baoyushan Mine in Dengfeng coalfield was adopted as the research object. Through the experiment and field test, the gas parameters of No. 2₁ coal seam were obtained, and the outburst danger was analyzed. Through studying the overburden coal-rock mass displacement and distortion, the mining fracture development characteristics of No. 2₁ coal seam, and the coal seam pressure relief gas migration and convergence rules, the authors hope that the research findings can guide Baoyushan Mine to conduct site protective seam mining. The research of the extremely thin

protective seam mining combined with the pressure relief gas extraction under the hard and extremely thick limestone condition is the first of its kind. The research findings are of vital significance to the prevention and control of coal and gas outburst dynamic disasters during the in-depth mining of No. 2₁ coal seam in Dengfeng coalfield.

2. Geological Background

Baoyushan Mine is located in the westmost Dengfeng coalfield and the junction of Ruyang County, Linru County, and Yichuan County. It is about 100 km away from Zhengzhou City, capital city of Henan Province. Its geographical coordinates are 112°34'37.4" ~ 112°41' east longitude and 34°18'02.4" ~ 34°21'54.4" north altitude. Its traffic situation is shown in Figure 1. The mine is about 5~11 km long and 1.1~3.0 km wide and covers an area of 21.2186 km². It is a coal and gas outburst mine with a design production capacity of 600,000 ton per annum. No. 2₁ coal seam is the major mining area of the mine.

The mine adopts the inclined shaft and the vertical shaft mixed exploitation method, the full-seam mining method, and the fully caving roof management. There are two major minable coal seams, namely, No. 2₁ coal seam and No. 1₇ coal seam. The composite histogram of the mine is shown in Figure 2. No. 2₁ coal seam is about 0~18.98 m thick, which is averaged at 3.1 m. The coal bed pitch is 30°. The gas content of No. 2₁ coal seam is high. The gas content is above 8 m³/t. The mine mainly treats the gas outbursts through the drainage borehole, bleeder off hole, and increase of the wind amount for the mining working face. However, due to high gas content of No. 2₁ coal seam, the coal seam is soft and has poor permeability. As a result, the gas extraction effect is poor. During the mining process, the gas density in the ventilation roadway often exceeds the limit, which seriously threatens the safe production of the mine. Even if the wind amount for the working face is increased to above 1,000 m³/min, the problem still remains unresolved. During the blasting process, the gas exceeds the limit more seriously. At the same time, due to the large wind amount for the working face, the working face is filled with the coal dust, thus worsening the working environment of miners. It is apt to say that gas disasters directly restrain the safe and efficient production of the mine.

In order to solve the difficulties facing the prevention and control of gas disaster, based on Detailed Rules of Coal and Gas Outburst Prevention and Control and the conditions of the coal seam, the authors decided to adopt the protective seam mining combined with pressure relief gas extraction technique. No. 1₇ coal seam of the mine was adopted as the lower protective seam for prior mining. At the same time, the gas extraction roadway was placed in the proper position of the chassis of No. 2₁ coal seam. The pressure relief gas was extracted from No. 2₁ coal seam through the boreholes. The thickness of No. 1₇ coal seam in Baoyushan Mine is about 0.12~1.1 m, which averages 0.5 m. It belongs to the extremely thin coal seam and the coal seam gas content is low, which is about 0.5 ~ 1.5 m³/t, so No. 1₇ coal seam has no outburst danger. No. 1₇ coal seam is mined



FIGURE 1: Maps showing the traffic situation of the study area. (It is reproduced from [17].)

Thickness (m)	Rock columnar	Lithology
3.1		No.2 ₁ coal seam
2.5		sandy mudstone
11.0		fine sandstone
2.6		sandy mudstone
7.3		L ₇ limestone
0.5		No.1 ₇ coal seam
0.8		mudstone

FIGURE 2: The composite histogram of Baoyushan Mine.

using spiral drilling machine and adopts the gradual sagging method to manage the roof [17]. The average mining height of No. 1₇ coal seam is 0.5 m.

3. Parametric Measurement and Outburst Danger Evaluation of No. 2₁ Coal Seam

3.1. Parametric Measurement of No. 2₁ Coal Seam

3.1.1. *Industrial Analysis and Absorption Performance Experiment Results.* The coal absorption performance experiment was based on the coal’s gas absorption theory. Generally speaking, the absorption constants, *a* and *b*, are the two indexes evaluating the coal’s gas absorption performance. The measurement of coal’s gas absorption constants was conducted in the lab according to the national

standard, Measurement Method of Coal’s Gas Absorption Amount. First, the sample of No. 2₁ coal seam was obtained from Baoyushan Mine. Using the HCA high-pressure volume method, the gas absorption experiment devices, and 5E-MAG6600 full-automatic industrial analyzer, the gas absorption constants, moisture, ash content, and volatile components of No. 2₁ coal seam were measured, respectively. The experiment devices are shown in Figure 3. The actually measured value of *a*, an absorption constant of No. 2₁ coal seam, was 28.834 m³/t; the actually measured value of *b*, the other absorption constant, was 0.835 MPa⁻¹; the moisture of No. 2₁ coal seam was 1.12%; the ash content was 8.98%; and the volatile components were 13.03%.

The coal’s porosity refers to the ratio of the bulk volume of the hole to the bulk volume of the coal. This index decides the absorbability, permeability, and strength of coal and the gas migration characteristics within the coal. The porosity of No. 2₁ coal was calculated through the actually measured true and false proportion of No. 2₁ coal sample. The result showed that the porosity of No. 2₁ coal was 2.82%.

3.1.2. *Coal Structure, Gas Diffusion Initial Velocity, and Firmness Coefficient.* Detailed Rules of Coal and Gas Outburst Prevention and Control clearly divides the coal destruction types into five. I and II are the nontectonic coal without outburst dangers. III, IV, and V coal are the tectonic coal; they are basically corresponding to the tectonically crashed coal, the fractionalized coal, and the mylonitic coal. The site observation of No. 2₁ coal seam in Baoyushan Mine shows that No. 2₁ coal seam has the following characteristics: the coal mass is mainly powdery and seldom granulous or flaky. It lacks luster and has no bedding. Its strength is low and can be twiddled into powder by hand. The protogenesis structure of the coal has been seriously damaged. The lump coal formed through press of the pulverized coal is mixed in the coal mass now and then. The strength is low, and it can be fragmented by the press of a finger. It belongs to the full-thickness tectonic coal, and the destruction type of its coal mass belongs to IV-V coal.

The WT-1 gas diffusion rate tester and the coal firmness coefficient tester were employed to test the gas diffusion initial velocity and the coal firmness coefficient of No. 2₁ coal seam. The experiment devices are shown in Figure 3. The actually measured gas initial velocity of No. 2₁ coal seam in Baoyushan Mine was 12~27 mmHg, and the firmness coefficient of the coal mass was 0.1~0.18.

3.1.3. *Gas Pressure and Gas Content of No. 2₁ Coal Seam.* Seam gas pressure refers to the acting force generated by the free thermal motion of the gas molecules within the hole of the coal seam, namely, the gas pressure exerted on the hole wall. The gas pressure of the coal seam is an important index to evaluate the outburst danger and the gas content of the coal seam [18]. At the same time, the gas pressure is also the basic parameter which decides the gas migration power and the potential of gas power. It plays a guiding role in the research and evaluation of gas emission, gas migration, gas extraction, and gas outburst [13, 19–22].

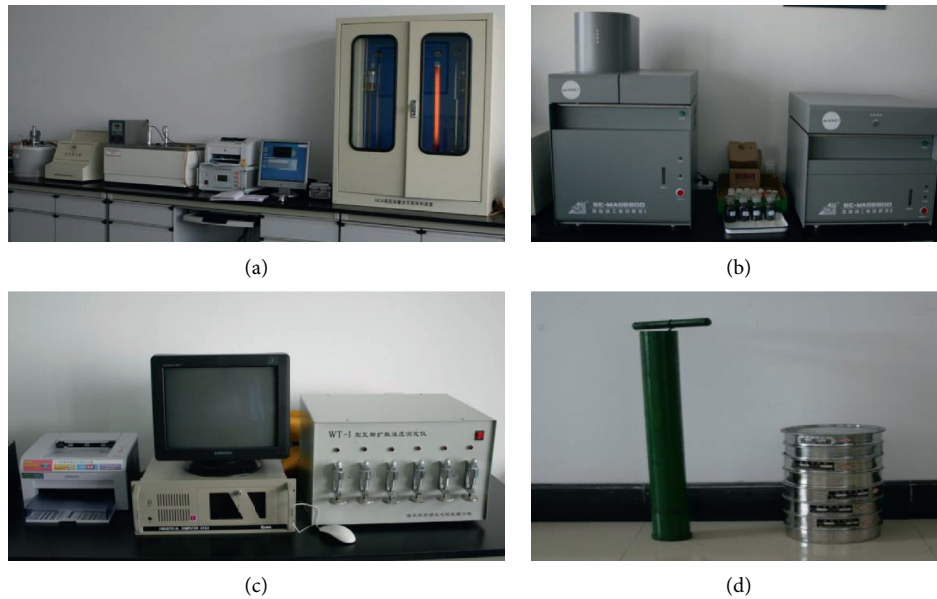


FIGURE 3: Instruments used in the determination of coal seam gas parameters: (a) gas absorption experiment device; (b) 5E-MAG6600 full-automatic industrial analyzer; (c) WT-1 gas diffusion rate tester; (d) coal firmness coefficient tester.

According to the requirements of direct measurement methods of the gas pressure of the coal seam under the coal mine, slip casting and hole sealing pressure measurement method was adopted to test the gas pressure of No. 2₁ coal seam in Baoyushan Mine. The piezometer tube with the holder was installed to the predetermined pressure depth under the mine. The porthole was sealed with the chuck and the quick-drying cement. The slip casting tube was installed. The use amount of the puff and nonshrink cement was determined by the depth of hole sealing. The hole sealing cement paste was prepared according to certain proportion (water-cement ratio was 2:1; the mixing amount of the swelling agent was 12% of the cement). The hole sealing cement paste was continuously injected into the borehole at once with the injection pump. After the slip casting lasted for 24 h, the triple-channel devices and the piezometer were installed in the porthole. Based on the natural permeation principle of gas in No. 2₁ coal seam, the gas pressure to achieve the balance in the borehole disclosed area was tested (see Figure 4). The site's actually tested gas pressure of No. 2₁ coal seam in Baoyushan Mine was 1.17 MPa.

The coal seam gas content refers to the gas content in the unit mass or volume of the original coal mass. According to the requirements of direct measurement methods of the gas pressure of the coal seam under the coal mine, a hole was drilled in Baoyushan Mine. Through hole drilling, No. 2₁ sample coal was fetched from the in-depth coal seam and was sealed in the bottle immediately. The field test of the gas desorption amount lasted for two hours. According to the gas desorption rule of the coal sample, the gas loss amount before the gas was sealed in the coal sample bottle was deducted. Then, the coal sample bottle was taken to the lab to conduct the remaining gas content test. The test devices are shown in Figure 5. The coal seam gas content is the sum of the gas loss amount, gas desorption amount, and remaining

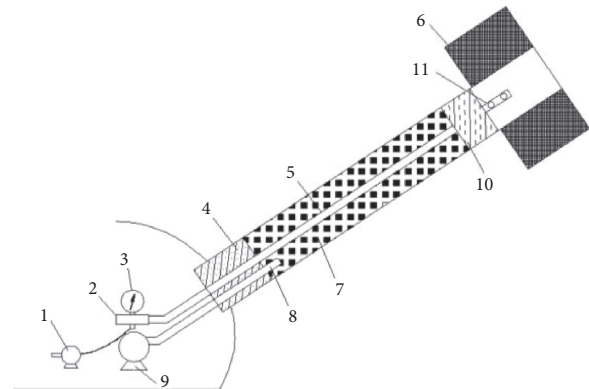


FIGURE 4: Schematic diagram of coal seam gas pressure grouting method: (1) air charging system; (2) three direct links; (3) pressure gage; (4) wooden wedge; (5) piezometer tube; (6) coal seam; (7) blocking material; (8) injection pipe; (9) grouting pump; (10) holder; (11) small holes.

gas amount. The actually measured gas content of No. 2₁ coal seam of Baoyushan Mine was 9.74 m³/t.

3.2. Analysis of the Outburst Danger of No. 2₁ Coal Seam

3.2.1. Coal and Gas Outburst Disasters of No. 2₁ Coal Seam of the Adjacent Coal Mines. The coal mines which focus on mining the shallow part of No. 2₁ coal seam and which are adjacent to the Baoyushan Mine include Pochi Mine, Poxin Mine, Lugou No. 8 Mine, and Lugou Mine. The coal mine adjacent to Baoyushan Mine in the east is Hezhuang Mine and in the west Changhong Mine. The coal mines which focus on mining the shallow include Shangzhuang Mine and Baoyushan No. 2 Mine. The relative position relationship of coal mines adjacent to Baoyushan Mine is shown in Figure 6.



FIGURE 5: Coal seam gas content measurement instrument.

According to the investigation, the gas dynamic phenomenon of the adjacent mines is shown as follows: Pochi Mine, Poxin Mine, Lugou No. 8 Mine, and Lugou Mine are the coal mines which mined the shallow part of No. 2₁ coal seam. During the mining period, the coal seam gas emission is low. In recent years, the gas grade has been identified as the low level. No coal and gas outburst dynamic phenomena have ever happened.

Shangzhuang Mine is located in the shallow part of Changhong Mine. In February 1977, there was a gas explosion accident. Two persons died and 17 were burned. In August 1981, gas combustion occurred, leading to the death of one person. It has ceased production.

Baoyushan No. 2 Mine is located in the shallow part of Changhong Mine and in the west of Shangzhuang Mine. On September 5, 2000, in +250 m horizontal transportation avenue, an extremely serious coal and gas outburst happened, leading to the death of 14 persons and the injury of 8 persons. On November 21, 2001, a gas stifling accident caused the death of two. Now, it has ceased production.

Hezhuang Mine and Baoyushan Mine are not connected with each other but are close to each other. The gas dynamic phenomena happened here several times. In 2007, it was identified as coal and gas outburst mine. On April 8, 2009, in the 11030 Transportation Avenue, a medium-size coal and gas outburst happened. The outburst coal and rock amount was 215 t and that of the gas amount was 10,089 m³.

Changhong Mine is connected with the west part of Baoyushan Mine. On October 16, 2004, during the tunneling process of the roadway on No. 2₁ coal seam, a coal and gas outburst happened. The sound of coal blasting lasted for a long time, and the gas emission was abnormal. The gas concentration rose to 1.69% within a short time. The outburst coal amount reached about 13 t, and the outburst gas was about 500 m³. The actually measured gas content near the outburst point when the outburst happened was 5.34 m³/t. In 2008, it was identified as the coal and gas outburst coal mine. On March 21, 2014, during the tunneling face of the roadway in Changhong Mine, a serious coal and gas outburst happened, leading to the death of 13 persons.

3.2.2. Gas Outburst Parameters and Outburst Danger Evaluation of No. 2₁ Coal Seam. The actually measured gas outburst parameters of No. 2₁ coal seam in Baoyushan Mine are shown in Table 1.

From Table 1, the following can be seen: (1) the gas pressure and gas content of No. 2₁ coal seam in Baoyushan Mine were high. Gas pressure was 1.17 MPa, which was higher than the critical value, 0.74 MPa, specified in Detailed Rules of Coal and Gas Outburst Prevention and Control. Gas content was 9.74 m³/t, which was higher than the critical value of 8 m³/t specified in Detailed Rules of Coal and Gas Outburst Prevention and Control and was far higher than that of No. 2₁ coal seam in the outburst point of Changhong Mine, which was 5.34 m³/t. (2) The initial velocity of gas emission of No. 2₁ coal seam was 12~27 mmHg, which was higher than the critical value of 10 mmHg. (3) The coal mass structure of No. 2₁ coal seam features the pulverized coal, which was a full-thickness tectonic soft coal. The proto-genesis structure of the coal seam suffered serious damage, and the strength is extremely low. The firmness coefficient of No. 2₁ coal seam was 0.1~0.18, and the destruction type is V. The original permeability of No. 2₁ coal seam was 0.0012 mD, so the seam permeability is extremely poor. The gas outburst parameters of No. 2₁ coal seam in Baoyushan Mine are far higher than the outburst critical indexes specified in Detailed Rules of Coal and Gas Outburst Prevention and Control, so the outburst danger is high. No. 2₁ coal seam of the adjacent coal mines underwent several coal and gas outbursts. To sum up, No. 2₁ coal seam of Baoyushan Mine is a low permeability high gas outburst coal seam.

4. Feasibility Analysis and Outburst Elimination Principle of the Extremely Thin Protective Seam Mining Combined with the Pressure Relief Gas Extraction Technique

Since No. 2₁ coal seam is characterized by strong outburst danger, we decided to adopt the protective seam mining combined with the pressure relief gas extraction technique to eliminate the coal seam outburst danger. According to the protective coal seam mining theory, the feasibility analysis of No. 1₇ coal seam acting as the lower protective seam was first conducted.

4.1. Feasibility Analysis of the Extremely Thin Protective Seam Mining

4.1.1. The Minimum Interlayer Spacing for the Lower Protective Layer Mining. According to the requirements of Detailed Rules of Coal and Gas Outburst Prevention and Control, during the lower protective seam mining, the minimum interlayer spacing not ruining the upper protective seam could be defined through the following formula: $\alpha < 60^\circ$ in the formula $H = KM \cos \alpha$, where H stands for the minimum interlayer spacing of the minable protective seam, M stands for the mining thickness of the protective seam and is set to be 0.5 m, α stands for the coal bed pitch and is set to be 30° , and K stands for the roof management

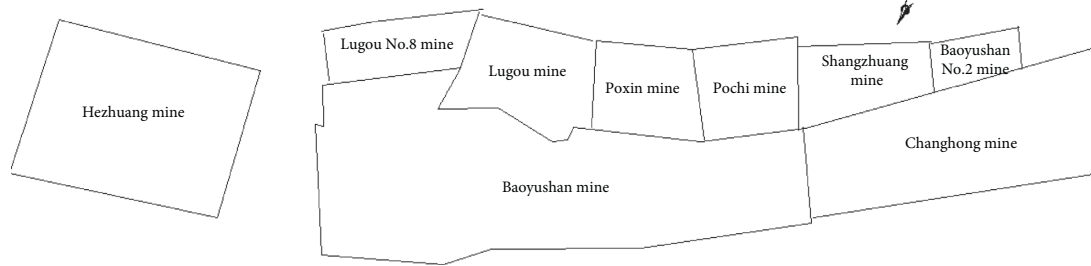


FIGURE 6: The relative position relationship of coal mines adjacent to Baoyushan Mine.

TABLE 1: Gas outburst parameters of No. 2₁ coal seam.

Gas outburst parameters	Measured value	Detailed Rules of Coal and Gas Outburst Prevention and Control	Overweight (yes or no)	Conclusion
Gas pressure (MPa)	1.17	0.74		No. 2 ₁ coal seam has serious outburst danger
Gas content (m ³ /t)	9.74	8		
Damage type of coal	IV, V	III, IV, V	Yes	
Initial speed of gas diffusion (mmHg)	12~27	10		
Solidity factor	0.1~0.18	0.5		
Dynamic phenomenon of mine gas disasters	No. 2 ₁ coal seam in the adjacent mines has experienced many coal and gas outburst accidents.			

coefficient; when the caving method is adopted to manage the roof, K is set as 10.

Through calculation, the minimum interlayer spacing, H , for mining No. 1₇ coal seam without damaging the upper No. 2₁ coal seam, was 4.3 m, which was smaller than 23.4 m, the interlayer spacing between No. 1₇ coal seam and No. 2₁ coal seam. Thus, the requirement was met.

4.1.2. The Maximum Protection Vertical Distance for the Lower Protective Layer Mining. The maximum protection vertical distance for the lower protective layer mining, S , was calculated according to the requirement of Detailed Rules of Coal and Gas Outburst Prevention and Control: $S = S_{\text{lower}}\beta_1\beta_2$. In the formula, S_{lower} stands for the maximum protection vertical distance of the protective seam, m . It is related to the working face length, L , and the mining depth, H . According to Detailed Rules of Coal and Gas Outburst Prevention and Control about S_{lower} , the following can be found: (1) When the working face depth and length of No. 1₇ coal seam are 400m and 125 m, respectively, S_{lower} is 66 m. (2) β_1 stands for the influence coefficient of the protective seam mining, $\beta_1 = M/M_0$, in which M stands for the mining depth of the protective seam, m . (3) M_0 stands for the minimum valid thickness of the protective seam mining, m . (4) The average thickness of No. 1₇ coal seam is 0.5 m, and the minimum mining depth is 0.5 m; then $\beta_1 = 1$. (5) β_2 stands for the coefficient of the interlayer hard rock. Considering that there is a 7.3 m thick hard limestone above No. 1₇ coal seam, β_2 is set to be 1 and $S = S_{\text{lower}}\beta_1\beta_2 = 66\text{m}$.

Like the lower protective seam mining of No. 2₁ coal seam, No. 1₇ coal seam has a maximum valid protection distance of 66 m and a minimum protection distance of 4.3 m. The interlayer spacing between No. 1₇ coal seam and

No. 2₁ coal seam is 23.4 m. Thus, it meets the requirement of the maximum protection seam spacing and the minimum protection distance, and it is a very ideal lower protection seam.

Therefore, the method of adopting No. 1₇ coal seam as the lower protective seam mining to protect the upper No. 2₁ coal seam and extracting the pressure relief gas in No. 2₁ coal seam through drilling holes in the roadway is feasible.

4.1.3. The Slanted Direction and Trend Protection Scope of the Lower Protective Seam Mining. The protection range on the slanted direction of the lower protective seam mining was decided according to the pressure relief angle of δ , specified in Detailed Rules of Coal and Gas Outburst Prevention and Control. Through the field test, the pressure relief angle on the slanted direction of No. 1₇ coal seam was $\delta_1 = 71^\circ$ and $\delta_2 = 89^\circ$ (see Figure 7). When the slanted mining length of the working face of No. 2₁ coal seam is designed to be 120 m, the mining length of No. 1₇ coal seam should be calculated according to the following formula: $L = 120 + 23.4/\tan 71^\circ + 23.4/\tan 89^\circ = 128.5\text{m}$. Thus, when the slanted length of the working face of No. 2₁ coal seam is 120 m, the slanted length of the working face of No. 1₇ coal seam must be larger than 128.5 m.

Through the field test, the mining pressure relief angle of No. 1₇ coal seam along its trend direction in Baoyushan Mine was $\delta_3 = 56^\circ$, and the mining interval caving valid protective angle is $\delta_4 = 60^\circ$ (see Figure 7). When the trend mining length of the working face of No. 2₁ coal seam is designed to be 500 m, the mining trend length, L , of No. 1₇ coal seam should be calculated according to the following formula: $L = 500 + 23.4/\tan 56^\circ + 23.4/\tan 60^\circ = 529.3\text{m}$. Thus, when the trend length of the working face of No. 2₁

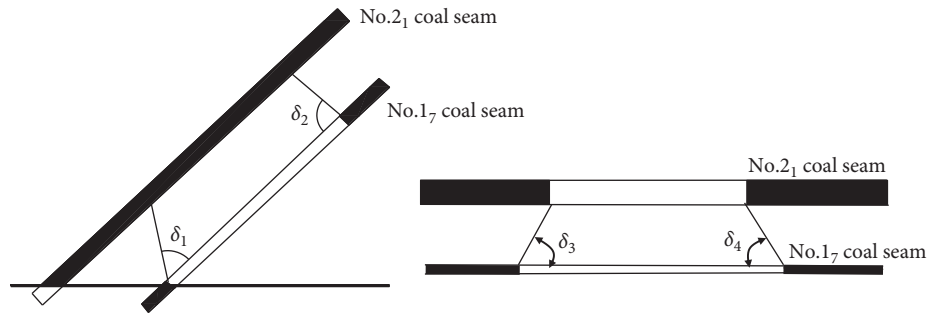


FIGURE 7: The mining pressure relief angle of the slanted direction and the trend direction.

coal seam is 500 m, the mining trend length of No. 17 coal seam must be larger than 529.3 m.

4.2. Protective Seam Mining Principle of Prevention of Coal and Gas Outburst. After mining the protective seam, a free space will be formed in the rock mass, destroying the balance of the primary rock stress, redistributing the ground stress, moving the rock mass to the goaf, and resulting in phenomena including roof caving and sagging, chassis heaving, and so on [23–25]. The coal seam and the rock mass will undergo pressure relief and dilatation and lead to fractures of different sizes. The increase of the permeability coefficient will result in the increase of the gas flow. The gas emission will cause the decrease of the coal seam gas content, pressure, and potential. The gas emission enhances the coal mass strength. In other words, the antioutburst performance of the coal is intensified. Thus, it can be seen that the cause and basis of the serious of changes are the deformation and movement of the rock (coal) seam. The larger the deformation and movement are, the more adequate the pressure relief is and the better the protection effect is. The closer to the mining seam, the better the protective effect is; otherwise, the poorer it is. The protection effect is mainly decided by the mining geological and technical conditions.

To sum up, after mining the protective seam, the change order of the stress, deformation, gas, and the other parameters of the seam to be protected is shown as follows: first, the rock seam undergoes movement and deformation. The seam to be protected shows the pressure relief phenomenon. The ground stress of the coal seam decreases. The coal seam is inflated and deformed. The permeability of the coal seam is increased. With the gas desorption in the coal seam, the gas changes from the absorption state to the unbound state. With the increase of the borehole gas flow, the gas extraction amount increases, the coal seam gas pressure decreases, the coal seam gas content is reduced, and the mechanical strength of the coal seam is increased. All the above parametric changes suggest that the protection effect of the protective seam is the comprehensive function of pressure relief, permeability increase, and gas emission [26, 27]. The pressure relief and permeability increase after the start of the protective seam mining plays the most important and decisive role in parametric changes. As long as the seam to be protected plays the role of pressure relief and permeability increase, the major parameters, including

coal mass structure, gas pressure, gas content, and coal seam permeability, follow the above order. All these parametric changes will decrease or eliminate the coal seam outburst danger.

4.3. The Function of the Pressure Relief Gas Extraction. Detailed Rules of Coal and Gas Outburst Prevention and Control specifies that, “during the protective seam mining, the pressure relief gas of the seam to be protected shall be extracted as well.” The thickness of the protective seam in Baoyushan Mine is 0.5 m, and there is a hard 7.3 m thick limestone between seams, which would definitely cause unfavorable influence to the pressure relief and permeability increase effect of the overburden No. 21 coal seam. In order to accelerate and expand the pressure relief and permeability increase function of the protective seam mining, the protective seam mining must extract the pressure relief gas of No. 21 coal seam. Such extraction might further decrease the ground stress, increase the coal strength, and reach the goal of comprehensive prevention and control of outbursts.

5. Movement and Deformation of the Overburden Coal Mass, Mining Fracture Development Characteristics of No. 21 Coal Seam, Pressure Relief Gas Migration Rule, and Gas Extraction Methods

Since the mining thickness of No. 17 coal seam is 0.5 m, the average interlayer spacing between No. 17 coal seam and No. 21 coal seam is 23.4 m, and there is a hard 7.3 m thick limestone in between, it is necessary to analyze and study the pressure relief and permeability increase effect of the overburden No. 21 coal seam after mining No. 17 coal seam, the movement and deformation of the overburden coal mass, the mining fracture development characteristics of No. 21 coal seam, and the pressure relief gas migration rules. Based on the research findings, the corresponding gas extraction methods can be adopted.

5.1. Movement and Deformation of the Overburden Coal Mass, Fracture Development of No. 21 Coal Seam, and Pressure Relief Gas Migration. Through the theoretical analysis and the field experiment, it was found that, during the mining process of No. 17 coal seam, the whole overburden coal mass

is bent, sagged, and deformed along with the hard limestone roof, but there is no craving zone formed. No. 2₁ coal seam is located within the bent and sagged zone; thus, it cannot form a vertically smooth fracture with No. 1₇ coal seam. Affected by mining No. 1₇ coal seam, No. 2₁ coal seam undergoes pressure relief and dilatational deformation. In No. 2₁ coal seam, a lot of bedding fractures are formed. In the bedding direction, the permeability of No. 2₁ coal seam is increased by a large margin.

Mining No. 1₇ coal seam leads to the destruction of the balance state of the original stress of the overburden No. 2₁ coal seam, and the deformation, movement, and fractures of the coal seam. As a result, the balance of the gas absorption and desorption will be destroyed, a lot of gas is turned from the absorption state to the free state, and the desorption gas of the coal mass expands to the fracture, leading to the dramatic increase of the gas concentration in the fractures. Thus, under the mining effect of No. 1₇ coal seam, the migration conditions of the pressure relief gas, namely, “desorption→diffusion→transfusion,” are formed.

Due to the dominant fracture distribution of bedding fracture in No. 2₁ coal seam, the pressure relief gas has good bedding migration conditions. Therefore, the pressure relief gas in the protected seam only flows in the bedding fracture.

In order to effectively and evenly extract the gas in the protected seam during the migration active period of the pressure relief gas, it is necessary to create the conditions to enable the bedding migration and convergence of the pressure relief gas. Through the special extraction roadway of No. 2₁ coal seam, the borehole was made for the extraction of the pressure relief gas. It can be seen that the gas is turned from the absorption state to the free state. Through the bedding separation fracture flow and the convergence in the borehole, and affected by the extraction negative pressure, a lot of pressure relief gas of No. 2₁ coal seam is extracted.

It should be noticed that when No. 1₇ coal seam is mined for a period of time, the overburden coal mass movement and deformation are gradually stabilized. The pressure relief effect exerted on No. 2₁ coal seam gradually disappears, the permeability of the coal seam is reduced correspondingly, and the desorbed gas will be reabsorbed by the coal mass. Thus, it is necessary to extract the gas within the valid pressure relief period of No. 2₁ coal seam and realize the goal of reducing the coal seam gas content and eliminating the coal seam outburst danger.

What is interesting in this study is that the overburden hard and extremely thick limestone roof sagged slowly but led to no craving zone. Now, let us focus on explaining this phenomenon. As the working face of No. 1₇ coal seam is mined forward, the working face is directly overhanging. Because the immediate roof of No. 1₇ coal seam is *L*₇ hard and extra-thick limestone roof, which is stable and not easy to collapse, there is no obvious movement and deformation of the overlying coal-rock mass in the early mining stage. As a large amount of coal is mined in the working face of No. 1₇ coal seam, the hard and extra-thick limestone roof of *L*₇ begins to bend and sink slowly under the action of gravity of the overlying coal and rock mass. It can be seen that the overlying coal and rock mass produce the overall slow

bending subsidence deformation, without falling zone and obvious fault zone, and No. 2₁ coal seam is in the bending subsidence zone. There are separation cracks at the boundary of soft and hard strata of the overlying coal-rock mass, but there are few vertical fracture cracks. It can be seen from the field measurement that the gas pressure of No. 2₁ coal seam drops gradually and slowly without sudden drop, which can also indicate that the roof is slowly sinking without caving phenomenon. The reason for these phenomena is that the mining height of No. 1₇ coal seam is only 0.5 m, and the roof of No. 1₇ coal seam is very hard and extra-thick limestone roof. It is found that there are many bedding tensile fractures on the surface of No. 2₁ coal seam, some of which have gone deep into the interior of the coal seam, while the number of vertical fracture fractures is few and not obvious. As the overlying strata are gradually compacted, the width and number of separation cracks between strata are reduced. A careful observation of No. 2₁ coal seam shows that the coal seam is also gradually compacted and the width and number of bedding tensile cracks in the coal seam are obviously reduced.

5.2. Extraction Methods of the Pressure Relief Gas in No. 2₁ Coal Seam. Concerning the actual mining geological conditions of Baoyushan Mine and in order to accelerate and expand the pressure relief and permeability increase function of No. 1₇ coal seam, mining No. 1₇ coal seam should extract the pressure relief gas of No. 2₁ coal seam as well. During the mining process of No. 1₇ coal seam, the pressure relief gas of the overburden No. 2₁ coal seam has sound bedding migration conditions. The chassis grid drilling method can be adopted to extract the gas in the drill hole. To put it specifically, the method is to tunnel a special roadway for the gas extraction in the chassis rock seam; in the roadway, a drill site is dug at the interval of certain distance. Within the drill site, an upward drill hole is made in No. 2₁ coal seam. The drill holes are evenly distributed in the coal seam in the form of grid. Relying on the pressure relief and permeability increase effect, the gas in No. 2₁ coal seam is evenly and effectively extracted.

5.2.1. The Selection of the Special Gas Extraction Roadway. Concerning the practical geological conditions of Baoyushan Mine, No. 1₇ coal seam roof is a layer of 7.3 m thick *L*₇ limestone. The upper part is a 2.6 m thick sandy mudstone, 11 m thick silty-fine sand, 2.5 m thick sandy mudstone, and 3.1 m thick No. 2₁ coal seam. Therefore, the gas extraction roadway in the chassis should be conducted along the *L*₇ limestone roof. The distance from the extraction roadway to No. 2₁ coal seam is maintained above 10 m, and the roadway construction fracture surface is above 6 m².

5.2.2. The Layout of the Cross-Layer Borehole for the Gas Extraction Roadway. A 5 m long extraction drill site perpendicular to the extraction roadway is set up every 20 m. In the drill site, the borehole is made and the gas is extracted. Every drill site sets up a group of fan-shaped gas extraction

boreholes. The borehole features a diameter of 91 mm. Every drill site sets up seven cross-layer boreholes. The borehole space within the fully pressure relief area is 20 m and in the inadequate pressure relief area is 10 m. The borehole spacing adopts the coal seam medium thickness as the standard. The two zones of the extraction roadways tunnel the connection roadway on the interior section and the end section. The fully negative pressure ventilation is formed. The gas extraction of the upward borehole on the grid is shown in Figure 8. All the extraction boreholes must finish their construction before mining No. 1₇ coal seam. After the hole sealing, the gas extraction pipeline is switched on. After mining No. 1₇ coal seam, the coal mass of No. 2₁ coal seam undergoes dilatation, deformation, and pressure relief. The gas is thus activated. Under the joint effect of the mine negative pressure and the coal seam gas pressure, the pressure relief gas is extracted. With the decrease of the coal seam gas content, the outburst danger of No. 2₁ coal seam is eliminated.

5.2.3. Gas Extraction Devices. Two sets of 2BEC-40 gas extraction pumps are set up on the ground, whose exhaust capacity is 90 m³/min. One is in use and the other stands by. The drilling devices feature the ZYG-150, 220, and 330 drill with the drill pipe having a diameter of 50 mm~63 mm and a drill bit of 110 mm to make the boreholes for the gas extraction.

6. The Pressure Relief, Permeability Increase, and Gas Extraction Effect after Mining the Extremely Thin Protective Seam

The pressure relief and permeability increase effect of the protective seam is related to the interlayer spacing, the protective seam mining height, the interlayer lithology, and so on. Since No. 1₇ coal seam thickness of Baoyushan Mine is just 0.5 m, the interlayer space between No. 1₇ and No. 2₁ coal seam averages 23.4 m, and there is a hard 7.3 m thick limestone in between, field inspection and experiment are needed to study the pressure relief and permeability increase of the overburden No. 2₁ coal seam after mining No. 1₇ coal seam. Two indexes, namely, coal seam pressure relief, and deformation and permeability changes, are adopted to directly reflect the pressure relief and permeability increase effect of the protective seam.

6.1. The Pressure Relief and Permeability Increase Effect of the Protective Seam. The permeability of the coal seam is an important parameter to reflect the difficulty degree of the gas migration and one of the feasible indexes to evaluate the gas extraction. It is also one of the indexes to judge the coal and gas outburst danger. The original coal mass permeability of No. 2₁ coal seam is 0.0012 mD. After mining No. 1₇ coal seam, No. 2₁ coal seam undergoes pressure relief, dilatational deformation. The permeability of No. 2₁ coal seam also undergoes corresponding changes. The permeability increases greatly. By comparing the permeability before and after the pressure relief of No. 2₁ coal seam, an in-depth

understanding of the changes of No. 2₁ coal seam before and after the protective seam mining can be gained. Through the hole drill under the shaft, the actually measured permeability coefficient of No. 2₁ coal seam after mining the protective seam is increased by about 400 times, about 0.4732 mD.

The permeability of coal seam increases by nearly 400 times, and the analysis reasons are as follows: in the process of mining No. 1₇ coal seam, the overlying coal and rock mass gradually bends and sinks without caving zone and obvious fault zone. Due to the slow subsidence deformation of the overlying coal-rock mass, there are stratification fissures along the layers between different soft and hard rock strata, resulting in the expansion deformation of No. 2₁ coal seam. A large number of bedding tensile fractures are produced in No. 2₁ coal seam, so the permeability of the coal seam increases, and the pressure relief gas in No. 2₁ coal seam flows along the bedding tensile fractures formed between layers. At this time, the pressure relief gas of No. 2₁ coal seam must be strengthened to be extracted.

The site experiment suggests that, after mining No. 1₇ coal seam, the roof and chassis of No. 2₁ coal seam slowly sag along with the limestone. However, the sagging speed of No. 2₁ coal seam chassis is more quick than that of the roof. In this way, No. 2₁ coal seam is stretched. In other words, the roof and chassis of No. 2₁ coal seam undergo dilatational deformation. The relative deformation of the roof and chassis of No. 2₁ coal seam obtained through the deep point method can be employed to reflect the pressure relief and permeability increase effect of No. 2₁ coal seam. During the construction of deformation borehole, the borehole is required to enter the coal seam roof by 1.0 m. A pair of steel wedges is installed on the roof and chassis of the coal seam to fix the deep points. The steel wedges are made up of steel pipes and steel plates, which look like inverted wedge-shaped rock bolt, but they are not solid inside. A reinforcing steel bar of about 10 mm thickness is welded to the steel wedge of the coal seam roof, which goes through the steel wedge of the coal seam chassis to the porthole. The steel wedge is welded with a seamless steel tube with a diameter of about 15 mm, which is covered on the reinforcing steel bar connected with the steel wedge. The dial indicator and the micrometer calipers are used to measure the relative displacement of the steel pipe and the reinforcing steel bar. Then, the relative deformation of the coal seam roof and chassis is calculated. On 1# borehole, the deep point method is used to test the dilatational deformation of the chassis and roof of No. 2₁ coal seam. The coal thickness in 1# deformed hole is about 3.5 m. The actually measured dilatation deformation is 72 mm, and the maximum dilatational deformation ratio is $72/3,500 = 20.6\%$. The maximum dilatational deformation is found in the 20 m of the working face. This suggests that the protective seam mining results in great reduction of the ground stress of No. 2₁ coal seam. Due to the pressure relief, dilatational deformation of the coal seam within the coal layer to form the bedding fractures, it is beneficial for the migration of the pressure relief gas within the coal seam. The advance distance between the deformation of No. 2₁ coal seam chassis and roof in 1# borehole of No. 2 drill site and the working face of the protective seam is shown in Figure 9.

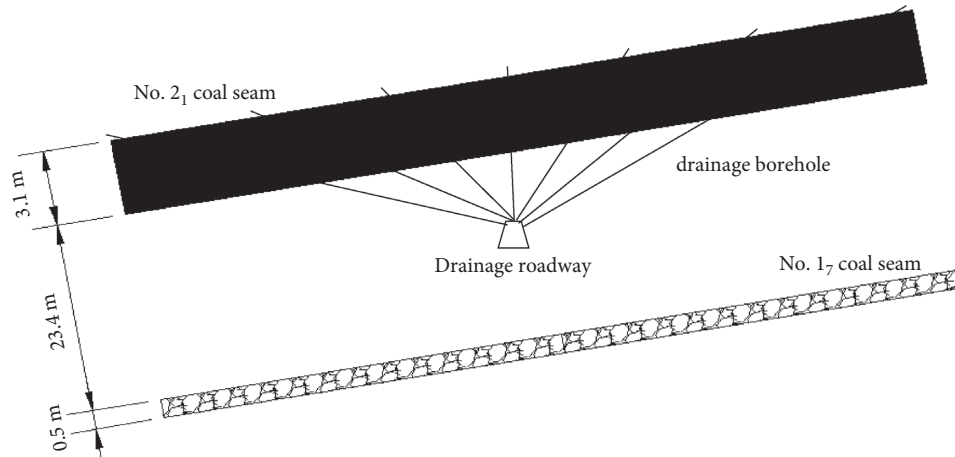


FIGURE 8: The layout of the drainage borehole for the drainage roadway.

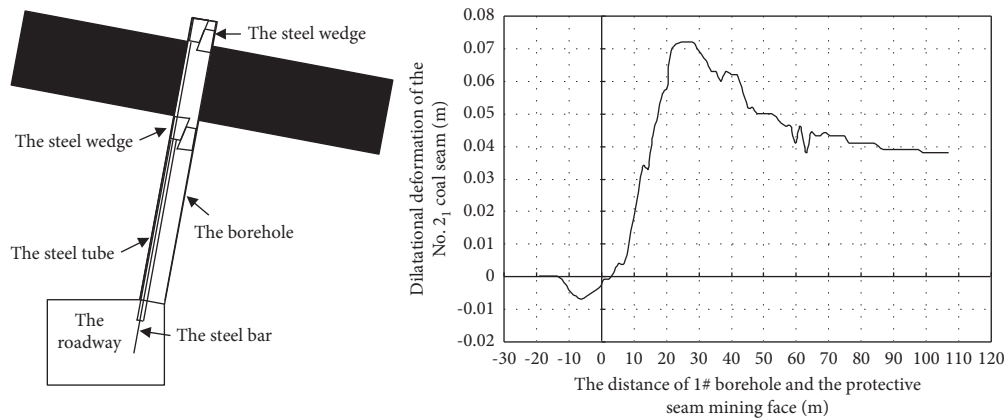


FIGURE 9: The dilatational deformation of No. 21 coal seam.

Based on the analysis of Figure 9, the following conclusions can be drawn: (1) the protective seam mining has a great influence on the deformation of No. 21 coal seam chassis and roof. With the progress of the protective seam mining, the deformation follows the change of compression, rapid dilatation, dilatational deformation reduction, and stabilization. In other words, the corresponding lower protective seam of No. 21 coal seam is compressed by the upper coal mass before the mining. From the mining start line, the coal seam experiences compression stage and expansion stage. About 20 m above the mining start line, the dilatation and the deformation of No. 21 coal seam reach the maximum. At the same time, the permeability of the coal seam increases dramatically. Within certain area, the dilatational deformation of No. 21 coal seam tends to be stable. The area is called No. 21 coal seam stable pressure relief and dilatation area. (2) The protective seam mining results in the redistribution of the stress of the overburden No. 21 coal seam. The maximum compressive deformation of No. 21 coal seam reaches 7 mm. The maximum dilatational deformation of No. 21 coal seam reaches 72 m. (3) When No. 21 coal seam is in a compressive deformation state, No. 21 coal

seam is in a pressure increase state, which might squeeze the free gas within the coal seam. The drill hole might be filled with the high concentration gas, but the gas amount is low. When the compressive deformation turns into the dilatational deformation, the coal seam will rapidly undergo pressure relief and permeability increase. The permeability will increase by a hundred times. The borehole will be filled with the high concentration gas, which will be emitted along with the pressure relief gas. It is the best time for the extraction of the pressure relief gas. With the increasing mining distance of the working face of the coal seam, since the overburden coal mass is formed and slowly sags, No. 21 coal seam is gradually compacted and the dilatational deformation of No. 21 coal seam gradually decreases. After reaching certain level, it will tend to be stable. At the moment, due to the gradual close of the fracture, the gas channels will be closed, the gas concentration within the borehole will rapidly decrease, and the gas amount will be reduced as well. This is the intermission for the gas extraction in the borehole. With the reduction of the remaining gas amount of No. 21 coal seam and the significant reduction of the gas concentration and gas amount in the borehole, the extraction of the pressure relief gas is generally completed.

TABLE 2: The investigated relief protective effect parameters of No. 2₁ coal seam.

Permeability coefficient (mD)			Gas pressure (MPa)		Gas extraction rate (%)	Gas content (m ³ /t)		Measured expansion displacement of coal seam (mm)
Original	After relief	Additional magnification	Original	After relief		Original	Remnant	
0.0012	0.473	394	1.17	0.12	68	9.74	3.1	72

6.2. The Gas Extraction Effect and the Outburst Elimination Field Verification

6.2.1. Gas Extraction Effect. Currently, the gas extraction amount in the mine is about 30~35 m³/min, the gas concentration is 33%, the pure gas amount is 10~12 m³/min, and the annual pure gas extraction amount reaches above 4 million m³. The gas extraction rate of the mine reaches 35~45%. With the intensification of the gas extraction, the gas extraction rate increases correspondingly.

In this experiment, apart from the measurement of the original gas pressure and the gas content of No. 2₁ coal seam, the remaining gas pressure and the gas content of No. 2₁ coal seam after mining the protective seam are measured. Before mining the extremely thin protective seam, the maximum value of the gas pressure of No. 2₁ coal seam reaches 1.17 MPa. The maximum gas content is about 9.73 m³/t. After the combination of the extremely thin protective seam and the pressure relief gas extraction, the maximum remaining gas pressure of No. 2₁ coal seam is 0.12 MPa, and the remaining gas content is 3.1 m³/t. The pressure relief protective effect of No. 2₁ coal seam after mining the extremely thin protective seam is listed in Table 2.

In the process of the protective seam mining, the gas pressure of the drill hole decreases gradually, and no sharp drop occurs. Therefore, it can be deduced that there is no direct fracture between the goaf of the protective seam working face and No. 2₁ coal seam. This also proves that, after mining the extremely thin protective seam working face, the overburden limestone roof sags gradually and shows no caving.

6.2.2. The Site Verification of the Outburst Elimination Effect. After the protective seam mining is combined with the pressure relief gas extraction, the blast capacity of No. 2₁ coal seam mining working face is decreased from 950 m³/min to 500 m³/min. The return air gas concentration of subroadway under the working face is decreased from the critical state to 0.3~0.5%. The absolute gas emission quantity decreases from 8.5~10 m³/min to the current level of below 3 m³/min. The absolute gas emission rate of the return air of the mining working face decreases by 70%. During the production process, the gas never exceeds the limit, which well solves the problem of excessive gas and coal dust flying during the production process. The working face output is also increased by a large margin.

In the past, the tunneling of the roadway in No. 2₁ coal seam without the mining protective seam was fulfilled by the 2*15 kW pivot axial flow fan. Under the condition of 300 m³/min wind supply, the gas concentration of the return air

reached above 0.6%. During the gas emission period, the gas often exceeded the limit. The monthly footage should not exceed 50 m. When the gas amount was high, the tunneling had to be stopped. Now, after the adoption of the mining protective seam, the gas concentration ranges within 0.15~0.3%, when the tunneling is conducted in the protected roadway with the adoption of the 2*15 kW pivot axial flow fan and the wind supply of 200 m³/min. The tunneling speed is increased from less than 50 m to about 120 m now, which not only eliminates the phenomenon of the excessive gas concentration and ensures the safe tunneling in the roadway of the mine but also alleviates the tension of production alternation and achieves good social and economic benefits.

7. Conclusions

- (1) The actually measured gas pressure of No. 2₁ coal seam of Baoyushan Mine in Dengfeng coalfield is 1.17 MPa, the gas content is 9.74 m³/t, and the gas emission initial velocity is 12~27 mmHg. The original structure of the coal has been seriously damaged. The coal mass is filled with the block coal formed by the pressed pulverized coal. The strength is low and is fragile. It belongs to the full-thickness tectonic coal. The coal destruction type belongs to IV ~ V coal. The firmness coefficient of No. 2₁ coal ranges within 0.1~0.18. The permeability rate of the original coal seam is 0.0012 mD. The permeability of the coal seam is extremely poor. The parameters of No. 2₁ coal seam gas outburst in Baoyushan Mine are far higher than the outburst critical indexes specified in Detailed Rules of Coal and Gas Outburst Prevention and Control, so the outburst danger is high and the coal and gas outburst dynamic disasters are very serious. According to the gas geological conditions of the Baoyushan Mine in Dengfeng coalfield, No. 1₇ coal seam, being about 23.4 m under No. 2₁ coal seam and having a thickness of 0.5 m, is regarded as the lower protective seam for prior mining. At the same time, the special gas extraction roadway is set up in the chassis of No. 2₁ coal seam. The borehole is made to extract the pressure relief gas of No. 2₁ coal seam to achieve comprehensive treatment of the gas.
- (2) During mining the extremely thin protective seam, the overburden coal and rock mass shows no caving zone. The whole overburden coal and rock mass bends, sags, and deforms along with the generation of the hard limestone roof. No. 2₁ coal seam is located above the extremely thin protective seam roof and the bent sagging zone. Macroscopically speaking, there are no obvious cross-layer fractures, and a

vertically smooth fracture cannot be formed between the extremely thin protective seams. Due to the function of the extremely thin protective seam, No. 2₁ coal seam undergoes pressure relief and dilatational deformation. Therefore, a lot of bedding fractures are formed in No. 2₁ coal seam. The permeability of the coal seam along the bedding direction is increased by a large margin, while the permeability vertical to the bedding direction is relatively small. After No. 2₁ coal seam obtains the pressure relief protection effect, the coal seam gas is desorbed. However, since a lot of bedding fractures are formed in the coal seam, the pressure relief gas in the coal seam flows along the bedding fractures. Concerning the distribution characteristics of the mining fractures of No. 2₁ coal seam and the sound bedding migration conditions of the pressure relief gas, the gas extraction method is adopted in the borehole in the chassis.

- (3) The field experiment results showed that, after mining No. 1₇ coal seam, the permeability rate of No. 2₁ coal seam was increased by about 394 times, from 0.0012 mD to 0.473 mD. After adopting the chassis grid borehole to extract the gas, the gas pressure of No. 2₁ coal seam decreased from 1.17 MPa to 0.12 MPa. The gas content decreased from 9.74 m³/t to 3.1 m³/t, which fully eliminates the coal and gas outburst dynamic disasters of No. 2₁ coal seam and realizes the safe and effective mining of the mine.
- (4) The adoption of No. 1₇ as the protective seam in combination with the pressure relief gas extraction technique for the comprehensive treatment of No. 2₁ coal seam can eliminate the problem threatening the safe production of the mine. The gas concentration of the return air of No. 2₁ coal seam working face is maintained within 0.3%~0.4%, which wipes out the phenomenon of excessive gas and achieves significant results for the gas treatment. In this way, the high gas outburst coal seam can be mined safely under the low gas state, and the mine achieves significant economic and safety benefits [28, 29].

Data Availability

The data used to support the findings of this study are available from the corresponding author upon request.

Conflicts of Interest

The authors declare that they have no conflicts of interest.

References

- [1] B. P. Plc, *BP Statistical Review of World Energy*, 2010.
- [2] C. Cattaneo, M. Manera, and E. Scarpa, "Industrial coal demand in China: a provincial analysis," *Resource and Energy Economics*, vol. 33, no. 1, pp. 12–35, 2011.
- [3] L. Wang and Y.-P. Cheng, "Drainage and utilization of Chinese coal mine methane with a coal-methane co-exploitation model: analysis and projections," *Resources Policy*, vol. 37, no. 3, pp. 315–321, 2012a.
- [4] Y. P. Cheng, *Mine Gas hazard Control Theory and Engineering Application*, China university of mining and technology press, Beijing, China, 2010.
- [5] S. Xue, Y. Wang, J. Xie, and G. Wang, "A coupled approach to simulate initiation of outbursts of coal and gas - model development," *International Journal of Coal Geology*, vol. 86, no. 2-3, pp. 222–230, 2011.
- [6] Y. P. Cheng, L. Wang, and X. L. Zhang, "Environmental impact of coal mine methane emissions and responding strategies in China," *International Journal of Greenhouse Gas Control*, vol. 5, no. 1, pp. 157–166, 2011.
- [7] L. Wang, Y. P. Cheng, L. Wang, P. K. Guo, and W. Li, "Safety line method for the prediction of deep coal-seam gas pressure and its application in coal mines," *Safety Science*, vol. 50, no. 3, pp. 523–529, 2012b.
- [8] Y. P. Cheng, Q. X. Yu, and L. Yuan, "Experimental research of safe and high-efficient exploitation of coal and pressure relief gas in long distance," *China University of Mining and Technology*, vol. 33, pp. 132–136, 2004.
- [9] M. Tu, N. B. Huang, and B. A. Liu, "Research on pressure-relief effect of overlying coal rock body using far distance lower protective seam exploitation method," *Mining and Safety Engineering*, vol. 24, pp. 418–426, 2007.
- [10] L. Wang, Y. P. Cheng, F. R. Li, H. F. Wang, and H. B. Liu, "Fracture evolution and pressure relief gas drainage from distant protected coal seams under an extremely thick key stratum," *Journal of China University of Mining and Technology*, vol. 18, no. 2, pp. 182–186, 2008.
- [11] L. Yuan, "Research on gas drainage technology for seam group with complicated and difficult conditions," *Coal Science and Technology*, vol. 31, pp. 1–4, 2003.
- [12] J. Brandt and R. Sdunowski, "Gas drainage in high efficiency workings in German Coal mines," in *Proceedings of the 2007 China (Huainan) International Symposium on Coal Gas Control Technology*, pp. 22–29, China university of mining and technology press, Huainan, China, 2007.
- [13] Y. P. Cheng, J. H. Fu, and Q. X. Yu, "Development of gas extraction technology in coal mines of China," *Mining and Safety Engineering*, vol. 26, pp. 127–139, 2009.
- [14] T. B. L. Daniel, B. Alireza, N. Chikezie, and A. W. David, "A review of Australia's natural gas resources and their exploitation," *Journal of Natural Gas and Science Engineering*, vol. 10, pp. 68–88, 2013.
- [15] L. Ying-ke, Z. Fu-bao, L. Lang, L. Chun, and H. Shen-yong, "An experimental and numerical investigation on the deformation of overlying coal seams above double-seam extraction for controlling coal mine methane emissions," *International Journal of Coal Geology*, vol. 87, pp. 139–149, 2011.
- [16] Q. X. Yu, Y. P. Cheng, C. L. Jiang, and S. -N. Zhou, "Principles and applications of exploitation of coal and pressure relief gas in thick and high-gas seams," *China University of Mining and Technology*, vol. 33, pp. 127–131, 2004.
- [17] H. Liu, H. Liu, and Y. Cheng, "The elimination of coal and gas outburst disasters by ultrathin protective seam drilling combined with stress-relief gas drainage in Xinggong coal-field," *Journal of Natural Gas Science and Engineering*, vol. 21, pp. 837–844, 2014.
- [18] P. D. William and J. S. Steven, "Measuring the gas content of coal: a review," *International Journal of Coal Geology*, vol. 35, pp. 311–331, 1998.

- [19] X. He, W. Chen, B. Nie, and M. Zhang, "Classification technique for danger classes of coal and gas outburst in deep coal mines," *Safety Science*, vol. 48, no. 2, pp. 173–178, 2010.
- [20] L. Liu, Y. P. Cheng, H. F. Wang, L. Wang, and X. Q. Ma, "Principle and engineering application of pressure relief gas drainage in low permeability outburst coal seam," *Mining Science and Technology*, vol. 19, no. 3, pp. 342–345, 2009.
- [21] T. Xu, C. A. Tang, T. H. Yang, W. C. Zhu, and J. Liu, "Numerical investigation of coal and gas outbursts in underground collieries," *International Journal of Rock Mechanics and Mining Sciences*, vol. 43, no. 6, pp. 905–919, 2006.
- [22] R. L. Zhang and I. S. Lowndes, "The application of a coupled artificial neural network and fault tree analysis model to predict coal and gas outbursts," *International Journal of Coal Geology*, vol. 84, pp. 141–152, 2010.
- [23] H. Guo, L. Yuan, B. Shen, Q. Qu, and J. Xue, "Mining-induced strata stress changes, fractures and gas flow dynamics in multi-seam longwall mining," *International Journal of Rock Mechanics and Mining Sciences*, vol. 54, pp. 129–139, 2012.
- [24] W. Yang, B. Q. Lin, Y. A. Qu et al., "Mechanism of strata deformation under protective seam and its application for relieved methane control," *International Journal of Coal Geology*, vol. 85, no. 3-4, pp. 300–306, 2011a.
- [25] W. Yang, B. Q. Lin, Y. Q. Qu et al., "Stress evolution with time and space during mining of a coal seam," *International Journal of Rock Mechanics and Mining Sciences*, vol. 48, no. 7, pp. 1145–1152, 2011b.
- [26] M. B. A. Díaz and C. N. González, "Control and prevention of gas outbursts in coal mines, Riosa-Olloniego coalfield, Spain," *International Journal of Coal Geology*, vol. 69, no. 4, pp. 253–266, 2007.
- [27] K. Noack, "Control of gas emissions in underground coal mines," *International Journal of Coal Geology*, vol. 35, no. 1-4, pp. 57–82, 1998.
- [28] China State Administration of Work Safety, *Detailed Rules of Coal and Gas Outburst Prevention and Control*, China Coal Industry Press, Beijing, China, 2019.
- [29] State administration of work safety (SAWS), *Protective Mining Technical Specifications. AQ 1050-2008*, China Coal Industry Publishing House, Beijing, China, 2008.

Research Article

Deflection Laws of Gas Drainage Boreholes in Interbedded Soft and Hard Seams: A Case Study at Xinzheng Coal Mine, China

Xiaoyan Sun,¹ Zhiheng Cheng ,² Liang Chen,² Zhenhua Li ,³ Hongbing Wang,⁴ and Shuaifeng Yin²

¹Chengdu University of Technology, Chengdu, Sichuan 610051, China

²School of Safety Engineering, North China Institute of Science and Technology, Beijing 101601, China

³School of Energy Science and Engineering, Henan Polytechnic University, Jiaozuo, Henan 454000, China

⁴School of Civil and Resource Engineering, State Key Laboratory of High-Efficiency Mining and Safety of Metal Mine, Ministry of Education, University of Science and Technology Beijing, Beijing, China

Correspondence should be addressed to Zhiheng Cheng; an958158@163.com

Received 10 February 2021; Revised 8 April 2021; Accepted 8 July 2021; Published 9 September 2021

Academic Editor: Jian Ji

Copyright © 2021 Xiaoyan Sun et al. This is an open access article distributed under the Creative Commons Attribution License, which permits unrestricted use, distribution, and reproduction in any medium, provided the original work is properly cited.

Coal and gas outbursts can lead to serious disasters in coal mines. The drilling of boreholes to predrain the gas is an effective measure for preventing such accidents. However, due to the complexity of the geological situation, the drilling trajectory often deviates from the design trajectory, resulting in poor gas extraction. To solve the problem of gas drainage borehole deflection, an analytic hierarchy process (AHP) model is established based on geological factors, technical factors, and human factors. The AHP model is used to rank the weights of various influencing factors, and the analysis is combined with a drilling model and engineering examples. Finally, the results show that soft and hard interlayers are the most important factors affecting the deflection of the borehole. The rock drilling model is mainly affected by the formation forces. The regularity of the change in the azimuth angle during drilling is not obvious when the angle of the encountered layer is less than some critical value. When the borehole is skewed downward, the deflection angle ranges from 0 to 4°, and the deflection of the borehole occurs mainly at the interface of the rock layers. When the angle of the encountered layer is greater than the critical value, the borehole is skewed upward, with a deflection angle of 0–6°, and the deflection occurs at the rock interface. The trajectory curve obtained by theoretical predictions from field data is found to be consistent with that of an actual project.

1. Introduction

Coal and gas outbursts can result in serious disasters in coal mines [1–5]. In response to this problem, many scholars have conducted research related to rock mechanics and gas flow [6–13]. At present, the use of drilling boreholes to predrain coal-seam gas is a common and effective measure for preventing such accidents [14, 15]. However, when drilling in soft and outburst-prone coal seams, problems such as buried drilling, injection boreholes, and stuck drills are prone to occur, and the actual drilling trajectory often deviates from the designed trajectory [16, 17]. This leads to unqualified gas control drilling, which not only wastes construction time, manpower, materials, and financial

resources but also seriously affects the gas drainage effect. Therefore, it is necessary to study the deflection law of gas drilling in soft outburst-prone coal seams [18, 19].

Aiming at the problem of borehole deflection, Gao et al. [20] analyzed the lateral penetration ability of the drill bit, which is different from its axial penetration ability. The inclination angle and lateral force of the drill bit were determined based on a weighted residual method. Wang et al. [21] obtained the contact characteristics between boreholes and calculated the dynamic lateral force on the drill bit, which led to a deviation control mechanism based on the motion stability and dynamic lateral force. Gao and Zheng [22] studied the changes in the formation characteristics of the bottom borehole in the process of air drilling. A large

anisotropy index in air drilling was found to lead to more serious well deviation, and an increase in the penetration depth of the bit teeth aggravates this deviation. Morin and Wilkens [23] reported that the bit tends to be perpendicular to the fracture strike in the drilling process and used the deviation logarithm to describe the trajectory of the borehole in three-dimensional space. Chen et al. [24] proposed a bit formation wellbore model for a nonlinear coupled bottom borehole assembly under full screw drilling. Liu et al. [25] established a linear elastic model of borehole collapse failure based on pore fluid seepage and obtained the attenuation law for the soft coal seam collapse pressure with gas seepage; the basic mechanical parameters of the coal seam and fluid seepage and the space of the borehole trajectory were also analyzed. The influence of factors such as the azimuth angle of drilling on the borehole collapse provides theoretical support for soft rock formations and the deflection of boreholes in coal seams.

Although the abovementioned studies covered research on the law and control of borehole deflection, the resulting deflection laws are somewhat vague, making a qualitative and quantitative analysis of the deflection law impossible. There have been few studies on borehole deflection in gas treatment, so this work focuses on solving the problem of the blind area of gas drainage and the inability to achieve effective gas drainage. The deflection law and main influencing factors of gas treatment boreholes are analyzed, and the borehole deflection trajectory equation is determined. Additionally, the relationship between the magnitude of deflection and the main influencing factors is identified. This paper describes the use of an analytic hierarchy process (AHP) model to sort the weights of the influencing factors and analyzes the drilling model and engineering examples. The deflection law is then derived, allowing effective predictions of coal-seam gas to be realized. Pumping provides a strong guarantee of preventing the occurrence of coal and gas outbursts and gas overruns and ensures a certain basis for the study and control of borehole deflection in high-gas mines and coal/gas outburst mines.

2. Factors Affecting Borehole Deflection

A literature review and field investigations suggest that the main factors influencing borehole deflection during natural gas extraction are drilling depth, lithology, rock inclination, drilling speed, drilling rig performance, and supporting facilities. These influencing factors can be divided into three aspects: geological factors, technological factors, and human factors.

2.1. Geological Factors. Geological factors are the objective causes of borehole deflection. The main geological factors are rock anisotropy, weak interlayers, and rock angles:

- (i) *Rock Anisotropy.* The rock anisotropy has an important influence on the choice of drilling direction and method. In other words, the degree of rock anisotropy determines the techniques and technologies used for drilling in the formation.

- (ii) *Weak Interlayers.* The principle that soft and hard interlayers affect the drilling trajectory is that when drilling through a hard rock formation at an acute angle, the different pressure resistance of the soft rock and hard rock causes the trajectory of drilling to curve along the direction perpendicular to the rock formation. When passing into soft rock from hard rock, the axis of the drilling tool in the borehole will deviate from the normal line of the rock layer. However, the lithology of the borehole wall of the hard rock above is relatively hard, which limits the drilling tool in the borehole. The final result is that the trajectory of the borehole will basically be offset in the original direction; when the borehole passes into hard rock from soft rock and then through the hard rock, the final result is still an offset along the route of the hard rock facet.
- (iii) *Rock Angles.* In the stratum where gneiss is developed and the rock angle is acute, the drilling trajectory will bend in the direction perpendicular to the stratum angle.

2.2. Technical Factors. Technical factors influence the whole lifecycle of the drilling process. The main technical factors are equipment installation, drilling tool structure, and drilling tool weight:

- (i) *Equipment Installation.* The uneven foundation of drilling sites and the restricted space mean that the borehole inclination is often less than required. Additionally, the magnetism of the field equipment will interfere with the compass used to determine the borehole position. These factors will affect the drilling trajectory. When the equipment is not adequately stabilized, the equipment will swing back and forth during the drilling process, causing deviations in the drilling trajectory and producing serious safety hazards.
- (ii) *Drilling Tool Structure.* The influence of the drilling tool structure on the drilling trajectory is mainly reflected in the drilling tool length, borehole wall clearance, and drilling tool rigidity. The size of the borehole wall clearance and the length of the drill tool determine the deflection angle of the drill tool in the borehole. When the borehole wall gap increases or the length of the drill tool decreases, the deflection angle of the drill tool in the borehole will increase. A more rigid drilling tool will undergo less deformation under the action of axial pressure, thus reducing the impact on the drilling trajectory.
- (iii) *Self-Weight of Drilling Tool.* In the process of directional drilling, the main drilling tools in the borehole include the drill bit, screw motor, nonmagnetic lower tube, probe pipe, nonmagnetic upper tube, and drill pipe. As the borehole depth increases, the weight of the drill pipe becomes heavier and the impact on the trajectory of the borehole becomes greater.

2.3. Human Factors. Human factors determine the efficiency of drilling. The main human factors are the drilling method, drilling procedure parameters, weight on bit (WOB) selection, and drilling speed selection:

- (i) *Drilling Method.* There are many construction methods for underground drilling in coal mines. Different drilling methods have different characteristics in terms of the broken rock and borehole wall gaps, which ultimately affect the deviation of the drilling trajectory. The current drilling methods include percussion drilling, rotary drilling, percussive rotary drilling, vibration drilling, and hybrid drilling. Adopting reasonable drilling methods for the site conditions can effectively control the drilling trajectory while improving the drilling efficiency.
- (ii) *Drilling Procedure Parameters.* The influence of drilling parameters on the drilling trajectory is mainly reflected in the coordination of the drilling pressure and the drilling speed. If the drilling pressure of the drilling rig is too large, it will cause the drilling tool in the borehole to bend, and the drill bit will be biased to the side of the borehole wall. The optimized processing and reasonable coordination of the drilling pressure and the drilling speed can effectively reduce the deviation of the drilling trajectory.
- (iii) *WOB Selection.* When the drilling pressure is too high, the cutting volume will be excessive and the cutting tool will become completely buried in the rock formation. At the same time, the cooling and powder discharge conditions at the bottom of the drill hole deteriorate, and the wear on the bit increases, making the drilling less effective. The choice of drill weight depends on the rock abrasiveness, drillability, particle size, quantity, grade, bottom lip area of the diamond bit, and other factors.
- (iv) *Drilling Speed Selection.* Rotation speed is the main aspect affecting drilling efficiency. Strict control of the drilling speed of the drill pipe so as to achieve more grinding and less advancement improves the qualification rate of drilling. For softer and less abrasive rocks, the drilling speed can be increased by increasing the rotation speed; for hard and abrasive rocks, too high a rotation speed not only reduces the drilling effect but also harms the drilling advancement process. When selecting the drilling speed, the drill bit type, flushing fluid (with or without lubricant), ability of the drilling rig, strength of the drill string, and cutting tool should also be considered, and the appropriate speed should be determined through comprehensive analysis.

3. AHP Model

AHP [26, 27] is an effective method for transforming semiquantitative and semiquantitative problems into

quantitative systems. It is applicable to systems with complex evaluation structures. The basic principle and main steps of AHP are as follows: first, according to the characteristics of the actual scenario, the problem is decomposed layer by layer, and the AHP structure model of the overall target and the hierarchical target is established; second, the judgment matrix from the lower-level target to the higher-level target is constructed, and the evaluation indexes of the same level are compared in pairs to calculate the weight value relative to the higher-level target (hierarchical single ranking table). Finally, the results are combined with the total target weight value to obtain the total ranking table.

3.1. Establishment of AHP Model. To determine the deflection from internal and external causes and considering the factor of quantitative maneuverability, a selection of geological factors (U_1), technology factors (U_2), and human factors (U_3) were incorporated into the AHP model. Specifically, the proposed AHP model considers the rock anisotropy (U_{11}), hard and soft interbed layers (U_{12}), angle of bedding (U_{13}), equipment installation (U_{21}), drilling tool structure (U_{22}), weight of drill tool (U_{23}), drilling method (U_{31}), drilling parameters (U_{32}), weight on bit (U_{33}), and drilling rate selection (U_{34}), a total of 10 impact factors. The structure of the proposed AHP model is shown in Figure 1.

3.2. Determination of the Weight. According to the AHP model described above, judgment matrices for the second- and third-level targets were constructed using the 1–9 scale method. Combined with practical experience, this allowed the weight values of each impact factor in each judgment matrix to be calculated (Tables 1–4). Finally, the weight values of the third- and second-level targets were multiplied from the bottom, and the results were further synthesized with the total target to obtain the total weight ranking of each impact factor [28, 29].

- (i) *Determine the Judgment Matrix of Each Level.* On the basis of each criterion layer, the result table from comparing each pair of elements was established, and the judgment matrices of each layer versus the next were obtained from Tables 1–4. The results are as follows:

- (a) Judgment matrix A_Z of the criterion layer to the target layer Z [30]:

$$A_Z = \begin{bmatrix} 1 & 2 & 5 \\ \frac{1}{2} & 1 & 2 \\ \frac{1}{5} & \frac{1}{2} & 1 \end{bmatrix}. \quad (1)$$

- (b) Judgment matrix A_{U1} between indicator layer and criterion layer Z :

$$A_{U_1} = \begin{bmatrix} 1 & \frac{1}{6} & \frac{1}{2} \\ 6 & 1 & 3 \\ 2 & \frac{1}{3} & 1 \end{bmatrix}. \quad (2)$$

(c) Judgment matrix A_{U_2} between indicator layer and criterion layer U_2 :

$$A_{U_2} = \begin{bmatrix} 1 & \frac{1}{2} & 1 \\ 2 & 1 & 1 \\ 1 & 1 & 1 \end{bmatrix}. \quad (3)$$

(d) Judgment matrix A_{U_3} between indicator layer and criterion layer U_3 :

$$A_{U_3} = \begin{bmatrix} 1 & 1 & \frac{1}{2} & \frac{1}{2} \\ 1 & 1 & \frac{1}{2} & \frac{1}{2} \\ 1 & 2 & 1 & 1 \\ 2 & 2 & 1 & 1 \end{bmatrix}. \quad (4)$$

(ii) *Calculate the Importance Ranking.* According to the judgment matrices, the eigenvector corresponding to the maximum eigenvalue can be calculated using the following equation, where P is the judgment matrix and the eigenvector W is normalized to form the order of importance of each evaluation factor, that is, the weight allocation:

$$PW = \lambda_{\max} W. \quad (5)$$

Using the square root method to solve this equation, we calculate the judgment matrix P for the product of each row of elements M and then calculate the cubic root W of M_i . The vector $W = (W_1, W_2, W_3)$ is normalized according to $W_i = W_i / [\sum_{i=1}^3 W_i]$, and the resulting $W = (W_1, W_2, W_3)$ is the eigenvector. According to the above steps, the eigenvector of the judgment matrix A_z can be calculated as (0.606, 0.265, 0.129).

(iii) *Consistency Test.* To determine whether the weight distribution is reasonable, the consistency of the judgment matrix needs to be tested using the following expression:

$$\begin{aligned} CR &= \frac{CI}{RI}, \\ CI &= \frac{(\lambda_{\max} - n)}{(n - 1)}. \end{aligned} \quad (6)$$

where CR is the consistency index value, CI is the random consistency ratio of the judgment matrix, RI is the average consistency index of the judgment matrix, and N is the order of the judgment matrix; the RI values of the judgment matrix, ordered from 1–9, are presented in Table 5.

The maximum eigenvalue of the judgment matrix is calculated and converted to

$$\lambda_{\max} = \sum_{i=1}^3 \frac{(PW)_i}{nW_i} = \frac{1}{n} \sum_{i=1}^3 \frac{(PW)_i}{W_i}, \quad (7)$$

where $(PW)_i$ represents the i -th element of PW , and the order of the judgment matrix is $n = 3$.

$$PW = \begin{pmatrix} (PW)_1 \\ (PW)_2 \\ (PW)_3 \end{pmatrix}. \quad (8)$$

The known data in Table 5 are substituted into equation (3) and the maximum eigenvalue is calculated; in this case, $\text{Max} = 3.03$. As shown in Table 6, $RI = 0.58$ and $CR = 0.025 < 0.1$. This indicates that the judgment matrix has satisfactory consistency, so each component of $W = (W_1, W_2, W_3)$ can be used as a weight coefficient. Similarly, the second-level weight set can be calculated: $\text{Max} = 3.01$, $CR1 = 0.01 < 0.1$, $\text{Max} = 3.08$, $CR2 = 0.060 < 0.1$, and $\text{Max} = 4.06$, $CR3 = 0.02 < 0.1$.

(iv) *Calculate the Composite Weight of Each Layer to the Target Layer.* The synthetic weight of each element to the target layer refers to the synthesis of the relative weight of each factor of each judgment matrix to the target layer (the topmost layer). This weight is calculated using a top-down method, that is, layer-by-layer synthesis. The composite weights and their total rankings are listed in Table 6.

(v) Overall ranking consistency ratio is as follows:

$$CR = \frac{\sum_{i=1}^3 W_i CI_i}{\sum_{i=1}^3 W_i RI_i} = \frac{0.606 * 0.01 + 0.265 * 0.06 + 0.129 * 0.02}{0.606 * 0.58 + 0.265 * 0.58 + 0.129 * 1.12} = 0.026 < 0.1. \quad (9)$$

Thus, the total sorting results of the hierarchy meet the consistency requirement.

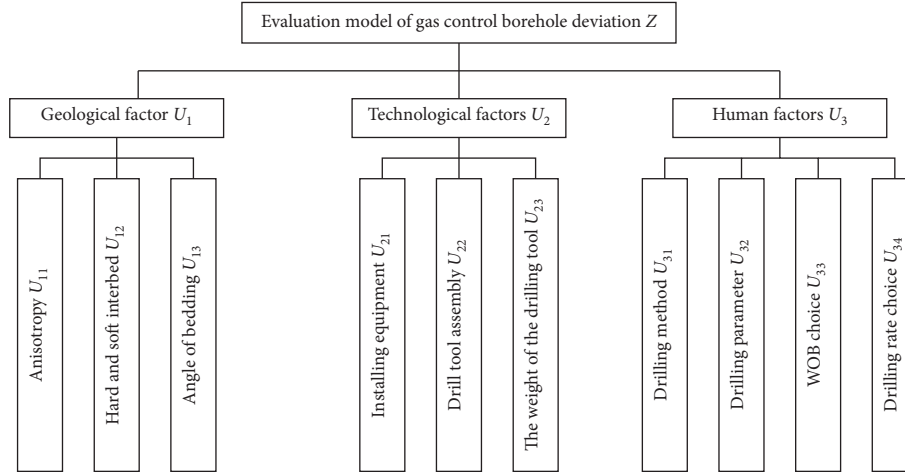


FIGURE 1: Hierarchical structure model of borehole deflection evaluation.

TABLE 1: Judgment matrix table Z.

Borehole deflection Z	U_1	U_2	U_3	Weight
U_1	1	2	5	0.606
U_2	1/2	1	2	0.265
U_3	1/5	1/2	1	0.129

4. Field Test

4.1. *Overview of the Test Site.* The 14205 working face of Xinzheng Coal and Electricity Co., Ltd., is a flat surface with a ground elevation of +134.9–+137.2 m. The working face elevation ranges from –152.0 m to –193.0 m, the working face slope is 187 m, the strike length is 668 m, and the coal seam inclination is 0–11°. The coal thickness is 0.5–12 m, and the bottom roadway is 12–15 m away from the coal seam. On-site surveys indicate that the mining area was mainly used in the initial stage of the drilling site, and a gas control borehole was drilled on the roadway wall at a later stage. The site layout is shown in Figure 2.

4.2. *Test Results.* A total of 421 sets of drilling inclination data from the bottom-draining roadway of site 14205 were collected. The changes in the top angle (θ) and azimuth angle (α) of each borehole section are summarized in Table 7. Due to the large amount of drilling data, not all of the statistics can be listed here. Note, however, that both the vertex angle and the azimuth angle change in 81.9% of cases; that is, deviation occurred in the majority of drilling processes .

(i) *Change in Azimuth.* Figure 3 shows the azimuth angle change diagram of boreholes 40–53. The general characteristics of the overall upper azimuth angle change are as follows. During the drilling process, the azimuth angle body exhibits an increasing trend. Half of the cases are skewed to the left with a deflection angle of 0–2°, and the other half are skewed to the right with a deflection angle of 0–1.7°, with an overall increasing trend.

(ii) *Inclination Angle Change.* According to the field survey data collected by the bottom alley roadway of site 14205, the main constituents of the drilling zone are limestone (L7 and L8), sandy mudstone, and a 2–1 coal seam. The L7 limestone with L8 limestone has the greatest strength, with a uniaxial compressive strength of around 62.0–62.3 MPa. The sandy mudstone is relatively weak, with a uniaxial compressive strength generally in the range of 19.0–42.3 MPa. Thus, at the bottom alley roadway of site 14205, drilling extraction from above will involve drilling through hard and soft interbed structures.

(a) *When the Angle of the Encountered Layer is Less Than the Critical Value.* Using the SPSS data platform to sort the field data, the critical angle was found to be 25–35°. Figure 4 shows that when the angle of the encountered layer is less than the critical value, the overall downward deflection of the borehole is between 0 and 4° and the overall offset is from 1 to 6.1 m (average of 3.0 m). When the angle of the encountered layer is less than the critical value, the offset in the vertical direction is larger in deeper boreholes. The vertical displacement tends to increase over the extent of the borehole, and so the borehole trajectory gradually moves away from the design trajectory (Figure 5).

The borehole trajectory deflection condition is compared with a geological model of the regional change corresponding to L8 limestone in Figure 6. The relatively soft sandy mudstone produces small deviations when drilling, whereas drilling through

TABLE 2: Judgment matrix table U_1 .

Geological factors U_1	U_{11}	U_{12}	U_{13}	Weight
U_{11}	1	1/6	1/2	0.11
U_{12}	6	1	3	0.67
U_{13}	2	1/3	1	0.22

TABLE 3: Judgment matrix table U_2 .

Technological factors U_2	U_{21}	U_{22}	U_{23}	Weight
U_{21}	1	1/2	1	0.25
U_{22}	2	1	1	0.5
U_{23}	1	1	1	0.25

TABLE 4: Judgment matrix table U_3 .

Human factors U_3	U_{31}	U_{32}	U_{33}	U_{34}	Weight
U_{31}	1	1	1/2	1/2	0.2
U_{32}	1	1	1/2	1/2	0.2
U_{33}	1	2	1	2	0.2
U_{34}	2	2	1/2	1	0.4

TABLE 5: RI values of average random consistency index.

n	RI
1	0
2	0
3	0.58
4	0.90
5	1.12
6	1.24
7	1.32
8	1.41
9	1.45

TABLE 6: Overall ranking of synthetic weights of evaluation indicators.

Impact factor	Total sorts	Weight W_i
Hard and soft interbed	1	0.406
Angle of bedding	2	0.133
Device structure	3	0.133
Anisotropy	4	0.067
Rig-up	5	0.066
Drilling tool weight	6	0.066
Drilling rate choice	7	0.052
Drilling method	8	0.026
Drilling parameter	9	0.026
WOB choice	10	0.025

the rock to the L8 limestone produces large deviations. The “soft-hard-soft” rock formation means that it is necessary to drill through the interface between hard rock and soft rock. When the angle of the encountered layer is less than the critical angle, the main force results in downward deflection.

(b) *When the Angle of the Encountered Layer is Greater Than the Critical Value.* When the angle of the encountered layer is greater than the critical value, Figures 7 and 8 show that there is an overall upward deflection, with a drilling deflection angle of 0–6° and an overall offset of 1–7.2 m (average of 4.1 m). The



FIGURE 2: Inclination test site. (a) Drilling site at the early stage of treatment. (b) Drilling at the later stage of treatment.

TABLE 7: Drilling deviation.

Data classification	Proportion (%)
Vertex angle θ and azimuth angle α are unchanged	0.5
Vertex angle θ changes; azimuth angle α is unchanged	10.9
Vertex angle θ and azimuth angle α both change	81.9
Apex angle θ remains unchanged; azimuth angle α changes	6.7

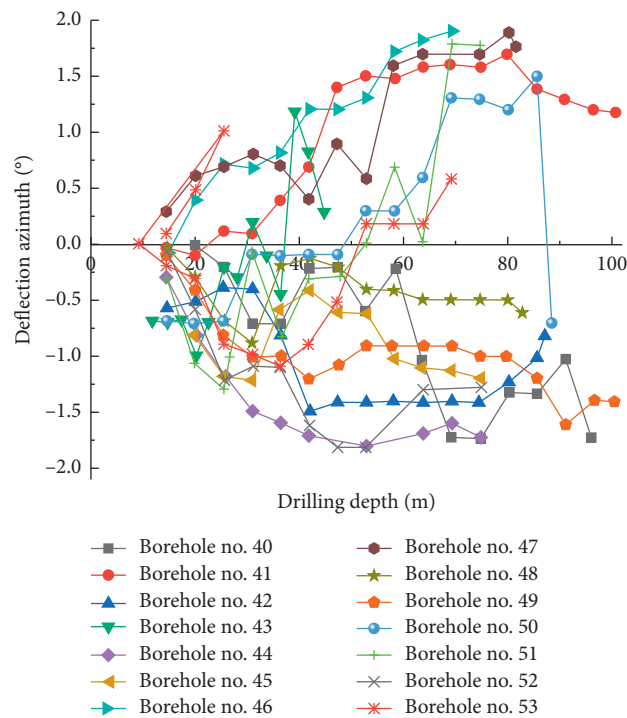


FIGURE 3: Azimuth change diagram.

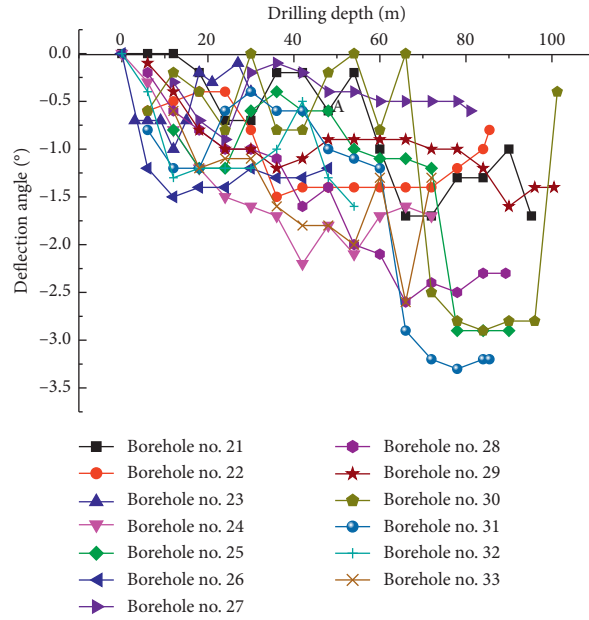


FIGURE 4: Change in the dip angle when the angle of encountered layer is less than the critical value.

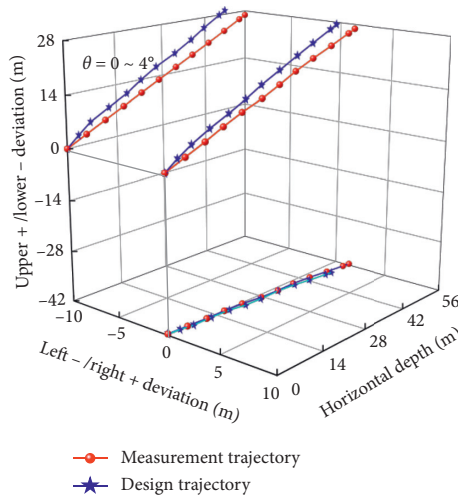


FIGURE 5: Borehole offset when the angle of encountered layer is less than the critical value.

offset in the vertical direction due to the angle of the layer being greater than the critical value grows as the borehole becomes deeper. Therefore, over the extent of the slanted borehole trajectory, the offset gradually increases.

The borehole deflection is compared with a geological model figure corresponding to L8 limestone in Figure 9. Sandy mudstone induces small deviations, whereas drilling through the L8 limestone produces significant deflections. When drilling through “soft-hard-soft” rock interfaces, if the angle of the encountered layer is greater than the critical angle, the resultant force is mainly towards the hard rock interface, and so the main deflection is upward.

4.3. *Inclinometer Trajectory Fitting and Prediction.* From the rock coring drilling trajectory data collected in this study, a borehole trajectory nonlinear regression equation was constructed. A scatter plot of the trajectories is shown in Figure 10.

The final fitting results were obtained as follows:

$$\theta = (-2.35484 \pm 0.89571) \cdot e^{(-L/(3.53216 \pm 3.00351))} + (2.13432 \pm 0.2785). \tag{10}$$

Comprehensive analysis, theoretical analysis, and the prediction model exhibit good consistency. Therefore, the proposed approach can adequately represent the deflection in the process of drilling, allowing adjustable control to be implemented during the drilling process.

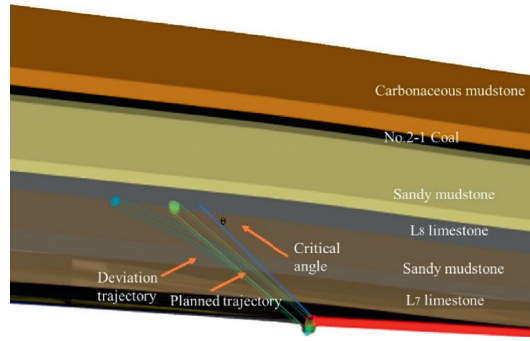


FIGURE 6: Comparison of stratigraphic restoration.

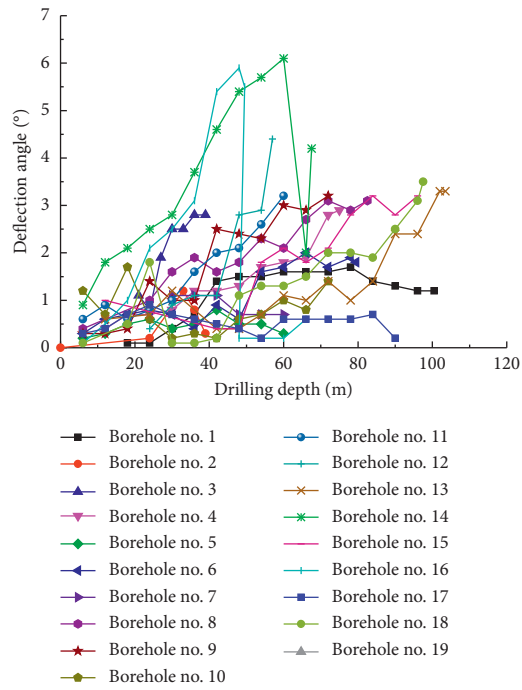


FIGURE 7: Change in the dip angle when the angle of encountered layer is greater than the critical value.

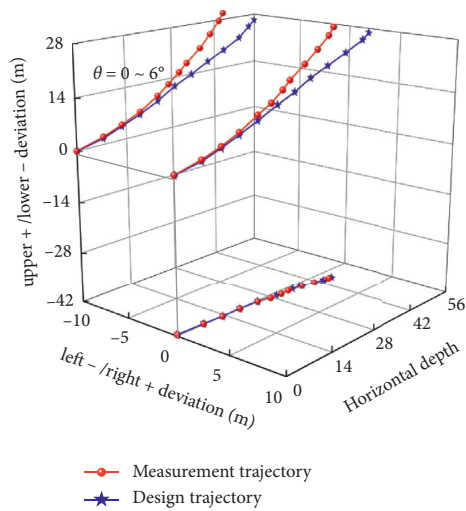


FIGURE 8: Borehole offset when the angle of encountered layer is greater than the critical value.

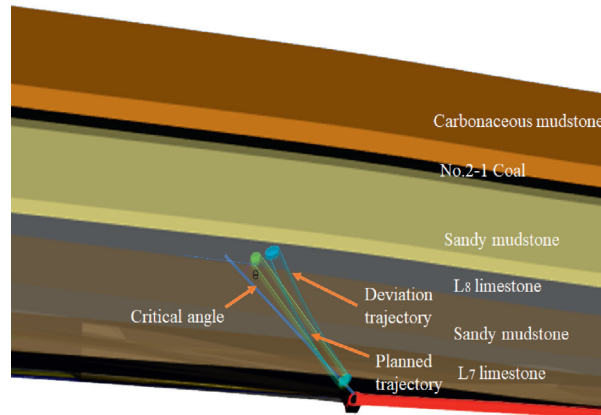


FIGURE 9: Comparison of stratigraphic restoration.

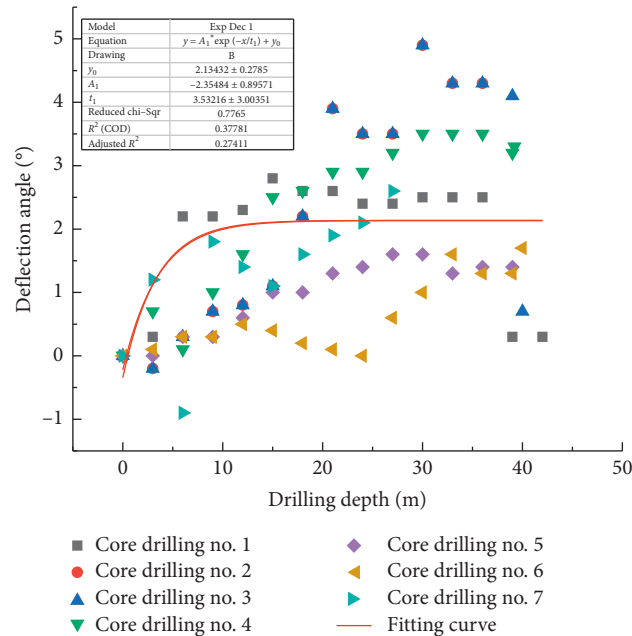


FIGURE 10: Scatter plot.

5. Conclusions

For the problem of gas drainage borehole deflection, an AHP model has been established to rank the weights of various influencing factors, and the analysis has been combined with a drilling model and engineering examples. The primary conclusions from this study are as follows:

- (1) The soft and hard interlayers are critical factors influencing gas drainage borehole deflection.
- (2) In the process of drilling, when there are soft and hard interlayers at the interface, the critical drilling inclination angle ranges from 25 to 35°. When the dip angle is greater than the critical angle, the inclination angle generally moves upward with a deflection angle of 0–6°, and the borehole deflection occurs mainly in the rock layer interface. When the angle of the

encountered layer is less than the critical value, the overall drilling angle is deflected downward, and the skew angle is from 0 to 4°.

- (3) The theoretical model and field data for predicting the trajectory curve are consistent, enabling preliminary control of the drilling process. This provides a new way of thinking for borehole deflection governance.

Data Availability

All data, models, or code generated or used during the study is available from the corresponding author upon request.

Conflicts of Interest

The authors declare that they have no conflicts of interest.

Acknowledgments

This work was financially supported by the National Natural Science Foundation of China (52074120), Program for Science & Technology Innovation Talents in Universities of Henan Province (19HASTIT047), and Science and Technology Project of Henan Province (182102310012). This support is gratefully acknowledged.

References

- [1] X. Li, Z. Cao, and Y. Xu, "Characteristics and trends of coal mine safety development," *Energy Sources, Part A: Recovery, Utilization, and Environmental Effects*, pp. 1–19, 2020.
- [2] Q. Zou, H. Liu, Y. Zhang, Q. Li, J. Fu, and Q. Hu, "Rationality evaluation of production deployment of outburst-prone coal mines: a case study of nantong coal mine in Chongqing, China," *Safety Science*, vol. 122, Article ID 104515, 2020.
- [3] J. Dennis, "Black . Review of coal and gas outburst in Australian underground coal mines," *International Journal of Mining Science and Technology*, vol. 29, no. 6, pp. 815–824, 2019.
- [4] C. Fan, S. Li, and M. Luo, "Coal and gas outburst dynamic system," *International Journal of Mining Science and Technology*, vol. 27, no. 1, pp. 49–55, 2017.
- [5] J. Geng, X. Jiang, and N. Wen, "Regression analysis of major parameters affecting the intensity of coal and gas outbursts in laboratory," *International Journal of Mining Science and Technology*, vol. 27, no. 2, pp. 327–332, 2017.
- [6] F. Wu, H. Zhang, Q. Zou, C. Li, J. Chen, and R. Gao, "Viscoelastic-plastic damage creep model for salt rock based on fractional derivative theory," *Mechanics of Materials*, vol. 150, no. 103600, 2020.
- [7] F. Wu, J. Liu, Q. Zou, C. Li, J. Chen, and R. Gao, "A triaxial creep model for salt rocks based on variable-order fractional derivative," *Mechanics of Time-dependent Materials*, vol. 25, pp. 101–118, 2020.
- [8] B. Zhang, H. Sun, Y. Liang, K. Wang, and Q. Zou, "Characterization and quantification of mining-induced fractures in overlying strata: implications for coalbed methane drainage," *Natural Resources Research*, vol. 29, no. 4, 2019.
- [9] D. Rudakov and V. Sobolev, "A mathematical model of gas flow during coal outburst initiation," *International Journal of Mining Science and Technology*, vol. 29, no. 5, pp. 791–796, 2019.
- [10] J. Ou, M. Liu, and C. Zhang, "Determination of indices and critical values of gas parameters of the first gas outburst in a coal seam of the Xieqiao Mine," *International Journal of Mining Science and Technology*, vol. 22, no. 1, pp. 29–93, 2012.
- [11] Q. Zou, L. Han, Z. Cheng, T. Zhang, and B. Lin, "Effect of slot inclination angle and borehole-slot ratio on mechanical property of pre-cracked coal: implications for ECBM recovery using hydraulic slotting," *Natural Resources Research*, vol. 29, pp. 1705–1729, 2020.
- [12] T. Liu, B. Lin, X. Fu et al., "Experimental study on gas diffusion dynamics in fractured coal: a better understanding of gas migration in in-situ coal seam," *Energy*, vol. 195, Article ID 117005, 2020.
- [13] T. Liu, S. Liu, B. Lin, X. Fu et al., "Stress response during in-situ gas depletion and its impact on permeability and stability of CBM reservoir," *Fuel*, vol. 266, Article ID 117083, 2020.
- [14] Q. Zou, B. Lin, C. Zheng et al., "Novel integrated techniques of drilling–slotting–separation–sealing for enhanced coal bed methane recovery in underground coal mines," *Journal of Natural Gas Science and Engineering*, vol. 26, pp. 960–973, 2015.
- [15] H. Jiang and Y. Luo, "Development of a roof bolter drilling control process to reduce the generation of respirable dust," *International Journal of Coal Science & Technology*, vol. 8, no. 2, pp. 199–204, 2021.
- [16] H. Gao, Qi Wang, and B. Jiang, "Relationship between rock uniaxial compressive strength and digital core drilling parameters and its forecast method," *International Journal of Coal Science & Technology*, 2021.
- [17] Y. Hui, H. Jia, and S. Liu, "Macro and micro grouting process and the influence mechanism of cracks in soft coal seam," *International Journal of Coal Science & Technology*, 2021.
- [18] Z. F. Wang, T. Hen, F. M. An et al., "Experimental research of gas drainage in extremely short-distance over-lying adjacent seam," *Journal of Henan Polytechnic University(Natural Science)*, vol. 36, no. 1, pp. 12–16, 2017.
- [19] G. Y. Li and Y. P. Xu, "Gas drainage technology with super long high directional drilling in goaf roof," *Coal Engineering*, vol. 49, no. 8, pp. 88–91, 2017.
- [20] D. Gao, Z. Dong, and H. Zhang, "On appropriately matching the bottomborehole pendulum assembly with the anisotropic drill bit, to control the borehole-deviation," *Computer Modeling in Engineering and Sciences*, vol. 89, no. 2, pp. 111–122, 2012.
- [21] W. Wang, H. Zhang, N. Li et al., "The dynamic deviation control mechanism of the prebent pendulum BHA in air drilling," *Journal of Petroleum Science and Engineering*, 2019.
- [22] D. Gao and D. Zheng, "Study of a mechanism for well deviation in air drilling and its control," *Petroleum Science and Technology*, vol. 29, no. 4, pp. 358–365, 2011.
- [23] R. H. Morin and R. H. Wilkens, "Structure and stress state of Hawaiian island basalts penetrated by the Hawaii Scientific Drilling Project deep core borehole," *Journal of Geophysical Research: Solid Earth*, vol. 110, no. 404, pp. 1–8, 2005.
- [24] Y. Chen, J. Fu, T. Ma et al., "Numerical modeling of dynamic behavior and steering ability of a bottom borehole assembly with a bent-housing positive displacement motor under rotary drilling conditions," *Energies*, vol. 11, no. 10, 2018.
- [25] C. Liu, F. Zhou, and K. Yang, "Failure analysis of borehole liners in soft coal seam for gas drainage," *Engineering Failure Analysis*, vol. 42, pp. 274–283, 2014.
- [26] F. Gao, Z. Zhang, Y. Gao et al., "Risk assessment model of rockburst based on blind number theory," *Journal of China Coal Society*, vol. 35, no. S1, pp. 28–32, 2010.
- [27] X. Wang and D. Huo, "Application of fuzzy comprehensive evaluation method in coal mine safety evaluation," *China Mining Industry*, vol. 4, no. 5, pp. 75–78, 2008.
- [28] X. S. Guo and N. Kapucu, "Assessing social vulnerability to earthquake disaster using rough analytic hierarchy process method: a case study of Hanzhong City, China," *Safety Science*, vol. 125, Article ID 104625, 2020.
- [29] A. Petruni, E. Giagloglou, E. Douglas, J. Geng, M. C. Leva, and M. Demichela, "Applying Analytic Hierarchy Process (AHP) to choose a human factors technique: choosing the suitable Human Reliability Analysis technique for the automotive industry," *Safety Science*, vol. 119, pp. 229–239, 2019.
- [30] L. I. Ning, L. Wang, and M. Jia, "Fuzzy comprehensive evaluation of six mine systems based on analytic hierarchy process," *Journal of Central South University: Science and Technology*, vol. 46, no. 2, pp. 631–637, 2015.

Research Article

Similarity Model Test on the Spatiotemporal Evolution Law of Deformation and Failure of Surrounding Rock-Induced Caving in Multi-Mined-Out Areas

Fengyu Ren , Yanjun Zhou , Rongxing He , Jianli Cao , and Kaihua Zou 

School of Resources and Civil Engineering, Northeastern University, Shenyang 110000, China

Correspondence should be addressed to Yanjun Zhou; zhouyanjun0218@163.com

Received 19 June 2021; Revised 14 August 2021; Accepted 18 August 2021; Published 2 September 2021

Academic Editor: Jia Lin

Copyright © 2021 Fengyu Ren et al. This is an open access article distributed under the Creative Commons Attribution License, which permits unrestricted use, distribution, and reproduction in any medium, provided the original work is properly cited.

Taking the deep mined-out areas of Paishanlou Gold Mine as the research object, we designed the indoor similar physical model test and used VIC-3D and resistance pressure sensors to record the vertical stress and strain of the model during the test. And based on the results of digital image correlation (DIC) analysis, we deeply analyzed the deformation and failure characteristics of the surrounding rock in the process of goaf caving. At the same time, the failure mechanism of surrounding rock mass and the law of temporal and spatial evolution during the excavation process of pillars between the mined-out areas were studied. According to the characteristics of the caving process, it can be divided into three stages: initial caving in a small range at the arch angle, continuous vault collapse, and instantaneous huge caving of the roof. Before the occurrence of instantaneous large caving at the top, the phenomenon of sudden increase of caving arch curvature appears. Based on the monitoring results, it can also be seen that the deformation of overlying rock mass is most affected by the span of the cavity, and the vertical strain is inversely proportional to the depth. The rock mass stress and strain caused by the excavation of isolation pillars between adjacent two goafs have an obvious time delay phenomenon. The time delay effect of the strain is proportional to the span of the cavity; conversely, it is inversely proportional to the span of the cavity. Specifically, throughout the experiment, the subsidence of the target area of the test model is larger in the middle and smaller on both sides; simultaneously, the upper part is high, and the lower part is low. However, the variation of the stress value shows the characteristics of higher on both sides and lower on the middle area and higher on the upper part and lower on the lower part. To sum up, the experimental results show that the caving process can be predicted and effectively controlled manually, and a new treatment method can be provided for the control and prevention of the large caving and mining subsidence damage in the goaf combined with the field monitoring method.

1. Introduction

Over the years, the induced caving method has gradually been applied to the treatment of the goaf. It does not have bottom structure and does not have strict requirements for the caving time and lumpiness. Because it is essentially different from the natural caving method in terms of technology, it can be considered as a natural caving method improved in the form of undercutting and the structure of the ore extraction. For this reason, it is called the induced caving method [1–5]. The main process is to apply disturbances to expand the effective exposure area of the mined-out area artificially (including elimination of supporting

pillars, undercutting, precracking, and other auxiliary works) in specific rock mass projects, providing internal stress concentration effects in the orebody and rock mass, and inducing the deformation and caving of the roof. The main difficulty lies in the fact that the support of the pillars has accumulated caving energy in the roof of the goaf to be caved, and the concentrated release of the energy will lead to the instantaneous collapse of the roof surrounding rock, endangering the safety of the mine. Therefore, it is necessary to use advanced theory of induced rock breaking to artificially intervene the caving process, so that the roof surrounding rock can complete the caving process in the form of sporadic caving [2, 5, 6].

At present, the main methods for studying the caving of orebody and rock mass include similar material simulation experiment, numerical simulation analysis, theoretical analysis, and on-site monitoring [7–13]. The simulation of surrounding rock stress and deformation is the key to the development or improvement of new treatment methods for goafs, and similarity physical model test is one of the typical research methods. It can reverse the relationship between the physical quantities obtained during the test to the simulated prototype, thereby directly reflecting the corresponding deformation and failure characteristics and evolution process of the actual engineering object. It has the characteristics of easy operation, low cost, and high simulation. Besides, it can also carry out some research that cannot be realized in actual engineering, so it has been widely used in recent years [11, 13, 14]. He et al. [9] established a support-surrounding rock mechanical model considering the behavior of an elastic cantilever beam in order to study the hard roof fracturing characteristics and mining-induced stress behaviors. Ren et al. [11] designed physical simulation experiments to analyze the deformation and failure characteristics of the surface and surrounding rock around the goaf, as well as the creep behavior and failure mechanism of surrounding rock deformation. Wang et al. [15] and Chen et al. [16] conducted physical and numerical simulation of field monitoring for the movement and structure of the overlaying strata on the fully mechanized top-coal caving face. But nowadays, most of the similar material model experiments can only qualitatively reflect the caving phenomena, which can only be used as a reference for analysis of rock caving process. Even if some monitoring equipment is introduced, due to the lack of accuracy and simplicity of test method, there is still a lack of in-depth study on the caving process of multi-mined-out areas and the law of temporal and spatial evolution of the three-dimensional morphology of caving arches. These years, the development of computer analysis software, sensors, and imaging technology makes it possible to obtain the temporal and spatial evolution rules of caving process, caving arch, and cracks during the test. In addition, the introduction of on-site drilling monitoring equipment has further optimized the goaf management scheme [12, 17, 18].

This paper takes the treatment of multi-mined-out areas of Paishanlou Gold Mine as the research background, based on similarity theory, and uses VIC-3D (noncontact full-field strain measurement system) and resistive pressure sensor as measurement tools to design a similar physical model simulation test. Through the test, we studied the caving mechanism of the roof surrounding rock during the excavation of the pillars in the deep mined-out areas and the process of simulated undercutting and explored the internal law of the induced caving process. Combining the experimental research results with the RG underground TV monitoring technology, we can effectively control the caving process of the goafs, so as to safely deal with the goaf while recovering the residual ore and convert the overstocked ore in goafs into available resources.

2. Geological Conditions of the Experimental Prototype

Paishanlou gold deposit belongs to a large metamorphosed hydrothermal gold deposit in the same ductile shear zone. The surrounding rocks of near-orebody are mylonite, and the surrounding rocks far away from the orebody are primary mylonite and mylonitized rocks. The orebody thickness of Paishanlou Gold Mine is medium to thick, the dip angle is generally 35° – 55° , the stability of roof surrounding rock is good, and the ore grade is low. Due to the large thickness of the orebody and the slow attitude and concentrated distribution of orebody, the open-pit mining method is used in the upper orebody. After mining to the level of +300 m, it is transferred to underground mining, and the open-pit method is used in the process of transferring from open-pit to underground. And then the whole upper mined-out areas are induced to penetrate the surface, and the subsidence area is filled from the surface and reclaimed land (see Figure 1). Because it is located in a scenic protection area, the surface is not allowed to collapse (see Figure 1(c)). Based on the treatment experience of the upper goaf, the safe and efficient mining technology of zoned open stope with subsequent filling was developed.

Based on the field geological survey and the classification of rock mass stability, the mechanical parameters of rock mass in Paishanlou Gold Mine are obtained (see Table 1). The stability level of surrounding rock in each level of Paishanlou Gold Mine belongs to medium stable~stable. The borehole monitoring shows that the current height of the mined-out area from the ground surface is 245~410 m, and the goaf is already in a caving state, and the current caving height of the mined-out area is about 13~70 m, so it is urgent to deal with the mined-out areas at present.

In this paper, we took the deep mined-out areas of Paishanlou Gold Mine as the experimental prototype, simulated the process of cutting through between multi-mined-out areas and rock strata induced caving, and studied the rock mass failure mechanism and caving law in the process of penetration and caving of multi-mined-out areas. The simulated range of the test was roughly from level of +225 m to level of +125 m, with a dip length of about 240 m. This design scheme adopts the induced caving method; that is, the pillars between the goafs are excavated first, and then the undercutting project is arranged in the rock mass at the bottom of the goaf to induce the natural caving of the upper orebody.

3. Description of the Similar Physical Model Simulation Test

3.1. Test Equipment

3.1.1. Similar Physical Model Simulation Test Bench. The main equipment for this test is an electrohydraulic servo multichannel similar material test bench (see Figure 2(a)). It is a plane loading system that adopts active loading mode. The equipment adopts multichannel independent control technology that simulates distributed loads. It can simulate

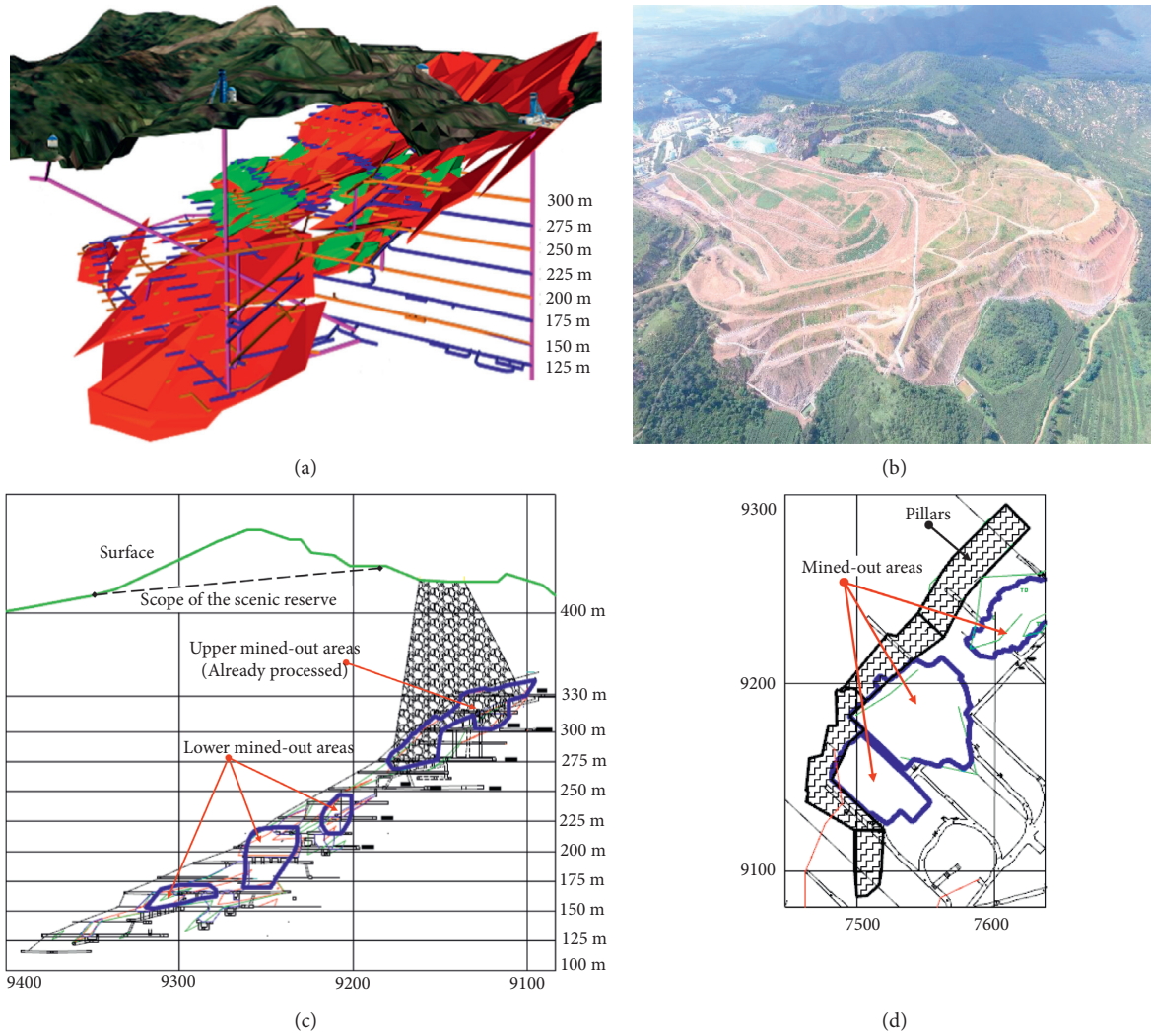


FIGURE 1: Topographic maps of the orebody and surface. (a) 3D model of geology. (b) Map of surface topography. (c) Current profile of the mined-out areas. (d) Current plan of the mined-out areas.

TABLE 1: The mechanical parameters of rock mass in Paishanlou Gold Mine.

Type of rock body	Ore	Surrounding rocks in the upper wall	Bed rocks of the footwall
Compressive strength (MPa)	22.1	25.19	27.4
Strength of extension (MPa)	1.85	2.5	2.54
Elasticity modulus (GPa)	34	43.1	42.17
Cohesion (MPa)	5.63	6.53	7.03
Internal friction angle (°)	36	35.1	35.7

the excavation process in mining and geotechnical engineering indoors. Multichannel independent control technology can simulate distributed loads. The upper part of the test bench is equipped with 7 vertical oil cylinders, that is, 7 channels. Each channel can be individually controlled and nonlinearly loaded. Each channel can load a maximum of 150 kN test force, and the actual control accuracy is 0.5 kN. The three oil cylinders of the test bench are combined into one channel, and the maximum load is 600 kN. The test bench can realize the constant rate loading of the test force, can carry out the experiment under the constant load within

a given accuracy range, and can ensure the long-term stability of the axial and horizontal load during the experiment.

3.1.2. Equipment and Principle of Strain Measuring. Because the surface displacement meter has a large direct measurement error and is not easy to install, we use a noncontact full-field displacement measurement system (VIC-3D for short) (see Figure 2(b)) to monitor the displacement change of the model surface. The DIC (Digital Image Correlation) used by VIC-3D is a simple optical

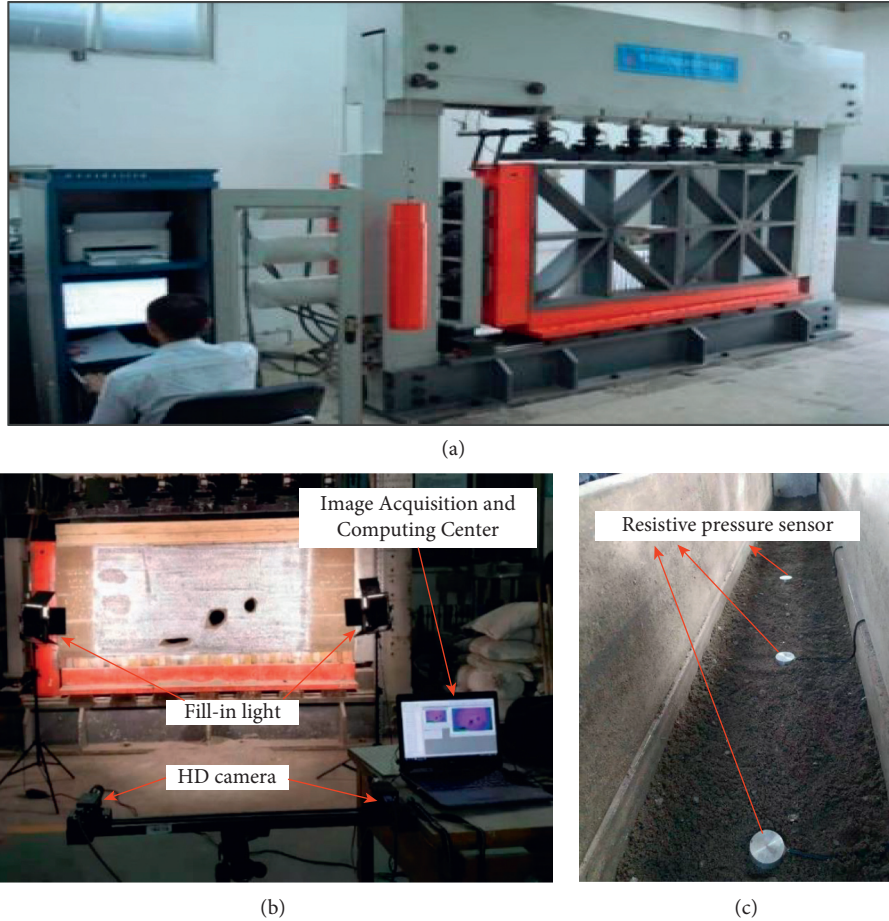


FIGURE 2: Main test equipment. (a) Electrohydraulic servo multichannel similar material test bench. (b) Noncontact full-field displacement measurement system. (c) Resistive pressure sensor.

measurement method to measure surface deformation of objects. DIC technology can be used in general indoor and outdoor environments, and the strain measurement range is from 0.005% (50 microstrains) to 2000%. The size of the measuring object can be from 0.8 mm to tens of meters. In principle, strain can be measured as long as the image can be obtained. It mainly adopts the method of spraying speckle on the surface of the model, combined with industrial close-up photography technology, with real-time acquisition of digital images of the region of interest (speckle pattern) in each deformation stage of the object. DIC tracks the smaller areas with gray value patterns during the deformation process, which we call the subset subarea. Find the relevant area of the image by grayscale and calculate the strain on the surface of the object by using an algorithm similar to that used in finite element analysis software to obtain the surface displacement and strain distribution [17]. Then the displacement field data is smoothed, and the corresponding deformation information is visualized to realize fast, high-precision, real-time, noncontact, full-field deformation and strain measurement (see Figure 3).

After the simulation experiment, photos are analyzed in order to obtain the deformation and strain. The strain calculation in VIC-3D can be briefly summarized as follows (see Figure 3).

The strain calculation in Vic-3D is similar to the algorithm generally used by FEA software. The input for the strain calculation is the grid of data points from the correlation—a cloud of X, Y, Z points and U, V, W displacement vectors (see Figure 3A).

The separation between these points (in pixels) is dictated by the step size. The separation between the points in physical space will vary depending on magnification and the shape of the specimen. With this grid as the input, we consider each point separately and create a local mesh of triangles; here, we consider the highlighted point from above (see Figure 3B).

Next, we consider the deformation of each triangle separately (see Figure 3C).

Rigid body motion is easy to remove at this point (see Figure 3D).

The remaining deformation of the triangle gives us exactly enough data to compute a single, constant strain tensor for this triangle. We repeat this for each triangle (see Figure 3E).

Since we want a strain for each existing data point, we interpolate from the surrounding strains (see Figure 3F).

We repeat this process for each point until we have a strain tensor at each initial data point (see Figure 3G).

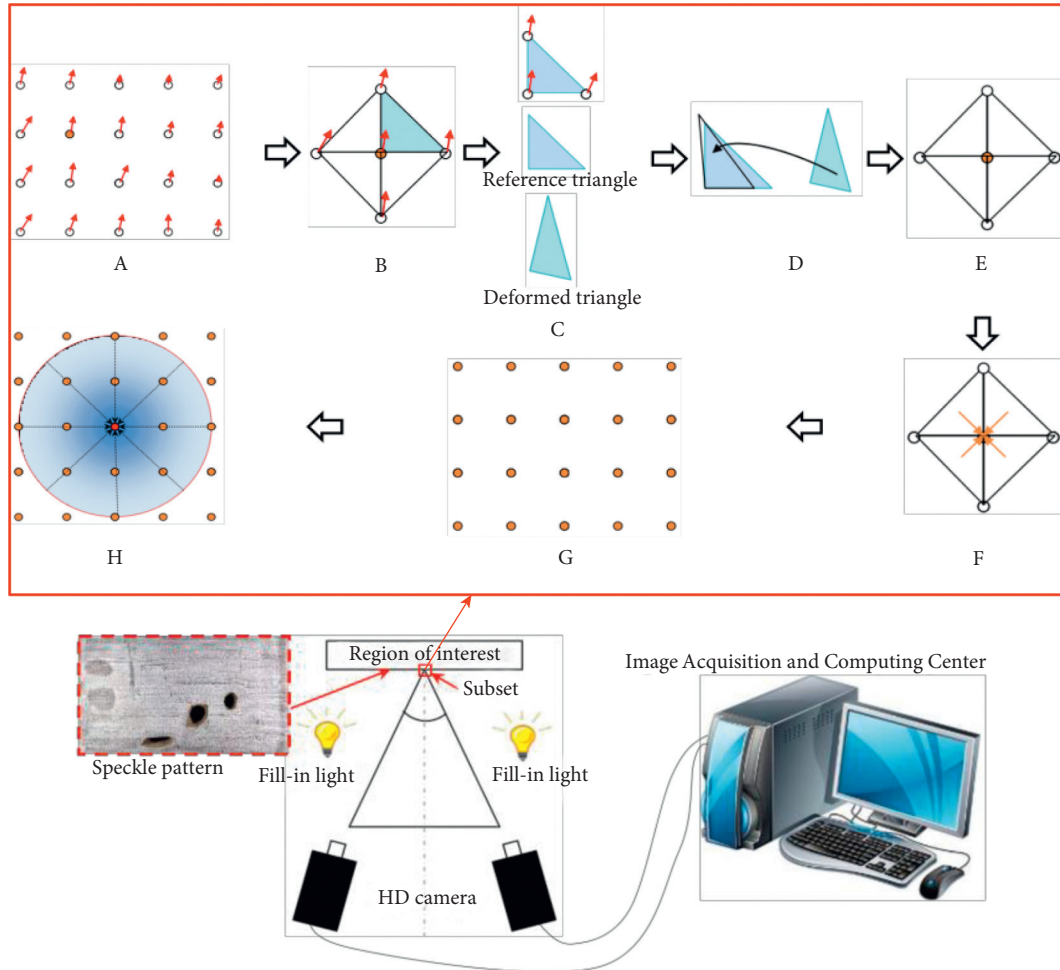


FIGURE 3: Methodology and principle for strain measurement.

Because the local triangles are small, the directly calculated strain tensors can be noisy, so at this point we smooth over a group of points. The size of this smoothing group is dictated by the user (“filter size”) and is a Gaussian (center-weighted) filter (see Figure 3H). The region of interest in the model is composed of these smoothed points, forming the final strain cloud image.

3.1.3. Equipment and Principle of Stress Measuring. For the measurement of the internal pressure of the model, we adopted the resistance strain sensor (see Figure 2(c)), whose resistance strain gage has the strain effect of metal; that is, mechanical deformation is generated under the action of external force, so that the resistance value changes accordingly. According to the principle of resistance strain effect, the deformation of the measured object is transformed into the change of the resistance parameter of the sensitive element, which is transformed into the output of voltage or current signal by the circuit, so as to realize the measurement of nonelectric quantity such as pressure.

3.2. Mechanical Parameters of the Strata and Determination of Similar Model Material Ratios. The principle of the simulation experiment of similar materials is to use materials with

similar mechanical properties to the mine prototype. Based on the three theorems of the similarity theory, the model is made according to the geometric similarity constant and the specific engineering conditions on-site, and the similar physical model is used to simulate all kinds of mine engineering. Then the phenomenon and data obtained can be used to speculate and analyze the rock mass change law in the mine prototype, so as to improve the production process.

The geometric shape of the model is similar to the engineering entity and satisfies the length ratio as a constant, that is,

$$a_L = \frac{L_p}{L_m}, \tag{1}$$

where a_L is geometric similarity ratio; L_p is entity size; L_m is model size.

According to the mine geological data, in the induced caving mining scheme, it is necessary to focus on the caving law of the roof surrounding rock at a height of about 100 m. Considering the size of the experimental equipment, the geometric similarity constant is selected as 100.

According to the data provided by the mine, the bulk density of mylonite ore is taken as $\gamma_m = 2.74 \text{ t/m}^3$, and the bulk density of marble is taken as $\gamma_n = 2.62 \text{ t/m}^3$. According

to the proportioning experiment, the bulk density of similar materials with different proportions is close, which is $\gamma_s = 1.70 \text{ t/m}^3$. Therefore, the ore rock bulk density similarity constant is

$$a_\gamma = \frac{\gamma_n}{\gamma_s} = 1.50. \quad (2)$$

The stress similarity constant is calculated by the similarity theorem, $a_\sigma = a_\gamma a_L = 150$, after calculation, $a_\sigma = 150$. At the same time, the elastic model similarity constant $a_E = a_\sigma = a_\gamma a_L = 150$ can also be calculated. Take the time similarity constant as

$$a_t = \sqrt{a_L} = 10. \quad (3)$$

According to on-site investigation, the surrounding area of the project can be regarded as a homogeneous gravitational field. The vertical ground stress of the target orebody at +175 m is $\sigma_p = 10.508 \text{ MPa}$. After calculation, the vertical loading stress of the model is

$$\sigma_m = \frac{\sigma_p}{a_\sigma} = 0.070 \text{ MPa}. \quad (4)$$

This paper simplifies the structural characteristics of the mine prototype, only simulating the horizontal layered rock mass structure, and aims to find the mechanism and basic laws of rock mass caving and then gradually simulates rock mass caving under complex conditions in subsequent studies. According to similar theory, the boundary conditions of the model should be as consistent as possible with the prototype. The first mining level in the mine prototype has sufficient width and length. For homogeneous rock mass, the range of stress redistribution caused by excavation is approximately equal to 3 to 5 times the excavation space. Therefore, when using the applied load method to study the problem, the simulation range should be at least 3 times larger than the excavation space. The excavation height of this simulation experiment is 0.1 m, so the model size is at least height \times length = $0.5 \times 0.5 \text{ m}$. According to the loading space size of the electrohydraulic servo multichannel similar material experimental platform, the size of the model produced this time is designed to be length \times thickness \times height = $2400 \text{ mm} \times 200 \text{ mm} \times 100 \text{ mm}$, and the model size can meet the requirements of similar theories [11].

3.3. Determination of Similar Physical Model Material Ratios.

“Similar physical model material ratio” refers to the proportion of various materials contained in the model stacked on the test bench. In order to find the appropriate ratio of similar physical model materials, we mainly studied the influence of sand-to-rubber ratio, gypsum-cement ratio, water content, and rosin alcohol solution content on the strength of similar materials. Firstly, according to the experience of similar mines, 11 sets of material proportioning schemes were screened out through orthogonal experiment. Each set of proportioning schemes produced 5 compressive test pieces and 5 tensile test pieces. The test specimens produced in the compressive strength experiment are $\phi 50 \times 100 \text{ mm}$. The tensile strength test specimen is a test

piece of $\phi 50 \times 50 \text{ mm}$ (see Figure 4(c)). Regression orthogonal experiment method is used to carry out rock strength test on samples with different proportions. The compressive strength can be obtained by using an extensometer to test the deformation of the specimen (see Figure 4(a)), and the tensile strength can be measured by the Brazilian split test (see Figure 4(b)), taking uniaxial compressive strength, tensile strength, elastic modulus, and Poisson’s ratio as the control targets for the strength of similar materials, and summarizing the regression equation for simulating the ratio of similar materials, so as to obtain the simulation material that satisfies the similar physical simulation test. The mechanical properties require the optimal proportioning scheme [7] (see Table 2).

3.4. Establishment of the Similarity Model

3.4.1. Test Model Design. The electrohydraulic servo multichannel similar material test bench can simulate the excavation process in mining and geotechnical engineering indoors. The equipment adopts active loading mode to simulate the excavation process under deep conditions. The equipment adopts multichannel independent control technology, which can simulate distributed load. The 7 axial loading cylinders are independently controlled, and the 3 horizontal loading cylinders are controlled synchronously. The loading force of the test can be loaded at a constant rate, and the test under constant load can be carried out within a given accuracy range. The long-term stability of axial load and horizontal load can be ensured during the test.

The size of the test model is length \times thickness \times height = $2400 \text{ mm} \times 200 \text{ mm} \times 1000 \text{ mm}$. The model is stacked in layers, and the upper part of the wood is used for layered compaction. The lowermost part is 200 mm high as the excavation space, and a preburied layer of extractable bricks is used for the test block (length \times thickness \times height = $200 \text{ mm} \times 50 \text{ mm} \times 100 \text{ mm}$). In the test, the wood blocks are removed one by one to simulate the excavation process of the orebody. At this moment, we observe the development of roof cracks in the excavation space and the caving of the upper mined-out areas (see Figure 5(a)) below. After 3 days of stacking the model, three holes of different sizes are drilled at predefined positions in the model according to the similarity ratio. After stacking the model for 7 days, speckles are sprayed on the position shown in the figure (as shown in Figure 5(b)); then we can carry out the loading and excavation tests.

3.4.2. Procedure of the Model Test. The purpose of this test is to study the failure mechanism and caving law of rock mass in the process of induced caving in the deep multi-mined-out areas of Paishanlou Gold Mine. K_1 , K_2 , and K_3 represent three mined-out areas, respectively, and the process of excavation is mainly divided into four steps. A total of 9 resistive stress sensors are arranged inside the model, which are, respectively, buried at points A, B, D, E, F, G, H, I, and J to monitor the trend of stress changes during the entire experiment.

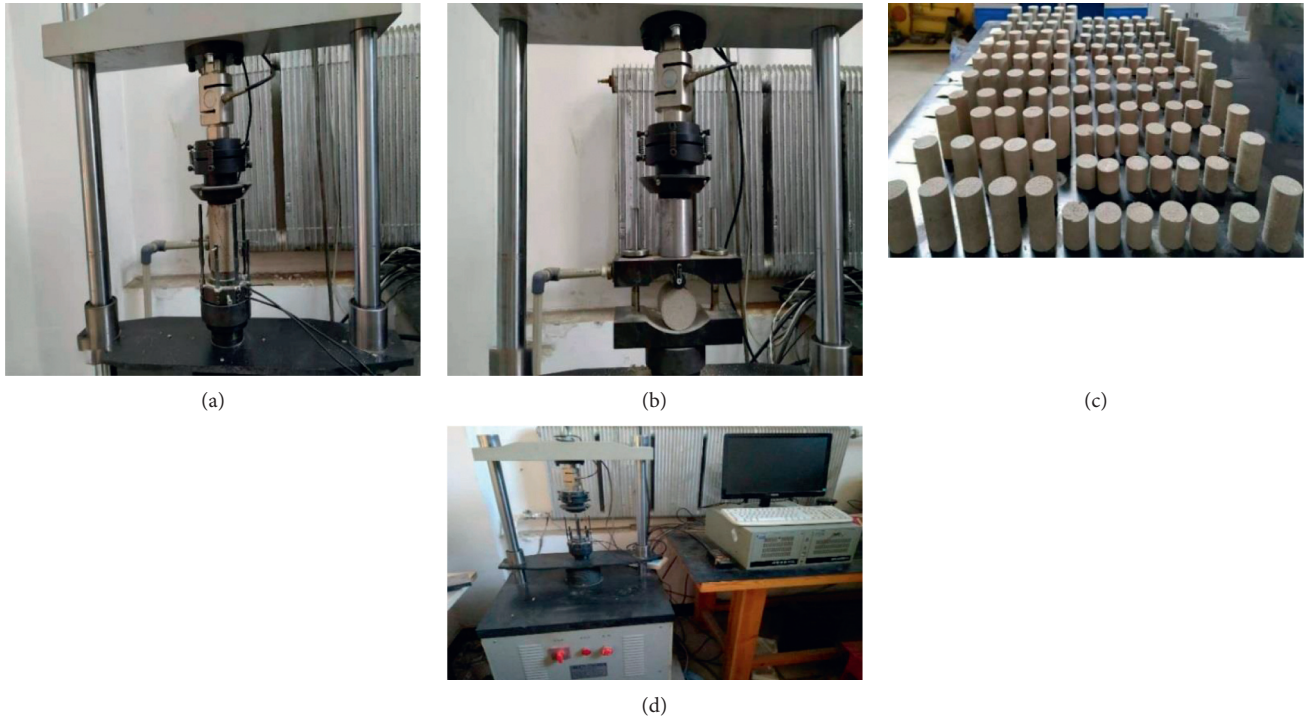


FIGURE 4: Physics experiments to find the material ratio of the test model. (a) Uniaxial compressive. (b) Brazil splitting experiment. (c) Molded specimen test. (d) Mechanical properties test of similar simulated materials.

TABLE 2: The ratio of similar materials' model test.

Materials	River sand (%)	Plaster (%)	Cement (%)	Rosin alcohol saturated solution (%)	Water (%)	Mica slice (%)
Ratio	78	4	7	2	8	1

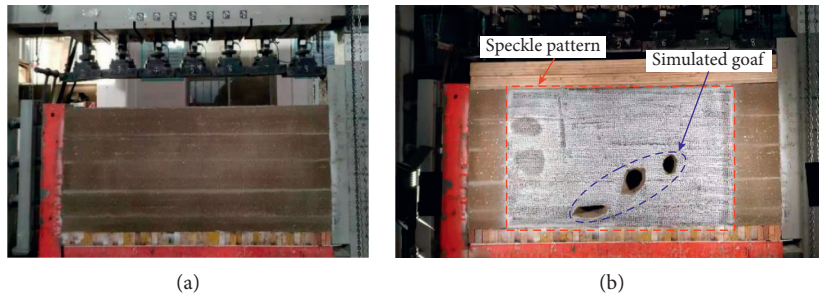


FIGURE 5: Construction of the similar physical model. (a) Initial similar physical model. (b) Similar physical model after processing.

In the test, we apply uniform pressure to the model according to the magnitude of the crustal stress, and the vertical load of 10 kN is applied to the 7 channels of the model before the model is excavated; then we keep the load constant. After about 10 minutes, we start to excavate No. 1 (between K_1 and K_2) and No. 2 pillars (between K_2 and K_3) in turn. After the excavation of each pillar, a period of time should be set aside to wait for the model to stabilize. Then we begin to continuously remove wood blocks from the bottom starting point which is 700 mm to left side of the model to simulate the caving of the surrounding rock on the roof. In this process, in addition to the VIC-3D monitoring test process, another high-definition camera is also needed to

record the formation of fracture line and rock caving process of similar physical models (see Figure 6).

4. Results and Discussion

4.1. Deformation and Failure Characteristics of Rock Mass

4.1.1. *The Process of Deformation and Failure.* Firstly, the vertical load is increased from 35 kN (load after the initialization of loading equipment) to 70 kN. Throughout the process of the test, the vertical load is kept constant without active horizontal loading. The model failure process is shown in Figure 7. When the model load is stable, it is found from

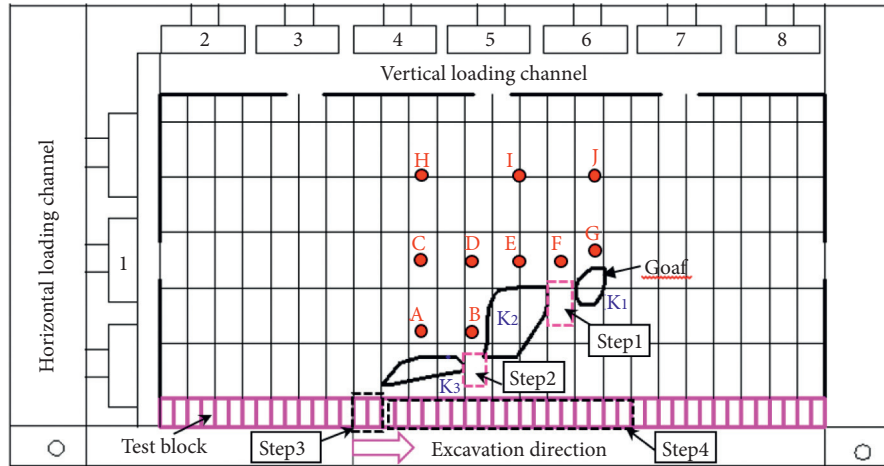


FIGURE 6: Schematic diagram of a similar material test process (1 represents the horizontal loading channel; 2~8 represent the vertical loading channels; K_1 , K_2 , and K_3 represent the goaf area; A~G represent the stress and strain monitoring points; Step 1~Step 4 represent the excavation sequence).

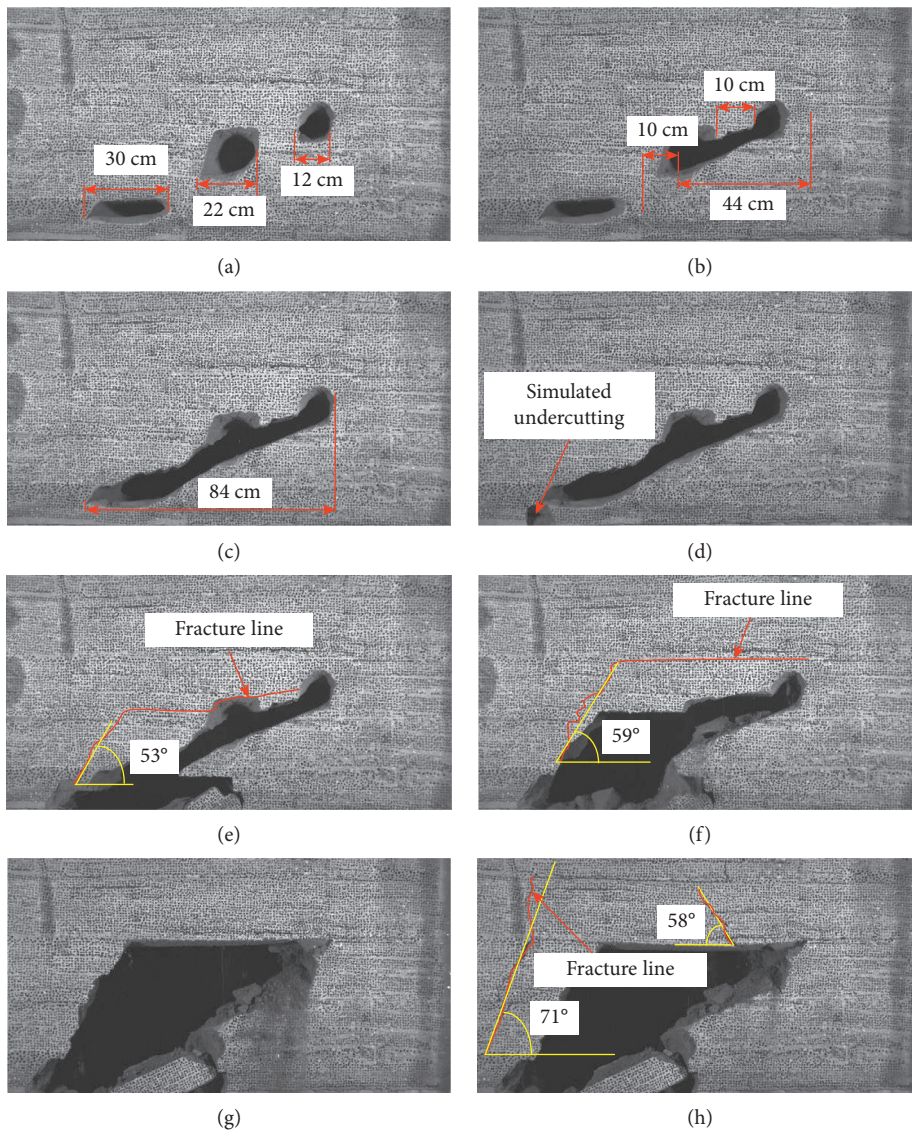


FIGURE 7: Schematic diagram of the failure process of the test model.

the vertical strain cloud diagram (Figure 8(a)) that the overall displacement of the model gradually decreases with the increase in depth, and the greater the span of the empty area, the greater the vertical displacement above it. At this time, the centerline of the settlement zone is close to goaf K_3 with a larger span. From Figures 8(b) and 8(c), we know that when the pillar No. 1 between the goafs K_1 and K_2 (all the following texts will be referred to as “pillar No. 1”) is excavated, a 30~55 cm thick cone-shaped subsidence zone is quickly formed above the goaf after penetration, and the larger the goaf span, the more the vertical subsidence. The average displacement at this time is 0.4 mm, but after about 200 s, the subsidence zone gradually shifts to the top of the pillar 1 and then continually spreads to left of the upper of the model (the region is above K_3) to the top of the model, and the average displacement increases to 0.5 mm. Then we excavate the No. 2 pillar between K_2 and K_3 (all the following texts will be referred to as “pillar No. 2”) (see Figures 8(d) and 8(e)). The displacement above No. 2 pillar increased rapidly. Meanwhile, a 30 cm deep butterfly-shaped subsidence zone is formed in the middle of the model with an average deformation of 0.7 mm. After about 5 minutes, the large deformation area gradually evolves into a chimney shape, and the average amount of deformation increased to 1 mm. At this very moment, two strip-shaped deformation areas that spread to the top of the model were formed above the goafs K_1 and K_2 , and the average amount of deformation was 0.85 mm. After that, the third step of the simulated undercutting project is carried out. After the excavation of the left corner of K_3 , the chimney-shaped deformation zone gradually expands, and the gourd-shaped deformation zone appears in the central area. The displacement of the central area was 1.3 mm, and the displacement of the upper part of K_3 was 1 mm (see Figures 8(f) and 8(g)); simultaneously, a 53° crack appears above K_3 (see Figure 7(e)). With the excavation in the fourth step, the deformation area gradually develops into a rectangle with a displacement of 2.48 mm, followed by a caving, which is now in the sporadic caving stage. After a strip-shaped deformation zone with an average deformation of 4.3 mm appeared again in the lower left of the rectangular displacement zone, a fracture line of 59° appeared in the left side of the roof (Figure 7(f)), and then a continuous caving occurs. After the continuous caving, the remaining roof maintained a stable period of about 3 minutes, and then large cracks of 71° and 58° penetrating to the top were formed on the left and right sides of the model, and then a large caving occurs rapidly until the model collapses (see Figures 7(g) and 7(h)).

4.1.2. Analyses of Deformation and Failure Mechanisms. According to the analysis of the similar test process, the entire destruction process of the goafs can be divided into five stages, namely, the deformation and failure of rock mass, the instability stage of sporadic caving, the continuous caving stage of separation layer of roof, and the instantaneous huge caving stage of the roof. The rock mass of

original goafs is in a state of squeezing, and the mining of the pillar will unload the surrounding pressure, and the goaf that loses its original support will cause the redistribution of the surrounding rock stress.

- ① After the No. 1 pillar is excavated (the mined-out area after the penetration of K_1 and K_2 is called K_{12}), the roof of the mined-out areas under the action of gravity of the overlying rock mass will bend to the free surface (see Figure 8(b)). After the spontaneous stress redistribution process of the surrounding rock, a stable deformation zone “a” is formed in the upper area of the goaf K_{12} , and the average deformation is the largest (Figure 8(c)).

Similarly, when the No. 2 pillar is excavated, the main deformation zone gradually shifts from the upper area of K_{12} to the position of the No. 2 pillar, and finally the deformation zone “b” is formed (Figure 8(e)). The two steps have undergone the process of elastic deformation-plastic deformation, and the transition from elastic deformation to plastic deformation is due to the redistribution of stress around the goaf caused by the excavation of the pillar. According to the analysis of the cloud diagram, the pressure properties of the roof of the goafs in the deformation zone “a” are mainly compressed, and the exposed area of the roof expanded with the excavation of the pillar, which makes the stress properties of the roof of the goaf transform from the compressed state to tension state.

As known from the foregoing, the ore rock in the goaf is medium-hard rock with poor ductility, so the main form of ore rock failure is brittle failure. From the perspective of failure mechanism, it can be divided into two categories: tensile failure and shear failure. With the progress of the simulated undercutting project, the span of the mined-out area has further increased, the tensile stress of the surrounding rock of the roof exceeds the allowable tensile strength of the rock mass, and the left lower foot of model begins to show 53° crack failure line under the action of shear stress (as shown in Figure 7(e)).

- ② With the progress of the undercutting project, the stress concentration phenomenon at the undercutting position makes the crack failure further expand upward. Caving occurs when the surrounding rock stress is not enough to support the self-weight of the rock formation, and the caving rock lumpiness is small, and we call this stage sporadic caving.
- ③ The undercutting project destroys the stress balance of the surrounding rock. With the progress of sporadic caving, the fracture damage gradually extends upward under the combined action of the tensile and compressive stress of the roof. At this time, the roof layer began to gradually delaminate, followed by continuous caving (Figures 8(e)–8(g)).
- ④ In the later period of the continuous caving, a 71° large-angle fracture line appeared on the left side of

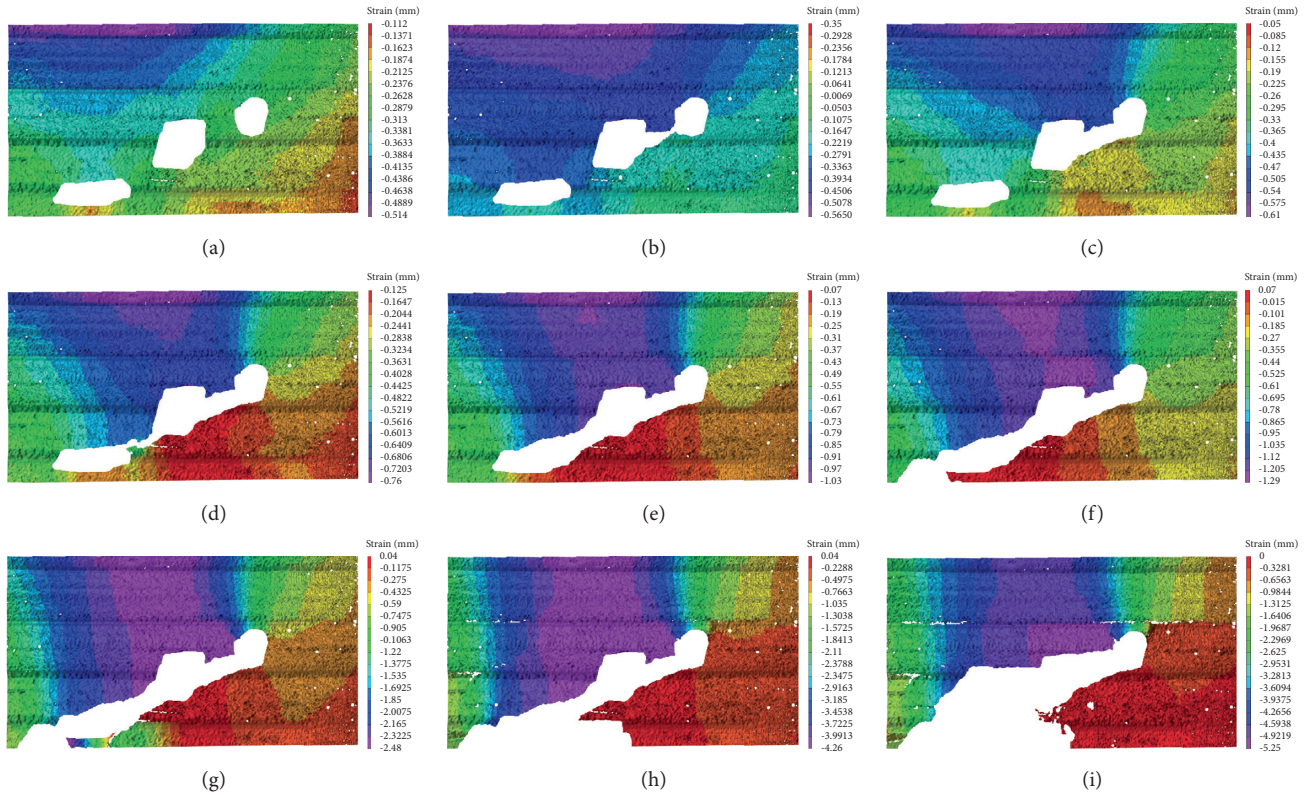


FIGURE 8: Vertical strain cloud diagram of the whole field of the test model.

the model. After a period of development of the fracture, instantaneous roof collapse occurred in the model.

4.2. Strain and Stress Analysis. The VIC-3D data analysis software is used to extract the local displacement values of points A, B, C, D, E, F, G, H, I, and J on the surface of the model (see Figure 6), and the displacement trend during the whole experiment is plotted (see Figures 9(a) and 9(b)). In addition, the pressure values of points A, B, D, E, F, G, H, I, and J collected by the pressure sensor are plotted as curves (see Figures 10(a) and 10(b)).

As can be seen from the displacement trend diagram in Figure 9, after the excavation of No. 1 pillar, all monitoring points begin to settle, and the sedimentation rate of E, F, and I points rises first, and the settlement rate is the largest. After the excavation of No. 1 pillar is completed, points E, F, G, and J will continue to settle for about 50 s. During the excavation of the No. 1 pillar, the settlement amount is large in the middle of the goaf and small in the two sides. Due to the effect of No. 2 pillar, the excavation of No. 1 pillar has less influence on the settlement of four monitoring points A, B, C, and D. After the excavation of No. 2 pillar, the settlement rates of B and D near the pillar roof begin to rise first and reach the maximum. The overall settlement shows the characteristics of large in the middle and small in the two sides and large in the upper part and small in the lower part. After the excavation of No. 2 pillar, all monitoring sites still

keep the settlement trend of about 220 s. After the simulated bottom drawing project starts, the settlement rates of points A, B, G, and J begin to rise first and reach the maximum, and then the overall settlement trend is regular. The settlement of the whole simulated bottom drawing process presents the characteristics of large, middle, and small two sides, and the settlement of G and J points at the other end of the excavation position is the least. When continuous caving occurs, the displacement of points G and J rises. This is because the effect of cantilever beam causes the pressure in the middle of the model to produce a component force along the direction of gravity on the slope before caving occurs. After caving is completed, the pressure disappears, so the displacement of points G and J rises.

It can be seen from the vertical pressure variation trend diagram in Figure 10, after the excavation of No. 1 pillar, since the span of K_1 pillar is small, positions of F and G are close, and their variation trends are also similar. E is close to the center the connected goaf of A and B, and the pressure value at point I drops first, and then point I drops accordingly. The rate and range of decline at point E are greater than those at point I, while H and J at the top rise slowly. Points D and B are located above pillar 2. After the excavation of No. 1 pillar, the pressure was transferred to both sides, resulting in the pressure value of B and D increasing at the same speed and range. At the same time, the pressure value of points F and G increases, and the pressure value of point G increases faster than that of points F and J. After the excavation of No. 2 pillar, the

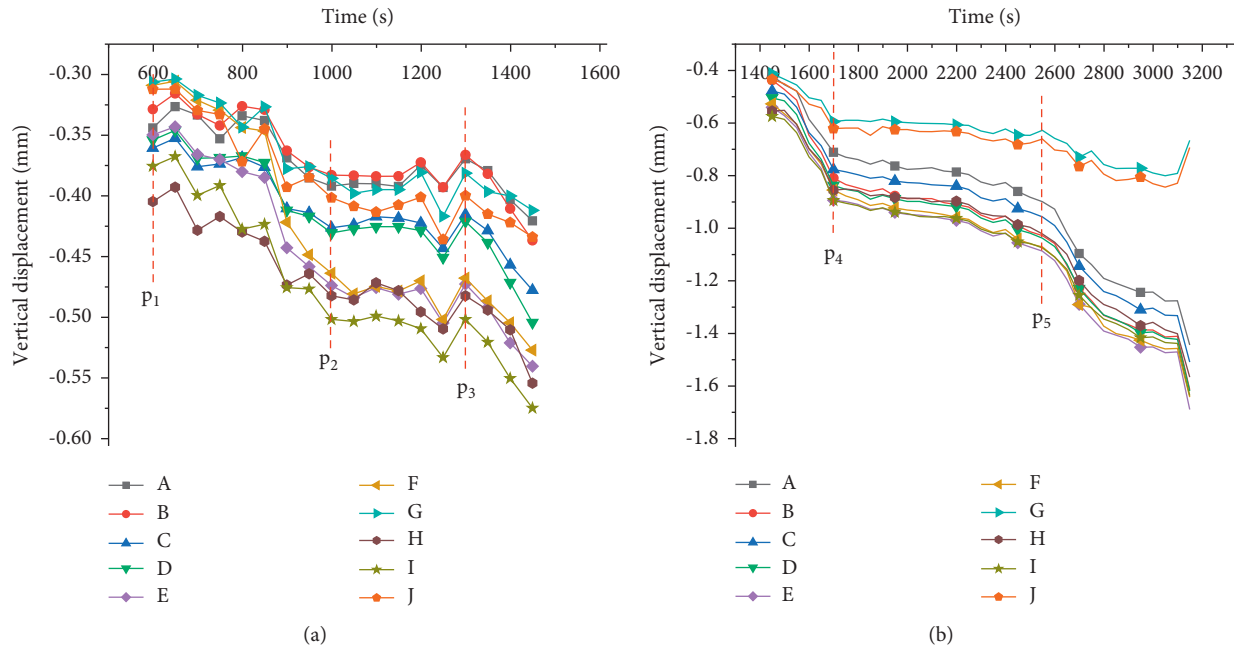


FIGURE 9: Vertical displacement trend of each monitoring point (p1 stands for No. 1 pillar before excavation; p2 stands for No. 1 pillar after excavation; p3 stands for No. 2 pillar before excavation; p4 stands for No. 2 pillar after excavation; p5 stands for the start of simulated bottoming).

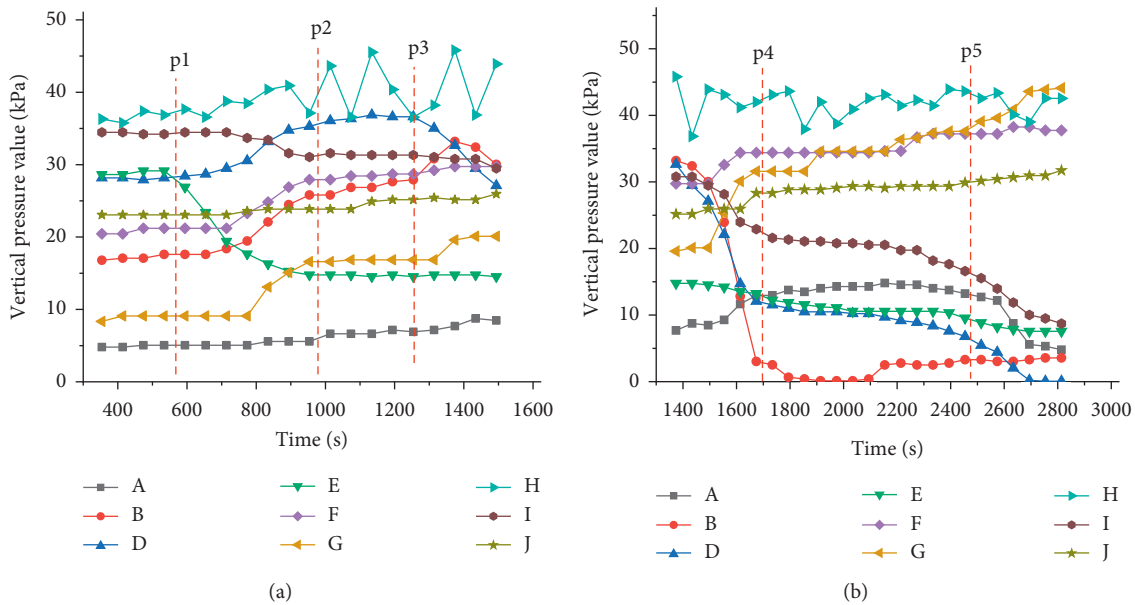


FIGURE 10: Vertical pressure trend of each monitoring point (p1 stands for No. 1 pillar before excavation; p2 stands for No. 1 pillar after excavation; p3 stands for No. 2 pillar before excavation; p4 stands for No. 2 pillar after excavation; p5 stands for the start of simulated bottoming).

pressure values of B and D begin to decrease first, and the pressure values of E and I then decrease. The decreasing rate of B is greater than that of D, and the decreasing rate of E is less than that of D. On the contrary, the pressure values of points H, G, and J all show an upward trend, and the growth rate is greater than that of H, and the growth rate of G is greater than that of J. After the beginning of the drawing project, the pressure at points F, G, and J increased, while the pressure at other points decreased to

some extent. Point A starts to decline first and has the largest rate of decline; then points A, D, and E decline in turn.

4.3. Discussion

- (1) In order to ascertain the temporal and spatial evolution of the deformation and failure of the surrounding rock induced by multi-mined-out areas,

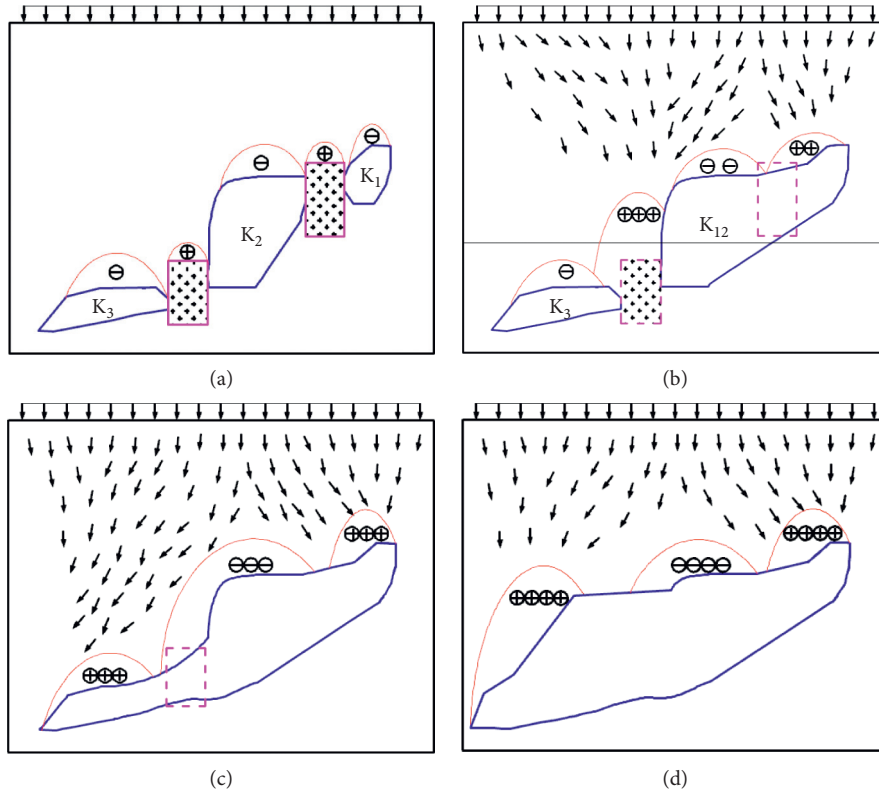


FIGURE 11: Schematic diagram of stress transfer of the roof-pillar system.

we need to analyze the impact mechanism of rock mass instability on the safety of mine production and the stability of the mined-out areas system. Therefore, based on the rock deformation and failure mechanism obtained by the analysis in 4.1, combined with the stress and strain change law obtained during the experiment (Figures 8 and 9), we discuss the overall instability law of the coordinated effect of the roof-pillar system in the mined-out area and propose the caving control and safety management technology in the goafs of Paishanlou. After the excavation of the pillars between the mined-out areas in a balanced state, the surrounding rock deforms, which leads to changes in stress. For purpose of maintaining the balance, the surrounding stress field transfers spontaneously to seek a new balance. Therefore, the balance of goaf system is essentially a stress balance. In order to ascertain the law of caving in the goaf, the transfer of the stress field and the law of pressure increase and release of the roof-pillar system are first studied.

Before the excavation of the pillar, the roof-pillar system is in a balanced state. There is a pressure-bearing area above the pillar (indicated by “ \oplus ” in the figure, and the number of \oplus qualitatively indicates the pressure-bearing value), and the upper area of mined-out areas is the pressure relief area (indicated by “ \ominus ” in the figure, and the number of \ominus qualitatively represents the pressure relief value) (Figure 11(a)); the arrows represent the transfer of pressure.

After the excavation of the No. 1 pillar, the upper area of K_{12} begins to relieve pressure, then the pressure gradually shifted to the No. 2 pillar and the right side bank, and the No. 2 pillar was the main pressure-bearing area. At this time, the stress above the goaf of K_1 does not change significantly, indicating that the stress transfer was blocked by the No. 2 pillar, and the No. 2 pillar shows obvious stress concentration (see Figure 11(b)).

After the excavation of the No. 2 pillar, the goaf is connected as a whole. The sudden release of the high stress above the No. 2 pillar caused an instantaneous pressure relief in the middle part, and the stress shifted to the two sides and the pressure value of the left slope was greater than that of the right slope. This is on account of the excavation sequence of the pillars and the buried depth of the goaf (see Figure 11(c)). After the start of the induced undercutting project, with the increase of the span of the mined-out area, the rock mass began to cave sporadically, and the pressure above the caving zone was slowly relieved at this time. At the same time as the phenomenon of separation of rock mass occurs, the pressure relief rate of the caving zone suddenly increases, and the two slopes on both sides also increase suddenly, and the rock mass begins to cave continuously. The fracture line caused by the caving gradually developed to the near-surface area, and after a period of stability, a sudden and instantaneous large caving occurs (see Figure 11(d)).

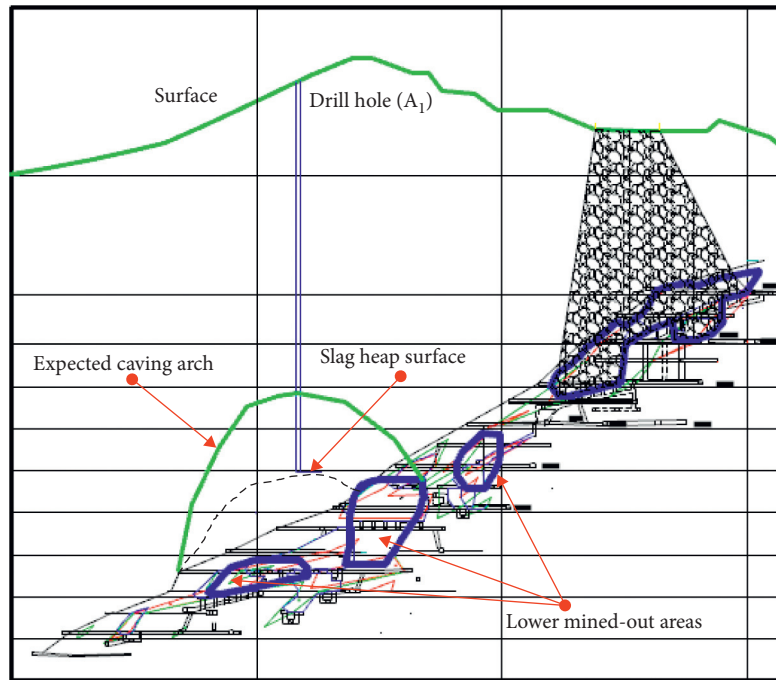


FIGURE 12: Schematic diagram of the goaf caving monitoring and filling scheme.

- (2) Since the lower mined-out areas are not allowed to penetrate to the ground surface, so as to achieve reasonable and efficient recovery of ore while dealing with the goaf, we have formulated a coordinated scheme for pillar mining and goaf filling through surface borehole. Taking into account the safety and efficiency factors, it is better to wait for the mined-out areas to cave to a certain height before filling it, but it is necessary to prevent sudden penetration to the ground. Because the higher the caving height of the goaf is, the smaller the drilling depth is, and the larger the filling range is. It can be seen from the test that, during the entire caving process, sporadic caving is the least destructive to the stability of the rock mass, and instantaneous large caving is the most destructive. Therefore, we should control the caving process in the later period of the sporadic caving to the initial period of continuous caving.

According to the results of the previous analysis, there will be obvious roof separation phenomena during the transition from sporadic caving to continuous caving. In addition, the angle of the fracture line inside the rock mass, the vertical strain, and the pressure of slopes on the two sides have increased significantly. Hence, we monitor the roof rock caving process of the mined-out areas by drilling surface monitoring holes, combined with the RG underground TV, and expand the monitoring boreholes at a predetermined time and then fill the mined-out areas through borehole A_1 to control the caving process. Through monitoring, we can see that the mined-out areas are currently in the sporadic caving phase (Figure 12). Test has proved that the process of

induced caving in the multi-mined-out areas can be controlled artificially, and the mined-out areas can be treated efficiently while the residual ore is mined, which has certain guiding significance for the production of similar mines.

5. Conclusion

Through indoor similar physical model tests, using noncontact full-field displacement measurement systems and resistive pressure sensors as monitoring methods, we recorded in detail the stress and strain trend of surrounding rock during the process of penetration and undercutting of the multi-mined-out areas and summarized and analyzed the deformation and failure characteristics of the rock mass and the temporal and spatial evolution law of the stress and strain with the caving of the mined-out area. The main conclusions are as follows:

- (1) The rock caving is mainly divided into three stages: the first stage occurs above the left arch angle of the first undercutting project, the fracture angle is 59° , the caving in this stage is slower, and the lumpiness is small. The stage occurs at the top of the caving arch, and the fracture angle is 57° . This stage has a large caving block; the third stage is an instantaneous roof caving, and there is a stable period of about 3 minutes before the roof caving. The fracture angles of the sides are 71° and 58° , respectively, because the large horizontal stress of the roof will limit the dilatancy space of the surrounding rock of the roof.

- (2) A sudden increase in the fracture angle occurred in the upper area of the undercutting position before the instantaneous caving of the top, and the curvature of the caving suddenly increased. The instantaneous caving of the top plate is the continuation of the caving of the vault, which can be safely drilled. The shape of the caving arch is monitored to ensure that the goaf cave is naturally in the form of sporadic caving in the initial caving stage; that is, the time of huge caving can be safely monitored and the caving process is controllable.
- (3) Rock deformation is most affected by the span of the goaf, and the vertical strain is inversely proportional to the depth; the rock mass stress and strain caused by the excavation of the void space column have a significant time delay phenomenon, and the time delay effect of the stress is inversely proportional to the void span. The time delay effect is inversely proportional to the gap span. During the test, the strain value shows the characteristics of high in the middle of model and low in the slope of both sides and high in the upper area and low in the lower area, while the stress shows the characteristics of high in the slope of both sides and low in the middle and high in the upper area and low in the lower area.
- (4) The excavation sequence of the pillar will affect the stability of the roof-pillar system in the goaf. The pillar excavated first will have a stress concentration effect on the pillar excavated later and the surrounding rock mass, resulting in the local destruction of the rock mass, thereby affecting the layout of the inducing project and the process of caving in the mined-out area.
- (5) According to the law of caving in multi-mined-out areas obtained from the test, combined with the RG underground drilling monitoring technology, the caving process of the goafs can be effectively controlled. Thereby it can provide favorable conditions for the filling, mining, and ore drawing work of the goaf. At the same time, it has reference significance for the management of multi-mined-out areas in similar mines.

Data Availability

No data were used to support this study.

Conflicts of Interest

The authors declare that they have no conflicts of interest.

Acknowledgments

This study was supported by the National Natural Science Foundation of China (no. 51534003) and National Key R&D Program Project of China (no. 2016YFC0801601). The agencies' funding is gratefully acknowledged.

References

- [1] F. Y. Re, N. Li, S. Chan, K. Jiang, J. Xiao, and X. Liu, "Study on the induced caving method in transferring from open-pit to underground mining in main mining area of Yanqianshan iron mine," *Mental Mine*, vol. 2, pp. 42–45, 2010.
- [2] F. Y. Ren, H. Y. Li, M. L. Ren, B.-d. Liang, and F.-y. Hu, "Technique of induced caving on adjacent mined-out areas in Shujigou iron mine," *China Mining*, vol. 21, no. S1, pp. 378–380, 2012.
- [3] F. Y. Ren, S. Z. Shan, and J. F. Huo, "Study of mining method for difficult mining ore-body in Yushiwa iron mine," *Mental Mine*, vol. 1994, no. 7, 16 pages, 1994.
- [4] Z. H. Zhou, F. Y. Ren, W. X. Wang, and H. Jiang, "Study on the high efficient mining scheme of inclined fractured orebody in Houhemushan iron mine," *China Mining*, vol. 2006, no. 3, 50 pages, 2006.
- [5] Z. H. Zhou, F. Y. Ren, and G. Q. Yuan, "Study on treatment method of the mined area in Taochong iron mine," *China Mining*, vol. 2005, no. 2, 18 pages, 2005.
- [6] R. X. He, F. Y. Ren, and B. H. Tan, "Discussion on Induced caving and block caving," *Mental Mine*, vol. 3, pp. 9–14, 2017.
- [7] S. Chen, H. Wang, J. Zhang, H. Xing, and H. Wang, "Experimental study on low-strength similar-material proportioning and properties for coal mining," *Advances in Materials Science and Engineering*, vol. 2015, Article ID 696501, 2015.
- [8] F. Gao, K. Zhou, W. Dong, and J. Su, "Similar material simulation of time series system for induced caving of roof in continuous mining under backfill," *Journal of Central South University of Technology*, vol. 15, no. 3, pp. 356–360, 2008.
- [9] Z. He, H. Xie, M. Gao, L. Ding, G. Peng, and C. Li, "The fracturing models of hard roofs and spatiotemporal law of mining-induced stress in a top coal caving face with an extra-thick coal seam," *Geomechanics and Geophysics for Geo-Energy and Geo-Resources*, vol. 7, no. 1, 2020.
- [10] L. Mao, H. Liu, Y. Wang, M. Gao, Y. Ju, and F. Chiang, "3-D strain estimation in sandstone using improved digital volumetric speckle photography algorithm," *International Journal of Rock Mechanics and Mining Sciences*, vol. 141, Article ID 104736, 2021.
- [11] W. Ren, C. Guo, Z. Peng, and Y. Wang, "Model experimental research on deformation and subsidence characteristics of ground and wall rock due to mining under thick overlying terrane," *International Journal of Rock Mechanics and Mining Sciences*, vol. 47, no. 4, pp. 614–624, 2010.
- [12] C.-F. Yuan, Z.-J. Yuan, Y.-T. Wang, and C.-M. Li, "Analysis of the diffusion process of mining overburden separation strata based on the digital speckle correlation coefficient field," *International Journal of Rock Mechanics and Mining Sciences*, vol. 119, pp. 13–21, 2019.
- [13] J. Zhang and B. Shen, "Coal mining under aquifers in China: a case study," *International Journal of Rock Mechanics and Mining Sciences*, vol. 41, no. 4, pp. 629–639, 2004.
- [14] C. O. Aksoy, H. Kose, T. Onargan, Y. Koca, and K. Heasley, "Estimation of limit angle using laminated displacement discontinuity analysis in the Soma coal field, Western Turkey," *International Journal of Rock Mechanics and Mining Sciences*, vol. 41, no. 4, pp. 547–556, 2004.
- [15] X. Wang, Q. Qin, and C. Fan, "Failure characteristic and fracture evolution law of overburden of thick coal in fully mechanized sub-level caving mining," *Sains Malaysiana*, vol. 46, no. 11, pp. 2041–2048, 2017.
- [16] Y. Chen, S. Ma, and Y. Yu, "Stability Control of underground roadways subjected to stresses caused by extraction of a 10-m-

thick coal seam: a case study,” *Rock Mechanics and Rock Engineering*, vol. 50, no. 9, pp. 2511–2520, 2017.

- [17] H. Kong, L. Wang, G. Gu, and B. Xu, “Application of DICM on similar material simulation experiment for rock-like materials,” *Advances in Civil Engineering*, vol. 2018, Article ID 5634109, 2018.
- [18] Q. Zheng, N. Mashiwa, and T. Furushima, “Evaluation of large plastic deformation for metals by a non-contacting technique using digital image correlation with laser speckles,” *Materials & Design*, vol. 191, Article ID 108626, 2020.

Research Article

Study on the Key Technology of Controlling the Instability of Deep High-Stress Coal and Rock Mass and Relieving the Danger

Zhijing Zhang,¹ Jianghong Zuo,¹ and Dongji Lei² 

¹Wuyang Coal Mine of Shanxi Lu'an Environmental Protection and Energy Development Co., Ltd., Changzhi City, Shanxi Province 046000, China

²State Key Laboratory Cultivation Base for Gas Geology and Gas Control, Henan Polytechnic University, Henan Province 454000, China

Correspondence should be addressed to Dongji Lei; leidongji@126.com

Received 28 May 2021; Accepted 26 July 2021; Published 6 August 2021

Academic Editor: Wei-yao Guo

Copyright © 2021 Zhijing Zhang et al. This is an open access article distributed under the Creative Commons Attribution License, which permits unrestricted use, distribution, and reproduction in any medium, provided the original work is properly cited.

In order to solve the problem of stress concentration and gas overrun in the process of uncovering high gas and thick coal seam, combined with the occurrence characteristics of coal seams in Wuyang Coal Mine, the measures of “hydraulic and mechanical cavity making + steel screen pipe + surrounding rock grouting” are adopted to establish a method for mutual verification of multiple effect test indexes of residual stress, residual gas content, coal seam moisture content, and microseismic signal characteristics, and the three-dimensional accurate analysis of the influence range of hydraulic cavitation is effectively realized. By comparing and analyzing the gas extraction amount, the surrounding borehole stress change and the microseismic monitoring signals before and after the application of hydraulic cavitation technology are studied. The results show the following. (1) The pressure relief effect of the hydraulic cavity on surrounding coal decreases with the increase of distance, and the pressure relief effect is most obvious at 1.0~2.5 m, in the range of 2.5~3.5 m around the hydraulic drilling hole, the duration, rate, and amplitude of pressure relief are reduced compared with those in the range of less than 2.5 m, while in the range of more than 3.5 m, the effect of pressure relief is very weak. (2) During the period of hydraulic cavitation release hole, the radius of water supply to coal seam is within 1.5 m, which accounts for 79% of coal wall area. (3) It is also a process where the stress distribution in the coal and rock body needs to be rebalanced before and after hydraulic caverning, which is often accompanied by microfracture of coal and rock mass. The analysis shows that, before hydraulic caverning, the waveform of coal and rock fracture signal has a short duration, large amplitude, and obvious signal mutation, and the dominant frequency of the signal is about 250 Hz, with large total energy. After hydraulic caverning, the intensity of coal and rock fracture events is greatly reduced. The research results can effectively identify the influence range of hydraulic cavitation, improve the detection accuracy and efficiency of hydraulic cavitation range, effectively predict and warn the hidden danger of mine safety, and provide a reference for the work of similar mines.

1. Introduction

At present, China's coal mines have entered deep mining areas, and the characteristics of high gas content, strong adsorption, and poor air permeability of coal seams have more obvious constraints on the efficient mining of the mine, and because of the increase of the scale of coal mining, the impact on the environment is bigger and bigger [1]. The key to efficient mining is to improve the permeability of coal seam, realize the efficient predrainage of gas before mining, and effectively reduce the content of gas in the coal seam. At

the moment, measures such as loose blasting [2–4], hydraulic slitting [5, 6], hydraulic punching [7, 8], and hydraulic fracturing [9–11] have been widely adopted to relieve pressure and improve reflection of coal seams. But due to the limitations of these measures, applicable conditions, such as loose blasting and hydraulic slotting easily induced by coal and gas outburst, stress, high hydraulic fracturing cracks easily closed, and hydraulic punching limited by the rigidity coefficient of coal, are susceptible to the limitation of geological structure and construction equipment; at the same time, the effect evaluation of hydraulic hole forming is

imminent. Microseismic monitoring technology is a geophysical real-time monitoring technology that studies and evaluates the stability of coal and rock mass by using the microseismic signals generated in the process of coal rock failure under load [12, 13]. It can effectively identify different coal and rock dynamic disaster signal types and characteristics, evaluate the stability of coal internal structure, and provide theoretical support for coal and rock dynamic disaster prevention in underground operation.

The technology of hydraulic hole punching and cavitation is to cut the coal around the drilling hole with a high-pressure water jet under the condition of no one in the working face to form a larger hole, increase the exposed area of the coal body, relieve the pressure inside the coal seam, and take the cut coal out of the hole with water flow. In the process of hydraulic cavitation, a large number of coal bodies are crushed and rushed out of the borehole under the impact of high-pressure water flow, which can greatly reduce the in situ stress of coal bodies. At the same time, cavitation causes a large amount of coal caving to form several depressurized caverns with a larger diameter, which increases the exposed area of the coal seam, and forms a huge fracture network around the caverns, which provides a large space for gas migration and extraction and improves the permeability of coal seam. In addition, hydraulic perforation and cavitation make a large amount of water enter the coal body, improve the desorption rate of gas in the coal body, and further reduce the risk of coal and gas outburst [14]. Many scholars have conducted in-depth research on this. Wang and Li [5] and others conducted numerical simulation by using the field measured data and found that after the implementation of hydraulic extrusion measures in the heading face, the stress of coal body in front of the heading face was redistributed, the elasticity was reduced, the plasticity was increased, and the permeability of coal body was enhanced. Through analysis, Li [6] concluded that water injection by hydraulic extrusion can effectively reduce the gas content and gas emission in coal, greatly reducing the risk of outburst; Yang and Hu [7] and others pointed out that hydraulic punching in high outburst coal seam can not only eliminate the outburst risk of working face but also improve the driving speed and working environment. Liu et al. [9] and others elaborated the basic principle of hydraulic cavitation technology based on the research background of Jiulishan Mine with serious coal and gas outburst and pointed out that hydraulic cavitation technology could effectively eliminate the stress of excitation outburst, reduce the risk of coal seam outburst, and increase the driving speed of roadway by 2-3 times. Lu and others [11] used 40~60 MPa high-pressure water jet cutting measures for gas control in Rujigou coal mine, effectively improved the coal seam permeability, increased the gas drainage efficiency by 3~6 times, and eliminated the outburst risk in the process of mining. Zhang [15] combined theoretical analysis with the field test, studied the application effect of hydraulic hole making pressure relief and permeability enhancement technology in coal roadway bottom drainage, and showed that hydraulic hole making drilling can have the effect of pressure relief and permeability enhancement on coal body. Compared with

ordinary through-layer drilling, hydraulic hole making technology increases the initial gas drainage concentration, and the influence radius of drilling also increases by one time. It can be seen that hydraulic cavitation has a good improvement and promotion effect on coal seam gas release and pressure relief, so it is extremely urgent to develop hydraulic cavitation technology to prevent coal and gas outbursts in the roadway.

The coal mining depth of the Wuyang Coal Mine of Shanxi Lu'an Group has reached more than 700 meters. With the increase of mining depth, the permeability of the coal seam itself and surrounding rock is reduced, and the amount of gas is also increasing, and there are many times of coal blasting in the excavation. In order to solve the problems of stress concentration and gas overrun in the process of uncovering high gassy thick coal seam, combined with the occurrence characteristics of the coal seam in Wuyang Coal Mine, by using the combination of "hydraulic and mechanical cavity making + steel screen pipe + surrounding rock grouting" outburst prevention technology, the mutual verification method of multiple effect inspection indexes such as residual gas pressure, residual gas content, K1 value, coal swelling deformation, coal seam moisture content, and surrounding rock deformation is established, which effectively realizes regional pressure relief, water supplement, and surrounding rock stress control. In this paper, by comparing the changes of gas drainage amount and surrounding borehole stress before and after hydraulic punching, the gas drainage effect after hydraulic punching and the activated drainage radius after stress release are studied. Combined with the microseismic monitoring technology, the whole process monitoring and comparative analysis of the spatial-temporal distribution characteristics of microseismic events before and after the measures and the dynamic response characteristics of the signal waveform are carried out, and the activated extraction radius after hydraulic cavity building is verified by contact and noncontact means, which provides a theoretical basis for preventing mine rock burst disaster.

2. Hydraulic Cavern Engineering Test

Wuyang Coal Mine mainly adopts 3# coal seam, and the gas control measures are mainly prepumping coal seam gas by drilling along the seam. In daily work, there are many problems, such as a large amount of drilling engineering, the easy collapse of drilling, and the low net quantity of single hole, which directly lead to a long time of reaching the standard of drainage and then cause a serious imbalance of mining and drainage balance. The attenuation coefficient of borehole coalbed methane flow in 3# coal seam of Wuyang Coal Mine is 0.0063 d^{-1} , the permeability coefficient is $0.412\sim 0.88 \text{ m}^2/\text{MPa}^2\cdot\text{d}$, and the firmness coefficient is $f=0.2\sim 0.5$. According to the daily underground gas content measurement results, the coal seam coalbed methane desorption speed in this area is slow, and 60~70% of the coalbed methane is comminuted desorption volume, which directly leads to low single hole drainage volume of drainage borehole. The in situ stress in this area is large, complex, and

changeable, and it is easy to collapse after drilling. It is difficult to release the in situ stress in the drainage area and then inhibit the coalbed methane desorption, resulting in the rapid attenuation of single hole drainage volume. In view of this, it is urgent to adopt effective pressure relief and permeability enhancement technology to improve the gas drainage effect.

2.1. Engineering Principle of Hydraulic Cavitation.

Assuming that the shape of the hole after hydraulic punching is still circular, when the broken coal is discharged from the hole, the diameter of the hole increases, and the radius of the pressure relief zone is as follows:

$$R_x = (R_x + x) \exp \left[\frac{(\sigma_{r,d}/\sigma_{ci} + s/m_b)}{(s/m_b)} \right]^{1-a} \cdot \left\{ \frac{(\sigma_c - \sigma_{cr})}{Q[(2 - 2\mu)\sigma_0 - \sigma_{r,d}](1 + \mu)} + 1 \right\}^{-1/(1+Np)} \quad (1)$$

After hydraulic punching, the radius of the broken area of the borehole increases, the pressure relief area increases, the strain affects the stress change, and the stress around the borehole obviously decreases. Based on the strain-softening model of the H-B criterion, when the drilling hole is impacted by a high-pressure water jet, the strength of coal decreases. The place where the coal is thus damaged and displaced is called the crushing area. The more distant it is, the greater stress the coal body suffers, ending up going beyond its own strength. This happens in the plastic area. When the stress of the coal body is less than its own strength, the coal body will have elastic deformation within a certain range, which is called the elastic area. Therefore, the stress-strain curve of coal can be divided into an elastic stage, softening stage, and residual stress stage, and the area of corresponding coal around the drilling hole can also be divided into an elastic zone, plastic zone, and crushing zone. According to the distance from the hole, it can be divided into pressure relief zone, stress concentration zone, and original stress zone. And its distribution changes are shown in Figure 1.

In the process of hydraulic pressure relief, the stress of the coal body is released, the strength of the coal body is destroyed, the permeability of the coal body in the pressure relief area is increased, and the gas drainage rate is effectively improved. The stress around the hole drilling meets the following equation:

$$\frac{d\sigma_r}{dr} + \frac{\sigma_r - \sigma_\theta}{r} = 0, \quad (2)$$

where σ_r is the borehole stress, and σ_θ is the borehole tangential stress.

To sum up, the evaluation of the scope and effect of hydraulic cavity building should first examine whether it can increase the pressure relief range of drilling along the coal seam, whether it can concentrate the stress to move far away and reduce the relative stress of the coal seam around the cavity building area. Therefore, the borehole stress meter will

be used to test the change of relative stress at different distances around the hole, and then, the influence range of hydraulic cavitation can be analyzed.

2.2. Engineering Design of Hydraulic Cavity Making.

Combined with the actual situation of the Wuyang Coal Mine, two types of test boreholes were constructed in this study, which is hydraulic hole making boreholes and stress test boreholes. They are divided into three groups, with 5 boreholes in each group, 3 hydraulic hole making boreholes and 2 stress test boreholes. Now, 5 boreholes have been tested in the 8006 air-return roadway. During the process of drilling construction, high-pressure hydraulic punching is carried out for hydraulic hole drilling; after the construction of stress test drilling, the stress meter is installed, and the stress meter is pressed to make the flexible detection unit expand to the preset pressure of 5 MPa and test the stress condition during hydraulic hole drilling, and the drilling is shown in Figure 2.

Drilling type: 2 stress test holes, Y1 and Y2, respectively; 3 hydraulic holes, S1, S2, and S3, respectively. Opening height: the upper row of boreholes is hydraulic hole making boreholes with an opening height of 1.8 m; the lower row of boreholes is stress testing boreholes with an opening height of 1.6 m. Opening spacing: nonequal spacing, as shown in Figure 1. Drilling azimuth: all azimuth angles are 90° (0° for the middle line of roadway). Borehole dip angle: coal seam dip angle +1°. Drilling length: the hydraulic hole drilling is the same as the daily construction, but it needs to be conducted once in the 1 m section of 15-16 m; the stress test drilling length is 16 m. Drilling diameter: the hydraulic hole drilling is the same as the daily construction; the stress test drilling is $\Phi 55$ mm.

3. Influence Range Analysis of Hydraulic Cavitation

3.1. Stress Change Analysis of Surrounding Coal Body

3.1.1. *Stress Data during Punching.* Figure 3 shows the relative stress drop values at different intervals during the process of hydraulic cavitation, as shown in Figure 3:

- ① In the process of hydraulic cavitation, the relative stress of the coal seam at the distance of 1.0 m and 1.5 m from the cavitation hole decreases significantly, reaching 0.6 MPa and 0.8 MPa, respectively, indicating that hydraulic cavitation at the above position has played a relatively good pressure relief effect. As the initial stress value at 1.0 m is higher than 4.5 MPa, the pressure drop is more likely to occur when subjected to coal seam strain. Therefore, the relative stress drop at the distance of 1.5 m is larger than that at the distance of 1.0 m.
- ② In the process of hydraulic cavitation, the relative stress of the coal seam at the distance of 2.5 m from the cavitation hole has a certain decrease, which is 0.3 MPa, indicating that the hydraulic cavitation can still play a certain pressure relief role at this position,

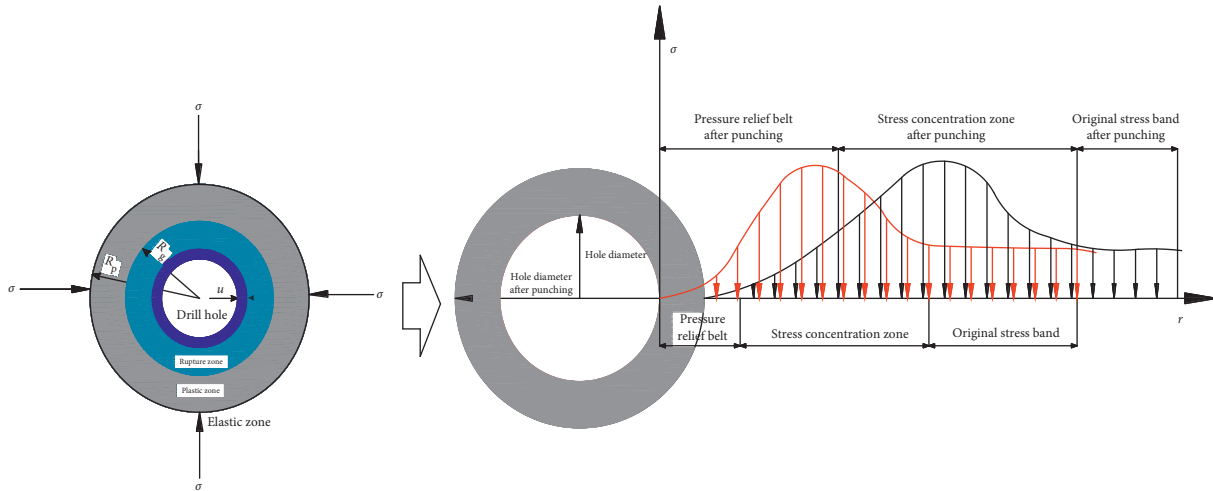


FIGURE 1: Schematic diagram of stress change before and after acupoint making.

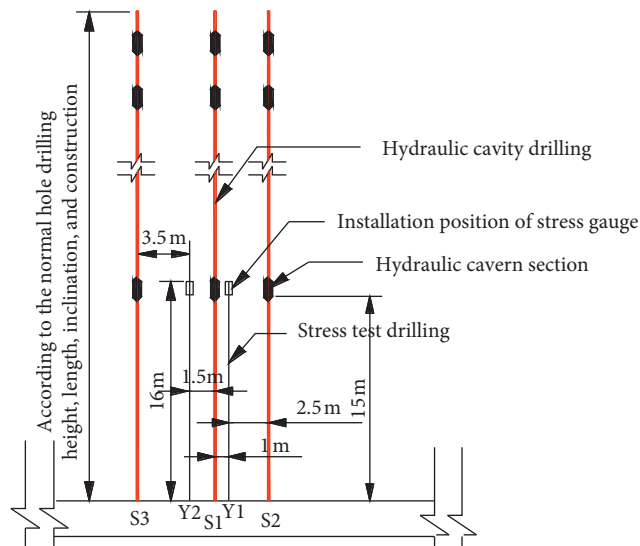


FIGURE 2: Layout plan of test boreholes.

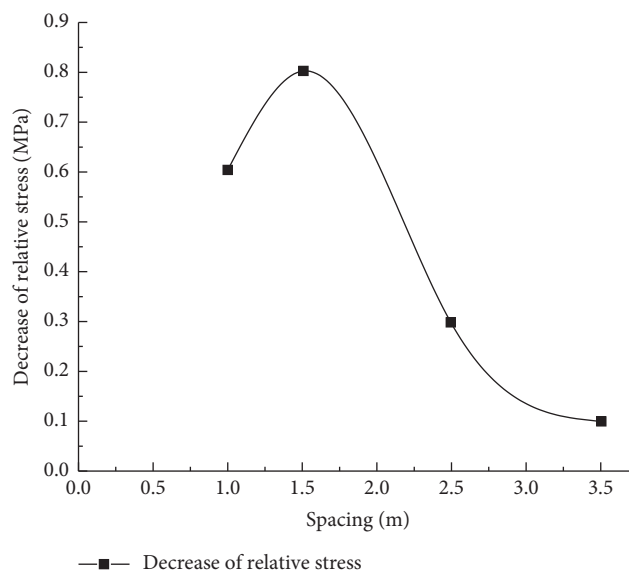


FIGURE 3: Relative stress drop values at different spacing.

but it is weaker than that at the distance of 1.0 m and 1.5 m.

- ③ In the process of hydraulic cavitation, the relative stress of the coal seam at the 3.5 m interval of the cavitation hole almost does not decrease, which is only 0.1 MPa, indicating that the pressure relief effect caused by hydraulic cavitation at this position is very weak.

3.1.2. *Stress Data after Punching.* After hydraulic cavitation, the relative stress data at different distances were continuously tracked, and the variation of the relative stress values with time was analyzed, as shown in Figure 4.

- ① At 1.0 m and 1.5 m spacing between cavitation holes, the relative stress of coal seam decreases obviously, and the decrease speed is fast, the decrease duration is long, and the decrease amount is large. The decrease amount at the distance of 1.0 m and 1.5 m from the cavitation hole is 2.0 MPa and 1.1 MPa, respectively. At a 1.0 m interval, the decrease rate is 0.049 MPa/h, and the decrease rate is stable after 41 h. After a continuous decrease for 31 h at a distance of 1.5 m, the decrease rate is 0.035 MPa/h. It shows that the pressure relief effect in the above area is very obvious.
- ② At the 2.5 m spacing of cavitation holes, the relative stress of coal seam drops relatively small, and the amount of decrease is 0.3 MPa. It remains stable after a continuous decrease for 22 h, and the rate of decline is 0.014 MPa/h. The decrease time is short and the rate of decline is low, indicating that the pressure relief effect here is weaker than that at the 1.0 m and 1.5 m spacing.
- ③ At the 3.5 m spacing of cavitation holes, the relative stress of coal seam drops less, with a decrease amount of 0.2 MPa, which remains stable after a continuous decrease of 20 h and a decline rate of 0.010 MPa/h, indicating that the pressure relief effect here is weaker than that at the 2.5 m spacing.

According to relevant studies, the change rule of permeability coefficient of coal seam around hydraulic cavitation drilling is as follows:

$$\lambda = \begin{cases} \lambda', & r = r_0, \\ \frac{K}{4\mu p_n} + \frac{\lambda'}{2}e^{-ar}, & r_0 < r < L, \\ \lambda_0, & r \geq L. \end{cases} \quad (3)$$

λ' is the permeability coefficient of the borehole wall, $m^2/(MPa^2 \cdot d)$; λ_0 is the permeability coefficient of the original coal seam, $m^2/(MPa^2 \cdot d)$; L is the stress distribution range of borehole surrounding rock, m; r_0 is the borehole radius of line cavitation, m; p_n is atmospheric pressure, 0.101325 MPa; K is the permeability of coal, m^2 ; μ is the dynamic viscosity coefficient, $\mu = 1.08 \times 10^{-5}$ Pa·s.

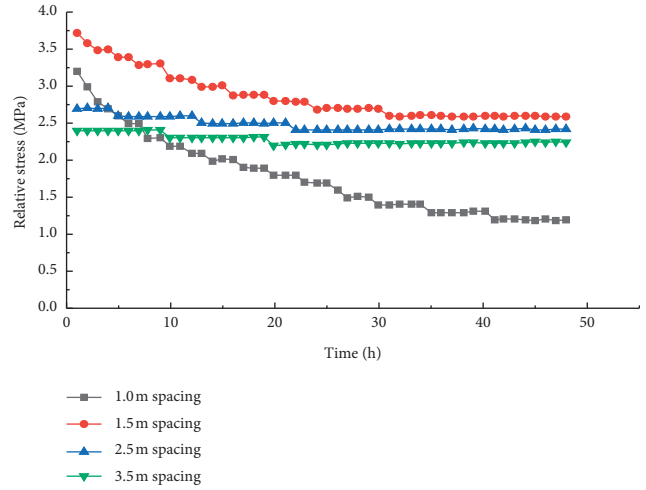


FIGURE 4: Changes of relative stress data at different spacing with time after hydraulic cavitation.

According to the above equation, hydraulic made hole drilling hole wall of the coal seam permeability coefficient is the largest, extending outward along the borehole diameter direction of the broken zone, plastic zone of coal gas permeability coefficient of the original coal seam permeability is obviously improved and made the hole stress, high coefficient of permeability of coal seam is the broken zone, and the plastic zone is on the decline and gradually tends to be the original coal seam permeability coefficient.

In conclusion, with the increase of the distance, the pressure relief effect of hydraulic cavitation on the surrounding coal decreases. The pressure relief effect can be obvious at 1.0~2.5 m, while the pressure relief effect is very weak after 3.5 m. This is shown in Figure 5.

In order to ensure the safety and efficiency of roadway excavation, the surrounding area of hydraulic hole drilling >3.5 m, the stress direction and gas content of roadway are large, and the prevention and control measures of “hydraulic and mechanical cavity making + steel screen pipe + surrounding rock grouting” are adopted. There are 8 hole making boreholes in a single drilling field, with a depth of 120 m. The adjacent boreholes start to make holes at 18 m and 15 m, respectively, and the hole making spacing is 7 m. After verification, it is found that the effective gas fracturing burst pressure to reduce the frequency of coal blasting is more than 190 MPa. In order to fully grasp the occurrence of roof strata and bedding and fracture development, the changes of bedding and fracture in borehole before and after fracturing were compared. Before and after fracturing, the borehole imager is used to peep the borehole. The peep image results are shown in Figure 6.

- (1) Peep before fracturing: before fracturing, the borehole wall is smooth, bedding and fracture are not developed.
- (2) Peep after fracturing:
 - ① The maximum peeping depth of the hole peeper is 17 m, and the part with the hole depth greater than 17 m cannot be observed temporarily.

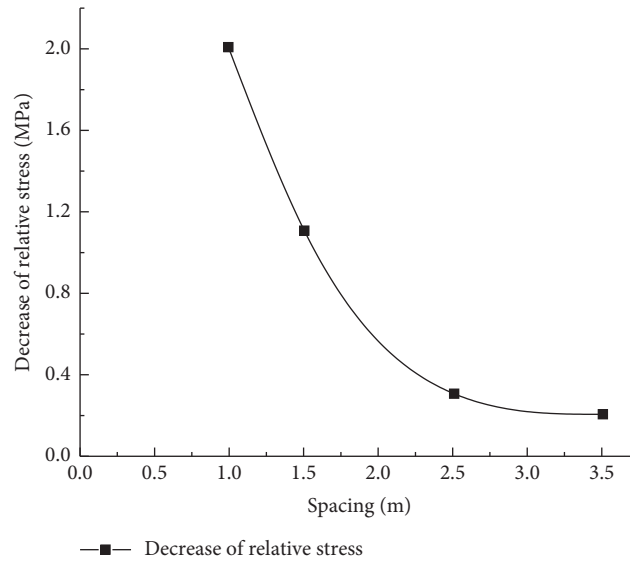


FIGURE 5: Relative stress drop values at different spacing.

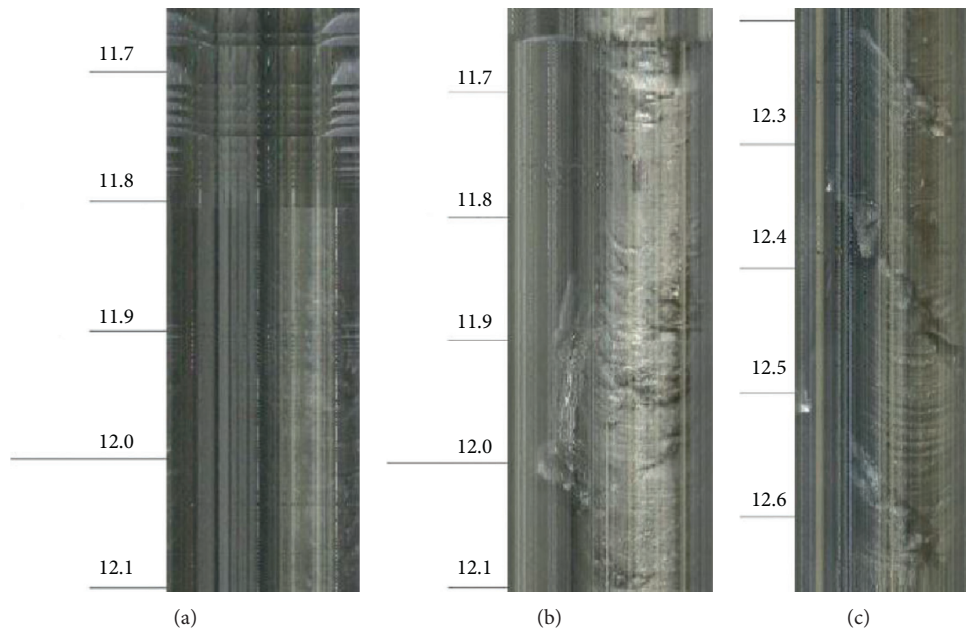


FIGURE 6: Peep image (a) before fracturing, (b) after fracturing, and (c) 7 days after fracturing.

- ② The number of microfractures, fracture expansibility, and fracture number increase significantly in the fracturing area.
- ③ On the seventh day after fracturing, the fractures closed obviously and the dynamic events of surrounding rock began to increase.

3.2. Spectrum Analysis of Microseismic Events in Hydraulic Cavitation of Coal Roadway. Coal and rock dynamic disasters occur in large intensity and are highly destructive. Coal and gas outburst is one of the biggest coal and rock dynamic disasters in mine production, which seriously threatens the safe mining of the mine [16]. Underground

mining disturbance induces coal and rock to release a large amount of elastic energy and high gas internal energy. Under such conditions, the possibility of coal outburst is greater and the probability of coal and rock dynamic disasters is also greater [17]. In order to reveal the relationship between the law of seismic activity and the change of stress before and after hole making, the Canadian ESG microseismic monitoring system is used to monitor the whole process of driving roadway and summarize and analyze the data and the temporal and spatial evolution process of microseismic events before and after hole making, and the qualitative analysis of roadway surrounding seismic dynamic response waveform signal spectrum characteristics and

implementation of rock burst signal remote, real-time, dynamic, automatic monitoring identify each time the vibration of the vibration types and judge the stress source of microseismic events to face danger degree evaluation. Table 1, for February 19–29 coal mine ring number and position, from February 19 to 24, shows the underground coal and cannons, 44 noise cannons according to the noise source and noise microseismic monitoring system for real-time positioning from the roof and the ram position, monitoring of more than 40 significantly coal YanWei burst incidents, and calculation of wavelet packet energy $1.00 e + 07$ J above 26, February 21, which is thus around roadway roof where microfracture occurs, the highest energy at $3.6 e + 09$ J. In this case, the miner has successively adopted hydraulic cavitation to relieve pressure on the coal seams from many sources in the roadway. After the implementation, 21 sound coal cannons were recorded from February 25 to 29, and only 11 microseismic events with obvious power were statistically found, with small sound and energy. In addition, it is found that the frequency of crosstalk is the most frequent at 8 o'clock every day. The main reason is that 8 o'clock is the main driving time. During this time, the driving speed is accelerated, the fault zone of the coal roadway is active, and the coal gun is fired. As can be seen from Figure 7, after adopting hydraulic cavitation to relieve the danger, both the gas content and gas pressure in the coal seam are released, and the number of underground sounding coal gunners and microseismic events is significantly reduced. It can be seen that this measure can keep the internal stress in the coal seam in balance and has a good effect on maintaining the stable state of the roadway and accelerating the driving speed.

Research shows that coal and rock dynamic disasters often occur in the axis of anticline and syncline, especially near faults, coal seam dip angle change zone, coal seam fold, and tectonic stress zone [18]. 8006 transport lane is located in an active fault zone, the coal seam inclination of the roadway is $4\text{--}14^\circ$, the tunneling face is close to the Eastern Zhou anticline, the geological structure is complex, the excavation activity caused by the increase of fault shear stress and the decrease of normal stress is likely to induce mine seismic activity, with the continuous advancement of tunneling work, and the roof activity is intense. According to the dynamic event microseismic signal of coal and rock in the roadway, the short-time Fourier transform and wavelet packet transform are used to analyze the spectrum characteristics. The short-time Fourier transform (STFT) is derived from the classical Fourier transform, on the basis of which the time window function is added. STFT overcomes the interference of cross term in nonstationary signal analysis and is a powerful tool for nonstationary signal analysis. The expression is in the following form, including $t = \tau$:

$$\text{STFT}(\tau, f) = \int_{-\infty}^{\infty} h(t)g(t - \tau)e^{(-2i\pi f)t}dt, \quad (4)$$

where f is the frequency, $H(t)$ is the analyzed signal, $g(t)$ is the window function, and T is the time.

Figure 8 shows seismic signal spectrum analysis of coal and rock burst. As shown in Figure 7 (February 21–24), three times more large vibration signals, where, on February 21, roadway roof fracture happens, analyze the acquisition signal where the signal length is about 0.4–0.5 milliseconds, there is the short duration of the signal and large amplitude (has reached the maximum amplitude of sensor that can accept 4096 mv), the signal total energy is $3.6 e + 09$ J, the wavelet package signal energy is concentrated in the first band, since 2-band energy gradually decreased, and 16-band wavelet packet energy almost reduced to 0 J. Therefore, it is ruled out that internal microfracture signal occurs in coal and rock mass. For further analysis, reasons of roof fracture to provide theoretical support for XieWei measures and the monitoring signal Fourier transform to get the signal frequency of 250 Hz satisfy large intensity spectrum characteristics of vibration signals, and by the S transformation of its verification, it was found that the strength of large rupture occurred ahead of the side of roadway roof rock mass, rock burst, support, and pressure transfer to coal.

According to the analysis of coal and rock fracture that occurred from 21 to 24 and formulate measures to relieve the danger, hydraulic cavitation was adopted to relieve the pressure in the roadway. After the measures were adopted, three obvious coal and rock dynamic phenomena occurred successively from 25 to 29 days. Figure 9 makes hydraulic hole after microseismic signal spectrum analysis, discovered by Figure 8 after the hydraulic hole builds microseismic signal waveform amplitude slash, remaining within the 2000 mv, of which 200–800 mv, the signal frequency is obtained by Fourier transform concentrated in about 200 Hz, mostly in 200 Hz, significantly lower than building hole before the main frequency, and the frequency range is also greatly narrowed; through the frequency domain analysis of S-transform, it is found that the main frequency points of surrounding rock dynamic events are low after hydraulic cavern building; most of them are caused by small coal rock falling, which will not affect the normal driving of coal roadway. Visible XieWei measures after execution and the coal and rock dynamic events are small rock failure or tunneling roadway coal drop ahead and will not affect drivage work, also not to endanger the safety of staff and facilities of the safety of life.

3.3. Moisture Change Analysis of Surrounding Coal. After the hydraulic measures, the surrounding coal mass moves toward the borehole, causing the crack expansion, and at the same time, the high-pressure water will also flow along with the crack expansion to supplement the water of the coal seam [19–21]. Therefore, the water replenishment range of coal seam is approximately consistent with the crack expansion range. Since the crack extension range directly measured in the coal wall of the working face is affected by the visible width of the crack and the continuous expansion of mining-induced stress [22, 23], the reliability of the measured crack extension range is not high (as shown in Figure 10, only obvious cracks can be observed and it is

TABLE 1: Statistics of noise coal gun in the roadway.

Date	Frequency of sound	Frequent noise frequency	Sound frequency	Position
February 20th	12	8 o'clock	6	Middle of roof
February 21th	2	4 o'clock	1	Roof fracture
February 22th	2	8 o'clock	2	—
February 23th	13	8 o'clock	8	Wind tunnel gang
February 24th	15	8 o'clock	7	There are 4 air ducts and two pedestrians
February 25th	13	8 o'clock	9	Air duct, pedestrian, 10–15 m from head to back 10-15 m
February 26th	2	8 o'clock	9	—
February 27th	6	4 o'clock	—	—
February 28-29th	0	—	—	—

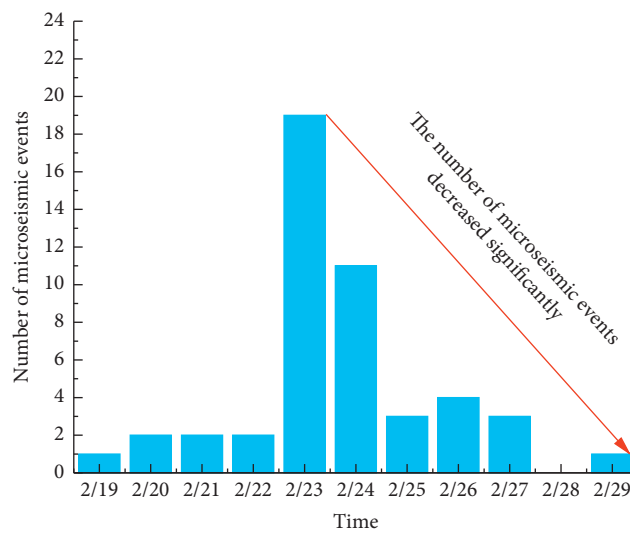
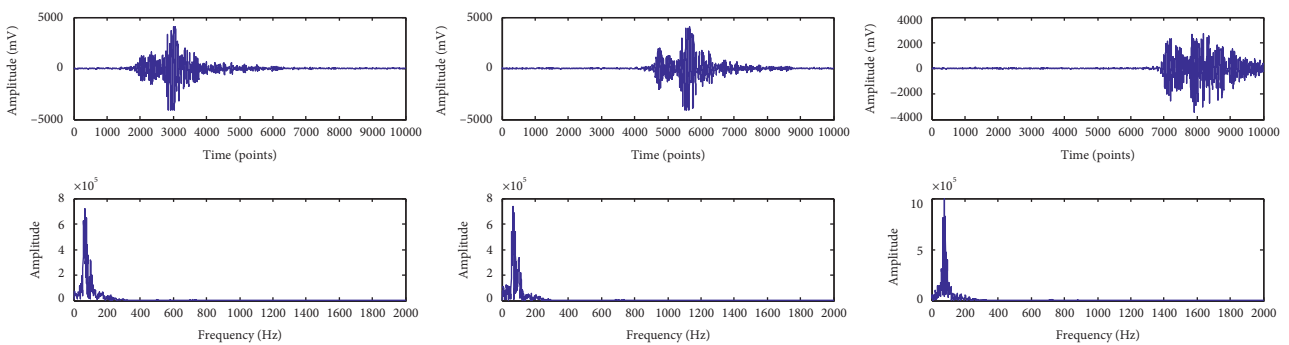


FIGURE 7: Diagram of the daily number of microseismic events.



(a)

FIGURE 8: Continued.

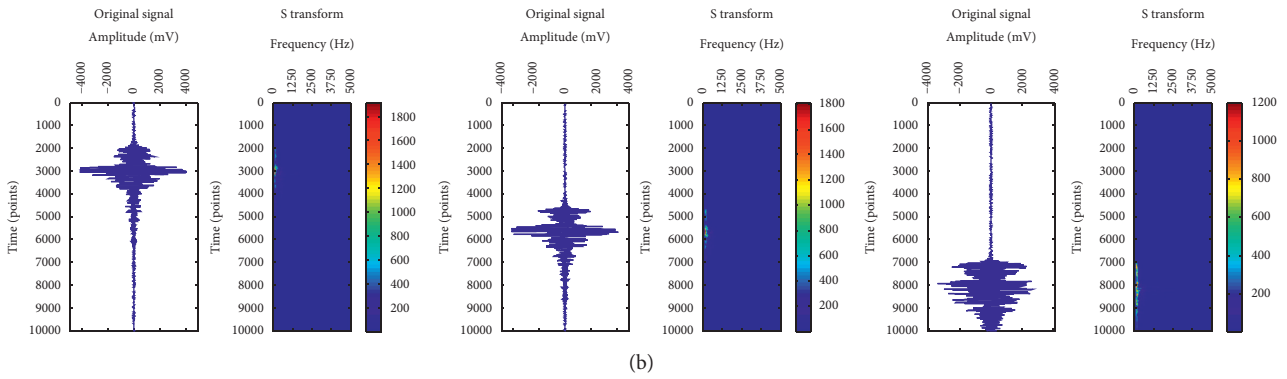


FIGURE 8: Spectrum diagram of coal rock fracture signal from February 21 to 24. (a) Fourier transform results of coal rock fracture. (b) S-transform results of coal rock fracture.

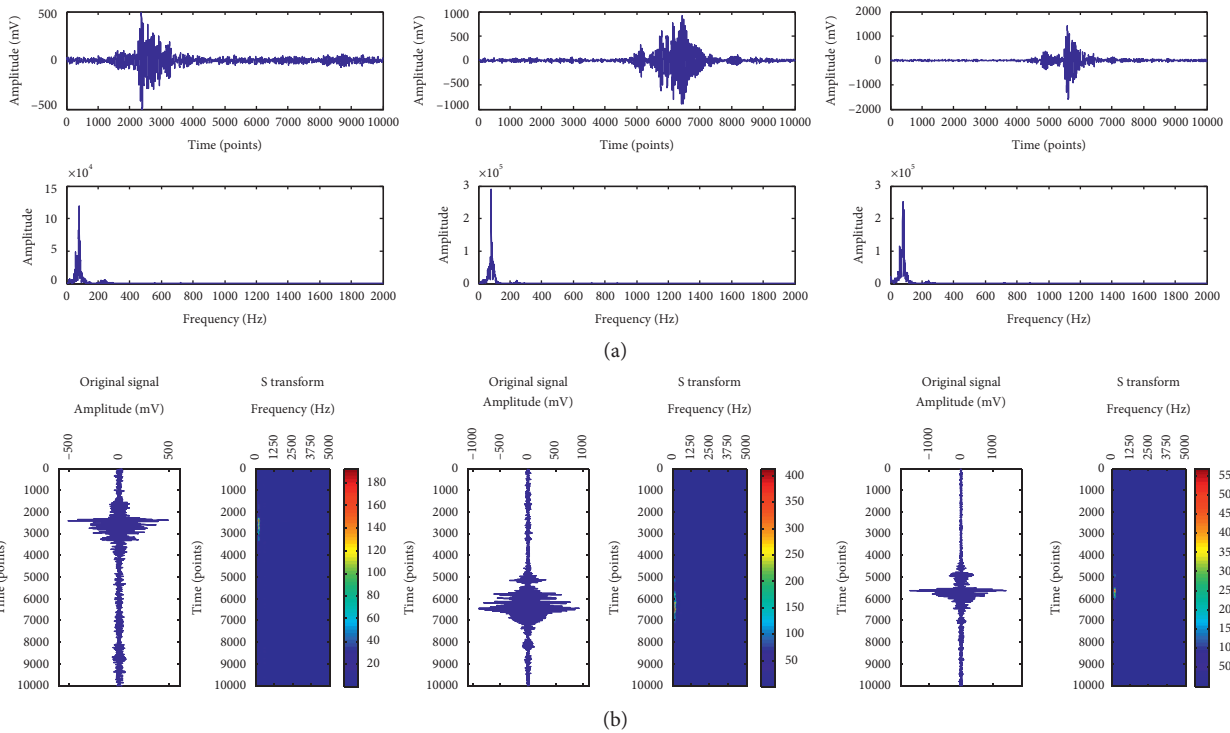


FIGURE 9: Frequency spectrum characteristics of microseismic signals after hydrocavern building. (a) Fourier transform results of coal rock fracture. (b) S-transform results of coal rock fracture.

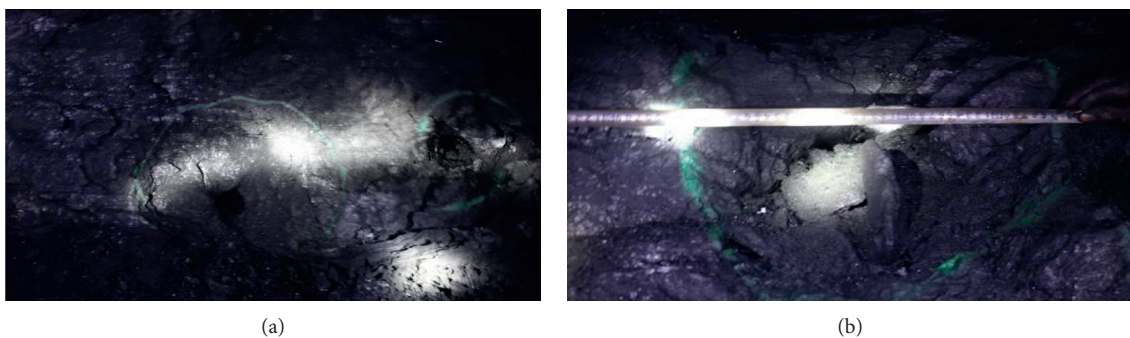


FIGURE 10: Fracture expansion range. (a) The distance between the two hole making holes is 3 m, and the cracks are completely connected. (b) The diameter of a single hole is 0.7 m, and it has collapsed after coal cutting.

difficult to determine the cause of the crack), so the water test is used to calculate the coal seam water supply range.

According to the data in Figure 11, it can be seen that the average moisture of coal seam within the test range increases from 1.09% of raw coal to 3.16%, and the maximum reaches 5.15%. During the test, considering the influence of two ordinary holes in the middle of the roadway, the radius of the test area was 1.1 m, and the water content at the edge of the test area was still far greater than that of the raw coal. According to the variation law of each water test point, the radius of the water replenishing range was 1.5 m, so the water replenishing range of the working face by the hydraulic cavitation release hole technology exceeded 79% of the area of the coal wall.

On the one hand, hydraulic cavitation release drill plays the role of pressure relief and reflection improvement, speeding up the release of gas from the broken coal body, and on the other hand, it also plays the role of water replenishing and wetting the coal body around the cave and inhibiting the desorption of gas from the wet coal body [24–27]. After sampling at the opening of 8006 return air roadway, the coal sample with 0.17–0.25 mm, and the particle size was obtained from No. 3 coal seam of Wuxiang Coal Mine through grinding. Natural desorption experiments of coal under different moisture and unified equilibrium pressures were carried out. The variation curve of gas desorption velocity over time is shown in Figure 12.

The following can be seen from the above experimental results:

- (1) The desorption law of coal samples with different water contents conforms to the power exponential function.
- (2) The coal sample with 1% moisture has the highest coalbed methane desorption rate, and the fitting coefficient B value reaches 1.7233, which indicates that the methane desorption of coal sample with 1% moisture has the characteristics of high initial gas desorption rate and fast decay rate. With the increase of water content, the B value of the injected coal samples decreased from 1.7233 to 0.9342, which indicated that water injection affected the desorption rate of methane in the coal samples, making the initial desorption rate smaller and the attenuation rate slower. The initial desorption velocity is reduced by water injection, and the desorption process becomes more gentle, avoiding the sudden release of a large amount of coalbed methane.
- (3) With the increase of water content, the initial gas desorption velocity B value decreases continuously. The decrease of the initial gas desorption rate in the water-injected coal sample can effectively prevent the sudden and massive gas desorption, which is beneficial to the prevention and control of coal and gas outbursts. With the increase of moisture, the attenuation rate slows down, and the desorption of methane in coal becomes more uniform, and it is not easy to release a large amount of methane in case of a slight disturbance.

The above experimental results are the important reason for the slow attenuation of the extraction pure volume of hydraulic cavitation borehole and the fundamental reason for the low gas concentration in the backflow during coal cutting in the tunneling face under the action of hydraulic cavitation release hole.

3.4. Analysis of Gas Change in Surrounding Coal. Through the statistical analysis of the content test results of 8006 air-return roadway and haulage roadway and the air-return flow data of developing face, it is found that the content is not the root cause affecting the air-return flow concentration of developing face, but the root cause lies in the desorption characteristics of coal in a short time. The coal breaking process during coal cutting is the direct reason for the increase of gas concentration in return for air flow. Generally, the whole coal cutting time lasts about 40 minutes, and the coalbed methane sources include free gas in the coal body, $W1 + W2$, and fresh head-on natural release. Table 2 shows the comparison of gas content test results after taking danger relief measures.

According to the calculation formula of coalbed methane content, various indexes of coal content and free gas in the 8006 air-return roadway and haulage roadway are obtained.

$$x = \frac{abp}{1+bp} \times \frac{100 - A_d - M_{ad}}{100} \times \frac{1}{1 + 0.31M_{ad}} + \frac{10\pi p}{\gamma} \quad (5)$$

In the formula, x is the residual gas content of coal seam, m^3/t ; a and b are the adsorption constant; p is the residual gas pressure of coal seam, MPa; A_d is the ash content of coal, %; M_{ad} is the moisture of coal, %; π is the porosity of coal, m^3/m^3 ; γ is the bulk density of coal proportion (false), t/m^3 .

Among them $(abp/(1+bp)) \times ((100 - A_d - M_{ad})/100) \times (1/(1 + 0.31M_{ad}))$. $10\pi p/\gamma$ is adsorbed gas and free gas.

As shown in Table 2, after the implementation of hydraulic hole making and hazard relief measures, the free gas content, fresh head natural gas release content, gas pressure, and total gas released by coal body during coal cutting have been reduced. It can be seen that hydraulic hole punching and hazard relief measures have a good effect on reducing gas content.

4. Results and Analysis

Based on the test and research background of 8006 haulage roadway in the Wuyang Coal Mine expansion area, this paper analyzes the influence scope of hydraulic punching and the stress transformation of surrounding coal body by arranging stress test boreholes and hydraulic hole making boreholes in different directions; it is found that the pressure relief effect of hydraulic cavitation on surrounding coal decreases with the increase of distance, and the pressure relief effect is obvious at 1.0–2.5 m, but it is very weak after 3.5 m; meanwhile, the water content of coal seam is greatly increased by hydraulic cavitation measures, the maximum water content reaches 5.15%, and the radius of water supplement for coal seam is 1.5 m. Combined with microseismic monitoring technology, the intensity change of coal rock dynamic events before and after hydraulic cavern building was analyzed. It was found that the amplitude of microseismic signal waveform decreased greatly after hydraulic cavern building, the frequency also decreased from above 250 Hz to about 150 Hz, and the intensity of coal rock

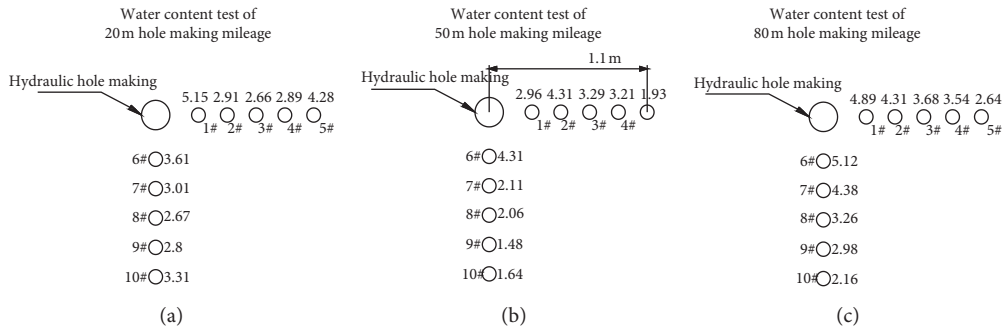


FIGURE 11: Water supplement of coal seam around cavern forming a hole at (a) 20 m, (b) 50 m, and (c) 80 m of cavern forming mileage.

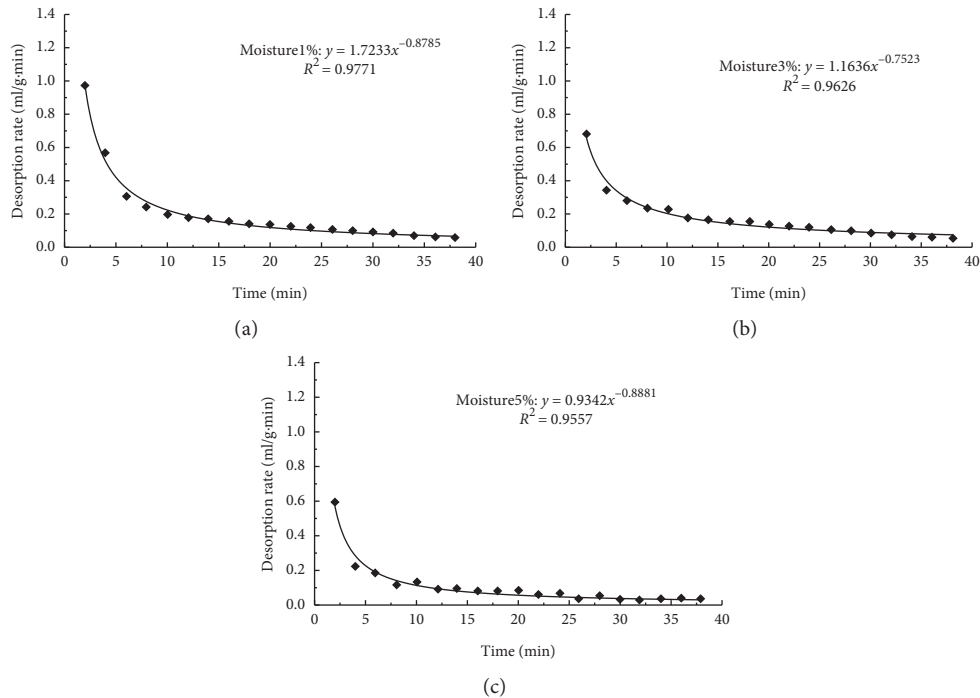


FIGURE 12: Gas desorption rate of coal sample under different moisture conditions (gas desorption speed when equilibrium pressure is 2.5 MPa and water content is 1%, 3%, and 5%).

TABLE 2: Comparison of gas content test results after taking measures.

Test tunnel	Before and after the measures	Average W1 + W2	Average W	Average W3 m ³ /t	Pressure MPa	Free gas	During coal cutting total amount of gas released from coal	(w1 + w2)/w
8006 air-return	Before	4.06	14.33	7.60	1.56	0.38	4.06	0.29
	After	2.61	12.14	7.17	1.02	0.25	2.61	0.21
8006 haulageway	Before	4.16	14.38	8.42	1.38	0.35	4.16	0.30
	After	3.08	12.90	7.44	1.10	0.28	3.08 < X < 3.36	0.24

dynamic events was far less than that before hydraulic cavern building and pressure relief. Based on the analysis of water content and coalbed methane change of coal body around the hydraulic cavern, it is found that hydraulic cavern can effectively prevent a sudden large amount of coalbed methane desorption, which is very beneficial to the prevention and control of coal and coalbed methane outburst. The research shows that the hydraulic cavity can release the pressure of coal

seam coalbed methane greatly, keep the roadway stable, and improve the driving speed. However, the selection of test sites is limited, the spatial analysis of coal and rock dynamic events monitored by the microseismic monitoring system is not deep enough, and the research on the relative position relationship between coal and rock dynamic events and hydraulic cavern formation is not specific enough. This part should be emphasized in the follow-up research.

5. Conclusion

- (1) The paper makes a comparative analysis of the stress variation of coal seam during and after hydraulic cavitation and finds that the relative stress of coal seam decreases gradually with the extension of time, and the pressure relief effect gradually appears. In the range of less than 2.5 m around the hydraulic hole drilling, the pressure relief duration is long, the pressure relief rate is fast, and the pressure relief amplitude is large. The pressure relief effect of hydraulic hole drilling is the best. In the range of 2.5–3.5 m around the hole, the duration, rate, and amplitude of pressure relief are reduced. Although the hydraulic cavity can produce a certain pressure relief effect, it is relatively weak. Within the range of above 3.5 m around the hole, the available pressure relief effect can hardly be observed.
- (2) Through the analysis of the moisture change of the surrounding coal body during hydraulic cavitation, the conclusions are as follows: during the process of drilling, the coal body in the face of the working face is basically communicated through the cavity making fissures, and the free coalbed methane also dissipates through these fissures in advance. However, the disturbance of the common hole to the coal seam is far less than that of the hydraulic hole. The hydraulic hole making and releasing technology is of great significance to the construction. The head-on water supply scope of the working face should exceed 79% of the coal wall area.
- (3) Through time-frequency analysis of tunnel microseismic events before and after hydraulic cavitation found that the main frequency of coal rock fracture signal before hydraulic cavern building is about 250 Hz, and the signal is continuous. Multiple groups of signals are similar, with rapid attenuation, short duration, high main frequency, large specific gravity value, large signal duration, and released energy. It shows that the impact of microseismic events will cause the sudden increase of deformation energy of surrounding rock of mine roadway and cause large-scale damage events, which will cause the collapse of coal rock. With the increase of coalbed methane content and coalbed methane pressure, the intensity of coal rock fracture dynamic event is greatly weakened after the implementation of hydraulic cavity-making measures, which shows that this measure has a good effect on coal seam pressure relief.

Data Availability

The data used to support the findings of this study are included within the article.

Conflicts of Interest

The authors declare that there are no conflicts of interest regarding the publication of this article.

Acknowledgments

The authors are grateful for the financial support of the research from the National Natural Science Foundation of China (51704101), Key Scientific and Technological Research Projects in Henan Province (182102310780 and 192102310199), and the 65th General Program of China Postdoctoral Science Foundation (2019M6525352536), supported by “the Fundamental Research Funds for the Universities of Henan Province (NSFRF200307).

References

- [1] H. Wang, X. Fang, F. Du et al., “Three-dimensional distribution and oxidation degree analysis of coal gangue dump fire area: a case study,” *The Science of the Total Environment*, vol. 772, Article ID 145606, 2021.
- [2] R. Zhiyuan, J. Yang, and Y. Zhaoguo, “Application of shallow hole loosening blasting in geological disaster control engineering,” *Chinese Journal of Underground Space and Engineering*, vol. 6, no. z2, pp. 1696–1698, 2010.
- [3] S. Biming and Yu Qixiang, “Analysis of outburst prevention effect of deep hole pre-cracking control loosening blasting in low air permeability coal seams,” *Mine Construction Technology*, vol. 5, pp. 27–30, 2002.
- [4] Z. Fujun, “Application of loose blasting in coal mining,” *Blasting*, vol. 19, no. 1, pp. 40–42, 2002.
- [5] Z. Wang and Z. Li, “Research on the elimination mechanism of hydraulic squeeze measures,” *Safety In Coal Mines*, vol. 35, no. 12, pp. 1–4, 2004.
- [6] P. Li, “Application of hydraulic extrusion technology in outburst coal seam,” *Coal Science and Technology*, vol. 35, no. 8, pp. 45–47, 2007.
- [7] H. Yang and B. Hu, “High outburst coal seam hydraulic extrusion technology application,” *Coal Science and Technology*, vol. 35, no. 6, pp. 31–33, 2007.
- [8] L. Ximing and Z. Jing, “Safety analysis of anti-outburst measures for hydraulic cutting,” *China Mining Magazine*, vol. 18, no. 3, pp. 92–99, 2009.
- [9] M. Liu, L. Kong, and F. Hao, “Application of hydraulic punching technology in severely outburst coal seams,” *Journal of China Coal Society*, vol. 30, no. 4, pp. 451–454, 2005.
- [10] M. Liu, Z. Li, and Y. Liu, “Research on the mechanism of eliminating outbursts of hydraulic cutting measures,” *Coal*, vol. 15, no. 3, pp. 1–2, 2006.
- [11] T. Lu, H. Yu, T. Zhou, J. S. Mao, and B. H. Guo, “Improvement of methane drainage in high gassy coal seam using waterjet technique,” *International Journal of Coal Geology*, vol. 79, no. 1–2, pp. 40–48, 2009.
- [12] R. Hardy, *Acoustic Emission/Microseismic Activity*, Vol. 1, A.A.Balkema Publishers, Netherlands, 2003.
- [13] Ge Maochen, “Efficient mine microseismic monitoring,” *International Journal of Coal Geology*, vol. 64, no. 8, pp. 44–56, 2005.
- [14] W. Jianbin, W. Hongchao, and G. Xiaoliang, “Application by hydraulic flushing cavity technology while drilling in pressure relief hole of low-permeability coal roadway,” *Coal Technology*, vol. 40, no. 2, pp. 72–74, 2021.
- [15] J. Zhang, “Application research on technology of hydraulic caving pressure-relief and permeability-enhancement in bottom rock roadway,” *Safety In Coal Mines*, vol. 46, no. 7, pp. 69–72, 2020.

- [16] F. Du, K. Wang, X. Zhang, C. Xin, L. Shu, and G. Wang, "Experimental study of coal-gas outburst: insights from coal-rock structure, gas pressure and adsorptivity," *Natural Resources Research*, vol. 29, no. 4, pp. 2481–2493, 2020.
- [17] C. Xin, F. Du, K. Wang, C. Xu, S. Huang, and J. Shen, "Damage evolution analysis and gas-solid coupling model for coal containing gas," *Geomechanics and Geophysics for Geo-Energy and Geo-Resources*, vol. 7, no. 1, p. 7, 2021.
- [18] Li Zhihua, *Mechanism of Coal Rock Burst Induced by Fault Slip under Mining*, China University of mining and technology, Xuzhou, China, 2009.
- [19] T. Shuanglong, W. Qingguo, and Z. Lianjun, "Application of permeability enhancement induced by hydraulic jet cavity in hongyang no. 2 colliery," *China Coalbed Methane*, vol. 14, no. 4, pp. 39–42, 2017.
- [20] W. Yaofeng, He Xueqiu, W. Enyuan, and Y. Li, "Research progress and development tendency of the hydraulic technology for increasing the permeability of coal seams," *Journal of China Coal Society*, vol. 39, no. 10, pp. 1945–1955, 2014.
- [21] Z. Cheng, Li Xianzhong, and Li Quangui, "Research and application of coal seam pulsating hydraulic fracturing pressure relief and permeability enhancement technology," *Journal of China Coal Society*, vol. 36, no. 12, pp. 1996–2001, 2011.
- [22] Li Guoqi, Ye Qing, Li Jian Xin et al., "Theoretical analysis and practical study on reasonable water pressure of hydro-fracturing technology," *China Safety Science Journal*, vol. 20, no. 12, pp. 73–78, 2010.
- [23] L. Yanwei, R. Peiliang, X. Shibai et al., "Analysis of pressure-relief and permeability improvement effect of hydraulic flushing," *Journal of Henan Polytechnic University(Natural Science)*, vol. 28, no. 6, pp. 695–699, 2009.
- [24] X. Shibai, Z. Wenwu, L. Yanwei et al., "Effect analysis of rapid outburst elimination by hydraulic punching," *Safety In Coal Mines*, vol. 36, no. 2, pp. 105–107, 2012.
- [25] W. Xinxin, X. Shibai, S. biming et al., "Experiment research on hydraulic borehole flushing in no.13-1 seam of pansan mine," *Coal Science and Technology*, vol. 39, no. 4, pp. 60–64, 2011.
- [26] B. Guoji, Z. Chunru, J. Xugang, and Y. Liu, "Eliminating outburst effect and main influencing factors analysis of hydraulic flushing," *J Journal of Henan Polytechnic University(Natural Science)*, vol. 29, no. 4, pp. 440–443, 2010.
- [27] F. Yanjun, "Hydraulic fracturing initiation and propagation," *Chinese Journal of Rock Mechanics and Engineering*, vol. 30, no. z2, pp. 3169–3179, 2013.

Research Article

Analysis and Monitoring Technology of Upper Seam Mining in Multiunderlayer Goaf

Han Liang , Pengfei Li, and Chen Cao

College of Mining Engineering, Liaoning Technical University, Fuxin 123000, China

Correspondence should be addressed to Han Liang; 18641822228@163.com

Received 14 May 2021; Accepted 15 July 2021; Published 22 July 2021

Academic Editor: Shangtong Yang

Copyright © 2021 Han Liang et al. This is an open access article distributed under the Creative Commons Attribution License, which permits unrestricted use, distribution, and reproduction in any medium, provided the original work is properly cited.

Based on the background of close coal seam mining in the Qianjiaying coal mine, Tangshan, China, the feasibility of the upper seam mining in complex underlaying goaf is analysed using the roof caving analysis and numerical method. The deformation of the mining seam and roadways is monitored and analysed by field measurement and 3D laser scanning. The deformation characteristics of #5 seam after mining 1378P, 2071P, 2072P, and 2091P working panels with a depth of 39–54 m below the #5 seam are analysed using roof caving analysis and numerical method. Results show that the maximum deformation of #5 seam in the superimposed area of the lower goafs reaches 2.5 m and the maximum deformation in the single coal goaf is 1.5 m. The maximum seam inclination is 1.9°. The subsidence of the floor of 1359P roadways is obtained by field measurement, and the result is consistent with numerical calculation. ZEB-HORIZON 3D laser scanner was used to measure and model the roadway deformation. Based on the analysis of multiple scanning data, the deformation of the 1359P roadways was obtained. Results show that the deformation of the surrounding rock of the roadway is not great, the maximum displacement of the roof fall is 30 mm, and the maximum rib convergence is 25 mm. It can be concluded that the #5 seam can be recovered in this complex underlying lower seams' mining condition.

1. Introduction

Close multiseams mining refers to the coal seams with mutual influence. As excavation has greater impact on the roof than the floor, the downward mining method is often used to reduce the influence on adjacent seams [1]. In practice, due to uncertainty of geological exploration or unsatisfied mining conditions, the lower seam may be mined firstly, namely, upward mining. Upward mining faces the challenges of upper seam and surrounding rock subsidence, fracturing and bending, gas immitation, and stress concentration directly above lower seam pillar [2–7]. Considering the timed effect of lower goaf compaction, the situation of upward mining for close multiple coal seams is complex; thus, it is often studied case-by-case in practice.

The lower seams' mining causes upper seam movements and ground stress unloading, which introduce fractures influencing the stability of surrounding rock of upper seam [8–15]. The research of the upward mining method mainly focuses on the overburden damage analysis caused by lower

seam mining and the deformation monitoring and strata control technology while upper seam mining. The former addresses the feasibility of upper seam mining. For example, based on the statistics of more than 200 upward mining cases, Wang and Li [8] suggested that the feasibility of upward mining can be determined using three zones' discrimination and surrounding rock equilibrium methods. Han et al. [9] classified the extent of damnification of upper seam caused by lower seam mining and established the criterion for the upward mining of close seams using the multivariate regression analysis. Wang et al. [16] identified the overburden stress distribution and fracture field for upward mining. In a case study, Zhang et al. [17] found that the fracture in upper seam located above the caving zone was recovered after a certain period, indicating that the upper seam could be mined. Jiang et al. [18] obtained roof stress distribution using the continuous beam model under uniformly distributed load, which can be used to study the feasibility of upper seam mining above large goaf area.

Another key of upward mining is strata deformation monitoring and related ground control technologies in upper seam development and excavation [19–23]. Suchowska et al. [19] studied the vertical stress redistribution in close seam mining. Shao et al. [20] conducted simulation experiment study on the overlying rock fracture and stability of interlayer strata in upward mining, and result showed that the upper seam working face could pass through the fracture zone safely under proper support technique. Based on the theory of composite overburden structure, Huang et al. [24] considered the fracture zone inclined to the inner side of the goaf and proposed two schemes of upward mining, namely, the overlaying method and the staggering pillar method. Zhang [25] monitored the overburden movement during upward seam excavation, and the roof caving angle, overburden displacement, and large and small periodic weighting intervals were studied. Zhao et al. [26] calculated the range of upper seam influenced by lower seam mining in Qianjiaying and proposed a roadway reinforcing scheme for passing through lower seam pillars. Based on theoretical analysis and numerical calculation, Wang et al. [27] studied the upper seam floor subsidence upon lower seam open cut, and it showed that the working face was unstable while passing through the lower seam open cut, and special support should be implemented.

Qianjiaying colliery, located in Tanshan, China, is a typical close multiseams' coal mine. After mining out two lower seams, it is necessary to determine the possibility of upward mining [28]. In this paper, the influence of the lower seams' mining on the overlying strata is determined based on the roof caving analysis. Then, the subsidence and bending angles of the upper seam due to lower seams mining are calculated using numerical method, so as to provide a criterion for the feasibility of upward mining. After roadway development of the upper panel, the actual subsidence of the upper seam floor is measured based on elevation data. Before panel excavation, multiple 3D laser scanning was carried out in the roadways using the ZEB-HORIZON 3D laser scanner, and the deformation of the upper roadways beyond lower seam coal mass, goaf, roadway, and coal pillars was evaluated to provide a basis for monitoring and strata control in the excavation. This paper conducts a case study of upper seam mining over complex lower seam conditions using theoretical, numerical, and field monitoring methods, which provide a reference for feasibility judgement and premining confirmation of upward mining under similar geo-condition.

1.1. Field Conditions. Qianjiaying coalmine is 17 km east of Tangshan, China, with a mining area of 42.6 km². The minable coal includes #5, #7, #9, and #12 seams with total recoverable coal 600 Mt and annual production of around 6.0 Mt. The seams have medium thickness with composite overlaying strata; the bury depth is about 600–800 m underground. *In situ* stress measurements suggest that the major and medium principle stresses of the Qianjiaying coalmine are in horizontal direction, and the major principal stress to vertical stress ratio is around 1.6.

The seams are mainly formed by clarain and semiclarain. The average thickness of #5, #7, and #9 seams is 1.4, 3.6, and 1.8 m, respectively; their dipping angle is 1°–10°. The distance between #5 and #7 seam is 39 m and is 54 m between #5 and 9 seam. The comprehensive stratigraphic column of related seams is shown in Figure 1. The mining method of #7 and #9 coal seams is full roof caving longwall mining.

Before mining of 1359 panel (shorten as 1359P hereafter) in #5 seam, 1378P, 2071P, and 2072P in #7 seam were mined out in 2006, 2009, and 2012, respectively; 2091P in #9 seam was mined out in 2017. The layout of the related panels is shown in Figure 2.

The roadway and mining direction of 1359P is nearly vertical to lower seams. The roadway development and face retreat of 1359P need to cross 4 gobs and 2 pillars.

The aim of this study is to evaluate the excavation possibility of 1359P. Before roadway excavation of 1359P, the influence of lower seams' mining towards #5 seam should be studied quantitatively. During roadway excavation, *in situ* measurement and data analysis should be conducted to confirm the prediction result. Before panel retreat, the deformation behaviour of 1359P roadways over different underlaying strata conditions should be monitored and evaluated to guarantee a safe environment of working face retreat.

1.2. Overlaying Strata Caving Analysis. After panel excavation, the overlying strata form caving zone, fracture zone, and subsidence zone from the bottom to the top. For upward mining, if the upper panel is within the caving zone of lower seam gob, the seam and surrounding rock are seriously broken and cannot be driven or mined. If the upper panel is within the fracture zone, the roadway is unstable as the fracture cannot be restored for a long time, *i.e.*, the upper seam cannot be mined. If the upper panel is beyond the middle section of the fracture zone or within the subsidence zone, the upper seam keeps certain integrity although there are a large number of fractures developed in the coal and surrounding rock. After a certain period of compaction, the strata can restore stability and the seam can be safely mined [29–33].

The height of each zone is related to geological condition and mining method, which are often evaluated using the semitheoretical and semiempirical method [1, 8]. According to the geological characteristics of Qianjiaying (Figure 1), the height of one single coal seam caving zone can be calculated using the following equation:

$$H_m = \frac{M - W}{(K - 1)\cos \alpha} \quad (1)$$

And, the height of the fracture zone can be calculated using

$$H_1 = \frac{100 \sum M}{1.6 \sum M + 3.6} \pm 5.6, \quad (2)$$

$$H_2 = \sqrt{\sum M} + 10, \quad (3)$$

Stratum	Histogram	Ave thickness (m)
Siltstone	•••••	34.6
Mudstone	•••••	0.2
5 seam	•••••	1.4
Siltstone	•••••	3.0
Mudstone	•••••	4.1
Siltstone	•••••	3.6
6 seam	•••••	0.3
Siltstone	•••••	7.8
Medium sand	•••••	8.5
Siltstone	•••••	7.7
7 seam	•••••	3.2
Siltstone	•••••	12.6
9 seam	•••••	2.2
Fine sandstone	•••••	4.8
Mudstone	•••••	9.0
Siltstone	•••••	10.6

FIGURE 1: Stratigraphic diagram of the studied area.

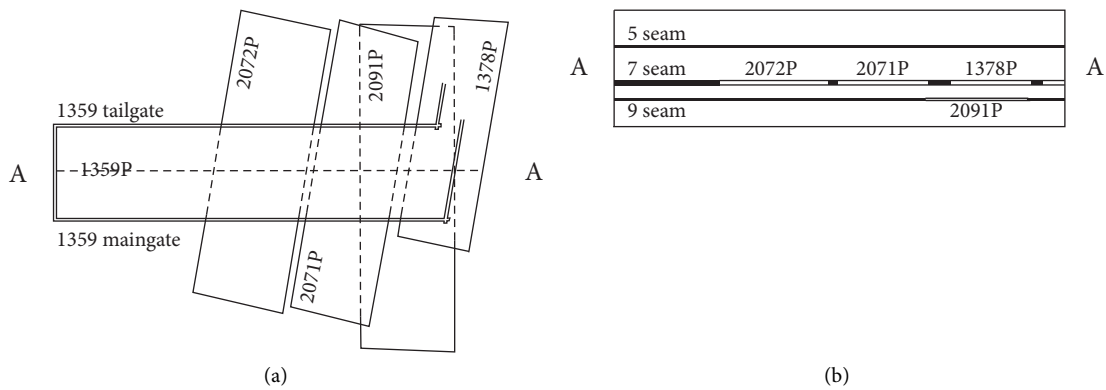


FIGURE 2: Layout and cross-section view of the studied area.

where M is the excavation thickness, W is the roof subsidence, K is the volumetric expansion coefficient of crushed rock, normally 1.1~1.4, and α is the seam dipping angle.

The mining height of 2071P is 3.4 m and the seam dipping angle is 8°. The roof fall is around 400 mm and the volumetric expansion coefficient of crushed rock is supposed to be 1.4. Then, the height of the caving zone can be estimated as 7.57 m; the height of the fracture zone can be calculated as 32.0–43.2 m and 46.9 m based on equation (2) or (3), respectively. Based on safety consideration, the height of the fracture zone of 2071P can be estimated as 46.9 m. The

heights of the caving zone and the fracture zone of each lower seam panel can be calculated in a similar manner, and the result is summarized in Table 1.

The average distance between #5 and #7 seam is 39 m, *i.e.*, 1359P is located in the upper position of fracture zone of #7 seam gob. Accordingly, #7 seam gob has less influence on the deformation of #5 seam. The distance between #5 and #7 seam is 54 m, so #5 seam is within the subsidence zone of #9 gob. The deformation of #5 seam due to #9 seam mining is small. The gob of 2091P overlaps with 1378P and 2071P gobs, and the deformation of #5 seam over this area is expected large.

TABLE 1: The height (in meters) of the caving zone and the fracture zone of related lower panels.

	2071P	2072P	1378P	2091P
Caving zone (m)	7.57	8.08	7.71	4.03
Fracture zone (m)	46.9	48.0	47.3	36.8

1.3. Numerical Calculation. To quantify the deformation of #5 seam induced by lower seams' mining, a FLAC 3D calculation model is constructed to calculate the subsidence consequence of #5 seam due to lower seams' mining. The model size is 1223(L) × 566(W) × 114(H) m using a total of 1193600 elements, as shown in Figure 3.

The mechanical properties of the surrounding rock used in the model are shown in Table 2.

The calculation procedure followed the consequence of lower seam mining [34]. After 2071P is mined out, the deformation nephogram and numerical simulation of #5 seam floor are shown in Figure 4. It shows that the subsidence of the middle sections of 2071P gob and 1378P gob is large, up to 1.22 m, and gradually decrease towards mining boundary.

Figure 5 shows side view of vertical displacement of A-A cross section. The maximum subsidence is 3.1 m, occurs at the #7 seam roof, and gradually decreases upwards. The subsidence of #5 seam floor is around 1.0–1.2 m.

After all lower panels are mined out, the subsidence of #5 seam floor is shown in Figure 6. It shows that, after excavation of #7 and #9 seams, the subsidence of #5 seam floor over the gob areas is 1.0–2.5 m, and the maximum deformation is on the overlapped area of 1378P gob and 2091P gob.

Figure 7 shows the subsidence of middle axial of 1359P (A-A in Figure 2). The maximum subsidence is 2.5 m. The bending angle of the seam is calculated based on the subsidence geometry. It shows that the maximum bending angle is around 1.9°, according to studies related to deformational behaviour of coal mass [31, 35–37], and it suggests that the rock integrity of 1359P is favourable.

1.4. Field Measurement. The results of roof caving analysis and numerical calculation suggest that the 1359P is minable. After roadway development, the subsidence of #5 seam should be measured to confirm pre-excavation prediction. In reality, due to the coal seam pinch out, the final length of the tailgate is 544.6 m, *i.e.*, 112 m beyond the 2072P goaf boundary. The final length of the maingate is 583.9 m and 76 m beyond the 2072P goaf boundary.

Based on the survey, the subsidence of the 1359P roadway floor is analysed. The roadways of 1359P are developed along the floor. The elevation at the corner of tailgate and open cut is −618.37 m, and the elevation at the corner of the maingate and open cut is −611.9 m. The subsidence contours of the roadway floor are obtained by the comparison of the elevation data before and after lower seams' excavation, as shown in Figures 8 and 9. The dashed line is the floor elevation before lower seams' mining.

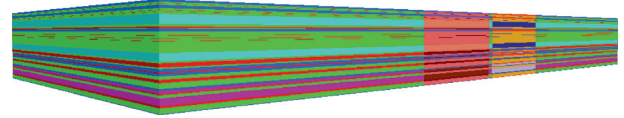


FIGURE 3: Numerical model.

Figures 8 and 9 show that the maximum subsidence of the 1359P tailgate is about 2.5 m, which is located in the overlapping area of 1378P gob and 2091P gob. The maximum subsidence of the 1359P maingate is about 2.7 m, which is located in the overlapping area of 2071P gob and 2091P gob. Figure 10 shows the measured and calculated subsidence data of the 1359P roadway floor. The numerical calculation is in good agreement with field measurement.

1.5. Roadway Deformation Monitoring. 3D laser scanning can obtain precise chamber profile data and quick modeling, which has been tested and trialed in deformation monitoring of underground roadway in the coal mine [38–42]. ZEB-HORIZON 3D laser scanner is used to analyse the roadway deformation of 1359P. ZEB-HORIZON is a mobile 3D laser scanner based on SLAM algorithm. It can dynamically measure and record 3D spatial information without GPS. Its scanning range is 30 m, the data acquisition rate is 43,200 points/s, the accuracy is 4 mm/100 m, and the angle accuracy is 60 mrad. It is the IP64 level that can be used in harsh environment. Its weigh is 3.5 kg and can be carried personally.

The deformation of roadway can be obtained by multiple scanning. The 3D laser scanning model of the tailgate and maingate of 1359P over 2072P is shown in Figure 11.

Figure 12 shows the outline of the maingate of 1359P, and they are (a) underlying coal mass, (b) over 2072P gob, (c) over pillar between 2072P and 2071P, (d) over 2071P gob, (e) over pillar between 2071P and 1378P, and (f) over 1378P gob. The red and blue lines are two measurements, after roadway development and before 1359 panel excavation, respectively. The calculation results of roof fall and rib convergence are shown in Table 3.

For large deformation of surrounding rock of the roadways, a special ground support scheme should be implemented based on the reinforcement principles and field conditions [43–46]. The maximum roof fall is 30 mm, and the maximum rib convergence is 25 mm. The overall deformation of the roadway is small. At the same time, it was observed that the roof, floor, and ribs of the roadway remained in good condition. Combining with result of theoretical analysis, it can be concluded that the roadway of 1359 panel in #5 seam is stable, and the panel can be mined as normal.

TABLE 2: Parameters of coal and rock used in the calculation.

Rock	Density (kg/m ³)	Tensile strength (MPa)	Elastic modulus (MPa)	Poisson's ratio	Cohesion (MPa)	Internal friction angle (°)
Siltstone	2.600	1.10	15.125	0.26	1.30	34
Coal	1.323	0.28	2.173	0.28	0.28	32
Medium sand	2.502	0.66	35.696	0.20	0.66	33
Mudstone	2.668	0.36	11.399	0.25	0.83	31

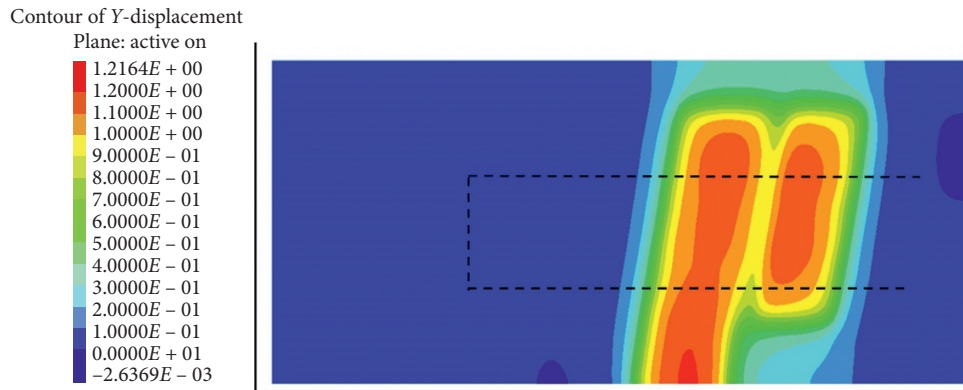


FIGURE 4: Subsidence of #5 seam floor after 1378P and 2071P are mined out.



FIGURE 5: Overlaying strata subsidence of A-A cross section after 2071P is mined out.

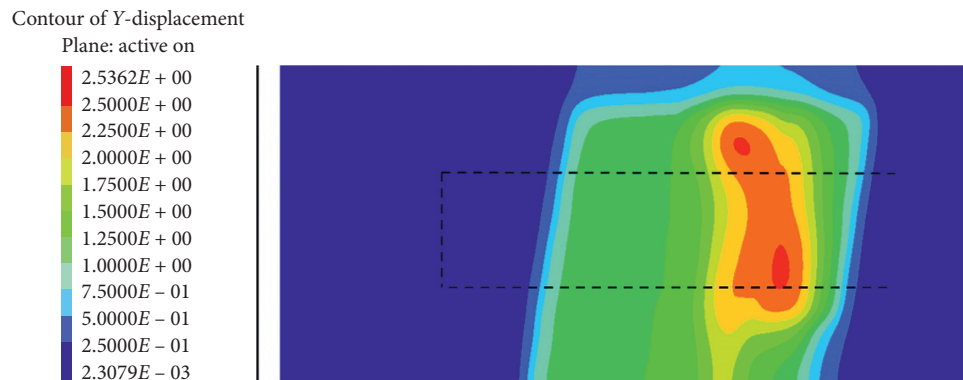


FIGURE 6: Floor subsidence of #5 coal seam after lower seam mining.

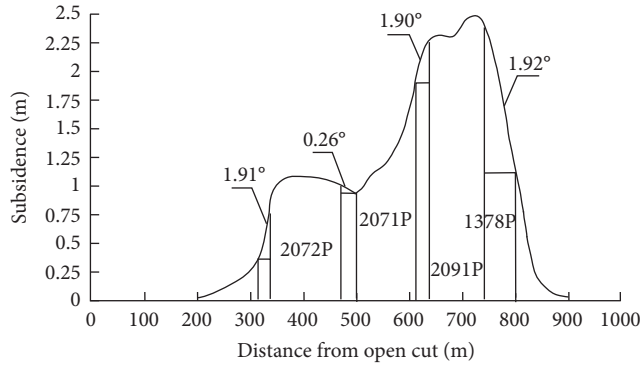
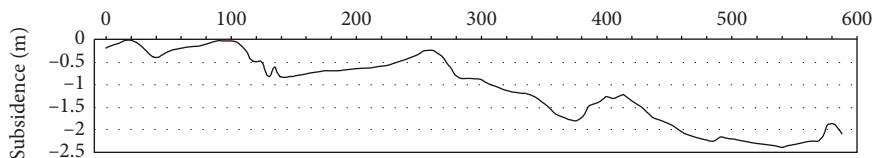
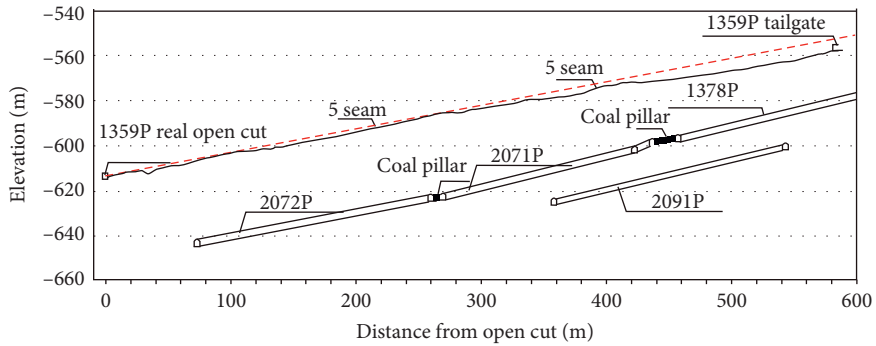


FIGURE 7: Floor subsidence and dipping angles of 1359P after lower seam mining.

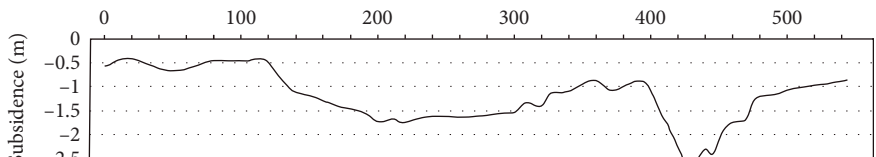


(a)

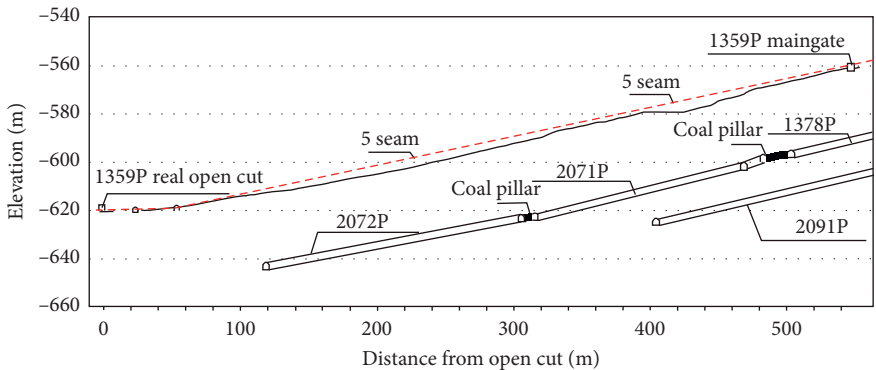


(b)

FIGURE 8: Subsidence of 1359P maingate floor.



(a)



(b)

FIGURE 9: Subsidence of 1359P tailgate floor.

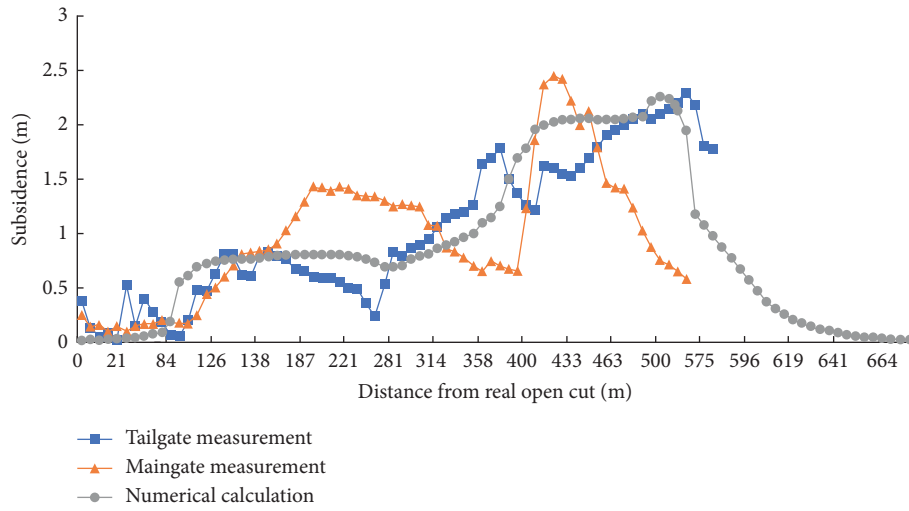


FIGURE 10: Comparison of calculated and measured subsidence of 1359P roadway floor.

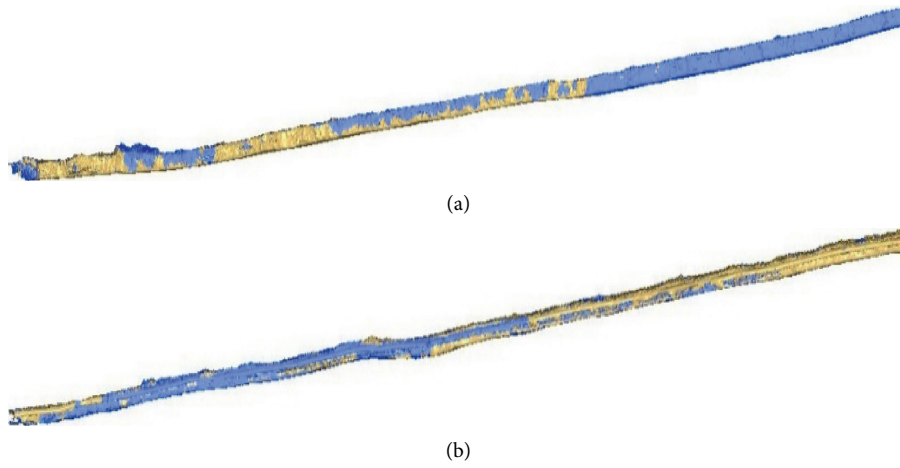


FIGURE 11: 3D scanning model of 1359P over 2072P gob: (a) tailgate and (b) maingate.

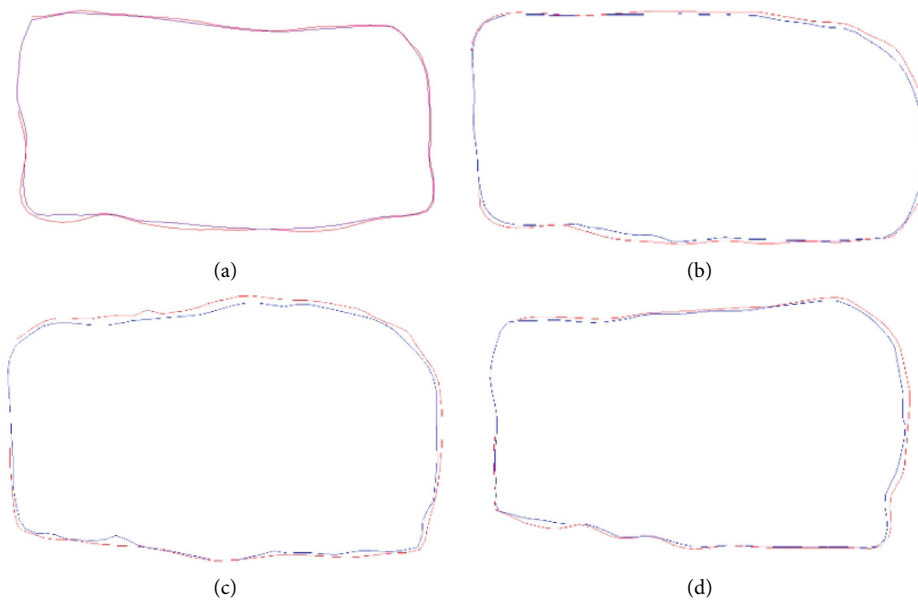


FIGURE 12: Continued.

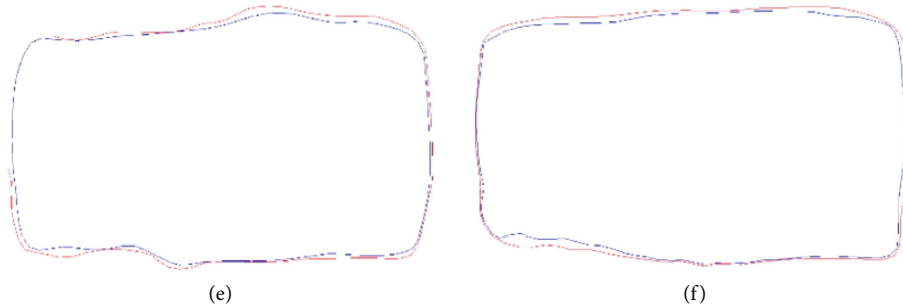


FIGURE 12: The profile of 1359P maingate. (a) Underlying coal mass (40 m from open cut). (b) Over 2072P gob (1730 m from open cut). (c) Over pillar between 2072P and 2071P (268 m from open cut). (d) Over 2071P gob (357 m from open cut). (e) Over pillar between 2071P and 1378P (455 m from open cut). (f) Over 1378P gob (502 m from open cut).

TABLE 3: The maximum roadway deformation.

Distance from open cut (m)	40	173	268	357	455	502
Roof fall (mm)	24	20	30	19	29	18
Rib convergence (mm)	12	19	25	17	20	14

2. Conclusion

Based on the upward mining engineering background of the Qianjiaying coal mine, this paper comprehensively uses roof caving analysis and numerical calculation to analyse the mining feasibility of 1350P. In the stage of the roadway development, the roadway subsidence is measured and the roadway deformation is modeled. The following conclusions can be drawn:

- (1) The results of caving analysis and numerical calculation show that, under the condition of 2071P, 2091P, 1378P, and 2091P are mined out, and the subsidence of #5 seam 5 is 1.0–2.5 m. The maximum bending angle of #5 seam is 1.9°. The subsidence and bending angle results of #5 seam show that 1359P roadway can be developed.
- (2) Through field measurement, the floor subsidence of 1359P roadway is obtained. The maximum subsidence of 1359P tailgate is about 2.5 m, located in the overlapping area of 1378P gob and 2091P gob. The maximum subsidence of the maingate is about 2.7 m, which is located in the overlapping area of 2071P gob and 2091P gob. The numerical results are in good agreement with the field measurements.
- (3) The roadway deformation is monitored using the multiple 3D laser scanning method. The maximum roof fall and rib convergence is 30 and 25 mm, respectively. So, 1359P can be mined as normal.

Data Availability

All data used to support the findings of the study are included within the article.

Conflicts of Interest

The authors declare that there are no conflicts of interest regarding the publication of this paper.

References

- [1] J. Han, W. H. Song, and Z. J. Zhu, *Overmining Technology of Closed Multi Coal Seams*, China Coal Industry Publishing House, Beijing, China, 2013.
- [2] L. Zhang, J. H. Li, J. H. Xue et al., “Experimental studies on the changing characteristics of the gas flow capacity on bituminous coal in CO₂-ECBM and N₂-ECBM,” *Fuel*, vol. 291, Article ID 120115, 2021.
- [3] J. Lin, T. Ren, Y. P. Cheng et al., “Cyclic N₂ injection for enhanced coal seam gas recovery: a laboratory study,” *Inside Energy*, vol. 188, Article ID 116115, 2019.
- [4] J. Lin, T. Ren, G. Wang, P. Booth, and J. Nencik, “Experimental investigation of N₂ injection to enhance gas drainage in CO₂-rich low permeable seam,” *Fuel*, vol. 215, pp. 665–674, 2018.
- [5] D. Xue, J. Wang, Y. Zhao, and H. Zhou, “Quantitative determination of mining-induced discontinuous stress drop in coal,” *International Journal of Rock Mechanics and Mining Sciences*, vol. 111, pp. 1–11, 2018.
- [6] X. W. Feng, N. Zhang, F. Xue, and Z. Xie, “Practices, experience, and lessons learned based on field observations of support failures in some Chinese coal mines,” *International Journal of Rock Mechanics and Mining Sciences*, vol. 123, Article ID 104097, 2019.
- [7] D. J. Xue, J. Zhou, Y. T. Liu et al., “On the excavation-induced stress drop in damaged coal considering a coupled yield and failure criterion,” *International Journal of Coal Science & Technology*, vol. 7, no. 5, pp. 58–67, 2020.
- [8] L. Q. Wang and Z. H. Li, *Overmining Technology of Coal Seams*, China Coal Industry Publishing House, Beijing, China, 1995.
- [9] J. Han, H. W. Zhang, P. T. Zhang et al., “Feasibility study on upward mining in seam group with short distance to each other in Kailuan mining area,” *Coal Science and Technology*, vol. 39, no. 10, pp. 14–17, 2011.
- [10] L. Zhang, S. Chen, C. Zhang et al., “The characterization of bituminous coal microstructure and permeability by liquid nitrogen fracturing based on μ CT technology,” *Fuel*, vol. 262, Article ID 116635, 2020.

- [11] D. J. Xue, L. L. Lu, J. Zhou et al., "Cluster modeling of the short-range correlation of acoustically emitted scattering signals," *International Journal of Coal Science & Technology*, pp. 1–15, 2020.
- [12] D. J. Xue, Y. T. Liu, H. W. Zhou, J. Q. Wang, J. F. Liu, and J. Zhou, "Fractal characterization on anisotropy and fractal reconstruction of rough surface of granite under orthogonal shear," *Rock Mechanics and Rock Engineering*, vol. 53, no. 3, pp. 1225–1242, 2020.
- [13] Q. Wang, Z. H. Jiang, B. Jiang et al., "Research on an automatic roadway formation method in deep mining areas by roof cutting with high-strength bolt-grouting," *International Journal of Rock Mechanics and Mining Sciences*, vol. 128, Article ID 104264, 2020.
- [14] D. Cao, A. Wang, S. Ning et al., "Coalfield structure and structural controls on coal in China," *International Journal of Coal Science & Technology*, vol. 7, no. 2, pp. 220–239, 2020.
- [15] H. Shi, J. Xie, X. Wang, J. Li, and X. Ge, "An operation optimization method of a fully mechanized coal mining face based on semi-physical virtual simulation," *International Journal of Coal Science and Technology*, vol. 7, no. 1, pp. 147–163, 2020.
- [16] C. Wang, N. Zhang, G. C. Li et al., "Control principles for roadway roof stabilization in different zones during ascending mining," *Journal of China University of Mining & Technology*, vol. 41, no. 4, pp. 543–550, 2012.
- [17] H. W. Zhang, J. Han, L. X. Hai et al., "Study on closed multiple-seam in the ascending mining technology," *Journal of Mining & Safety Engineering*, vol. 30, no. 1, pp. 63–67, 2013.
- [18] Y. D. Jiang, Y. M. Yang, Z. Q. Ma et al., "Breakage mechanism of roof strata above widespread mined-out area with roadway mining method and feasibility analysis of upward mining," *Journal of China Coal Society*, vol. 41, no. 4, pp. 801–807, 2016.
- [19] A. M. Suchowerska, R. S. Merifield, and J. P. Carter, "Vertical stress changes in multi-seam mining under supercritical longwall panels," *International Journal of Rock Mechanics and Mining Sciences*, vol. 61, pp. 306–320, 2013.
- [20] X. P. Shao, J. T. Wu, J. F. Zhang et al., "Study on crack evolution law of overburden strata and stability of interlayer rock in upward coal mining," *Coal Science and Technology*, vol. 44, no. 9, pp. 61–66, 2016.
- [21] C. Cao, T. Ren, C. Cook, and Y. Cao, "Analytical approach in optimising selection of rebar bolts in preventing rock bolting failure," *International Journal of Rock Mechanics and Mining Sciences*, vol. 72, pp. 16–25, 2014.
- [22] Q. Wang, Y. Wang, M. C. He et al., "Experimental research and application of automatically formed roadway without advance tunneling," *Tunnelling and Underground Space Technology*, vol. 114, no. 3, Article ID 103999, 2021.
- [23] C. Cao, T. Ren, and C. Chris, "Introducing aggregate into grouting material and its influence on load transfer of the rock bolting system," *International Journal of Mining Science and Technology*, vol. 24, no. 3, pp. 325–328, 2014.
- [24] W. P. Huang, W. B. Xing, Y. S. Zheng et al., "Reasonable layout of roadways for upward mining technology of close coal seams," *Chinese Journal of Rock Mechanics and Engineering*, vol. 36, no. 12, pp. 3028–3039, 2017.
- [25] C. L. Zhang, "Study on overlying strata caving and movement regularity of ascending mining in contiguous seams," *Coal Science and Technology*, vol. 46, no. 8, pp. 1–7, 2018.
- [26] X. Z. Zhao, Z. Y. Gao, T. Wu et al., "Study on roadway layout of the ascending mining panels in closed distance coal seams," *Chinese Journal of Underground Space and Engineering*, vol. 15, no. 1, pp. 194–201, 2019.
- [27] Y. Wang, X. Y. Fu, L. H. Kong et al., "Study on the stability of dangling structure in ascending mining close distance coal seams," *Coal Science and Technology*, vol. 48, no. 12, pp. 95–100, 2020.
- [28] "State Administration of safety supervision, State Administration of coal mine safety, National Energy Administration, State Railway Administration," *Code for Coal Pillar Setting and Coal Pressure Mining in Buildings, Water Bodies, Railways and Main Roadways*, http://www.mem.gov.cn/gk/gwgg/201707/t20170703_241729.shtml, 2017.
- [29] Z. Bi, J. Han, B. Liang, B. Huo, C. Cao, and S. Ma, "Analysis of strata stress and its effect on lower-level seam exploitation under room-and-pillar shallow coal mining," *Journal of Engineering Science and Technology Review*, vol. 14, no. 1, pp. 79–85, 2021.
- [30] S. R. Wang, X. G. Wu, Y. H. Zhao et al., "Evolution characteristics of composite pressure-arch in thin bedrock of overlying strata during shallow coal mining," *International journal of applied mechanics*, vol. 11, no. 3, Article ID 1950030, 2019.
- [31] J. Han, H. Liang, C. Cao, Z. Bi, and Z. Zhu, "A mechanical model for sheared joints based on Mohr-Coulomb material properties," *Géotechnique Letters*, vol. 8, no. 2, pp. 92–96, 2018.
- [32] P. Luo, S. Wang, P. Hagan et al., "Mechanical performances of cement-gypsum composite material containing a weak interlayer with different angles," *Dyna*, vol. 94, no. 4, pp. 447–454, 2019.
- [33] C. Zhu, M. C. He, M. Karakus, X. H. Zhang, and Z. Guo, "The collision experiment between rolling stones of different shapes and protective cushion in open-pit mines," *Journal of Mountain Science*, vol. 18, no. 5, pp. 1391–1403, 2021.
- [34] C. Zhu, M. He, M. Karakus, X. Zhang, and Z. Tao, "Numerical simulations of the failure process of anaclinal slope physical model and control mechanism of negative Poisson's ratio cable," *Bulletin of Engineering Geology and the Environment*, vol. 80, no. 4, pp. 3365–3380, 2021.
- [35] D. Xue, H. Zhou, Y. Zhao, L. Zhang, L. Deng, and X. Wang, "Real-time SEM observation of mesoscale failures under thermal-mechanical coupling sequences in granite," *International Journal of Rock Mechanics and Mining Sciences*, vol. 112, pp. 35–46, 2018.
- [36] X. Lian, H. Hu, T. Li, and D. Hu, "Main geological and mining factors affecting ground cracks induced by underground coal mining in Shanxi Province, China," *International Journal of Coal Science and Technology*, vol. 7, no. 2, pp. 362–370, 2020.
- [37] B. Chen, "Stress-induced trend: the clustering feature of coal mine disasters and earthquakes in China," *International Journal of Coal Science & Technology*, vol. 7, no. 4, pp. 676–692, 2020.
- [38] V. Kajzar, R. Kukutsch, P. Waclawik, and J. Nemcik, "Innovative approach to monitoring coal pillar deformation and roof movement using 3D laser technology," *Procedia Engineering*, vol. 191, pp. 873–879, 2017.
- [39] X. Y. Liu, Q. S. Hu, and H. J. Li, "Research on coal mine roof monitoring based on three-dimensional laser scanning technology," *China Coal*, vol. 43, no. 7, pp. 81–83, 2017.
- [40] L. L. Guo, D. W. Zhou, D. M. Zhang et al., "Deformation and failure law of surrounding rock of roadway of mining action," *Journal of Mining and Strata Control Engineering*, vol. 3, no. 2, Article ID 023038, 2021.
- [41] D. J. Xue, H. W. Zhou, Y. T. Liu, L. S. Deng, and L. Zhang, "Study of drainage and percolation of nitrogen-water flooding

- in tight coal by NMR imaging,” *Rock Mechanics and Rock Engineering*, vol. 51, no. 11, pp. 3421–3437, 2018.
- [42] S. Mao, “Development of coal geological information technologies in China,” *International Journal of Coal Science & Technology*, vol. 7, no. 2, pp. 320–328, 2020.
- [43] X. Feng, N. Zhang, S. Yang, and F. He, “Mechanical response of fully bonded bolts under cyclic load,” *International Journal of Rock Mechanics and Mining Sciences*, vol. 109, pp. 138–154, 2018.
- [44] J. Han, S. Wang, Y. Chen, and C. Cao, “Analytical derivation of rib bearing angle of reinforcing bar subject to axial loading,” *Magazine of Concrete Research*, vol. 71, no. 4, pp. 175–183, 2019.
- [45] C. Cao, T. Ren, and C. Cook, “Calculation of the effect of Poisson’s ratio in laboratory push and pull testing of resin-encapsulated bolts,” *International Journal of Rock Mechanics and Mining Sciences*, vol. 64, pp. 175–180, 2013.
- [46] X. W. Feng, N. Zhang, Z. J. Wen et al., “Mechanical responses and acoustic emission properties of bolting system under short encapsulation cyclic thrust tests,” *International Journal of Fatigue*, vol. 121, pp. 39–54, 2018.

Research Article

A Case Study of Optimization and Application of Soft-Rock Roadway Support in Xiaokang Coal Mine, China

Shuai Guo ¹, Xun-Guo Zhu ², Xun Liu ³ and Hong-Fei Duan ⁴

¹State Key Laboratory for GeoMechanics and Deep Underground Engineering, China University of Mining and Technology, Xuzhou 221116, China

²College of Architectural Engineering, Dalian University, Liaoning, Dalian 116622, China

³School of Mines, China University of Mining and Technology, Xuzhou 221116, China

⁴Jinneng Holding Group Co. Ltd., Datong 037000, China

Correspondence should be addressed to Xun-Guo Zhu; zhu_xunguo@hotmail.com

Received 11 May 2021; Accepted 28 June 2021; Published 15 July 2021

Academic Editor: Jia Lin

Copyright © 2021 Shuai Guo et al. This is an open access article distributed under the Creative Commons Attribution License, which permits unrestricted use, distribution, and reproduction in any medium, provided the original work is properly cited.

The roadway of S2S2 fully mechanized caving face (FMCF) in Xiaokang Coal Mine is one of the most typical deep-buried soft-rock roadways in China and had been repaired several times. In order to figure out the failure reasons of the original roadway support, the geological conditions were investigated, the surrounding rock stress was monitored, the rib displacement, roof separation, and floor heave were in situ measured, and the performance of the U-shaped steel support was simulated. The above analysis results indicated that the support failure was mainly caused by (1) the unreasonable arch roadway section, (2) the high and complex surrounding rock stress, (3) the failure control of the floor heave, and (4) the inadequate self-supporting capacity of the surrounding rock. For optimizing, the roadway section was changed to circle and a new full-section combined support system of “belt-cable-mesh-shotcrete and U-shaped steel-filling behind the support” was adopted, which could specifically control the floor heave, allow the roadway deformation in control, and improve the self-supporting ability and stress field of the surrounding rock. To determine the support parameters, the selected U-shaped steel support was verified by simulation, and various bolt-cable support schemes were simulated and compared. Finally, such an optimized support scheme was applied in the roadway of the next replacement FMCF. The in situ monitoring showed that the rib-to-rib convergence and roof-to-floor convergence were both controlled within 600 mm, which indicated that the roadway was effectively controlled. This case study has important reference value and guiding function for the optimal design of the soft-rock roadway support with similar geological conditions.

1. Introduction

As coal mining depth increases, the roadway support is generally faced with the difficult problems caused by soft rock and high ground stress [1–3]. In addition, the severe strata behavior, the large and long-time roadway deformation, serious floor heave, and serious support structure damage lead to over 70% of the repair rate in such kind of roadways [4–6]. The induced vicious cycle of “digging and repairing” during mining [7–9] wastes a lot of manpower and material, directly affects the efficient production of coal mine, and endangers the safety of human life and property [10–12].

The research on the theory and technology of the soft-rock roadway support under high ground stress is active, and a series of research results have been obtained. For instance, He et al. [13] proposed the coupling support concept of roadway and developed the technical system of active support; Kang and Wang [14] put forward the theory of high pretensioned stress and intensive bolting system and developed a complete technology of bolt support for coal mine; Gao et al. [15] developed the concrete-filled steel tube support technology; Jiang et al. [16] analyzed the mechanism of different types of roadway floor heaves and proposed corresponding prevention and control measures. In addition, Yang et al. [17] revealed the deformation and failure

mechanism of deep soft-rock roadway and put forward a new “bolt-cable-mesh-shotcrete + shell” combined support; Shen [18] optimized the spacing and pretightening force of the bolt and anchor cable by UDEC; Kang et al. [19] analyzed the soft-rock roadway deformation and failure characteristics with different support types by the numerical simulation method; Wang et al. [20] first adopted grouting to enhance the surrounding rock’s self-bearing ability and then used the bolt to control the deformation and failure of the soft surrounding rock.

These studies laid the theoretical foundation and provided new ideas and methods for the support of deep-buried soft-rock roadway. As for specific applications, the geological conditions and the key factors affecting the stability of surrounding rocks are complex and numerous [20–23]. Hence, the design and optimization of the support scheme should be carried out according to the in situ conditions and a suitable support theory and technology should be adopted [24–27].

In Xiaokang Coal Mine, during the first fully mechanized caving face (FMCF) of S1W3, during the whole mining period, the cumulative roof-to-floor convergence of the two mining roadways is 3800 mm and 6500 mm, respectively, and the cumulative rib-to-rib convergence is 1400 mm and 3200 mm, respectively, which is 10~20 times and 2~3 times that of other mines where the surrounding rock is relatively stable and soft. Coupled with serious floor heave and complex surrounding rock stress, the soft-rock roadway in Xiaokang Coal Mine is extremely difficult to maintain in China and even in the world [28].

The purpose of this paper is to optimize and design the support scheme of the deep-buried soft-rock roadway in Xiaokang Coal Mine based on the initial soft-rock roadway support system in S2S2 FMCF. Thus, the performance of the original support scheme in S2S2 FMCF was first analyzed by in situ measurement and numerical simulation to figure out the failure mechanism, based on which the corresponding control technology was developed and the support scheme was optimized. Finally, the new proposed support scheme was carried out in the roadway of the next replacement FMCF, and the in situ monitoring was carried out to identify the effect of the new support system.

2. Engineering Background

2.1. The Geological Conditions. As shown in Figure 1, Xiaokang Coal Mine with an area of 28.99 km² is located in Liaoning Province, China. Its north-south length is 6.03 km and the east-west width is 4.81 km.

In Xiaokang Coal Mine, the S2S2 FMCF and its replacement FMCF are both located in southern No. 2 mining area (S2) and share the same geological conditions. The width of the S2S2 FMCF is 232 m, and the advancing length is 1281 m. As for the coal seam, the thickness is 7.50 m to 10.24 m, with an average of 8.50 m; the buried depth is 640 m to 720 m, with an average of 665 m; and the dip is 3° to 10°, with an average of 5°.

The immediate roof of the coal seam is oil shale with stepped fracture. It is carbonaceous, oil-rich, and easily weathered and would be crushed after drying, which make it

not easy to maintain. Its thickness is 6.31 m to 14.2 m with an average of 8.5 m. The mining height of the machine is 2.8 m, the coal drawing height is 5.7 m, and the caving ratio is 1 : 2.04. The basic roof is mainly composed of mudstone with obvious beddings and joints. Its thickness is 11.2 m to 21.3 m with an average of 15.6 m.

The thickness of the coal seam floor is 6.51 m to 12.3 m with an average of 7.62 m. It was relatively highly cemented by argillaceous material. More than 50% of the clay minerals in floor strata are Aemon interbeds, and the other clay minerals are mainly kaolin and illite, so they are easy to be weathered and have strong dilatibility, resulting in a very serious floor heave.

2.2. The Initial Support Scheme. The arch-section mining roadways of the S2S2 FMCF with a sectional area of 13.7 m² initially adopted the combined support scheme of “bolt-mesh-shotcrete and U-shaped steel”. The specific support parameters are as follows.

As shown in Figure 2(a), the anchor bolts were just installed at the top and shoulder of the roadway. The anchor bolt used the thread steel of M22 × 2400 mm with a spacing of 800 × 800 mm and a pretightening force of 60 kN. The lengthened resin anchorage was applied with two Z2335 resin anchor agents and one Z2540 resin anchor agent in each hole. The high-intensity tray of 120 mm × 120 mm × 10 mm was selected. The U36 steel support was adopted with a spacing of 1000 mm. The rhombic metal mesh was used with a bar of 8 mm and a grid spacing of 100 mm. The back-filling thickness was 300 mm. There almost no support was conducted to control the floor. The support effect is shown in Figure 2(b).

2.3. Complex Stress Field of the Roadway Surrounding Rock. To reveal the stress environment of the roadway in the S2S2 workface, three observation stations of P1, P2, and P3 were arranged at a distance of 50 m, 500 m, and 1000 m away from the open-off cut, respectively, as shown in Figure 3(a). The stresses were measured by using the SY-56 hydrofracturing in situ stress measurement device in the drilling of the roadway surrounding rock, as shown in Figure 3(b). The drilling depth was 10 m and the bore diameter was 56 ± 2 mm. The horizontal stresses on the two ribs and the vertical stresses on the roof are shown in Figure 3(c).

The results indicated that the rock stress varied with the positions along the roadway: at P1 position, the stress on the two ribs (21 MPa) is two times that of the roof (10 MPa), while at P2 position the roof stress (21 MPa) is two times that of the ribs (10 MPa), and when it turns to P3 position, the right rib stress is the largest. It can be concluded that the rock stresses were not even around the roadway and changed along the length direction, and such high and uneven stress field far exceed the resistance of the surrounding rock which only has a saturated compressive strength of 3 MPa–5 MPa, resulting in large displacement and damage depth of the roadway and high pressure on the support structures. Under the complex and uneven stress field at different positions, the

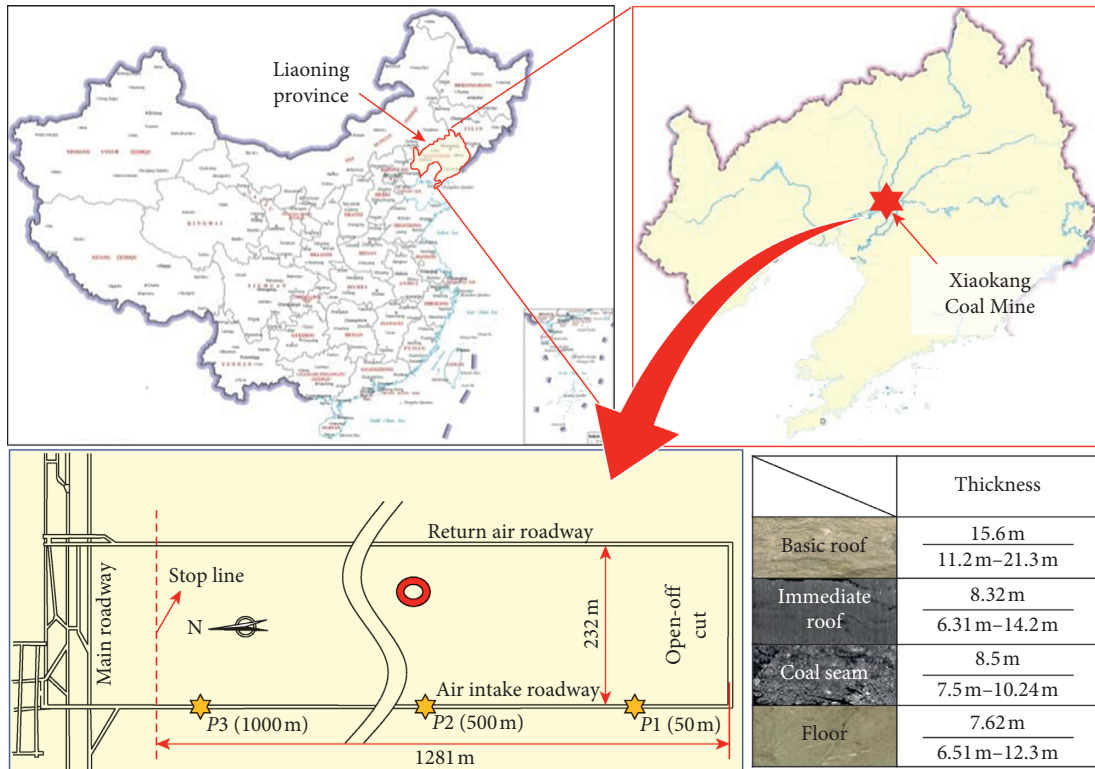


FIGURE 1: Location of the Xiaokang Coal Mine.

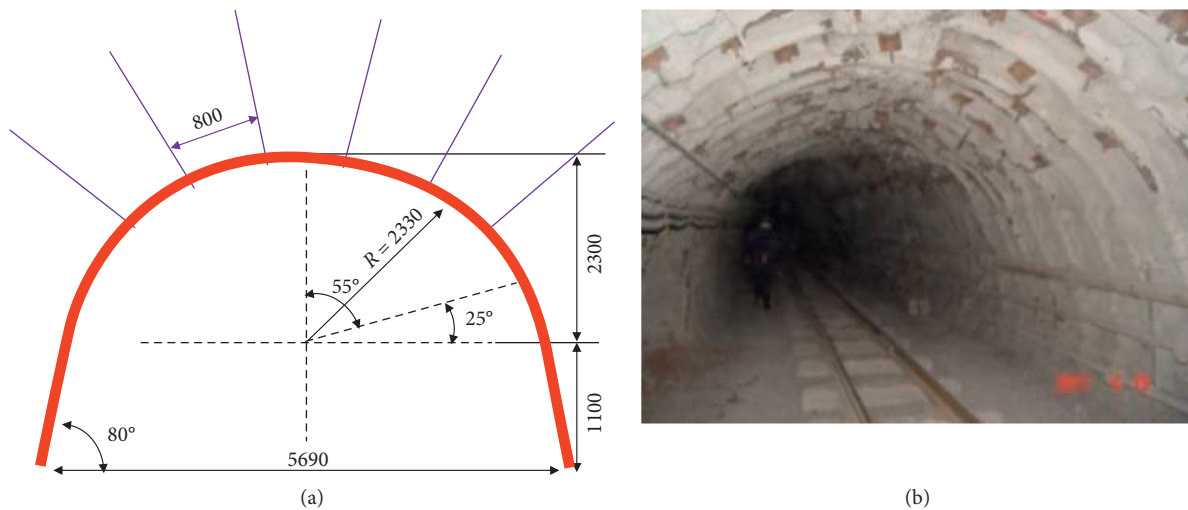


FIGURE 2: The original support. (a) Support parameters; (b) support effect.

performance of the U-shaped steel support will be simulated and analyzed in Section 3. In addition, in the new optimized support scheme, the selected U-shaped steel must adapt to such complex stress field environment which will be verified in Section 4.

2.4. The Roadway Deformation and Failure Characteristics. In order to analyze the roadway deformation and failure characteristics, three observation stations were set at observation stations of P1, P2, and P3 to monitor the rib-to-rib

convergence, roof separation, and floor heave during the stopping period under the influence of mining.

2.4.1. Displacement of Ribs. The crossing method is commonly used to measure the displacement of ribs, as shown in Figure 4. The pegs were used to fix the ends of the line on two ribs, roof, and floor of the roadway at P1 observation station (50 m away from the open-off cut). The surrounding rock on ribs moved inward towards the roadway under the actions of the horizontal stress causing the lateral displacement of the

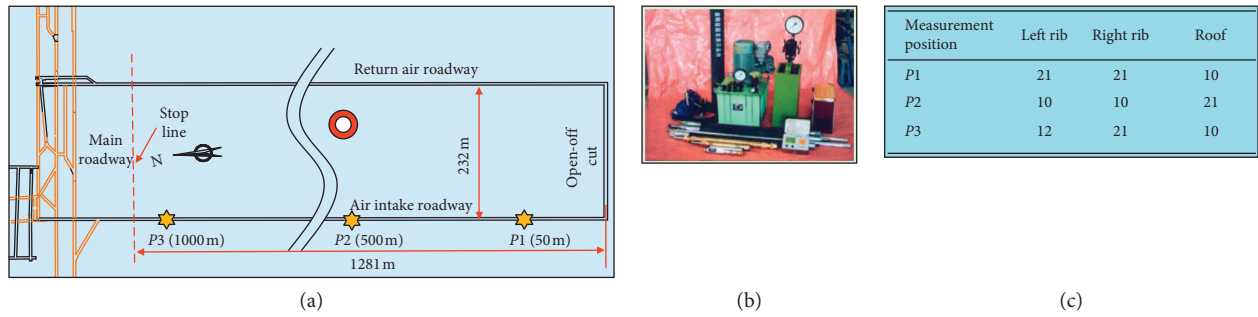


FIGURE 3: In situ stress measurement of the roadway surrounding rock. (a) In situ stress measurement position. (b) In situ stress measuring device. (c) Stress measurement results.

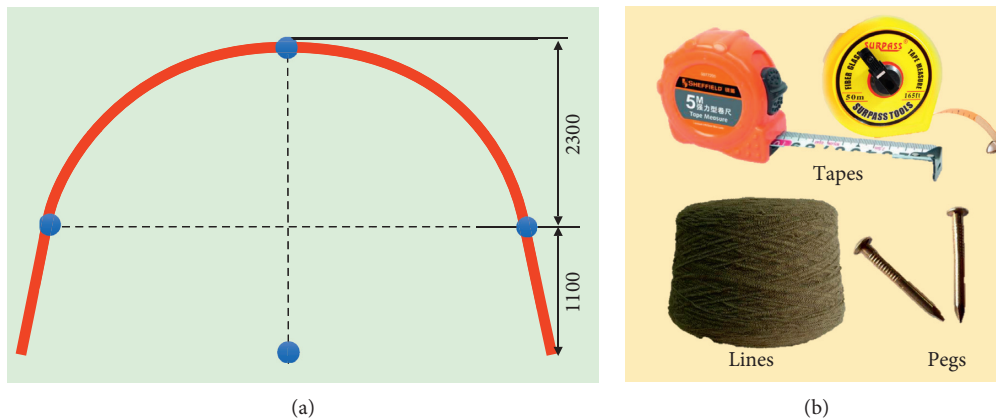


FIGURE 4: The monitoring scheme and devices.

surrounding rock. A tape was used to measure the displacement on ribs, as Figure 4(b). The monitoring results of rib-to-rib convergence are shown in Figure 5.

Figure 5 indicates that (1) there were three stages of rib-to-rib convergence, that is, slow stage, accelerated stage, and instability stage, with the corresponding periods of 0~4 days, 4~10 days, and 10~18 days, respectively; (2) the rib-to-rib convergence was 99 mm, 783 mm, and 1300.5 mm in the three stages, respectively, and the total convergence was 2182.5 mm, and the average speed was 138.9 mm/d since 4 to 18 days; and (3) at the instability stage, the failure of the U-shaped steel support and the anchor bolt occurred and the roadway ribs were out of control.

2.4.2. Roof Separation. The roadway roof activities mainly include bending deformation, separation, and caving, which could be monitored by using the SMJ-2 roof separation device. The SMJ-2 is made up of anchor head of the base point, measuring line, casting, external cylinder, and internal cylinder. As shown in Figure 6(a), the roof separation device was mainly used to monitor the roof separation values within depths of 0–2.4 m and 0–8.0 m in the roof strata. The anchor head of the deep base point (8.0 m) was fixed within the stable deep bedrock, and the anchor head of the shallow base point (2.4 m) was fixed at the anchor end. The observation station was 500 m away from the open-off cut (i.e., P2 observation station).

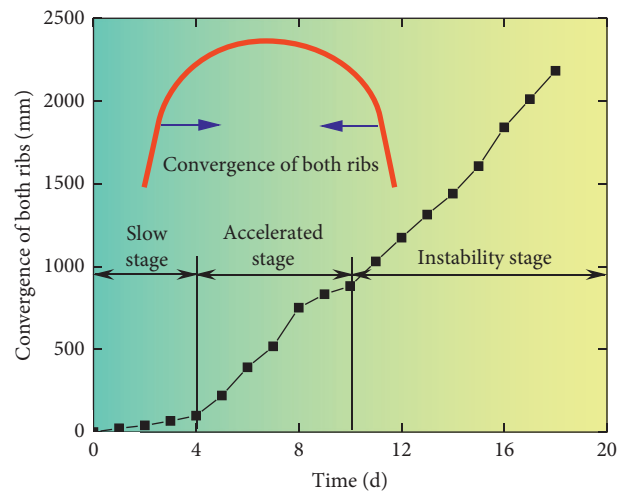


FIGURE 5: The rib-to-rib convergence.

The results of the shallow base points could be seen in Figure 6(b), which indicated that (1) the roadway roof experienced three stages, that is, the slow stage, accelerated stage, and stable stage with the periods of 0~4 days, 4~11 days, and 11~18 days, respectively; (2) the roof subsidence amounts were 101.6 mm, 843.4 mm, and 84.0 mm at the three stages, respectively, and the total amount was

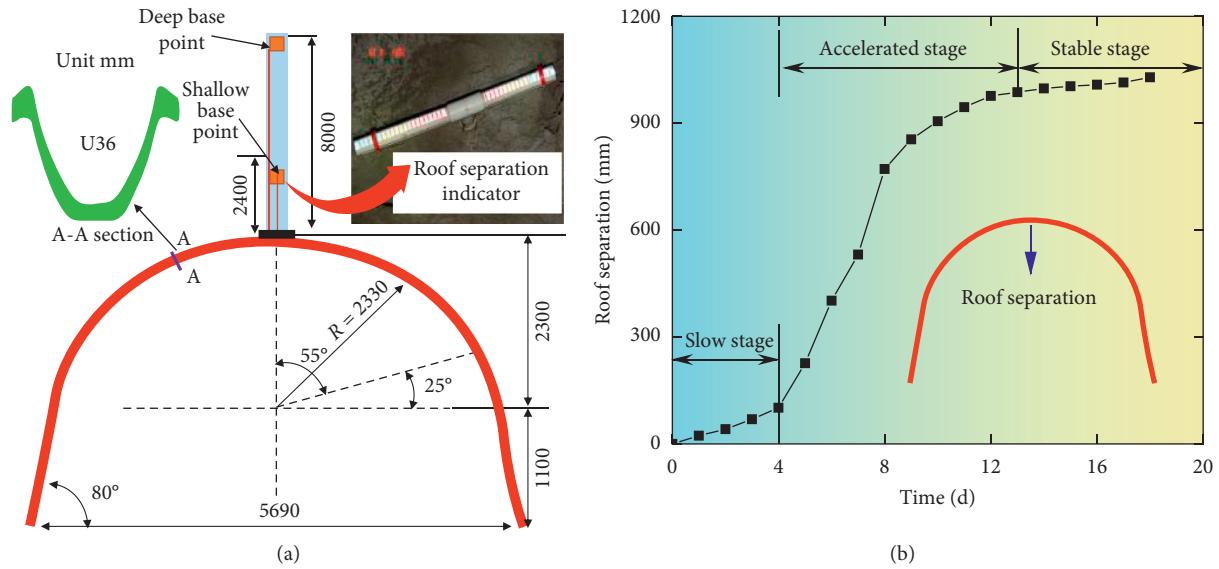


FIGURE 6: Roof separation. (a) The measurement scheme; (b) the results.

1029 mm; and (3) at the stable stage, the roof deformation basically kept unchanged because a single prop was used for timely maintenance.

2.4.3. The Amount of Floor Heave. The floor heave is caused by the uplift of the roadway floor due to mining, as shown in Figure 7(a). It could reduce the roadway section, hinder the transportation and pedestrians, affect mine ventilation, and greatly limit the safe production of the mine. In the worst situation, the roadway has to be abandoned. To solve the severe floor heave, a lot of manpower and material resources are needed. The floor heave amounts were obtained 1000 m away from the cut-open, as shown in Figure 7(b).

Figure 7(b) indicates that (1) the roadway roof experienced three stages, that is, slow stage, accelerated stage, and stable stage with the periods of 0~6 days, 6~15 days, and 15~18 days, respectively; (2) the floor heave amounts were 168.0 mm, 828.0 mm, and 48.8 mm, respectively, at the three stages, and the total floor heave amount was 1044.8 mm; and (3) at the stable stage, the floor deformation basically remained unchanged. As the original arched roadway adopted an open support system with no measurement to control the floor heave, the serious floor heave is mainly caused by stress extrusion and floor rock water expansion.

3. Numerical Analysis of Deformation and Failure Characteristics of the U-Shaped Steel Support

A shed is often used for soft-rock roadway support. In this support method, the bearing capacity of the U-shaped steel support is the basis to ensure the control effects of the roadway surrounding rock. When the loads applied on the U-shaped steel support exceed its bearing capacity, the support will undergo significant deformation and failure. According to the obtained roadway surrounding rock

stresses in Section 2.3, the numerical simulation method was used to analyze the deformation and failure characteristics of the U-shaped steel support in this part.

3.1. The Numerical Model

3.1.1. The Constitutive Model of the Material. The materials of the U-shaped steel are usually 20MnK, 25MnK, and 20MnVK. According to the requirements of international standard GB/T228-2010, the aforementioned three materials were used to make tensile specimens with circular cross sections with a size of $100 \times \Phi 10$ mm to conduct tensile tests at room temperature. The tensile testing machine is shown in Figure 8(a). It could realize automatic data acquisition, processing and storage, and real-time display of test status and curves.

Figure 8(b) shows the stress-strain curve of the specimens, which have undergone the elastic stage, yield stage, strengthened stage, and failure stage. The properties of the stress-strain curve were used to determine the materials' elastic modulus E_1 , yield limit σ_s , and tensile limit σ_b . The bilinear isotropic hardening model was used to select the material type. The MATLAB was used to write program and fix the material's tangent modulus E_2 . The electrical measurement method was applied to get the Poisson ratios μ . Table 1 shows the detailed results.

3.1.2. Model Establishment. The establishment of the U-shaped steel support could be divided into the establishment of the solid model, the selection of the element type, the constitutive model of materials, and the boundary conditions. The specific process is as follows:

- (1) The establishment of the solid model: according to the international standards of U-shaped steel, a 3D modeling software was applied to build an U36 section model, which was then saved in *sat.file*

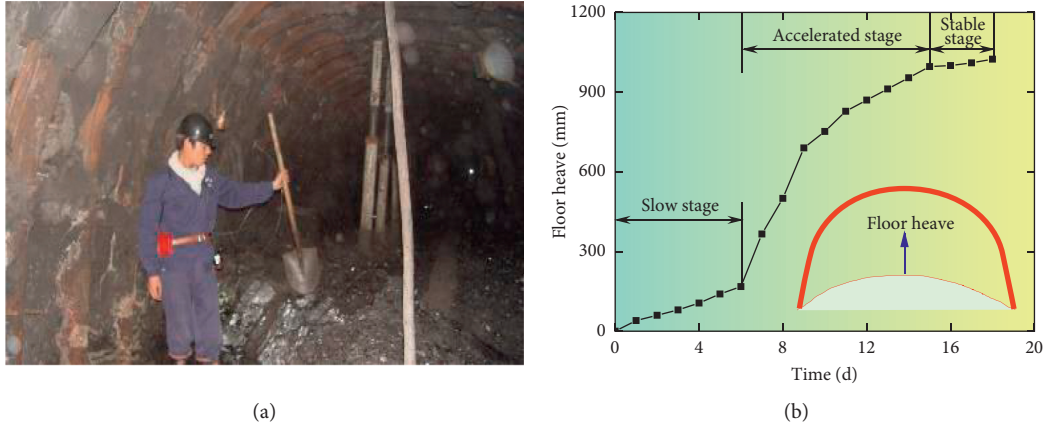


FIGURE 7: Roadway floor heave. (a) Floor heave; (b) floor deformation.

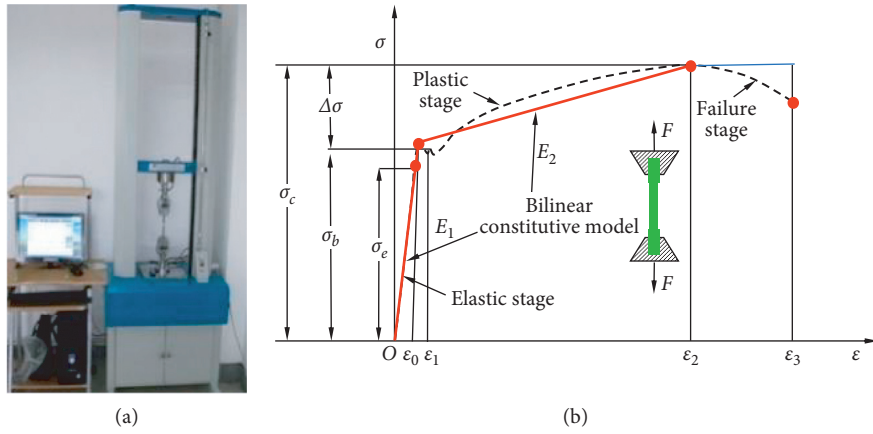


FIGURE 8: Pull-out test. (a) The synthetic material tensile testing machine; (b) the stress-strain curve.

TABLE 1: Main parameters of the U-shaped steel support.

Type	Material	Elastic modulus E_1 (GPa)	Poisson ratio μ	Tangent modulus E_2 (GPa)	Yield strength σ_s (MPa)	Tensile strength σ_b (MPa)
25U	25MnK	206	0.3	21	335	530
29U	25MnK	206	0.3	21	335	530
36U	20MnK	210	0.3	19	350	530
40U	20MnVK	215	0.3	20	390	580

format and imported into the solver. Finally, the U-shaped steel support contour along the axial direction was constructed.

- (2) The selection of the element type: the U-shaped steel support with shed is composed of a straight beam and a curved beam. Therefore, the straight beam element CBEAM and the curved beam element CBEAN were used in the numerical model. The former one required the neutral axis to coincide with the shear center and did not consider the effects of warping on the torsional stiffness as well as the influence of transverse shear [26]. The curved beam did not require the neutral axis to coincide with the shear center, and it also considered the impacts of warping

on the torsional stiffness as well as the influence of transverse shear.

- (3) The constitutive model of materials: based on the stress-strain curve of the pull-out test of the U-shaped steel support metal materials, the bilinear isotropic hardening elastic-plastic material model was selected. Table 1 shows the concrete parameters [28, 29].
- (4) The boundary conditions: the constraint was simply supported at both ends [30–33]. According to the measured results of the roadway stress field obtained in Section 2.3, three types of the corresponding loads were applied on the axis of the U-shaped steel support. The above four steps were used to establish

the U-shaped steel support numerical model, as shown in Figure 9.

3.2. The Deformation and Failure Characteristics. The deformation and failure characteristics of the U-shaped steel support at $P1$, $P2$, and $P3$ observation stations were extracted and compared with field measurement, as shown in Figures 10(a)–10(c), respectively.

It could be obtained that

- (1) The U-shaped steel support presented various deformation and failure characteristics under different stress states.
- (2) As shown in Figure 10(a), the stresses on the two ribs of the roadway were greatly larger than the vertical stresses, which leads to the two sides of the U-shaped steel support being obviously moved inward at $P1$ observation station. The maximum Mises stress was 440 MPa at the leg of the shed. It was beyond the limit of the material and caused bending and failure.
- (3) As shown in Figure 10(b), the vertical stresses on the top of the U-shaped steel shed were significantly larger than those on two legs, and obvious subsidence could be found on top of the U-shaped steel support at $P2$ observation station, 500 m away from the cut-open. The maximum Mises stress was 463 MPa at the top.
- (4) As shown in Figure 10(c), the stresses on the right side of U-shaped steel shed were obviously larger than those on the left side, and the U-shaped steel support inclined to the left. The maximum Mises stress was 650 MPa at the right side of the shed leg and caused bedding.

The analyses indicated that the arch roadway had poor adaptability under uneven and complex stress environment, and the stresses acted on the support by the surrounding rock exceeded its bearing capacity.

4. Optimization and Design of Soft-Rock Roadway Support under Complex Stress Field

As analyzed and discussed above, it is the precise factors such as the roadway being deep-buried, the surrounding rocks being weak and easy to expand and undergo weathering, the floor control not being included in the support system, the support structure not being able to fully mobilize the self-supporting capacity of surrounding rocks, the roadway section being unreasonable, etc., that finally cause the complex surrounding rock stress and the serious roadway deformation and failure.

In order to overcome the support difficulty of a deep-buried soft-rock roadway, the floor heave control must be incorporated into the support system [34]. However, as previously discussed, in the initial open support system, the roadway was constructed with an arch section and the floor reinforcement and control was ignored, so the self-supporting capacity of surrounding rocks failed to be effectively

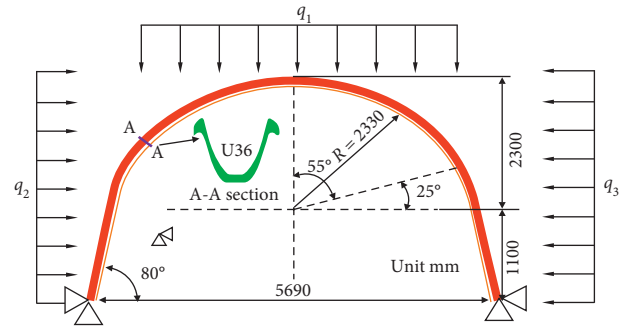


FIGURE 9: The numerical model of the arched U-shaped steel support.

manipulated and the support performance of the U-shaped steel could not be fully developed as analyzed in Section 3. Even if floor bolts were added later, the floor heave was still out of control.

Thus, aimed at overcoming the aforementioned support defects, which make the original supporting system unable to adapt to the deformation and failure characteristics of the deep-buried soft-rock roadway, it is critical to select an appropriate roadway section and improve the supporting system. According to the experience from the existing roadway support in Xiaokang Coal Mine, it is more reasonable for the roadway section to select circle than arch and ellipse. In order to reduce the actions of the surrounding rock on the support, the section size should be reduced as much as possible. To meet the minimum requirements of transportation and ventilation, the roadway section was designed with a diameter of 4.6 m and a net area of 13.9 m².

Furthermore, matching with the redesigned circular roadway section, a new full-section combined support scheme of “belt-mesh-cable-shotcrete + U-shaped steel and wall back filling” was suggested, in which the positive support of the “belt-mesh-cable” could improve the self-supporting ability of the surrounding rock, and the passive and rigid support of the “U-shaped steel and wall back filling” not only allows the roadway deformation in control to relieve the surrounding rock pressure, but also effectively resists excessive deformation to ensure that the roadway can be normally used. In this way, the new support system was expected to control the displacement and failure of such deep-buried soft-rock roadway.

4.1. Parameters of the U-Shaped Steel Support. To verify the bearing capacity of the U36 support with the diameter of 4.6 m under a complex stress field environment, the numerical simulation of the circular section U-shaped steel support was constructed. The in situ stress values obtained in Section 2.3 were applied.

As shown in Figure 11, when the circular section support was dominated by horizontal stress, vertical stress, and right horizontal stress, the corresponding deformation amounts were 465 mm, 636 mm, and 763 mm, respectively, and the maximum Mises stresses were 293 MPa, 312 MPa, and 342 MPa, respectively. It implied that the circular U-shaped

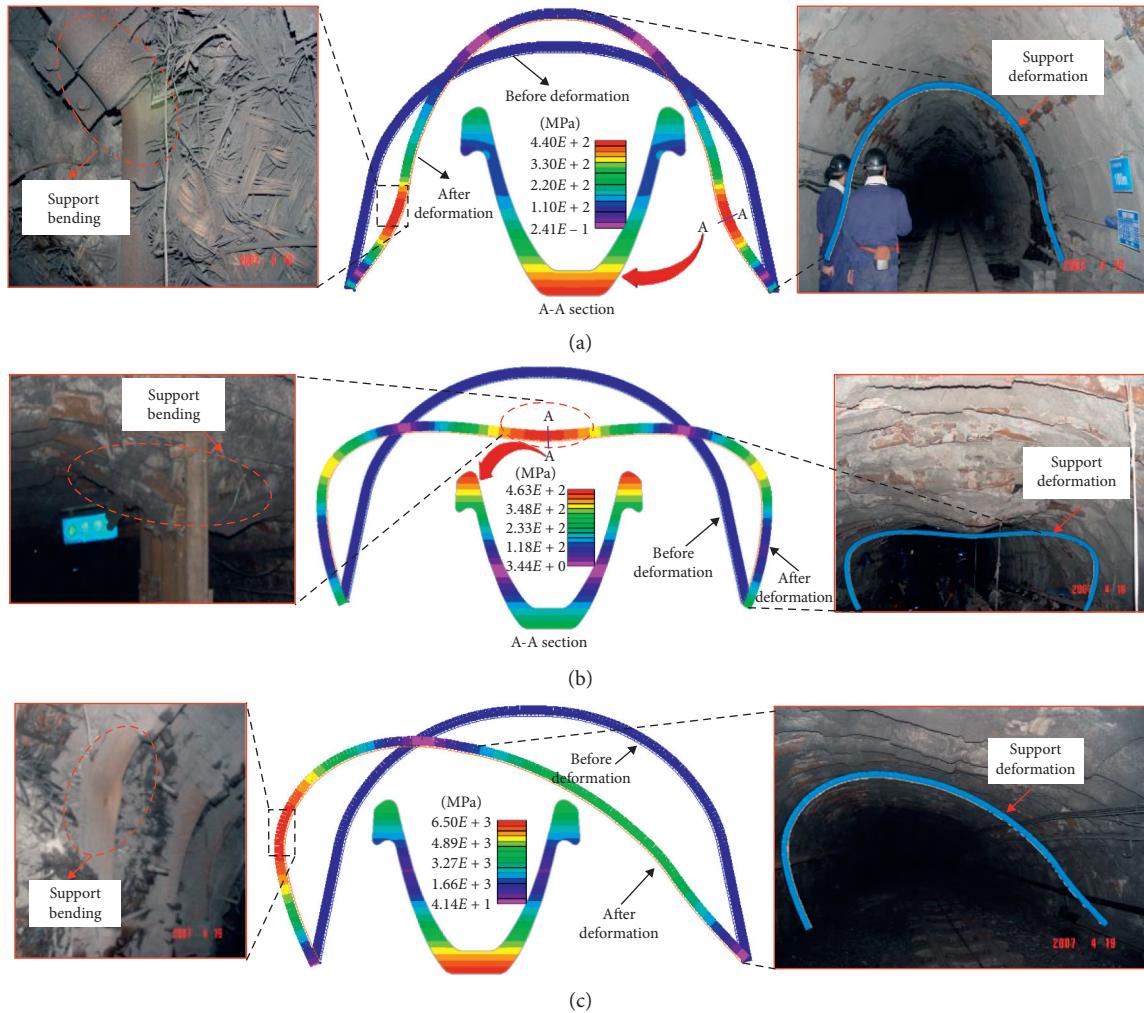


FIGURE 10: The deformation and failure characteristics of the U-shaped steel support. (a) At P1 observation station, 50 m; (b) at P2 observation station, 500 m; (c) at P3 observation station, 1000 m.

steel support had high ability to resist deformation, and the roadway deformation was well controlled to a certain degree.

4.2. The Filling behind the Support. During the process of construction, it is inevitable to leave a certain space between the U-shaped steel shed and the surrounding rock. Therefore, at the beginning, the shed almost has no support effect on the roadway, and its supporting resistance could not exert timely, resulting in the roadway deformation. Then, the surrounding rock will contact the U-shaped steel shed unevenly, leading the support to suffer extremely complex stress, which is manifested as the uneven distribution of the U-shaped steel support load around the roadway and along the axial direction of the roadway. This is the main cause of bending, torsional deformation, and bearing capacity loss of the shed. However, the filling behind the shed support could eliminate such space, make the shed support and the surrounding rock come in close contact and make the shed suffer uniform load, so as to give full play to the supporting performance of the U-shaped steel shed.

The characteristics of the filling materials are as follows:

- (1) The curing time of the filling materials should be short and the intensity should increase rapidly. That is, the filling materials should have certain early and later intensity.
- (2) The filling materials should have certain compressibility. In the case of the surrounding rock deformation, the filling material could produce yielding effects.
- (3) After curing, the filling materials should not undergo volume shrinkage, and they should have slight expansion.
- (4) The filling materials should have abundant sources of raw materials, and also should be low-cost, easy to transport, and easy to construct underground.
- (5) The filling materials should have favorable processing properties such as pumpability and timely support.

According to the above requirements and based on the existing engineering experience, the mixing proportions of the filling materials were given as follows:

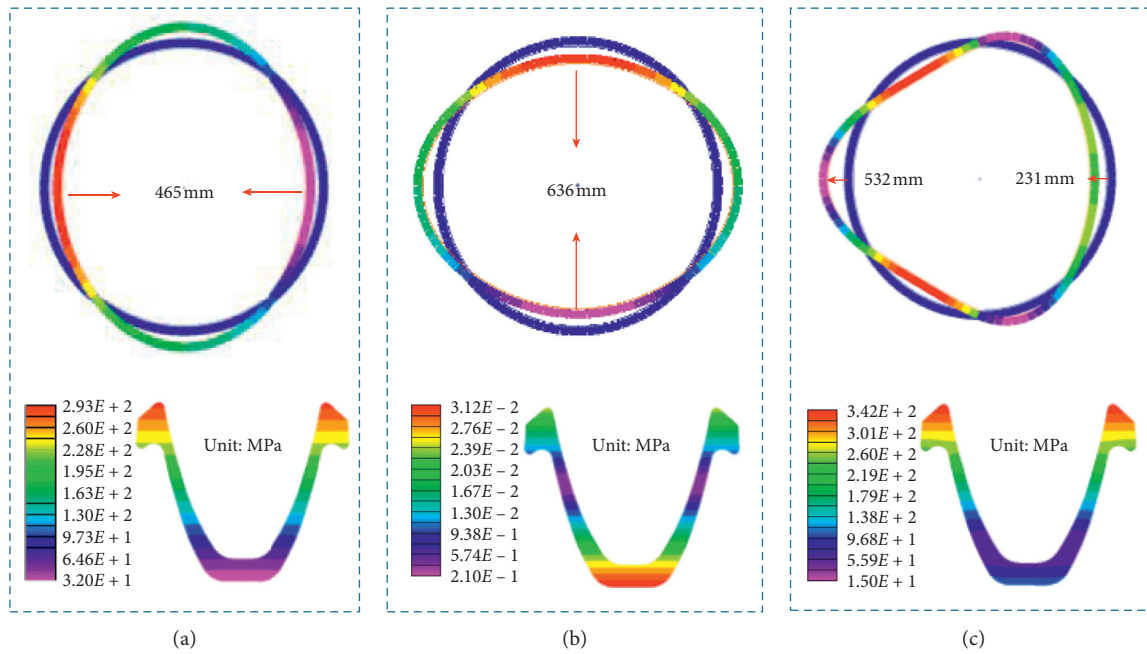


FIGURE 11: The deformation and failure laws of the circular section U-shaped steel support. (a) Horizontal stress, (b) vertical stress, and (c) horizontal unbalance loading.

- (1) The raw materials of back wall filling consisted of cement, gypsum, coal ash, and plasticizer. The 425# ordinary Portland cement and dihydrate gypsum were used [35–37]. The coal ash was the high-quality fly ash discharged from power plants.
- (2) According to multiple trial ratios and on-site engineering experience, the cement-gypsum-coal ash ratio was 1 : 1 : 3. The water-cement ratio was 0.4. The admixture dosages accounted for 2% of the cement weight [38].

4.3. Parameters of Anchor Bolt and Cable. Another key to control the surrounding rock is to select the parameters of the anchor bolt and cable appropriately. Scholars have put forward many theories, such as the suspension theory and loose circle theory. These theories are useful to determine these parameters. In recent years, the prestress theory [39, 40] has been proposed, which suggests that a complete compressive stress layer within the surrounding rock of the roadway should be formed under the action of prestressed anchor bolt and prestressed anchor cable. The prestress theory has been generally accepted and has been widely used in industrial practice to provide basis for the determination of the anchor bolt and cable parameters.

According to the theory, without considering the original rock stress, if there exists a near-zero compressive stress layer within the supporting area of the anchor cable and bolt, it means that the bolt and cable fail to reinforce the surrounding rock in this area. If the compressive stress zones generated by different bolts and cables are isolated from each other, and a continuous ring of compressive stress is not formed, it means that the integral support effect of bolts and

cables has not fully played [41–43]. Therefore, reasonable and effective bolt-cable support should generate as high compressive stress as possible within their support range, eliminate as much as possible the area of near-zero compressive stress, and make the area of compressive stress contiguous to form as large as possible the scale of compressive stress circle layer.

Thus, in order to clearly reflect the stress field generated by the prestressed anchor bolt and cable in the surrounding rock, the supporting effect is simulated numerically without considering the original rock stress, and the alternative support parameters are considered as shown in Figure 12: bolts with different spaces of 1200 mm, 1000 mm, and 800 mm, lengths of 1.8 m, 2.2 m, and 2.4 m, and pretightening forces of 40 kN, 60 kN, and 100 kN, and cables with different lengths of 5.3 m, 6.3 m, and 7.3 m and pretightening force of 60 kN, 105 kN, and 150 kN. In addition, the simulation scheme is listed in Table 2.

As shown in Figure 12(a), under the pretightening force of 100 kN and the length of 2.4 m, with the decrease in the bolt support space from 1200 mm to 800 mm, the compressive stress in the surrounding rock increases continuously, and the isolated compressive stress area begins to form a continuous compressive stress circle layer, and its range is obviously expanded outward. When the bolt spacing is 800 mm, the continuous compressive stress circle layer has formed in the whole length of the bolt, and there is basically no near-zero compressive stress area and isolated compressive stress area. That is, the space of 800 mm is better than 1000 mm and 1200 mm.

As shown in Figures 12(b) and 12(d), for both the anchor bolt and the cable, the increase in the pretightening force has a significant control effect on the magnitude of compressive

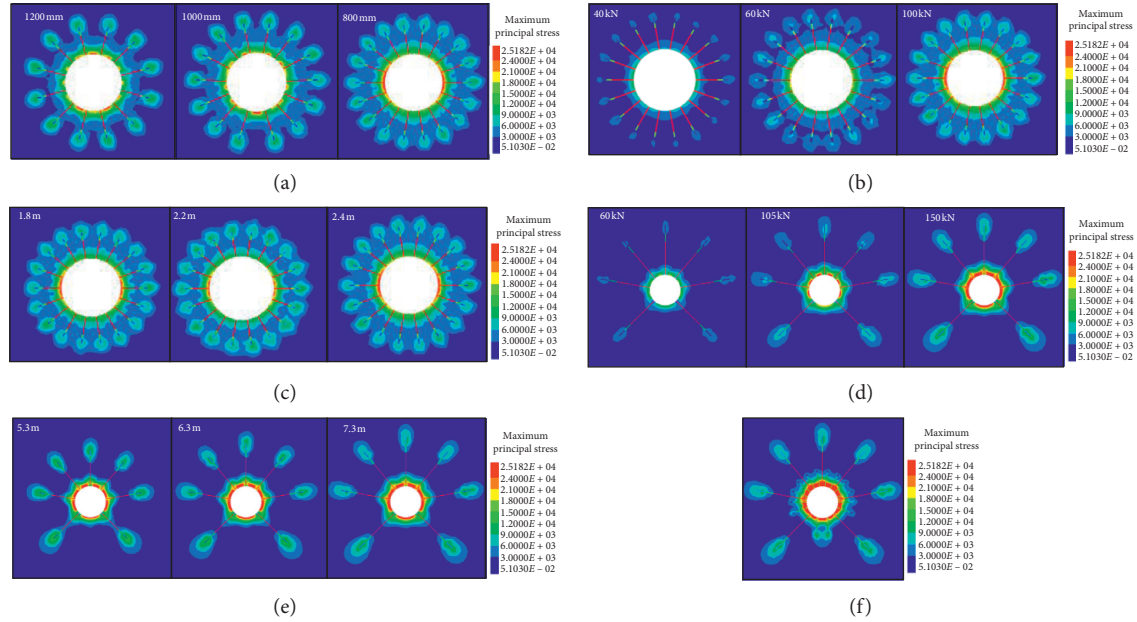


FIGURE 12: Parameter optimization of the anchor bolt and cable. (a) The space of the anchor bolt; (b) the pretightening force of the anchor bolt; (c) the length of the anchor bolt; (d) the pretightening force of the anchor cable; (e) the length of the anchor cable; (f) matching of bolts and cables.

TABLE 2: Simulation scheme for parameter optimization of the anchor bolt and cable.

Support type	Plans in Figure 12	Parameters		
		Space (mm)	Pretightening force (kN)	Length (mm)
Anchor bolt	(a)	1200, 1000, 800	100	2.4
	(b)	800	40, 60, 100	2.4
	(c)	800	100	1.8, 2.2, 2.4
Anchor cable	(d)	—	60, 105, 150	7.3
	(e)	—	150	5.3, 6.3, 7.3

stress and the range of a continuous compressive stress layer, so it is more appropriate to choose a higher pretightening force.

As shown in Figures 12(c) and 12(e), under the same pretightening force and support space, the length of the anchor bolt and cable has no significant effect on the improvement of the support effect. However, considering the complex geological conditions of soft rock and the existing support experience in this mine, it is suggested to choose the 2.4 m anchor bolt and 7.3 m anchor cable which have larger support range and higher safety coefficient.

According to the above simulation and analysis, the final support scheme is formed, that is, the anchor bolt with a length of 2.4 m, an interval of $0.8\text{ m} \times 0.8\text{ m}$, and a pretightening force of 100 kN, and the anchor cable with a length of 7.3 m, a pretightening force of 150 kN, an interval of $1.6\text{ m} \times 1.6\text{ m}$, and a density of 7. The combined supporting effect of the anchor bolt and the cable is shown in Figure 12(f), and a complete compressive stress layer was formed around the roadway.

5. Engineering Application

5.1. The Scheme. First, instead of blasting, the road header was used to cut the roadway profile, which could reduce the impact of driving activities. Then, the anchor bolt and cable were applied. The diamond wire mesh was arranged on the roadway surface, and the U-shaped steel support shed was set. Finally, the filling behind the support was applied. The specific support parameters are shown in Figure 13.

U-shaped steel support: the diameter of the roadway section was 4.6 m. 5 sets of U-shaped screw type connectors were set at each lap section. A set of strong draw plates was applied in the middle of the U-shaped steel to enhance the whole supporting capacity. The central angle of the round vault was 90° . To make the support have better bearing capacity and yieldable performance, the curvature radius R_1 of the vault should meet $N = R_2/R_1$. The curvature radius of the lateral arch was R_2 . Therefore, when $N = 1.0$, the support had the best bearing capacity, and the space between two sheds was 800 mm.

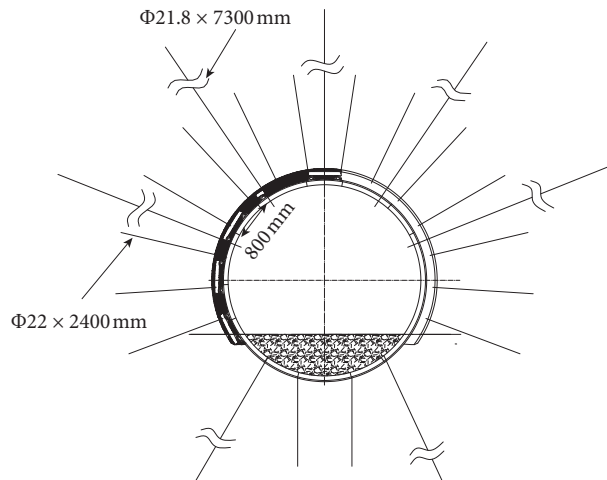


FIGURE 13: The scheme of the roadway support.

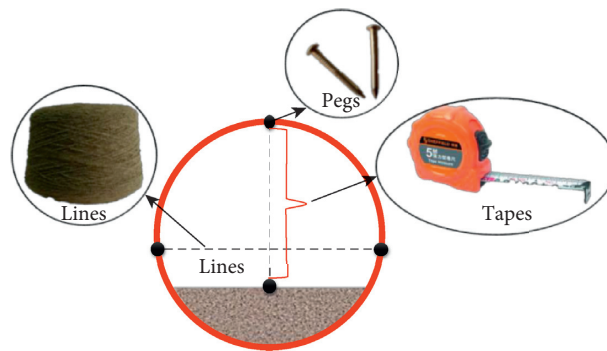


FIGURE 14: The monitoring scheme.

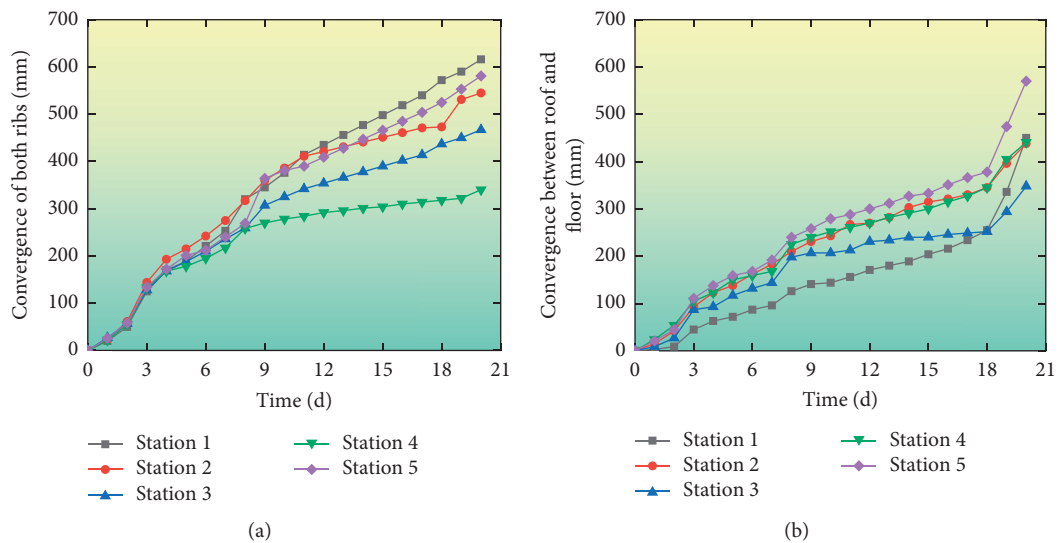


FIGURE 15: The roadway deformation under new support scheme. (a) Rib-to-rib convergence; (b) roof-to-floor convergence.

Anchor bolt: the left-hand threaded steel bolt without longitudinal reinforcement was used for the anchor bolt. The yield strength was 600 MPa and the tensile

strength was 800 MPa. The bolt had a diameter of 22 mm and a length of 2.4 m. The interval of the bolt was 0.8 m × 0.8 m. The resin full-column anchorage was

used, and the pretightening force of the bolt was 100 kN. The high-intensity tray was used with the size of 130 mm × 130 mm × 10 mm.

Anchor cable: the anchor cable had a diameter of 21.8 mm and a length of 7.3 m. The pretightening force of the anchor cable was 150 kN. A total of 7 cables were adopted. The high-intensity tray was used with the size of 300 mm × 300 mm × 16 mm.

Shotcrete and filling behind the support: the first spraying thickness is 50 mm, and the second spraying thickness is 100 mm.

Other supports: the W-type steel band had a thickness of 4 mm and a width of 250 mm. The self-made 10# diamond metal net with a mesh spacing of 40 mm × 40 mm was installed to protect the roof.

5.2. The Monitoring Scheme of the Roadway. In order to verify that the proposed new support method could effectively control the deformation and failure of the mining roadway with soft rocks under complex geological conditions, the roadway of the replacement workface of S2S2 FMCF in Xiaokang Coal Mine was taken as the example. 5 observation stations were distributed evenly in the roadway to monitor the surface displacement of the soft-rock roadway under the mining influence. The crossing method was also applied to monitor the rib-to-rib convergence and the roof-to-floor convergence. Figure 14 shows the specific monitoring method.

5.3. The Roadway Deformation Monitoring. The support quality of the roadway was judged by comparing the monitoring data with those of the original data. The underground roadway deformation was monitored continuously, and the rib-to-rib convergence and roof-to-floor convergence were monitored and given every other day, as shown in Figure 15.

Figure 15 indicates that

- (1) Within 20 days of roadway monitoring, the rib-to-rib convergence was 616 mm, 545 mm, 467 mm, 340 mm, and 581 mm from No. 1 to No. 5 observation points, respectively. That of original support scheme was 2182.5 mm. Therefore, the deformation of the ribs was effectively controlled.
- (2) Within 20 days of roadway monitoring, the roof-to-floor convergence was 450 mm, 438 mm, 348 mm, 441 mm, and 570 mm from No. 1 to No. 5 observation points, respectively. Compared with the original support scheme with a roof separation of 1029 mm and a floor heave of 1044.8 mm, the roadway roof and floor deformations were well controlled.

The obtained roadway deformation laws verify that the new support scheme could effectively control the surrounding rock deformation.

6. Conclusions

Based on the on-site monitoring and numerical simulation of the original roadway support effect, the U-shaped steel support, the anchor cable, and the bolt were optimized and verified, a new full-section combined support system of “belt-cable-mesh-shotcrete and U-shaped steel-filling behind the support” was proposed, and the support effects were simulated and in situ measured. The main conclusions are as follows:

- (1) The roadway in the S2S2 working face underwent serious deformation and damage with a rib-to-rib convergence of 2183 mm, a roof separation of 1029 mm, and a floor heave of 1045 mm. In addition, it was the overload pressure that caused the failure of the U-shaped steel support.

The in situ measurement and simulation results indicated that it was the unreasonable roadway section and the failure control of the floor heave that weakened the self-supporting capacity of the surrounding rock, caused the complex surrounding rock stress, and finally resulted in the failure of the initial soft-rock roadway support.

- (2) For optimization, the roadway section in the replacement FMCF was changed from arch to circle and a new full-section combined support scheme of “belt-cable-mesh-shotcrete and U-shaped steel-filling behind the support” was proposed.

The redesigned U-shaped steel support was verified by simulation and it exhibited high adaptability to different types of surrounding rock stress, and the roadway deformation could be effectively controlled within 770 mm. The support parameters of the belt and cable were determined by simulation with the pretightening theory.

- (3) The optimized full-section combined support scheme was practiced and applied in the roadway of the replacement FMCF. In addition, the in situ measured rib-to-rib convergence and roof-to-floor convergence were both controlled within 600 mm, i.e., the roadway deformation and failure were controlled effectively.

Data Availability

The data used to support the findings of this study are included within the article.

Conflicts of Interest

The authors declare that they have no conflicts of interest.

Acknowledgments

This work was supported by the Fundamental Research Funds for the Central Universities (2017BSCXB50) and Postgraduate Research & Practice Innovation Program of

Jiangsu Province (KYCX17_1528). The authors gratefully acknowledge the financial support from the organization.

References

- [1] J. P. Bennett, B. W. Riggs, K. S. Kwong, and J. Nakano, "Mechanisms of Wear Reduction in High Chrome Oxide Refractories Containing Phosphate Additions Exposed to Coal Slag," John Wiley & Sons, Ltd., Hoboken, NJ, USA, 2014.
- [2] S. Bhaskaran, A. Ganesh, S. Mahajani, P. Aghalayam, R. K. Sapru, and D. K. Mathur, "Comparison between two types of Indian coals for the feasibility of underground coal gasification through laboratory scale experiments," *Fuel*, vol. 113, pp. 837–843, 2013.
- [3] D. Ma, H. Duan, X. Li, Z. Li, Z. Zhou, and T. Li, "Effects of seepage-induced erosion on nonlinear hydraulic properties of broken red sandstones," *Tunnelling and Underground Space Technology*, vol. 91, Article ID 102993, 2019.
- [4] C. H. An, G. B. Zhang, Z. D. Liu, K. Zhao, W. Guo, and H. L. Liu, "Deformation failure analysis and stability control technology of large section soft rock chamber in deep coal mine," *Applied Mechanics and Materials*, vol. 353-356, pp. 1035–1039, 2013.
- [5] N. Zhang, J. B. Bai, J. Y. Zhou, X. M. Cheng, Z. L. Zhu, and L. C. Chang, "Strata control technology by grouting in soft rock roadway," *Rock Mechanics Symposium*, vol. 5, 2001.
- [6] D. Ma, H. Duan, J. Liu, X. Li, and Z. Zhou, "The role of gangue on the mitigation of mining-induced hazards and environmental pollution: an experimental investigation," *The Science of the Total Environment*, vol. 664, no. 10, pp. 436–448, 2019.
- [7] H. A. Lazemi, M. Fatehi Marji, A. R. Yarahmadi Bafghi, and K. Goshtasbi, "Rock failure analysis of the broken zone around a circular opening/analiza pęknięcia skały w strefie naruszonej wokół otworu kolistego," *Archives of Mining Sciences*, vol. 58, no. 1, pp. 165–188, 2013.
- [8] C. O. Aksoy, M. Geniş, G. Uyar Aldaş, V. Özacar, S. C. Özer, and Ö. Yilmaz, "A comparative study of the determination of rock mass deformation modulus by using different empirical approaches," *Engineering Geology*, vol. 131-132, pp. 19–28, 2012.
- [9] P. Hamdi, D. Stead, and D. Elmo, "Characterizing the influence of stress-induced microcracks on the laboratory strength and fracture development in brittle rocks using a finite-discrete element method-micro discrete fracture network FDEM- μ DFN approach," *Journal of Rock Mechanics and Geotechnical Engineering*, vol. 7, no. 6, pp. 609–625, 2015.
- [10] D. H. Wu, W. G. Qiao, W. J. Song, and P. Vladimir, "Research on secondary support time of soft rock roadway," *Journal of China Coal Society*, vol. 40, pp. 5–10, 2016.
- [11] J. L. Zhao, P. Song, B. Z. Liu, K. Tian, and L. R. Liu, "Study on stagger arrangement roadway layout under the condition of high stress soft rock in the medium-thickness coal seam," in *Proceedings of the International Conference on New Energy and Renewable Resources (ICNERR)*, Guangzhou, China, 2015.
- [12] D. Ma, J. Zhang, H. Duan et al., "Reutilization of gangue wastes in underground backfilling mining: overburden aquifer protection," *Chemosphere*, vol. 264, no. 1, Article ID 128400, 2021.
- [13] M. C. He, H. H. Jing, and X. M. Sun, *Engineering Mechanics of Soft Rock*, Science Press, Beijing, China, 2002.
- [14] H. P. Kang and J. H. Wang, *Rock Bolting Theory and Complete Technology for Coal Roadways*, China Coal Industry Publishing House, Beijing, China, 2007.
- [15] Y. F. Gao, B. Wang, J. Wang et al., "Test on structural property and application of concrete-filled steel tube support of deep mine and soft rock roadway," *Chinese Journal of Rock Mechanics and Engineering*, vol. 29, no. s1, pp. 2604–2609, 2010.
- [16] Y. D. Jiang, Y. X. Zhao, W. G. Liu, and Q. Li, "Research on floor heave of roadway in deep mining," *Chinese Journal of Rock Mechanics and Engineering*, vol. 23, no. 14, pp. 2396–2401, 2004.
- [17] S.-Q. Yang, M. Chen, H.-W. Jing, K.-F. Chen, and B. Meng, "A case study on large deformation failure mechanism of deep soft rock roadway in xin'An coal mine, China," *Engineering Geology*, vol. 217, pp. 89–101, 2017.
- [18] B. Shen, "Coal mine roadway stability in soft rock: a case study," *Rock Mechanics and Rock Engineering*, vol. 47, no. 6, pp. 2225–2238, 2014.
- [19] H. P. Kang, J. Lin, and M. J. Fan, "Investigation on support pattern of a coal mine roadway within soft rocks - a case study," *International Journal of Coal Geology*, vol. 140, pp. 31–40, 2015.
- [20] L. G. Wang, H. L. Li, and J. Zhang, "Numerical simulation of creep characteristics of soft roadway with bolt-grouting support," *Journal of Central South University of Technology*, vol. 15, no. 1, pp. 391–396, 2008.
- [21] H. J. Zhang, H. Y. Li, S. C. Li, J. W. Bai, T. Y. Hao, and H. W. Li, "Deformation mechanism of surrounding rock and support technology in deep soft rock roadway," *Journal of Mining and Safety Engineering*, vol. 32, no. 6, pp. 955–962, 2015.
- [22] P. Song, J. L. Zhao, and T. Xue, "Studying the reasonable roadway layout under the condition of high stress soft rock," in *Proceedings of the 5th International Conference on Advanced Design and Manufacturing Engineering*, pp. 1482–1485, Atlantis Press, Shenzhen, China, September 2015..
- [23] Y. Huang, J. Li, D. Ma, H. Gao, Y. Guo, and S. Ouyang, "Triaxial compression behaviour of gangue solid wastes under effects of particle size and confining pressure," *The Science of the Total Environment*, vol. 693, Article ID 133607, 2019.
- [24] C. Lu, C. Zang, F. Yu, and X. Yu, "Optimization on gateway section of soft coal seam and hard roof and supporting technology," *Applied Mechanics and Materials*, vol. 90-93, pp. 622–625, 2011.
- [25] H. Bei, Y. Z. Xia, R. I. Barabash, and Y. F. Gao, "A tale of two mechanisms: strain-softening versus strain-hardening in single crystals under small stressed volumes," *Scripta Materialia*, vol. 110, pp. 48–52, 2016.
- [26] F. Tonon, "ADECO full-face tunnel excavation of two 260m² tubes in clays with sub-horizontal jet-grouting under minimal urban cover," *Tunnelling and Underground Space Technology*, vol. 26, no. 2, pp. 253–266, 2011.
- [27] D. Ma, H. Duan, W. Liu, X. Ma, and M. Tao, "Water-sediment two-phase flow inrush hazard in rock fractures of overburden strata during coal mining," *Mine Water and the Environment*, vol. 39, no. 2, pp. 308–319, 2020.
- [28] S. H. Yang and S. Y. Wang, "Application of coupling support in soft rock mining roadway," *Journal of Coal Technology*, vol. 27, no. 5, pp. 53–56, 2008.
- [29] H. Yan, J.-x. Zhang, L.-y. Li, and R.-m. Feng, "Stability assessment of rock surrounding an I-beam supported retreating roadway," *Journal of Central South University*, vol. 22, no. 9, pp. 3598–3607, 2015.
- [30] Y. Tai, X. Han, P. Huang, and B. F. An, "The mining pressure in mixed workface using a gangue backfilling and caving method," *Journal of Geophysics and Engineering*, vol. 16, no. 1, pp. 1–15, 2019.

- [31] Y. Tai, S. Guo, and B. F. An, "The influence of gangue particle size and gangue feeding rate on the dynamic response of suspended buffer and engineering application," *Journal of Geophysics and Engineering*, vol. 16, no. 2, pp. 275–288, 2019.
- [32] D. Ma, H. Y. Duan, Q. Zhang et al., "A numerical gas fracturing model of coupled thermal, flowing and mechanical effects," *Computers, Materials & Continua*, vol. 65, no. 3, pp. 2123–2141, 2020.
- [33] D. Ma, J. J. Wang, X. Cai et al., "Effects of height/diameter ratio on failure and damage properties of granite under coupled bending and splitting deformation," *Engineering Fracture Mechanics*, vol. 220, Article ID 106640, 2019.
- [34] Y. Tai, F. Ju, and X. L. Han, "Investigation of the kinetic energy transformation pattern of gangue particles in a buffer system," *Powder Technology*, vol. 344, pp. 926–936, 2019.
- [35] Y. Tai, S. Guo, B. F. An, and F. Ju, "Analysis of the nonlinear dynamic response of guide rails for a suspended buffer," *PLoS One*, vol. 14, Article ID e210185, 2019.
- [36] F. S. Zhang, X. Y. Xie, and H. W. Huang, "Application of ground penetrating radar in grouting evaluation for shield tunnel construction," *Tunnelling and Underground Space Technology*, vol. 25, no. 2, pp. 99–107, 2010.
- [37] S. Swedenborg and L. O. Dahlström, "Rock mechanics effects of cement grouting in hard rock masses," in *Proceedings of the 3rd International Conference: Grouting and Ground Treatment*, pp. 1089–1102, New Orleans, Louisiana, February 2003.
- [38] D. J. Pan, N. Zhang, C. H. Zhang, D. Qian, C. L. Han, and S. Yang, "Long-term mechanical behavior of nano silica sol grouting," *Nanomaterials*, vol. 8, no. 1, 2018.
- [39] Y. G. Hu, R. Li, X. X. Wu, G. Zhao, and Q. L. Zhang, "Blasting damage depth in layered jointed basalt before and after grouting," *Journal of Geotechnical and Geoenvironmental Engineering*, vol. 145, no. 3, Article ID 4018113, 2019.
- [40] H. S. Tu, S. H. Tu, C. Wang, D. Y. Hao, and D. F. Zhu, "Mechanical analysis of a vertical-wall, semicircular-arch roadway and a repair technique using double-shell support," *Environmental Earth Sciences*, vol. 77, no. 13, 509 pages, 2018.
- [41] H. P. Kang, T. M. Jiang, and F. Q. Gao, "Effect of pre-tensioned stress to rock bolting," *Journal of China Coal Society*, vol. 32, no. 7, pp. 680–685, 2007.
- [42] H. P. Kang, T. M. Jiang, and F. Q. Gao, "Design for pre-tensioned rock bolting parameters," *Journal of China Coal Society*, vol. 33, no. 7, pp. 721–726, 2008.
- [43] J. Z. Li, H. P. Kang, F. Q. Gao, and J. F. Lou, "Analysis of bolt support stress field and bolt support effect under in-situ stress field," *Journal of China Coal Society*, vol. 45, no. s1, pp. 99–109, 2020.

Research Article

Width Design of Small Coal Pillar of Gob-Side Entry Driving in Soft Rock Working Face and Its Application of Zaoquan Coal Mine

Ai Chen ^{1,2}

¹School of Energy and Mining Engineering, Shandong University of Science and Technology, Qingdao 266590, China

²Ningxia Coal Industry Co., Ltd., of China Energy Group, Yinchuan 750000, China

Correspondence should be addressed to Ai Chen; aichenm@163.com

Received 12 April 2021; Revised 25 May 2021; Accepted 21 June 2021; Published 3 July 2021

Academic Editor: Jia Lin

Copyright © 2021 Ai Chen. This is an open access article distributed under the Creative Commons Attribution License, which permits unrestricted use, distribution, and reproduction in any medium, provided the original work is properly cited.

Reasonable width of gob-side coal pillar can reduce the waste of coal resources and is conducive to roadway stability. According to the distribution of internal and external stress fields at the working face, a method for determining the width of gob-side coal pillar was proposed. The coal pillar and roadway should be set within the internal stress field, and support is provided through the anchored part and the intact part of the coal pillar. The method was used in the design of the coal pillar at No. 130205 working face of Zaoquan Coal Mine. The calculation results indicated that the width of a coal pillar suitable for gob-side entry is 6.0 m. It is reasonable to arrange the roadway and coal pillar in the low-stress zone with a width of 11 m. During tunnelling of roadway and stoping of the working face, the deformation of the roadway increased with a reduction in the distance from the working face. Even during stoping of the working face, there was an approximately 1.5 m intact zone in the coal pillar. This indicates that the proposed method of designing small coal pillar of gob-side entry driving is reliable.

1. Introduction

With the continuous improvement of coal mining methods and the enhancement of the mechanical equipment level, fully mechanised caving has become an important mining method for thick coal seam [1–3]. It can achieve high-yield and high-efficiency mining of thick coal seams, but roadways in mining area face challenges of surrounding rock control, for example, the large cross section, strong mining influence, and soft and thick coal roof and floor [4–7]. Over the past few years, China has called for the construction of resource-saving mines [8]. Fully mechanised caving mining projects involving large-cross section roadway driving along goafs under narrow coal pillar conditions have become increasingly common, and the difficulty in controlling the stability of the surrounding rocks in these projects has increased.

A key issue in the fully mechanised caving of small coal pillars is the design of a reasonable width. A reasonable coal pillar width can not only reduce the deformation of the coal pillar and the maintenance costs, but also maximise the

recovery of coal resources [9–11]. A century ago in the United States, the design of coal pillar dimensions depended heavily on intuition or established rules of thumb [12]. However, currently, various coal pillar design guidelines have been developed on the basis of indoor tests and theoretical analyses [13–16]. Sheorey et al. [13] analysed 23 cases of pillar instability and 20 cases of safe and stable pillars and proposed a new pillar strength equation for practical values of the width-to-height ratio. Aiming at the defect of traditional coal pillar safety evaluation method which regards safety factor as fixed value, Najafi et al. [14] proposed a coal pillar stability evaluation method which regards safety factor as probability function. He et al. [15] studied the correlation between the gob-side entry (GSE) stability and coal pillar width during longwall top-coal caving mining in extra-thick coal seams and found that the GSE with an 8 m coal pillar was distressed and minimal GSE deformation occurs. Fan et al. [16] calculated the range of the internal stress field from the perspective of the stress distribution in the surrounding rock, thereby determining the width of coal pillars and validating them onsite.

In addition, with the advancement of field measurement and numerical simulation techniques, they have been increasingly applied to coal pillar design [17–24]. Focusing on the potential variation in strength due to the strength properties of the surrounding rock, Gale [17] proposed a design method for coal pillar arrangement. Jaiswal and Shrivastva [18] proposed a method for establishing the strain-softening constitutive relation of coal via calibration of a numerical model, and they determined the most appropriate strain-softening parameters and hence identified a reasonable coal pillar width. Esterhuizen et al. [19] calibrated the numerical model of coal pillar strength using FLAC3D according to triaxial test data of coal samples together with the failure depth and peak resistance of the coal pillar. Wu et al. [20] studied the initiation, propagation, and failure of cracks within a 7 m gob-side coal pillar during its formation and suggest that the most appropriate pillar width is 10 m in the Sijiazhuang Coal Mine in China.

In the foregoing studies, the width of the coal pillar was designed to maintain stability only under specific stress conditions. However, the design of the coal pillar is related to not only its own bearing capacity but also the stress environment in which it is located. When the coal pillar is designed to be in a high-stress area, its bearing capacity must be high, that is, a large width. Conversely, a coal pillar in a low-stress area must have a low bearing capacity and small width [25]. This study focused on soft rock roadway driving along the goaf of Zaoquan Coal Mine. A design method for the width of the coal pillar along the goaf was developed by combining the position of the chain pillar (stress conditions) and the bearing capacity of the coal pillar. The method was applied to Zaoquan Coal Mine.

2. Study Area

2.1. Geological Overview. Zaoquan Coal Mine is located at the edge of the Mu Us Desert, southeast of Lingwu City in Ningxia in northwestern China. The mine field is 13 km long from north to south and approximately 4 km wide from east to west, with an area of 52 km². The bedrock strata in the mine field include the Upper Triassic Shangtian Formation, Middle Jurassic Yan'an Formation (coal-bearing strata), and Zhiluo Formation, as well as the Upper Jurassic Anding Formation, with the bedrock extensively covered by Quaternary wind-deposited sand or Palaeogene purplish-red clay. There are three main workable coal seams: No. 2, No. 6, and No. 8, which have thicknesses of 8.4 m, 2.6 m, and 5.5 m, respectively. The coal seam currently being mined is No. 2.

2.2. Overview of Working Face. The coal seam mined at working face 130205—coal seam No. 2—is buried at a depth of approximately 615 m. Its thickness ranges from 8.2 to 10.7 m, with an average of 8.4 m. It contains a layer of gangue (black carbonaceous mudstone) with an average thickness of 0.3 m, which is 0.7 m from the immediate floor of the coal seam. The lithology of the pseudoroof of No. 2 coal seam is carbonaceous mudstone (average thickness of 0.4 m), while that of the immediate roof is siltstone (average thickness of

4.6 m) and fine sandstone (average thickness of 3.2 m), with the part above it being medium sandstone (average thickness of 12.7 m) and fine sandstone (average thickness of 5.0 m). The coal seam floor is siltstone (average thickness of 11.8 m).

Airway 130205 opens at the return airway moving downhill of mining area No. 13, and the machine tunnel opens at the downhill belt conveyor of working face 130203 (where mining is completed) is above working face 130205. Coal safety pillars (35 m high) were set up in airway 130205 and machine tunnel 130203. The working face is bounded by normal fault F201 to the north and the shaft pillar in mining area No. 13 to the south. The part below working face 130205 is a primitive coal seam that has not been extracted; thus, there is no mining activity affecting the excavation of the working face.

The airway of working face 130205 has a length of 2,198 m, with a cross section of length \times width = 5,000 mm \times 4,000 mm. The machine tunnel has a length of 1,976 m, with a cross section of length \times width = 5,200 mm \times 4,000 mm. The working face has a strike length of 1,910 m (with a workable length of 1,583 m) and an inclination length of 332 m (cutting hole). The mining method of retreating longwall along the strike, the fully mechanised top-coal caving technique, and the full-caving method were adopted at the working face for the treatment of the goaf. The mining layout plan of working face 130205 is shown in Figure 1.

3. Methodology

3.1. Coal Pillar Design Method Based on Internal and External Stress Fields. During roadway excavation and maintenance, the sources of mine pressure and their corresponding excavation locations and timings under different chain pillar mining conditions were divided into three types, as shown in Figure 2 [25–27].

The first type was the excavation of a small coal pillar within the internal stress field and advancement due to mining of the relative working face before the formation and stabilisation of the internal stress field (Position 1 in Figure 2). The second type was advancement due to delayed mining of the working face after the stabilisation of the internal stress field (Position 2 in Figure 2). The third type was a roadway protection scheme using a large coal pillar, in which excavation was conducted in the high-stress area (Position 3 in Figure 2), with a low recovery rate owing to the large coal pillar and a large stress concentration factor.

For improving the coal recovery rate and reducing the stress concentration factor of coal pillar, the narrower the coal pillar is, the better. But considering the supporting effect of the coal pillar on the roof and the deformation degree of the surrounding rock of the roadway, the designed width of the coal pillar has a minimum value. If it is less than this value, the coal pillar will be easily broken, and the roadway will produce large deformation.

The width of the small coal pillar in the section was based on the comprehensive analysis of the effects of the stress, displacement, and width of the small coal pillar on the deformation of the roadway when the coal pillar was affected

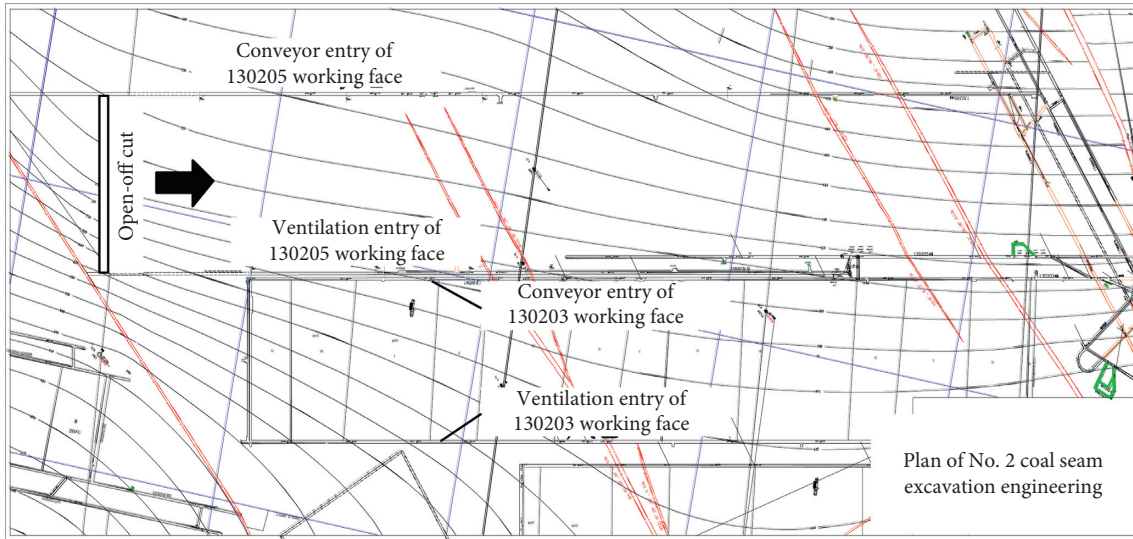


FIGURE 1: Relationship between the movement of the surrounding rock of the roadway and the abutment pressure distribution.

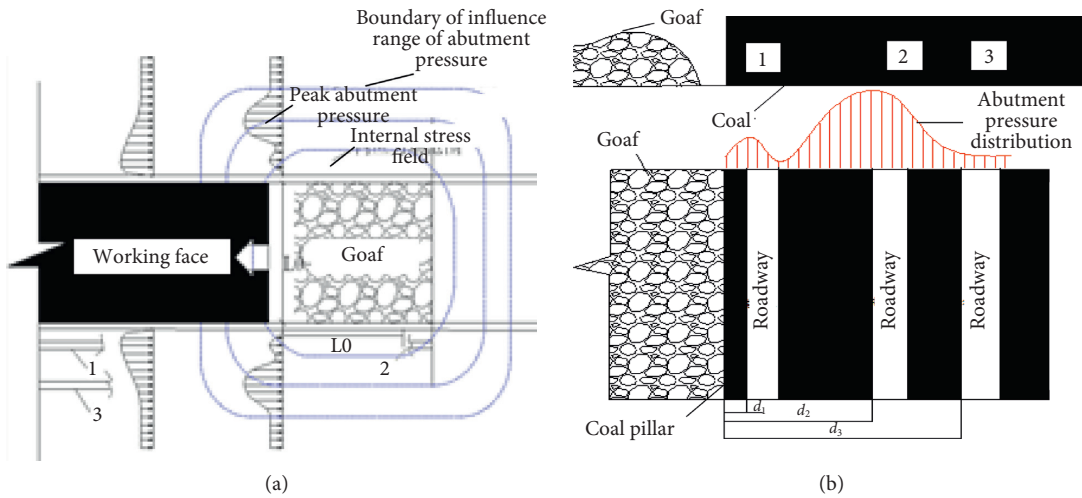


FIGURE 2: Relationship between the movement of the surrounding rock of the roadway and the abutment pressure distribution. (a) Plan and (b) profile.

by stoping of the working face in this section. The main factors affecting the working condition of the coal pillar included the following:

- ① **Loading time:** if the service time of the roadway was relatively long, a strength factor of prolonged service (with a value of 0.7 to 0.8) was used to correct the compressive strength of the specimen.
- ② **Width-to-height ratio:** the relationship between the coal pillar strength and width-to-height ratio (S_p) can be expressed by the following equation [28]:

$$S_p = \left(\frac{B}{h}\right)^{(1/2)} S_c, \quad (1)$$

where S_c represents the strength at $B/h = 1$ (i.e., the cubic strength) and S_p represents the coal pillar strength at a width-to-height ratio of B/h .

- ③ **Load size:** the degree of filling of the immediate roof in the goaf is directly related to the load size of the coal pillar. If the degree of filling was low, dynamic loading was significant. If the filling thickness was 3 to 5 times larger than the mining height, dynamic loading was not significant.
- ④ **Anchor reinforcement:** after the roadway was excavated, stress failure occurred within the surface layer of the coal seam on both sides of the coal pillar, forming a failure zone in the internal stress field. Moreover, the coal pillar was reinforced with an anchor bolt, which significantly increased the lateral pressure of the coal pillar under certain conditions.

3.2. Calculation Method for Coal Pillar Width. The stability of roadway driving along the goaf must be maintained with the installation of a small coal pillar in this section of the

roadway. The width of the coal pillar should be greater than the sum of the widths of the crushing zone on the side of the goaf and the anchorage zone. That is, it must be ensured that an intact zone is retained in the middle of the coal pillar to provide support, as shown in Figure 3. Hence, the reasonable minimum width B of small coal pillars in the section of roadway driving along the goaf is calculated as follows:

$$B = S_1 + S_2 + S_3, \quad (2)$$

where S_1 represents the crushing zone created in the small coal pillar in the roadway driving along goaf in this section, whose width is given as follows [29]:

$$S_1 = \frac{mA}{2tg\phi_0} \ln \left[\frac{k\gamma H + (C_0/tg\phi_0)}{(C_0/tg\phi_0) + (P_x/A)} \right], \quad (3)$$

where m represents the height of the roadway (in m), A is the coefficient of lateral pressure, k is the stress concentration factor caused by excavation of the roadway, γ represents the average unit weight of the overlying strata (in kN/m^3), H represents the mining depth (in m), P_x represents the strength provided by the roadway support to the coal wall (in MPa), and C_0 and ϕ_0 represent the cohesive force (MPa) and the angle of internal friction ($^\circ$) of the interface of the laminae of the coal mass, respectively.

S_2 represents the effective length of the anchor bolt in the sidewall of the roadway (in m), with an additional reinforcement factor of 15%.

S_3 represents the width of the elastic core zone in the middle of the coal pillar (in m). Assuming that the crushing zone of the coal pillar does not provide load bearing and that only the anchorage zone and the elastic core zone provide support, the width of the elastic core zone can be determined using the width-to-height ratio of this part of the coal pillar (equation (1)).

4. Results and Discussion

4.1. Calculation of Width of Coal Pillar at Working Face 130205. According to the equation for calculating the width of the coal pillar and the geological parameters of working face 130205, the width of the crushing zone of the small coal pillar S_1 was calculated as 1.8 m, where $m = 4$ m, $A = 1.6$, $k = 2.5$, $\gamma = 2512 \text{ kN/m}^3$, $H = 615$ m, $P_x = 0.1$ MPa, $C_0 = 1.5$ MPa, and $\phi_0 = 27^\circ$. The effective length of the anchor bolt in the sidewall of roadway was $S_2 = 2.3 \times (1 + 15\%) = 2.6$ m. According to the uniaxial compressive strength (24.6 MPa) and the coal mass strength of the plastic anchorage zone (22.3 MPa) of coal seam No. 2 of Zaoquan Coal Mine, it was found that the elastic core zone S_3 in the middle of the coal pillar was 1.7 m in width. Combining the three parts, the minimum width of the coal pillar was determined to be 5.8 m. The width of the small coal pillar was set to 6.0 m in this study.

4.2. Distribution of Advanced Abutment Pressure. Excavation and maintenance of roadways under a stable internal stress field are crucial for preventing and controlling the large deformation of roadways and related disasters.

Numerical simulations were performed to study the characteristics of the distribution of advanced abutment pressure during mining of working face 130203 and the deformation and failure of the airway of working face 130205 during excavation and stoping. An FLAC3D numerical simulation model was established according to the physical and mechanical parameters of coal and the geological characteristics of Zaoquan Coal Mine, as shown in Figure 4. The working face and the roadway were arranged in the central area of the model, and the grid was densely divided in the part around the roadway. The numerical model comprised 285,600 grid units. The left and right boundaries of the model were constrained by horizontal displacement conditions, and the lower boundary was constrained by vertical displacement. The upper boundary was a free boundary with a uniform load. The size of the computational model was set as 311 m \times 300 m \times 227 m.

During the simulation, excavation of working face 130203 was first conducted to observe the lateral abutment pressure distribution characteristics of the working face, and the results are presented in Figure 5. The lateral stress distribution of the working face was divided into low-stress (0~5 m), high-stress (5~11 m), peak-stress (11~20 m), and stress-relief zones (20~50 m). This indicates that the range of lateral impact due to the excavation of the working face was approximately 50 m. The 6 m coal pillar was just outside the peak-stress zone, verifying the accuracy of the calculation results.

4.3. Deformation and Failure Pattern of Coal Pillar during Excavation. After the excavation of working face 130203 was completed and the movement of the overlying strata was stabilised, excavation of the airway of working face 130205 was conducted. The deformation and failure of the surrounding rocks of the roadway 150 and 180 m from the cutting hole during the excavation are shown in Figures 6 and 7, respectively.

The results suggest that the deformation of the rock around the airway gradually increased. The deformation value was particularly large near the vault. The maximum deformation near the airway was 114.4 mm (180 m from the cutting hole). The vault extended upwards, and the deformation of strata converged quickly. The deformation of the surrounding rock was within 10 mm, after extending 5 m into the rock. The maximum uplift at the bottom was approximately 45 mm. The two sidewalls exhibited highly asymmetric deformation distributions owing to the heterogeneity of the cross section.

4.4. Deformation and Failure Pattern of Coal Pillar during Stopping. After the excavation of the airway of working face 130205 was complete, the excavation of working face 130205 was conducted. The deformation and failure of the coal pillar were observed, and the failure of the surrounding rocks of the roadway 150 and 180 m from the cutting hole is shown in Figure 8. During the advancement of the working face with a large mining height, the coal wall of the working face failed in a certain range along the advancement direction under the action of abutment pressure. The depth range of 0 to 2.0 m in

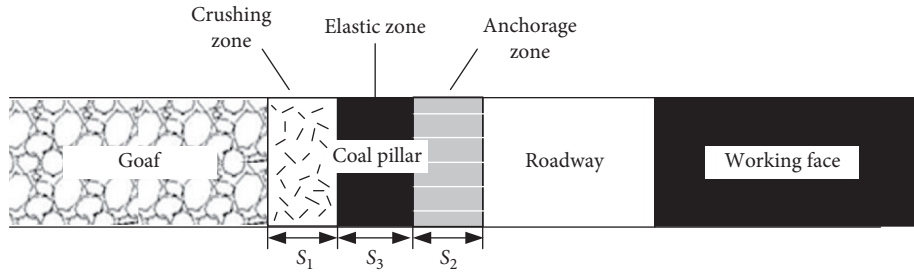


FIGURE 3: Schematic of roadway driving along the goaf and the small coal pillar.

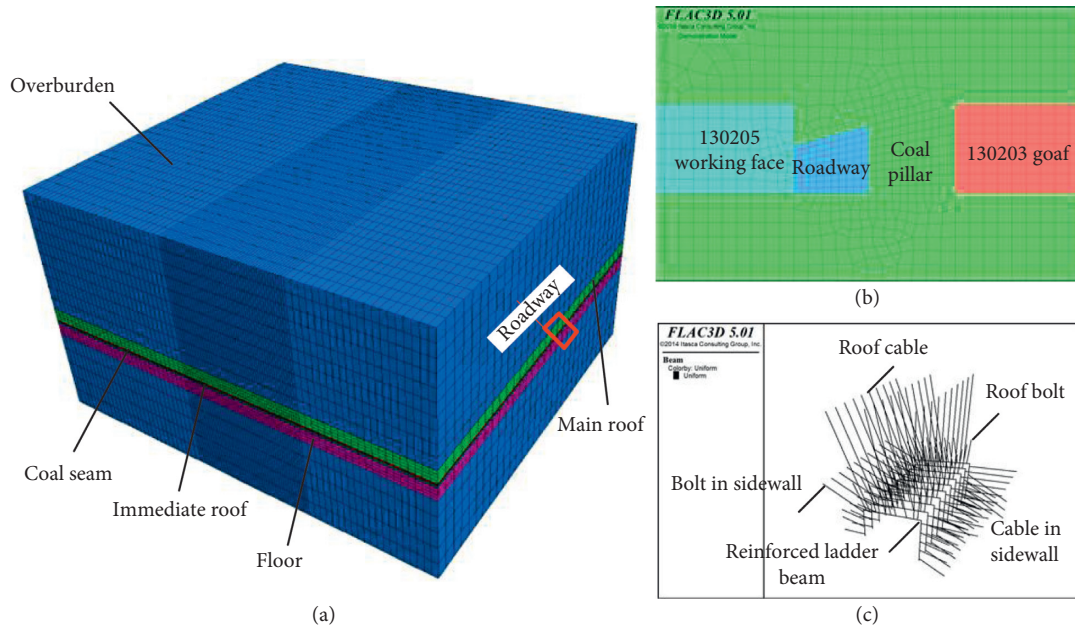


FIGURE 4: Grid diagram of the three-dimensional numerical model.

the coal wall on the side of mining face 130205 was the tensile and shear plastic zone, which was characterised by a typical failure in the form of outward bulging. Under the action of the abutment pressure, the reduction in the strength of the coal mass caused the coal wall at the working face to bulge outward. The depth range of 0 to 1.5 m in the coal wall on the side of mining face 130203 was the tensile and shear plastic zone. Under the action of the abutment pressure, the reduction of the strength of the coal mass led to the outward bulging of the coal wall at the working face. Within the range of 2.0 to 4.5 m in the centre of the small coal pillar, although part of the coal seam was in the plastic zone, the coal seam was mainly in the shear plastic zone, and the degree of rock fragmentation was not severe.

The comprehensive analysis indicated that there was approximately 1.5 m of noncrushing zone in the centre of the 6 m small coal pillar.

4.5. Application Results. The cross-point method [30] was used to monitor the degree of deformation of the surrounding rock of airway 130205. Measuring pins were installed at the centres of the roof, floor, and two sidewalls. The

degrees of deformation of these parts were measured once a day using a steel tape measure. The deformation of the roadway 150 m and 180 m from the cutting hole during the advancement of the working face is shown in Figure 9.

The deformation of the two sidewalls of the roadway was greater than those of the roof and floor during the advancement of the working face. The maximum sinkage of the roof was 55 mm, the maximum heave of the floor was 55 mm, the maximum upper-wall bulge was 30 mm, and the maximum lower-wall bulge was 70 mm. The bulging of the upper wall of the airway was the smallest among all the changes, indicating that a 6 m coal pillar can maintain the stability of the roadway. Within 50 m from the working face, the deformation of the surrounding rock of the roadway became increasingly apparent. The deformation accelerated significantly within 35 m, and the deformation rate was maximised at approximately 20 m. Thus, the influence range during the process of stoping of the working face was roughly within 50 m. The deformation of the roof increased significantly within 20 m ahead of the working face, and a sharp increase occurred at approximately 15 m. This indicates that the coal seam mining generally affected a range 50 m ahead of the coal wall and that the impact of the mining intensified within the range of 15 m.

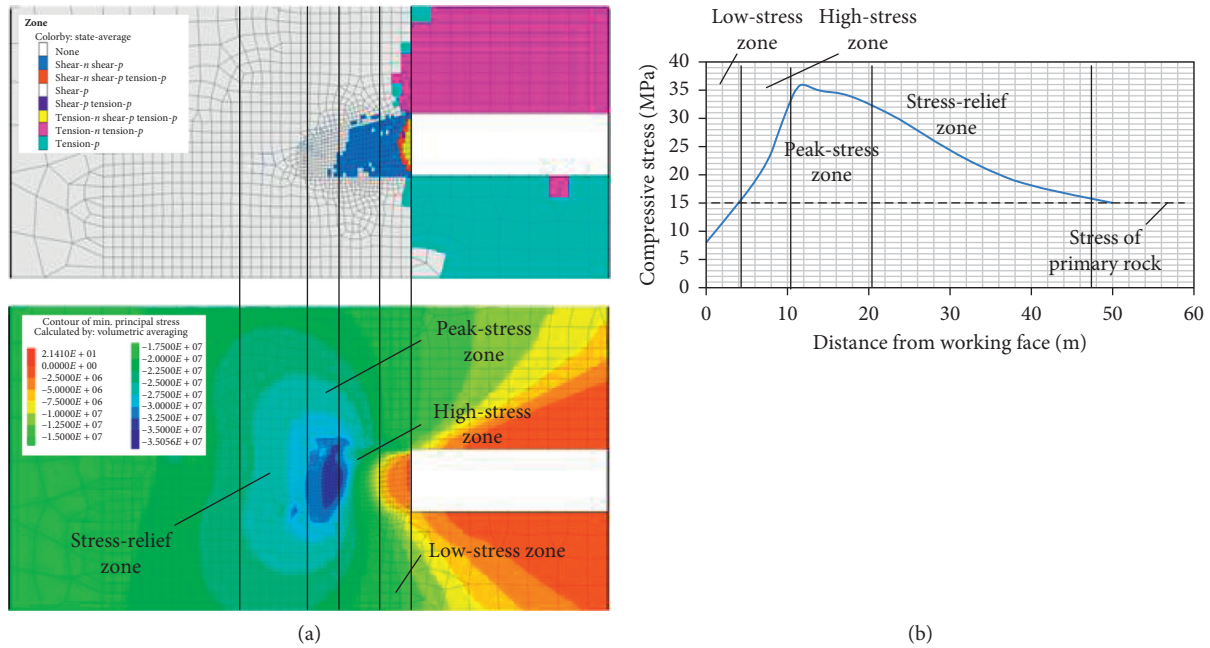


FIGURE 5: Distribution of the advanced abutment pressure at the working face during stoping. (a) Vertical view and (b) stress distribution curve.

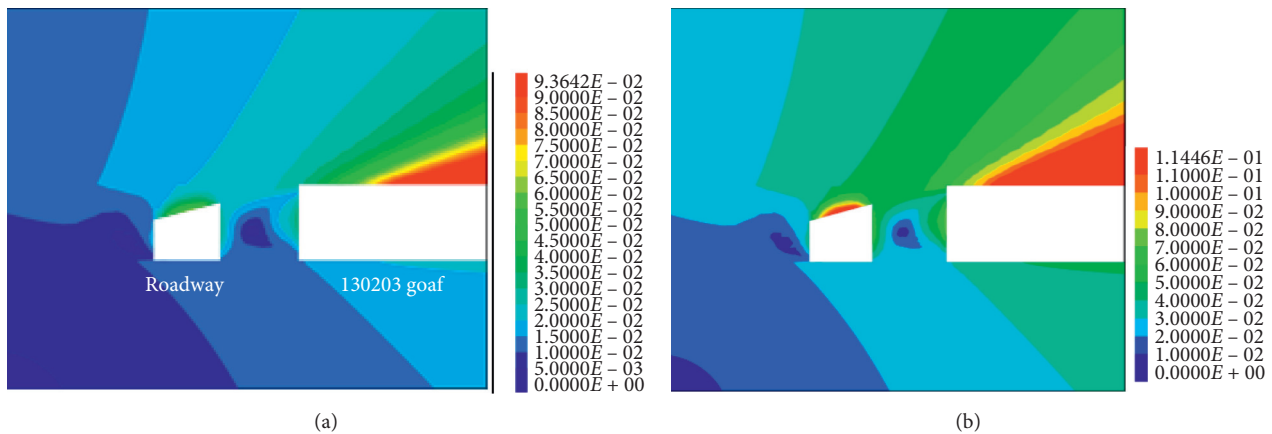


FIGURE 6: Nephograms indicating the rock deformation during airway excavation. (a) 150 m from the cutting hole and (b) 180 m from the cutting hole.

The YS(B) explosion-proof electronic borescope for mines (as shown in Figure 10) was used to detect the failure in the coal pillar 50 m ahead of the working face, and the results are shown in Figure 11. At the front end of the borehole (i.e., near working face 130203), fractures developed in the borehole, and the coal mass was crushed. At the middle of the borehole, the borehole wall was relatively smooth, with high integrity. At the back end of the borehole (i.e., near working face 130205), the borehole wall appeared to be bright black under the illumination of the probe, indicating that the coal mass here was also in the plastic state. The detection results indicated that both sides of the coal pillar were in a state of plastic failure, while there was still an intact elastic core zone in the middle, which indicates that the design of the coal pillar is reasonable. This was supported by the overall results for the deformation control of the roadway. The

effects on the roadway 50 and 100 m ahead of the working face are presented in Figure 12. As shown, the deformation of the roadway along the goaf with a 6 m small coal pillar was not apparent within the influence range of advanced abutment pressure, which can ensure normal stoping of the working face.

4.6. Discussion. The method for determining the width of gob-side coal pillar proposed in this paper is applicable to all coal mines in theory. However, when the roadway roof is hard, it needs to be supplemented by roof cutting and other measures to prevent excessive stress on the coal pillar. The broken position of soft roof is close to the coal pillar, so it is not necessary to take other measures, so the method in this paper can be directly used for design.

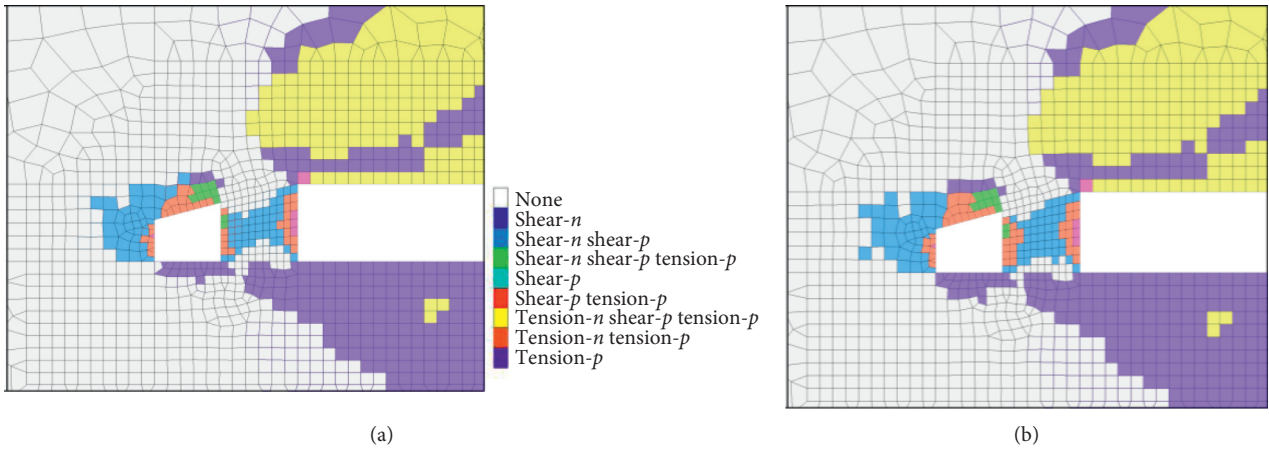


FIGURE 7: Distribution of the plastic zone of the rock during the airway excavation. (a) 150 m from the cutting hole and (b) 180 m from the cutting hole.

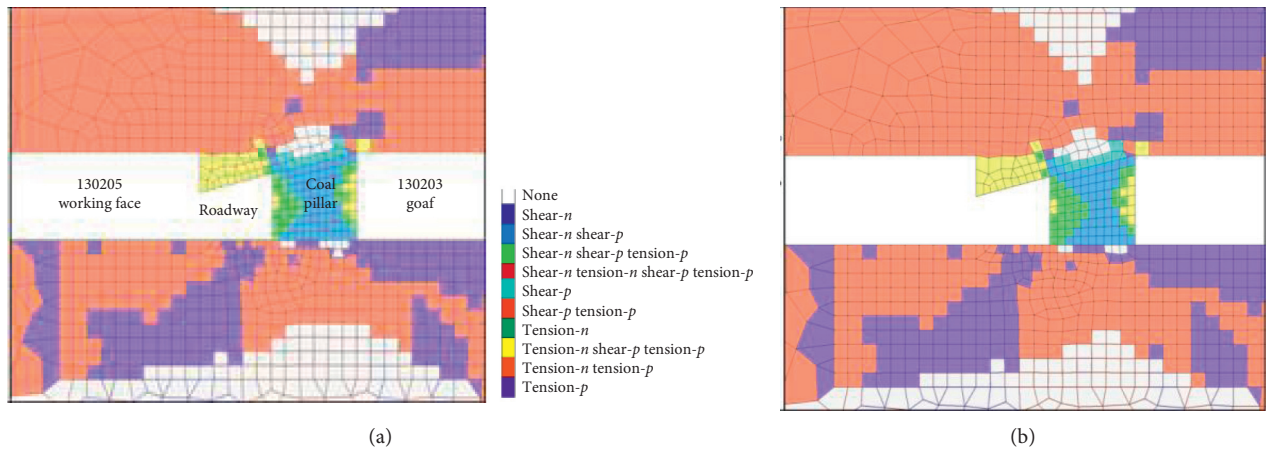


FIGURE 8: Distribution of the plastic zone of the rock body at the working face during stoping. (a) 150 m from the cutting hole and (b) 180 m from the cutting hole.

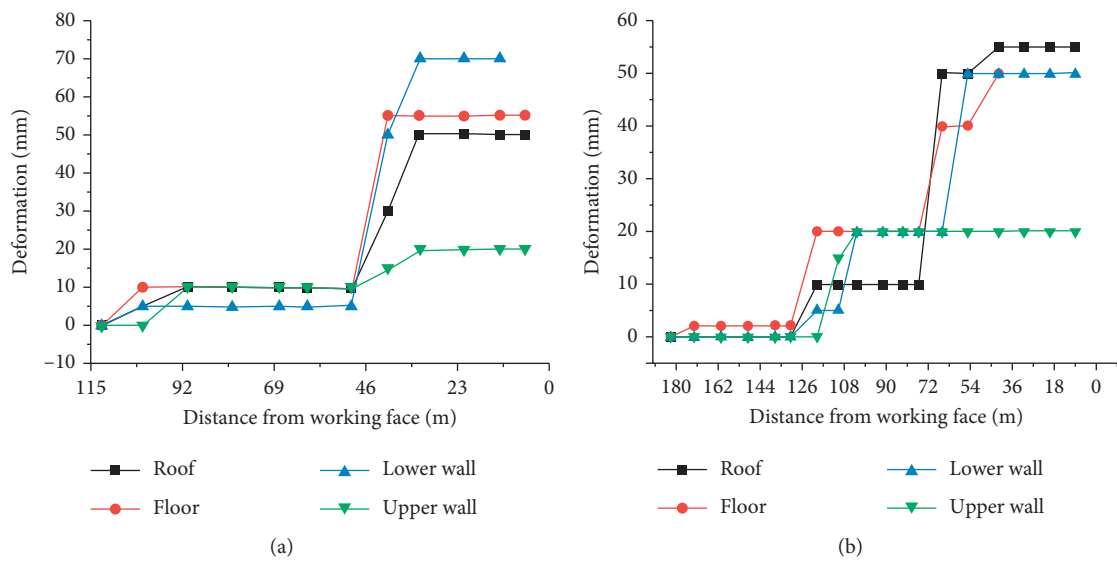


FIGURE 9: Deformation of the surrounding rocks of the roadway at different distances from the cutting hole. (a) 150 m from the cutting hole and (b) 180 m from the cutting hole.

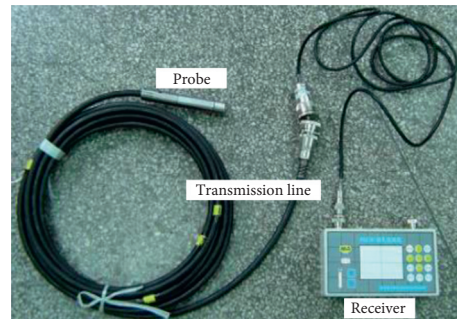


FIGURE 10: Detection equipment for internal fracture of the coal mass.

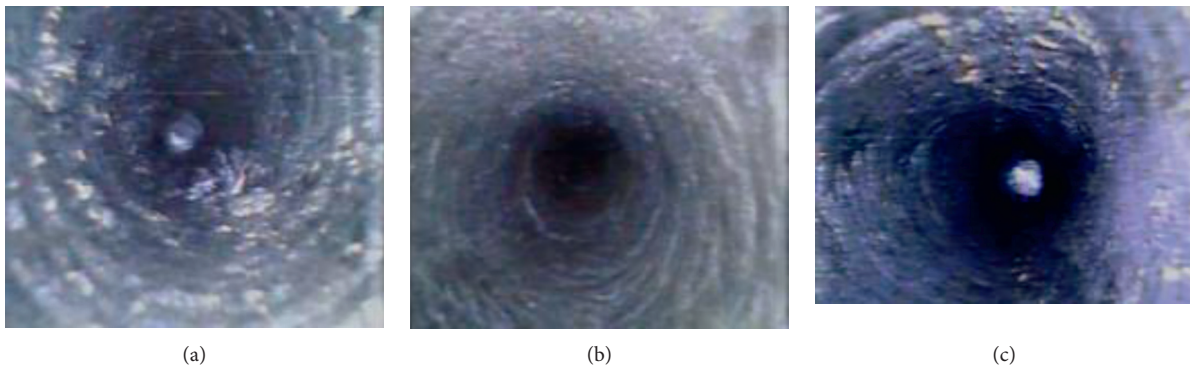


FIGURE 11: Internal fracture development in the coal mass. (a) Front-end crushing zone, (b) middle intact zone, and (c) back-end anchorage zone.



FIGURE 12: Effects on the roadway with 50 and 100 m of working face advancement. (a) 50 m of advancement and (b) 100 m of advancement.

5. Conclusions

In the design of a coal pillar in roadway driving along a goaf, not only the width of the coal pillar but also its location must be considered. In this study, a method for determining the location and width of a small coal pillar was developed on the distribution of the internal and external stress fields at the working face. The method was applied to working face 130205 of Zaoquan Coal Mine.

- (1) According to the calculation of the width of the limit equilibrium zone generated in the coal pillar at

working face 130205 and the mechanical calculation of the joint loading in the limit equilibrium zone and the elastic core zone of the coal pillar, a reasonable width of the coal pillar of the section was found to be 6 m. This result is consistent with the simulation results for the distribution of the lateral abutment pressure after the mining of working face 130203.

- (2) During the excavation of the roadway and stoping of the working face, the deformation of the roadway increased with a reduction in the distance from the working face. Owing to the asymmetry of the

roadway, plastic failure of the solid coal side of the roadway was apparent. Although plastic failure also occurred in the coal pillar, its bearing capacity was still relatively high. There was approximately 1.5 m of intact zone in the middle of the coal pillar even during the stopping of the working face.

- (3) The influence range during the stopping of the working face was roughly 50 m, and the deformation of the roof increased significantly within 20 m ahead of the working face. The deformation of the two sidewalls of the roadway exceeded those of the roof and floor, and the bulging of the upper wall was the smallest among all the changes, indicating that a 6 m small coal pillar can effectively maintain the stability of the roadway. This is consistent with the conclusion from the exploration of the coal pillar through the borehole onsite that there is an intact zone in the centre of the coal pillar.
- (4) The proposed design method for small coal pillars in deep roadway driving along goafs is scientific and reliable. It provides a scientific basis for the determination of the reasonable width of narrow coal pillars, which can improve the maintenance status of deep roadways and increase the coal recovery rate.

Data Availability

The data used to support the findings of this study are available from the corresponding author upon request.

Conflicts of Interest

The author declares that he has no conflicts of interest.

Acknowledgments

This work was supported by the Key R&D Program of Shandong Province (no. 2019GSF111020). The support was greatly appreciated.

References

- [1] J. Martin and W. Holger, "Progress in the research and application of coal mining with stowing," *International Journal of Mining Science and Technology*, vol. 23, pp. 7–12, 2013.
- [2] M. L. Hu, W. L. Zhao, Z. Lu, J. X. Ren, and Y. P. Miao, "Research on the reasonable width of the waterproof coal pillar during the mining of a shallow coal seam located close to a reservoir," *Advances in Civil Engineering*, vol. 2019, Article ID 3532784, 14 pages, 2019.
- [3] Q. Wang, Y. P. Fan, G. Li, W. X. Guo, D. H. Yan, and L. P. Zhang, "Determination of coal pillar width between roadways of fully mechanised caving face with double roadways layout in a thick coal seam," *Rock and Soil Mechanics*, vol. 38, pp. 3009–3016, 2017.
- [4] K. Wang, T. Zhao, K. Yetilmezsoy, and X. Q. Zhang, "Cutting-caving ratio optimization of fully mechanized caving mining with large mining height of extremely thick coal seam," *Advances in Civil Engineering*, vol. 2019, Article ID 7246841, 11 pages, 2019.
- [5] W. Liu, Z. Guo, J. Hou, and D. Chen, "Research and application of support technology for re-mining roadway in goaf under regenerated roof in thick coal seam," *Geotechnical & Geological Engineering*, vol. 37, no. 5, pp. 4327–4335, 2019.
- [6] Y. Xue, P. G. Ranjith, F. Dang et al., "Analysis of deformation, permeability and energy evolution characteristics of coal mass around borehole after excavation," *Natural Resources Research*, vol. 29, no. 5, pp. 3159–3177, 2020.
- [7] X. S. Liu, D. Y. Fan, Y. L. Tan et al., "Failure evolution and instability mechanism of surrounding rock for close-distance chambers with super-large section in deep coal mines," *International Journal of Geomechanics*, vol. 21, no. 5, Article ID 04021049, 2021.
- [8] Y. Xue, T. Teng, F. Dang, Z. Ma, S. Wang, and H. Xue, "Productivity analysis of fractured wells in reservoir of hydrogen and carbon based on dual-porosity medium model," *International Journal of Hydrogen Energy*, vol. 45, no. 39, pp. 20240–20249, 2020.
- [9] J. Zhang, F. Jiang, S. Zhu, and L. Zhang, "Width design for gobs and isolated coal pillars based on overall burst-instability prevention in coal mines," *Journal of Rock Mechanics and Geotechnical Engineering*, vol. 8, no. 4, pp. 551–558, 2016.
- [10] Z. Zhu, H. Zhang, J. Nemcik, T. Lan, J. Han, and Y. Chen, "Overburden movement characteristics of top-coal caving mining in multi-seam areas," *The Quarterly Journal of Engineering Geology and Hydrogeology*, vol. 51, no. 2, pp. 276–286, 2018.
- [11] Y. L. Tan, F. H. Yu, J. G. Ning, and T. B. Zhao, "Design and construction of entry retaining wall along a gob side under hard roof stratum," *International Journal of Rock Mechanics and Mining Sciences*, vol. 77, pp. 115–121, 2015.
- [12] E. Ghasemi and K. Shahriar, "A new coal pillars design method in order to enhance safety of the retreat mining in room and pillar mines," *Safety Science*, vol. 50, no. 3, pp. 579–585, 2012.
- [13] P. R. Sheorey, M. N. Das, D. Barat, R. K. Prasad, and B. Singh, "Coal pillar strength estimation from failed and stable cases," *International Journal of Rock Mechanics and Mining Science & Geomechanics Abstracts*, vol. 24, no. 6, pp. 347–355, 1987.
- [14] M. Najafi, S. E. Jalali, A. R. Y. Bafghi, and F. Sereshki, "Prediction of the confidence interval for stability analysis of chain pillars in coal mines," *Safety Science*, vol. 49, no. 5, pp. 651–657, 2011.
- [15] W. He, F. He, and Y. Zhao, "Field and simulation study of the rational coal pillar width in extra-thick coal seams," *Energy Science & Engineering*, vol. 8, no. 3, pp. 627–646, 2020.
- [16] N. Fan, J. Wang, B. Zhang, D. Liu, and R. Wang, "Reasonable width of segment pillar of fully-mechanized caving face in inclined extra-thick coal seam," *Geotechnical & Geological Engineering*, vol. 38, no. 4, pp. 4189–4200, 2020.
- [17] W. J. Gale, "Experience of field measurement and computer simulation methods for pillar design," in *Proceedings of the Second International Workshop on Coal Pillar Mechanics and Design*, US National Institute for Occupational Safety and Health, Pittsburgh, PA, USA, June 1999.
- [18] A. Jaiswal and B. K. Shrivastva, "Numerical simulation of coal pillar strength," *International Journal of Rock Mechanics and Mining Sciences*, vol. 46, no. 4, pp. 779–788, 2009.
- [19] G. S. Esterhuizen, C. Mark, and M. M. Murphy, "Numerical model calibration for simulating pillars, gob and overburden response in coal mines," in *Proceedings of the 29th International Conference on Ground Control in Mining*, West Virginia University, Morgantown, WV, USA, July 2010.

- [20] W.-d. Wu, J.-b. Bai, X.-y. Wang, S. Yan, and S.-x. Wu, "Numerical study of failure mechanisms and control techniques for a gob-side yield pillar in the Sijiazhuang coal mine, China," *Rock Mechanics and Rock Engineering*, vol. 52, no. 4, pp. 1231–1245, 2019.
- [21] J. B. Bai, C. J. Hou, and H. F. Huang, "Numerical simulation study on stability of narrow coal pillar of roadway driving along goaf," *Chinese Journal of Rock Mechanics and Engineering*, vol. 20, pp. 3475–3479, 2004.
- [22] K. Chen, J. B. Bai, and Q. Zhu, "Failure law of small coal pillar and determination of reasonable width in gob side entry driving," *Safety in Coal Mines*, vol. 40, no. 8, pp. 100–102, 2009.
- [23] X. G. Zheng, Z. G. Yao, and N. Zhang, "Study on stress distribution of small coal pillar in gob side entry driving in the whole process of mining," *Journal of Mining and Safety Engineering*, vol. 29, no. 4, pp. 459–465, 2012.
- [24] X. S. Liu, D. Y. Fan, Y. L. Tan et al., "New detecting method on the connecting fractured zone above the coal face and a case study," *Rock Mechanics and Rock Engineering*, 2021.
- [25] G. Zhang, L. Chen, Z. Wen et al., "Squeezing failure behavior of roof-coal masses in a gob-side entry driven under unstable overlying strata," *Energy Science & Engineering*, vol. 8, no. 7, pp. 2443–2456, 2020.
- [26] Z. Zhao, W. Sun, S. Chen, D. Yin, H. Liu, and B. Chen, "Determination of critical criterion of tensile-shear failure in Brazilian disc based on theoretical analysis and meso-macro numerical simulation," *Computers and Geotechnics*, vol. 134, Article ID 104096, 2021.
- [27] B. Wang, F. Dang, S. Gu, R. Huang, Y. Miao, and W. Chao, "Method for determining the width of protective coal pillar in the pre-driven longwall recovery room considering main roof failure form," *International Journal of Rock Mechanics and Mining Sciences*, vol. 130, Article ID 104340, 2020.
- [28] S. H. Prassettyo, M. A. Irnawan, G. M. Simangunsong, R. K. Wattimena, I. Arif, and M. A. Rai, "New coal pillar strength formulae considering the effect of interface friction," *International Journal of Rock Mechanics and Mining Sciences*, vol. 123, Article ID 104102, 2019.
- [29] G. S. Jia and L. J. Kang, "Study on the chain pillar stability of the developing entry in longwall top-coal mining," *Journal of China Coal Society*, vol. 27, pp. 6–10, 2002.
- [30] J. Ning, J. Wang, Y. Tan, and Q. Xu, "Mechanical mechanism of overlying strata breaking and development of fractured zone during close-distance coal seam group mining," *International Journal of Mining Science and Technology*, vol. 30, no. 2, pp. 207–215, 2020.

Research Article

Characteristics of Pressure Relief Gas Extraction in the Protected Layer by Surface Drilling in Huainan

Xiaozhang Tong ^{1,2,3,4}, Hu Wen ^{1,2}, Xiaojiao Cheng ^{1,2}, Shixing Fan ^{1,2}, Chunhui Ye,^{3,4}
Mingyang Liu,^{1,2} and Hu Wang ^{1,2}

¹College of Safety Science and Engineering, Xi'an University of Science and Technology, Xi'an 710054, China

²Shaanxi Key Laboratory of Prevention and Control of Coal Fire, Xi'an 710054, China

³National Engineering Research Center for Coal Gas Control, Huainan, Anhui 232001, China

⁴Huainan Mining Group Co., Huainan, Anhui 232001, China

Correspondence should be addressed to Xiaozhang Tong; 183042045@qq.com and Xiaojiao Cheng; 201512713@stu.xust.edu.cn

Received 25 March 2021; Accepted 24 May 2021; Published 8 June 2021

Academic Editor: Jia Lin

Copyright © 2021 Xiaozhang Tong et al. This is an open access article distributed under the Creative Commons Attribution License, which permits unrestricted use, distribution, and reproduction in any medium, provided the original work is properly cited.

To study the behavior of gas extraction from the protected layer by surface drilling, the common characteristics of gas extraction concentration and gas extraction quantity are summarized through the collection of key parameters of surface drilling and a combination of data and figures, with the background of 11⁻² coal protection 13⁻¹ coal in the Huainan mining area. The research results show that the flow of pressure relief gas extraction of the protected layer by surface drilling has three stages: a rising period, stable period, and decay period. When the extraction processes of multiple surface wells on the same working face are coordinated, the extraction flow is superimposed, and the extraction volume of surface drilling shows an increasing trend and fluctuates with the location of the drilling. The extraction flow rate before ground drilling is relatively small, and the extraction flow rate increases after ground drilling. This behavior is further confirmed by field observation of mining changes in the protective layer and the expansion and deformation of the protected layer. The periodic variation in the surface drilling and extraction quantity is affected primarily by the mining movement of the working face of the protective layer. Specifically, it is affected by factors such as the mining progress of the working face of the protective layer, mining height, degree of compacted goaf, degree of pressure relief of the protected layer, original gas content, and other measures taken to extract the protected layer.

1. Introduction

China is rich in coal resources and coalbed methane (CBM) resources. According to the second national coal resource prediction results, the volume of the reserves of CBM buried at depths less than 2000 m in China is $3.68 \times 10^{13} \text{ m}^3$, equivalent to $4.2 \times 10^{10} \text{ t}$ standard coal [1]. China's coal mine methane (CMM) resources are less plentiful than those of Russia and the United States, ranking third in the world, accounting for 13% of the total CMM resources in the 12 countries richest in CMM. In 2012, 3284 high gas outburst coal mines were distributed in 26 major coal-producing provinces, mainly in the southwest and mid-eastern regions. China's coal mine safety regulations stipulate that the coal seam must be predrained before mining so that the gas

pressure and gas content are reduced to 0.74 MPa and 8 m³/t, respectively. Otherwise, it is easy to cause coal and gas outbursts, excesses of gas in the working face, and gas explosion accidents [2–5]. In addition, the damage to the ozone layer and the greenhouse effect caused by gas emission into the atmosphere are 7 and 21 times greater than that of CO₂, respectively [6]. However, coalbed methane is a clean and efficient energy source, and its calorific value is 2–5 times that of general coal [7].

Coal seam permeability enhancement mainly includes protective layer mining, hydraulic fracturing, hydraulic cutting, hydraulic punching, presplitting blasting, shock wave fracturing, liquid CO₂ blasting, and other hole fracture reconstruction technologies. At present, hydraulic fracturing, hydraulic cutting, and hydraulic flushing have made

great progress in increasing the production of shale gas and CBM [8–11]. However, these methods also introduce some problems. When water enters the microhole fracture of the coal body, under the influence of “water lock,” gas desorption decays rapidly, resulting in poor water injection. It is difficult to ensure that fracturing water is evenly distributed in the fine cracks and pores of the coal seam, and it cannot fully wet the coal. Hydraulic technology requires high water consumption, which has become a problem in areas such as Texas, North Dakota, and Kansas [12]. In addition, the water and groundwater used by the hydration technology return to the ground; this water can contain hydraulic additives or harmful substances.

Presplitting blasting has made some achievements in increasing the permeability of coal seams and strengthening gas drainage [13]. However, it is extremely difficult to deal with abnormal conditions such as “dumb blasting” and “blind blasting” when using explosives. In addition, explosives cause the coal and rock mass to be crushed during the blasting process, and the crushed coal will hinder the propagation of the blasting wave, resulting in higher energy consumption. The fracture circle area is small, and the crushed coal and rock mass can easily block the fracture, making extraction ineffective. Shock wave fracturing of coal seams is an innovative technology for enhanced permeability gas drainage [14]. The coal reservoir is reconstructed through breaking, tearing, and elastic acoustic wave disturbance, which have the basic characteristics of segmentation and frequency bands. This basic feature is combined with the fatigue effect of repeated loading, which makes controllable shock wave technology advantageous in reservoir reconstruction technology; however, large-scale underground applications have not yet been realized.

In recent years, domestic and foreign researchers have carried out numerous liquid CO₂ blasting tests in major coal mines [15]. The field results show that the technology has a significant effect on coal reservoir reconstruction and coal seam methane recovery, but the range of influence is small. Wen et al. [16–24] proposed liquid CO₂ permeability enhancement and gas displacement technology in coal mines, carried out several underground engineering tests, and achieved good results. However, these studies had problems such as small test areas and difficulty of CO₂ transportation. Protective layer mining is the most effective regional measure for preventing and controlling gas disasters. Protective layer mining changes the deformation degree of the coal skeleton, destroys the stress state of the overlying coal and rock mass, effectively improves the permeability of the protected layer, and promotes desorption, flow, and discharge of pressure relief gas [25–28]. In addition, Jin confirmed that the protected areas generated by protective layer mining were larger than those predicted theoretically [29], but the technology was greatly affected by geological conditions. With the deepening of mining depth year by year, there are fewer and fewer coal seams or low outburst-prone coal seams with an interlayer spacing of 20–50 m. Therefore, the protective layer mining method is greatly affected by the occurrence characteristics of coal seams.

The typical geological feature of the Huainan mining area is the high occurrence of coal seam groups, and the protective layer mining strategy has been fully implemented. In the process of mining the protective layer, the stress field and fracture field evolution caused by mining action are used to relieve pressure, increase the permeability of gas, and improve the storage and transportation of pressure relief gas. The pressure relief gas of the protected layer is efficiently extracted, and coal and gas are mined together to eliminate the risk of coal and gas outbursts in the protected layer.

Pressure relief gas extraction methods mainly include underground roadway extraction, coal pillarless borehole extraction, and surface drilling extraction [30]. Gas extraction by surface drilling is a type of green mining technology that does not interfere with the normal operation of the mine from the surface construction, reduces the amount of underground engineering technology, and is conducive to safe operation of the mine. This process is generally divided into predrainage before mining, mining-induced drainage, and goaf drainage. Surface drilling technology has been applied in Huainan, Huaibei, Jincheng, Lu’an, and other high gas mining areas and has become increasingly effective [31–37]. Based on the drainage results of surface drilling of a typical working face during the exploitation of the protective layer in the Huainan mining area, the characteristics of relief gas extraction from the protective layer by surface drilling are summarized.

1.1. Application of Surface Drilling for Pressure Relief Gas Extraction in the Huainan Mining Area. Since the successful application of pressure relief gas extraction technology by surface drilling in the 2352(1) protective layer working face of the Panyi Coal Mine in 2002, more than 100 wells have been tested in the Pansan Coal Mine, Xieqiao Coal Mine, Zhangji Coal Mine, and Guqiao Coal Mine. The geographical distribution of coal mines is shown in Figure 1. Surface drilling in the Huainan mining area is mainly used for pressure relief gas extraction during the mining of the 11⁻² coal protective seam face, that is, the construction of surface drilling before the 11⁻² coal mining. With the mining of the 11⁻² coal protective layer, the overlying coal and rock layers continue to collapse, crack, and sink, causing the pores and cracks of the originally closed geological body to proliferate and open, and the air permeability coefficient of the surrounding rock and its coal seam greatly increases, as shown in Figure 2. The mining of the protective layer promotes full pressure relief of the protective and protected layers. The pressure relief gas of the protective layer, the gas flowing into the goaf, and the pressure relief gas of the protected layer flow into the well through the screen and are then pumped to the ground from the well.

2. Characteristics of Surface Drilling Types in the Huainan Mining Area

To adapt surface drilling technology for pressure relief gas extraction to various types of working faces of mining protective layers and improve gas extraction, Huainan

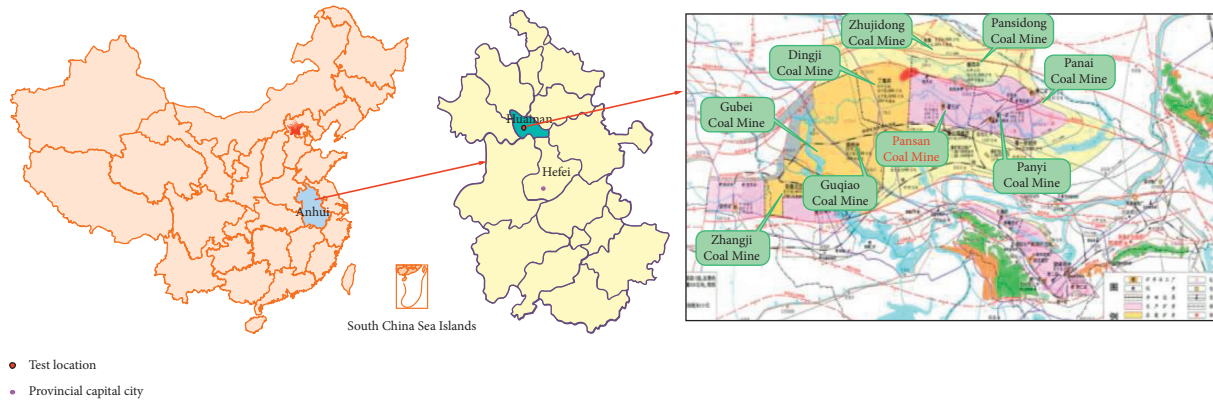


FIGURE 1: Geographical location of the study area and locations of the engineering test sites [17].

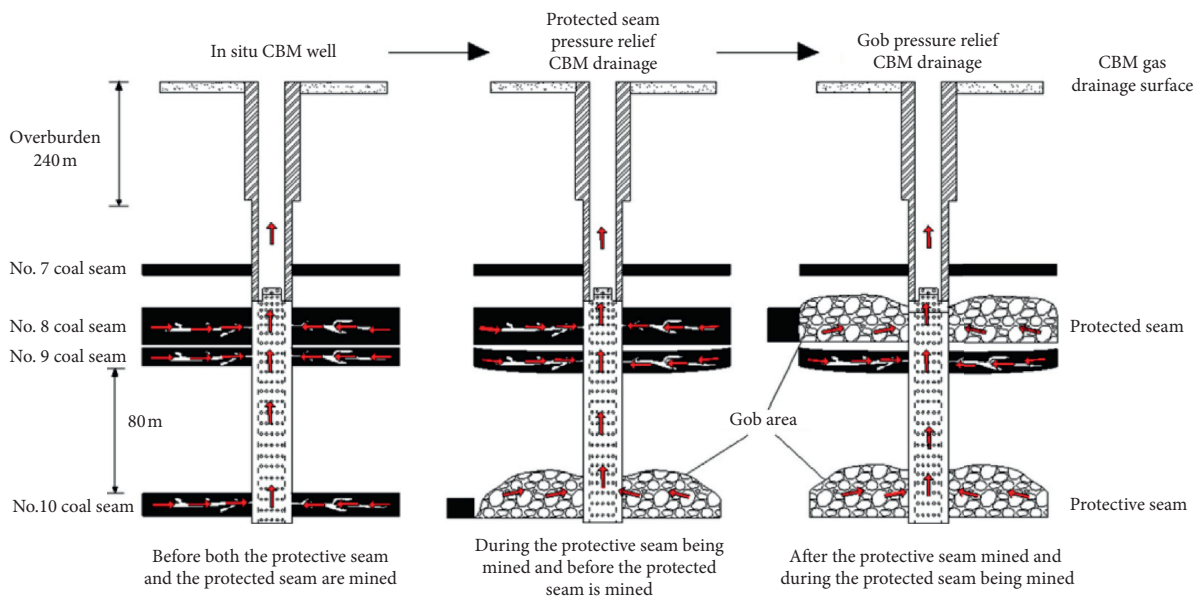


FIGURE 2: Different stages of pressure relief CMM extraction of the multipurpose well modified from the work of Wang et al. [38].

Mining Group has improved and innovated upon the drilling well structure, drilling construction technology, and drilling well location layout. The Huainan mining area successfully applied well structure types I, II, III, and IV, as shown in Table 1. Furthermore, the Huainan Mining Group formed a drilling well structure and drilling well location layout suitable for different mining conditions, mastered the key drilling construction technologies of different well body structures, and enriched the theoretical basis of pressure relief gas extraction in the protective layer.

3. Characteristics of Gas Extraction in Pressure Relief by Typical Surface Drilling in the Huainan Mining Area

3.1. Measurement of Gas Extraction Flow from Surface Drilling. To extract pressure relief gas from the protected layer by surface drilling, an independent extraction system was established with sufficient extraction capacity and negative pressure of 20–50 kPa. The highly concentrated gas

extracted can be used directly as clean energy for gas power generation or civil use. During the extraction of surface wells, special personnel were deployed to maintain the extraction system. The gas extraction concentration, negative pressure, flow rate, temperature, and other parameters were measured daily. A daily extraction report was formulated, and the extraction effect of surface drilling was analyzed regularly.

3.2. Typical Characteristics of Pressure Relief Gas from Single Ground Drilling. The ground drilling No. 1 in the protective layer working face 2662(1) is a type I drilling structure, with a total of 214 days of extraction and 20.91 million m³ of gas extraction. Figure 3(a) shows that the gas flow of No. 1 surface drilling has a significant periodicity, which can be divided into a rising period, stable period, and decay period. The ground well (No. 1) passed 12 m through the mining face to begin the extraction; the gas extraction concentration was 20%, and the gas extraction rate was 2.99 m³/min. From that point, the gas extraction concentration and extraction

TABLE 1: Surface gas extraction wells of different structural types in the Huainan mining area.

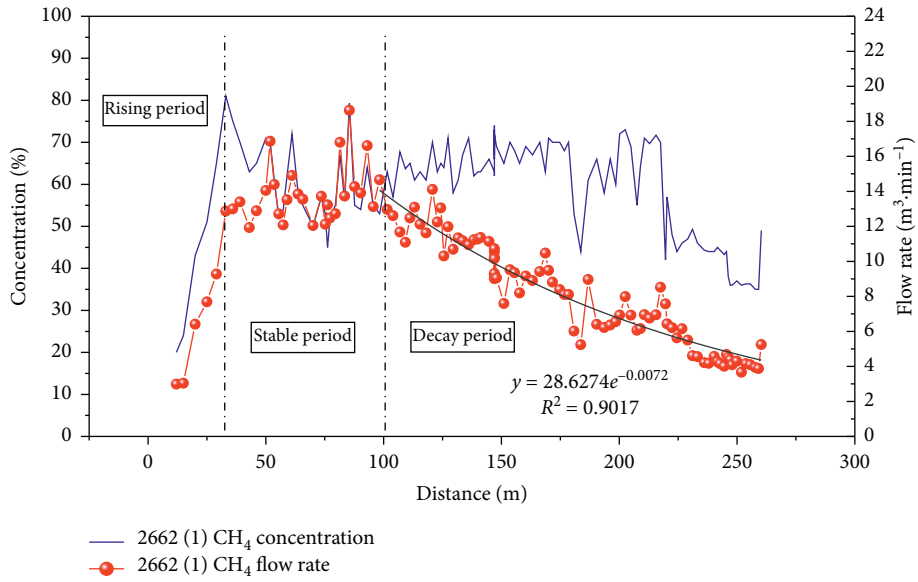
Type	Structural representation	Coal mines featuring successful application	Result
I		<p>Panyi coal mine, Xieqiao coal mine, and Pansan coal mine</p>	<p>The maximum single-well gas extraction volume is close to 1,000,000 m³</p>
II		<p>Dingji coal mine</p>	<p>The cumulative gas output of a single well is close to 1,000,000 m³</p>

TABLE 1: Continued.

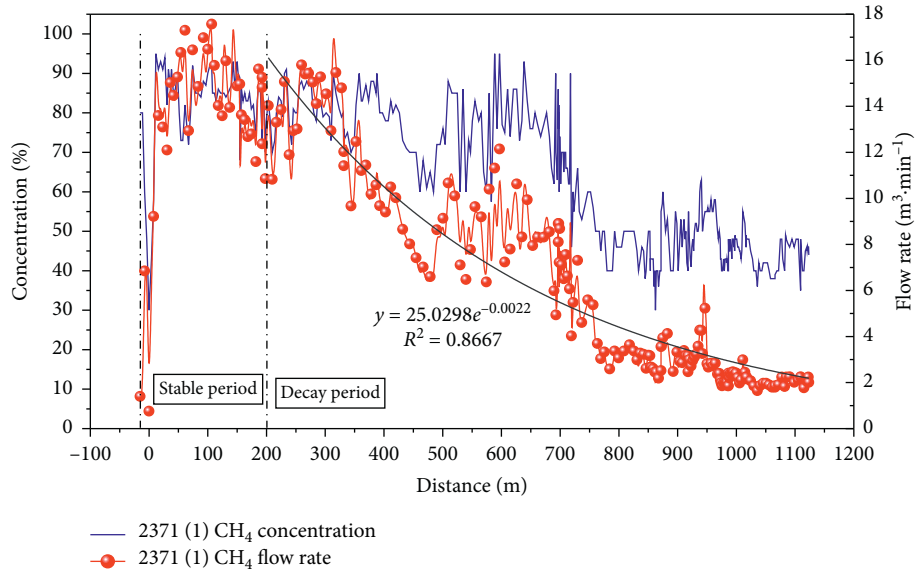
Type	Structural representation	Coal mines featuring successful application	Result
III		<p>Guqiao coal mine, as well as other coal mines in the Huainan mining area</p>	<p>The gas output of a single well is more than 1,000,000 m³, which solves the problem of gas extraction and pressure relief by rapidly advancing surface gas extraction drilling in complex geological and hydrogeological environments</p>
IV		<p>Pansan coal mine, as well as other coal mines in the Huainan mining area</p>	<p>The maximum single well gas extraction volume reached 7,500,000 m³</p>

rate were in the rising period until the mining face passed the drilling at 33 m; the gas extraction concentration was 81%, and the extraction rate was 15.89 m³/min. The working face

then passed through 33–109.2 m of drilling, and the extraction rate was stable during this period. The average gas extraction concentration was 64%, and the average



(a)



(b)

FIGURE 3: Continued.

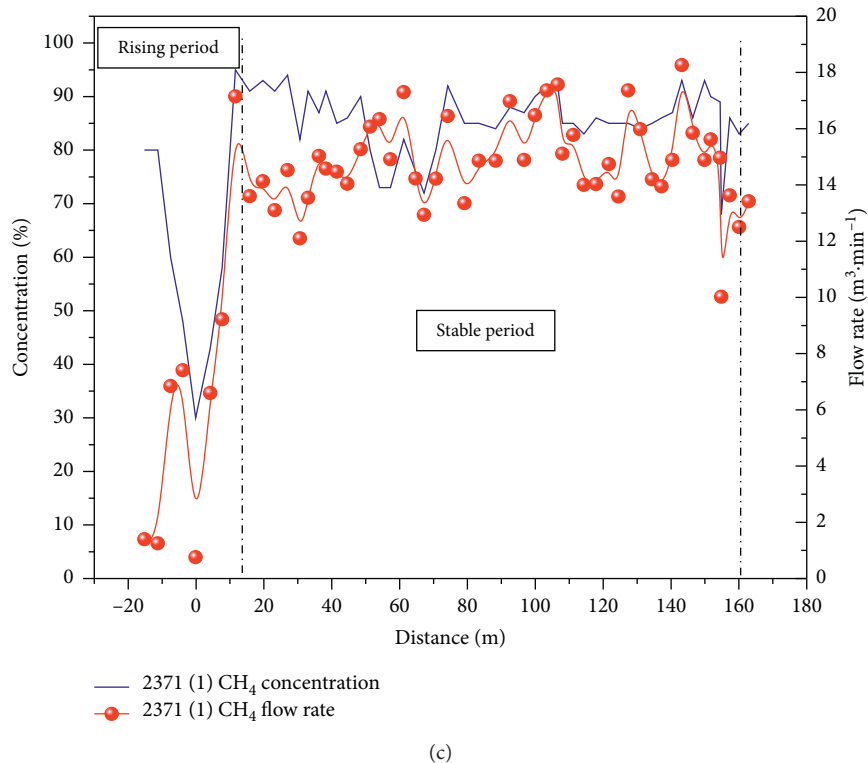


FIGURE 3: Diagram illustrating gas concentration and flow rate in gas extraction and pressure relief for typical single surface wells: (a) protective layer working face 2662(1), (b) protective layer working face 2371(1), and (c) protective layer working face 2371(1) rising period.

extraction rate was $11.84 \text{ m}^3/\text{min}$. After the working face passed the drilling (109.2 m), the extraction rate was in the attenuation period, and the extraction rate and mining progress (time) decreased exponentially.

The ground drilling No. 1 in the protective layer working face 2371(1) is a type II drilling structure, with a total of 427 days of extraction and 542.54 million m^3 of gas extraction. Figures 3(b) and 3(c) show that the periodic variation behavior of “rising period, stable period, and decay period” described previously is exhibited in this drilling system as well. The working face was 15.2 m away from the No. 1 ground drilling system, the gas extraction concentration was 80%, and the extraction rate was $1.25\text{--}1.4 \text{ m}^3/\text{min}$, which is the original coal extraction. When the working face was 7.5 m away from the No. 1 well, the gas extraction concentration was 60%, the extraction rate was $6.85 \text{ m}^3/\text{min}$, and the extraction rate was greatly increased, indicating that the protected layer 13^{-1} coal was released. When the working face was mined to the position of the No. 1 well on the ground, the gas extraction concentration was 30%, the extraction rate was $0.76 \text{ m}^3/\text{min}$, and the extraction concentration of ground drilling was significantly lower. Subsequently, the gas extraction concentration and extraction rate entered the rising period. When the working face passed a drilling depth of 11.6 m, the gas extraction concentration was 95% and the extraction rate reached $17.15 \text{ m}^3/\text{min}$. The working face passed through the drilling depths of 11.6–162.9 m, and the extraction rate was in the stable period. The average gas extraction concentration was

85.8% , and the average extraction rate was $14.86 \text{ m}^3/\text{min}$. After the working face passed the drilling depth of 162.9 m, the extraction rate entered the attenuation period, and the extraction rate and working face progress (time) decreased exponentially.

The structures of the No. 1 wells on the ground of the 2662(1) working face and 2371(1) working face are different, and the extraction time and amount are different, although both follow the periodic pattern of the “rising period, stable period, and decay period.” Therefore, after analyzing the extraction of surface drilling in the Huainan mining area, it was found that the typical characteristics of pressure relief gas extraction by surface drilling follow the periodic pattern of the “rising period, stable period, and decay period.”

3.3. Analysis of Gas Extraction by Multiple Ground Drilling Systems in the Same Working Face. The distance between ground drilling and extraction of pressure relief gas in the protective layer in the Huainan mining area is generally less than 300 m. Therefore, multiple drilling systems are arranged in the same working face. As shown in Figure 4, a total of five ground wells were arranged in the 1581(1) working face, and the ground well spacing was 230–260 m. After the working face was recovered from the No. 1 surface drilling system, the surface drilling extraction rate rose rapidly by $21.08 \text{ m}^3/\text{min}$, and after a short stable period, it entered a decay period. Before the working face mining to No. 2 surface drilling, the surface drilling extraction rate was

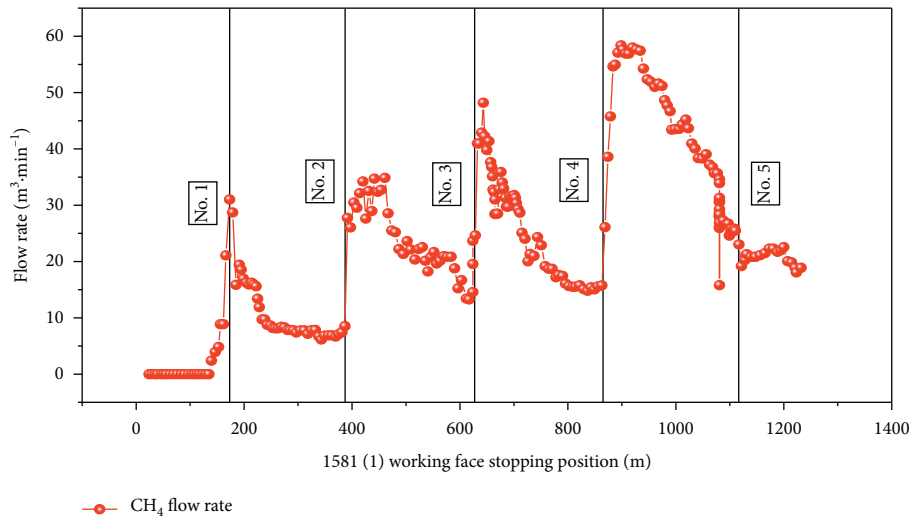


FIGURE 4: Cooperative extraction of five surface wells in 1581(1) working face.

attenuated to about $7 \text{ m}^3/\text{min}$, and the extraction volume of the working face recovered rapidly to $27.74 \text{ m}^3/\text{min}$ after the surface drilling of No. 2 was recovered. The extraction process of surface drilling at different positions in the same working face follows the periodic pattern of “rising period, stable period, and decay period.”

Because of the different locations and times at which surface drilling was conducted in the working face, the extraction rates of multiple surface drilling systems in the same working face were combined, the trend of the surface drilling extraction rate increased, and the extraction rate fluctuated with the position of surface drilling. When the working face was close to No. 4 surface drilling, the extraction volume decreased to $14.81 \text{ m}^3/\text{min}$. After the working face was recovered from No. 4 surface drilling, the surface drilling extraction volume rose rapidly to $58.38 \text{ m}^3/\text{min}$. After a short stabilization period, it entered the decay period. No. 5 surface drilling which was close to the retraction line of the working face; the recovery progress of the working face slowed down, the gas emission volume was reduced, and the combination of multiple surface drilling extraction rates was not obvious. In summary, when multiple ground drilling systems in the same working face perform extraction concurrently, the extraction rate of ground drilling increases with an increase in the number of drilling systems extracting simultaneously, and the extraction rate fluctuates with different ground drilling positions.

3.4. Analysis of the Causes of Surface Drilling Extraction Characteristics. In the mining process of the 11^{-2} coal protective layer working face in the Huainan mining area, the pressure relief gas extraction by surface drilling of the 13^{-1} coal protective layer was taken as an example for analysis. The influence of the mining-induced 11^{-2} coal protective layer on gas extraction in the goaf of the 11^{-2} coal face includes several main aspects. When the 11^{-2} coal working face passed through the ground drilling, the ground drilling system communicated with the 11^{-2} coal goaf, and

the air leakage in the goaf was large. With the 11^{-2} coal face advancing, the ground drilling and 11^{-2} coal goaf gradually compacted and the goaf air leakage was reduced and then gradually stabilized.

To determine the influence of mining changes in the 11^{-2} coal protective layer working face on the 13^{-1} coal protected layer, the expansion deformation rate of the protected layer working face was studied as an evaluation index, as shown in Figure 5. When the working face was 37.75 m away from the measuring point, the deformation rate of the 13^{-1} coal seam was 0. When the working face was 33.8 m away from the measuring point, the 13^{-1} coal seam expanded and deformed. When the working face was 0 m away, the expansion deformation rate of the 13^{-1} coal seam was 7.2% . When the working face passed the measuring point of 16.3 m , the expansion deformation rate of the 13^{-1} coal seam was 28.5% . After that, the 13^{-1} coal seam has contracted slightly, and when the working face passed the measuring point of 66.45 m , the expansion deformation rate of the 13^{-1} coal seam was 23.2% .

Before the surface drilling of the 11^{-2} coal face in the Huainan mining area, the protective layer of 13^{-1} coal generally began to unload pressure. When the working face passed through the ground drilling, the ground drilling communicated with the goaf of the 11^{-2} coal working face, the extraction volume was reduced, and the gas extraction concentration was generally at its lowest value. With the advancement of the 11^{-2} coal working face, the goaf of ground drilling and the 11^{-2} coal working face was gradually compacted, and the air leakage was gradually reduced. The expansion and pressure relief of the 13^{-1} coal protected layer in ground drilling and the amount of desorbed gas both increased, while the concentration and rate of gas extraction entered the rising period. With an increase in the goaf distance between the 11^{-2} coal face and the ground drilling, the goaf of the 11^{-2} coal face during ground drilling was basically stable. The range of the fully pressure relief zone of protected layer 13^{-1} extracted by ground drilling increased, and the amount of ground drilling extraction entered a stable period.

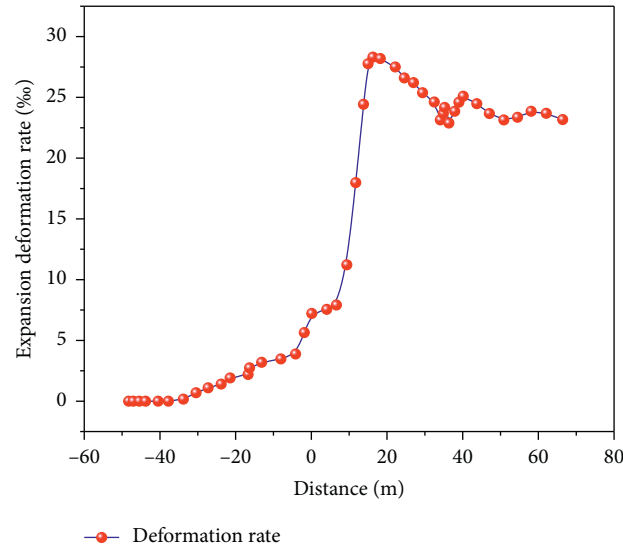


FIGURE 5: 1672(1) expansion deformation rate of the protected layer.

When the distance between the working face of the 11^{-2} coal seam and the ground drilling goaf increased to a certain range, the protected layer of 13^{-1} coal during ground drilling gradually entered the recompaction area from the fully depressurized area, and the gas content in the fully depressurized area decreased significantly, and the ground drilling pumping quantity entered the attenuation period. In summary, the periodic variation in the surface drilling extraction is mainly affected by changes in the mining of the protective layer working face. The rate of surface drilling extraction and the variation thereof are affected by the mining progress of the protective layer working face, mining height, degree of goaf compaction, degree of pressure relief of the protected layer, original gas content, and other measures for extraction of the protected layer.

After the protective layer working face passes through the drilling, the mined-out area is not fully compacted, and the air leakage is gradually reduced. Gas drilling occurs in the rising period, mainly manifested as an increase in the gas extraction concentration and extraction rate. The goaf of the protective layer working face is fully compacted, and the leakage is stable. Gas extraction by surface drilling occurs in the stable or attenuation period. The rate of gas extraction by surface drilling is mainly determined by the amount of pressure relief gas in the protective layer within the range of influence of surface drilling in the stable or decay period. In the range of influence of ground drilling, the amount of pressure relief gas in the protected layer is large, the gas extraction rate of ground drilling is stable, the fluctuation is small, and the trend line of the fitting curve is in a horizontal state, which represents the stable period of gas extraction from ground drilling. In the range of influence of ground drilling, the amount of gas released by the protective layer decreases, and the rate of gas extraction decreases.

The main feature of the surface drilling extraction volume from the rising stage to the stable stage is that the gas

extraction concentration reaches a maximum. Simultaneously, the variation trend of the extraction volume is considered. The fluctuation of extraction quantity in the stable period is small, the trend line of the fitting curve is in the horizontal state, and the gas extraction concentration is generally stable. The stable period transitions to the decay period mainly because the extraction volume begins to decline, and the extraction volume and stopping schedule or time in the decay period decrease exponentially.

4. Conclusions

- (1) Through the analysis of pressure relief gas flow and extraction concentration of protected layer extraction by surface drilling in different working faces, it was found that, after the protected layer working face was pushed through the surface drilling, the gas extracted by surface drilling showed a periodic variation summarized as the “rising period, stable period, and decay period.”
- (2) When multiple ground drilling systems were used in the same working face coordinate extraction, the extraction rate is superimposed, and the extraction rate increases with an increase in the number of drilling systems. The extraction rate fluctuated with different ground drilling positions. The extraction rate was small before the working face was pushed through ground drilling, and increased afterward.
- (3) The periodic variation in surface drilling extraction is mainly affected by the mining progress of the protective layer working face, mining height, degree of goaf compaction, degree of pressure relief of the protected layer, original gas content, and other protective layer measures. The rate of gas extraction by surface drilling is mainly determined by the amount of pressure relief gas in the protective layer within the influence range of surface drilling in the stable or decay period.

- (4) The main change from the rising period to the stable period is that the gas extraction concentration reaches the maximum value, considering the trend of the extraction volume. The main change from the stable period to the attenuation period is that the extraction rate begins to decline, and the extraction rate in the decay period decreases exponentially with the recovery progress or time.

Data Availability

The data used to support the findings of the study are all available within the article.

Conflicts of Interest

The authors declare that there are no conflicts of interest regarding the publication of this paper.

Acknowledgments

This study was supported by the Natural Science Foundation of China (51974240) and the Key Special Projects of National Key R&D Plan (2016YFC0801802).

References

- [1] F. Zhou, T. Xia, X. Wang et al., "Recent developments in coal mine methane extraction and utilization in China: a review," *Journal of Natural Gas Science and Engineering*, vol. 31, pp. 437–458, 2016.
- [2] J. J. Zhang, K. L. Xu, G. Reniers, and G. You, "Statistical analysis the characteristics of extraordinarily severe coal mine accidents (ESCMAs) in China from 1950 to 2018," *Process Safety and Environmental Protection*, vol. 133, pp. 332–340, 2019.
- [3] H. Wen, X. J. Cheng, S. X. Fan et al., "A method for detecting hidden fire source in deep mine goafs based on radon measurement and its experimental verification," *Applied Geochemistry*, vol. 117, Article ID 104603, 2020.
- [4] Z. Li, G. R. Feng, H. N. Jiang et al., "The correlation between crushed coal porosity and permeability under various methane pressure gradients: a case study using Jincheng anthracite," *Greenhouse Gases: Science and Technology*, vol. 8, pp. 493–509, 2018.
- [5] Z. Li, G. R. Feng, Y. Luo et al., "Multi-tests for pore structure characterization-A case study using lamprophyre," *AIP Advances*, vol. 7, no. 8, Article ID 085204, 2017.
- [6] IPCC, "IPCC fourth assessment report: climate change," Technical Report, AR4, Geneva, Switzerland, 2007.
- [7] B. H. Shen, J. Z. Liu, and H. Zhang, "The technical measures of gas control in China coal mines," *Journal of China Coal Society*, vol. 7, pp. 673–679, 2007.
- [8] Q. Zhang, X. P. Zhang, and W. Sun, "A review of laboratory studies and theoretical analysis for the interaction mode between induced hydraulic fractures and pre-existing fractures," *Journal of Natural Gas Science and Engineering*, vol. 86, Article ID 103719, 2020.
- [9] W. Yang, B. Q. Lin, Y. B. Gao et al., "Optimal coal discharge of hydraulic cutting inside coal seams for stimulating gas production: a case study in Pingmei coalfield," *Journal of Natural Gas Science and Engineering*, vol. 28, pp. 379–388, 2016.
- [10] D. D. Chen, W. R. He, S. R. Xie et al., "Increased permeability and coal and gas outburst prevention using hydraulic flushing technology with cross-seam borehole," *Journal of Natural Gas Science and Engineering*, vol. 73, Article ID 103067, 2019.
- [11] R. Zhang, Y. P. Cheng, L. Yuan et al., "Enhancement of gas drainage efficiency in a special thick coal seam through hydraulic flushing," *International Journal of Rock Mechanics and Mining Sciences*, vol. 124, Article ID 104085, 2019.
- [12] X. H. Song, Y. T. Guo, J. Zhang et al., "Fracturing with carbon dioxide: from microscopic mechanism to reservoir application," *Joule*, vol. 3, no. 8, pp. 1913–1926, 2019.
- [13] L. Y. Yang, A. Y. Yang, S. Y. Chen et al., "Model experimental study on the effects of in situ stresses on pre-splitting blasting damage and strain development," *International Journal of Rock Mechanics and Mining Sciences*, vol. 138, Article ID 104587, 2021.
- [14] A. T. Zhou, L. P. Fan, K. Wang et al., "Multiscale modeling of shock wave propagation induced by coal and gas outbursts," *Process Safety and Environmental Protection*, vol. 125, pp. 164–171, 2019.
- [15] G. Z. Hu, W. R. He, and M. Sun, "Enhancing coal seam gas using liquid CO₂ phase-transition blasting with cross-measure borehole," *Journal of Natural Gas Science and Engineering*, vol. 60, pp. 164–173, 2018.
- [16] H. Wen, X. J. Cheng, J. Chen et al., "Micro-pilot test for optimized pre-extraction boreholes and enhanced coalbed methane recovery by injection of liquid carbon dioxide in the Sangshuping coal mine," *Process Safety and Environmental Protection*, vol. 136, pp. 39–48, 2020.
- [17] X. J. Cheng, H. Wen, S. X. Fan et al., "Liquid CO₂ high-pressure fracturing of coal seams and gas extraction engineering tests using crossing holes: a case study of Panji coal mine no. 3, Huainan, China," *International Journal of Energy Research*, vol. 45, 2020.
- [18] G. M. Wei, H. Wen, J. Deng et al., "Enhanced coalbed permeability and methane recovery via hydraulic slotting combined with liquid CO₂ injection," *Process Safety and Environmental Protection*, vol. 136, pp. 234–244, 2020.
- [19] G. M. Wei, H. Wen, J. Deng et al., "Liquid CO₂ injection to enhance coalbed methane recovery: an experiment and in-situ application test," *Fuel*, vol. 284, Article ID 119403, 2020.
- [20] H. Wen, Z. B. Li, J. Deng et al., "Influence on coal pore structure during liquid CO₂-ECBM process for CO₂ utilization," *Journal Of CO₂ Utilization*, vol. 21, pp. 543–552, 2017.
- [21] H. Wen, M. Y. Liu, G. M. Wei et al., "Gas displacement engineering test by combination of low and medium pressure injection with liquid CO₂ in high gas and low permeability coal seam," *Geofluids*, vol. 2020, Article ID 8840602, 13 pages, 2020.
- [22] S. X. Fan, D. Zhang, H. Wen et al., "Enhancing coalbed methane recovery with liquid CO₂ fracturing in underground coal mine: from experiment to field application," *Fuel*, vol. 290, Article ID 119793, 2020.
- [23] S. X. Fan, H. Wen, Y. F. Jin et al., "Initiation pressure model for liquid CO₂ fracturing through upward penetrating boreholes and its engineering verification," *Journal of Rock Mechanics and Engineering*, vol. 40, no. 4, pp. 703–712, 2021.
- [24] S. X. Fan, H. Wen, X. J. Cheng et al., "Research and application of set equipment of permeability enhancements induced by high-pressure (30 MPa) L-CO₂ fracturing," *Journal of China Coal Society*, pp. 1–12, 2021.
- [25] H. D. Chen, Y. P. Cheng, H. X. Zhou et al., "Damage and permeability development in coal during unloading," *Rock Mechanics and Rock Engineering*, vol. 46, pp. 1377–1390, 2013.

- [26] S. Q. Lu, Y. P. Cheng, and W. Li, "Model development and analysis of the evolution of coal permeability under different boundary conditions," *Journal of Natural Gas Science Engineering*, vol. 31, pp. 129–138, 2016.
- [27] S. G. Wang, D. Elsworth, and J. Liu, "Permeability evolution during progressive deformation of intact coal and implications for instability in underground coal seams," *International Journal of Rock Mechanics Mining Sciences*, vol. 58, pp. 34–45, 2013.
- [28] M. Tu, N. B. Huang, B. A. Liu et al., "Research on pressure-relief effect of overlying coal rock body using far distance lower protective seam exploitation method," *Journal of Mining and Safety Engineering*, vol. 24, no. 4, pp. 418–421, 2007.
- [29] J. Kan, Y. P. Cheng, W. Wei et al., "Evaluation of the remote lower protective seam mining for coal mine gas control: a typical case study from the Zhuxianzhuang coal mine, Huaibei coalfield, China," *Journal Natural Gas Science and Engineering*, vol. 33, pp. 44–55, 2016.
- [30] L. Yuan, "Theory of pressure-relieved gas extraction and technique system of integrated coal production and gas extraction," *Journal of China Coal Society*, vol. 34, no. 1, pp. 1–8, 2009.
- [31] J. L. Xu and M. G. Qian, "Study on drainage of relieved methane from overlying coal seam far away from the protective seam by surface well," *Journal of China University of Mining & Technology*, vol. 1, pp. 78–81, 2000.
- [32] L. Yuan, H. Guo, P. Li et al., "Theory and technology of goaf gas drainage with largediameter surface boreholes," *Journal of China Coal Society*, vol. 38, no. 1, pp. 1–8, 2013.
- [33] F. X. Lian, "Completion technology of surface gas extraction wells," *Coal Geology & Exploration*, vol. 40, no. 6, pp. 29–38, 2012.
- [34] Z. J. Wang, "Optimum surface drilling gas drainage technique based on "O" ring theory," *Coal Mining Technology*, vol. 22, no. 5, pp. 96–101, 2017.
- [35] J. G. Wu, "Integrated technology of coalbed methane drainage with ground well in Luling coal mine," *Coal Geology & Exploration*, vol. 1, pp. 27–29+33, 2008.
- [36] G. C. Hao, S. Y. Hu, X. Q. Guo et al., "Study on destruction characteristics of surface vertical wells in mining area of Sihe coal mine," *Safety in Coal Mines*, vol. 51, no. 3, pp. 48–51, 2020.
- [37] P. Liu, J. Y. Fan, D. Y. Jiang et al., "Evaluation of underground coal gas drainage performance: mine site measurements and sensitivity analysis of fracture-matrix interaction parameters," *Process Safety and Environmental Protection*, vol. 148, pp. 711–723, 2021.
- [38] L. Wang, Y. P. Cheng, F. H. An et al., "Characteristics of gas disaster in the Huaibei coalfield and its control and development technologies," *Natural Hazards*, vol. 71, no. 1, pp. 85–107, 2014.

Research Article

Distribution Characteristics and Formation Mechanism of Surface Crack Induced by Extrathick Near Horizontal Seam Mining: An Example from the Datong Coal Field, China

Yueguan Yan ¹, Weitao Yan ², Huayang Dai,¹ and Junting Guo³

¹College of Geoscience and Surveying Engineering, China University of Mining and Technology, Beijing 100083, China

²School of Surveying and Land Information Engineering, Henan Polytechnic University, Jiaozuo, Henan 454003, China

³State Key Laboratory of Groundwater Protection and Utilization by Coal Mining, Beijing 102009, China

Correspondence should be addressed to Weitao Yan; yanweitao@hpu.edu.cn

Received 18 February 2021; Revised 7 April 2021; Accepted 21 May 2021; Published 30 May 2021

Academic Editor: Jia Lin

Copyright © 2021 Yueguan Yan et al. This is an open access article distributed under the Creative Commons Attribution License, which permits unrestricted use, distribution, and reproduction in any medium, provided the original work is properly cited.

Under the mining condition of extrathick coal seam, the overburden moves violently, the surface is destroyed seriously, and the discontinuous deformation such as cracks is fully developed. Taking Datong mining area as an example, this paper studies and analyzes the development characteristics and generation mechanism of surface cracks in loose layer covered area and bedrock exposed area by means of field measurement and similar model experiment. In the bedrock exposed area, there is no main crack. The width, length, number, and step drop of surface cracks are relatively small. There are many cracks with the same scale and distributed evenly and parallel. However, in the loose covered area, the main cracks are mainly located above the open-off cut and the stoppage line side that is deviated from the working face. There are many secondary cracks around the main crack, with a large crack density and a few cracks in the outer edge of the main crack. Through research, it is found that three mining faces belong to the typical three-zone mining mode and the main fracture is consistent with the O-ring fracture distribution theory. This research's results can provide theoretical and technical support for the follow-up land remediation and ecological restoration.

1. Introduction

Coal industry is closely related to sustainable development. From the social, economic, and environmental aspects, it has both positive and negative driving effects [1, 2]. Coal is a widely distributed energy source in China, mainly concentrated in Xinjiang, Qinghai, Shaanxi, Inner Mongolia, Shanxi, Henan, Hebei, Shandong, Jiangsu, Anhui, and other provinces. The mining of underground coal resources often leads to large-scale overburden movement and surface subsidence. According to the mining subsidence knowledge, the greater the mining thickness, the more serious the surface subsidence. So, when mining the thick seam and extrathick seam, the surface subsidence is the most serious. When the mining thickness of the coal seam is thick or extrathick, the roof is broken seriously. After the mining influence transmits to the ground surface, cracks, collapse pits, landslides, and other disasters are formed. As a result, the buildings in the mining

area are seriously damaged, the groundwater level is lowered, the railway and highway are blocked, and the other secondary geological disasters are produced [3–7].

The mining of extrathick coal seam often causes discontinuous damage to the ground surface and then forms the surface cracks [8, 9]. Up to now, some scholars at home and abroad have studied the distribution law of surface cracks after mining of extrathick coal seam [10, 11]. Due to the large mining thickness, the failure height of overlying strata can reach 200–350 m with the mining of extrathick coal seam under the hard roofs [12]. Gao et al. obtained the surface subsidence prediction parameters and angular parameters of Dongpo coal mine and studied the surface subsidence law and its particularity of fully mechanized top coal caving mining in extrathick coal seam under the conditions of near shallow buried depth and medium-thick bedrock [13]. Guo et al. derived the calculation method of surface mining crack width according to the basic

characteristics of surface movement and surface limit deformation [14]. Gao et al. investigated and analyzed the influence of hard rock crack in different layers on the surface stress distribution under the mining conditions of extrathick coal seam [15, 16]. Ma et al. used a variety of algorithms to analyze the possibility of landslide caused by thick coal seam mining [17, 18]. Guo et al. discussed the roof support technology under the condition of fully mechanized mining in hard overburden and extrathick coal seam [19]. Lan et al. measured and analyzed the rock movement characteristics of thick coal seam mining under the action of a thick hard roof [20]. Chen et al. analyzed and studied the influence of mining on the underground roadway under the condition of 10 m mining height and constructed the safety evaluation method [21]. Singh et al. studied the movement mode of overburden under the condition of large mining height in the mountainous area [22]. Huang et al. established the prediction method of residual deformation in the mining of extrathick and steeply inclined coal seam [23]. Wang and Wang studied the movement law and control technology of surrounding rock system under thick coal seam mining [24]. Nayzar et al. analyzed the interaction effects in double extrathick coal seams mining [25]. Matsui et al. studied the underground mining systems for extrathick coal seams [26].

According to the above literature analysis, there are many studies on the surface subsidence law and the distribution characteristics of mining cracks caused by the mining of extrathick steeply inclined coal seams, but there are few studies on the surface mining cracks of extrathick near horizontal coal seams. Therefore, this paper takes a coal mine in Datong City as the research object and uses similar material model experiments to conduct in-depth research on the distribution characteristics and formation mechanism of surface cracks caused by the mining of extrathick near horizontal coal seams.

2. Survey of Research Area

2.1. Geological and Mining Conditions of Research Area. The research area is located in a coal mine in Datong City, with a design production capacity of 3 million Ton/year, and the mining face is supported by suspended support. This mine adopts the strike longwall mining method to excavate and the all caving method to manage the roof. The recovery rate is more than 80%. Coal seam 3 is mined in this study area. The buried depth of the coal seam 3 is 295~380 m, the full thickness is 21.38~28.01 m, and the dip angle is about 3°. The overlying strata are mostly sandstone and mudstone.

Three longwall working faces are mined, including working faces 1505, 1506, and 1502 successively from south to north. The thickness of the coal seams of the three working faces is 21.20~32.43 m. The inclination angle of the coal seam is about 3°. In China, when the thickness of the coal seam is more than 3.5 m, it is a thick coal seam, and when the thickness of the coal seam is more than 8.0 m, it is an extrathick coal seam. When the dip angle of the coal seam is less than 8°, it is a near horizontal coal seam. So, these three working surfaces are typical extrathick near horizontal seam mining. The relative position of those working faces is shown in Figure 1.

The mining method of three working faces is fully mechanized top coal caving. The top view and cross-sectional view of the caving situation are shown in Figure 2.

2.2. Measured Distribution Characteristics of Surface Cracks. After the three working faces were mined in sequence, various cracks occurred on the surface, as shown in Figure 3.

In Figure 3, the red thick curve represents the large crack with the drop greater than 1 m and the width greater than 20 cm, also known as the main crack; the blue thin curve represents the crack with the drop less than 1 m and the width less than 20 cm, referred to as the small crack. It can be seen from Figure 3 that the crack area is located around the goaf, and the crack width and depth in different areas are different. Working face 1502 is close to the mountain, the mountain is steep, and the cracks on the mountain are mainly tensile cracks. The side near the mountain body of working face 1502 is mainly exposed bedrock area, and the north side is the mountain body. The surfaces above the working faces 1505 and 1506 are mainly covered by loess. Compared with the loess area, the shape and distribution of cracks in the bedrock exposed area are different.

2.2.1. Distribution of Surface Cracks in Loess-Covered Area.

Open-off cut side: In working faces 1505 and 1506, the crack area appears above and outside the open-off cut along the open-off cut direction. The main crack strikes in the north-south direction and is continuous along this direction. There are two main cracks along the strike direction above the goaf of 1505 working face (Figure 4(a)). The length is 200–220 m. Two main cracks are located at the edge of the goaf, and many small cracks are generated around the main crack about 50 m, which is consistent with the trend of the main crack. The length of small parallel cracks is 50–180 m.

Stop mining line side: The cracks at the stop line of working faces 1505 and 1506 are located on the inner side of the working face, and there are several similar cracks with large lengths and widths. There are many small- and medium-sized cracks at the stop line of working face 1505 near the farmland, which have great density and complexity, and seriously damage the farmland. A large area of stepped arc-shaped cracks appeared at the stop line of working face 1506. The depth of the main crack is about 2.4 m. The distribution of the cracks is regular. There are few cracks in the outer edge of several main cracks. The cracks are mainly close to the side of the belt roadway, just above the mining area.

Above the goaf: The middle part of the goaf of working faces 1505 and 1506 showed overall collapse, there are large cracks and many cracks of different sizes (Figure 4(b)). The distribution density of cracks is not uniform, the strike direction is not consistent, and the damage degree is different. Through field survey, the large-scale surface deformation area of this type of goaf occurs within the boundary of working face 130 m. The surface deformation is a typical “cutting and caving form,” which shows that the deformation of the upper part of the mining boundary and the surrounding area is strong, and the deformation outside the crack is greatly weakened (Figure 4(c)).

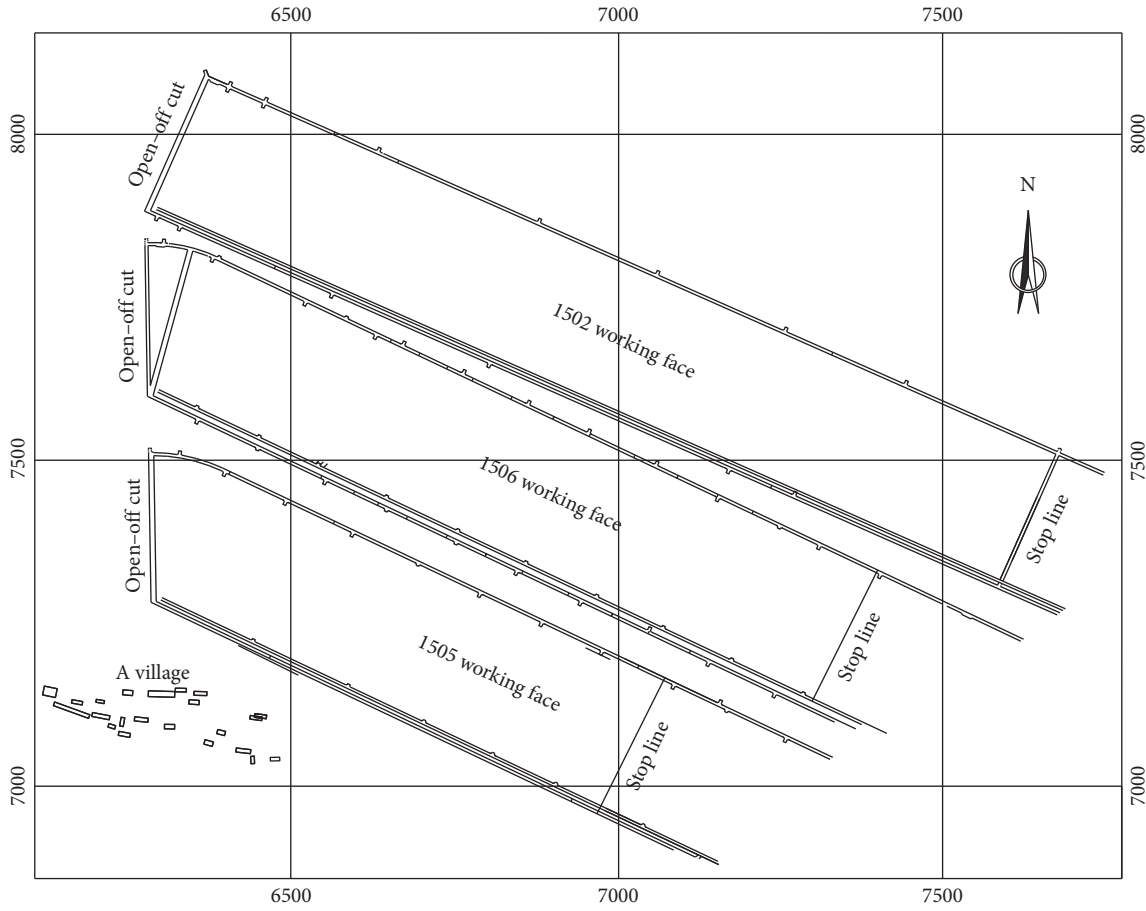
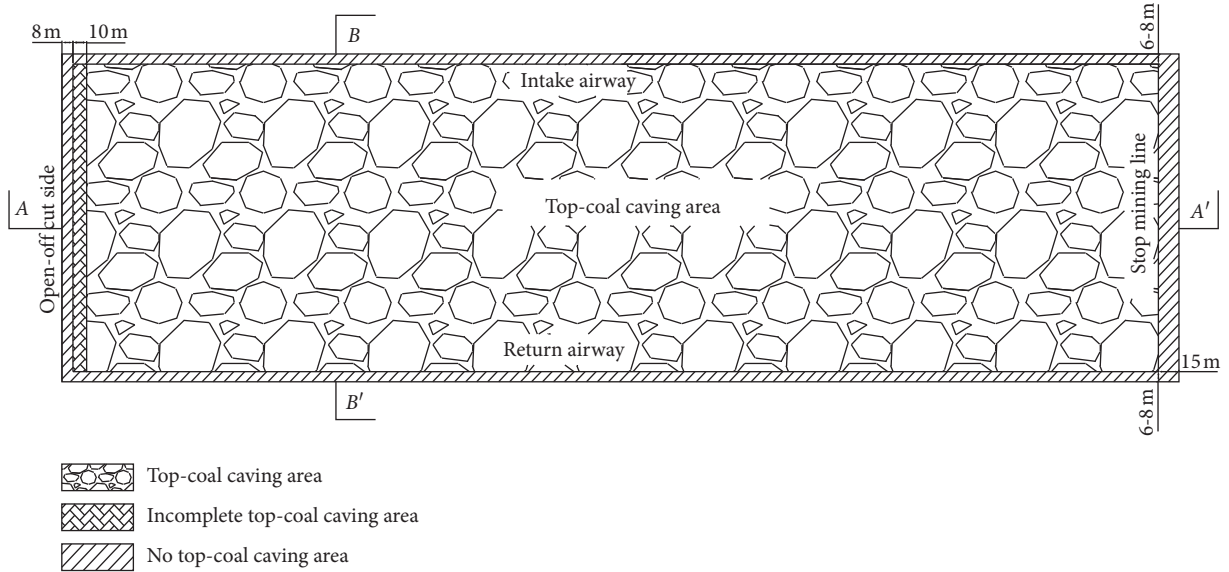


FIGURE 1: Working face layout.



(a)

FIGURE 2: Continued.

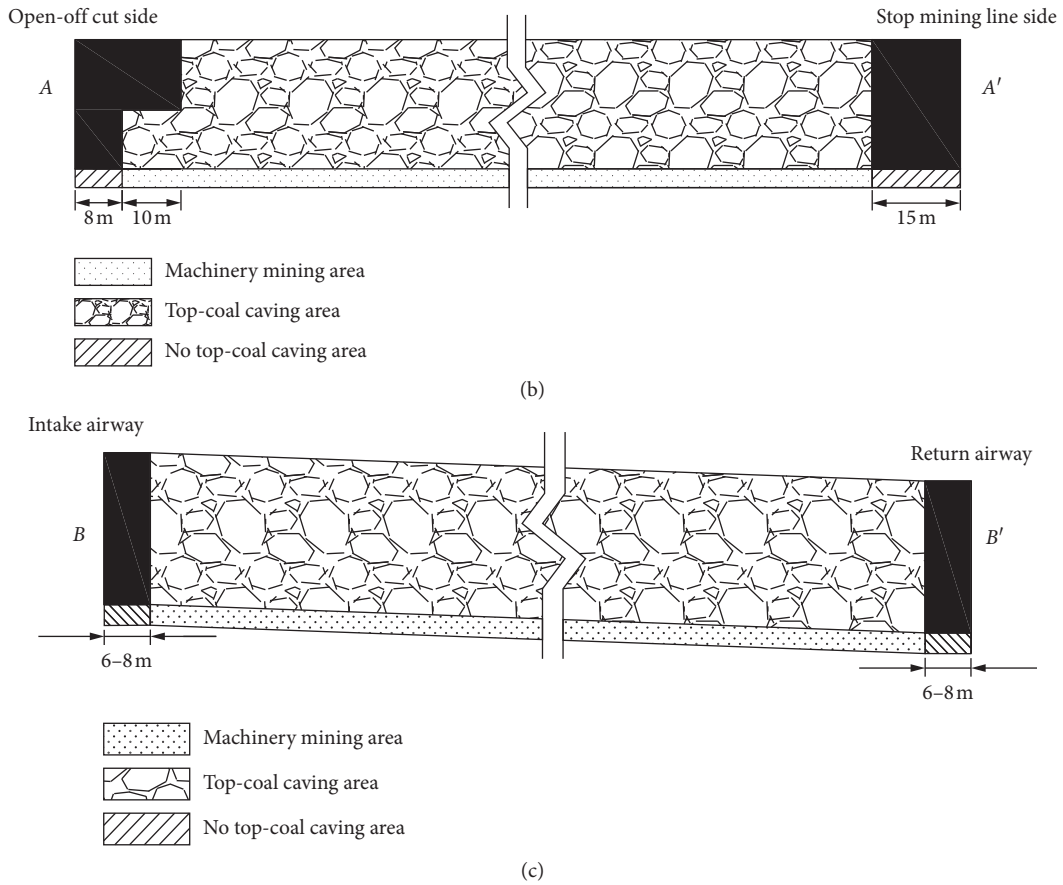


FIGURE 2: Top and cross-sectional view of the caving situation. (a) Top view. (b) Cross-sectional view of line AA'. (c) Cross-sectional view of line BB'.

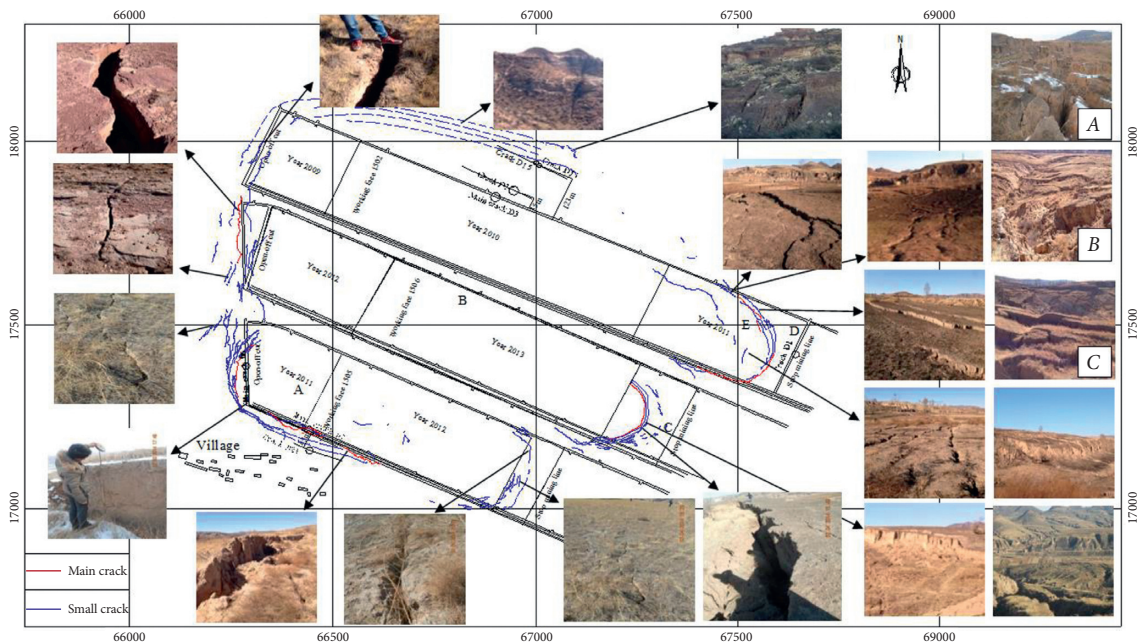


FIGURE 3: Distribution of surface cracks and cracks relative position and cracks photos.

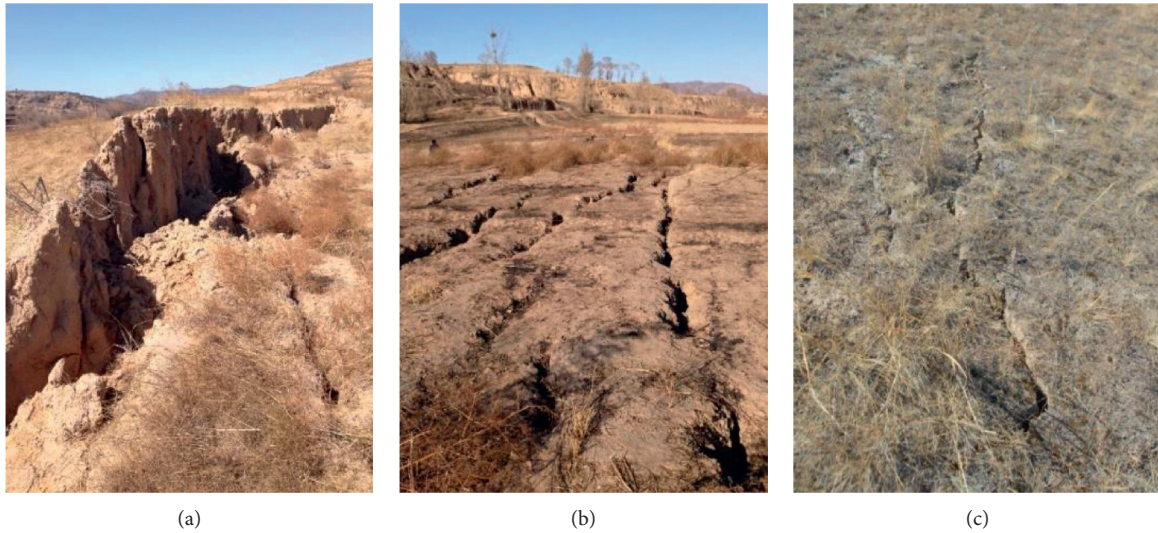


FIGURE 4: Morphology of surface cracks in loess-covered area. (a) Surface cracks near the boundary of goaf (main crack). (b) Crack right above the middle of goaf. (c) Crack near the surface movement basin margin.

2.2.2. Distribution Law of Surface Cracks in Bedrock Exposed Area. In 1502 working face, the main crack appears in the upward direction of the open-off cut near the mountain (Figure 5). The main crack is located in the bedrock exposed area. Compared with the main crack in the loess area, the width and drop of cracks are small. At the same time, the length of other cracks is shorter than that in the loess area. The uphill direction of working face 1502 is the mountain. There is no main crack in the mountain, but many parallel cracks with the same scale and uniform distribution are formed. In working face 1502, the terrain of the stoppage line is gentle, and many medium cracks are evenly distributed. With the generation of large cracks, there are few small cracks.

3. Research Method

3.1. Experimental Model Making. This simulation is limited by the size of the model frame, only working faces 1505 and 1506 are simulated. The comprehensive histogram of the mining area is shown in Figure 6. According to the actual geological and mining conditions of the mining area, a similar material model of the dip section of the coal face is established.

The size of the experimental frame model is 2990 mm × 1610 mm × 250 mm, the geometric similarity constant of similar material model is 350, the similarity constant of bulk density is 0.6, the strength ratio is 210, and the time ratio is 20. The measuring points are evenly arranged on the surface of the model. The two sides of the observation points on the same floor are equally spaced by 5 cm, and other points are spaced every 10 cm in the middle part. A total of six lines are arranged, from top to bottom as A, B, C, D, E, and F, as shown in Figure 7. Line A is the surface observation line, line B is arranged on the interface between loose layer and bedrock, and lines C, D, E, and F are placed on the bedrock of different layers.

3.2. Material Ratio. According to the similarity constant, the parameters of model laying are calculated. Quartz sand is selected as aggregate, and gypsum and lime mixture is used as cementation material. Combined with the bulk density and compressive strength of the simulation material, the material ratio and model making are carried out. Table 1 shows the geometric parameters and proportioning parameters of similar material model experiments.

3.3. Model Mining and Observation. After the completion of the model, first mining working face 1505, and then mining working face 1506, the subsidence is observed four times, two times before mining, and the average value was taken as the initial value, and once after the mining of working faces 1505 and 1506, respectively. The accuracy of the observed subsidence is higher than ±0.2 mm.

4. Results and Discussion

4.1. Distribution Laws of Mining Crack. After the mining, the upper roof collapsed and a large range of collapse occurred. The width of the caving zone was 540 mm and the height was 432 mm. The height of the caving zone was about 5~6 times the coal thickness. The height of the fracture zone is 220 mm, and the bending zone reaches the ground surface. There are three kinds of mining affected zones in overlying strata, including caving zone, fracture zone, and bending zone, which is a typical “three-zone” model.

After the mining of working faces 1505 and 1506, cracks appear on the left and right sides of the goaf. On the left, a large crack appears just above the open-off cut of working face 1505 (such as crack 2 in Figures 8 and 9). With the passage of time, the crack gradually becomes larger and forms the main crack. The depth of the main crack runs through the whole loose layer and reaches the bedrock surface. The width of the main crack is consistent with the

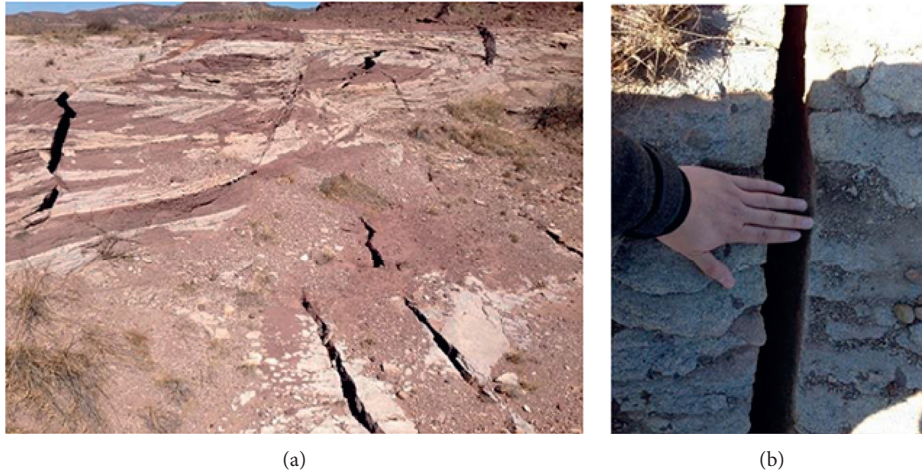


FIGURE 5: Morphology of surface cracks in bedrock exposed area.

measured situation and finally forms the step shape shown in crack 2. At the side where the large crack is far away from the goaf, some small cracks (such as crack 1) are gradually produced, and the distance between the outermost crack of the goaf and the large crack is 328 mm.

On the right, two cracks also appear on the side of the 1506 working face that deviates from the working face (such as crack 3 and crack 4). The main characteristics of the cracks on the right side of the goaf are that the distance between the outermost crack and the crack above the mining boundary is 231 mm. With the gradual transfer of overburden movement to the surface, both sides of the surface main crack (crack 3) above the mining boundary of working face 1505 gradually subsided and moved, and the subsidence difference on both sides of the crack gradually increased and finally formed a bench crack with a drop of 1.5 m. The maximum width of crack 3 is 2.1 m, and the final depth of crack 3 is 140 m. It is quite different from the general mining subsidence studies or the maximum depth of cracks measured in other areas (generally less than 10 m). The main reason is that the lithology of overburden rock in the study area is hard and sudden subsidence occurs in the mining process, resulting in the surface deformation rate is large, thus forming cracks throughout the loose layer. There are cracks on both sides of the goaf, and the development morphology and geometric characteristics of the cracks are basically consistent.

Overall, the above mining face belongs to the typical three-zone mining mode. The main fractures are mainly distributed near the edge of the goaf, which is consistent with the O-ring fracture distribution theory.

4.2. Reasons for the Difference of Crack Development in Different Surface Coverage Areas. The distribution of surface fractures is consistent with the O-ring theory. According to the O-ring theory, after mining, the fractures are mainly distributed around the goaf, similar to the O-shape circle. However, in different geotechnical coverage areas, the development rules of surface cracks are different.

- (1) The cracks in the loess-covered area are fully developed, with various types and different laws. The reasons are as follows:
 - (a) In the loess-covered area, the loess structure is soft and has significant anisotropy. Due to the existence of loess, it is equivalent to softening the overlying layer.
 - (b) The mechanical strength of resistance to tensile deformation, resistance to compression deformation, and resistance to bending deformation is very low. In particular, the tensile deformation resistance is very weak. When the tensile deformation capacity of the ground surface exceeds 2-3 mm/m, the ground surface will be broken and cracks will appear. So, the surface cracks in the loess-covered area are fully developed, with both large and small cracks.
 - (c) At the same time, the vertical joints in the loess are fully developed, and vertical cracks are easily formed after being disturbed by mining. Due to the development of vertical joints in the loess and the soft shear resistance, large vertical cracks of the cut-off type are easily formed in the loess above the cracks in the bedrock surface; and around the large cracks, the loess has a very weak tensile deformation resistance. Therefore, many small irregular cracks are formed around the large crack.
- (2) Compared to the loess-covered area, the cracks in the bedrock exposed area are relatively small but have strong regularity. The reasons are as follows:
 - (a) The bedrock in the bedrock exposed area is directly exposed on the ground surface without loose layer covering. Compared with the loess-covered area, the overlying rock is generally stronger in lithology, and the bedrock has stronger resistance to deformation. Therefore, the number of surface cracks in the bedrock exposed area is small, the width is small, and the depth is shallow.

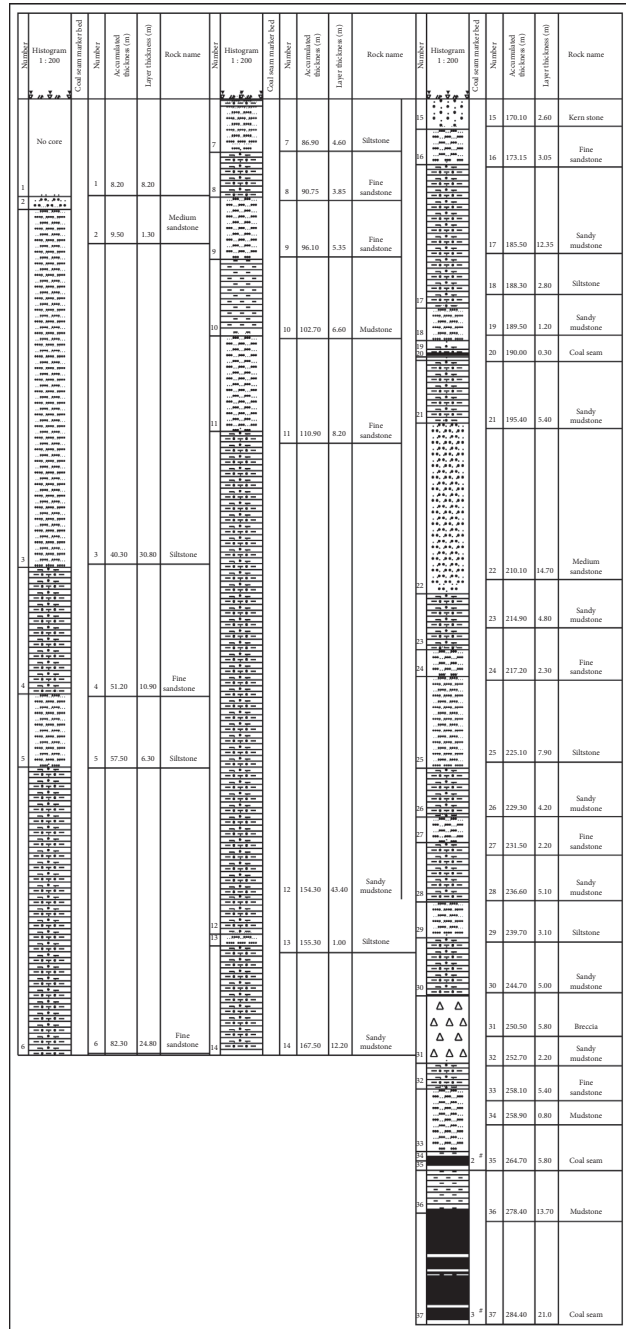


FIGURE 6: Comprehensive histogram of the borehole.



FIGURE 7: Experimental model and measuring point layout.

TABLE 1: Material ratio table of model test.

Rock stratum	Layer thickness (mm)	Material ratio Sand:lime:gypsum	Sand (kg)	Lime (g)	Gypsum (g)	Water (ml) 7% calculation
1 Loose layer	150					
2 Sandy mudstone	540	120:4:6	536.3	17876.9	26815	40670
3 Fine sandstone	105	40:3:2	107.6	5377.8	8067	8470
4 Coal seam	60	20:3:7	19.5	1200.0	300	1470
5 Sandy mudstone	250	120:4:6	248.4	8280.0	12420	18837

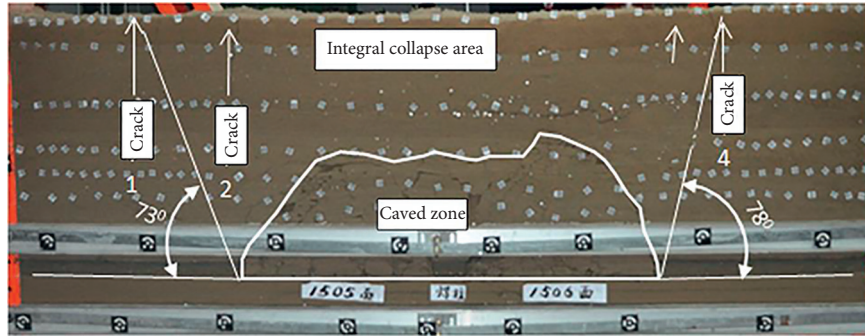


FIGURE 8: Crack distribution and overburden failure map of model mining.

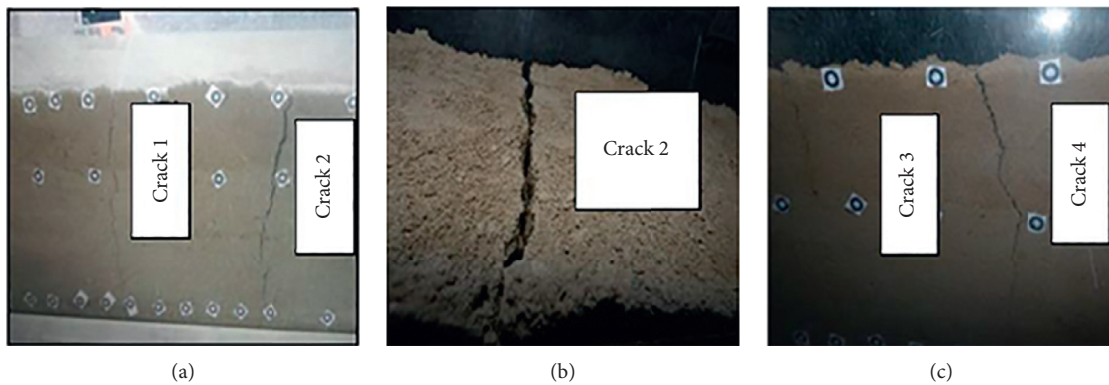


FIGURE 9: Local enlarged map of surface crack distribution.

(b) The generation of cracks in the bedrock mainly develops along the weak surface of the rock mass. Because the distribution of weak surfaces in the rock body has a strong regularity overall, the distribution of the cracks in the bedrock also has a strong regularity. After the cracks are exposed on the surface, they also have strong regularity; there are many cracks with the same scale and distributed evenly and in parallel.

5. Conclusion

Based on the analysis of the existing and measured data of the extrathick coal seam in the Datong mining area, combined with the similar material model test research, the following main conclusions are drawn.

(1) Three mining faces belong to the typical three-zone mining mode. The main fracture is consistent with the O-ring fracture distribution theory.

(2) In the loess-covered area, cracks are fully developed. The main cracks are mainly located above the open-off cut, outside of the open-off cut and the stoppage line side that is deviated from the working face. There are many secondary cracks around the main crack, with a large crack density and few cracks in the outer edge of the main crack.

(3) Compared with the loess-covered area, the width, length, number, and step drop of surface cracks in the bedrock exposed area are smaller. There is no main crack, and there are many cracks with the same scale and distributed evenly and in parallel.

Data Availability

The data used to support the findings of this study are available from the corresponding author upon request.

Conflicts of Interest

The authors declare no conflicts of interest.

Authors' Contributions

W.Y. conceptualized the study. Y.Y. developed methodology. W.Y. provided the software. H.D. and J.G. performed validation. W.Y. performed formal analysis. Y.Y. performed investigation. Y.Y. provided the resources. J.G. performed data curation. Y.Y. wrote the original draft. W.Y. reviewed and edited the article. J.G. performed visualization. H.D. supervised the study. Y.Y. performed project administration. Y.Y. was responsible for funding acquisition. All authors have read and agreed to the published version of the manuscript.

Acknowledgments

This research was funded by the Fundamental Research Funds for the Central Universities (2021YQDC09), National Natural Science Foundation of China (Grants nos. 50974122 and U1810203), the Youth Backbone Teacher Support Program of Henan Polytechnic University (Grants no. 2019XQG-07), the Fundamental Research Funds for the Universities of Henan Province (Grant no. NSFRF200314), the Henan Scientific and Technological Projection (Grant no. 212102310012), the Open Fund of State Key Laboratory of Water Resource Protection and Utilization in Coal Mining (Grants nos. WPUKFJJ2019-20 and WPUKFJJ2019-17).




References

- [1] T. A. Elmira, K. Reza, A. Mohammad, and R. T. Mohammad, "A review of studies on sustainable development in mining life cycle," *Journal of Cleaner Production*, vol. 229, pp. 213–231, 2019.
- [2] Anonymous, "Sustainable management of mining operations," *Mining Engineering*, vol. 61, no. 2, p. 22, 2009.
- [3] C. Li, H. Xie, M. Gao, J. Xie, G. Deng, and Z. He, "Case study on the mining-induced stress evolution of an extra-thick coal seam under hard roof conditions," *Energy Science & Engineering*, vol. 8, no. 9, pp. 3174–3185, 2020.
- [4] B. Unver and N. E. Yasitli, "Modelling of strata movement with a special reference to caving mechanism in thick seam coal mining," *International Journal of Coal Geology*, vol. 66, no. 4, pp. 227–252, 2006.
- [5] Y. H. Pang and G. F. Wang, "Top-coal caving structure and technology for increasing recovery rate at extra-thick hard coal seam," *Journal of China Coal Society*, vol. 42, pp. 817–824, 2017.
- [6] J. Caron, S. Durand, and H. Asselin, "Principles and criteria of sustainable development for the mineral exploration industry," *Journal of Cleaner Production*, vol. 119, pp. 215–222, 2016.
- [7] R. I. Maczkowiack, C. S. Smith, G. J. Slaughter, D. R. Mulligan, and D. C. Cameron, "Grazing as a post-mining land use: a conceptual model of the risk factors," *Agricultural Systems*, vol. 109, pp. 76–89, 2012.
- [8] B. Xia, J. Jia, B. Yu, X. Zhang, and X. Li, "Coupling effects of coal pillars of thick coal seams in large-space stopes and hard stratum on mine pressure," *International Journal of Mining Science and Technology*, vol. 27, no. 6, pp. 965–972, 2017.
- [9] J. Ju and J. Xu, "Structural characteristics of key strata and strata behaviour of a fully mechanized longwall face with 7.0 m height chocks," *International Journal of Rock Mechanics and Mining Sciences*, vol. 58, pp. 46–54, 2013.
- [10] B. Yu, "Behaviors of overlying strata in extra-thick coal seams using top-coal caving method," *Journal of Rock Mechanics and Geotechnical Engineering*, vol. 8, no. 2, pp. 238–247, 2016.
- [11] B. Yu, J. Zhao, T. Kuang, and X. Meng, "In situ investigations into overburden failures of a super-thick coal seam for longwall top coal caving," *International Journal of Rock Mechanics and Mining Sciences*, vol. 78, pp. 155–162, 2015.
- [12] H. M. Li, D. J. Jiang, and D. Y. Li, "Analysis of ground pressure and roof movement in fully-mechanized top coal caving with large mining height in ultra-thick seam," *Journal of China Coal Society*, vol. 39, pp. 1956–1960, 2014.
- [13] C. Gao, N. Z. Xu, and G. Liu, "Research on actual measurement of surface subsidence law for fully-mechanized top coal caving in extra thick seam," *International Journal of Coal Science & Technology*, vol. 42, pp. 106–109, 2014.
- [14] J. T. Guo, Y. G. Yan, and H. Y. Dai, "Determination of ground movement parameters under insufficient mining condition based on simulation results of FLAC3D," *Journal of Mechanical Engineering Research*, vol. 25, pp. 43–46, 2010.
- [15] R. Gao, J. X. Yang, T. J. Kuang, and H. J. Liu, "Investigation on the ground pressure induced by hard roof fracturing at different layers during extra thick coal seam mining," *Geofluids*, vol. 2020, Article ID 8834235, 15 pages, 2020.
- [16] R. Gao, B. J. Huo, H. C. Xia, and X. B. Meng, "Numerical simulation on fracturing behaviour of hard roofs at different levels during extra-thick coal seam mining," *Royal Society Open Science*, vol. 7, Article ID 191383, 2020.
- [17] L. Ma, J. G. Zhang, and X. Chen, "Comprehensive evaluation of blast casting results based on unascertained measurement and intuitionistic fuzzy set," *Shock and Vibration*, vol. 2021, Article ID 8864618, 14 pages, 2021.
- [18] L. Ma, J. Q. Zhao, and J. G. Zhang, "Slope stability analysis based on leader dolphins herd algorithm and simplified bishop method," *IEEE Access*, vol. 9, p. 1, 2021.
- [19] W.-B. Guo, H.-S. Wang, G.-W. Dong, L. Li, and Y.-G. Huang, "A case study of effective support working resistance and roof support technology in thick seam fully-mechanized face mining with hard roof conditions," *Sustainability*, vol. 9, no. 6, p. 935, 2017.
- [20] Y. Lan, R. Gao, B. Yu, and X. Meng, "In situ studies on the characteristics of strata structures and behaviors in mining of a thick coal seam with hard roofs," *Energies*, vol. 11, no. 9, Article ID 2470, 2018.
- [21] Y. Chen, S. Ma, and Y. Yu, "Stability control of underground roadways subjected to stresses caused by extraction of a 10-m-thick coal seam: a case study," *Rock Mechanics and Rock Engineering*, vol. 50, no. 9, pp. 2511–2520, 2017.
- [22] R. Singh, P. K. Mandal, A. K. Singh, R. Kumar, J. Maiti, and A. K. Ghosh, "Upshot of strata movement during underground mining of a thick coal seam below hilly terrain," *International Journal of Rock Mechanics and Mining Sciences*, vol. 45, no. 1, pp. 29–46, 2008.
- [23] C. Huang, Q. Li, and S. Tian, "Research on prediction of residual deformation in goaf of steeply inclined extra-thick coal seam," *PLoS One*, vol. 15, Article ID e0240428, 2020.
- [24] J. Wang and Z. Wang, "Systematic principles of surrounding rock control in longwall mining within thick coal seams," *International Journal of Mining Science and Technology*, vol. 29, no. 1, pp. 65–71, 2019.

- [25] L. Nayzar, S. Takashi, S. Hideki, H. Akihiro, and M. Kikuo, "Numerical analysis of interaction effects in double extra-thick coal seams mining," *Procedia Earth and Planetary Science*, vol. 6, pp. 343–349, 2013.
- [26] K. Matsui, H. Shimada, and T. Sasaoka, "Some consideration in underground mining systems for extra thick coal seam," *Coal International*, vol. 2, pp. 38–41, 2011.

Research Article

Experimental Study on Impermeability Law of Aquiclude Reconstructed by Mudstone of External Dump in Arid Zone

Li Ma ^{1,2}, **Chendong Liu** ^{1,2}, **Yinli Bi**³, **Suping Peng**⁴, **Kaisheng Jiang**⁵, **Hui Zhang**⁶, **Qiang Luo** ^{1,2}, **Fei Xue**^{1,2}, **Tianxin Xu**^{1,2}, **Tianxiang Li**^{1,2}, **Jing Wu**¹, **Jiahao Tian**¹, and **Dongxu Zhang**⁷

¹School of Energy Engineering, Xi'an University of Science and Technology, Xi'an, Shaanxi 710054, China

²Institute of Surface Mining Technology, Xi'an University of Science and Technology, Xi'an, Shaanxi 710054, China

³College of Geology and Environment, Xi'an University of Science and Technology, Xi'an 710054, China

⁴State Key Laboratory for Coal Resources and Safe Mining, China University of Mining & Technology (Beijing), Beijing 100083, China

⁵Shenhua Xinjiang Qitai Energy Co., Ltd., Changji 831799, Xinjiang, China

⁶International Exchange and Cooperation Office, Xi'an University of Science and Technology, Xi'an 710054, Shaanxi, China

⁷CCTEG Shenyang Research Institute, Fushun 113122, Liaoning, China

Correspondence should be addressed to Chendong Liu; lcd6552@yeah.net

Received 6 January 2021; Accepted 6 May 2021; Published 18 May 2021

Academic Editor: Xueping Fan

Copyright © 2021 Li Ma et al. This is an open access article distributed under the Creative Commons Attribution License, which permits unrestricted use, distribution, and reproduction in any medium, provided the original work is properly cited.

In order to achieve the goal of ecological restoration, plant irrigation, and water retention in the external dump of open-pit coal mine in the arid desert area, it is proposed to use the mudstone in the stripped material to reconstruct the surface aquiclude and improve the water holding capacity of the topsoil. By taking the Hongshaquan Open-Pit Coal Mine as the study object, the red mudstone of mining level +650 was selected as the topsoil aquiclude material through the geological survey. XRD diffraction experiments are used to determine the composition of red mudstone including kaolinite mineral, quartz, potash feldspar, albite, and illite. The moisture content of the red mudstone is 4.16% as measured by the indoor drying experiment. And the particle size of 0.5 mm, 1 mm, and 2 mm and the thickness of 5 cm, 10 cm, and 20 cm rock samples were selected to conduct the indoor soil column experiment. Three indicators of initial infiltration rate, stable infiltration rate, and average infiltration rate were obtained according to the analysis and calculation of the water column drop rate, wet peak drop rate, and cumulative infiltration rate so that the permeability law and coefficient of each group of tests can be known. The finite element transient analysis theory and numerical simulation method were adopted to verify the results of physical experiments. The research results show that +650 level red mudstone has a strong antiseepage ability, and the smaller the particle size, the better the antiseepage performance. For 0.5 mm and 2 mm particle sizes, as the paving height increases, the water-proof effect is better. The laying height of 1 mm particle size has no obvious influence on the water barrier effect. The physical simulation was confirmed to have the same result trend as the numerical simulation, both of which are quadratic functions with the error within a reasonable range.

1. Introduction

In the process of open-pit coal mining, a large amount of topsoil and stone is removed and an empty site is needed for disposal, which damages the original terrain of the mining

area and leads to the deterioration of soil and regional ecological environment. Therefore, it is of great significance to carry out mine land reclamation and ecological restoration in the process of mining and after mine closure [1] (Ma et al. 2017). Especially for the arid desert areas, as it has

the characteristics of less rainfall and large evaporation, combined with the impact of open-pit mining on the terrain structure, the topsoil structure of the dump site has a loose structure, strong permeability, poor water retention capacity, and large irrigation water requirements. Hence, it is necessary to study the permeability law and parameters of water barrier reconstruction for maintaining the ecological restoration, irrigation cycle, and water consumption in the open-pit mine of the arid area.

Under natural conditions, the soil profile in the stratum has a layered structure, which can maintain certain infiltration characteristics and rate. The external dump material of open-pit mine is made of loose material such as rock, mudstone, and sandstone, which has large porosity and strong water permeability between materials. In addition, due to the low rainfall and large evaporation in the mining area, there is no groundwater in the lower part of the reconstructed external dump. Only a small part of the water is absorbed by plants, most of the irrigation water is lost along the vertical direction of the external dump, and it has poor water function to maintain plant growth, which is easy to cause water loss in topsoil prematurely, seriously affecting plant growth or increasing irrigation water consumption.

According to the structural characteristics and principle of the vadose zone, the water barrier is reconstructed inside the external dump to reduce or prevent the vertical infiltration of atmospheric precipitation and irrigation water. In line with the phreatic impact layer, a stagnant water layer is formed on the upper part of the water barrier. The water layer allows the water blocked by the water barrier layer to rise along the soil pores through capillary action, as a result, capillary water supply from stagnant water layer to plant root. The structure is shown in Figure 1.

There are several studies related to the reconstruction of the aquifer at home and abroad. Some scholars obtained the variation curve of permeability coefficient with time through variable head experiment and carried out a feasibility analysis for the error [2–6] (Ma et al., 2020; Wang, 2019; Zhao et al., 2018; Li et al., 2016; and Cao et al., 2010). Based on the experiment of bentonite and nonbentonite, Chen et al. (2010) and Bojana (2009) concluded that there is an obvious relationship between water conductivity and soil properties [7, 8]. By studying the permeability change of the coal seam under the action of plastic flow, Guo et al. (2019, 2020) obtained the relationship between the permeability and the relative residual strain and the influence coefficient of the confining pressure [9, 10]. Burger et al. (2001), Niu et al. (2009), Robert et al. (2004), and Aubertin et al. (2003) obtained equations that are more suitable for experiments by modifying and optimizing theoretical equations [11–14]; Zhu et al. (2014), Zhang et al. (2013), and Robert et al. (2001) discussed the experimental methods of different soil permeability coefficients, determined the error range through comparative experiments, and summarized the error sources to determine the appropriate functional relationship [15–17].

In order to provide a theoretical foundation for realizing ecological restoration of external dump and topsoil water conservation in the open-pit mine of arid areas, the red mudstone of mine level +650 from the Hongshaquan open-

pit coal was taken as the research object. The physical soil column experiments and numerical simulation were adapted to explore the permeability coefficient and permeability law of the red mudstone.

2. Project Overview of Hongshaquan Open-Pit Coal Mine

2.1. The Environment of Mine Area. Hongshaquan Open-Pit Coal Mine is located in the southeast of Junggar Basin. It belongs to the temperate continental climate, and the annual average temperature is 5.5°C. The annual average precipitation is 269.4 mm, and summer generally accounts for 40–50% of the total annual precipitation; spring and autumn are nearly equivalent, each accounting for 20–30%, the winter precipitation is the least, accounting for less than 10% of the annual precipitation. The evaporation capacity is 2141 mm, the annual average wind period is about 100 d, and the wind speed is generally 3~4 m/s. Low rainfall, large evaporation, and frequent winds resulting from the surface water storage around the stope and dump are scarce, while the irrigation water demand is large. Figure 2 shows the exterior view of the external dump site of the Hongshaquan Open-Pit Coal Mine.

2.2. Selection of Mudstone Antiseepage Materials. As the open-pit mine is located on the northern edge of the eastern part of the Junggar Basin, the exposed strata such as Paleozoic Carboniferous and Permian, Mesozoic Triassic and Jurassic, Neogene of Cainozoic and the fourth series, and the Paleozoic strata constituting the base of the Mesozoic strata were included.

By geological surveys, it is found that the rock of mining level +650 on the east side of the stope has good physical and chemical properties of mudstone (Figure 3). The mudstone belongs to the Shishugou Group of the Middle-Upper Mesozoic Jurassic System (J₂₋₃sh). Its lithology is variegated fluke-lacustrine facies. The upper subgroup mainly consists of red argillaceous siltstone, mudstone intercalated with sandstone. The lower subgroup mainly consists of green argillaceous siltstone, mudstone, and silicified wood. And the storage is abundant, with a thickness of 116 m–900 m.

In order to further confirm the mineral composition content of mudstone, XD-3X-ray diffractometer was used to perform XRD diffraction experiments on the rock samples. First grinding the granular solid into powder with a mortar, then pouring the clean powder sample into the center of a clean sample pan, covering with a clean iron sheet to make the surface of the sample flat, and finally entering the test parameters with the scanning angle from 0 to 90°, scanning speed of 4°/min, working voltage of 36 kV, and electric current of 20 A, the XRD experimental map shown in Figure 4 is obtained.

It can be seen from Figure 4 that the peak intensity of the curve has obvious peaks ④ and ⑤ when the 2θ is 27.5° and 29°. The diffraction peaks ①, ⑥, and ⑦ are illite, ② and ③ are quartz, and the diffraction peaks ④ and ⑤ are the

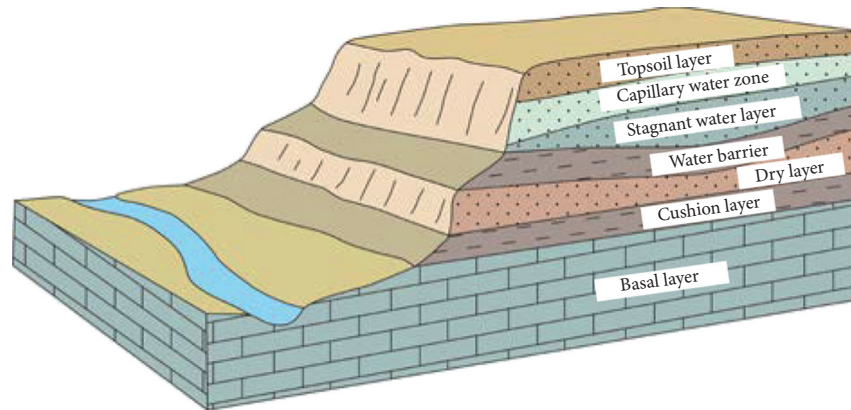


FIGURE 1: Schematic diagram of aquiclude reconstruction of the external dump.

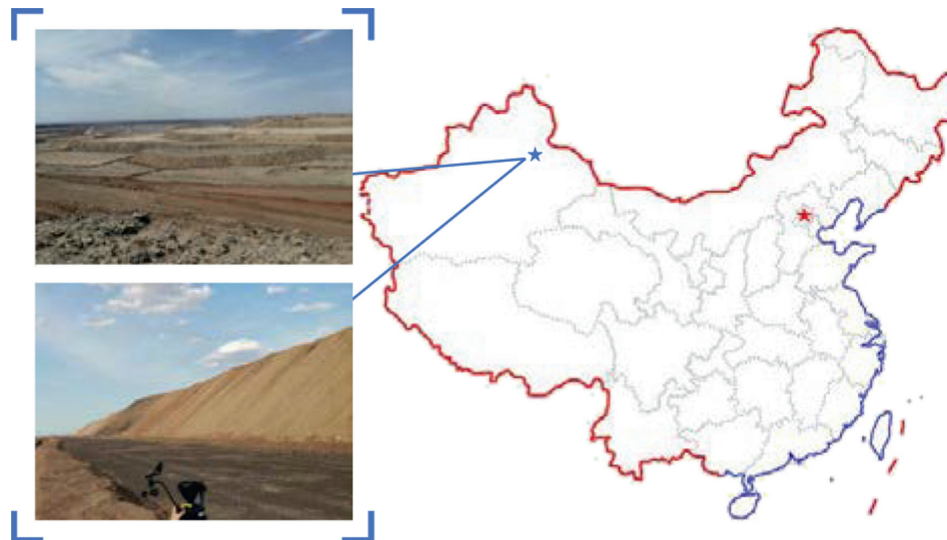


FIGURE 2: The location and external dump site of Hongshaquan open-pit mine.

diffraction peaks of potassium feldspar and albite, respectively. Due to the presence of potash feldspar and albite in mudstone, the mudstone is reddish-brown.

Considering that there may be other impurities in the rock sample which may interfere with the results of the XRD diffraction experiment, the known identified minerals are reconfirmed. The rock samples were calcined at different high temperatures, and the XRD diffraction experiment was continued. The treatment temperature was 300°C, 500°C, and 800°C, and the calcination time was 30 minutes. The comparison chart is shown in Figure 5.

The comparison of the experimental results shows that the diffraction peaks ⑤ and ⑥ of the rock sample have a tendency to weaken after the high temperature calcination treatment at 800°C; especially the diffraction peak ⑥ weakens more significantly, and it is indicated that potash feldspar and albite will gradually disappear after high temperature treatment. The diffraction peak ② has no change in the peak after high temperature treatment; it is

indicated that the crystal plane distance remains unchanged after high temperature treatment. This peak indicates that the mineral is illite. Thus, the final mineral composition is kaolinite mineral, quartz, potash feldspar, albite, and illite.

3. Soil Column Experiment on Seepage Control Law of Mudstone in Water Isolation Layer

3.1. Experiment Preparation

3.1.1. Seepage Test Materials. To explore the permeation law of different material parameters, particle size and thickness are key influence factors to be considered. By crushing and sieving repeatedly, the experimental materials were sorted into 9 groups of soil columns with three different particle sizes of 0.5 mm, 1 mm, and 2 mm and different heights of 5 cm, 10 cm, and 20 cm [18]. The experimental material packing density parameters are shown in Table 1. After the drying experiment, the initial soil moisture content was 4.16%.



FIGURE 3: On-site rock sample collection.

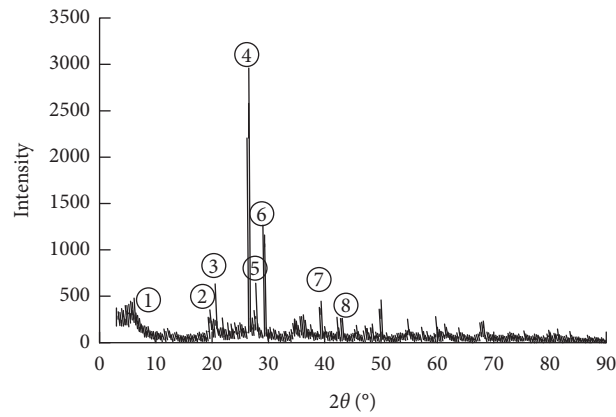


FIGURE 4: The experimental map of XRD.

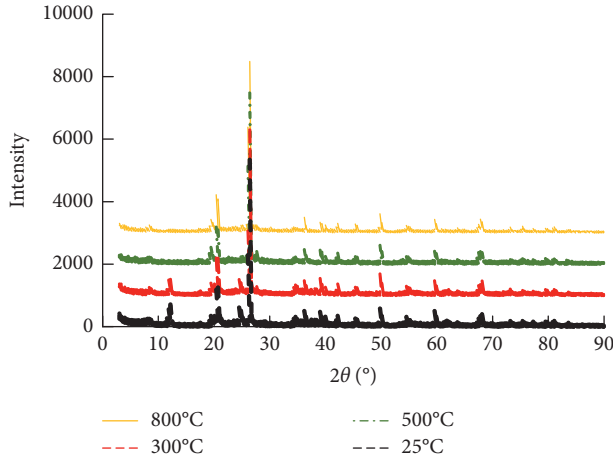


FIGURE 5: Comparison of XRD diffraction experiments at different temperatures.

TABLE 1: Experimental material density.

Size (mm)	Height (cm)		
	5	10	20
0.5	1360 kg/m ³	1400 kg/m ³	1327 kg/m ³
1	1093 kg/m ³	1067 kg/m ³	1047 kg/m ³
2	1000 kg/m ³	1140 kg/m ³	1033 kg/m ³

3.1.2. Equipment Required for Soil Column Experiment. The experiment requires a plexiglass tube with an inner diameter of 14 cm and height of 50 cm; 3L beaker; 200 mesh geo-sieve of 0.25 mm, 0.5 mm, 1 mm, 2 mm, and 5 mm; crusher; geo-hammer; material basket; tamping pestle; filter paper; gauze; red and blue ink; scale bars; and so forth.

3.2. Experimental Principle of Soil Column Based on Variable Head Method. The infiltration performance of soil water can be described by soil physical characteristic parameters. In this paper, through the analysis and calculation of the water column drop rate, wet peak drop rate, and cumulative infiltration rate, three indicators of initial infiltration rate, stable infiltration rate, and average infiltration rate are obtained. Among them are the following:

- (1) The initial infiltration rate:

The initial infiltration rate refers to the ratio of the drop height of the liquid level to the time within the first 6 hours:

$$v_0 = \frac{h_1}{6}, \quad (1)$$

where v_0 is the initial infiltration rate, cm/h, and h_1 is the height change corresponding to the first 6 hours, cm.

- (2) The stable infiltration rate:

The stable infiltration rate refers to the ratio of the drop height of the wet peak to the time during the stable water penetration period.

$$v_1 = \frac{h_3 - h_2}{t_3 - t_2}, \quad (2)$$

where v_1 is the stable infiltration rate, cm/h; h_2 and h_3 are the height at the beginning and ending of stable infiltration, cm; t_2 and t_3 are the time of stable infiltration and the time to end the stable infiltration, h .

- (3) The average infiltration rate:

The average infiltration rate is the ratio of the cumulative infiltration amount to the time used from the beginning of the test to the end of the test:

$$v_2 = \frac{h_z}{t_z}, \quad (3)$$

where v_2 is the average infiltration rate, cm/h; h_z is the total height, cm; and t_z is the total time of infiltration, h .

3.3. Seepage Experiment Method. The constant head method of the indoor permeability test is suitable for sandy soil and noncohesive soil with a small amount of gravel, and the variable head method is suitable for silt and cohesive soil [19]. The experiment was carried out in a closed laboratory without natural light, so the effect of evaporation was not considered. As the mudstone used has a strong antiseepage ability, the variable head method should be adopted for the permeability test with one-time adding water for simulating field irrigation. After the water level is stabilized, the infiltration rate of different particle sizes and heights can be calculated to determine the antiseepage effect by observing the height change of the water column, the distance of the wet peak migration, and the cumulative infiltration volume.

The sieved particles are added to a plexiglass column with an inner diameter of 14 cm and a height of 50 cm for filling. The bottom of the soil column needs to be added with gauze to prevent mudstone from clogging the mesh. Filter paper is added above the mudstone to relieve the impact of water during the water addition process. The experimental principle and device are shown in Figure 6. Measure the change of the wet peak, water column level, and water depth of the beaker which is also the cumulative infiltration volume. After the experiment, the results are processed. The corresponding curves of the wet peak, liquid level, and water depth of the beaker with time are shown in Figure 7.

The water depth of the test beaker can be converted into the cumulative infiltration amount in line with the size of the beaker. According to Figures 7(c) and 7(f), it can be seen that the 0.5 mm/20 cm and 1 mm/20 cm schemes never seeped or seeped rarely during the experiment, showing that the antiseepage effect of the two experimental schemes is excellent, and the cumulative infiltration amount has nothing to do with time. For the other 7 groups of experimental results obtained in Figure 7, the cumulative infiltration volume and time curve under different particle sizes and heights are summarized as shown in Figure 8. The horizontal axis of the fitting curve in this paper is the time, the vertical

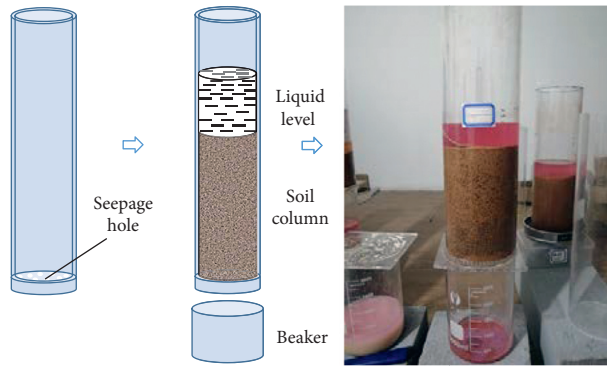


FIGURE 6: Experimental principle and device diagram.

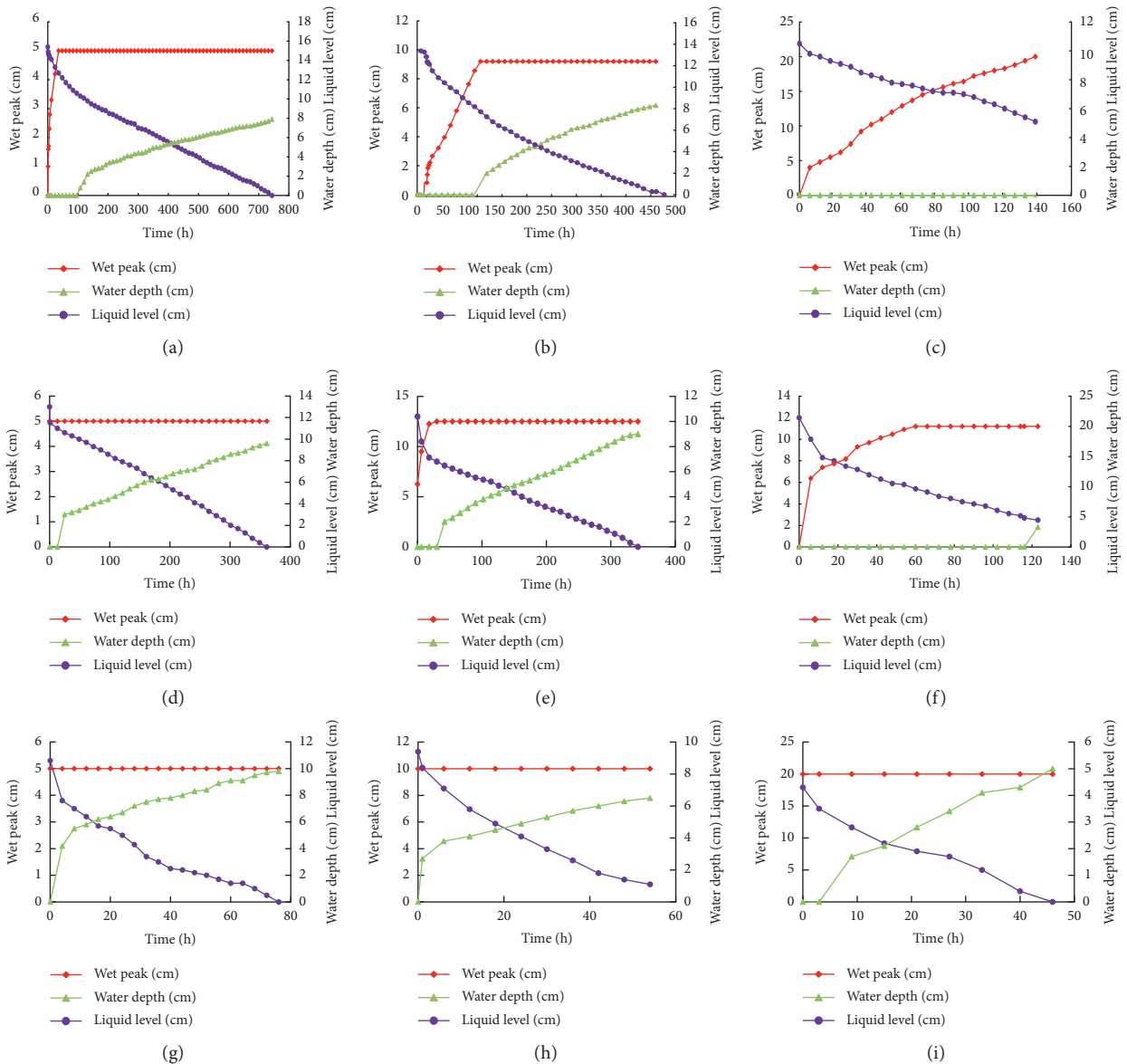


FIGURE 7: Curve of the relationship between wetting front, liquid level, water depth of beaker, and time: (a) 0.5 mm/5 cm seepage curve of soil column experiment. (b) 0.5 mm/10 cm seepage curve of soil column experiment. (c) 0.5 mm/20 cm seepage curve of soil column experiment. (d) 1 mm/5 cm seepage curve of soil column experiment. (e) 1 mm/10 cm seepage curve of soil column experiment. (f) 1 mm/20 cm seepage curve of soil column experiment. (g) 2 mm/5 cm seepage curve of soil column experiment. (h) 2 mm/10 cm seepage curve of soil column experiment. (i) 2 mm/20 cm seepage curve of soil column experiment.

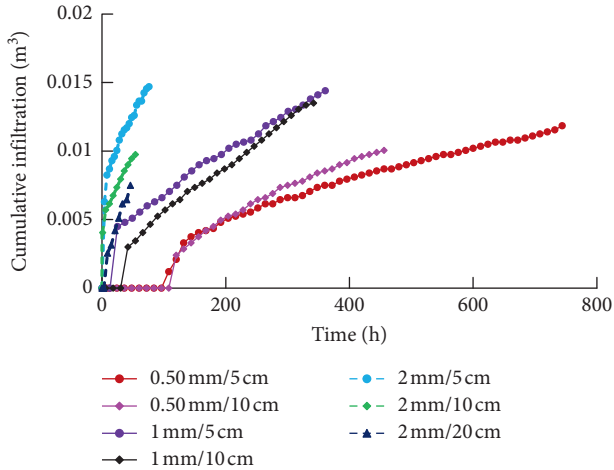


FIGURE 8: Relationship curve between cumulative infiltration volume and infiltration time.

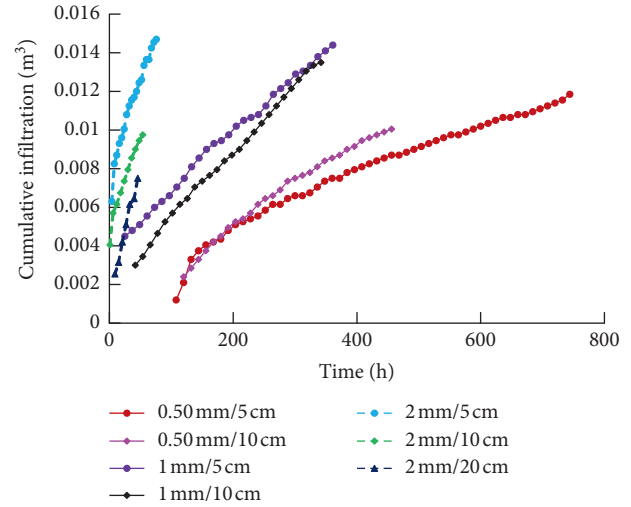


FIGURE 10: The relationship curve between cumulative infiltration volume and infiltration time after treatment.

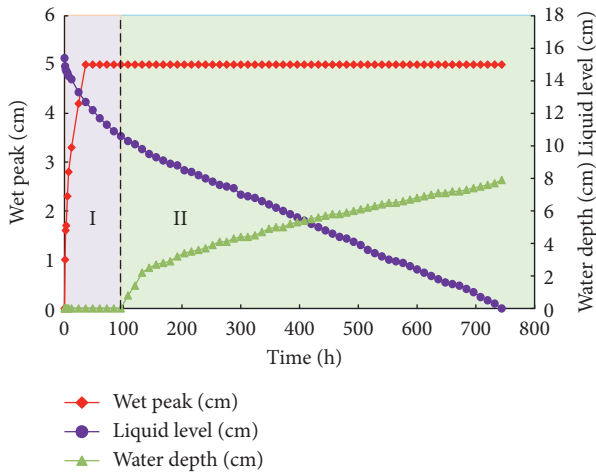


FIGURE 9: Demonstration of seepage experiment stage.

axis is the cumulative infiltration volume, and its slope is the infiltration rate.

Since mudstone has strong disintegration, the seepage process can be divided into two stages shown in Figure 9. The first stage is the stage of water absorption, expansion, and disintegration of mudstone. It takes various times for mudstones of different particle sizes and thicknesses to disintegrate. The second stage is after the completely disintegrated mudstone reaches a saturated state; it begins to enter the infiltration stage. Therefore, the permeability coefficient at the initial stage is unstable. Due to the characteristic relationship of the permeability, the initial disintegration stage of the experimental results of Figure 8 is pretreated as shown in Figure 10.

As shown in Figure 10, the relationship between the cumulative infiltration volume and time meets the growth trend of the quadratic function curve, and the growth rate is from fast to slow, and then tends to be linear. The fitting function can be listed in Table 2.

3.4. *Physical Experiment Data Processing.* According to formulas (1)–(3), the initial infiltration rate, stable infiltration rate, and average infiltration rate were calculated by combining the wet peak height, liquid level height, and cumulative infiltration volume of each group of experiments. The results are shown in Table 3.

The average infiltration rate corresponding to each particle size and height is fitted to form a three-dimensional surface diagram shown in Figure 11. The relationship among the average infiltration rate, the particle size, and height is obtained:

$$\begin{cases} f(x, y) = p_{00} + p_{10}x + p_{01}y, \\ p_{00} = -0.03056 \in (-0.0519, 0.009214), \\ p_{10} = 0.07762 \in (0.06552, 0.08972), \\ p_{01} = -0.0006667 \in (-0.001877, 0.0005433), \end{cases} \quad (4)$$

where $f(x, y)$ is the average infiltration rate of permeability coefficient, x is the particle size of mudstone, in mm; and y is the height of laying mudstone, in cm.

It can be seen from Figure 11 that the average infiltration rate of rock samples gradually increases with the increase of mudstone particle size and gradually decreases with the increase of paving thickness. The higher the average infiltration rate, the stronger the permeability, and the worse the antiseepage effect. That is, the smaller the mudstone particle size and the thicker the soil layer, the better the antiseepage effect.

4. Numerical Simulation Method of Mudstone Permeability

4.1. *Principles of Transient Analysis.* In the physical experiment of mudstone permeable soil column, water is added once, and related variables are measured at certain time intervals. It is the basic point to define the initial total head

TABLE 2: The fitting function of physical experiment.

Size/mm	Height/cm		
	5	10	20
0.5	$y = -1.31 \times 10^{-8}x^2 + 2.97 \times 10^{-5}x + 1.76 \times 10^{-4}$	$y = -3.28 \times 10^{-8}x^2 + 4.10 \times 10^{-5}x - 1.88 \times 10^{-3}$	—
1	$y = -1.45 \times 10^{-8}x^2 + 3.52 \times 10^{-5}x + 3.5 \times 10^{-3}$	$y = -9.57 \times 10^{-9}x^2 + 3.82 \times 10^{-5}x + 1.67 \times 10^{-3}$	—
2	$y = -7.62 \times 10^{-7}x^2 + 1.63 \times 10^{-4}x + 6.57 \times 10^{-3}$	$y = -1.03 \times 10^{-6}x^2 + 1.56 \times 10^{-4}x + 4.31 \times 10^{-3}$	$y = -6.21 \times 10^{-7}x^2 + 1.69 \times 10^{-4}x + 9.5 \times 10^{-4}$

TABLE 3: Summary of experimental data processing results.

Size (mm)	Height (cm)	Type	Infiltration rate cm/h		
			Initial	Stable	Average
0.5	5	Wet peak	0.43	0.07	0.14
		Liquid level	0.17	0.02	0.02
		Cumulative	0	0.01	0.01
	10	Wet peak	0.38	0.08	0.09
		Liquid level	0.12	0.02	0.03
		Cumulative	0	0.02	0.01
	20	Wet peak	0.67	0.11	0.14
		Liquid level	0.12	0.04	0.04
		Cumulative	0	0	0
1	5	Wet peak	—	—	—
		Liquid level	0.28	0.03	0.04
		Cumulative	0	0.02	0.03
	10	Wet peak	—	—	—
		Liquid level	0.42	0.03	0.04
		Cumulative	0	0.02	0.03
	20	Wet peak	1.9	0.11	0.33
		Liquid level	0.33	0.05	0.08
		Cumulative	0	2.12	0.03
2	5	Wet peak	—	—	—
		Liquid level	0.55	0.08	0.14
		Cumulative	0.8	0.06	0.13
	10	Wet peak	—	—	—
		Liquid level	0.38	0.13	0.15
		Cumulative	0.63	0.06	0.12
	20	Wet peak	—	—	—
		Liquid level	0.2	0.06	0.09
		Cumulative	0.17	0.11	0.11

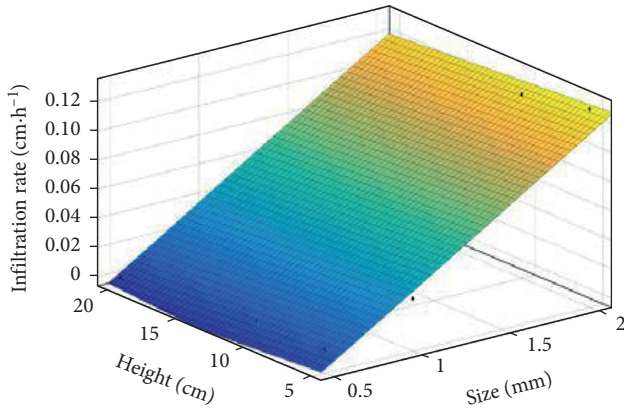


FIGURE 11: The average infiltration rate varies with the height of the particle size.

on all nodes. The two-dimensional seepage control differential equation using the transient analysis method can be expressed as

$$\frac{\partial}{\partial x} \left(k_x \frac{\partial H}{\partial x} \right) + \frac{\partial}{\partial y} \left(k_y \frac{\partial H}{\partial y} \right) + Q = \frac{\partial \theta}{\partial t}, \quad (5)$$

where H is the total head; K_x is the permeability coefficient in the x direction; K_y is the permeability coefficient in the y direction; Q is the imposed boundary flow; θ is the water content per unit volume; and t is the time.

The change of volumetric water content depends on the change of stress state and the properties of soil. Both saturated and unsaturated stress states can be expressed by two state quantities $\sigma - u_a$ and $u_a - u_w$ [20–22], where σ is the total stress, u_a is the atmospheric pressure in the pore, and u_w is the pore water pressure.

It is assumed that, for transient problems, the atmospheric pressure of the pore is kept at constant atmospheric pressure; that is, $(\sigma - u_a)$ remains unchanged [23, 24] and has no effect on the change of water content per unit volume. Therefore, the change of water content per unit volume only depends on $(u_a - u_w)$. When u_a remains unchanged, the water content per unit volume is only a function of water pressure. The relationship between water content per unit volume and pore water pressure is

$$\partial \theta = m_w \partial u_w, \quad (6)$$

where m_w is the slope of the water storage curve.

The total head H is defined as

$$H = \frac{u_w}{\gamma_w} + y, \quad (7)$$

where u_w is the pore water pressure; γ_w is the bulk density of water; and y is the elevation.

Substituting formulas (6) and (7) into formula (5), we can get

$$\frac{\partial}{\partial x} \left(k_x \frac{\partial H}{\partial x} \right) + \frac{\partial}{\partial y} \left(k_y \frac{\partial H}{\partial y} \right) + Q = m_w \gamma_w \frac{\partial (H - y)}{\partial t}. \quad (8)$$

Since the elevation is a constant, the derivative of y with respect to time is 0, and finally, the governing equation used in the finite element formula is [25–27]

$$\frac{\partial}{\partial x} \left(k_x \frac{\partial H}{\partial x} \right) + \frac{\partial}{\partial y} \left(k_y \frac{\partial H}{\partial y} \right) + Q = m_w \gamma_w \frac{\partial H}{\partial t}. \quad (9)$$

The Galerkin method with weighted margin is applied to the governing equation, and the finite element format of the two-dimensional seepage equation can be obtained:

$$\begin{aligned} & \tau \int_A ([B]^T [C] [B]) dA \{H\} + \tau \int A (\lambda \langle N \rangle^T \langle N \rangle) dA \{H\}, \\ t = q\tau \int_L (\langle N \rangle^T) dL, \end{aligned} \quad (10)$$

where $[B]$ is the gradient matrix; $[C]$ is the element permeability coefficient matrix; $\{H\}$ is the nodal head vector; $\langle N \rangle$ is the interpolation function vector; q is the unit flow across the element boundary; τ is the element thickness; t is the time; λ is the storage item, which is equal to $m_w \gamma_w$ for transient seepage; A is the sum sign on the unit area; L is the sum sign on the unit boundary length.

In the case of axisymmetric, the complete hoop distance is $2\pi R$. Since it is derived for 1 radian, the equivalent thickness is R . Therefore, the finite element equation in the case of axisymmetric is [28–30]

$$\begin{aligned} & \int_A ([B]^T [C] [B]) dA \{H\} + \int A (\lambda \langle N \rangle^T \langle N \rangle) dA \{H\}, \\ t = q\tau \int_L (\langle N \rangle^T) dL. \end{aligned} \quad (11)$$

In the two-dimensional analysis, the thickness τ is different, the radial distance R in an element is not a constant, and R is variable in the integrand, so the finite element seepage equation can be simplified as

$$[K]\{H\} + [M]\{H\}, t = \{Q\}, \quad (12)$$

where $[K]$ is the unit characteristic matrix; $[M]$ is the unit mass matrix; and $\{Q\}$ is the flow vector imposed on the unit.

The finite element solution of transient analysis is a function of time, and the time integration can be completed by the finite element difference approximation method. The finite element equation is written according to the finite difference to obtain the following equation:

$$\begin{aligned} (\omega \Delta t [K] + [M])\{H_1\} = \Delta t ((1 - \omega)\{Q_0\} + \omega\{Q_1\} \\ + ([M] - (1 - \omega)\Delta t [K])\{H_0\}, \end{aligned} \quad (13)$$

where t is the time increment; ω is a coefficient between 0 and 1; H_1 is the water head at the end of the time increment;

H_0 is the water head at the beginning of the time increment; Q_1 is the node flow at the end of the time increment; and Q_0 is the node flow at the beginning of the time increment.

4.2. Mudstone Seepage Law Based on Numerical Simulation.

Firstly, by selecting the transient analysis, the duration was set as the experimental time, and the appropriate number of steps and soil parameters was set in the meantime. And the different model heights of 5 mm, 10 mm, and 20 mm for the same particle sizes were established with the ratio of 1 : 10. Then, according to the experimental results of the soil column, the permeability coefficient k_T of each group of schemes can be calculated by [3, 7]

$$k_T = \delta \frac{aL}{A(t_2 - t_1)} \log \frac{H_1}{H_2}, \quad (14)$$

where a is the cross-sectional area of the variable head tube, cm^2 ; A is the sample area, cm^2 ; δ is the conversion factor of \ln and \log , $\delta = 2.3$; L is the height of permeation diameter of the sample, cm ; t_1 and t_2 are the start and end time of the measured water head, h ; H_1 and H_2 are the start and end of water head height, cm .

According to the physical experiment data, the corresponding heights of mudstones with different particle sizes and different heights can be obtained by formula (14); they are shown in Table 4.

Secondly, the boundary conditions were set for the model. The head boundary function was adapted at the top of the model, the boundary conditions of zero total flow for the two sides, and the boundary conditions of zero pressure head for the bottom, as well as a flow monitoring line at the bottom. By Taking 0.5 mm particle size as an example, the total head stress cloud diagram at different soil layer thicknesses is shown in Figure 12. The permeability decreases approximately linearly in line with the thickness of the clay layer increases. According to the simulation calculation of different higher transient water levels, a transient head-time-seepage flow relationship table is listed in Table 5. As the transient head drops, seepage flow increases with the accumulation of time. The change rate of seepage flow presents a phenomenon of starting at a slow speed, and then from fast to slow, finally tending to be stable.

Based on the data obtained from the numerical simulation results, a scatter plot of each program can be drawn as Figure 13. The curve of time and cumulative infiltration volume obtained by numerical simulation has the same trend as the results of the soil column physical simulation (Figure 10), and both are quadratic: the initial growth rate is fast and then tends to be linear. Similarly, the fitting function that can obtain the numerical simulation results is shown in Table 6.

It can be seen that the simulation results of 0.5 mm and 1 mm rock samples have the same trend as the experimental results, and the error is kept within the error range.

TABLE 4: The corresponding k value of each group of experiments.

Size/mm	Height/cm		
	5	10	20
0.5	0.0105	0.015	0.014
1	0.015	0.021	0.029
2	0.044	0.081	0.154

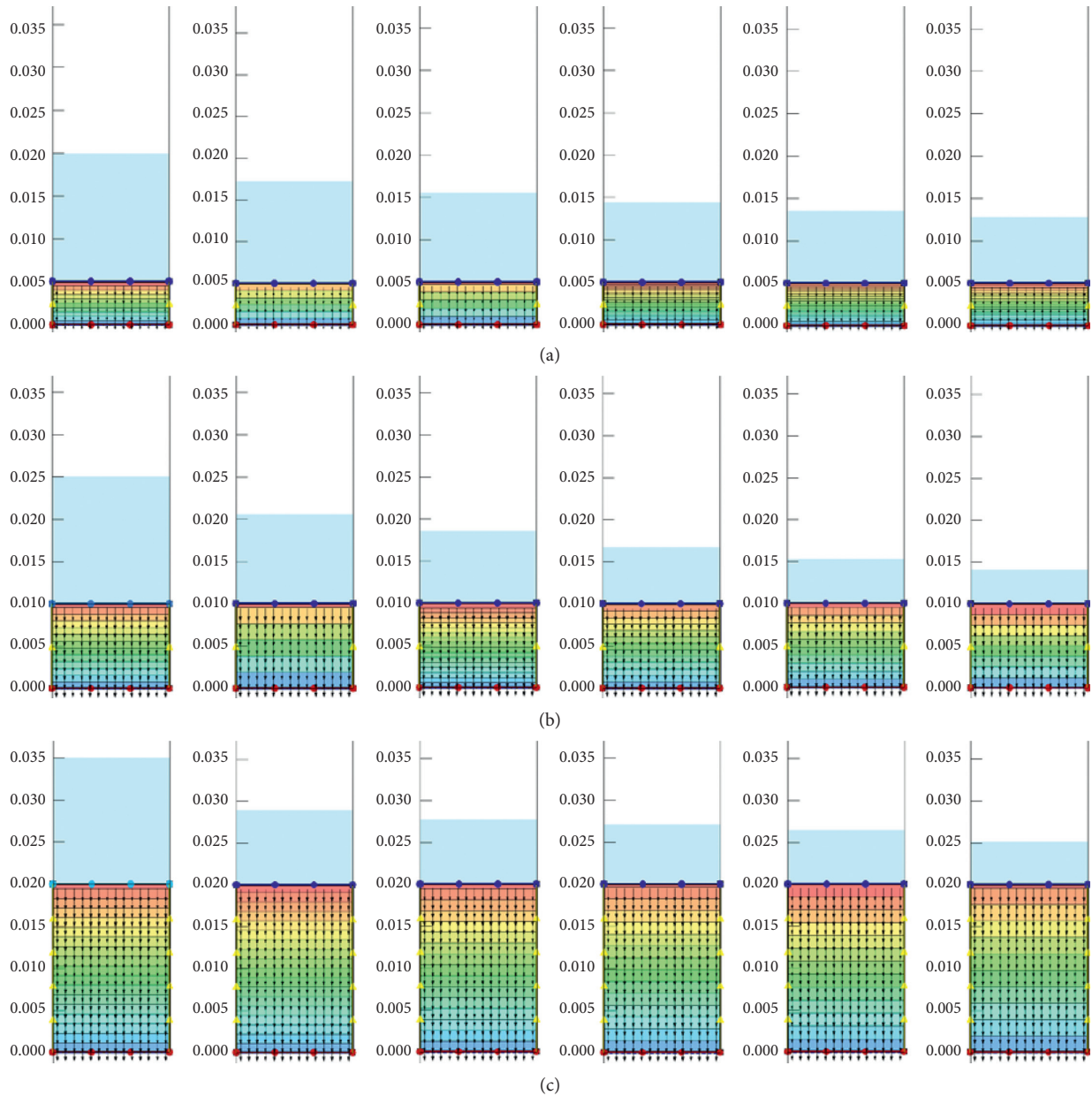


FIGURE 12: Numerical simulation total water head stress cloud diagram with different thickness and 0.5 mm at different times: (a) 0.5 mm/5 cm soil column pressure head at different times. (b) 0.5 mm/10 cm soil column pressure head at different times. (c).5 mm/20 cm soil column pressure head at different times.

TABLE 5: Transient head-time-seepage flow relationship.

Number	Transient head/cm			Time/h			Seepage flow/m ³		
	5 cm	10 cm	20 cm	5 cm	10 cm	20 cm	5 cm	10 cm	20 cm
1	15.4	13.8	10.5	0	0	0	0	0	0
2	12.1	10.7	9.0	50.6	48	29.5	0.0018	0.0021	0.0008
3	10.5	8.5	7.7	101.3	105	59.14	0.0034	0.0042	0.0017
4	9.4	6.7	7.1	152	151	88.7	0.0048	0.0058	0.0024
5	8.6	5.4	6.5	202.6	196	108.42	0.0061	0.0072	0.0030
6	7.8	4.2	5.1	253.3	250	138	0.0074	0.0086	0.0037

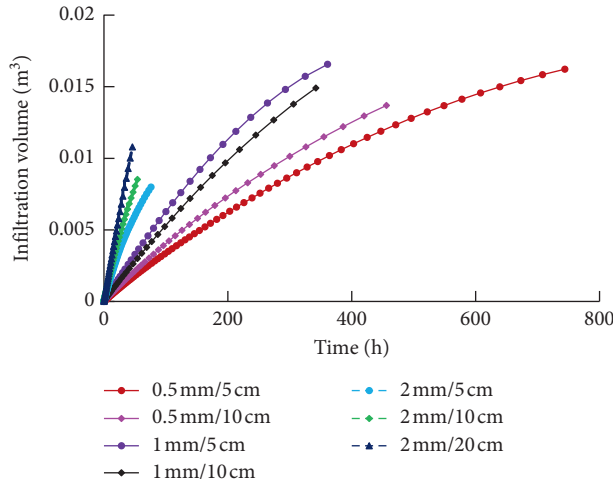


FIGURE 13: Numerical simulation cumulative infiltration volume and time relationship curve.

TABLE 6: Numerical simulation fitting function.

Size/mm	Height/cm		
	5	10	20
0.5	$y = -2 \times 10^{-8}x^2 + 3 \times 10^{-5}x + 9 \times 10^{-5}$	$y = -3 \times 10^{-8}x^2 + 4 \times 10^{-5}x + 6 \times 10^{-5}$	—
1	$y = -7 \times 10^{-8}x^2 + 7 \times 10^{-5}x - 2 \times 10^{-5}$	$y = -4 \times 10^{-8}x^2 + 6 \times 10^{-5}x + 3 \times 10^{-5}$	—
2	$y = -7 \times 10^{-7}x^2 + 2 \times 10^{-4}x + 6 \times 10^{-5}$	$y = -8 \times 10^{-7}x^2 + 2 \times 10^{-4}x + 6 \times 10^{-5}$	$y = -4 \times 10^{-7}x^2 + 3 \times 10^{-4}x - 5 \times 10^{-7}$

5. Results and Discussion

- (1) During the period of soil column experiment, there is no visible seepage of water from particle size 0.5 mm with height 20 cm and particle size 1 mm with height 20 cm, which proves that it has good antiseepage performance.
- (2) Due to the disintegration characteristics of mudstone in the seepage process, the small particle size mudstone disintegrates quickly, and the particle size is further reduced after disintegration, resulting in a denser soil structure. As the thickness increasing, the soil column does not seep out of water, which is one of the important factors affecting the permeability effect.
- (3) For mudstone with a small particle size, since its particle size is small, the degree of disintegration is also small, so the change of its liquid level is fast and then slow to a constant speed until the seepage is

complete. After the particle size increases, the degree of disintegration also increases. For the particle size of 2 mm with a height of 5 cm, the water is completely permeated due to the small height; for the particle size of 2 mm with a height of 10 cm, the water is not permeated.

- (4) In addition to disintegration, water absorption also has a certain impact on the experimental process. Particle size and height are positively correlated with water absorption, so the mudstone of 2 mm with a height of 20 cm seeps less water, and most of it is absorbed.

6. Conclusion

- (1) The particle size is negatively correlated with the infiltration effect, and the influence of mudstone paving thickness on the infiltration effect shows a certain difference. The paving height under the

condition of particle size of 0.5 mm and particle size of 2 mm is negatively related to the average infiltration rate. However, the thickness of 1 mm particle size has little effect on the antiseepage effect.

- (2) The relationship among the average infiltration rate, height, and particle size is obtained by fitting. The average infiltration rate is proportional to the particle size, inversely proportional to the laying height, and inversely proportional to the water barrier effect; the higher the average infiltration rate, the worse the water barrier.
- (3) The cumulative infiltration volume is in a quadratic function relationship with time. The infiltration rate gradually decreases with the increase of time and then tends to be linear.
- (4) The permeability coefficient calculated by physical experiment is used for numerical simulation, the obtained seepage curve can better restore the process of physical simulation, the results show a quadratic function growth, and the error is within a reasonable range.

Data Availability

The data used to support the findings of this study are available from the corresponding author upon request.

Conflicts of Interest

The authors declare that there are no conflicts of interest regarding the publication of this paper.

Acknowledgments

This study was supported by the National Energy Group 2030 Major Pilot Project (GJNY2030XDXM-19-03.2), Scientific Research Program Funded by Shaanxi Provincial Education Department (18JK0520, 18JS067), the China Postdoctoral Science Foundation (2018M643691, 2016M601913), Shaanxi Innovation Capacity Support Program (2018TD-038), and Young Faculty Innovation Program of Engineering School (XUST, 2017-NY-001). Support from these agencies is gratefully acknowledged.

References

- [1] L. Ma, K. Li, S. Xiao, and X. Ding, "Optimisation study on coordinated mining model of coal reserves buried between adjacent surface mines," *International Journal of Oil, Gas and Coal Technology*, vol. 1, no. 3, pp. 283–297, 2017.
- [2] X. Ma and Q. Fu, "Characteristics analysis and numerical simulation of soil water movement parameters in different freeze-thaw periods," *Journal of Applied Basic Science and Engineering*, vol. 2, no. 04, pp. 774–787, 2020.
- [3] J. Wang, *Experimental Study on Layer Reconstruction of Open-Pit Coal Mine Dump*, China University of Mining and Technology, Xuzhou, China, 2019.
- [4] K. Zhao, Q. Xu et al., "Comparative test study on permeability of shallow loess in Heifangtai," *Journal of Engineering Geology*, vol. 2, no. 2, pp. 459–466, 2018.
- [5] S. Li, D. Li, and P. Shi, "Analysis of influencing factors for the determination of permeability coefficient of cohesive soil," *Journal of Shandong University of Science and Technology*, vol. 3, no. 03, pp. 46–52, 2016.
- [6] S. Cao, L. Qiao, Y. Liu, Y. Jiang, and J. Xie, "Error analysis and feasibility study of bentonite permeability test," *Chinese Journal of Rock Mechanics and Engineering*, vol. 2, no. S2, pp. 4202–4206, 2010.
- [7] Y. Chen, W. Ye, Q. Wang, and C. Bao, "Research on influencing factors of permeability of sand-bentonite mixed barrier materials," *Journal of Engineering Geology*, vol. 1, no. 3, pp. 357–362, 2010.
- [8] B. Dolinar, "Predicting the hydraulic conductivity of saturated clays using plasticity-value correlations," *Applied Clay Science*, vol. 4, no. 1–2, pp. 90–94, 2009.
- [9] J. Guo, J. Liu, Q. Li et al., "Variation law of coal permeability under cyclic loading and unloading," *Thermal Science*, vol. 23, p. 215, 2019.
- [10] J. Guo, J. Liu, Q. Li et al., "Experimental study on the failure law of water-bearing coal and the evolution of permeability under plastic flow," *Environmental Earth Sciences*, vol. 7, no. 14, 2020.
- [11] C. A. Burger and C. D. Shackelford, "Evaluating dual porosity of pelletized diatomaceous earth using bimodal soil-water characteristic curve functions," *Canadian Geotechnical Journal*, vol. 3, no. 1, pp. 53–66, 2001.
- [12] W. Niu, W. Ye, C. Bao, and L. Qian, "Soil-water characteristic curve and permeability coefficient of Gaomiaozhi bentonite," *Chinese Journal of Underground Space and Engineering*, no. 5, pp. 952–955, 2009.
- [13] R. P. Chapuis, "Predicting the saturated hydraulic conductivity of sand and gravel using effective diameter and void ratio," *Canadian Geotechnical Journal*, vol. 4, no. 5, pp. 787–795, 2004.
- [14] M. Aubertin, R. P. Chapuis, A. Bouchentouf, and B. Bussière, "Unsaturated flow modeling of inclined layers for the analysis of covers," in *Proceedings of the 4th International Conference on Acid Rock Drainage*, pp. 731–746, Vancouver, Canada, May 1997.
- [15] X. Zhu, J. Yan, X. Wang, M. Chen, D. Zhao, and G. Yu, "Laboratory experimental study on the permeability coefficient of silt saturated soil," *Water Resources and Hydropower Technology*, vol. 4, no. 9, pp. 107–111, 2014.
- [16] M. Zhang, M. Jiang, and Y. Zhao, "Nonlinear permeability and parameter determination of dredger fill silt based on GDS consolidation apparatus," *Chinese Journal of Rock Mechanics and Engineering*, vol. 3, no. 3, pp. 625–632, 2013.
- [17] R. P. Chapuis, D. Chenaf, D. Marcotte, and M. Chouteau, "Essai de pompage dans un aquifère à nappe libre à Lachenaie, Québec," in *Proceedings of the 51st Canadian Geotechnical Conference*, pp. 515–522, Edmonton, Canada, October 1998.
- [18] X. Fu and R. Deng, *Indoor Rock Mechanics Experiments*, Southwest Jiaotong University Press, Chengdu, China, 2014.
- [19] C. R. R. Clarkson, Z. Pan, I. Palmer, and S. Harpalani, "Predicting sorption-induced strain and permeability increase with depletion for coalbed-methane reservoirs," *SPE Journal*, vol. 1, no. 1, pp. 152–159, 2010.
- [20] Canada GEO-SLOPE International Co., Ltd., *User Guide for Unsaturated Soil Seepage Analysis Software SEEP/W*, Metallurgical Industry Press, Beijing, China, 2011.
- [21] Y. Wang, B. Shi, L. Gao, and L. Jin, "Experimental study on temperature effect of cohesive soil permeability," *Journal of Engineering Geology*, vol. 1, no. 3, pp. 351–356, 2010.

- [22] B. Bai and C. Zhao, "Effect of temperature on mechanical properties of cohesive soil," *Rock and Soil Mechanics*, vol. 24, no. 4, pp. 533–537, 2000.
- [23] Z. Gu and B. Sun, "Experimental study on permeability of undisturbed soil, remolded soil and solidified soil," *Journal of Rock Mechanics and Engineering*, vol. 2, no. 3, pp. 505–508, 2003.
- [24] M. Mbonimpa, M. Aubertin, B. Bruno et al., "A model to predict the water retention curve from basic geotechnical properties," *Canadian Geotechnical Journal*, vol. 4, no. 6, pp. 1104–1122, 2003.
- [25] National Bureau of Quality and Technical Supervision, *National Standards of the People's Republic of China*, China Planning Press, Beijing, China, 1999.
- [26] M. Bi, Y. Qiao, and L. Wang, "Application of Seep/w in the structural optimization of dam foundation wall and curtain combined anti-seepage system," *Journal of China Three Gorges University*, vol. 3, no. 2, pp. 11–15, 2010.
- [27] H. Xiao, Z. Xia, D. Peng et al., "The effect of plant roots on the disintegration performance of purple soil in the water-level-fluctuating zone of the three gorges reservoir," *China Soil and Water Conservation Science*, vol. 1, no. 3, pp. 98–103, 2019.
- [28] B. J. Cosby, G. M. Hornberger, R. B. Clapp et al., "A statistical exploration of the relationships of soil moisture characteristics to the physical properties of soils," *Water Resources Research*, vol. 2, no. 6, 1984.
- [29] L. Ma, X. Lai, J. Zhang, S. Xiao, L. Zhang, and Y. Tu, "Blast-casting mechanism and parameter optimization of a benched deep-hole in an opencast coal mine," *Shock and Vibration*, vol. 202, no. 4, 11 pages, Article ID 1396483, 2020.
- [30] R. P. Chapuis and M. Aubertin, "A simplified method to estimate saturated and unsaturated seepage through dikes under steady-state conditions," *Canadian Geotechnical Journal*, vol. 3, no. 6, pp. 1321–1328, 2001.

Research Article

Simulation Analysis and Experimental Study on the Working State of Sinking Headframe in the Large Underground Shaft

Yin Qixiang ¹, Zhao Weiping ², Xin Wen,² Yang Hailin,² and Zhang Linglei¹

¹Jiangsu Vocational Institute of Architectural Technology, Xuzhou, Jiangsu 221116, China

²Tangshan Polytechnic College, Tangshan, Hebei 063299, China

Correspondence should be addressed to Zhao Weiping; zhaowphj@163.com

Received 26 January 2021; Revised 25 March 2021; Accepted 7 May 2021; Published 18 May 2021

Academic Editor: Jia Lin

Copyright © 2021 Yin Qixiang et al. This is an open access article distributed under the Creative Commons Attribution License, which permits unrestricted use, distribution, and reproduction in any medium, provided the original work is properly cited.

Based on the newly developed sinking headframe for the deep and large shaft, the finite element model of the full-scale headframe was established by using SAP2000. Through the calculation, the theoretical stress of the headframe at sinking depths of 40 m, 143 m, 223 m, 518 m, 762 m, 1000 m, 1250 m, and 1503 m was obtained and then compared with the field measured stress. The results show that with the increase of shaft sinking depth, the theoretical stress of finite element simulation and the field measured stress of each member of the sheave wheel platform and the headframe increase linearly, and for the maximum member stress in the upper, middle, and lower layers of the headframe, the numerical simulation value is greater than the field measured value and less than the designed steel strength. In other words, under normal working conditions, headframe members are in the elastic stress stage and meet the design requirements, and instability failure of headframe members will not occur. The end-restraint mode of the supporting bars has a great influence on the force of the top member. The reasonable selection of the restraint mode in the simulation is the key to the accuracy of the calculation results. The simulation results well reflect the actual stress of the headframe and provide a reliable guarantee for the follow-up work of the project.

1. Introduction

China has one of the richest coal reserves in the world. According to incomplete statistics, China's proven coal reserves are about 1 trillion tons, with complete coal types and wide distribution areas, which provides a reliable material guarantee for the development of the coal industry [1–5]. With the mining of mineral resources gradually shifting to the deep, the proportion of large diameter (more than 8 m) and deep shaft (more than 1000 m) exploitation will be further increased. In mine construction, the shaft construction is generally regarded as the key project, and the sinking headframe is the main stress component in the shaft construction process [6–9]. In the actual construction, the sinking headframe in the large shaft is subject to extremely complex stress, and its bearing capacity not only depends on its own structure but also closely related to the layout of the shaft sinking equipment and the ground winch lifting equipment [10–12]. The reason and limit value of derrick

inclination are determined by experiment and finite element modeling analysis. The inclination of derrick, support settlement, and corrosion of support beam are measured by experiment, and the bearing capacity is analyzed by considering defects in the finite element model [13–15].

With the development of test and analysis technology, field tests of prototype structure can be used to verify and develop the calculation theory and then directly applied to production practice to solve problems. More importantly, tracking and monitoring, fault alarm, and automatic control of important buildings are realized to ensure safe operation [16–18]. Due to the limitation of funds and conditions, it is impossible to monitor a large number of structures. Within the operation of structure for a certain time, field tests can be used to detect or diagnose the fault to achieve the purpose of troubleshooting [19–22]. Only through the field test of the prototype structure, various kinds of structural parameters, boundary conditions, and load distribution rules in line with the actual situation and the satisfactory results of the

theoretical analysis can be obtained. The field test is also the best way to develop the theory of prototype structure testing [23–25]. In a word, field tests and the monitoring of prototype structure play an irreplaceable role in both the theory development and the solution of practical production and scientific research problems [26, 27].

Kong [28] simulated and analyzed the structural changes of the headframe after lifting in the main and auxiliary shafts through the finite element analysis software and improved the stress state of some components of the headframe close to the critical stress state. Xiao et al. [29] used the anchoring agent, screw-thread steel, and concrete foundation reinforcement methods to reinforce the headframe leg foundation. As a result, the further settlement deviation of the headframe foundation was prevented after the use of the freezing method in a mine, and the construction safety and smooth sinking construction were ensured. In previous studies [30–33], the headframe stress caused by headframe deflection was analyzed. Gusella et al. [34] studied the dynamic characteristics of headframe structure and determined its influencing factors based on the simulation analysis. Link [35] regarded the element stiffness parameter as a modified parameter in the process of relevant research and modified the design scheme appropriately based on the obtained results. In these studies [36, 37], the fatigue stress and deformation of various components of headframe were intuitively and comprehensively analyzed based on the field measurement method [38, 39].

With the continuous increase of energy demand, the required sinking speed and production efficiency have been improved, and the diameter and depth of the construction shaft have been increased; thus, the lifting capacity of the headframe should be increased greatly. However, the conventional sinking headframe cannot meet the needs of deep and large shaft construction, and the stress analysis of the super large shaft headframe is rarely reported. In this study, the stress of the large sinking headframe developed for the auxiliary shaft (net diameter 10 m, depth 1503.9 m) in the Sishanling iron mine was comprehensively analyzed.

2. Selection of the Headframe for Large Shaft Sinking

The auxiliary shaft of the Sishanling iron mine was located in Benxi City, Liaoning Province. The net diameter of the shaft was 10.0 m, and the shaft neck section was 40 m in total. The temporary lock section was 3.7 m, which was supported by 1000 mm thick brick. The neck section of the shaft was supported by 1000 mm thick reinforced concrete. The shaft sinking equipment included the lifting system, transportation system, ventilation system, air pressure system, drainage system, and water supply system.

For the engineering conditions of the shaft with a diameter over 8 m and a depth over 1000 m, the existing V-type headframe with the largest specification cannot meet the construction conditions. According to the construction requirements of drilling equipment and the large shaft, the SA-III type headframe was selected. This headframe was developed by China University of Mining and Technology

and Handan Design Engineering China Coal Co., Ltd. meet the development trend of overdepth and large-diameter shaft in China. The Q345 steel was selected as the main and auxiliary materials of the large-scale sinking headframe. Figure 1 shows its structural form, and Figure 2 shows the sinking headframe in working condition.

According to the characteristics of large diameter and deep depth of the auxiliary shaft in Sishanling iron mine and the construction technology of the shaft, the shaft sinking equipment included a hoist and bucket, a Φ 9800 mm three-layer hanging plate, the YSJZ-6.12 hydraulic umbrella drill, and two HZ-6B central rotary rock grabs. According to the selected drilling equipment, eight kinds of drilling depth were obtained: 40 m, 143 m, 223 m, 518 m, 762 m, 1000 m, 1250 m, and 1503 m; then, the working loads of wire rope of sinking equipment under eight working conditions were obtained. The loads of wire rope were transmitted to the sheave wheel platform and then to the stress bars of the headframe. Figure 3 shows the number and corresponding position of the stress bars.

A FBD-2 \times 55 kW counter rotating fan with a Φ 1000 mm FRP air duct is installed near the wellhead for forced ventilation. Two 35 W \times 7 – Φ 42–1960 steel wire ropes and two JZ-40/1800 stable car suspensions are selected. A Φ 57 \times 3.5 water supply pipe is arranged in the shaft, and the surface is connected with the underground reservoir. A pressure reducing valve is installed in the water supply pipe in the shaft to meet the water pressure requirements of the rock drill.

3. Simulation Analysis of Working State of the Large Sinking Headframe

In the SAP2000 finite element numerical simulation analysis, the number and position of the large sinking headframe were consistent with the measuring points of the headframe, and working conditions of the numerical simulation analysis were consistent with the working condition of the sinking depth measured in the field. The corner columns and supporting bars of large sinking headframe were mainly axial force-bearing bars, and the normal stress at each point on the cross-section was $\sigma = N/A$, and the cross-sections were all Φ 325 mm \times 16 mm. According to the length, these members can be divided into eight types, I-II corner columns and III-VIII supporting bars. The end spring stiffness of the supporting bars was 1000 N/mm. Through the force analysis of members and side beam of the sheave wheel platform, the steel of the HN 1350 mm \times 600 mm \times 25 mm \times 45 mm was adopted for the sheave wheel platform. The calculated length coefficient of the supporting bars was taken as 0.9, and the calculated length coefficient of the axial compression member hinged at both ends is 1.0. Table 1 provides the parameters of the members.

Through the calculation of $\sigma = N/A$, the stress was obtained. The stress at the sinking depth of 40 m (the release of the hanging plate) was taken as the reference value in the field measurement. Through the above equations, the theoretical stress of corner column and supporting bars for the

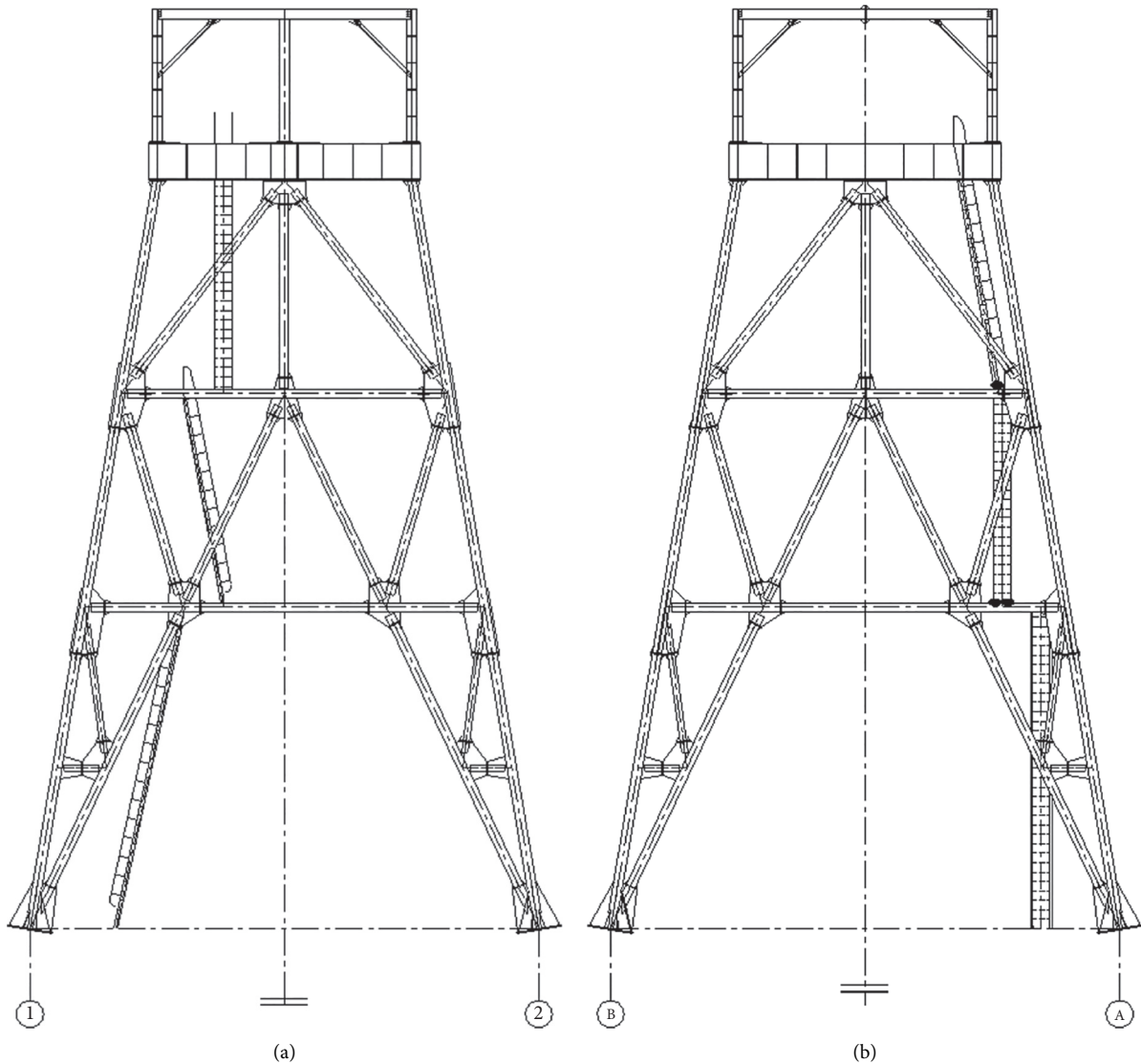


FIGURE 1: General drawing of SA-III sinking headframe. (a) Front elevation of headframe. (b) Side elevation of headframe.

headframe in the working condition of 40 m, 143 m, 223 m, 518 m, 762 m, 1000 m, 1250 m, and 1503 m was calculated.

3.1. Stress Analysis of Upper Members. With the increase of sinking depth, the theoretical stress curves of the upper corner column and supporting bars are obtained, as shown in Figure 4 and Figure 5, respectively.

As shown in Figures 4 and 5, the stress value of the upper member increases gradually with the increase of sinking depth. The stress growth rate of corner column G07 and supporting bar F17 is the fastest, while that of corner column G04 and supporting bar F01 is the slowest. The reason is that the load growth rate on the beam of the sheave wheel platform corresponding to G07 and F17 is greater than that of G04 and F01. When the sinking depth is 1503 m, the maximum compressive stress of G07 and F17 is 105.4 MPa and 69.7 MPa, which is far less than the designed tensile strength of Q345 steel ($f = 310$ MPa). It shows that the upper

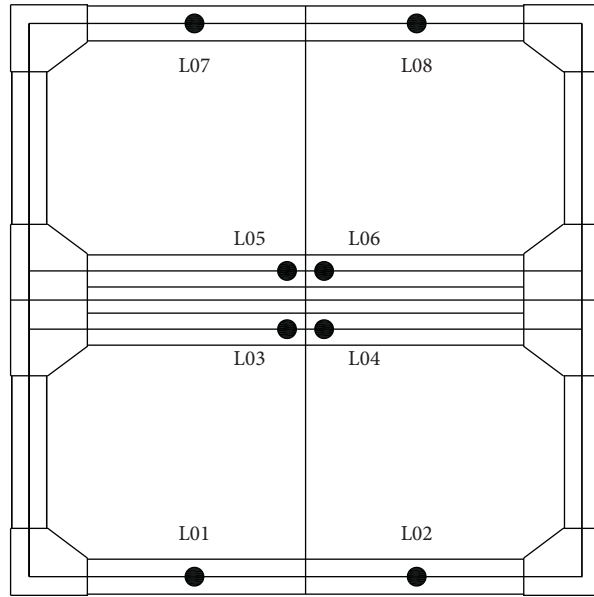
members are in the elastic stress stage, meeting the design requirements, and the instability failure of headframe members will not occur under the normal working condition within the sinking depth of 1503 m.

3.2. Stress Analysis of Middle Members. With the increase of sinking depth, the theoretical stress curves of the middle corner columns and supporting bars are shown in Figure 6 and Figure 7.

As shown in Figures 6 and 7, the stress value of the middle members gradually increases with the increase of the sinking depth. The growth rate of compressive stress and tensile stress of corner column G08 and supporting bar F22 is the fastest, while that of corner column G05 and supporting bar F06 and supporting bar F04 is the slowest. The reason is that the load growth rate of G08, F22, and F20 corresponding to the sheave platform beam is higher than that of G05, F06, and F04. When the shaft sinking depth is



FIGURE 2: The working condition of sinking headframe in the field.



(a)

FIGURE 3: Continued.

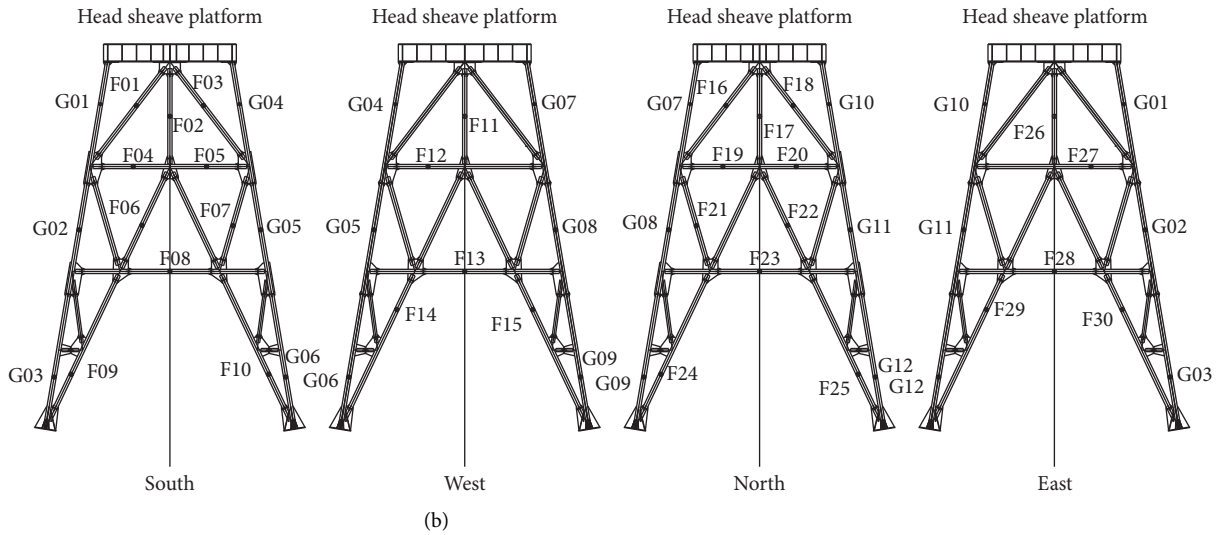


FIGURE 3: Number and corresponding positions. (a) Sheave wheel platform. (b) Headframe.

TABLE 1: Parameters of the members.

Types of member bar	l/mm	μ	I/mm^4	A/mm^2	λ	Member bar type
Class I	8228.0	1.0	1.86×10^8	1.55×10^4	75.2	Corner columns 01, 02, 04, 05, 07, 11
Class II	6171.0	1.0	1.86×10^8	1.55×10^4	56.4	Corner columns 03, 06, 09, 12
Class III	10157.8	0.9	1.86×10^8	1.55×10^4	83.6	Supporting bars F01, F03, F16, F18
Class IV	8114.8	0.9	1.86×10^8	1.55×10^4	66.8	Supporting bars 02 and 17
Class V	8962.1	0.9	1.86×10^8	1.55×10^4	73.7	Supporting bars 06 and 21
Class VI	8436.1	0.9	1.86×10^8	1.55×10^4	69.4	Supporting bars 07, F22
Class VII	7608.0	0.9	1.86×10^8	1.55×10^4	62.6	Supporting bars 08, 13, 23, F28
Class VIII	6721.6	0.9	1.86×10^8	1.55×10^4	55.3	Supporting bars 09, 10, 14, 15, 24, 25, 29, F30

Note. l is the length of the member; μ is the calculated length; I is the moment of inertia of the section; A is the area of the section; λ is the flexibility of the member.

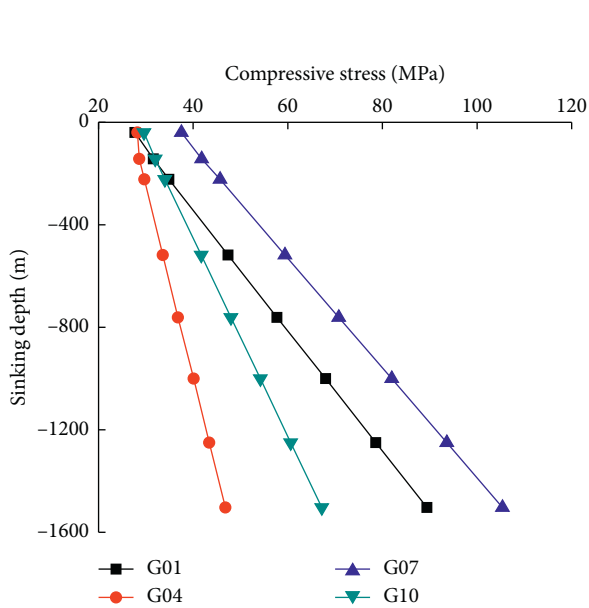


FIGURE 4: Theoretical stress curve of upper corner column under different working conditions.

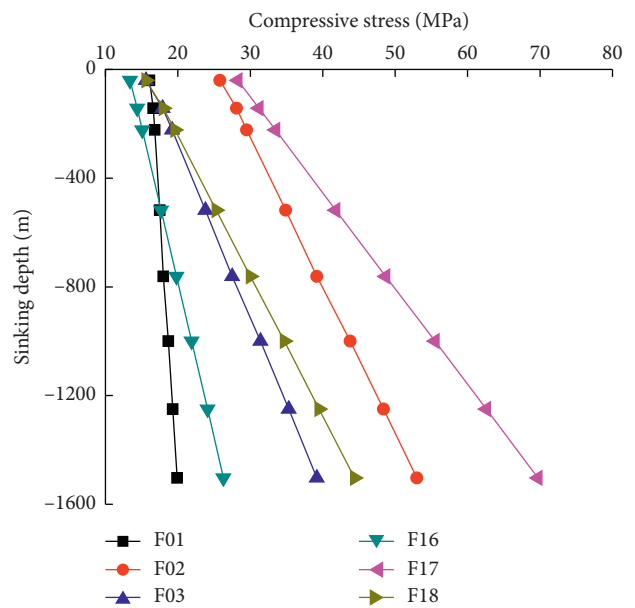


FIGURE 5: Theoretical stress curve of upper supporting bars under different working conditions.

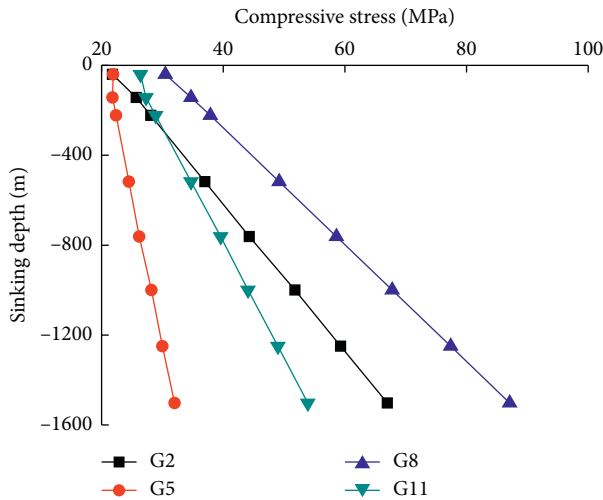


FIGURE 6: The theoretical stress curve of middle corner columns under different working conditions.

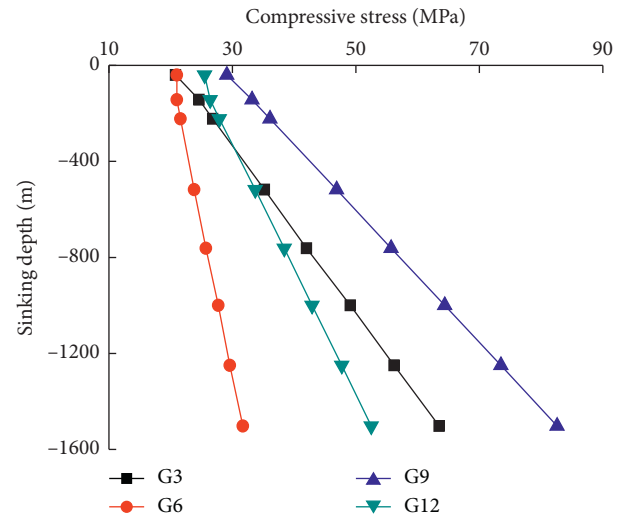


FIGURE 8: Theoretical stress curves of the lower corner column under different working conditions.

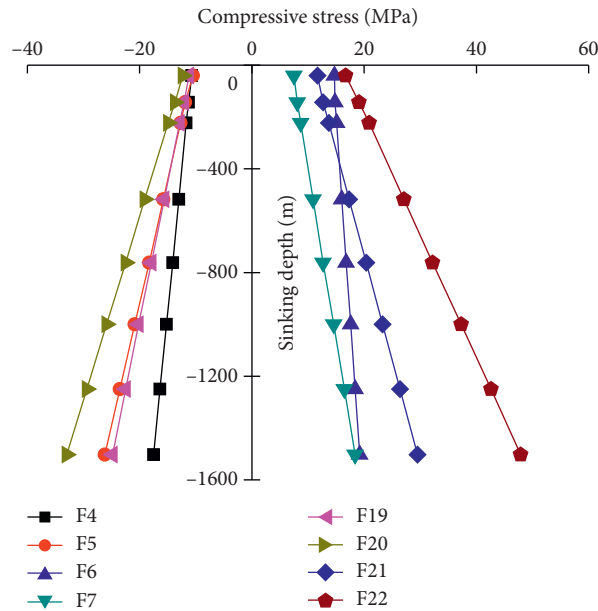


FIGURE 7: The theoretical stress curve of middle supporting bars under different working conditions.

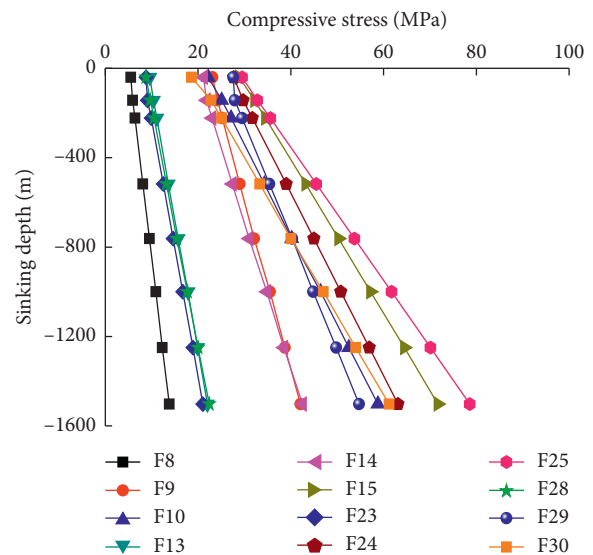


FIGURE 9: Theoretical stress curves of the lower supporting bars under different working conditions.

1503 m, the maximum compressive stress of G08 and F22 are 87.1 MPa and 47.9 MPa, which is far less than the designed tensile strength of Q345 steel ($f = 310$ MPa). It shows that the middle members are in the elastic stress stage, meeting the design requirements; the instability failure of headframe members will not occur under the normal working condition within the sinking depth of 1503 m.

3.3. Stress Analysis of Lower Members. With the increase of sinking depth, the theoretical stress curve of lower corner columns and supporting bars is obtained, as shown in Figure 8 and Figure 9.

As shown in Figures 8 and 9, the stress value of lower members gradually increases with the increase of the sinking

depth. The stress growth rate of corner column G09 and supporting bar F25 is the fastest, while that of corner column G06 and support bar F08 is the slowest. When the shaft sinking depth is 1503 m, the maximum compressive stress of G09 and F25 is 82.6 MPa and 78.6 MPa, which is far less than the designed tensile strength of Q345 steel ($f = 310$ MPa). It shows that the top members meet the design requirements and are in the elastic stress stage; the instability failure of headframe members will not occur under the normal working condition within the sinking depth of 1503 m.

3.4. Stress Analysis of Members in the Sheave Wheel Platform. In the establishment process of the finite element model of the sheave wheel platform in the headframe, the bending moment and torque at the end of the supporting member should be

transferred without the release. The calculation results of the bending normal stress at the measuring points of the cross-section of the sheave wheel platform beam under the working conditions of 40 m, 143 m, 223 m, 518 m, 762 m, 1000 m, 1250 m, and 1503 m are obtained, as shown in Figure 10.

As shown in Figure 10, with the increase of the sinking depth, the theoretical stress of four measuring points L03, L04, L05, and L06 of the two middle beams of the sheave wheel platform and the four measuring points L01, L02, L07, and L08 of the two side beams of the sheave wheel platform in the finite element numerical simulation increases linearly under normal working conditions. When the shaft sinking depth is 1503 m, the maximum stress of the middle beam L05 (L06) of the sheave wheel platform is 34.1 MPa, which is far less than the designed tensile strength ($f = 310$ MPa). It shows that the headframe members are in the elastic stress stage, meeting the design requirements, and the instability failure of headframe members will not occur under the normal working condition within the sinking depth of 1503 m.

As shown in Figure 10, the stress growth rate of measuring point L05 (L06) in the middle beam of the sheave wheel platform is the fastest and the largest and that of measuring point L07 in the side beam of the sheave wheel platform is the slowest. Through the analysis of the equipment layout on the beam of the sheave wheel platform in the headframe and the rigid connection at the end of the supporting bar, it can be concluded that there is no support constraint in the middle beam of the sheave wheel platform, and the middle beam is a single span simply supported beam. The load growth rate of measuring points L05 (L06) on the side beam of platform is faster than that of L03 (L04) on the middle beam of platform, and the stress in the midspan increases the fastest and the most. Because of the rigid connection at the end of the supporting bar, the center of the side beam of the platform is supported, so the side beam of the platform can be considered as the two-span continuous beam with a certain supporting function. Since the span is reduced by one time, the stress growth rate at the measuring point of the side beam of the platform is the slowest and the smallest.

4. Field Measurement and Analysis of the Working State of Sinking Headframe in the Large Shaft

According to the stress characteristics of the headframe in this project, the constraints of site construction conditions and economic cost and other factors are considered, and the strain gauge electrical measuring system was used as the static test scheme of the headframe working state in this project. According to the basic situation of the auxiliary shaft engineering in Sishanling iron mine, combined with the main test contents of headframe in the SA-III vertical shaft sinking, the main measured headframe strain on-site was

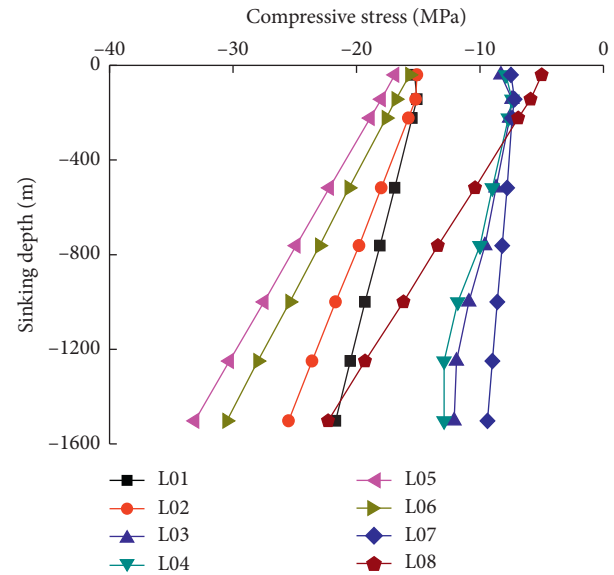


FIGURE 10: Theoretical stress curves of platform beams of sheave wheel platform under different working conditions.

considered, and the actual bearing condition of the headframe was judged, and the datataker test system was adopted.

Eight times of static data acquisition were carried out on-site, including eight working conditions of 40 m, 143 m, 223 m, 518 m, 762 m, 1000 m, 1250 m, and 1503 m. The field data acquisition is shown in Figure 11.

According to the field measurement results and the conclusion of numerical simulation analysis, the most representative members of the upper, middle, and lower layers are selected for analysis. In other words, the members with the maximum stress of corner columns, vertical supporting bars, and diagonal supporting bars in the upper, middle, and lower parts are selected for comparison, as shown in Figure 12.

As shown in Figure 12, the stress variation law of bars in the field measurement is consistent with that of simulation results. The stress of bars increases with the increase of shaft sinking depth, and the measured value is less than the theoretical value in the simulation calculation. Therefore, the bar stress of the headframe is far less than the maximum bearing capacity of the bar within 1503 m of shaft sinking depth. In other words, these bars meet the design requirements and are in the elastic stress stage, and the instability failure of headframe members will not occur. Besides, with the increase of the shaft sinking depth, the measured stress value of the bars is gradually close to the simulated value. At the shaft sinking depth of 1503 m, the measured stress value of the bars is basically consistent with the simulated value. It can be concluded that the simulation results can better reflect the actual situation.

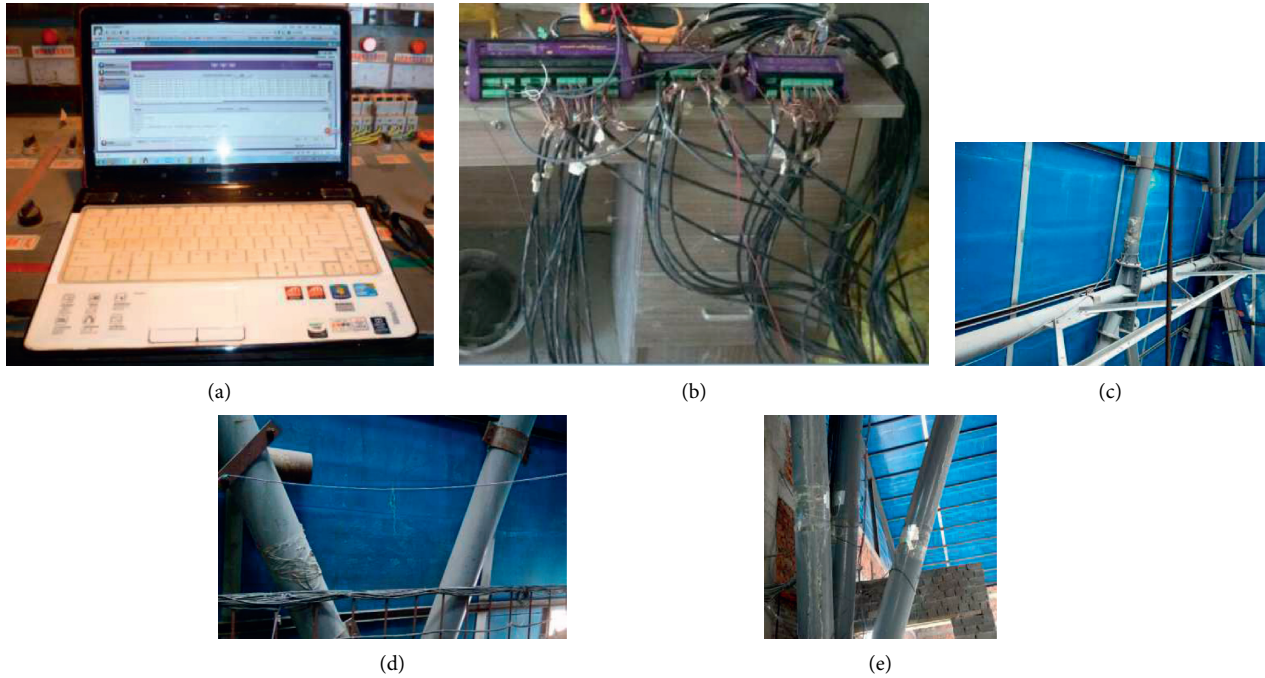


FIGURE 11: Field data acquisition. (a) Data acquisition equipment. (b) Datataker data acquisition. (c) Site map of upper measuring points. (d) Site map of middle measuring points. (e) Site map of lower measuring points.

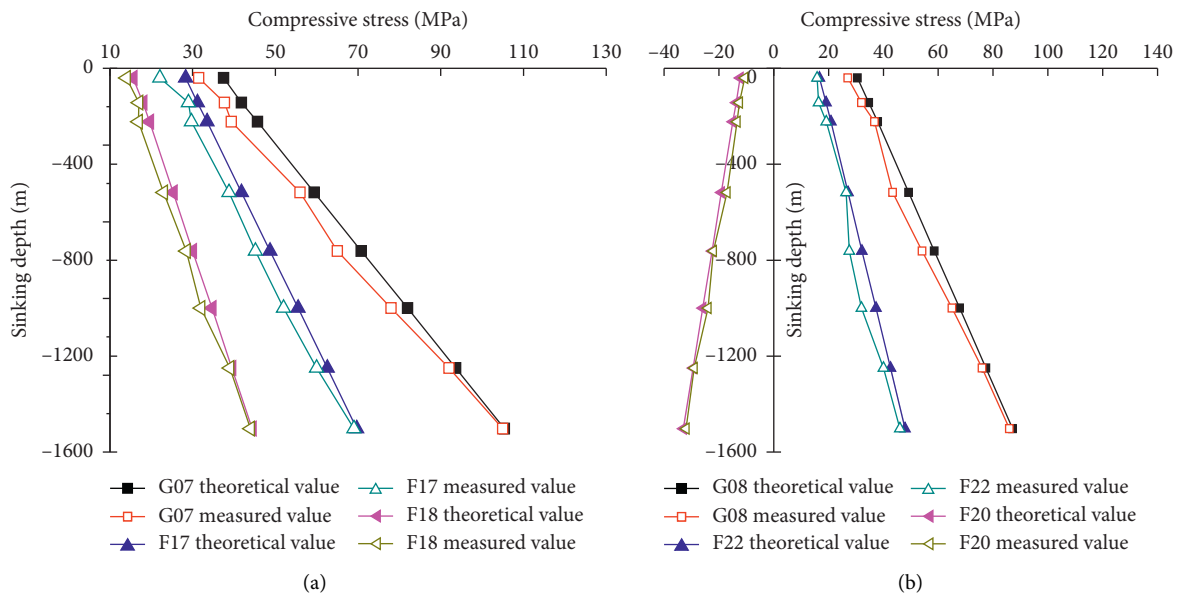


FIGURE 12: Continued.

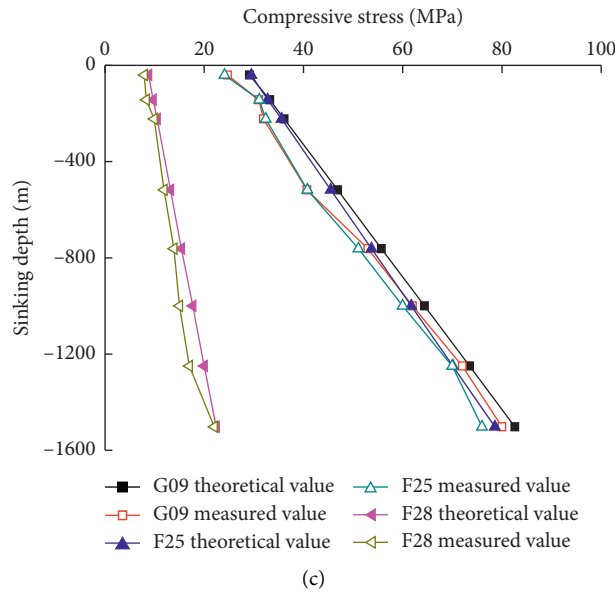


FIGURE 12: Comparison between measured values and theoretical values. (a) Upper members. (b) Middle members. (c) Lower members.

5. Analysis of the Influence of Different Constraint Modes on the Support End

The upper members mainly include corner column and supporting bar. According to the above simulation analysis and field measurement results, the top corner column G07, vertical supporting bars F17, and inclined supporting bars F18 are the most stressed. The stress variation curve of the upper member and the sheave wheel platform under different restraint modes with the shaft sinking depth is shown in Figure 13.

It can be seen that when the constraint of member changes from flexible to rigid, the slope of curves increases gradually. Within a certain range of sinking depth, the compressive stress of the flexible constraint has a greater change. Since the different constraint methods lead to different stress characteristics of the bar, the flexible constraint has a greater impact on the compressive stress of the bar.

As shown in Figure 13, the measured analysis results of the working state of the upper member are between the calculation results of the finite element numerical simulation of the rigid connection and the flexible connection. The corner column stress of the rigid connection at the end of the supporting bar is 55.7% lower than that of the flexible connection at the end of the supporting bar, and the supporting bar stress of the rigid connection at the end of the supporting bar is 36.17% and 58.3% higher than that of the flexible connection at the end of the supporting bar, respectively. It shows that the end-restraint mode of the supporting member has a great influence on the force of the uppermost member. Therefore, in the finite element numerical simulation, the determination of the end-restraint mode of supporting bars is particularly important for the calculation analysis and optimization design of the headframe in the large shaft sinking.

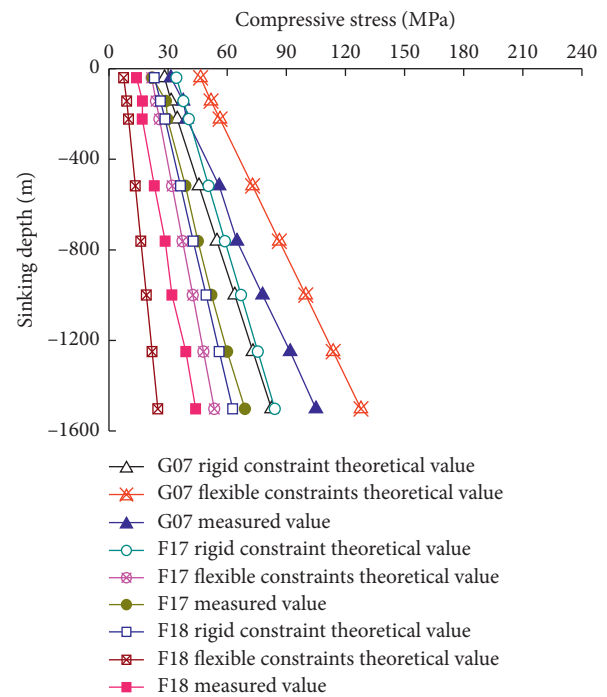


FIGURE 13: Variation curve of member stress with sinking depth under different restraint modes.

6. Conclusions

Aiming at the field application of the newly developed steel headframe for the superlarge and ultradeep shaft in the auxiliary shaft of the Sishanling iron mine, the working state and mechanical performance analysis of the headframe are carried out in combination with the actual project. The results of field measurement and finite element numerical

simulation are compared and analyzed. The conclusions are drawn as follows:

- (1) Numerical simulation analysis of the headframe members in eight sinking depths of 40 m, 143 m, 223 m, 518 m, 762 m, 1000 m, 1250 m, and 1503 m is performed. The results show that the stress of headframe members increases linearly with the increase of sinking depth;
- (2) The measured stress of headframe in the on-site working condition is less than the theoretical stress of headframe in the finite element numerical simulation. When the sinking depth is less than 1503 m, the reliability of this project is verified by the results of numerical simulation results and field measurement, that is, the headframe members are in the elastic stress stage, meeting the design requirements, and the instability failure of headframe members will not occur under the normal working condition within the sinking depth of 1503 m.
- (3) The end restraint mode of the supporting member has a great influence on the force of the top member. The reasonable selection of the end-restraint mode in the simulation is the key to the accuracy of the calculation results.

The numerical simulation in this study can better reflect the stress state of the shaft headframe in the actual project and provide a reliable guarantee for the follow-up mining work. The simulation results and measured results show that the internal force of the member bar has a large surplus, and the bar can be optimized to achieve the purpose of saving steel, which will be further studied.

Data Availability

The data used to support the findings of this study are included within the article.

Conflicts of Interest

The authors declare that they have no conflicts of interest.

Acknowledgments

This research was funded by the Tangshan Science and Technology Research and Development Plan (the Third Batch) Project of China (grant no.20150221C) and the Natural Science Foundation of the Jiangsu Higher Education Institutions of China (grant no. 20KJB560009).

References

- [1] H. Z. Zhao, X. Zhen, and M. J. Li, "Development status of open-pit coal mines in China," *China Mining Magazine*, vol. 25, no. 6, pp. 12–15, 2016.
- [2] H. Zhang, "Open-pit coal mine mining theory, technology and development trend," *OpenCast Mining Technology*, vol. 34, no. 1, pp. 1–9, 2019.
- [3] J. I. Rojas-Sola and I. Palomares-Munoz, "3d modelling and static analysis of a Spanish articulated metal headframe for mineral extraction," *Dyna*, vol. 90, no. 6, p. 602, 2015.
- [4] D. Ma, J. Zhang, H. Duan et al., "Reutilization of gangue wastes in underground backfilling mining: overburden aquifer protection," *Chemosphere*, vol. 264, no. 1, p. 128400, 2021.
- [5] E. Rusiński, P. Moczko, and P. Odyjas, "Estimating the remaining operating time of mining headframe with consideration of its current technical condition," *Procedia Engineering*, vol. 57, pp. 958–966, 2013.
- [6] A. Nechitailo, Y. Horokhov, and V. Kushchenko, "Analysis of the mode of deformation of the sub-pulley structures on shaft sloping headgear structures," in *Proceedings of the 18th International Conference on the Application of Computer Science and Mathematics in Architecture and Civil Engineering*, Istanbul, Turkey, June 2012.
- [7] V. Kushchenko and A. Nechitailo, "The analysis of the intense deformed condition of the basic bearing elements of frame mowing mine headgears," *Metal Constructions*, vol. 17, no. 3, pp. 151–165, 2011.
- [8] D. Ma, H. Duan, W. Liu, X. Ma, and M. Tao, "Water-sediment two-phase flow inrush hazard in rock fractures of overburden strata during coal mining," *Mine Water and the Environment*, vol. 39, no. 2, pp. 308–319, 2020.
- [9] V. Kushchenko and A. Nechitailo, "Computer simulation of the stress-strain state of the subsurface stitched mine frame structures," *Building Materials Science. Engineering Series: Computer Systems and Information Technology in Education, Science and Management*, vol. 23, no. 78, pp. 155–159, 2014.
- [10] E. G. Kassikhina, V. V. Pershin, and V. M. Volkov, "Assembling of steel angle headframe of multifunctional purpose. IOP conference series: materials science and engineering," *IOP Publishing*, vol. 253, no. 1, Article ID 012020, 2017.
- [11] D. Ma, H. Duan, Q. Zhang et al., "A numerical gas fracturing model of coupled thermal, flowing and mechanical effects," *Computers, Materials & Continua*, vol. 65, no. 3, pp. 2123–2141, 2020.
- [12] Y.-B. Wang, G.-Q. Li, S.-W. Chen, and F.-F. Sun, "Experimental and numerical study on the behavior of axially compressed high strength steel box-columns," *Engineering Structures*, vol. 58, pp. 79–91, 2014.
- [13] T.-J. Li, S.-W. Liu, G.-Q. Li, S.-L. Chan, and Y.-B. Wang, "Behavior of Q690 high-strength steel columns: Part 2: parametric study and design recommendations," *Journal of Constructional Steel Research*, vol. 122, pp. 379–394, 2016.
- [14] N. E. Shanmugam, S. P. Chiew, and S. L. Lee, "Strength of thin-walled square steel box columns," *Journal of Structural Engineering*, vol. 113, no. 4, pp. 818–831, 1987.
- [15] C. S. Stolle and J. D. Reid, "Development of a wire rope model for cable guardrail simulation," *International Journal of Crashworthiness*, vol. 16, no. 3, pp. 331–341, 2011.
- [16] O. Hasançebi and S. Carbas, "Bat inspired algorithm for discrete size optimization of steel frames," *Advances in Engineering Software*, vol. 67, pp. 173–185, 2014.
- [17] D. Ma, H. Duan, J. Liu, X. Li, and Z. Zhou, "The role of gangue on the mitigation of mining-induced hazards and environmental pollution: an experimental investigation," *Science of the Total Environment*, vol. 664, pp. 436–448, 2019.
- [18] M. Hartnett and P. Mitchell, "An analysis of the effects of the leg-spacing on spectral response of offshore structures," *Advances in Engineering Software*, vol. 31, no. 12, pp. 991–998, 2000.

- [19] E. Dogan and M. P. Saka, "Optimum design of unbraced steel frames to LRFD-AISC using particle swarm optimization," *Advances in Engineering Software*, no. 1, pp. 27–34, 2012.
- [20] V. Kushchenko and A. Nechitailo, "Analysis of the mode of deformation of the joints of guide pulley resting on shaft sloping headgear structures," *Metal Constructions*, vol. 18, no. 2, pp. 97–109, 2012.
- [21] K. Kuzniar and T. Tatara, "Dynamic investigations of various civil engineering structures due to ambient and mining tremors," *EDP Sciences*, vol. 24, Article ID 04008, 2015.
- [22] V. Kushchenko and A. E. Nechitailo, "Strength analysis of the nodes of the bearing of the guide pulleys of frame ukosny mine pile drivers," *Metal Constructions*, vol. 20, no. 1, pp. 15–27, 2014.
- [23] S. Sandun De Silva and D. P. Thambiratnam, "Dynamic characteristics of steel-deck composite floors under human-induced loads," *Computers & Structures*, vol. 87, no. 17-18, pp. 1067–1076, 2009.
- [24] V. Kushchenko and A. E. Nechitailo, "Factor analysis of the stress state of the support units of the guide pulleys of the frame shaft copers," *Construction Materials Engineering. Series: Life Safety*, vol. 71, no. 2, pp. 92–101, 2013.
- [25] V. Kushchenko and A. E. Nechitailo, "Rational design of bearing units for guide pulleys," *Budivelne Virobnitstvo*, vol. 57, no. 2, pp. 42–45, 2014.
- [26] S. Mustafa, "Artificial Bee Colony algorithm for optimization of truss structures," *Applied Soft Computing*, vol. 11, no. 2, pp. 2406–2418, 2011.
- [27] D. Ma, J. Wang, X. Cai et al., "Effects of height/diameter ratio on failure and damage properties of granite under coupled bending and splitting deformation," *Engineering Fracture Mechanics*, vol. 220, p. 106640, 2019.
- [28] D. Kong, "Unilateral sprag-type vertical shaft headframe rectification process," *China Coal*, vol. 39, no. 4, pp. 71–73, 2013.
- [29] Q. F. Xiao, M. Li, and B. G. Chen, "Freezing mine shaft headframe differential settlement," *Mine Onstruction Technology*, vol. 30, no. 4, pp. 37–39, 2009.
- [30] H. L. Zhang, W. F. Jia, and Z. L. Chen, "Application research of grouting reinforcing shaft headframe," *Modernization of Coal Mines*, vol. 22, no. 2, pp. 7–9, 2016.
- [31] C. Y. Zhang, W. H. Zheng, and X. M. Feng, "Research on the deformation monitoring method of a derrick," *Geomatics and Spatial Information Technology*, vol. 39, no. 3, pp. 202–204, 2016.
- [32] D. Ma, H. Duan, X. Li, Z. Li, Z. Zhou, and T. Li, "Effects of seepage-induced erosion on nonlinear hydraulic properties of broken red sandstones," *Tunnelling and Underground Space Technology*, vol. 91, p. 102993, 2019.
- [33] Z. Q. Wang, G. Y. Wang, W. H. Zhang, S. J. Zhang, Y. L. Ren, and Z. Q. Liu, "Analysis and forecast of shaft frame inclination and its rectification control," *Metal Mine*, vol. 31, no. 4, pp. 24–26, 2002.
- [34] V. Gusella, O. Spadaccini, and A. Vignoli, "Dynamic identification of vega platform drilling derrick," in *Proceedings of the Second International Offshore and Polar Engineering Conference*, pp. 314–321, June 1992, San Francisco, CA, USA.
- [35] M. Link, "Updating of analytical models - review of numerical procedures and application aspects," *Structural Dynamics*, vol. 2001, 2000.
- [36] Z. Q. Li and H. W. Li, "Structural optimization of mine hoist derrick based on ANSYS," *Coal Mine Machinery*, vol. 37, no. 6, pp. 18–20, 2016.
- [37] P. B. Xu, "Study on analysis of virtual fatigue life of two-pillar mask hydraulic support," *Coal Mine Machinery*, vol. 40, no. 3, pp. 34–36, 2019.
- [38] D. Ma, J. J. Wang, and Z. H. Li, "Effect of particle erosion on mining-induced water inrush hazard of karst collapse pillar," *Environmental Science and Pollution Research*, vol. 26, no. 19, pp. 19719–19728, 2019.
- [39] D. Ma, X. Miao, H. Bai et al., "Impact of particle transfer on flow properties of crushed mudstones," *Environmental Earth Sciences*, vol. 75, no. 7, p. 593, 2016.

Review Article

Mechanism and Classification of Coal and Gas Outbursts in China

Qi Zhang ¹, Chun-li Yang,² Xiang-chun Li ¹, Zhong-bei Li,¹ and Yi Li¹

¹*School of Emergency Management and Safety Engineering, China University of Mining and Technology-Beijing, Beijing 100083, China*

²*Occupational Hazards Control Technology Center, Beijing Municipal Institute of Labour Protection, Beijing 100054, China*

Correspondence should be addressed to Xiang-chun Li; chinalixc123@163.com

Received 1 March 2021; Revised 9 April 2021; Accepted 28 April 2021; Published 13 May 2021

Academic Editor: Jia Lin

Copyright © 2021 Qi Zhang et al. This is an open access article distributed under the Creative Commons Attribution License, which permits unrestricted use, distribution, and reproduction in any medium, provided the original work is properly cited.

Coal and gas outburst is a kind of complex dynamic disaster with short duration and strong explosiveness, and the modes and strength of the outburst are determined by the in situ stress, gas pressure, and physical and mechanical properties of the coal mass. In this paper, the status quo of research on the mechanism of coal and gas outburst in China is described from three aspects: the controlling effect of single factor, the controlling effect of multi-factor, and new understandings of the outburst mechanism in recent years. Firstly, controlling factors of coal and gas outburst are classified for an in-depth analysis of the main factors of the same type of disasters, and the research progress and new understandings of the mechanism of coal and gas outburst are systematically sorted out. Secondly, the influencing factors of the strength coal mass are analyzed, and the related issues of coal mass strength on coal and gas outburst disaster mechanism are discussed. The results show that the stages of incubation, occurrence, development, and stop on coal and gas outburst are affected by the coupling effects of in situ stress field, gas pressure field, and seepage field, and the coal strength becomes an important factor affecting outburst strength under the same in situ stress and gas pressure. Therefore, the scientific and reasonable improvement methods of such similar simulation experiment devices are proposed according to the existing experimental methods and devices, which is of great significance to provide ideas for the continuous transferring to deep mining and preventing coal and gas outburst in China in the future.

1. Introduction

Coal and gas outburst is a lump of typical coal and rock dynamic disaster in the process of coal mine production, which has become a key problem affecting the safety of coal production and causing serious casualties and property losses [1, 2]. Besides, coal and gas outbursts are extremely complex dynamic disasters with extremely short duration and strong explosiveness, and its disaster mechanism is fundamental to prevent coal and gas outburst [3, 4].

Currently, the mechanisms of coal and gas outburst are still in the stage of hypothesis, such as the hypothesis of gas action, ground stress, chemical action, and other single factor hypothesis, which cannot fully explain some special disasters reasonably [5–7]. However, in the practical explorations of the mechanism of coal and gas outburst, more and more scholars believe that coal and gas outbursts occur under the combined action of three main factors, namely,

gas pressure, in situ stress, and physical and mechanical properties of coal mass [8, 9]. Since the 1950s, the former Soviet Union expert B. B. Hodot conducted the simulation experiments on coal and gas outburst with soft coal for the first time, subsequently followed by a lot of coal and gas outbursts by many other researchers, but most of them utilized pulverized coal as the experimental materials and focused mainly on soft coal outburst. Besides, the coal strength is one of the important parameters of the coal physical and mechanical properties of coal, but it was not taken as the variable index of outbursts [10–12]. It is found that coal strength is closely related to outburst indexes such as coal quality, outburst distance, and hole depth. As a result, the change of coal strength affects the outburst strength under the same in situ stress and gas pressure [13–15].

Given this, the paper expounds the disaster mechanisms of coal and gas outbursts in China, assorts the types of the disaster mechanisms, and analyzes the main controlling

factors of coal and gas outburst. Besides, the influencing factors of coal strength and the causes of coal outburst are emphatically analyzed. Furthermore, the relevant scientific problems are discussed, and the research directions and urgent scientific problems about the mechanism of coal and gas outburst are put forward, so as to provide theoretical support for the prevention and control of coal and gas outburst accidents and the reduction of casualties and property losses.

2. Research Progress on Mechanism of Coal and Gas Outburst

The outburst processes occur with huge energy effects and sounds, which damage the facilities in the surrounding rock roadway facilities and discharge with harmful gases such as gas and carbon dioxide, resulting in suffocation casualties, which easily lead to gas explosion, fire, and other safety accidents [16–20]. Since the first recorded coal and gas outburst accident in 1834, it has become one of the most serious disasters in coal mines [21].

Since the 20th century, a large body of researches on the mechanism of coal and gas outbursts, and based on the experience of preventing and controlling outburst accidents [22–24]. At the same time, with laboratory tests and computer simulations, a series of hypotheses on the disaster mechanism are formed, such as spherical shell instability hypothesis [25–27], rheological hypothesis [28, 29], two-phase fluid hypothesis [30], unified instability theory [31], fluid-solid coupling instability theory [32, 33], and key layer stress wall outburst mechanism [34, 35]. In recent years, with the progress of technology and experimental methods, new theories and understandings are constantly put forward, which are mainly summarized as the following aspects.

2.1. Single-Factor Dominant Control Theory. The in situ stress, gas pressure, and the physical and mechanical properties of coal and rock mass fully determine the way and intensity of coal and gas outbursts. According to the current complex geological conditions and the control factors of the outburst, coal and gas outburst disasters can be classified with quantitative study for an in-depth exploration of the main control factors under the same type of coal and gas outburst disasters. Yuan [36] conducted experiments based on the comprehensive action hypothesis and found that coal and gas outbursts were mainly driven by gas. A large body of gas is stored in fractured coal, which supports the formation and growth of the bursts. Driven by the gas, the coal mass of low permeability are destroyed instantly, discharging huge energy and leading to coal and gas outbursts. Chen et al. [37] utilized the coal and gas outburst test system with multi-field coupling conditions and found that gas pressure had obvious pulverization effect on coal mass. The high gas pressure gradient of the gas makes it circulate in the cracks inside the coal mass, and a large amount of pulverization, particles, and small pieces of coal ash inhibit the further outburst.

Moreover, increasing studies show that coal and gas outbursts are closely related to geological tectonic

movement, and the uneven distribution of geological structure greatly changes the state of other factors such as in situ stress, gas pressure, and physical and mechanical properties and controls the process of coal and gas outburst. Cheng et al. and He and Chen [38, 39] found that tectonic stress controls the migration and occurrence of gas in coal seam by using the combination of theoretical analysis and field examples, which is the premise and basis of high gas stress in the coal mass, and is also the main controlling factor of coal and gas outburst accidents. Zhang and Liu et al. [40, 41] believed that the geological tectonic movement changed the closing-expansion states of the internal microstructures of the coal and rock mass, which promotes the development of the tectonic coal and the occurrence state of gas in the coal and rock mass, and controlled the occurrence of coal and gas outburst accidents. Han and Zhang [42] analyzed that the relationship between coal and gas outbursts and the tectonic evolution in North China, Northeast, and South China with tectonic evolution as the timeline. And they also found that large tectonic areas in the same region would evolve different small-level tectonic structures, which plays a controlling role in these small-scale tectonic regions. Besides, the factors such as coal structure, gas, and in situ stress in different regions have different impacts on each stage of coal and gas outbursts. Yan et al. [43] investigated and summarized the research on coal and gas outbursts in China and abroad and found that the geological conditions in high gas concentration are the prerequisite and key factors for the formation of outbursts. Besides, the destruction and permeability of the coal seam are changed due to the progress of mining and other works, resulting in the desorption of a large number of gases in the coal seam. As a result, the gas pressure increases sharply, and coal and gas outburst accidents occur.

In addition, it is also found that coal and gas outburst disasters are caused by the evolution of paleotectonic stress fields and modern stress fields. Zhu and Xu [44] found that the tectonic stress fields are the link connecting the in situ stress, gas pressure, and coal physical and mechanical properties, as an indivisible whole [44]. The long-lasting stable states of paleotectonic stress fields are the main reason for the intact existence and high concentration of the gas, while the continuous changes of modern tectonic stress fields are the main reason for the formation of high in situ stress and high gas pressure. In short, the evolution of the tectonic stress fields has become the main controlling factor for coal and gas outbursts.

What is more, the distribution of in situ stress and the weak geological structures in coal seam also play a role in controlling role in coal and gas outbursts. Shu et al. [45] believed that the primary coal mass transforms into structural coal mass due to the change of in situ stress and forms closed high gas stress environments, which accelerates the crushing process of tectonic coal and provides a good material and energy basis for the outburst excitation process. Meanwhile, the key structure model of coal and gas outburst is shown in Figure 1. The key structure 1 with the outburst hazard is the energy source and prerequisite for coal and gas outbursts, and the supporting structure 2 of the key structure

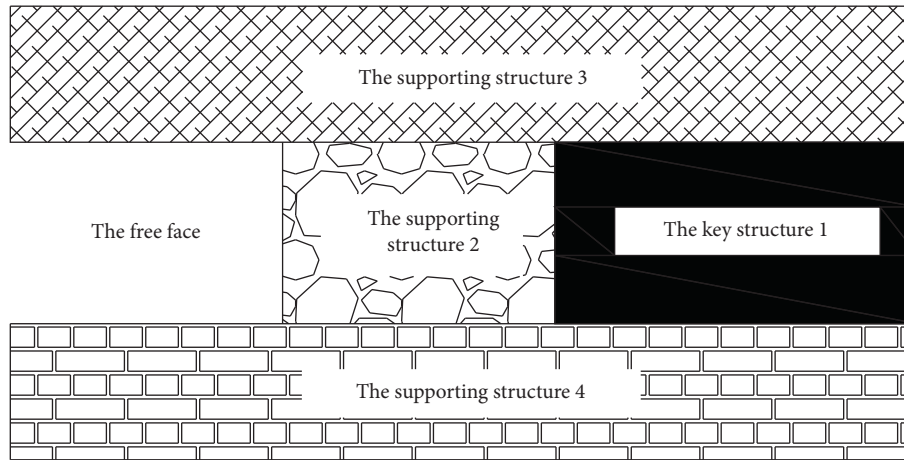


FIGURE 1: The key structure model of coal and gas outburst [45].

1 in the coal mass makes its gas and energy accumulate. At the same time, the supporting structure 3 and supporting structure 4 of the roof-floor of coal seam store a large amount of elastic potential energy, which promotes the continuous derivation and expansion of supporting structure 2. Eventually, the accumulated gas and elastic potential energy are released, resulting in coal and gas outbursts.

In Jiangjunling and Malingshan coal mine [46, 47], the sliding structures change the occurrence environments of stress, gas, and physical and mechanical parameters in coal seam, and they also found that the gas content gradient of the coal mass affected by the sliding structures is more obvious than that of the coal mass not affected by them. Furthermore, the reverse fault structures formed by the trailing edge of the sliding structures have better sealing; thus, the gas cannot spread easily and the gas pressure is high, more likely to cause outburst accidents. At present, computer technology has become an important means to understand the mechanism of coal and gas outbursts. Zhang et al. [48] conducted a series of numerical simulation experiments by using RFPA^{2D}-Flow solid-gas coupling dynamics software and analyzed the disaster mechanism of coal and gas outbursts in the process of cross-entries from the meso-perspective. In this case, the combined action of high gas pressure gradient, self-weight stress, stress concentration, and blasting stress shock is the main reason for the occurrence of coal and gas outbursts. And the stress concentration in front of tunneling plays an important role in the process of coal and gas outbursts, so that reduces stress concentration in front of tunneling work is an important measure and means to effectively reduce the coal and gas outburst.

Thus, single factors such as gas, in situ stress, and tectonic movement control the occurrence of coal and gas outburst accidents, but the single factor dominant control theory is based on specific geological conditions. The main controlling factors lead to coal and gas outburst by controlling other key factors and can theoretically explain the mechanism of coal and gas outbursts in some mines. Over the years, it is found that the processes of coal and gas outbursts have experienced four stages: preparation,

stimulation, development, and stop [49, 50], which is inevitably accompanied with changes of in situ stress, gas, and physical and mechanical properties of the coal mass. However, it is difficult to explain the process and critical conditions of the four stages of outbursts. Also, in situ stress, coal rock, gas, and other necessary conditions of coal and gas outbursts should be regarded as an organic system, and the coupling effects of various elements in each stage jointly lead to the coal and gas outbursts [51, 52].

2.2. Disaster-Causing Mechanism of Multi-Field Coupling.

Coal and gas outbursts are closely connected with the changes and coupling effects of in situ stress field, electromagnetic field, seepage field, and gas pressure field. Under the multi-field coupling conditions, the mechanical properties of gas-bearing coal and the occurrence state of gas are changed, which accelerates the instability of gas-bearing coal and rock and further leads to coal and gas outbursts. For example, the physical model of blasting disturbance structure of coal and rock outbursts was proposed in 2014. The model believes that the existence of the blasting stress wave in the outburst preparation stage breaks the equilibrium state of the initial stress [53], which makes the coal crack develop and forms the “geological weak face.” Also, the coupling effect of the gas pressure field and the stress field accelerates the crack propagation, which lead to a large number of gas desorption under the adsorption state. Besides, the coupling effect of gas pressure and blasting stress wave exacerbates coal and rock mass and accelerates the instability of “geological weak face.” Eventually, when the gas pressure in the coal seam reaches the critical state, the internal energy and elastic energy of the gas will burst out of the broken coal, leading to the occurrence of coal and rock outbursts.

The coal mining industry has shifted to the deep mining stage, and coal seam mining conditions are more complicated, which leads to the occurrence of coal and rock outbursts frequently. And the gas-bearing coal mass from the deep mining is in a three-dimensional complex in situ stress field [54]. Coal crushing in the mining face is caused

by the combined action of in situ stress and gas pressure, and the in situ stress becomes an important external factor to induce outbursts. Besides, gas pressure is the key internal power source for outburst initiation, and the experiments also prove this conclusion.

Moreover, the occurrence of coal and rock dynamic disasters involves many theories, such as the adsorption desorption, gas dynamics, seepage, and gas-solid two-phase flow theory. Sun et al. [55], by using classical gas dynamics theory, defined the two-phase flow, in the outburst cavity, reaching the sound velocity as a critical state, and the two-phase flow below the critical state was defined as non-expansion state. Besides, the instantaneous expansion of gas in lots of the nonexpansion two-phase flow will produce a huge momentum effect and burst out disasters in the outburst cavity. Xie et al. [51] also believed that the gas pressure provides the key power source for the initiation of outbursts. Under the coupling effect of in situ stress and gas leads to the continuous derivation and expansion of cracks, pores, and other defect structures in the coal mass, and they also extend along the direction of maximum tangential stress. Furthermore, when the energy of the gas power source is much greater than the energy consumed by the development and penetration of the cracks, the coal mass will collapse and breaks all of a sudden, which will form the coal and gas outburst accidents. Besides, Zhao et al. [56] conducted a series of experiments and found that there are obvious multi-physical field coupling effects between temperature and gas pressure field. After the outburst occurs, a large amount of gas is discharged, which causing the medium gas pressure to reduce. At the same time, the temperature is obviously reduced due to the endothermic reaction during the desorption.

With the development of computer and numerical technology, scholars begin to consider the coupling effect of damage field and fracture field, Zhao et al. [57] carried out many numerical simulation experiments and established the multi-field coupling model of gas pressure field, in situ stress field, damage field, and seepage field. They found that the mining disturbance causes the fracture closure and permeability reduction in the stress concentration area in front of the working face. The stress distribution in front of mining working face is shown in Figure 2. They also found that the mining disturbance would cause closure of the fracture and reduction of permeability in the area of stress concentration in front of the working area, thus increasing the gas pressure gradient in the area of stress relief and the area of stress concentration, which affects the occurrence of coal and gas outburst. Similarly, Zhang et al. [58] came to a similar conclusion that the coal and rock mass gradually break under the coupling of the mining stress field and fracture field, which leads to an increased gas concentration and pressure; driven by the gas pressure, the coal and rock outbursts occur. Nevertheless, Li et al. [59] found that the coupling effect of the vibration field, gas pressure field, in situ stress field, electromagnetic field, and seepage field affects the occurrence of coal and gas outbursts. The vibration caused by blasting and other excavation works further promotes the coupling effect between each other.

Through combining and analyzing related documents on the disaster mechanism of coal and gas outbursts under the coupling effect of multiple fields [16, 60], the in situ stress, gas pressure, and coal physical and mechanical properties have obvious differences in the various stages of coal and rock outbursts. And other internal and external factors, such as tectonic movement and mining disturbance, have changed the stress field environments of coal and rock, which accelerated the expansion and damage of coal and rock fractures. In this stage, it mainly depends on the crushing ability of in situ stress of mining stress to coal and rock, which provides the possibility for the occurrence of outbursts. Meanwhile, the adsorption and desorption state of gas changes due to the coupling effect of the in situ stress field and mining stress field, which changes the closing and open states of fractures and increases the internal energy of gas stored in coal and rock. When the accumulated gas internal energy and elastic energy makes the coal and rock mass broken to a certain extent and exceed the energy consumed by coal and rock breaking, which will cause the gas internal energy and elastic energy bursting out rapidly.

2.3. New Understanding of the Mechanism of Coal and Gas Outburst.

In recent years, some new theories have been obtained by some advanced techniques on coal and rock outbursts, which can explain some special phenomena of coal and gas outburst. Guo et al. [61] found that there was an obvious stick-slip instability phenomenon during the outburst processes by referring to the mechanism of stick-slip instability in rock bursts [53]. And they also proposed the mechanism of stick-slip instability in coal and gas outbursts, which can reveal the mechanism of vibration fluctuation, delayed outbursts, and intermittent outbursts during the outburst. Besides, Wang et al. [62] constructed the adsorption model between coal particle surfaces and methane gas by using the quantum chemical density functional theory (DFT) calculation method from a view of microscopic. They also found that the electromagnetic waves in the process of deformation and the failure of surrounding coal and rock in working face are due to the vibration, mining, and other works. Furthermore, coal and CH_4 molecules are adsorbed to form a companion molecular system that absorbs electromagnetic waves in a quantized form, which leads to CH_4 transforming from adsorption state to free state. Finally, a greater gas pressure is formed, which leads to CH_4 breaking through the structural surfaces and coal and gas outbursts. Ma and Yu [63] regarded the outburst coal mass as the pressure-bearing loose body, and they calculated the motion catastrophe potential function in the process of coal and gas outburst combined with the catastrophe theory from the perspective of the momentum of the coal-bearing loose body. Besides, they also analyzed the influencing factors and disaster-causing mechanism of the coal and gas outburst, which further put forward the mechanism of uncontrolled outburst of pressure-bearing loose body in coal and gas outburst.

Nowadays, Ma et al. [64–67] put forward the hypothesis of butterfly coal and gas outbursts in tunneling roadways

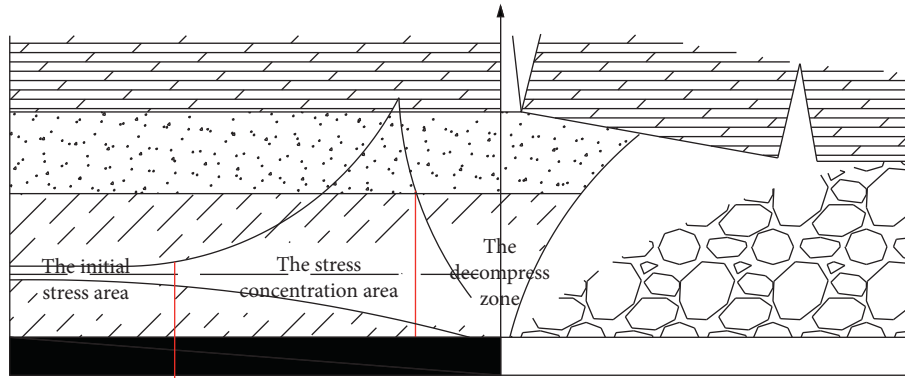


FIGURE 2: The stress distribution in front of mining working face [57].

based on the butterfly rock burst theory and nonlinear dynamic system theory, and they also established the deformation and failure model of circular roadway in the two-way nonisostatic pressure stress field. The theoretical calculation of butterfly-shaped plastic zone is shown in Figure 3. When the ratio of the maximum principal stress to the minimum principal stress increases continuously, the surrounding rock around the roadway will produce a plastic zone similar to the “Butterfly” shape. Besides, based on the Mohr–Coulomb failure criterion, the implicit equation of the plastic zone boundary of circular roadway surrounding rock in nonisobaric stress field is derived, which is called butterfly failure theory. Moreover, the conjecture holds that a certain amount of butterfly plastic zones appearing in the heading face in a short time due to the uneven distribution of in situ stress. When the increments of the plastic zones increase to the critical value, the elastic potential energy and gas energy stored in the coal rock mass will be released instantly, which thus leading to the coal and gas outburst.

It is believed that the hypothesis of stick-slip instability mechanism and microscopic outburst mechanism lead to a new idea and direction for the study of the mechanism of coal and gas outburst, which can explain specific coal and gas outbursts under certain conditions. However, it fails to give a judgement standard of the risk of coal and gas outbursts and is insufficient to a universal application to the outburst accidents, nor in applications to the coal seam with complicated geological conditions and burial conditions. Besides, as per the analysis, the outburst mechanism of the uncontrolled pressure-bearing loose mass holds that the pressure-bearing loose mass, within the range from the stress concentration area to the boundary of the pressure relief zone in front of the working face, is a practical engineering problem and in line with the characteristics of the general outburst coal mass. But the catastrophe potential function of the motion of the pressure-bearing loose mass, by the hypothesis, operates in the condition that the stress in front of the working face is in circular distribution and the coal mass in the stress concentration area is isotropous. And the original in situ stress and gas pressure are isobaric in all directions, it is different from the actual complex in situ stress environments of coal and gas outbursts, and there is a certain error with the actual movement increment about the

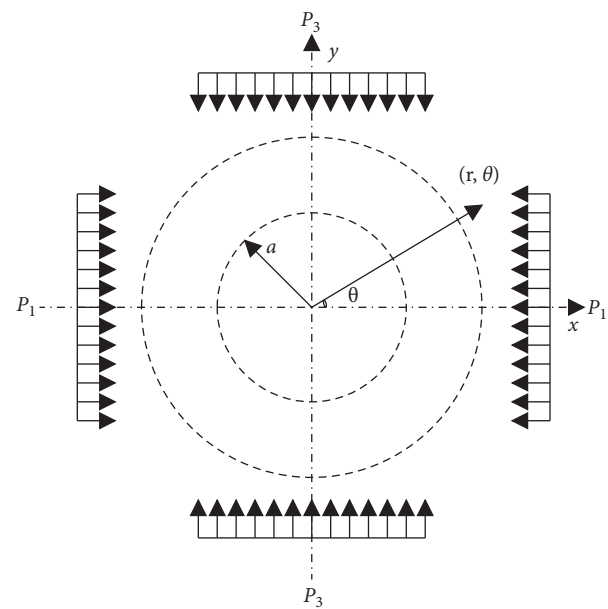


FIGURE 3: Theoretical calculation of butterfly-shaped plastic zone. P_1 and P_3 are the maximum and minimum principal stress in surrounding rock stress field; a is the radius of circular roadway; R , θ is the polar coordinates of any location.

motion increment of the confined bulk calculated by using the motion mutation potential function. Moreover, it is also believed [23] that the hypothesis of butterfly coal and gas outburst takes into account the uneven distribution of the ground stress caused by the excavation of the roadways in the working face and gives the stress field state and plastic zone boundary by using the implicit equation of the plastic zone boundary of circular roadway surrounding rock in nonisobaric stress field, which solves the quantitative interpretation of the risk indicators of coal and gas outburst risk indicators. However, the hypothesis is similar to the outburst mechanism hypothesis of pressure-bearing loose mass that the roadway is assumed to be in a plane stress state, which leaves a big difference from the complex stress environments of coal and gas outbursts in practice. Also, the conjecture does not consider the role of physical and mechanical properties of gas and coal in the whole outburst

process and how these three interact with each other to induce the coal and gas outbursts, thus leaving certain limitations.

Therefore, in spite of the full demonstration of the effects of in situ stress, gas, and tectonic movements by the above theories, researches on the action mechanism of the coal strength on coal and gas outbursts are rare due to the limited testing means and conditions. Strength is one of the important parameters of the physical and mechanical properties of the coal mass, also an essential index to predict the risk of coal and gas outbursts, and the strength value greatly affects the degree of damage of coal and gas outburst accidents [69].

3. Influencing Factors of Coal Strength

Differentiation of the coal strength is attributed to different occurrences under various geological conditions against the backdrop of the complicated geologic environment in China. It has been proved that the coal strength is affected by geological structure movement, gas pressure, size effect, and mining disturbance.

(1) Influence of tectonic movement on coal strength

The formation and evolution of structures are closely related to coal and gas outbursts, which change the bedding, joints, faults, fractures, and folds in the coal mass, as well as the microscopic pores inside the coal mass. Besides, the changes of the stress environment state of the coal mass have a certain influence on the strength of the coal mass [46]. Han et al. [70] found that the tectonic coal mass is relatively developed in areas where tectonic stress is concentrated, such as compressive fault zones and fold shafts caused by tectonic movements. Also, tectonic movements cause compaction or loosening of micropore structures in the coal mass, and the multi-stage evolution of tectonic stress fields makes most faults go through multi-stage activities, resulting in reduction of the coal strength. Moreover, Cao et al. [71] conducted uniaxial mechanical parameters experiments on coal samples from different areas and different coal ranks, and they also found that the tectonic movements change the tectonic stress fields combined with the statistics of previous uniaxial experiment data. Different tectonic stress fields affect the change speed of coal elastic modulus with uniaxial compression strength, as well as the interaction between the tectonic stress and the coal ranks causes the relationship between the elastic modulus and Poisson's ratio to change, which causes the change of the coal strength in turn. In addition, the tectonic movements have changed the microscopic pore structures inside the coal mass, leaving a significant increase in density and unstable direction of the fractures which causes the change of the coal strength [72].

(2) Influence of gas pressure on coal strength

The gas mainly exists in the micropores and microcracks in coal mass in the forms of adsorption and free state. And the existence of gas greatly causes the change of internal structures of coal mass, which further leads to the change of the coal strength in turn. Han et al. [73] believed that more than 90% of the coalbed methane is adsorbed on the coal base blocks, which reduces the permeability of coal mass. At the same time, the existence of adsorbed gas reduces the gas migration channels in the coal mass, which is extremely easy to cause the coal mass to fracture and reduce its strength. Similarly, Zhang [74] found that the content of adsorbed gas in coal mass increases with the increase of the gas pressure. Besides, the expansion and deformation of coal mass and the increase of gas pressure reduces the size of structural cohesion and effective stress between coal mass, resulting in the decrease of the coal strength. Generally, the coal structures will become more compact under the condition of gas desorption, with the coal strength increasing to some extent.

Other scholars believe that the existence of gas accelerates the derivation and expansion of internal cracks in coal mass, resulting in the change of the coal strength. Xu et al. [75] conducted a series of meso-pressure shear experiments on the gas-bearing coal mass and found that the coal cracks continue to expand in the process of experiments, which provides many channels for gas to infiltrate into coal mass. With the continuous development of pressure and shear experiments, the observation surfaces of the coal mass gradually break and fall off. Besides, the broken areas continue to increase, and more likely new cracks evolve, which eventually leads to the penetration of the cracks and the reduction of coal strength. On the basis of previous studies, Bai et al. [76] found that the defect structures such as microcracks and micropores in the coal mass further expand and fracture after the coal mass absorbs gas. Meanwhile, part of the elastic potential energy is transformed into solid surface energy during the fracture process of the defect structures. When the increasing rate of the solid surface energy is equal to the release rate of the elastic energy, the defect structures of the coal mass are in the critical state of fractures.

As a result, the coal strength decreases with the increase in the number of internal cracks, pores, and other defects, which leads to the increase of gas content in coal mass. Conversely, the increase of gas content will accelerate the derivation and expansion of internal cracks, pores, and other defects, in coal mass, which leads to the decrease of coal strength.

(3) Influence of size effect on coal strength

Physical similarity experiments and numerical simulation methods have become the important means to study the mechanism of coal and gas

outbursts. The research shows that the selection of engineering material specifications affects a series of strength indicators such as compressive strength, tensile strength, and flexural strength, and the size of the material also affects the final results of physical and numerical simulation experiments [77]. Deng [78] took the size effect as the starting point for the problem and found that there is a positive correlation between the coal strength value and size, which is in line with the theoretical function relationship of the Weibull strength size effect. And they also found that there are large number of pores and cracks of different sizes in the coal mass with the increase of the test size of coal mass.

The theoretical relationship between coal strength and size is as follows:

$$\sigma = \frac{\sigma_0}{(V/V_0)^{1/m}} \Gamma\left(\frac{1}{m+1}\right), \quad (1)$$

where σ is the strength of the coal sample; σ_0 is the strength value of reference sample; m is the test material homogeneity; V is the test sample volume; and V_0 is the reference sample volume, the laboratory standard sample is usually used as the reference sample.

Zhao et al. [77] believed that the size effect exhibits an obvious sensitivity to the coal strength with the increase of gas pressure when the coal is in the same homogeneous conditions, and the gas pressure has a significant impact on the size effect of coal compressive strength of coal, and heterogeneity of the coal controls the size effect of the coal. Herewith, the author thinks that the influence of size effect on coal strength is mainly manifested in the change of the defect structures such as micropores and microcracks inside the coal mass. In this stage, the increase of the tested coal size increases the possibility of the increase in the number of defect structures inside the coal mass, and this promotes the further initiation and evolution of new cracks due to the coupling effect between gas pressure and stress field, softening the coal further reducing the coal strength.

(4) Influence of mining disturbance on coal strength

The underground mining activities in coal mines make the stress redistribute in front of the mining face or heading working face and form the pressure relief zone, the concentrated stress zone, and the stress zone of the original rock with the continuous advancement of the working face [79]. Besides, the vibration of blasting, tunneling machine, shearer cutting, and other mining works will cause the change of internal microcracks of the surrounding coal and rock mass and then cause the change of the coal strength. Wang et al. [80] analyze the stress distribution of the two sides of the roadway in the mining working face by using the numerical simulation method. Also, a regularly concentrated

distribution area of stress on the two sides of the roadway in the mining face and the tunneling face is formed with the advance of the working face without considering the tectonic movements. Furthermore, the periodic weighting of the roof in the roadway causes periodic impact damage to the surrounding coal and rock mass, which further causes looseness and damage to the coal and rock. Ultimately, the overall strength of the coal mass is reduced. Li et al. [81] carried out many experiments and found that the vibration leads to the expansion and development of microcracks in coal mass, which gradually forms interpenetrated fissures between the cracks in coal mass and makes the coal strength reduced. They also found the vibration will change the stress state and the occurrence state of gas in coal mass, which increases the possibility of coal and gas outburst due to the rapid increase of the gas pressure.

In addition, the coal strength reduces by using the oftener water injection, hydraulic fracturing and other methods to solve the problems caused by the mining of harder coal. Also, gas extraction activities have a certain impact on the coal strength, which will affect the process of coal and gas outburst [82, 83]. To sum up, the change of the coal strength affects the distribution state of other factors, such as gas pressure and in situ stress, and it is of great significance to study the influence mechanism of coal strength on outburst prevention and control of coal and gas outburst.

4. Research Progress of Influence Mechanism of Coal Strength on Outburst

At present, theoretical achievements have been made on the disaster-causing mechanism of the in situ stress and gas pressure to the coal and gas outbursts in China, and the control effects of coal strength on the occurrence of coal and gas outbursts have been proved. Yuan et al. [84] found a negative correlation between the coal strength and coal and gas outburst. Also, they regard the coal mass as a prominent barrier, and it is more likely to cause coal and gas outburst with the lower coal strength. But there will still be gas outburst accidents under certain conditions with the higher coal strength, and it is lower about the outburst strength than that with the lower coal strength. In addition, some scholars have reached the opposite conclusions due to different experimental conditions. Yuan and Peng et al. [14, 15] found that the coal strength increases with the decrease of coal particle size by using their self-designed device of coal and gas outburst. In the outburst process, the quality of outburst coal increases with the increase of coal strength, and there is a linear positive correlation between the relative outburst strength and the coal strength. Furthermore, Zhang et al. [85] carried out a series of simulation experiments for the instant exposure of gas-bearing coals with different strengths and found that the indexes of outburst strength, such as the quality of the outburst coal

power, distance, and hole depth, decrease with the increase of the coal strength under the same in situ stress and gas pressure. Also, there is a linear negative correlation between outburst indexes and the coal strength, which is manifested as the hindrance of the coal strength against the occurrence of the outburst accidents. During the four stages of inoculation, occurrence, development, and termination of coal and gas outburst, the existence of gas pressure leads to the decrease of the effective stress, which accelerates the failure process of coal mass. Besides, the release of gas internal energy in the failure process of coal mass and its proportion in the total energy increase with the increase of the coal strength, and there is a linear positive correlation between gas internal energy, which becomes the main energy source affecting the occurrence of outburst accidents.

At present, the research on the mechanism of coal and gas outburst induced by the coal strength is relatively insufficient, and the definitive evaluation standard of the outburst strength is not unique. So that it is worth further discussing whether the definitive evaluation standard can be formed only by the single index, such as outburst coal quality, distance or hole depth. To sum up, in the action hypothesis on the four stages of incubation, start-up, development, and stop of coal and gas outburst in China, the effects of in situ stress, gas pressure, and the physical and mechanical properties of coal mass are taken into account comprehensively. Moreover, the control effects of the ground stress and gas pressure in the structural coal seams are believed to mainly lead to the occurrence of the coal and gas outburst. The above studies have indicated that the mechanical properties of coal mass are changed by the geological structure movements, which leads to the occurrence of outbursts, but it is focusing on the distribution laws of in situ stress and gas pressure in the coal seams about outbursts. Besides, the coal strength is one of the important physical mechanical parameters of coal mass, and how to further study coal and gas outburst induced by coal strength is of great significance to the improvement of outburst theories.

5. Discussion and Outlooks

By summarizing the mechanism of coal and gas outbursts in China, it can be seen that the existing research mainly focuses on influence of in situ stress, tectonic movement, and gas pressure on the coal and gas outburst. The coal strength is an important physical mechanical property of the coal mass and is closely related with the strength of the outburst. However, research on the effects of the coal strength on the disaster-causing mechanism of the coal and gas outburst is rarely reported. Therefore, further thinking should be given to the following aspect.

- (1) The influence mechanism of the coal strength to the coal and gas outburst requires further research. More and more scholars regard in situ stress, gas, physical and mechanical properties, and other influencing factors as an organic whole, and they also

comprehensively consider the processes of coal and gas outbursts by constructing different mathematical models, such as spherical shell instability model [25, 26] and butterfly coal and gas outburst conjecture [64, 65]. However, previous studies often set certain preconditions, for example, the hypothesis of spherical shell instability assumes that the coal seam is usually infinite with the isotropic original stress, and the stress concentration caused by mining work should be ignored. Also, the conjecture of butterfly coal and gas outburst simplifies the surrounding rock of the driving roadway into a plane, and the implicit equation of plastic zone boundary of surrounding rock in nonequal pressure stress field is calculated by means of elastic mechanics. By this conjecture, we can solve outburst problems like “pear-shaped cavity,” but the scientific issues related to coal and gas outburst, such as gas pressure and coal strength are ignored. How to further determine the critical conditions of the change of the coal strength in the four stages of incubation, occurrence, development, and stop of the outburst and how to quantitatively analyze the influence of coal strength on outburst are particularly important.

- (2) Coal and gas outburst includes four stages of incubation, occurrence, development, and stop, in which the coal mass is destroyed gradually under the coupling action of stress field, gas pressure field, vibration field, seepage field, fracture field, and electromagnetic field, and the gas pressure plays the most important role in the process of coal and gas outburst, following by coal strength and in situ stress [84]. Moreover, the tectonic movement has an extremely important impact on the coal strength and induces the coal and gas outburst [42–46]. But the researches only focus on the crushing effect of gas pressure and external stress on coal mass, ignoring the effect of in situ stress and tectonic movement on the coal mass' crushing and stripping. In addition, the in situ stress and tectonic movement can change the opening and closing states of the internal fractures of coal mass and change the gas migration at the same time. Generally, when the coal strength is large enough or the integrity of coal mass is good enough, the gas pressure is insufficient to strip and break the high-strength coal mass, and the coal mass plays an important role in preventing coal and gas outbursts, which affects the test results of coal and gas outbursts. Otherwise, some scholars consider the influence of coal strength on coal and gas outburst from another perspective [14, 15]. The particle size of the coal size changes the internal porosity of the coal mass, the smaller the particle size, the smaller the porosity, and the better the compactness of the coal mass. The test has indicated that the smaller the particle size of the coal, the better the adsorption feature of the coal, and the higher the temperature of

coal rises. Under effects of the temperature field, energy stored in the high-strength coal is relatively high; therefore the outburst is instantaneous with a high intensity. The current research focuses on the changing internal energy of the gas stored in the coal due to the changes of the adsorption feature of the gas. Enhancement of the adsorption feature of the gas rises the temperature within the coal mass, thus transporting energy to expand the gas continuously. As a result, the intensity of the outburst may be increased. Under the same gas pressure and ground stress, the coal strength is the main factor that affects the failure form of the coal mass at each stage of the outburst, which is the main influencing factor that controls the storage and release of the elastic energy and gas internal energy. At the same time, the author thinks that how to establish more suitable experiment conditions for underground outburst process and fully consider the coupling effect of multiple fields will be more conducive to study the influence mechanism of physical and mechanical parameters on coal and gas outburst and improve the disaster mechanism of coal and gas outburst.

- (3) Research methods of the disaster mechanism of coal and gas outburst need to be further improved in the future. In recent years, the mechanisms of coal and gas outburst have been studied by using rheological mechanics, elastic mechanics, chaos theory, plastic mechanics, rock mechanics, and gas-solid coupling theory, and by means of laboratory similar simulation experiments and numerical simulation methods, but no methods or theories are perfect. In short, they can explain specific coal and gas outburst accidents to a limited extent.

The size effects have greatly changed the coal strength value [77, 78, 86], and when for the similarity simulation experiments on coal and gas outburst, it is necessary to ensure that the physical and mechanical properties, geometric similarity, movement trend similarity and dynamic similarity of the simulated coal seams according to the similarity theory. But it is difficult to ensure that the final simulation results are consistent with the actual outburst process and outburst characteristics of the mine [87]. Therefore, the physical and mechanical properties of similar simulation materials and raw coal should be the same as possible, avoiding the influence of the size effects on the coal and gas processes caused by the coal strength, and ensuring the rationality of the design of the similar simulation experiments to achieve the quantification and accuracy of experiment on coal and gas outburst. However, the existing devices of the similar simulation experiment limit the accuracy of the experiment results of coal and gas outburst to a certain extent. For example, some of the existing devices [88] are designed with a small size, which is difficult to avoid the influence of boundary effect and hard to simulate the existence of the geological structure of the coal seam and the realization of engineering excavation function. In addition,

the sensors can only be placed in the model, which limits the data collection. Or some of the existing devices are designed with a large size, which increases the difficulty of device manufacturing and the periodicity of experiments. Or some of the existing devices are designed with a smaller volume of the gas cavity, which makes it difficult to maintain the adequacy of gas during the testing. Or some of the existing devices have poor airtightness and cannot provide the true triaxial stress loading which is more consistent with the actual engineering difficulty.

In view of the existing problems to the research methods and devices, the existing materials for the similarity simulation test should be improved to conform to the physical and mechanical properties of coal mass. The key factors of coal and gas outburst, such as in situ stress, gas stress, and physical and mechanical properties, should be comprehensively considered, and the scientific and reasonable size (avoiding boundary effects and size effects) should be designed to truly restore the geological structures of the coal seams and gas migration laws and truly restore the stress environment and excavation conditions of the coal seams. At the same time, the device of the similarity simulation test in terms of the four stages of preparation, excitation, development, and stopping (acquiring the critical conditions of each stage) can be obtained from multiple directions. Besides, the priority should be placed on the impact of changes of the macro-mechanical properties of coal mass on its microstructures, and how to use numerical simulation technology more reasonably by means of the computer numerical simulation technology.

6. Conclusions

Coal and gas outburst is a complex kinetic process. The current researches have revealed the disaster-causing mechanism of the coal strength to the coal and gas outburst, providing an idea for deep mining as well as prevention and control of the coal and gas outburst.

- (1) The research progresses and new understandings of the coal and gas outburst mechanism under the control of different factors are systematically summarized, providing an idea for the future deep mining as well as prevention and control of the coal and gas outburst in China.
- (2) Stages of incubation, occurrence, development, and stop of the coal and gas outburst are affected by the coupling effects of the multi-physical field such as in situ stress field, gas pressure field, fissure field, electromagnetic field, and seepage field. The coal strength is the main factor that affects the occurrence of outburst under the same gas pressure and ground stress.
- (3) Scientific methods are put forward to improve the research methods of the mechanism of coal and gas outburst. It is imperative to design a scientific size (boundary effects and size effects should be avoided), restore the real coupling conditions of multiple

geological fields, obtain the critical conditions of each stage from multiple directions, use numerical simulation technology comprehensively, and consider the influence of the changing mechanical properties of macrocoal on its microstructure.

Conflicts of Interest

The authors guarantee that they have no conflicts of interest to other research studies in this paper.

Acknowledgments

This work was financially supported by the Natural Science Foundation of Beijing Municipality (Grant no. 8192036), the National Key Research and Development Program of China (Grant no. 2018YFC0808301), the State Key Laboratory Cultivation Base for Gas Geology and Gas Control (Henan Polytechnic University)(Grant no. WS2018B04), the Municipal Research Institute Reform and Development Project (Grant No. BFAST-RD-BMILP202109-03), and the Municipal Research Institute Reform and Development Project (Grant No. BFAST-RD-BMILP202113).

References


- [1] Y. Song, Q. Zou, E. Su, Y. Zhang, and Y. Sun, "Changes in the microstructure of low-rank coal after supercritical CO₂ and water treatment," *Fuel*, vol. 279, no. 3, Article ID 118493, 2020.
- [2] Q. Zou, H. Liu, Y. Zhang, Q. Li, J. Fu, and Q. Hu, "Rationality evaluation of production deployment of outburst-prone coal mines: a case study of nantong coal mine in Chongqing, China," *Safety Science*, vol. 122, Article ID 104515, 2020.
- [3] H. Wang, Z. Cheng, Q. Zou et al., "Elimination of coal and gas outburst risk of an outburst-prone coal seam using controllable liquid CO₂ phase transition fracturing," *Fuel*, vol. 284, Article ID 119091, 2021.
- [4] M. Gao, S. Zhang, J. Li, and H. Wang, "The dynamic failure mechanism of coal and gas outbursts and response mechanism of support structure," *Thermal Science*, vol. 23, p. 122, 2019.
- [5] Y.-k. Ma, B.-s. Nie, X.-q. He, X.-c. Li, J.-q. Meng, and D.-z. Song, "Mechanism investigation on coal and gas outburst: an overview," *International Journal of Minerals, Metallurgy and Materials*, vol. 27, no. 7, pp. 872–887, 2020.
- [6] W. Gong and D. Guo, "Control of the tectonic stress field on coal and gas outburst," *Applied Ecology and Environmental Research*, vol. 16, no. 6, pp. 7413–7433, 2018.
- [7] W. P. Diamond and S. J. Schatzel, "Measuring the gas content of coal: a review," *International Journal of Coal Geology*, vol. 35, no. 1–4, pp. 311–331, 1998.
- [8] I. W. Farmer and F. D. Pooley, "A hypothesis to explain the occurrence of outbursts in coal, based on a study of west wales outburst coal," *International Journal of Rock Mechanics and Mining Sciences & Geomechanics Abstracts*, vol. 4, no. 2, pp. 189–193, 1967.
- [9] C. Dong, W. E. Yuan, and L. Nan, "Study on the microwave effect on the physical and mechanical properties of coal," *International Journal of Oil Gas and Coal Technology*, vol. 18, no. 1-2, 2018.
- [10] Z. Sun, L. Li, F. Wang, and G. Zhou, "Desorption characterization of soft and hard coal and its influence on outburst prediction index," *Energy Sources Part A Recovery Utilization and Environmental Effects*, vol. 2, pp. 1–15, 2019.
- [11] L. Wang, Z. Lu, D. P. Chen, Q. Q. Liu, and Z. J. Wen, "Safe strategy for coal and gas outburst prevention in deep-and-thick coal seams using a soft rock protective layer mining," *Safety Science*, vol. 129, Article ID 104800, 2020.
- [12] H. B. Zhao and G. Z. Yin, "Study on impact of coal and gas outburst strength caused by principal stress," *Disaster Advances*, vol. 3, no. 4, pp. 388–391, 2010.
- [13] C. Fan, S. Li, D. Elsworth, and Z. Yang, "Experimental investigation on dynamic strength and energy dissipation characteristics of gas outburst-prone coal," *Energy Science and Engineering*, vol. 8, no. 1–4, 2019.
- [14] R. F. Yuan and H. M. Li, *Simulation Test and Analysis on Coal-Gas Outburst at Condition of Different Coal Strength, Commemorating the 50th Anniversary of the Founding of China Coal Society*, Editorial Department of Shandong Coal Science and Technology, China Coal Society, Beijing, China, 2012.
- [15] S. J. Peng, X. W. Song, J. Xu et al., "Experiment of factors affected to coal and gas outburst intensity based on hypothesis of comprehensive effect," *Coal Science and Technology*, vol. 44, no. 12, pp. 81–84, 2016.
- [16] Q. X. Yu, *Mine Gas Prevention and Control*, China University of Mining and Technology Press, Xuzhou, China, 1992.
- [17] Y. G. Wang, J. P. Wei, and H. T. Sun, "Mechanism analysis of coal or rock dynamic disaster and its prevention and control," *Mining Safety & Environmental Protection*, vol. 37, no. 2, pp. 17–19, 2010.
- [18] L. J. Wei, S. Li, Z. K. Wei, and M. W. Wang, "Research status and prospects of the influence law of coal and gas outburst on ventilation system," *Coal Science and Technology*, pp. 1–7, 2021.
- [19] F. T. Miao, D. L. Sun, and Q. T. Hu, "The formation mechanism of shock waves in the coal and gas outburst process," *Journal of China Coal Society*, vol. 38, no. 3, pp. 367–372, 2013.
- [20] K. Wang, L. Wang, and F. Du, "Influence of coal powder particle sizes on dynamic characteristics of coal and gas outburst," *Journal of China Coal Society*, vol. 44, no. 5, pp. 1369–1377, 2019.
- [21] A. A. Haryoff, *Mine Ventilation*, Northeast Institute of technology, Guwahati, India, 1956.
- [22] J. Han, H. Zhang, and B. J. Huo, "Discussion of coal and gas outburst mechanism of syncline," *Journal of China Coal Society*, vol. 8, pp. 908–913, 2008.
- [23] Q. F. Wang, *Study on the Stress Evolution Process of Coal and Gas Outburst Mechanism in Excavation*, China University of Mining and Technology, Beijing, China, 2018.
- [24] B. Y. Zhang, Y. Yu, X. Gao, Q. Wu, and Q. Zhang, "Stress-strain characteristics of coal mine gas hydrate-coal mixture under confining pressure unloading," *Journal of China Coal Society*, pp. 1–12, 2020.
- [25] C. L. Jiang and Q. X. Yu, "The hypothesis of spherical shell destabilization of coal and gas outburst," *Safety in Coal Mines*, vol. 2, pp. 17–25, 1995.
- [26] C. L. Jiang, "Study of the reasons for the delay of the coal and gas outburst," *China Safety Science Journal*, vol. 4, no. 4, pp. 28–32, 1994.
- [27] C. L. Jiang, "Forecast model and indexes of coal and gas outburst," *Journal of China University of Mining and Technology*, vol. 4, pp. 3–5, 1998.
- [28] S. N. Zhou and X. Q. He, "Rheological hypothesis of coal and methane outburst mechanism," *Journal of China University of Mining and Technology*, vol. 19, no. 2, pp. 1–8, 1990.

- [29] X. Q. He and S. N. Zhou, "Rheological hypothesis of coal and methane outburst mechanism," *Safety in Coal Mines*, vol. 10, 1991.
- [30] P. F. Li, "Study on the hypothesis of coal and gas outburst mechanism: two phase fluid hypothesis," *Safety in Coal Mines*, vol. 11, 1989.
- [31] M. Zhang, Z. Xu, and Y. Pan, "A united instability theory on coal (rock) burst and outburst," *Journal of China Coal Society*, vol. 4, 1991.
- [32] B. Liang, *Study on the Theory of Solid Fluid Coupling Instability of Coal and Gas Outburst*, Northeastern University, Boston, MA, USA, 1994.
- [33] B. Liang, M. T. Zhang, Y. S. Pan, and L. G. Wang, "Theory of instability of flow fixation coupling for coal and gas outburst," *Journal of China Coal Society*, vol. 20, no. 5, pp. 492–496, 1995.
- [34] S. L. Lv and J. S. He, "Key layer and stress dike mechanism of coal and gas outbursts," *Journal of Chongqing University*, vol. 22, no. 6, pp. 80–84, 1999.
- [35] J. S. He and S. L. Lv, *Geophysical Study on Gas Outburst*, China Coal Industry Publishing House, Beijing, China, 1999.
- [36] X. Yuan, *Study on Mechanism of Coal and Gas Outburst Based on Gas-Driven*, Chongqing University, Chongqing, China, 2017.
- [37] J. Chen, X. K. Pan, D. Y. Jiang, X. Yuan, X. Jiang, and J. Y. Fan, "Development and application of coal and gas outburst test system based on gas driven," *Journal of China Coal Society*, vol. 43, no. S2, pp. 460–468, 2018.
- [38] Y. P. Cheng, X. L. Zhang, and L. Wang, "Controlling effect of ground stress on gas pressure and outburst disaster," *Journal of Mining & Safety Engineering*, vol. 30, no. 3, pp. 408–414, 2013.
- [39] H. J. He and X. S. Chen, "Research state and its development trends for control function of geological structure to coal and gas outburst," *Journal of Henan Polytechnic University (Natural Science)*, vol. 28, no. 1, pp. 1–7, 2009.
- [40] Z. M. Zhang and Y. G. Zhang, "Three grades of gas-geological maps and their application to gas controlling," *Journal of China Coal Society*, vol. 4, pp. 455–458, 2005.
- [41] M. J. Liu, X. L. Liu, and J. He, "Research on fractal prediction of coal and gas outburst," *Journal of China Coal Society*, vol. 6, pp. 3–5, 1998.
- [42] J. Han and H. W. Zhang, "The controlling of tectonic evolution to coal and gas outburst," *Journal of China Coal Society*, vol. 35, no. 7, pp. 1125–1130, 2010.
- [43] J. W. Yan, X. B. Zhang, and Z. M. Zhang, "Research on geological control mechanism of coal-gas outburst," *Journal of China Coal Society*, vol. 38, no. 7, pp. 1174–1178, 2013.
- [44] X. S. Zhu and F. Y. Xu, "The controlling effect of tectonic stress field and its evolution on coal and gas outburst," *Journal of China Coal Society*, vol. 19, no. 3, pp. 304–313, 1994.
- [45] L. Shu, K. Wang, Q. G. Qi, S. Fan, L. Zhang, and X. Fan, "Key structural body theory of coal and gas outburst," *Chinese Journal of Rock Mechanics and Engineering*, vol. 36, no. 3, pp. 347–356, 2017.
- [46] F. C. Hao, M. J. Liu, J. P. Wei, and Y. Q. Fu, "The controlling role of gravitational slide structure to coal and gas outburst," *Journal of China Coal Society*, vol. 37, no. 5, pp. 825–829, 2012.
- [47] F. J. Zhao, W. Qian, J. G. Deng, and M. J. Liu, "Tectonic control on coal and gas outburst of coal seam in Malingshan gliding structure," *Journal of China Coal Society*, vol. 38, no. S1, pp. 112–116, 2013.
- [48] C. H. Zhang, Z. G. Liu, T. Xu, J. Liu, and F. Cai, "Coal and gas outburst in steep inclined coal seam uncovered by two reverse drifts and technology of outburst elimination by increasing permeability with blasting," *Journal of China Coal Society*, vol. 35, no. 1, pp. 85–88, 2010.
- [49] Q. T. Hu, S. N. Zhou, and X. Q. Zhou, "Mechanical mechanism of coal and gas outburst process," *Journal of China Coal Society*, vol. 33, no. 12, pp. 1368–1372, 2008.
- [50] J. C. Ou, E. Y. Wang, G. Q. Ma et al., "Coal rupture evolution law of coal and gas outburst process," *Journal of China Coal Society*, vol. 37, no. 6, pp. 978–983, 2012.
- [51] D. Liu, J. Xu, G. Z. Yin, W. Z. Wang, Y. Q. Liang, and J. S. Peng, "Development and application of multifield coupling testing system for dynamic disaster in coal mine," *Chinese Journal of Rock Mechanics and Engineering*, vol. 32, no. 5, pp. 966–975, 2013.
- [52] K. Gao, G. D. Qiao, Z. G. Liu, J. Liu, F. H. Zhu, and S. C. Zhang, "On classification conception of coal and gas outburst mechanism and its application," *Journal of Mining & Safety Engineering*, vol. 36, no. 5, pp. 1043–1051, 2019.
- [53] J. P. Tang, S. L. Yang, Y. L. Wang, and J. Q. Lv, "Experiment of coal and gas outbursts under ground stress and gas pressure in deep mines," *Rock and Soil Mechanics*, vol. 35, no. 10, pp. 2769–2774, 2014.
- [54] D. L. Sun, Q. T. Hu, and F. T. Miao, "Motion state of coal-gas flow in the process of outburst," *Journal of China Coal Society*, vol. 37, no. 3, pp. 452–458, 2012.
- [55] X. G. Xie, T. Feng, Y. Wang, and S. Y. Huang, "The energy dynamic balance in coal and gas outburst," *Journal of China Coal Society*, vol. 35, no. 7, pp. 1120–1124, 2010.
- [56] Y. Zhao, B. Q. Lin, T. Liu et al., "Mechanism of multifield coupling-induced outburst in mining-disturbed coal seam," *Fuel*, vol. 272, Article ID 117716, 2020.
- [57] J. Zhang, H. Yan, Q. Zhang, B. Li, and S. Zhang, "Disaster-causing mechanism of extremely thick igneous rock induced by mining and prevention method by backfill mining," *European Journal of Environmental and Civil Engineering*, vol. 24, no. 3, pp. 307–320, 2020.
- [58] X. C. Li, B. S. Nie, L. K. Wang, L. C. Dai, and Z. Liu, "Analysis on coal and gas outburst mechanism under multifield coupling action," *Coal Science and Technology*, vol. 39, no. 5, pp. 64–66+69, 2011.
- [59] X. Q. He, *Disaster Dynamics of Gas Bearing Coal and Rock*, China University of Mining and Technology Press, Xuzhou, China, 1995.
- [60] D. Y. Guo and D. X. Han, "The stick-slip mechanism of coal and gas outburst," *Journal of China Coal Society*, vol. 6, pp. 598–602, 2003.
- [61] Q. X. Qi, Y. W. Shi, and T. Q. Liu, "Mechanism of instability caused by viscous sliding in rock burst," *Journal of China Coal Society*, vol. 22, no. 2, pp. 144–148, 1997.
- [62] J. R. Wang, C. B. Deng, and H. Z. Deng, "Study on the microcosmic mechanism for coal-gas outburst," *Journal of China Coal Society*, vol. 2, pp. 131–135, 2008.
- [63] Z. F. Ma and Q. X. Yu, "The pilot study on outburst mechanism for compression disseminated values of coal and gas out of control," *Journal of China Coal Society*, vol. 3, pp. 329–333, 2006.
- [64] N. J. Ma, X. D. Zhao, Z. Q. Zhao, X. F. Guo, H. T. Liu, and H. S. Jia, "Conjecture about mechanism of butterfly shape coal and gas outburst in excavation roadway," *Journal of Mining Science and Technology*, vol. 2, no. 2, pp. 137–149, 2017.
- [65] Z. Q. Zhao, N. J. Ma, X. F. Guo, X. D. Zhao, Y. X. Xia, and Z. K. Ma, "Mechanism conjecture of butterfly rock burst in coal seam roadway," *Journal of Mining Science and Technology*, vol. 41, no. 11, pp. 2689–2697, 2016.

- [66] Z. Q. Zhao, N. J. Ma, H. T. Liu, and X. F. Guo, "A butterfly failure theory of rock mass around roadway and its application prospect," *Journal of China University of Mining and Technology*, vol. 47, no. 5, pp. 969–978, 2018.
- [67] Z. Q. Zhao, *Study on Mechanism and Control Method of Deformation and Failure of Surrounding Rock in Lagged Deformation Mining Roadway*, China University of Mining and Technology, Beijing, China, 2014.
- [68] X. F. Guo, L. F. Guo, N. J. Ma, Z. Q. Zhao, and L. Chen, "Applicability analysis of the roadway butterfly failure theory," *Journal of China University of Mining and Technology*, vol. 49, no. 4, pp. 646–653, 2020.
- [69] X. S. Zhao, Q. T. Hu, Y. H. Zou, and J. N. Kang, "The fast measurement principium and its application of the consistent coefficient of distant coal beyond working face," *Journal of China Coal Society*, vol. 32, no. 1, pp. 38–41, 2007.
- [70] J. Han, H. W. Zhang, Z. M. Zhu, and J. C. Song, "Controlling of tectonic stress field evolution for coal and gas outburst in Fuxin basin," *Journal of China Coal Society*, vol. 9, pp. 934–938, 2007.
- [71] M. M. Cao, Y. S. Kang, Z. Deng, B. F. Tian, Q. Zhao, and H. Y. Wang, "Influence of coal rank and tectonic stress intensity on mechanical properties of coal rock," *Coal Science and Technology*, vol. 47, no. 12, pp. 45–55, 2019.
- [72] R. G. Zhang, L. T. Fang, B. Hu, L. Qin, and L. Xiong, "Tectonic coal structure and pore characteristics of Zhuxianzhuang mine," *Coal Geology and Exploration*, vol. 43, no. 4, pp. 6–10, 2015.
- [73] J. M. Han, Y. Wu, and D. Zhao, "Relationship between methane adsorption and strength about coal sample," *Coal*, vol. 21, no. 1, pp. 12–13, 2012.
- [74] J. S. Zhang, "Experimental study on influence of gas pressure on strength of coal body under adsorption condition," *Safety in Coal Mines*, vol. 51, no. 1, pp. 26–29, 2020.
- [75] J. Xu, X. P. Su, L. C. Cheng, L. Wang, J. Liu, and D. Feng, "Evolution characteristics of meso-cracks of gas-filled raw coal under compression-shear stress," *Chinese Journal of Rock Mechanics and Engineering*, vol. 33, no. 3, pp. 458–467, 2014.
- [76] B. Bai, X. C. Li, Y. F. Liu, Z. M. Fang, and W. Wang, "Preliminary theoretical study on impact on coal caused by interactions between CO₂ and coal," *Rock and Soil Mechanics*, vol. 4, pp. 823–826, 2007.
- [77] X. Zhao, J. X. Lv, and J. H. Jiang, "Size effect of modulus of rupture for the larch dimension lumber," *Journal of Building Materials*, vol. 17, no. 4, pp. 734–737, 2014.
- [78] Z. G. Deng, "Study on influencing factors of strength size effect based on bump-prone coal," *Coal Science and Technology*, vol. 47, no. 8, pp. 59–63, 2019.
- [79] J. Xu, W. Zhou, D. Liu, S. C. Li, and H. Y. Tan, "Temperature and acoustic emission characteristics of coal in the process of outburst under the influence of mining," *Journal of China Coal Society*, vol. 38, no. 2, pp. 239–244, 2013.
- [80] Z. Wang, Q. T. Hu, G. C. Wen, and D. L. Sun, "Study on the distribution laws of mining pressure field and its control action on dynamic disasters in coal mines," *Journal of China Coal Society*, vol. 36, no. 4, pp. 623–627, 2011.
- [81] X. C. Li, B. S. Nie, and X. Q. He, "Mechanism of coal and gas bursts caused by vibration," *Chinese Journal of Engineering*, vol. 33, no. 2, pp. 149–152, 2011.
- [82] X. Qi and J. J. Geng, "Experimental study on the effect of water injection to coal strength," *Shaanxi Coal*, vol. 31, no. 5, pp. 44–45, 2012.
- [83] Z. Y. Sun, Z. Zhang, and Z. G. Wu, "Field test analysis of gas drainage to coal strength and anchor character," *Coal Mining Technology*, vol. 22, no. 5, pp. 45–48, 2017.
- [84] J. Xu, D. Liu, S. J. Peng, X. Wu, and Q. Lu, "Experimental research on influence of particle diameter on coal and gas outburst," *Chinese Journal of Rock Mechanics and Engineering*, vol. 29, no. 6, pp. 1231–1237, 2010.
- [85] Q. H. Zhang, S. C. Li, H. P. Wang et al., "Influence mechanism and outburst characteristics during revealing different intensity coal containing gas," *Journal of Mining & Safety Engineering*, vol. 34, no. 4, pp. 817–824, 2017.
- [86] Y. Zhao, X. H. Li, Y. Y. Lu, and Y. Kang, "Influence of gas pressure on compressive strength size effect of inhomogenous coal," *Journal of China Coal Society*, vol. 34, no. 8, pp. 1081–1085, 2009.
- [87] Y. J. Liu, L. Yuan, J. H. Xue, Z. C. Tian, C. R. Duan, and B. L. Chen, "Research status and development trend of mechanism and simulation test of coal and gas outburst," *Industry and Mine Automation*, vol. 44, no. 2, pp. 43–50, 2018.
- [88] Y. Y. Lu, Z. Y. Peng, B. W. Xia, P. Yu, and C. N. Ou, "Multi-functional physical model testing system of deep coal petrography engineering-coal and gas outburst simulation experiment," *Journal of China Coal Society*, vol. 45, no. S1, pp. 272–283, 2020.

Research Article

Study on Rock Burst Early Warning in the Working Face of Deep Coal Mines Based on the Law of Gas Emission

Qinghua Zhang ^{1,2,3} and Shudong He^{2,3}

¹School of Safety Science and Engineering, Anhui University of Science and Technology, Huainan 232001, Anhui, China

²State Key Laboratory of the Gas Disaster Detecting, Preventing and Emergency Controlling, Chongqing 400037, China

³China Coal Technology and Engineering Group Chongqing Research Institute, Chongqing 400037, China

Correspondence should be addressed to Qinghua Zhang; 87217289@qq.com

Received 20 March 2021; Accepted 26 April 2021; Published 8 May 2021

Academic Editor: Jia Lin

Copyright © 2021 Qinghua Zhang and Shudong He. This is an open access article distributed under the Creative Commons Attribution License, which permits unrestricted use, distribution, and reproduction in any medium, provided the original work is properly cited.

This study is aimed at predicting rock burst disasters in high gas mines. First, the distribution law and correlation of gas and stress in the F₁₅₋₁₇-11111 working face of Pingdingshan No. 13 Mine were analyzed based on the coupling relationship between gas emission and stress in the working face. Next, the relationship between gas emission and stress distribution was revealed, and an early warning method of rock burst in the deep mine working face based on the law of gas emission was proposed and applied to the F₁₅₋₁₇-11111 working face. Finally, the critical value of the gas concentration indicator for rock burst early warning in the F₁₅₋₁₇-11111 working face was determined as 0.05%. The following research results were obtained. The gas emission and the mining stress in the F₁₅₋₁₇-11111 working face are negatively correlated. Mechanically, their correlation satisfies the typical coupling. Besides, the critical value of the gas concentration indicator determined by the proposed early warning method boasts high accuracy in predicting rock burst disasters. It can be used as an early warning method for underground rock burst disasters to promote the safety of working face mining. The research results provide reference and guidance for the monitoring and early warning of rock burst disasters in deep high gas mines.

1. Introduction

Rock burst [1] is a dynamic phenomenon in which the elastic energy accumulated in coal rock is released in a sudden, rapid, and violent way when the mechanical system of coal rock reaches its strength limit, scattering coal rock over roadways with great impact. This disaster, usually accompanied by huge vibration, will damage the roadway and equipment and causes casualties. Scholars at home and abroad have conducted extensive researches on the occurrence mechanism and monitoring and early warning methods of rock burst. A series of rock burst monitoring and early warning techniques have been proposed, including the microseismic method, the electromagnetic radiation method, the stress online method, the acoustic emission method, and the drilling cuttings method. However, these techniques cannot achieve early warning. When the

monitoring indicators reach the danger value, the rock burst disaster is about to occur, failing to leave sufficient time for pressure relief and disaster prevention. Besides, precursor information is needed to determine the risk of rock burst, which is of great inconvenience to the monitoring and prevention of rock burst in mines. At the same time, as the depth and extent of coal mining increase, the gas content and gas pressure in coal seams tend to increase, and the number of deep high gas mines is on the rise. Rock burst disasters occurred in many mines with high gas coal seams in China, such as Laohutai Coal Mine in Fushun, Wulong Coal Mine and Wangying Coal Mine in Fuxin, Tao'er Coal Mine in Handan, Jianxin Coal Mine in Fengcheng, and Pingdingshan No. 10 and 12 Mines [2–4]. The high gas in coal seams complicates the occurrence mechanism of rock burst, which poses a great obstacle to the monitoring and prevention of dynamic hazards in high gas coal seams. Therefore, special

studies on dynamic hazards in high gas coal seams are needed.

Scholars all over the world have done abundant studies on the occurrence mechanism and monitoring and early warning methods of rock burst in high gas mines. Petukhov [5], a scholar from former Soviet Union, was the first to research the combination of rock burst and gas outburst in 1987. Zhang et al. [6–8] were the first to analyze gas-induced coal instability and established a mathematical model of rock burst in gas-bearing coal seams. With the aid of microseisms, gas monitoring, and on-site investigation, Li et al. [9, 10] detected unusual gas emissions before, during, and after rock burst disasters, thus questioning the former idea that rock burst was a kind of coal outburst free from the impact of gas. They held that rock burst in deep mining was closely related to gas; high-pressure gas was highly likely to be involved in the occurrence of rock burst; and there was a kind of rock burst induced by the coupling between mining-induced stress relief and high-pressure adsorbed gas desorption and expansion in gas-bearing porous media and gas storage structures. Dong et al. [11] analyzed the influence of gas on the mechanical properties of coal and the law of gas seepage and fracture expansion and explored the conditions under which rock burst and gas outburst mutually converted in different stages. Yin et al. [12] studied the influence of stress field on gas field and established a gas-solid coupling model. Lu et al. [13] investigated the mechanism of rock burst occurrence in high gas coal seams. Zhang et al. [14] studied the coupling effect between the stress field and the gas field. Yuan et al. [15] summarized the characteristics and mechanism of rock burst in high gas coal seams and analyzed the problems in their study. Stanislaw [16] analyzed the effect of rock-burst-induced ore vibration on gas adsorption from multiple perspectives and factors and discussed the causes and conditions of emissions. Huo et al. [17, 18] proposed a solid-fluid coupling instability theory for coal and gas outburst based on the mechanism of coal rock deformation and gas seepage and established the intrinsic structure relationship of gas-bearing coal. Meanwhile, they proposed a method to determine material parameters. Shane and Tang [19] questioned whether rock burst induced gas, or gas induced rock burst, or both, based on the increase in gas concentration before, during, and after rock burst disasters. Ogieglo et al. [20] studied the effect of mine vibration on gas concentration. Zhou et al. [21, 22] established a one-dimensional flow model for coal and gas outburst, gave a crushing initiation criterion, and discussed the outburst process. Besides, they also studied large-scale outbursts corresponding to constant steady advancement and analyzed the important dimensionless parameters of coal and gas outburst, as well as the criterion. Wang et al. [23] probed into the unified mechanism of rock burst and outburst, explored the influences of coal burst proneness, pore gas pressure, and surrounding rock stress on outburst, and proposed a mathematical model of outburst. Wang et al. [24] researched the influence of gas during the implementation of the drill cuttings method in gas-bearing coal seams and used the classical theory to derive an index of the amount of drill cuttings for detecting rock burst in gas-bearing coal seams.

Liu et al. [25] put forward AVO technology (i.e., amplitude variation with offset) early warning theory of coal seam gas enrichment based on the comparison results of coal seam gas and conventional sandstone gas occurrence mechanism. Zhou et al. [26] analyzed the relationship between energy gathering and energy dissipation during uniaxial compression and cyclic loading of coal samples in different gas pressure environments and concluded that the gas shall be taken into account for burst proneness evaluation in deep mining of high gas mines.

The above studies mainly explain the mechanism behind the occurrence of rock burst in high gas coal seams and the effect of gas on rock burst. The results of these studies conduce to correcting the early warning indicators of the conventional rock burst monitoring technique to make it more applicable to the monitoring and early warning of high gas coal seams. However, methods for early warning of rock burst remain to be found. In this paper, the F₁₅₋₁₇-11111 working face of Pingdingshan No. 13 Mine was taken as the research background. First, the correlation between gas emission and rock burst was studied. Furthermore, a monitoring and early warning method of rock burst in the deep mine working face based on the law gas emission was proposed by using gas monitoring means. In this way, early warning of rock burst was achieved. Finally, the method was applied to engineering practice for verification. The research is expected to provide reference and guidance for the monitoring and early warning of rock burst disasters in deep high gas coal seams.

2. Study Area

2.1. Geological Conditions of Mines. Pingdingshan No. 13 Mine, with a design capacity of 1.80 Mt/a, is developed using double vertical shafts, two levels, rise and dip combined mining. The main minable seam is the lower F coal of the Shanxi Formation, and the main mining coal seam is the F₁₅₋₁₇ coal seam whose average thickness is 5.85 m. The mine field is located on the common flank of Likou syncline and Xiangjia anticline of the Pingdingshan coalfield, with the northeast oriented Gouli normal fault on the southeastern boundary, the coal outcrop near the Xiangjia fault on the northeastern boundary, and the northwest oriented Xingguosi normal fault on the western part. Overall, the strata strike and dip are NW 305°–340° and SW 215°–250°, respectively, and the dip angle is 10°–35°. The northeastern boundary of the mine field is close to the Xiangjia anticline axis, so it is significantly influenced by the Xiangjia anticline structure as a whole. The northwestern part of the mine field is a monoclinic structure that dips to the southwest, and it is accompanied by faults. Due to the Lingwushan syncline, the Baishishan anticline, and the secondary folds and faults perpendicular to the Lingwu syncline, the south-eastern part of the mine field is a complex structural area centered on the Lingwu syncline.

Pingdingshan No. 13 Mine is identified as a gas outburst mine. The distribution of gas occurrence in coal mine shows zonation. The gas content of the coal seam rises as the burial depth increases, and it increases from the west to the east,

resulting in a low gas concentration in the west and a high gas concentration in the east. Nevertheless, the gas concentration may vary locally due to the influence of faults, folds, and magmatic rocks. In the eastern part of the mine field, the gas contents of the F_1 and F_3 mining areas are the highest, with the measured maximum gas content at an elevation of -720 m being $16.09 \text{ m}^3/\text{t}$. All the three dynamic disasters that once threatened the mine occurred in the two mining areas. The gas content of the F_4 mining area in the western part of the mine field is relatively low, the measured maximum gas content at an elevation of -660 m being $10.28 \text{ m}^3/\text{t}$. The gas content in the central F_2 mining area is the lowest due to local faults.

2.2. Profile of the Working Face. The $F_{15-17-11111}$ working face of Pingdingshan No. 13 Mine is located in the sixth section of the east flank of the F_1 mining area. It extends to the Goulifeng normal fault in the east, the boundary of the security pillar at the rise and the Dongfeng shaft in the west, the goaf of the $F_{15-17-11090}$ mining face in the north, and the boundary of the F_1 mining area in the south. The F_3 mining area is under the F_1 mining area. The schematic diagram of the $F_{15-17-11111}$ working face is shown in Figure 1. The ground elevation of the working face is $+84.1$ m, and the elevation of it ranges from -465 m to -620 m. The mining coal seam in this working face is the F_{15-17} seam whose thickness and dip angle lie in the range of $3.8\text{--}6.5$ m and $8^\circ\text{--}16^\circ$, respectively, according to the coal exploration data. In addition, the seam has a simple and stable structure.

The F_1 mining area where the $F_{15-17-11111}$ working face is located and the adjacent F_3 mining area both experienced the compound dynamic disasters of rock burst and gas outburst. The $F_{15-17-11111}$ working face, located at the boundary of the F_1 mining area and near the F_3 mining area, belongs to an outburst coal seam. It is also prone to the compound dynamic disasters.

2.3. Overview of Rock Burst Accidents in the Mine. On March 12, 2002, the first compound dynamic disaster occurred at 12 m (i.e., at the open-off cut) of the $F_{15-17-11091}$ machine lane. Rock burst occurred first, resulting in local destruction of the roadway and bursting 196 t of coal. Then, the gas concentration surged sharply, and the volume of gas emission was $3,840 \text{ m}^3$. On January 20, 2008, 594 t of coal

was burst and $32,927 \text{ m}^3$ of gas was emitted at 830 m of the $F_{15-17-13031}$ machine lane. On June 13, 2010, $1,133$ t of coal was burst and $308,557 \text{ m}^3$ of gas was emitted at 272 m of the $F_{15-17-13031}$ low-level gas drainage roadway. Based on on-site cases of Pingdingshan No. 13 Mine, it was found that the gas concentration dropped first before rock burst, whereas it jumped sharply after that.

3. Methodology

3.1. Coupling Structural Model of Working Face Gas Emission and Stress. Rock burst generally occurs from the coal wall side of the working face. In the limit equilibrium zone ahead of the coal wall, stress is highly concentrated due to the suspension of overlying roof. As a result, a large amount of elastic strain energy is reserved in coal. In the high gas mine, the expansion energy of adsorbed gas is also reserved in coal.

The coupling structural model of gas emission and stress during deep high gas coal seam working face mining is shown in Figure 2.

During mining, three areas, namely, Areas A, B, and C, will be formed in front of the working face with the rupture of coal (Figure 2). Under high stress, the yield failure of coal in Area A leads to the loss of its bearing capacity, forming a pressure relief zone where the residual strength provides radial load for the internal coal. Under the support of the radial support force provided by the coal in Area A, the coal in Area B boasts enhanced strength, a great bearing capacity, and the highest stress, thus forming a stress concentration area. Stress in Area C gradually decreases to the initial rock stress, and this area is called the initial stress area.

When the working face experiences weighting, the hard roof is suspended above the coal wall, resulting in a certain range of "stress wall" in front of the coal wall. The "stress wall" gradually gets compacted, during which the gas emission is gradually reduced. Hence, a large amount of gas is accumulated inside the "stress wall." When the roof ruptures suddenly, the stress transfers to the deep area, which is equivalent to a sudden opening of the "stress wall." Accordingly, the gas emission increases sharply. Therefore, affected by mining stress, coal porosity and gas pressure will change dynamically. Xie et al. [27] held that the coal seam mining stress σ is a function where the gas pressure P and the porosity λ are variables (other parameters are constants for specific coal):

$$\sigma = \frac{(1 - \lambda_0)E}{(1 - \lambda)(1 - 2\mu)} \left[\frac{aK_0RT}{N_m S} \ln \frac{(1 + bP)}{(1 + bP_0)} - K_y (P - P_0) + 1 \right] - \frac{E}{(1 - 2\mu)}, \quad (1)$$

where λ_0 is the initial porosity of coal; P_0 is the initial gas pressure of coal seam, MPa; E is the elastic modulus of coal, GPa; μ is Poisson's ratio of coal; R is a universal gas constant, $\text{J}/(\text{mol}\cdot\text{K})$; T is the absolute temperature, K; N_m is the molar volume of gas, which equals 22.4 L/mol in the standard state; S is the specific surface area, m^2/g ; a is the adsorption

constant, m^3/t ; b is the adsorption constant, MPa^{-1} ; K_y is the compressibility coefficient of coal, MPa^{-1} .

Therefore, the stress has a significant influence on the distribution and extension of cracks in the coal. Cracks in the coal in Area A are interconnected, causing an increase in the porosity and a high permeability of the coal seam. In this case,

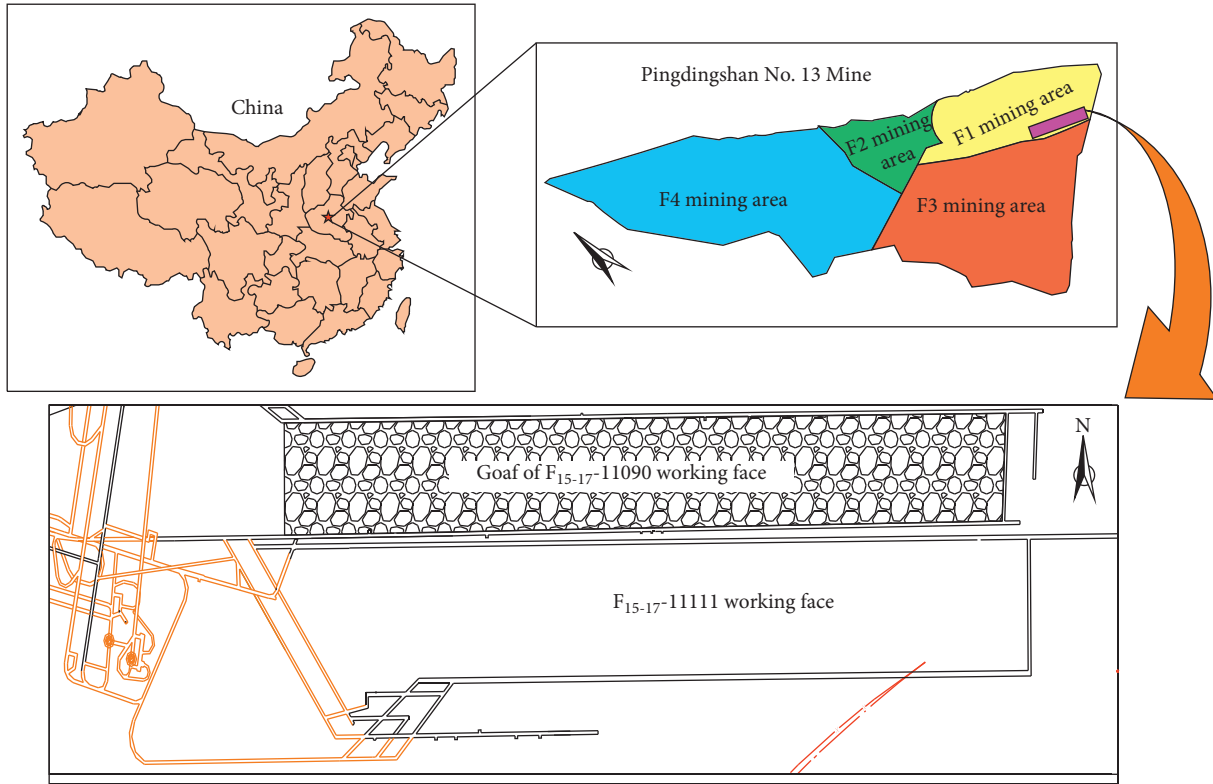


FIGURE 1: Schematic diagram of the location of the F₁₅₋₁₇₋₁₁₁₁₁ working face.

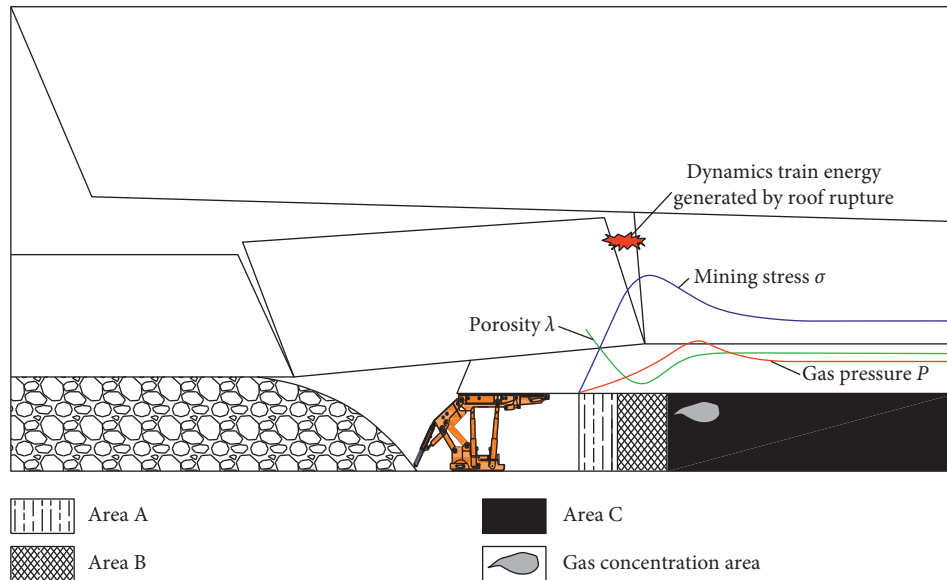


FIGURE 2: Coupling structural model of gas emission and stress in the working face.

gas can be fully emitted, so the gas content and gas pressure are relatively low. The coal in Area B is relatively integrated. Under the action of high stress, pores and cracks in the coal are compacted, bringing about a decrease in the porosity and a poor permeability. In this case, gas is accumulated, so the gas content and gas pressure are both high. Since Area B is close to the pressure relief area where the coal is ruptured seriously, a

high gas pressure gradient and a high gas content gradient tend to be formed. While the gas in Area A is emitted, the gas in Area B remains accumulated and rarely gets emitted because of the low porosity induced by stress concentration in the deep coal. The above phenomenon reflects the negative correlation between coal seam gas emission and mining stress in coal seam. Mechanically, their correlation satisfies the typical coupling.

3.2. Evolution Law of Stress and Gas in the Working Face during Mining. Since the working face is continuously advancing in the production process, the stress and gas states in the coal seam are changing cyclically and constantly. The following discussion is about the change of stress and gas states in the coal seam after the mining footage of the working face.

After the working face advances for a distance of S , the overlying load originally acting on the coal in Area S is transferred to the coal in the front, leading to a sudden rise of the stress borne by the newly exposed coal. At the same time, the amount of released gas in the coal seam is relatively small for a short time. Resultantly, a large stress gradient and a large gas gradient are formed (Curve 1 in Figure 3). When the stress exceeds the strength limit of the coal, the coal ruptures and the stress transfers to the inner part of the coal seam. Meanwhile, the cracks become interconnected after the coal ruptures, providing a channel for the migration and release of gas. The gas in the deep area transfers towards the working face (Curve 2 in Figure 3). After several ruptures of the coal in front of the working face, the stress and gas pressure gradually stabilize (Curve 3 in Figure 3). At this time, a footage of the working face is completed.

Under normal mining conditions, stress and gas pressure in front of the working face can transfer smoothly. However, once geological structures, coal seam thickness changes, and an excessively long suspended roof exist in front of the working face, stress transfer will become abnormal. Specifically, the stress and the stress gradient surge, so that gas becomes accumulated in local areas. Assuming there is an abnormal area (Area D, such as fault structures, coal seam thickness changes, soft layer thickness changes, and partings) in front of the working face, the stress transfer and variation law is shown in Figure 4. In this case, the stress no longer transfers forward along with working face advancement. Instead, it undergoes stress stagnation under the influence of Area D. As the pressure relief area (Area A) narrows, the stress peak becomes larger and increasingly closer to the working face. Besides, more and more gas is accumulated inside the coal, forming an increasing stress gradient and gas pressure gradient. A high gas content determines greater expansion energy of adsorbed gas. When Area A fails to provide enough radial support for the stress concentration area (Area B), the accumulated energy in Area B will be released outward suddenly, bringing about coal ruptures, rock burst dynamic disasters, and a rise of gas concentration.

3.3. An Early Warning Method of Rock Burst in the Deep Mine Working Face Based on the Law of Gas Emission. By analyzing stress and gas evolution in the working face during mining, it is concluded that abnormal mining conditions of the working face are likely to cause rock burst disasters. The gas concentration decreases first before the occurrence of rock burst, while it soars sharply after the occurrence. In areas where rock burst occurs, the stress increases gradually before the occurrence of rock burst, and rock burst occurs when the stress reaches the coal failure limit. Stress monitoring in

working face belongs to point monitoring which is discontinuous. When the stress reaches its maximum, the disaster is about to occur. Therefore, stress monitoring cannot support early warning. In contrast, the monitoring and control of gas concentration in the working face are continuous. As a result, based on the relationship between gas emission and stress in the working face, changes in the stress can be indirectly obtained by monitoring the gas concentration variation. In other words, rock burst can be monitored with the aid of gas concentration monitoring.

As revealed by the above analysis, the early warning of rock burst can be realized through a combination of rock burst monitoring and gas emission monitoring. In this study, by taking geological and mining conditions of the mine into account, based on the rational utilization of the existing monitoring facilities in the mine, a comprehensive monitoring scheme which can be used to monitor the gas concentration and the stress in the working face is designed, and an early warning method of rock burst in the deep mine working face based on the law of gas emission is proposed.

The flowchart of the proposed early warning method is shown in Figure 5. First of all, the monitoring points of gas concentration and stress in the working face are designed and arranged. Then, the monitoring data of gas concentration and stress are collected. Moreover, by analyzing the monitoring data, the law of gas emission and stress distribution is concluded, and the correlation between the gas concentration values and the data from the stress monitoring points is analyzed. Finally, the value of the gas concentration early warning indicator for early warning is determined, according to the data from the stress monitoring points at the moment when the dynamic changes of gas concentration are observed.

3.4. Design of Gas and Stress Monitoring in the Working Face.

According to the above introduction to the proposed early warning method, a field test was carried out with the F₁₅₋₁₇-11111 working face of Pingdingshan No. 13 Mine taken as the engineering geological background. The support pressure, which could reflect the stress change in the working face, was used for predicting the weighting time and weighting step distance. In accordance with the weighting condition, the rock burst and outburst hazards could be predicted. In this study, stress monitoring in the working face was realized online through the supports. A total of nine KJ21 support pressure online recorders were installed on the supports 18#, 27#, 31#, 36#, 45#, 50#, 72#, 81#, and 90# in the F₁₅₋₁₇-11111 working face, respectively. The roof periodic weighting step distance and pressure distribution were analyzed according to the monitored data. The gas concentration monitoring was realized through the KJ-2000 N safety monitoring system. The system included an MGTSV monitoring cable and two GJC40 (A) gas sensors. Of the two gas sensors, the internal gas sensor was installed in the return airway, being no more than 10 m away from the mining face. The layout of gas and stress monitoring points in working face is shown in Figure 6.

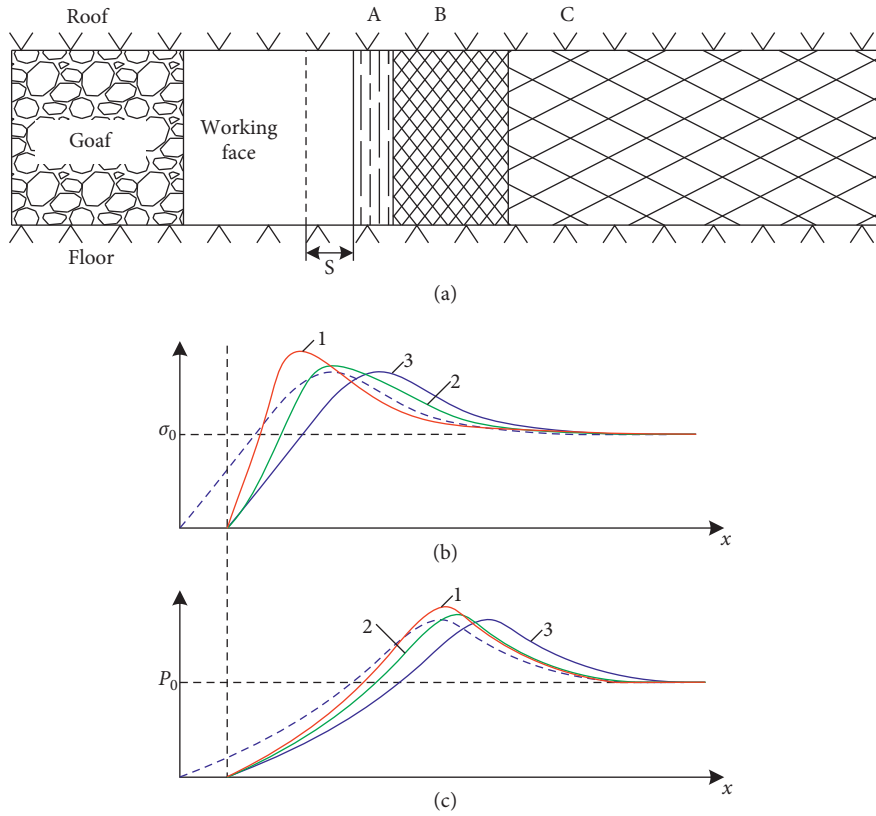


FIGURE 3: Diagram of stress and gas pressure changes.

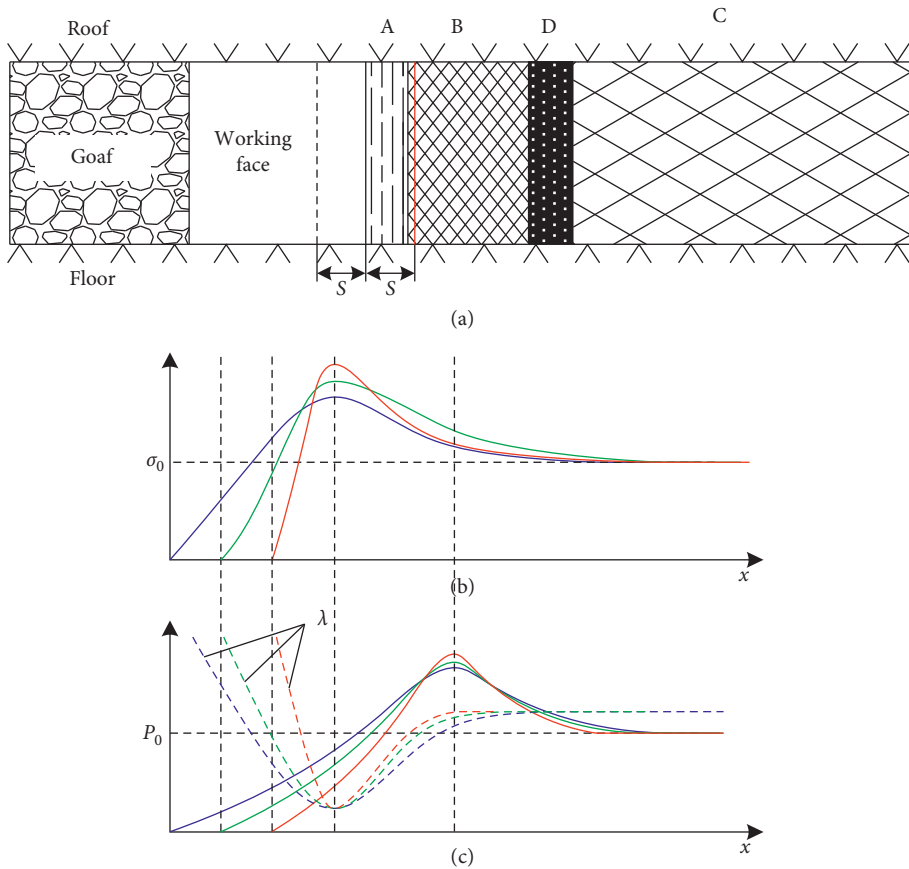


FIGURE 4: Influence of abnormal mining conditions on stress and gas pressure.

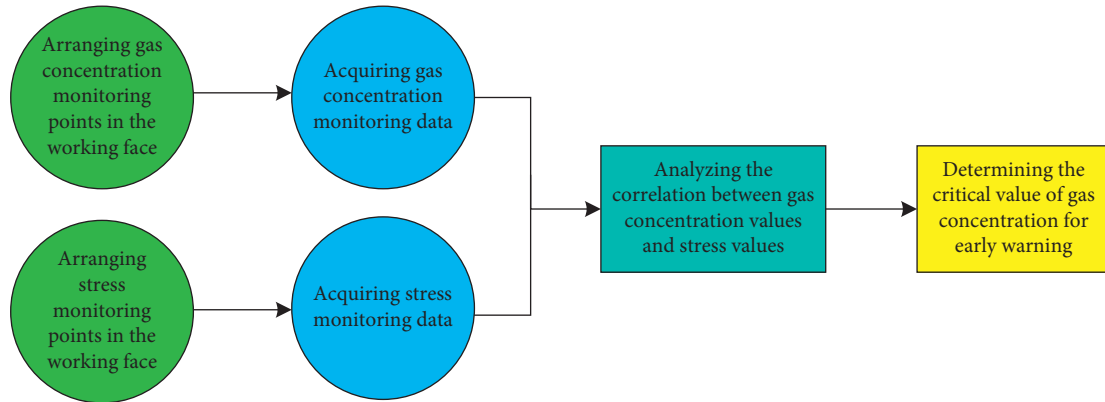


FIGURE 5: Flowchart of early warning method of rock burst in the deep mine working face based on the law of gas emission.

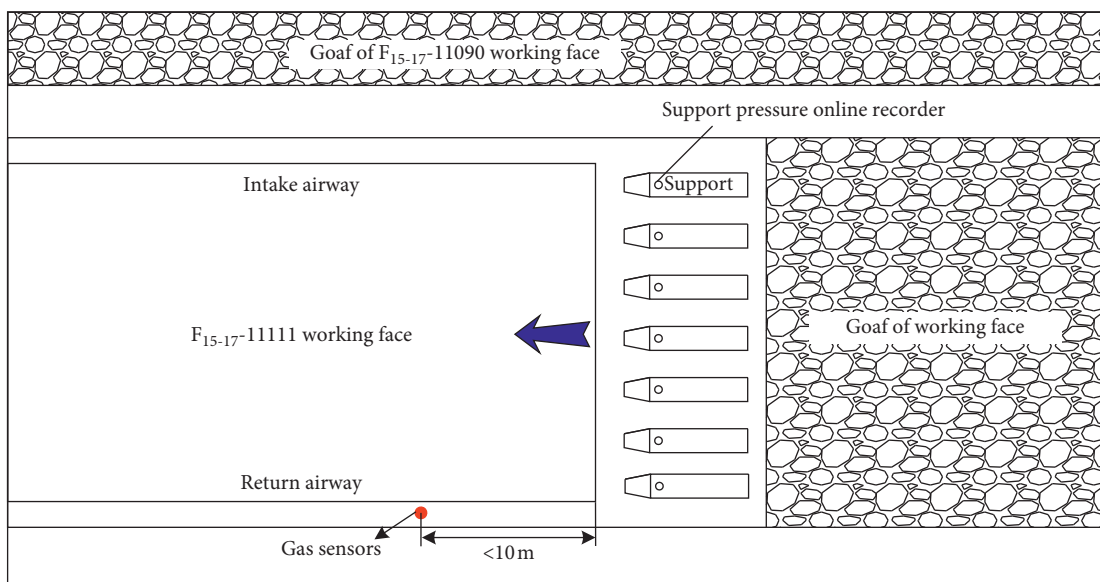


FIGURE 6: Schematic diagram of gas and stress monitoring design in the working face.

4. Results and Discussion

4.1. Law of Gas Emission and Stress Distribution in the F₁₅₋₁₇-11111 Working Face. In order to investigate the relationship between gas emission and stress distribution, the support pressure data in the working face and the gas concentration real-time data in the return airway were collected and statistically analyzed. On the basis of the analysis, the variation curves of support pressure and average gas concentration with the advancement distance of the working face are obtained (Figure 7).

According to the field data of Pingdingshan No. 13 Mine, the weighted average of support pressures in the F₁₅₋₁₇ coal seam is 25 MPa. If the support pressure exceeds the weighted average, it can be determined that periodic pressure is occurring in this area where the coal is under highly concentrated stress and possesses the risk of rock burst. Figure 7 shows that since the start of monitoring, as the advancement distance of the F₁₅₋₁₇-11111 working face increases, the roof of the working face gradually bends and sinks, accompanied

by periodic collapses. Correspondingly, the roof pressure increases to over 25 MPa, the maximum approaching 40 MPa. During normal advancement of the working face, the support pressure maintains a low value without significant changes and rarely exceeds the weighted average. However, when the working face advances to 21.4 m, 72.8 m, 108.5 m, and 140.1 m, the gas concentration of the working face falls notably, and meanwhile the working pressure of the support rises. As the working face continues to advance, roof collapse or rock burst occurs. Later, the support pressure drops, and the gas concentration jumps dramatically first and then falls. When the “8.16” rock burst occurs, the gas concentration reaches the minimum (0.03%) of the entire monitoring process, and the support pressure reaches the maximum (39.8 MPa). Afterwards, the gas concentration rises sharply to 38.65%.

4.2. Determination of the Critical Value of the Early Warning Indicator. As disclosed by the law of gas emission and stress

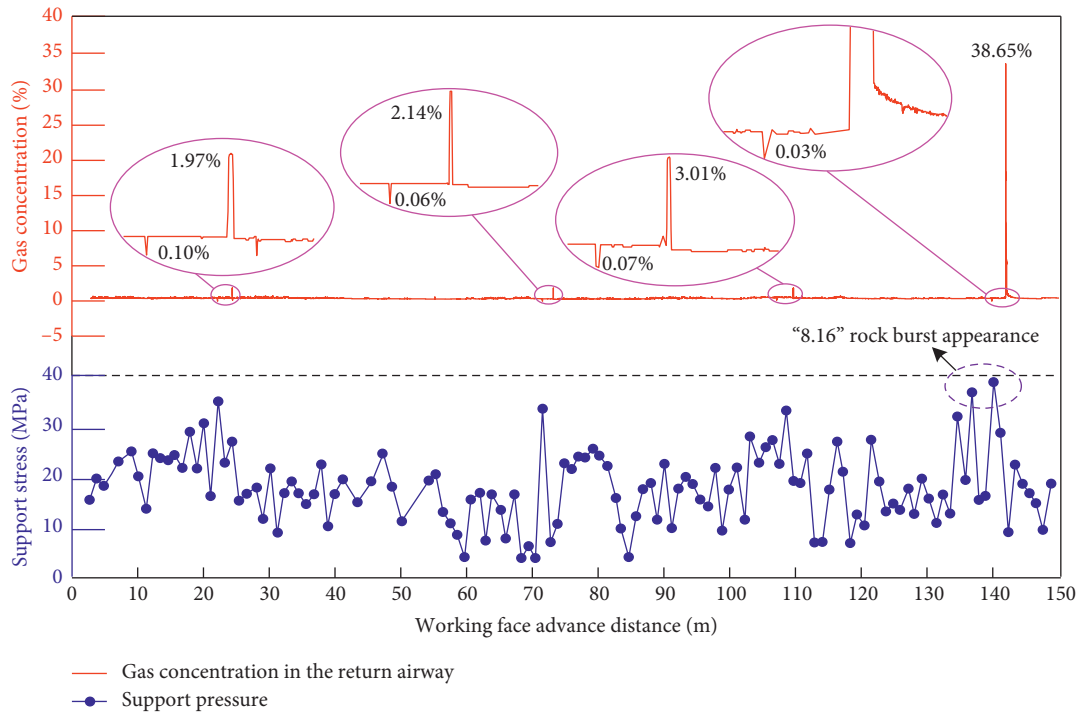


FIGURE 7: Variation curves of support pressure and average gas concentration with the advancement distance of the working face.

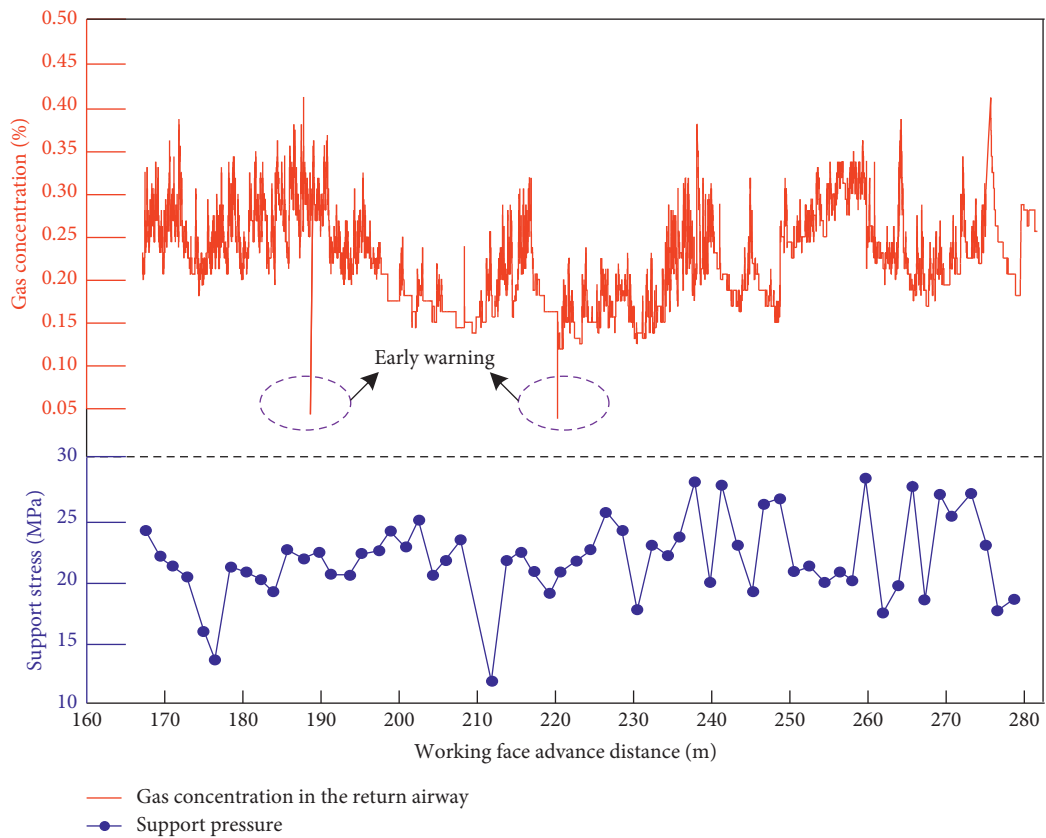


FIGURE 8: Early warning of support pressure and average gas concentration change curve after pressure relief.

distribution in the F₁₅₋₁₇₋₁₁₁₁₁ working face, during the periodic weighting, the gas emission often lags behind the periodic weighting. As the support pressure increases, the gas concentration experiences a great decrease. When it reaches the minimum, the support pressure is at its maximum. At this moment, the rock burst is the most likely to occur. By comparing the decrease in gas concentration with the usual gas concentration, the early warning of rock burst can be realized. According to the support pressure statistics during the mining of Pingdingshan No. 13 Mine, the minimum support pressure corresponding to coal and rock gas dynamic phenomena is 35 MPa, so 35 MPa is regarded as the critical value of support pressure. According to the support pressure data in the working face and the real-time gas concentration data in the return airway, during normal periodic weightings, the maximum support pressure is 34.7 MPa, and the gas concentration in the return airway ranges from 0.05% to 0.1%. When the support pressure exceeds 35 MPa, that is, when a coal and rock gas dynamic phenomenon occurs, the gas concentration is 0.03%, lower than 0.05%. Therefore, considering the correlation between the gas concentration value and the stress monitoring data, 0.05% is regarded as the critical value of gas concentration. When the gas concentration in the return airway undergoes a continuous decrease and falls to below 0.05%, rock burst warning is triggered.

4.3. Early Warning and Verification. In this study, the critical value of gas concentration for rock burst warning in the F₁₅₋₁₇₋₁₁₁₁₁ working face is determined as 0.05%. From November 2018 to January 2019, two impact hazards were predicted, with gas concentration reaching 0.042% and 0.047%, respectively, which reached the warning value, as shown in Figure 8. Therefore, when the pressure risk of impact ground pressure is detected, pressure relief measures are adopted. After pressure relief, the pressure of working face has not increased significantly, and no impact ground pressure accident occurred on the working face.

After that, the early warning results indicated rock burst risk for a total of 12 times of F₁₅₋₁₇₋₁₁₁₁₁ working face. After the pressure relief measures were adopted when the danger of rock burst was detected, the working face has been pushed forward for 400 meters, and the stopping line is safe, which has achieved significant economic, technical, and social benefits.

5. Conclusions

- (1) Through the analysis of the on-site rock burst accident of Pingdingshan No. 13 Mine, it is found that gas concentration changes regularly before and after the occurrence of rock burst. The gas concentration decreases first before the occurrence, while it jumps sharply after that.
- (2) The gas emission and the mining stress in the coal seam of the working face are negatively correlated. Mechanically, their correlation satisfies the typical coupling. In the direction of working face

advancement, the gas concentration in the working face increases as the stress decreases, and it decreases as the stress increases. In addition, the gas concentration reaches its minimum when the stress reaches its maximum.

- (3) The early warning method of rock burst in the deep mine working face based on the law of gas emission is proposed. Through field monitoring, the critical value of the gas concentration indicator for rock burst early warning in the F₁₅₋₁₇₋₁₁₁₁₁ working face is determined as 0.05%. On-site practice demonstrates that regarding the critical value as the early warning value is basically consistent with the field practical situation, and it succeeds in ensuring the safe mining of the working face.

Data Availability

The data used to support the findings of this study are included within the article.

Conflicts of Interest

The authors declare that they have no conflicts of interest regarding the publication of this work.

Acknowledgments

This study was supported by National Key Research and Development Program of China (No. 2018YFC0808305) and the support is gratefully acknowledged.


References

- [1] S. He, T. Chen, I. Vennes et al., "Dynamic modelling of seismic wave propagation due to a remote seismic source: a case study," *Rock Mechanics and Rock Engineering*, vol. 53, no. 11, pp. 5177–5201, 2020.
- [2] T.-B. Zhao, M.-L. Xing, W.-Y. Guo, C.-W. Wang, and B. Wang, "Anchoring effect and energy-absorbing support mechanism of large deformation bolt," *Journal of Central South University*, vol. 28, no. 2, pp. 572–581, 2021.
- [3] P. Zhang, Y. Ou, C. Liu, B. Sun, and C. Xu, "Stability of a roadway below a coal seam under dynamic pressure: a case study of the 11123 floor gas drainage roadway of a mine in huainan, China," *Data Mining in Civil Engineering*, vol. 2020, 15 pages, Article ID 8478043, 2020.
- [4] K. Ding, L. Wang, Y. Mei, W. Wang, and B. Ren, "Study on microseismic monitoring, early warning, and comprehensive prevention of a rock burst under complex conditions," *Shock and Vibration*, vol. 2020, Article ID 8863771, 12 pages, 2020.
- [5] K. Petukhov, "The theory and practice of rockburst prevention," in *Proceedings of the 22nd International Conference on Mining Safety*, Coal Industry Press, Beijing, China, 1987.
- [6] J. Zhang, Y. Li, Y. Pan et al., "Experiments and analysis on the influence of multiple closed cemented natural fractures on hydraulic fracture propagation in a tight sandstone reservoir," *Engineering Geology*, vol. 281, Article ID 105981, 2020.
- [7] X. Ding, X. Xiao, X. Lv, D. Wu, and Y. Pan, "Analysis of similarities and differences between acoustic emission and charge signal based on fractal characteristics of coal fracture,"

- Advances in Civil Engineering*, vol. 2020, Article ID 8745039, 12 pages, 2020.
- [8] Q. Ma, Y. Tan, X. Liu, Q. Gu, and X. Li, "Effect of coal thicknesses on energy evolution characteristics of roof rock-coal-floor rock sandwich composite structure and its damage constitutive model," *Composites Part B: Engineering*, vol. 198, Article ID 108086, 2020.
- [9] T. Li and M. Cai, "The mechanism of earth-quake-induced gas disaster nucleation in coal mines," *Journal of China Coal Society*, vol. 33, no. 10, pp. 1112–1117, 2008, [in Chinese].
- [10] Q. Ma, Y. Tan, X. Liu, Z. Zhao, and D.-Y. Fan, "Mechanical and energy characteristics of coal-rock composite sample with different height ratios: a numerical study based on particle flow code," *Environmental Earth Sciences*, vol. 80, p. 309, 2021.
- [11] G. Dong, X. Liang, and Z. Wang, "The properties of a coal body and prediction of compound coal-rock dynamic disasters," *Shock and Vibration*, vol. 2020, Article ID 8830371, 13 pages, 2020.
- [12] S. Yin, H. Ma, Z. Cheng et al., "Permeability enhancement mechanism of sand-carrying hydraulic fracturing in deep mining: a case study of uncovering coal in cross-cut," *Energy Science & Engineering*, vol. 7, no. 5, pp. 1867–1881, 2019.
- [13] J. Lu, G. Yin, H. Gao et al., "True triaxial experimental study of disturbed compound dynamic disaster in deep underground coal mine," *Rock Mechanics and Rock Engineering*, vol. 53, no. 5, pp. 2347–2364, 2020.
- [14] H. Zhang, Y. Zhong, E. Kuru, J. Kuang, and J. She, "Impacts of permeability stress sensitivity and aqueous phase trapping on the tight sandstone gas well productivity—a case study of the daniudi gas field," *Journal of Petroleum Science and Engineering*, vol. 177, pp. 261–269, 2019.
- [15] A. Yuan, P. Wang, and L. Yang, "Movement laws of overlying strata and prevention measures of dynamic disasters under deep adjacent coal seam group with high gas," *Geomatics Natural Hazards & Risk*, vol. 11, no. 1, pp. 2339–2359, 2020.
- [16] W. Stanislaw, "Gas-dynamic phenomena caused by rock mass tremors and rock bursts," *International Journal of Mining Science and Technology*, vol. 30, no. 3, pp. 413–420, 2020.
- [17] B. Huo, X. Jing, A. He, and C. Fan, "Hydraulic-mechanical coupling model with dual-porosity dual-permeability for anisotropy coal seams and its application in mine gas extraction," *Advances in Civil Engineering*, vol. 2019, Article ID 4534835, 12 pages, 2019.
- [18] B. Huo, X. Jing, C. Fan, and Y. Han, "Numerical investigation of flue gas injection enhanced underground coal seam gas drainage," *Energy Science & Engineering*, vol. 7, no. 6, pp. 3204–3219, 2019.
- [19] A. Shane, *Prediction and Prevention of Gas Dynamic Phenomena in Mines*, X. Tang trans, China Coal Industry Press, Beijing, China, 1992.
- [20] K. Ogieglo, M. Lubryka, J. Kutkowski et al., "Influence of mine shock to gas emission rate," *Ground Pressure and Strata Control*, vol. 22, no. 2, pp. 109–111, 2005.
- [21] B. Zhou, J. Xu, F. Yan et al., "Effects of gas pressure on dynamic response of two-phase flow for coal-gas outburst," *Powder Technology*, vol. 377, pp. 55–69, 2021.
- [22] B. Zhou, J. Xu, S. Peng et al., "Influence of geo-stress on dynamic response characteristics of coal and gas outburst," *Rock Mechanics and Rock Engineering*, vol. 53, no. 11, pp. 4819–4837, 2020.
- [23] L. Wang, Y.-P. Cheng, C. Xu, F.-H. An, K. Jin, and X.-L. Zhang, "The controlling effect of thick-hard igneous rock on pressure relief gas drainage and dynamic disasters in outburst coal seams," *Natural Hazards*, vol. 66, no. 2, pp. 1221–1241, 2013.
- [24] C. Wang, X. Li, C. Xu et al., "Study on factors influencing and the critical value of the drilling cuttings weight: an index for outburst risk prediction," *Process Safety and Environmental Protection*, vol. 140, pp. 356–366, 2020.
- [25] Z. Liu, G. Si, X. Chen, Q. Wang, and S. Deng, "Key pre-processing technology and its application for cbm avo analysis," *Acta Geophysica*, vol. 65, no. 5, pp. 1069–1079, 2017.
- [26] W. Zhou, K. Gao, S. Xue, Y. Han, C.-M. Shu, and P. Huang, "Experimental study of the effects of gas adsorption on the mechanical properties of coal," *Fuel*, vol. 281, p. 281, Article ID 118745, 2020.
- [27] G. Xie, Z. Hu, and L. Wang, "The coupling effect of the coal seam gas pressure and mining stress in working face," *Journal of China Coal Society*, vol. 39, no. 6, pp. 1089–1093, 2014, [in Chinese].

Research Article

Presplit Blasting Technique in Treating Hard Overlying Strata: From Numerical Simulation to Field Practice

Baisheng Zhang ^{1,2}, Zhiping Yang,¹ Xuming Yang,³ and Shuai Zhang⁴

¹College of Mining Engineering, Taiyuan University of Technology, Taiyuan, Shanxi 030024, China

²Shanxi Province Research Centre of Green Mining Engineering Technology, Taiyuan, Shanxi 030024, China

³Xinjin Company, Huayang New Material Technology Group Co., Ltd., Yangquan, Shanxi 045000, China

⁴Department of Construction Development, Jinneng Holding Equipment Manufacturing Group, Jincheng, Shanxi 048000, China

Correspondence should be addressed to Baisheng Zhang; bszhang2021@163.com

Received 23 January 2021; Revised 28 March 2021; Accepted 22 April 2021; Published 4 May 2021

Academic Editor: Jia Lin

Copyright © 2021 Baisheng Zhang et al. This is an open access article distributed under the Creative Commons Attribution License, which permits unrestricted use, distribution, and reproduction in any medium, provided the original work is properly cited.

The potential dynamic risk of the mined underground space with hard overlying strata is one of the main concerns for coal operators. This paper presents a comprehensive study on treating the hard overlying strata upon the coal seam through the presplit blasting technique. The properties of the overlying strata were firstly investigated and evaluated via the laboratory tests and theoretical analysis. With the consideration of the geological and mining condition of the research area, the critical parameters of the presplit blasting technique (e.g., unsaturation coefficient, borehole spacing, and the slit width) were consequently determined via the numerical simulation with the application of LS-DYNA. Then, the field practice in accordance with the determined parameters was carried out in Yuwu coal mine. The effectiveness of the presplit blasting technique was well verified when the microstructures of the surrounding rock were investigated. The success presented in this paper does not only demonstrate the feasibility of using the presplit blasting technique in treating the hard strata of underground mines but also provide a guideline in determining the critical parameters by the numerical simulation and theoretical analysis from the design aspect.

1. Introduction

It has been well noted that the hard overlying strata, which are also termed the hard roof upon the coal seams, are generally defined as the key strata by strata controlling engineers [1–4]. Different from other strata around the coal seam, the hard overlying strata generally consist of one or more layers of thick and strong strata (e.g., limestone or sandstone). The hard overlying strata will be hung for a long time rather than immediately be crushed and collapsed with the excavation process. During the past decades, a large amount of reported rock burst and coal and gas outburst accidents are attributed to the existence of these exposed and hung hard overlying strata after the extraction of coal resource [5–7]. The main reason for these unexpected dynamic accidents is that the concentrated stress and accumulated energy released within a very short time, once the hung roof

cannot sustain its integrity [8]. The dynamic accidents associated with the large deformation of surrounding rock and the severe damages of support structures even the injuries to miners have attracted much attention either from the academic researchers or the on-site managers [9, 10]. In addition, the sudden roof falls will result in the accumulation of gas and CO emission, leading to some other potential risks for underground coal operators [8]. How to effectively control or treat the hard overlying strata therefore becomes an urgent issue to be considered.

There are numerous underground coal mines facing the problematic issues in terms of the management of the hard overlying strata and the related dynamic accidents. From the design aspect, pretreating the hard overlying strata to weaken its strength and reduce the hung length is believed to be one of the most effective methods [11, 12]. Different pretreating techniques have been proposed and put into

practical applications to eliminate or prevent associated dynamic accidents caused by the exposed hard overlying strata. Among them, the presplit blasting technique (see Figure 1) and the hydraulic-fracturing technique are believed to be two most popular methods for weakening the hard overlying strata [8, 12–15].

The main aim of either the hydraulic-fracturing technique or the presplit blasting technique in treating the hard overlying strata is to generate a series of manmade cracks or fractures [16–18]. In practice, it is not very easy to maintain the accurate application of hydraulic fractures/cracks and therefore the effect of which will be somehow affected. Compared with the hydraulic-fracturing technique, the presplit blasting technique in treating the hard overlying strata obtains its comparative advantages including (1) ease of logistics, the requested equipment is with acceptable configurations and it is thus very suitable to be used in the narrow space in underground, when it is compared with the hydraulic-fracturing technique [8]; (2) cost effectiveness; and (3) the universal feasibility, which can be used to pretreat different types of hard overlying strata [8, 12]. Most importantly, the presplit blasting technique is believed to be the controllable method as verified from different practical applications in variable coal mines.

Currently, the application of the presplit blasting technique in weakening the hard overlying strata has been widely accepted, from which the critical parameters including the layout and depth of the blast holes, the usage of cartridge, and the design of associated support system are well recognized. The numerical modelling method has also been adopted to determine the final design of the presplit blasting technique. Different computing programmes (e.g., ABAQUS, ANSYS, etc.) have shown their superior advantages in numerical simulation of the presplit blasting technique [19–21], based on which the preliminary design can be proposed with some assumptions. Note that the surrounding rock is heterogeneous in nature; the results obtained from the finite element numerical simulation should be used together with the field investigation before the final design.

Previous research on the presplit blasting technique has provided the meaningful guideline for further applications of pretreating hard overlying strata. However, there are still some research gaps that should be investigated: (1) the comprehensive study on the presplit technique in different types of the roadway (e.g., large-scale cross section) is still requested; (2) the in-depth evaluation of the preblasting technique, from the initial proposal to the final design, should also be further conducted.

Against this background, the comprehensive research with the combined numerical simulation and field test was conducted on the representative coal mine operated by Luan Coal Ltd., China. Different from previous research, the effectiveness of the large-scale cross section cut-through of the underground mine is investigated. This paper starts with the concise introduction of the geological and mining conditions of the selected coal mine, followed by the numerical modelling covering the large range of parametric studies. This paper ends up with the case study with the application of the critical parameters obtained from the comprehensive

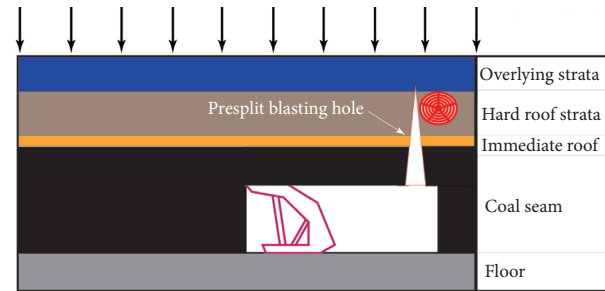


FIGURE 1: The sketch of the presplit blasting technique in treating the hard roof.

research. As expected, using the presplit blasting technique in weakening the hard overlying strata exhibited the superior advantages.

2. Geological and Mining Conditions

The N1202 longwall of Yuwu coal mine, located in Shanxi province China, was selected to verify the effectiveness of the presplit blasting technique in weakening the hard overlying strata. As depicted in Figure 2, the N1202 longwall is surrounded by the N1201 and N1203 longwall, the southern of which is the unmined coal seam. The width and the strike length of N1202 longwall are 295 m and 890 m, respectively. The average buried depth of investigated area ranges from 515 to 544 m. The 6.34-meter-thick coal seam numbered 3# is extracted by the top caving method with a mining depth of 3 m. The average dip angle of the coal seam is 6°. The black coal seam is in danger of explosion and outburst with a gas content of 10.05 m³/t.

Figure 3 presents the lithology of the N1202 longwall, in which there is an 8.10-meter-thick medium sandstone located upon the coal seam. According to the definition of the hard roof presented earlier, this medium sandstone can be regarded as the hard roof of N1202 longwall. Due to the existence of the hard overlying strata and the high-strength bolting system, the medium sandstone within the longwall is hung without obvious deformation observed, which is the other evidence to support the correction of the definition mentioned above.

The systematic laboratory tests were conducted to determine the mechanical properties of the surrounding rocks. These rock samples were collected through the drilling hole and then cut into the standard samples with a diameter of 50 mm and a height of 100 mm for compression tests in accordance with ASTM D7012-10 [22]. For tensile tests, the rock samples with a diameter of 50 mm and a height of 25 mm were also tested. Note that the values listed in Table 1 were all averaged from three identical specimens from each group.

It is apparent in Table 1 that the compressive strength of the overlying stratum upon the coal seam (e.g., sandy mudstone and fine sandstone) is much higher. Based on the mechanical properties of rock samples presented in Table 1 and the key strata theory proposed by Qian et al. [23], the length of the initial crushed hard roof can be then calculated by the following equation:

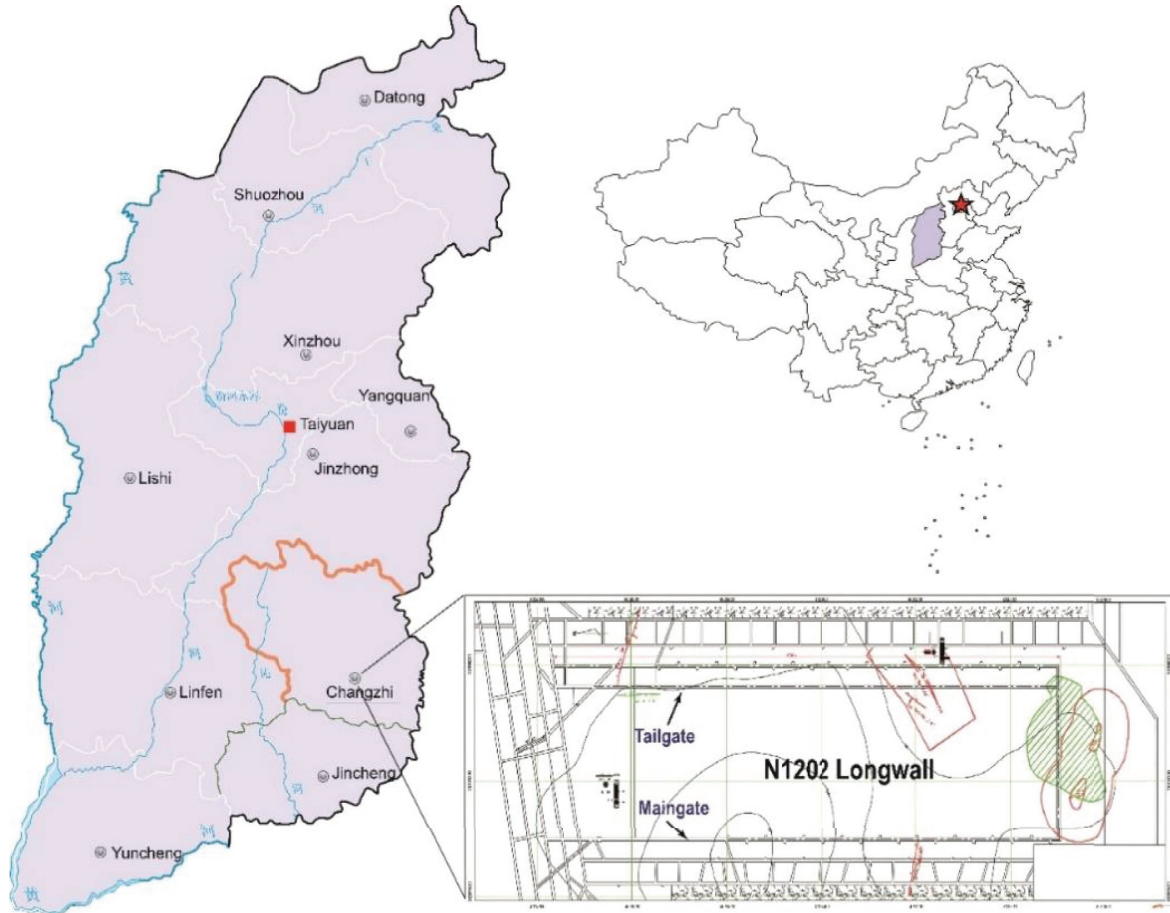


FIGURE 2: Geographical location and the plane view of the N1202 longwall.

$$L_m = \frac{L}{\sqrt{2}l_m} \sqrt{L^2 - \sqrt{L^4 - 4l_m^4}} = 48.59 \text{ m}, \quad (1)$$

in which L_m is the theoretical length of the crushed block, L is the length of the longwall, and l_m is defined as the length of the secondary key strata. The calculated length of the hung roof is about 50 m, and thus, it is urgent to take some measure to treating the hard roof from the perspective of controlling the stability of the surrounding rock.

To maintain the stability of the surrounding rock of N1202 longwall, the 8300-millimeter-length cables were installed associated with the blotting support system, the sketch of which can be seen in Figure 4. Note that the predriving roadway was excavated twice (Step 1 and Step 2); the GFRP bolts were installed in the working face. The additional support reinforcement increases the difficulty of the collapse of the hard roof, and thus, the presplit blasting technique is proposed to treat the hard roof strata by changing the integrity of the overlying strata.

3. Numerical Simulation

The embedded programme in the LS-DYNA covers the advantages of both Euler and Lagrange's algorithms, which is actually suitable to simulate the coupling of the fluid–solid coupling (e.g., the propagation process of the detonation

shock wave and the flow of the blasting gas). In this programme, the Euler algorithm is generally used to divide the internal cell grid whereas the boundary of the built model was usually achieved by the Lagrange algorithm. To prevent the occurrence of unexpected distortion of the grid, the division of the target zone should be manually adjusted. More detailed information about both the theoretical foundation and setup of the model can be found in the manual of the of LS-DYNA [24].

Figure 5 depicts the distribution of different zones of surrounding rock with the use of the presplit blasting technique. According to the propagation of the explosive energy, the surrounding rock around the blast hole can be divided into the crushed zone and the fractured zone. The explosive energy is initially generated around the surface of the blast hole and some of them will be consumed to crush the surrounding rock, leading to the generation of the crushed zone. With the shock waves gradually attenuating into stress waves, the original quasistatic pressure enlarges the initial cracks. If the peak intensity of the shock wave is larger than that of the compressive strength of the surrounding rock, the blast hole will be directly damaged and crushed. The radius of the crushed zone (i.e., R_1) can be marked from the numerical simulation if the monitored strength applied to the surrounding rock exceeds its peak strength.

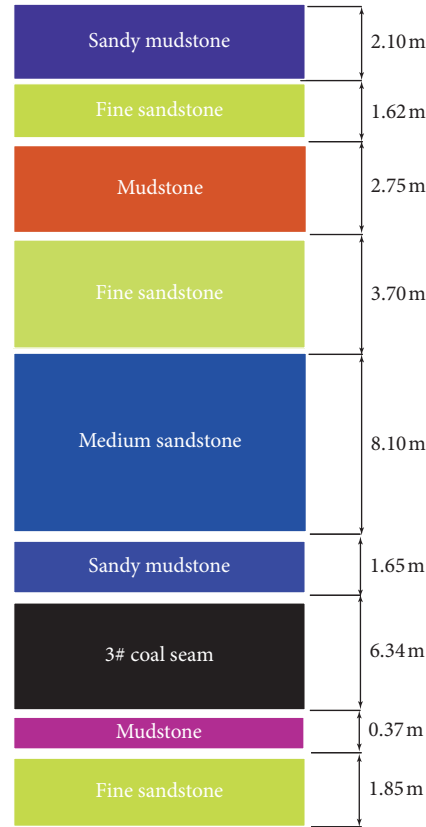


FIGURE 3: Lithology of the N1202 longwall.

TABLE 1: Key test results of rock samples.

Rock samples	UCS (MPa)	Tensile strength (MPa)	Elastic modulus (GPa)	Poisson's ratio	Friction angle
Fine sandstone	95.0	9.5	35.1	0.2	30.0
Medium sandstone	72.0	7.5	25.0	0.2	31.0
Sandy mudstone	55.0	2.5	14.0	0.2	34.0
3# coal seam	14.5	2.0	4.3	0.4	31.0
Mudstone	30.0	2.2	12.2	0.2	29.0

Apart from the crushed zone, there is a fractured zone, mainly generated attributed to the stress wave rather than the shock wave. If the maximum tensile stress obtained from the stress wave is larger than the tensile strength of the surrounding rock, the fractured zone featured with huge shear/tensile cracks will be then generated. The radius of the fractured zone (i.e., R_2) is closely related to the tensile strength of surrounding rock. With the combination of the crushed zone and the fractured zone, the integrity of the hard overlying strata will be somehow changed and the potential risks of dynamic accidents will be correspondingly prevented.

It has been well noted that the detonation shock wave will directly act on the surrounding rock around the blast borehole through the air medium associated with the reflection and transmission of the shock wave. During the propagation process, the shock wave gradually propagates and both the crushing zone and fissure zone will be formed. In this research, the following four critical parameters (e.g., the radial noncoupling coefficient, blasting borehole

spacing, group spacing, and the splitting width) were selected to investigate the effects of the presplit blasting technique.

3.1. Determination of Input Parameters. In this research, the input parameters were determined based on the geological and mining condition mentioned above. In accordance with the manual of LS-DYNA programme, the SOLID164 module was selected to generate the base model through the Euler grid. Differently, the ALE algorithm is used to establish the cartridge element. The air medium and the surrounding rock were obtained by the Lagrange algorithm. In building the numerical model, the blasting borehole was sealed with the 75-millimeter-diameter stemming. Considering the main strata above the coal seam to be the 8100-millimeter-thickness sandstone, they are selected to be the basic strata for the parametric studies presented in the following sections. Correspondingly, the mechanical properties of sandstone listed in Table 1 were adopted for numerical simulation.

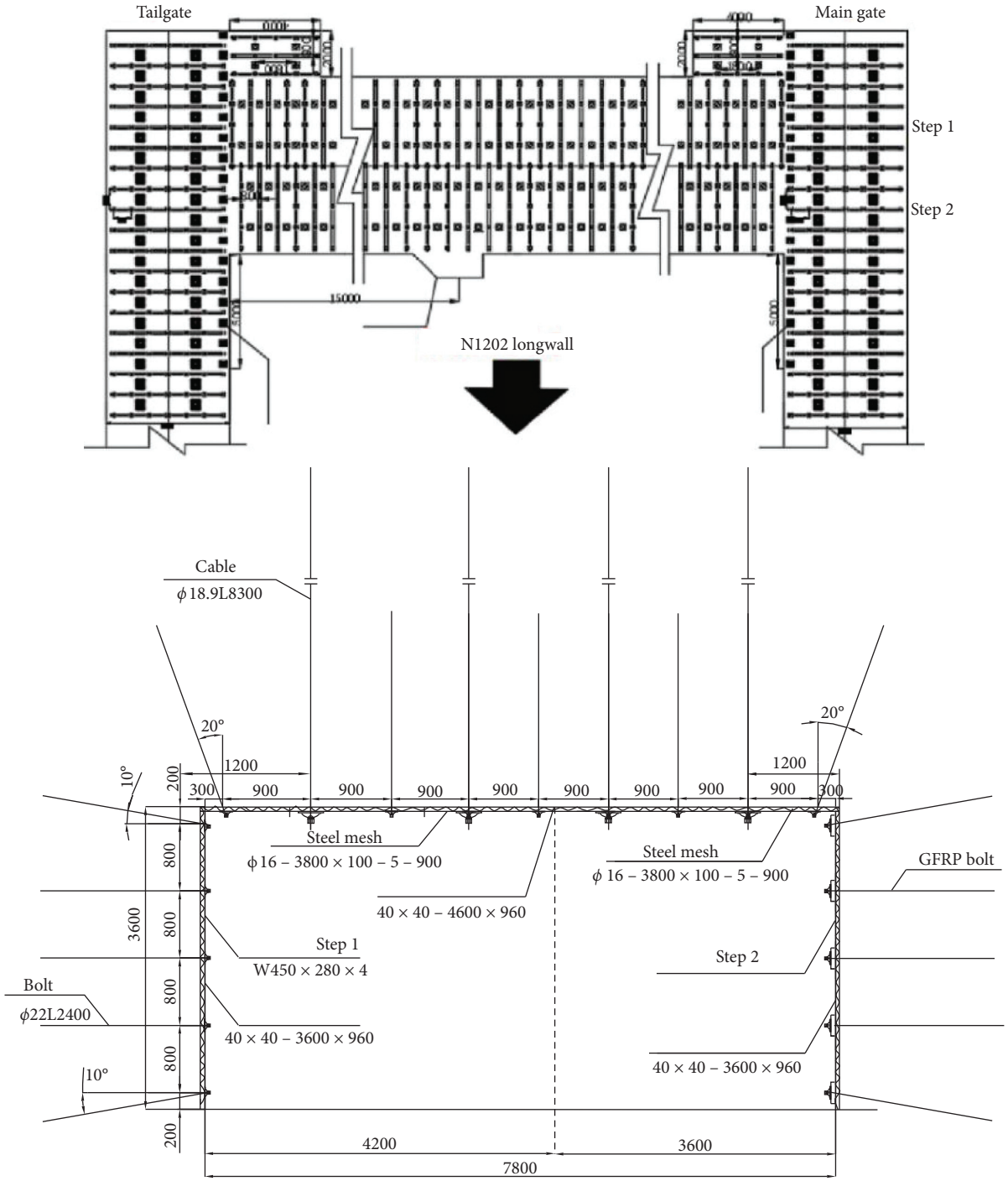


FIGURE 4: The cross section of the supported predriving roadway in the N1202 longwall.

The MAT-HIGH-EXPLOSIVE-BURN module was adopted to rebuild the cartridge element. The following equation represents the relationship between the shock stress (P) applied to the surrounding rock and the relative volume (V) [24]:

$$P = A1 - \frac{\omega}{R_1 V} e^{-R_1 V} + B \left(1 - \frac{\omega}{R_2 V} \right) e^{-R_2 V} + \frac{\omega E_0}{V}, \quad (2)$$

in which $A = 78.1$ GPa, $B = 0.552$ GPa, $R_1 = 4.02$, $R_2 = 0.91$, $\omega = 1.4$, and $E_0 = 51$ GPa.

The inherent element of “NULL” is adopted to generate the air element when the uncoupling blasting is considered.

$$P = c_0 + c_1 \mu + c_2 \mu + c_3 \mu + (c_4 + c_5 \mu + c_6 \mu) E_0, \quad (3)$$

in which $c_0 = 0.1$, $c_1 = c_2 = c_3 = c_6 = 0$, $c_4 = c_5 = 0.4$, and $E_0 = 250$ kJ.

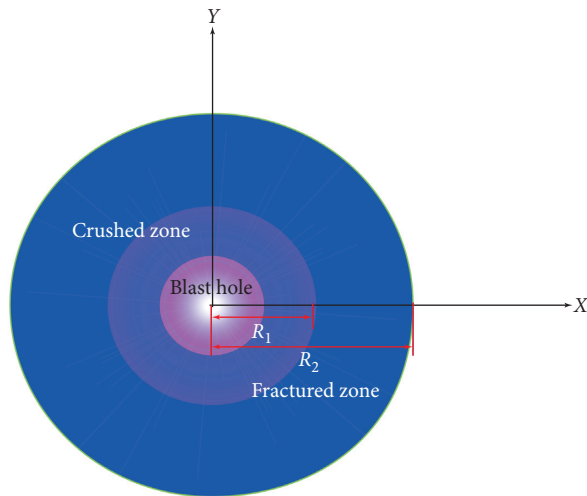


FIGURE 5: Classification of the crushed and fractured zones around the blast borehole.

The stemming was used to plug the blast borehole in the N1202 working face of Yuwu coal mine, which is simulated by the inherent MAT-SOIL-AND-FOAM element. With the consideration of conventional experience in underground blasting, the 4000-millimeter-length stemming is used in this research.

3.2. Effect of Noncoupling Coefficient. The value of the noncoupling coefficient is generally smaller than 2, and thus the following values (1.15, 1.25, 1.5, and 1.75) were adopted to investigate the effect of the noncoupling coefficient on the behaviour of the damaged surrounding rock. To obtain an in-depth understanding of the transmission of the shock wave and determine the radius of the crushed zone and fractured zone, the centre point of the blasting borehole is fixed as the reference point and the other five monitoring points apart from the reference point are nonuniformly distributed in accordance with the layout shown in Figure 6.

When the noncoupling coefficient is equal to 1, the distribution of the von Mises stress at different processes is presented in Figure 7. It is apparent that the shock wave decreased with the time and the stress applied to the surrounding rock nearby the blasting borehole experiences consequently a decrease. As can be seen from Figure 7, the effect of shock wave applied to the surrounding rock is not obvious when $T = 3.6$ ms. It is thus believed that the generation of the crushed and fractured zone is within 2.3 ms.

Figure 8 presents the monitored shock wave pressure at different times, in which the pressure is simultaneously recorded by the programme itself. It is obvious that the peak pressure at point A is larger than 320 MPa corresponding to the time equal to 0.3 ms, indicating that the crushed zone was generated within this time. From then on, the shock wave acted on the surrounding rock experiences a sharp decrease and the value of which tends to be zero when $T = 2.3$ ms.

To enhance the effects of presplit blasting, it is suggested to increase the effective time of the stress wave and the transmission of blasting air rather than the shock wave. If so, the radius of the crushed zone will be decreased and the fractured zone will be enlarged. It can be seen in Figure 9 that the maximum stress at point A is 320 MPa and the peak strength monitored at point B is 60 MPa at 0.4 ms. With the consideration of the mechanical properties of the surrounding rock listed in Table 1, it is supposed that the radii of the crushed zone and fractured zone are 1 m and 3.5 m, respectively. The generation of these fractured zones is within 2.3–4.0 ms, which is not good enough in respect of increasing the diameter of the fractured zone.

In the following section, the effects of noncoupling coefficient are investigated through the comparison of the numerical results. In these cases, the shock wave will be directly applied to the air layer, which is used to separate the cartridge rolls, rather than the surrounding rock. Because the air layer will absorb somewhat energy, the radius of the crushing zone will be correspondingly reduced and the effected zone of the fractured zone will be therefore increased, which can be seen in Figure 10.

Figure 11 presents the effective stress obtained from different monitoring points with different K values. When the value of K is equal to 1.15, the peak stresses obtained from different monitoring points (e.g., A, B, and C) are 140 MPa at 0.43 ms, 64 MPa at 0.9 ms, and 29 MPa at 1.9 ms. When it is compared with the coupling coefficient ($K = 1$), the reach of the shock wave on the surrounding rock has been significantly postponed. It can also be found that the stress obtained from point A experiences a decline, whereas the monitored stress at point C is larger than that when $K = 1$, indicating that the energy dissipation of the shock wave in the crushing zone is significantly reduced. As a result, much more energy will be used to increase the crack expansion, resulting in the increase of the radius of the fractured zone.

Given the dynamic compressive strength of surrounding rock listed in Table 1, the estimated diameter of the crushed zone is still smaller than 1 m, suggesting that the effect on the crushed zone is not obviously affected when the non-decomposition coefficient increased to 1.15. With the consideration of the monitored tensile stresses are 9 MPa at point C and 10 MPa at point D, the radius of the fractured zone is estimated to be around 3.5–4 m. The other notable observation is that the action time of the shock wave on surrounding rock is among 3–6 ms, which is much larger than that when $K = 1$.

It can be seen from Figure 11 that there is still a very high effective strength nearby the blasting borehole when $K = 1.25$. The positive pressure action time for the formation of the fractured zone is much longer in this case. Correspondingly, the minor cracks are further expanded and the radius of the fractured zone is enlarged. With the increase of the K value, the stress wave attenuates greatly at 3.5 ms. It can also be found that the effective stresses with the K value of 1.5 at different monitoring points are obviously smaller than their counterparts with the K value of 1.15 and 1.25, respectively.

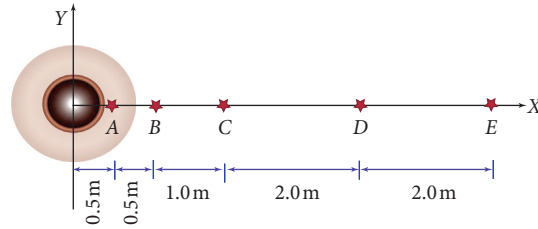


FIGURE 6: The schematic of monitoring points apart from the centre of the blast borehole.

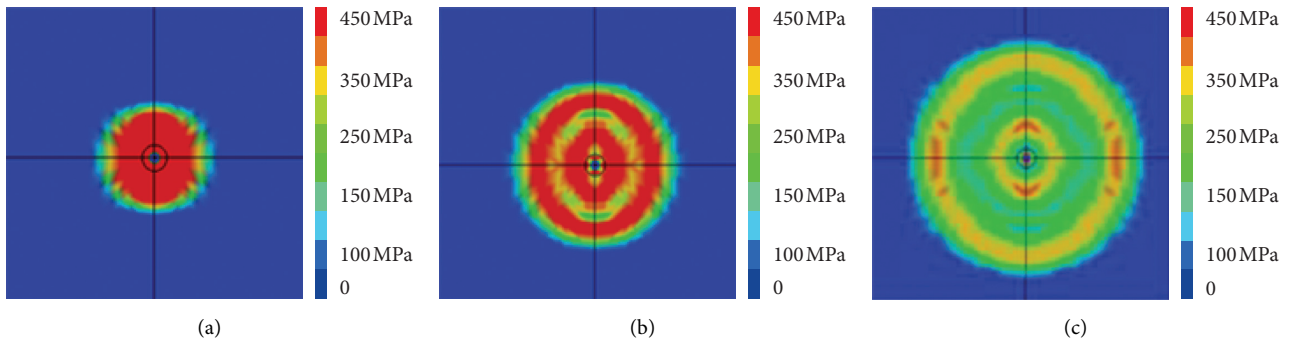


FIGURE 7: The evolution of the effective stress in the surrounding rock at different times. (a) $T=1.1$ ms. (b) $T=2.3$ ms. (c) $T=3.6$ ms.

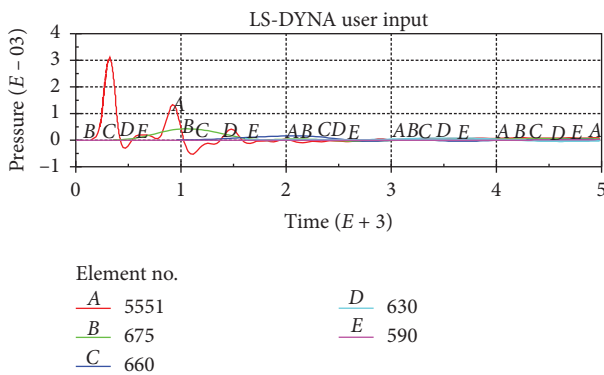


FIGURE 8: The effective stress obtained from different monitoring points.

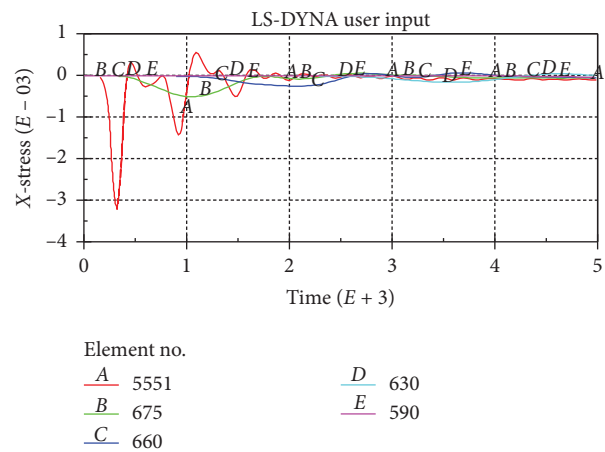


FIGURE 9: The stress-time curve for radial coupled charge.

When the value of K increases to 1.5, the peak stress at point A is 93.5 MPa at 0.45 ms, which is larger than that of the peak strength of surrounding rock. The monitored peak stress at point B is 46.5 MPa when $T=0.9$ ms, the value of which is larger than that of the mudstone and sandy mudstone. Even though, this stress is not enough to crush the sandstone and can only generate somewhat fractures and cracks. The declined peak stresses at points A and B are the direct evidence to support the assumption that the shock wave mainly works on the fractured zone with the increased radius. When the tensile stresses obtained from points C and D are all higher when they are compared with their counterparts with smaller K values, the increased tensile stress is actually suitable to generate much more cracks around the blasting borehole. As depicted in Figure 10, the radius of the

fractured zone is beyond 3.5 m, which is larger than that with other K values.

With the continuous increase of the K value, much more cracks and fractures may be generated. As illustrated in Figures 10-11, the radius of the crushed zone is too small when $K=1.75$. In this case, the limited numbers of initial cracks around the crushed zone cannot guarantee the requested distribution of the fractured zone. Although the shock wave and the explosion gas will work together to expand these cracks, they can only increase the length of these separated cracks, mainly attributed to the generated crushed zone with smaller radius (i.e., 0.4 m). According to the above analysis and discussions, the optimised K value is

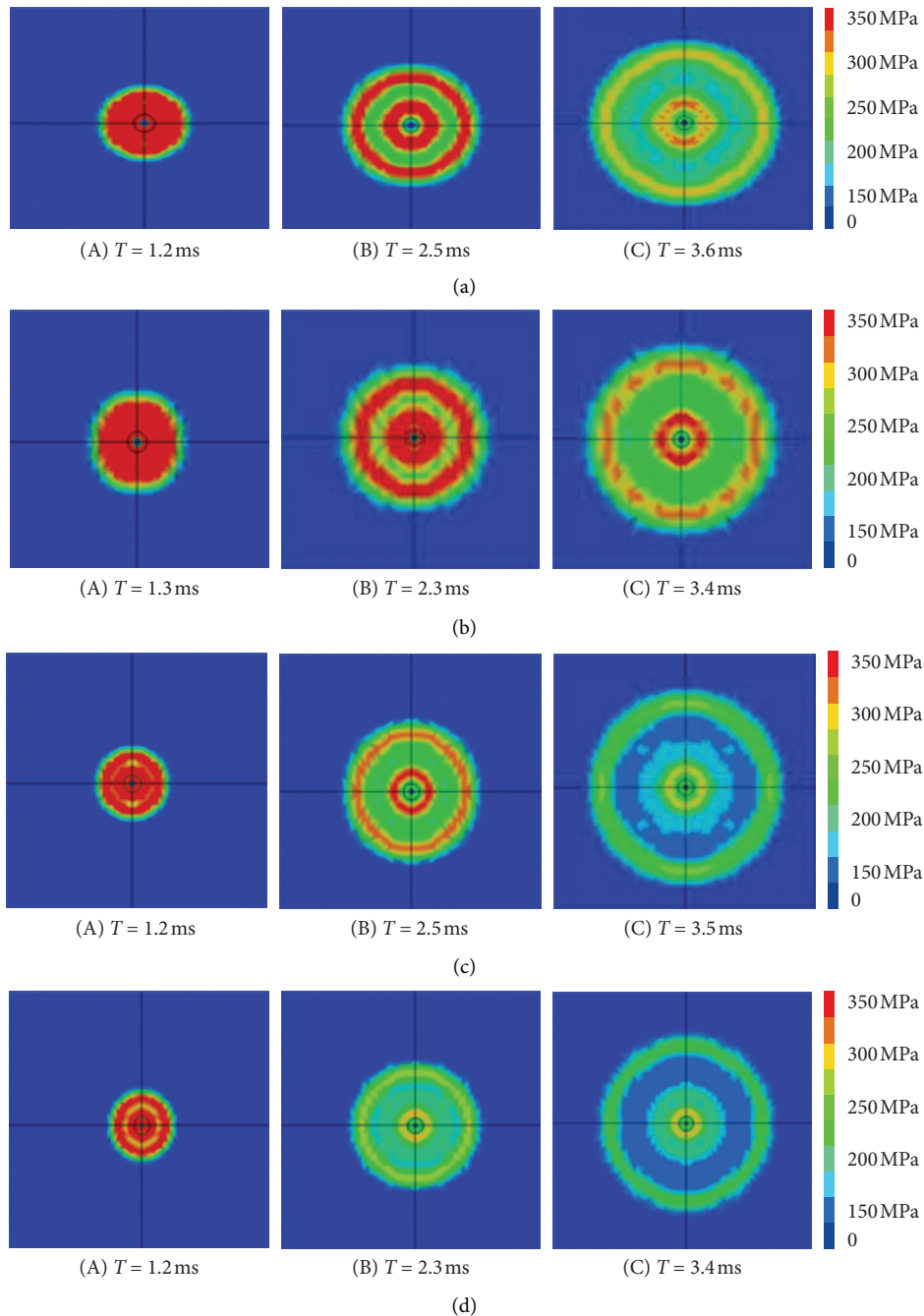


FIGURE 10: The evolution of the effective stress in the surrounding rock at different times. (a) $K = 1.15$. (b) $K = 1.25$. (c) $K = 1.5$. (d) $K = 1.75$.

1.5 from the numerical simulation with the simple assumption as stated earlier.

3.3. The Effect of the Borehole Spacing in the Same Group.

The above analysis of the single blasting borehole can help to deepen the understanding of the presplit blasting technique. However, the blast boreholes are either generally detonated in the group or some multiple blast boreholes are detonated together in practical applications. In this section, it is simply assumed that there are three blasting boreholes in the same

group; the numerical simulation was thus conducted to investigate the effect of different borehole spacing. With the consideration of the geological and mining conditions mentioned earlier, three typical borehole spacing values (e.g., 3 m, 6 m, and 9 m) were inputted. Different monitoring points were set up along the X- and Y-axes with the central point in the middle of the blasting borehole as illustrated in Figure 12.

It is expected to obtain the proper blasting borehole spacing based on the systematic of the monitored stresses from two different axes and the stress distribution

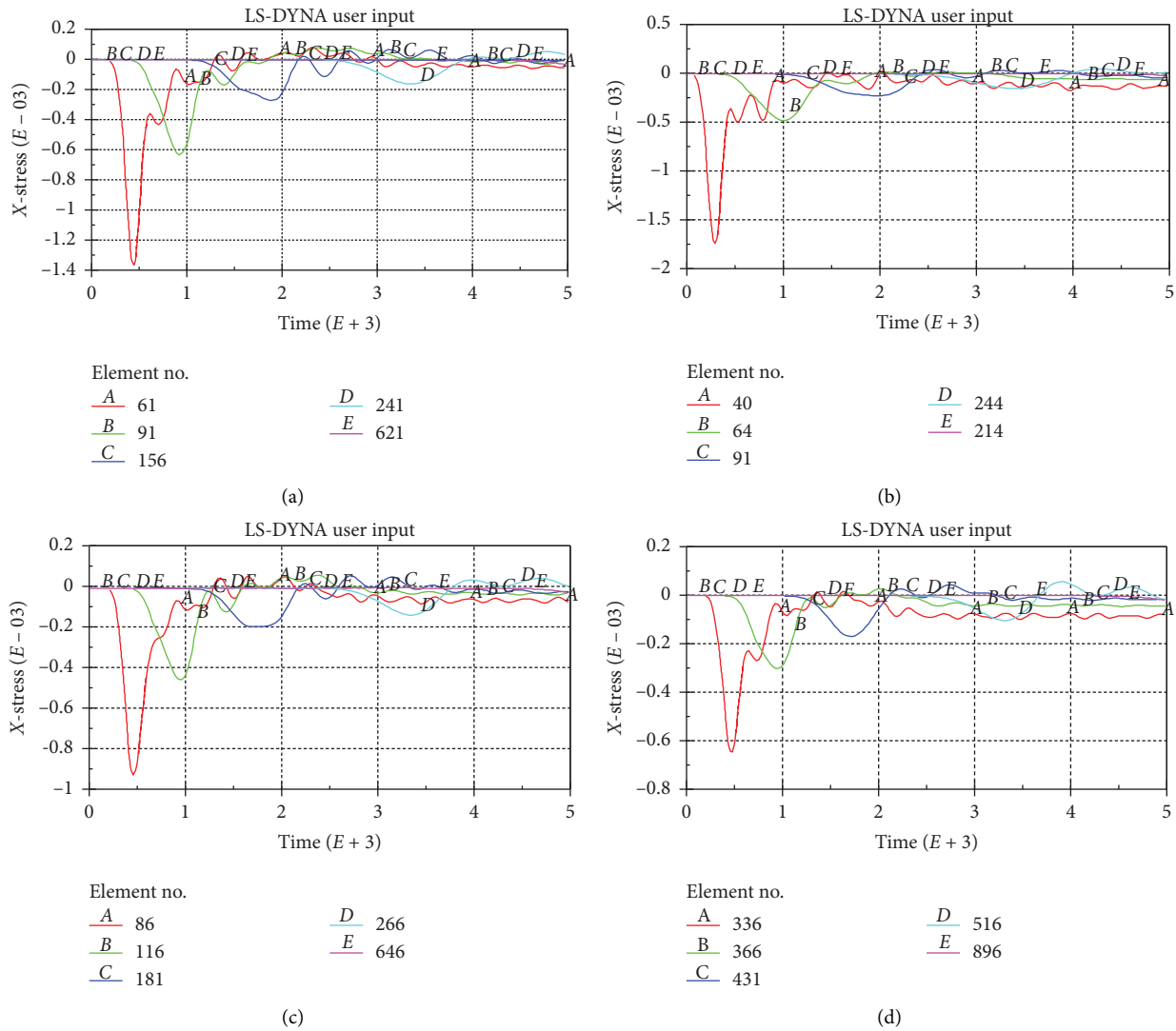


FIGURE 11: The effective stress obtained from different monitoring points with different K values. (a) $K = 1.15$. (b) $K = 1.25$. (c) $K = 1.5$. (d) $K = 1.75$.

characteristics. According to the monitoring results in two directions as shown in Figure 13, the occurrence of the stress increase will take place in some areas due to the superimposition of stress waves in the process of propagating in the rock formation. At these superimposition areas, the surrounding rock will be crushed and the radius of the fractured zone will be a little bit smaller.

Figures 14 and 15 present the effective pressure recorded at different monitoring points from different axis, respectively. When the value of the borehole spacing ranges from 3 m to 8 m, the radius of the signal fractured zone is 4 m and the sum radius of the crushed zone is 3 m, which can ensure the formation of the expected fractured zone between two blast boreholes in the same group. The suitable spacing between each borehole should be therefore in the range of 3–8 m. However, with the increase of the spacing between two blast boreholes, namely, $L > 8$ m, it becomes difficult to obtain enough cracks and fractures and the distance between each blast borehole should be within 3–6 m.

3.4. The Effect of the Borehole Spacing in Different Groups.

In practice, the blasting boreholes are drilled in rows and the fractures attributed to the blasting may be connected. In this section, the effects of the space between different blasting boreholes are investigated. In accordance with the geological and mining conditions, two typical spaces ($L_1 = 6$ m and $L_2 = 8$ m) were selected and compared. To evaluate the effect of the borehole spacing, six points were marked to record the maximum stress. More detailed information about the layout of the monitoring points can be found in Figure 16.

Figure 17 presents the monitored stress distributed around the Y-direction with different borehole spacing and Figures 18-19 present the distribution of the stress around the blasting boreholes. According to the results presented above, the peak tensile stress intensity of each tracking unit is weaker than when the group space is 6 m, and the peak intensity time is also delayed. If the group space is equal to 6 m, the peak compressive stresses obtained from points A, B, and C are 16 MPa at 2.6 ms, 17 MPa at 2.7 ms, and 19 MPa

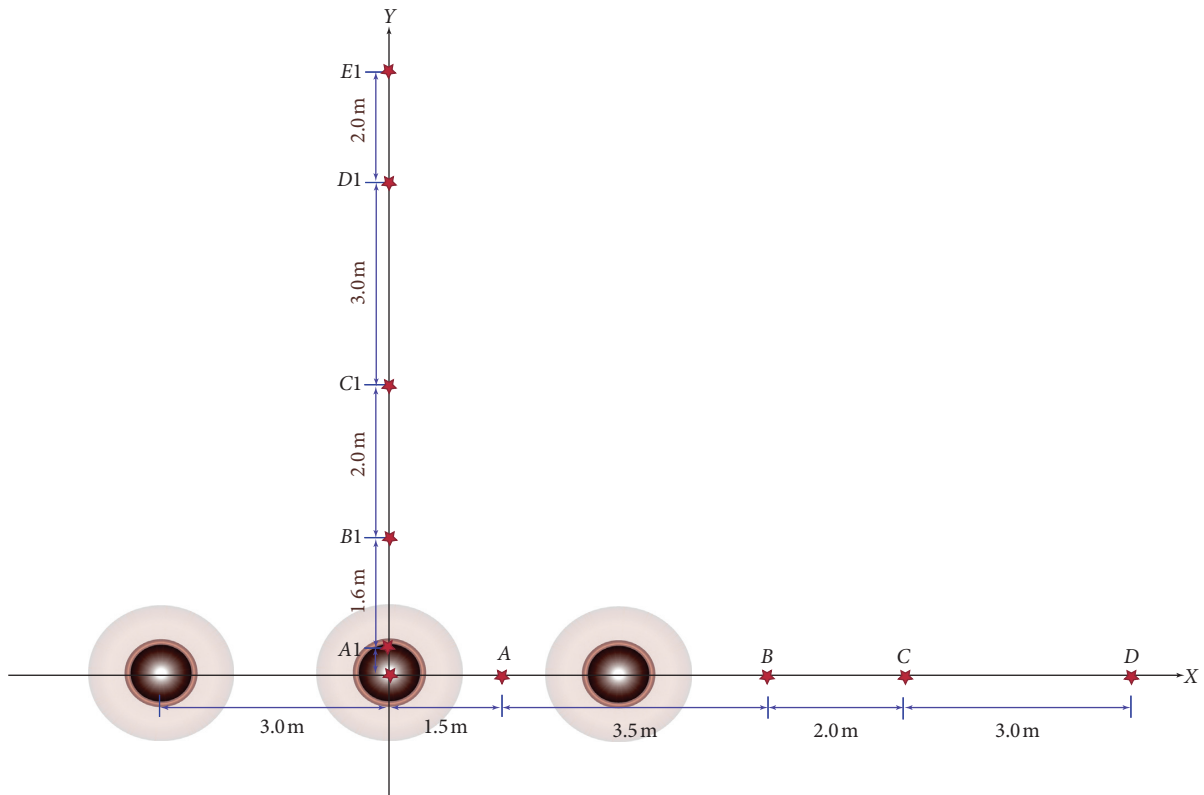


FIGURE 12: Layout of monitoring points.

at 3.5 ms, respectively. The cross section of the crushed zone along the Y-direction is about 4 m, which can cover the width of the working face. When the borehole spacing increased to 8 m, the crack expansion radius is between 2 and 4 m, which is significantly lower than that with a group spacing of 6 m.

It can be comprehensively known that in the actual engineering design, the blast borehole groups at both ends of the working face, the group spacing is generally designed to be within 8 m, which can better ensure that there are partial penetration cracks at the end position, and the partial penetration cracks will continue to extend and expand in the later stage, so as to realize the cutting of the entire working face roof along the cutting hole position of the working face to ensure the presplitting effect.

3.5. The Effect of the Split Width. The split width is the other critical parameter to be considered in practice. If the split width is too large, the energy cannot be concentrated which will not obtain an effective explosive. If the split width is too small, it will be very difficult to get the expected fractures. Therefore, in this section, the 15-millimeter-width split was adopted to investigate the effect of split width with the comparison between the normal cartridge pack. The diameter of the blasting hole is 64 mm, which is in accordance with the PVC tube used in practice.

Different from the stress distribution of normal cartridge pack shown in Figure 20, it is apparent that the energy from the shock wave is concentrated around the split. In

particular, the stresses applied to the surrounding rock are much larger when $T=1$ ms and $T=1.5$ ms. The main reason for this difference is that the shock wave will firstly be applied to the surrounding rock nearby the split line which acts as a pilot line. The shock wave will be generally transferred along the split line and then make the shock wave (stress wave) and explosive gas penetrate the initial crack along the direction of the incision. Then, the cracks will be further expanded and penetrated along the line of the blast borehole. Compared with the normal cartridge pack, the existing of the split reduces the excessive dissipation of explosion energy in other directions and thus improves the effect of presplit blasting effects.

Five monitoring points apart from the central point with various distance (0.5 m, 1 m, 2 m, 4 m, and 6 m) were set up to track the peak stress of the shock wave, the results of which are presented in Figures 21 and 22. It is obvious that the peak stress at point A is about 170 MPa at 0.3 ms if there is a split, whereas the peak value of the detonation wave pressure at point A is only 130 MPa corresponding to the time of 0.4 ms. With the consideration of the distance between point A and the split line, it is believed that the detonation wave pressure around the split is much greater than that where there is no split, indicating that the existence of the split is obvious. However, the pressure at points B, C, and D apart from the split line are slightly smaller than that if there is no split constructed. This observation is mainly attributed to the wave reflection associated with the energy loss. As a result, the radius of the crushed zone is smaller than that without the split. The slit-guided high-energy jet

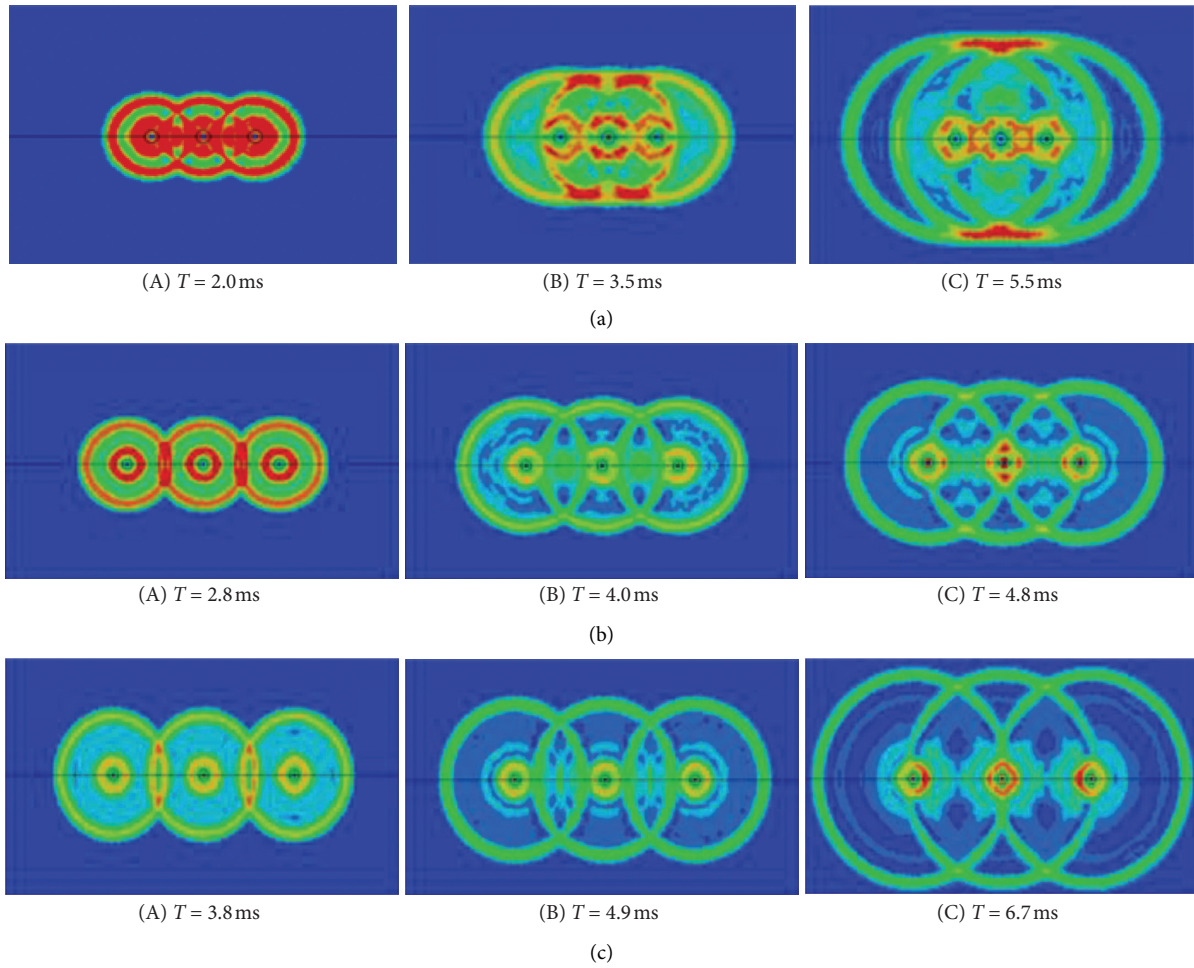


FIGURE 13: Distribution of stress with different blasting borehole spacing from the same group. (a) $L = 3.0$ m. (b) $L = 6.0$ m (c) $L = 8.0$ m.

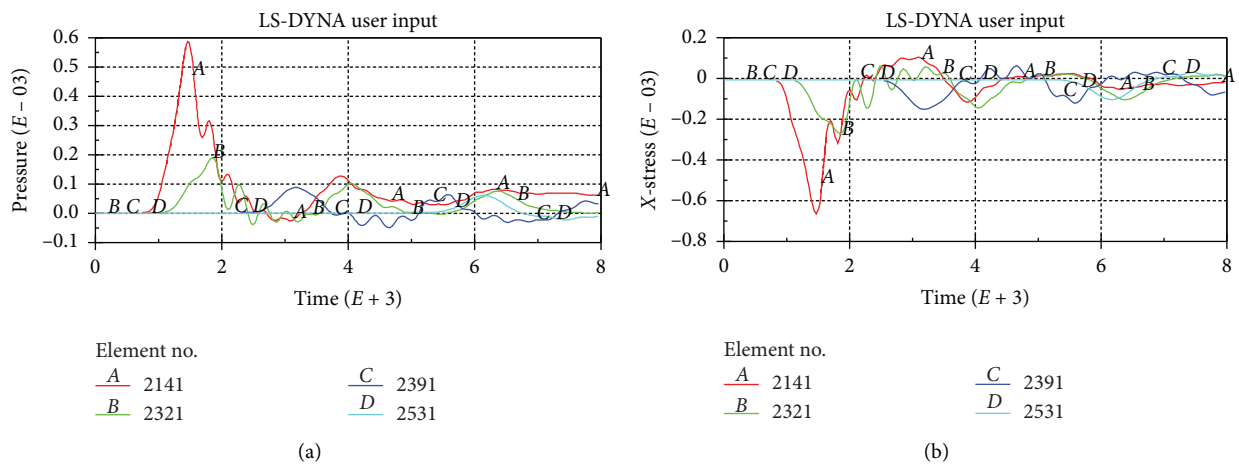


FIGURE 14: Continued.

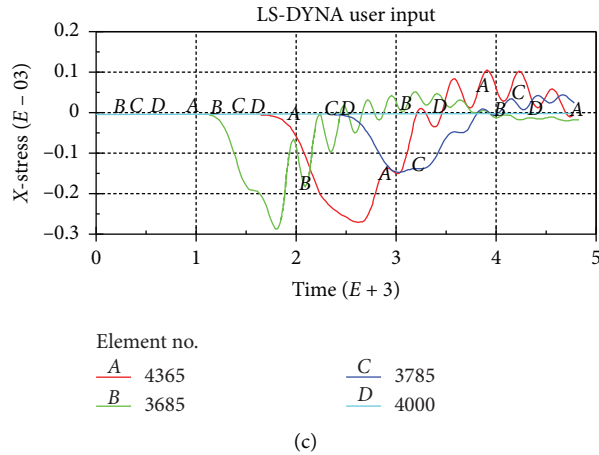


FIGURE 14: Stress at the X-axis in the blasting borehole with different values of L (a) L = 3 m. (b) L = 6 m. (c) L = 8 m.

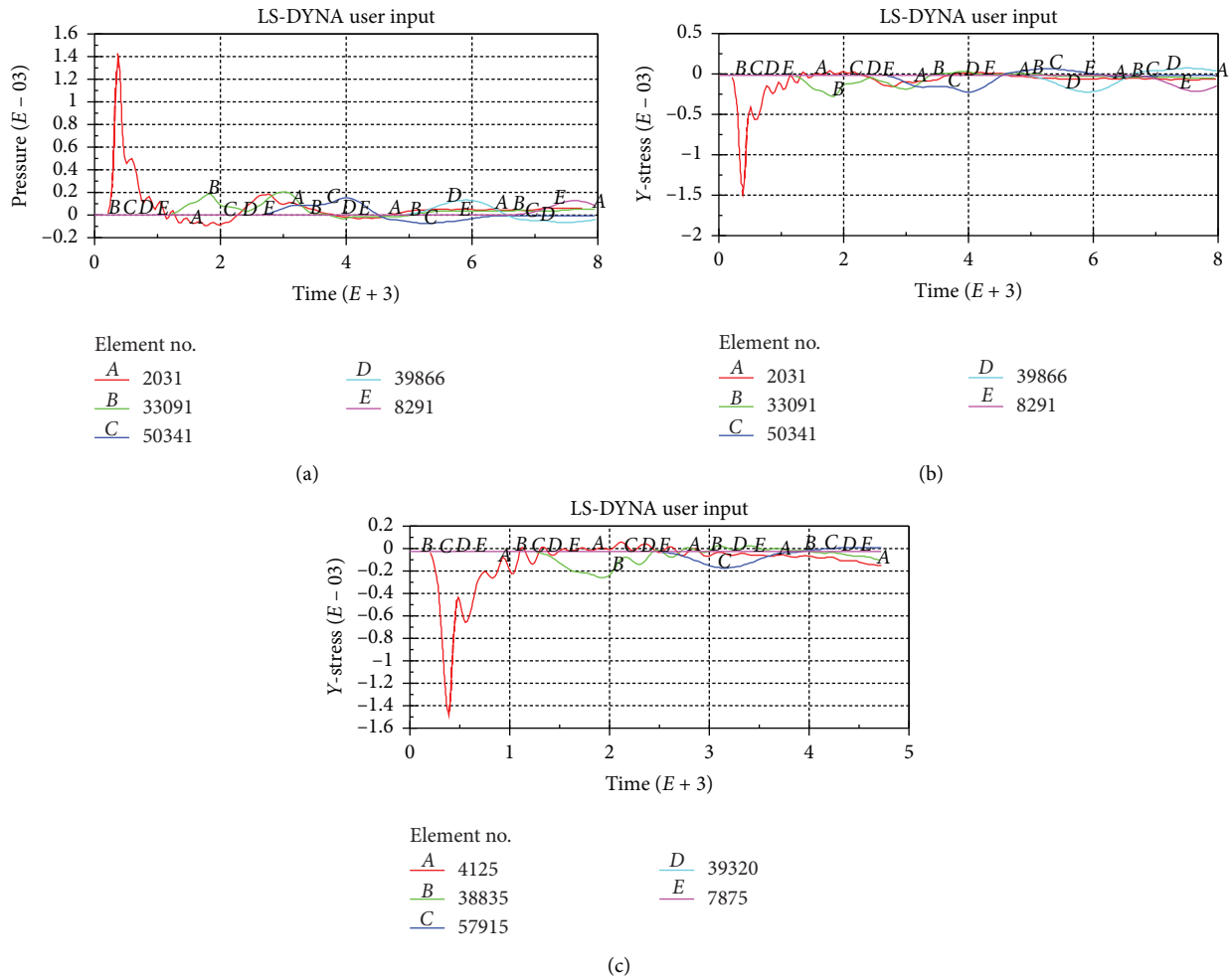


FIGURE 15: Stress at the Y-axis in the blasting borehole with different values of L (a) L = 3 m. (b) L = 6 m. (c) L = 8 m.

and explosive gas diffuse to both sides along the slit to further increase the residence time of the two in the initial fissure. In this case, more energy will work on the expansion

of the blast fissure. In general, the radius of the fissure zone is larger than that of the latter, which is conducive to the formation of through fissures along the central line of the

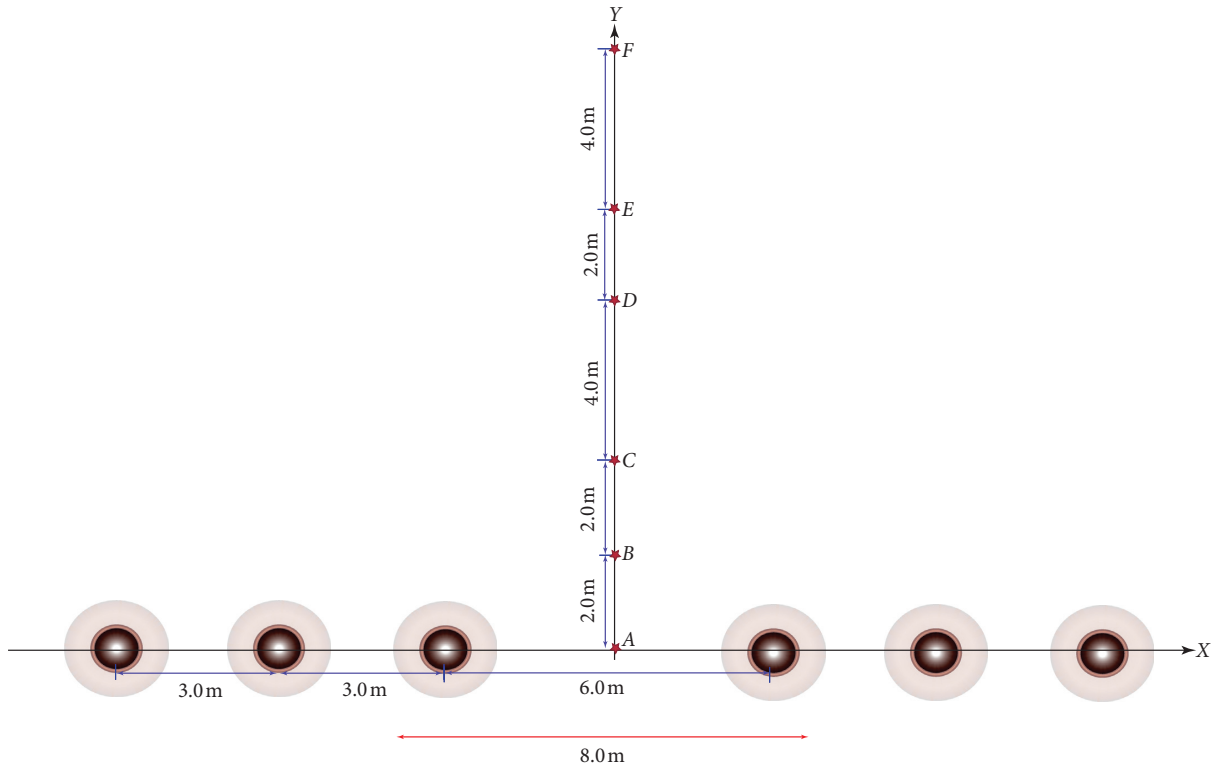


FIGURE 16: Layout of monitoring points.

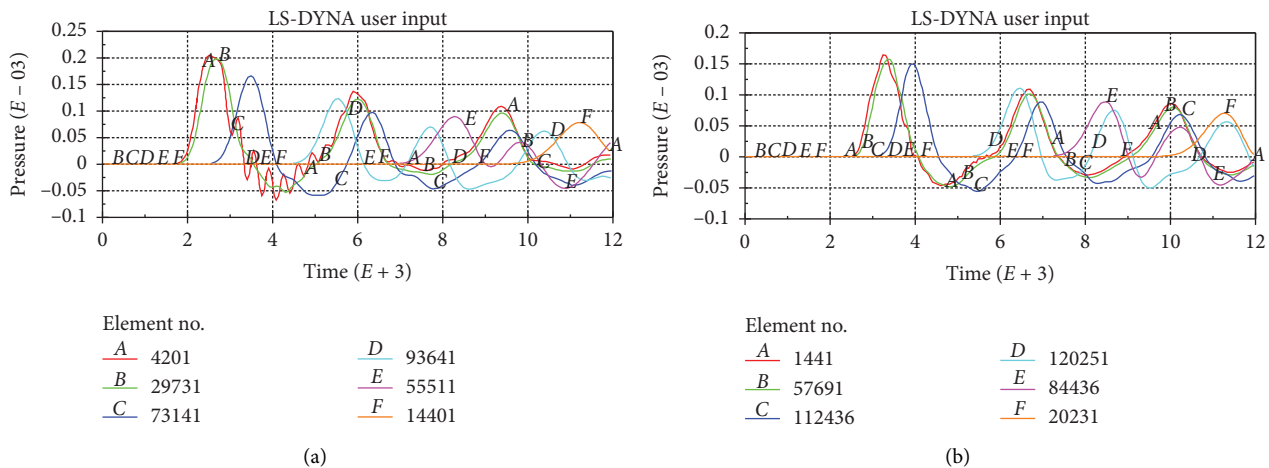


FIGURE 17: The effective stress obtained from different monitoring points with different spacing. (a) $L = 6$ m. (b) $L = 8$ m.

blast borehole to achieve the purpose of precracking the roof. According to above discussion, the 15-millimeter-width split is recommended.

4. Field Study

4.1. Overview. The layout of the blasting borehole to pretreat the hard roof of the longwall N1202 can be seen from Figure 23, in which the number is used to clarify the location

of the blasting borehole. A total of 49 blasting boreholes with the length of 15 m were drilled by the functions, among which two blasting boreholes were located at the corner of the main gate and the tailgate, respectively.

The critical parameters determined by the numerical simulation were adopted in this research to pretreat the hard roof. With the consideration of the existed fractures and cracks before the application of the presplit blasting technique, the radial noncoupling coefficient of 1.5 is applied.

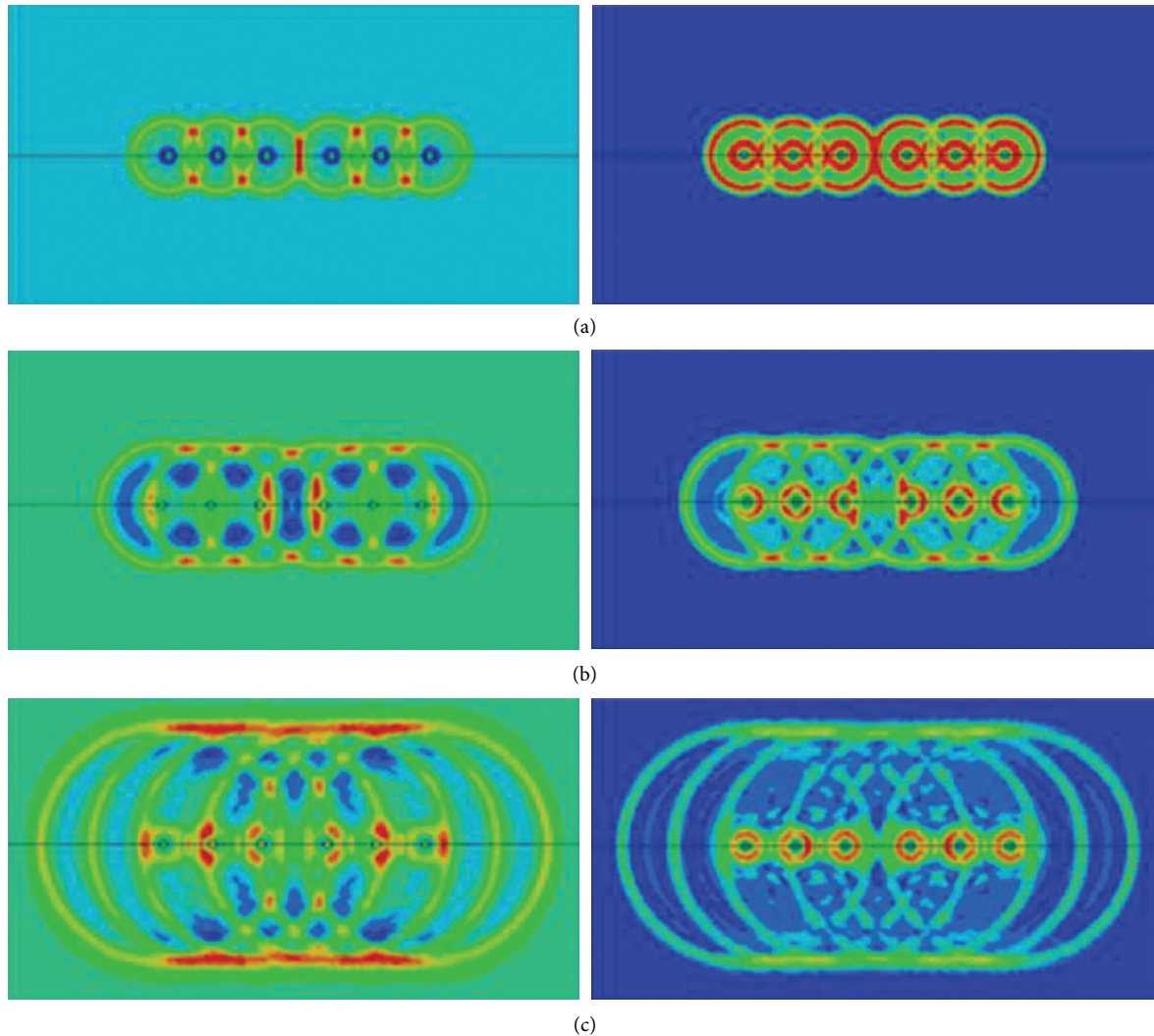


FIGURE 18: The evolution of the effective stress in the surrounding rock with the borehole spacing of 6 m at different times. (a) $T = 2.7$ ms. (b) $T = 4.6$ ms. (c) $T = 8.6$ ms.

The borehole spacing in the same group and different groups are 5 m and 6 m, respectively. The split width of 15 mm is used. In addition, two detonating cords and two detonators are designed to detonate the charge at the same time, which ensures that the charge can be detonated smoothly.

4.2. Evaluation of the Presplit Blasting Effects. To evaluate the effect of using presplit blasting technique in weakening the hard overlying strata, the breakage of the hard overlying strata and the inner structures of the surrounding rock nearby the blasting borehole were adopted in this research. The measured cracked length of the hard roof reduces to 18 m, which is acceptable for coal operators. As observed from field investigation, there was still somewhat deformation, the evidence of which is that some blasting boreholes drilled among the 130#-143#, 173#-3# hydraulic chocks were sealed due to the collapse of the top coal seam. To maintain the stability of the overlying strata, the timber chocks were installed as shown in Figure 24.

Figure 25 presents the inner structures of the blasting boreholes at different depth, from which the effect of presplit blasting technique can be further examined. It is apparent that the surrounding rock nearby the blasting borehole is crushed within the depth of 2–5 m. Most importantly, there is obvious separation between the top coal and the sandy mudstone. Starting from 3.8 m to 4.8 m, there are lots of fractures distributed along the blasting borehole. With the increase of the depth, the horizontal fractures were observed at the depth of 6–8 m, indicating the effective radius of the crushed zone is among this area. As expected, there is no crushed rock observed from the blasting borehole with the depth of 9–12 m. However, the horizontal fractures in these zones are much more obvious, which agrees well with the numerical modelling. As shown in Figure 25, the distribution of fractures is much more random and some surrounding rock experiences the crush. The main reason for this observation is probably attributed to the reflection of shock wave, which is located at the bottom of the blasting borehole.

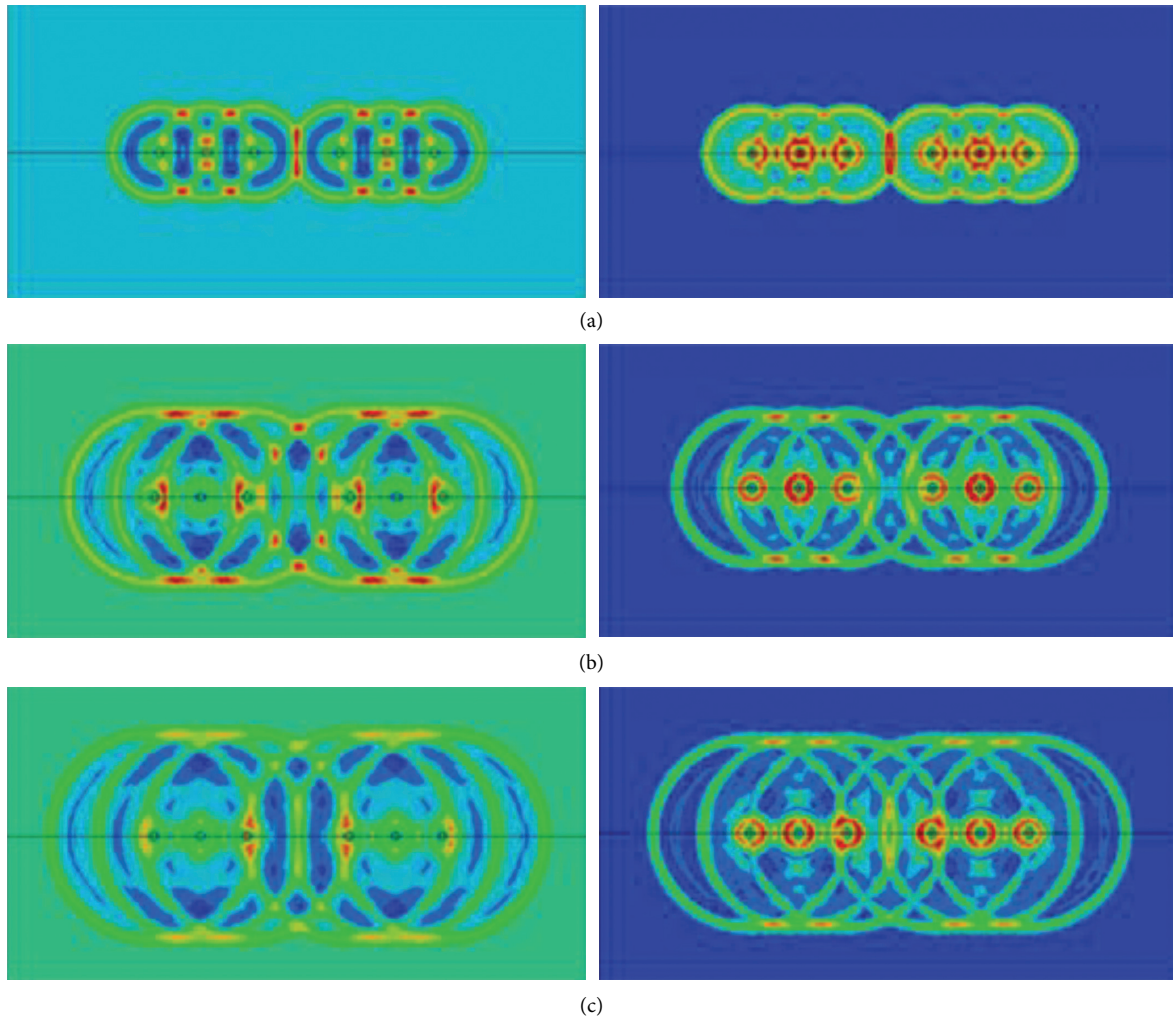


FIGURE 19: The evolution of the effective stress in the surrounding rock with the borehole spacing of 8 m at different times. (a) $T = 3.5$ ms. (b) $T = 5.5$ ms. (c) $T = 7.0$ ms.

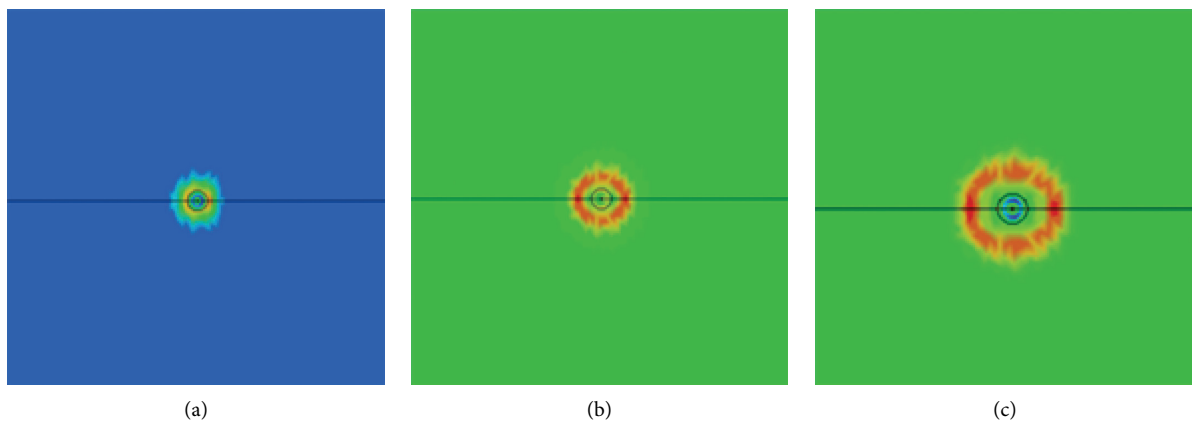


FIGURE 20: Continued.

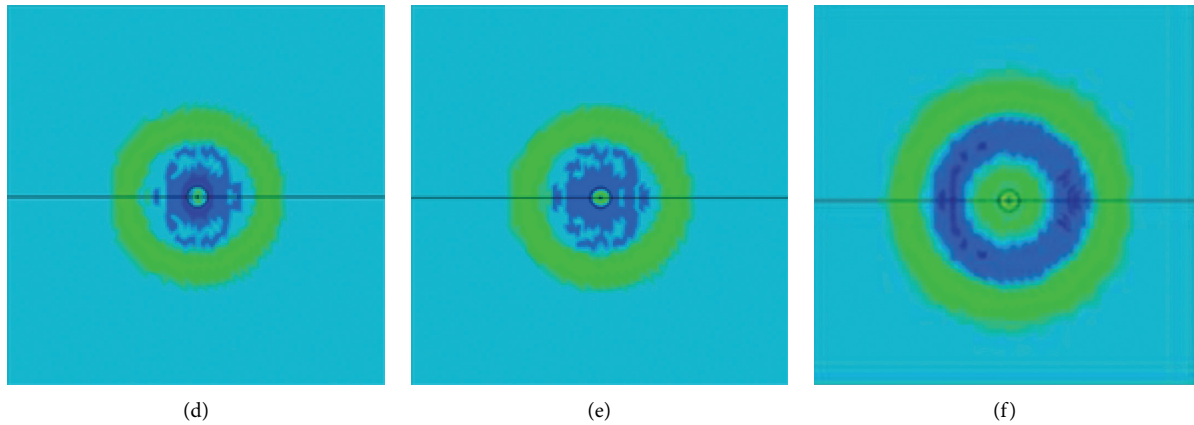


FIGURE 20: The evolution of the effective stress in the surrounding rock without split at different times. (a) $T = 0.58$ ms. (b) $T = 1.0$ ms. (c) $T = 1.42$ ms. (d) $T = 2.0$ ms. (e) $T = 2.50$ ms. (f) $T = 3.30$ ms.

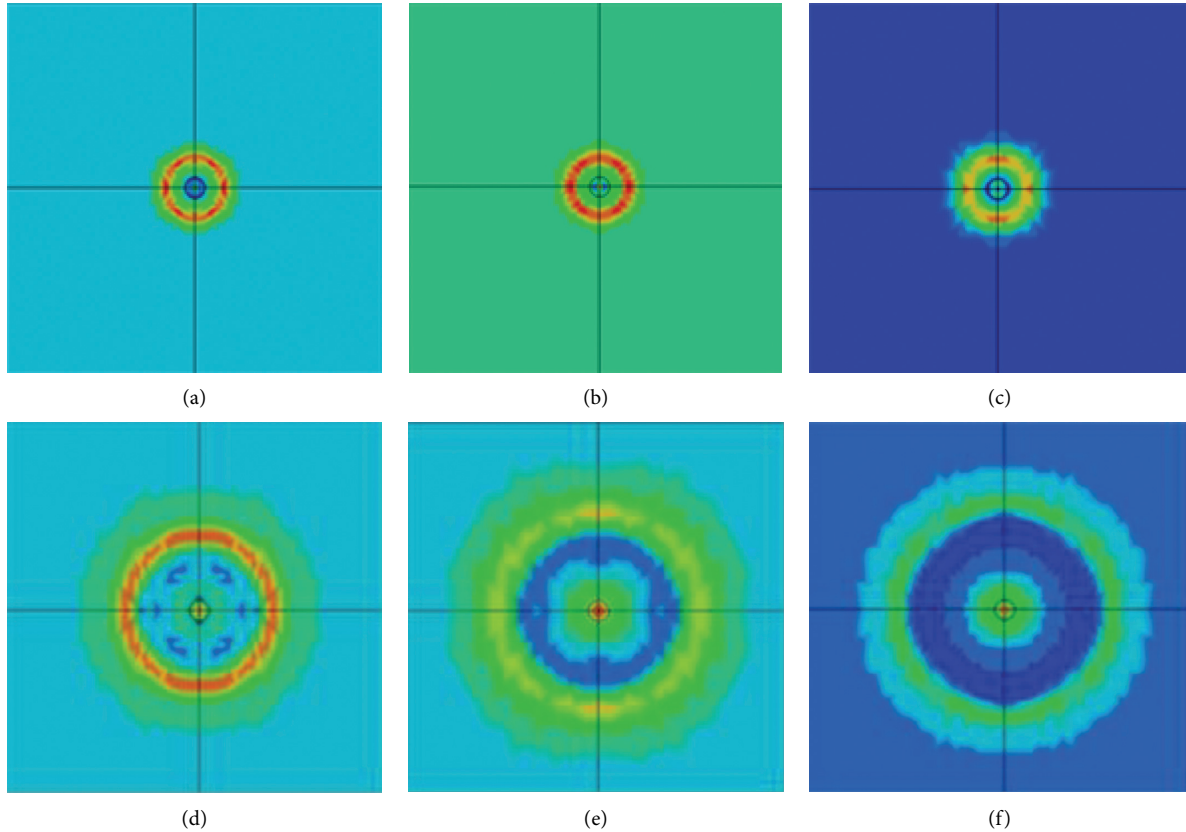


FIGURE 21: The evolution of the effective stress in the surrounding rock with a split spacing of 15 mm at different times. (a) $T = 0.60$ ms. (b) $T = 1.00$ ms. (c) $T = 1.50$ ms. (d) $T = 2.00$ ms. (e) $T = 2.51$ ms. (f) $T = 3.32$ ms.

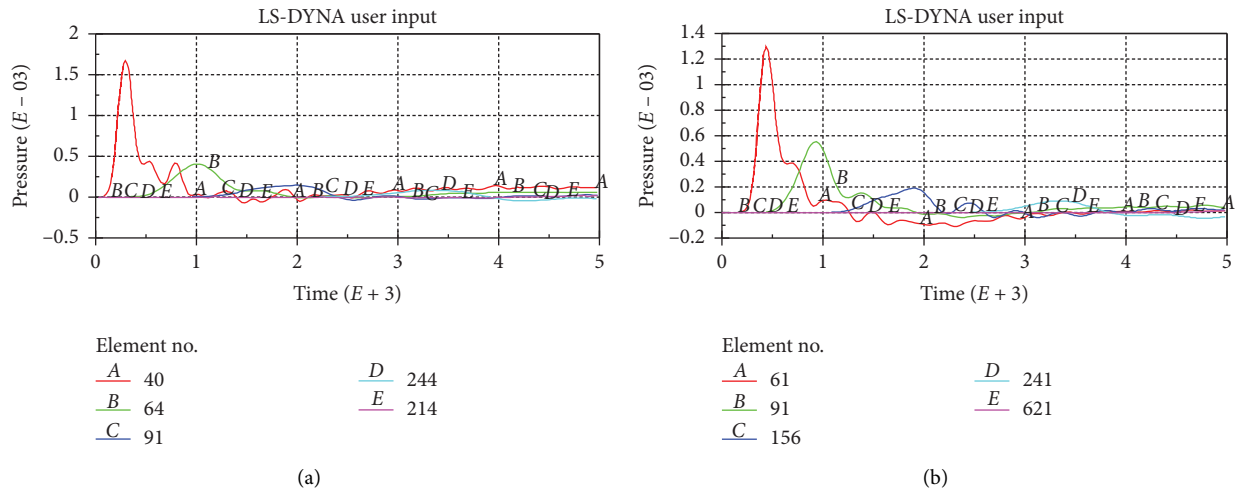


FIGURE 22: The effective stress obtained from different monitoring points with or without the presplit technique.

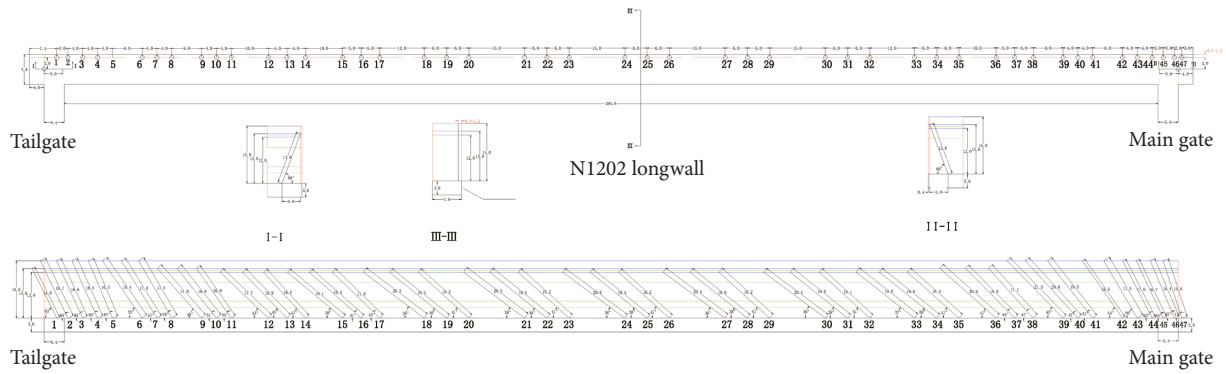


FIGURE 23: Layout of the blast boreholes in the N1202 longwall.

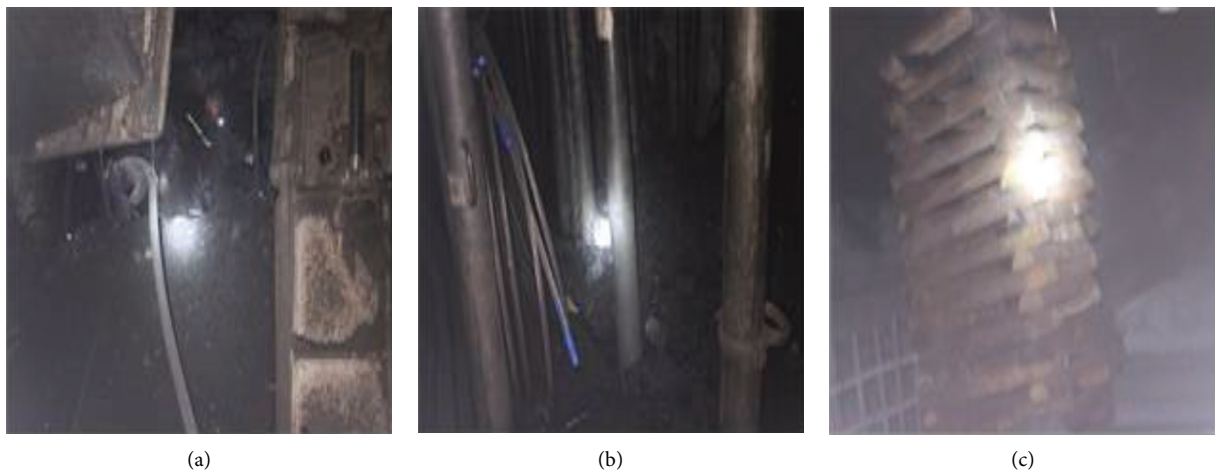


FIGURE 24: Roof deformation with the application of the presplit blasting technique. (a) Working face. (b) Main gate. (c) Tailgate.



FIGURE 25: The inner surface of the surrounding rock in the blast borehole.

5. Conclusions

The hanging of the hard overlying strata is believed to be one of the main reasons for the occurrence of the dynamic accident. This paper presents the case study of the application of presplit blasting technique in treating the pre-driving roadway through the longwall with the hard overlying strata. The following conclusions can be drawn based on the discussions in the present research:

- (1) Compared with the conventional layout of the blasting hole, the effect of the noncoupling coefficient is much obvious. With the increase of the noncoupling coefficient, the diameter of the crushed zone decreased, whereas the diameter of fractured zone experience somewhat increase.
- (2) Both the blasting borehole spacing and the split width will significantly affect the distribution of the stress and radius of the crushed zone and fracture zone. When other parameters are the same, the smaller borehole spacing and split width are highly recommended to reduce the radius of the crushed zone.
- (3) The advantages of the presplit blasting technique have been verified by the field study in weakening the large-scale pre-driving roadway with the hard overlying strata. The length of the hard roof block has been significantly decreased, which is the direct evidence to support the effectiveness of the presplit technique.

Note that the rock mass is generally regarded as a homogeneous medium in numerical calculation. However, there must be a lot of joints and fissures in practical engineering. Therefore, the critical parameters obtained from numerical simulation should be further verified by the field case study.

Data Availability

The research data used to support the findings of this study are currently under embargo while the research findings are commercialized. Requests for data, 12 months after publication of this article, will be considered by the corresponding author.

Conflicts of Interest

The authors declare that they have no conflicts of interest regarding the publication of this paper.

Acknowledgments

The authors acknowledge the financial support provided by the Key Research Programme (High-Tech) of Shanxi Province (201903D121075) and the Transformation of Scientific Technological Achievement Programme of Higher Education Institutions in Shanxi (JYT2019015).

References

- [1] P. Yiouta-Mitra and A. I. Sofianos, "Multi-jointed stratified hard rock roof analysis and design," *International Journal of Rock Mechanics and Mining Sciences*, vol. 106, 2018.
- [2] J. Hu, M. He, J. Wang, Z. Ma, Y. Wang, and X. Zhang, "Key parameters of roof cutting of gob-side entry retaining in a deep inclined thick coal seam with hard roof," *Energies*, vol. 12, no. 5, p. 934, 2019.
- [3] G. S. Esterhuizen, I. B. Tulu, D. F. Gearhart, H. Dougherty, and M. van Dyke, "Assessing support alternatives for longwall gateroads subject to changing stress," *International Journal of Mining Science and Technology*, vol. 31, 2021.
- [4] Y. L. Tan, X. S. Liu, B. Shen, J. G. Ning, and Q. H. Gu, "New approaches to testing and evaluating the impact capability of coal seam with hard roof and/or floor in coal mines," *Geomechanics and Engineering*, vol. 14, no. 4, pp. 367–376, 2018.
- [5] H. Li and H. Li, "Mechanical properties and acoustic emission characteristics of thick hard roof sandstone in Shendong coal field," *International Journal of Coal Science & Technology*, vol. 4, no. 2, pp. 147–158, 2017.
- [6] S. Zhang, Y. Li, B. Shen, X. Sun, and L. Gao, "Effective evaluation of pressure relief drilling for reducing rock bursts and its application in underground coal mines," *International Journal of Rock Mechanics and Mining Sciences*, vol. 114, 2019.
- [7] Z. Khademian and O. Ugur, "Computational framework for simulating rock burst in shear and compression," *International Journal of Rock Mechanics and Mining Sciences*, vol. 110, 2018.
- [8] J. Liu, C. Liu, Q. Yao, and G. Si, "The position of hydraulic fracturing to initiate vertical fractures in hard hanging roof for stress relief," *International Journal of Rock Mechanics and Mining Sciences*, vol. 132, 2020.
- [9] H. Kang, L. Wu, F. Gao, H. Lv, and J. Li, "Field study on the load transfer mechanics associated with longwall coal retreat mining," *International Journal of Rock Mechanics and Mining Sciences*, vol. 124, 2019.
- [10] D. Tuncay and T. Klemetti, "Investigating different methods used for approximating pillar loads in longwall coal mines," *International Journal of Mining Science and Technology*, vol. 31, 2020.
- [11] A. N. Dehghan, "An experimental investigation into the influence of pre-existing natural fracture on the behavior and length of propagating hydraulic fracture," *Engineering Fracture Mechanics*, vol. 240, 2020.
- [12] Z. Zhang, N. Zhang, H. Shimada, T. Sasaoka, and S. Wahyudi, "Optimization of hard roof structure over retained goaf-side gateroad by pre-split blasting technology," *International Journal of Rock Mechanics and Mining Sciences*, vol. 100, 2017.
- [13] Y. Shang, J. Wang, X. Li, J. Ning, and P. Qiu, "In situ investigations into mining-induced hard main roof fracture in longwall mining: a case study," *Engineering Failure Analysis*, vol. 106, 2019.
- [14] C.-P. Lu, Y. Liu, G.-J. Liu, and T.-B. Zhao, "Stress evolution caused by hard roof fracturing and associated multi-parameter precursors," *Tunnelling and Underground Space Technology*, vol. 84, 2019.
- [15] B. Huang, J. Liu, and Q. Zhang, "The reasonable breaking location of overhanging hard roof for directional hydraulic fracturing to control strong strata behaviour of gob-side entry," *International Journal of Rock Mechanics and Mining Sciences*, vol. 103, 2018.
- [16] A. Movassagh, M. Haghghi, X. Zhang, D. Kasperczyk, and M. Sayyafzadeh, "A fractal approach for surface roughness

- analysis of laboratory hydraulic fracture,” *Journal of Natural Gas Science and Engineering*, vol. 85, 2021.
- [17] Q. He, F. T. Suorineni, T. Ma, and J. Oh, “Parametric study and dimensional analysis on prescribed hydraulic fractures in cave mining,” *Tunnelling and Underground Space Technology*, vol. 78, 2018.
- [18] X. Huo, X. Shi, X. Qiu et al., “Rock damage control for large-diameter-hole lateral blasting excavation based on charge structure optimization,” *Tunnelling and Underground Space Technology*, vol. 106, 2020.
- [19] K. Liu, Q. Li, C. Wu, X. Li, and J. Li, “Optimization of spherical cartridge blasting mode in one-step raise excavation using pre-split blasting,” *International Journal of Rock Mechanics and Mining Sciences*, vol. 126, 2020.
- [20] R. Gao, B. Huo, H. Xia, and X. Meng, “Numerical simulation on fracturing behaviour of hard roofs at different levels during extra-thick coal seam mining,” *Royal Society Open Science*, vol. 7, no. 1, p. 191383, 2020.
- [21] H. P. Kang and Y. J. Feng, “Role of borehole transverse notching on hydraulic fracturing in hard rock,” in *ISRM SINOROCK 2013* International Society for Rock Mechanics and Rock Engineering, Lisbon, Portugal, 2013.
- [22] ASTM D7012-10, *Standard Test Method for Compressive Strength and Elastic Moduli of Intact Rock Core Specimens under Varying States of Stress and Temperatures*, ASTM, West Conshohocken, PA, USA, 2013.
- [23] M. Qian, X. Miao, and F. He, “Analysis of key block in the structure of voussoir beam in longwall mining,” *International Journal of Rock Mechanics and Mining Sciences and Geomechanics Abstracts*, vol. 4, no. 32, p. 191A, 1995.
- [24] Y. D. Murray, *Users Manual for LS-DYNA Concrete Material Model 159 (No. FHWA-HRT-05-062)*, Federal Highway Administration, Washington, DC, USA, 2007.

Research Article

Distribution and Variation of Mining-Induced Stress in the Reverse Fault-Affected Coal Body

Rui Zhou,^{1,2,3} Yujin Qin ,^{1,2} and Zhizhen Zhang ^{2,4}

¹China Coal Technology Engineering Group Shenyang Research Institute, Fushun 113122, China

²State Key Laboratory of Coal Mine Safety Technology, Fushun 113122, China

³Key Laboratory of Ministry of Education on Safe Mining of Deep Metal Mines, Northeastern University, Shenyang 110819, China

⁴State Key Laboratory of Geomechanics and Deep Underground Engineering, School of Mechanics and Civil Engineering, China University of Mining and Technology, Xuzhou 221116, China

Correspondence should be addressed to Yujin Qin; 359240092@qq.com and Zhizhen Zhang; zzzhang@cumt.edu.cn

Received 1 February 2021; Revised 14 March 2021; Accepted 17 April 2021; Published 29 April 2021

Academic Editor: Sanjay Nimbalkar

Copyright © 2021 Rui Zhou et al. This is an open access article distributed under the Creative Commons Attribution License, which permits unrestricted use, distribution, and reproduction in any medium, provided the original work is properly cited.

This study aimed to explore the stress distribution and variation of reverse fault-affected mined coal body. A mechanical analysis model of the coal body in the reverse fault area was first established, then the coal body stress characterization equation was derived, and the stress distribution pattern on the coal body was calculated. Subsequently, applying the Mohr–Coulomb strength criterion revealed the following relationship: the closer is the distance to the reverse fault, the worse is the stability of the coal body, and that the coal body strength influences the stress concentration of the coal body in front of the working face. Moreover, simulation with FLAC^{3D} was carried out to verify the coal body stress calculated by the mechanical model as well as the fluctuation of the coal body stress concentration. It could be concluded that while mining the hanging wall of the reverse fault, the stress concentration of mined coal body decreases with the increase of reverse fault dip angle, but increases with the increase of reverse fault throw; the stress concentration magnitude generated during footwall mining is lesser than that during hanging-wall mining. In other words, the magnitude of coal body stress concentration can be affected by the hanging wall and footwall mining, as well as parameters of the reverse fault. Finally, intrinsically safe GZY25 borehole stress sensors were used to monitor the coal body stresses in the reverse fault area under the influence of mining in Xinchun Coal Mine and ZuoQiuka Coal Mine. It was found that the coal body stress concentration in front of the working face either increased gradually or increased first before decreasing. It can be concluded that with the decrease of the distance between the working face and reverse fault, the vertical stress of the coal body increases, and the vertical stress of the coal body begins to increase obviously at a certain position. At this point, the vertical stress of the coal body can be generalized to 1.02–1.39 times of the initial vertical stress. Furthermore, the stress concentration coefficient of coal body is related to the distance from the reverse fault, and two changes occur: ① if the coal-bearing capacity does not exceed its strength, the coal stress in front of the working face increases gradually, and the stress concentration factor increases gradually; ② the stress concentration coefficient of mining coal body increases first, such that when the coal body bearing capacity exceeds its strength, the coal body fails and loses all its effective bearing capacity, followed by the decrease in coal body stress concentration coefficient.

1. Introduction

Reverse faults are common geological structures widely distributed in China's coal-producing areas [1–3], especially those in the southwest of the country, such as Guizhou, Yunnan, and Sichuan. Underground coal mine projects in

these areas often take place across or close to these reverse faults [4–6]. In fact, the coal bodies often lose their stability when the mining face gets too close to the reverse fault [7–11]. Also, reverse faults have sealing properties, so mining stress will also have an impact on gas bearing and its migration. Therefore, the mining activities in the reverse

fault area inflict massive challenges to the site construction and maintenance [12–14]. To ensure safety and improve mining productivity around the coal seam in the reverse fault area, it is necessary to study the stress variation trend of reverse fault-affected mined coal bodies.

At present, significant achievements have been made in the analysis of mined coal body stress in reverse fault regions. However, due to high susceptibility to rockbursts caused by the mining conditions-incurred reverse fault instability, plenty of research efforts have been focused on fields related to the prevention of rockbursts, such as stress variation, the stability of reverse fault zone, and the slip of reverse fault zone. To clarify the stress variation characteristics of reverse fault-affected mined coal bodies and explore the stress distribution characteristics of the mined coal bodies under various working faces, reverse fault distances, reverse fault dip angles, and fault throws, the actual working conditions of a typical working face in Guizhou mining area, were taken as the reference for the research herein.

2. Mechanical Model of the Reverse Fault-Affected Mined Coal Body

2.1. Theoretical Model. To study the stress distribution characteristics of the reverse fault-affected mined coal body, we established a geomechanical analysis model for coal rocks, measuring H and L along the X and Y axes respectively, as shown in Figure 1. A reverse fault was designed in front of the mining face, and O marks the intersection point of the reverse fault and the roof of the coal seam. It is vertically subject to the stress of the overburden above the roof of the coal seam and horizontally to the horizontal stress. Under normal circumstances, the horizontal and vertical stresses are approximately equal, but due to the existence of a reverse fault, the horizontal compression should become obvious in actuality, so the horizontal stress

is set herein as 1.5 times the vertical stress [4]. With the advancement of the mining face, the upper roof becomes an area subject to abutment stresses of various magnitudes and the front side of the working face and the rear side of the goaf become areas subject to increasing levels of abutment stress, whereas the goaf turns into an area subject to decreasing levels of abutment stress. With the advancement of the working face, the scope of the abutment stress also changes. Since hanging walls serve as the active plates in reverse faults, the effects of all mechanical stresses will also become more obvious. For this reason, the mining activities on the hanging wall of the reverse fault are taken as the object of mechanical analysis herein [15].

According to the distribution law of mine pressure [16], the vertical stress of roof can be divided into eight areas, the maximum stress value of AB and BC is $K_1 \cdot q_x$, the maximum stress value of FG and GH is $K_3 \cdot q_x$, the maximum stress value of CD and DF is $K_2 \cdot q_x$, and the stress value of OA and HJ is q_x .

The stress in the horizontal direction is q_y , according to the boundary conditions of the mechanical analysis model of reverse fault, the horizontal stress is $1.5q_x$ [4, 12]. In order to quantitatively calculate the law of coal stress variation, the vertical stress variation curve of roof stress support area is simplified as linear variation.

In the analysis process, it is assumed that the coal geological body is homogeneous and isotropic. According to rock mechanics [16], the concentrated force P acting on the plane will affect any point $M(x, y)$ below the plane, and its vertical stress value can be expressed as

$$\sigma_x = \frac{2P}{\pi} \cdot \frac{x^3}{(x^2 + y^2)^2}. \quad (1)$$

Therefore, under the combined action of horizontal stress and vertical stress in the reverse fault-affected area, the vertical stress of $M(x, y)$ can be expressed as

$$\begin{aligned} \sigma_x = & \frac{-2}{\pi} \cdot \int_0^a \frac{q_x \cdot x^3}{[x^2 + (y - \xi)^2]^2} d\xi + \frac{-2}{\pi} \cdot \int_a^b \frac{(((q_x - K_1 \cdot q_x)/(a - b)) \cdot y - ((b \cdot q_x - a \cdot K_1 \cdot q_x)/(a - b))) \cdot x^3}{[x^2 + (y - \xi)^2]^2} d\xi \\ & + \frac{-2}{\pi} \cdot \int_b^c \frac{(K_1 \cdot q_x/(b - c)) \cdot y - (c \cdot K_1 \cdot q_x/(b - c)) \cdot x^3}{[x^2 + (y - \xi)^2]^2} d\xi \\ & + \frac{-2}{\pi} \cdot \int_c^d \frac{(-(K_2 \cdot q_x/(c - d)) \cdot y + (c \cdot K_2 \cdot q_x/(c - d))) \cdot x^3}{[x^2 + (y - \xi)^2]^2} d\xi + \frac{-2}{\pi} \cdot \int_d^f \frac{K_2 \cdot q_x \cdot x^3}{[x^2 + (y - \xi)^2]^2} d\xi \\ & + \frac{-2}{\pi} \cdot \int_f^g \frac{(-(q_x - K_2 \cdot q_x/(f - g)) \cdot y - f \cdot q_x - g \cdot K_2 \cdot q_x/(f - g)) \cdot x^3}{[x^2 + (y - \xi)^2]^2} d\xi \\ & + \frac{-2}{\pi} \cdot \int_g^h \frac{(-(q_x - K_3 \cdot q_x/(g - h)) \cdot y + (g \cdot q_x - h \cdot K_3 \cdot q_x/(g - h))) \cdot x^3}{[x^2 + (y - \xi)^2]^2} d\xi + \frac{-2}{\pi} \cdot \int_h^j \frac{q_x \cdot x^3}{[x^2 + (y - \xi)^2]^2} d\xi \\ & + \frac{-2}{\pi} \cdot \int_0^H \frac{q_y \cdot y^3}{[y^2 + (y - \xi)^2]^2} d\xi, \end{aligned} \quad (2)$$

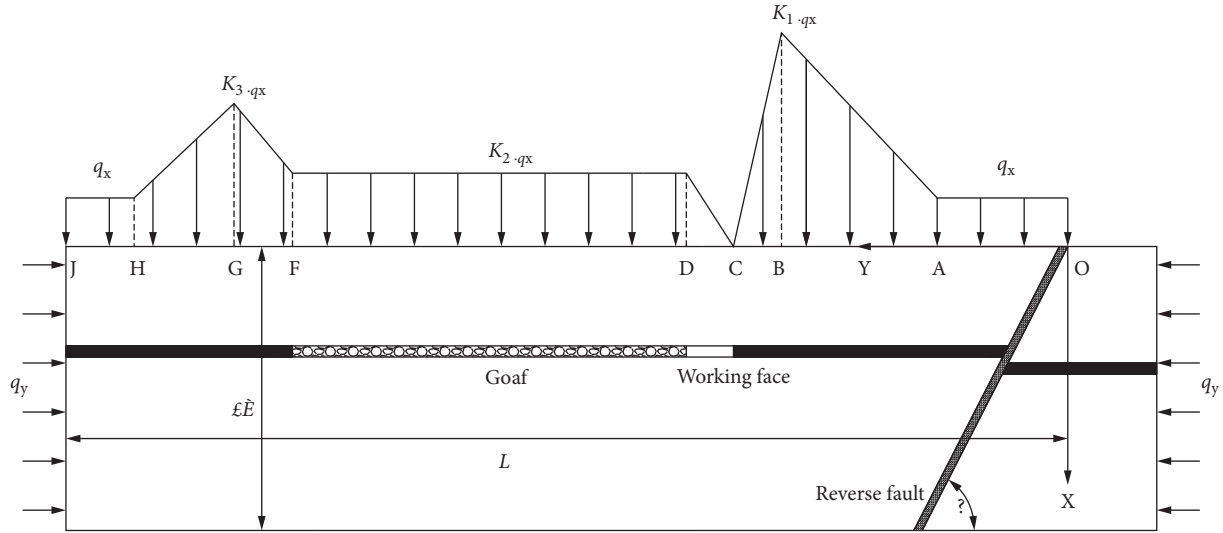


FIGURE 1: Mechanical model of mining coal under the influence of reverse fault.

where q_x is the vertical stress, MPa; q_y is the horizontal stress, MPa; A, B, C, D, F, G, H, and J are Y-axis lengths, and K_1 , K_2 , and K_3 are stress concentration factors.

When the coal load exceeds its strength, the coal body will undergo plastic deformation and fails, which leads to a reduction in stress. In view of this, the Mohr–Coulomb strength criterion was applied to analyze the stability of the coal body and determine whether failure occurs (see Equation (3)), before analyzing its stress characteristics.

$$\left\{ \begin{array}{l} \frac{\sigma_1 - \sigma_3}{\sigma_1 + \sigma_3 + 2 \cot \phi} < \sin \phi, \quad \text{stability,} \\ \frac{\sigma_1 - \sigma_3}{\sigma_1 + \sigma_3 + 2 \cot \phi} = \sin \phi, \quad \text{limit equilibrium,} \\ \frac{\sigma_1 - \sigma_3}{\sigma_1 + \sigma_3 + 2 \cot \phi} > \sin \phi, \quad \text{instability,} \end{array} \right. \quad (3)$$

where σ_1 is the first principal stress, MPa; σ_3 is the third principal stress, MPa; ϕ is the friction angle in coal body.

While mining the working face, shear stresses on mined coal bodies are relatively negligible in magnitude compared with the vertical and horizontal stresses, which makes it reasonable to omit their contributions in calculations. In fact, vertical stress of the coal body is generally taken as the first principal stress and the horizontal stress of working face inclination as the third principal stress [17]. With the decrease of the distance between working face and reverse fault, the stress concentration magnitude of coal body in front of working face and σ_1 increase gradually. σ_3 is influenced by the mining roadway on both sides of the working face, so stress will not be concentrated during mining activities. Moreover, when the position of coal body in front of the working face and the working face is the same, the difference in σ_3 is not large and hence can be simplified as equal. As such, Equation (3) $(\sigma_1 - \sigma_3)/(\sigma_1 + \sigma_3 + 2 \cot \phi)$ can be converted into $1 - ((2\sigma_3 + 2 \cot \phi)/(\sigma_1 + \sigma_3 + 2$

$\cot \phi))$, whose value increases gradually with the increase of σ_1 . This implies that $(\sigma_1 - \sigma_3)/(\sigma_1 + \sigma_3 + 2 \cot \phi)$ also increases gradually, which in turn indicates that, as the mining activity on the working face proceeds, the stability of mining-induced coal decreases gradually; when the coal-bearing capacity exceeds its strength, the coal will undergo plastic deformation and fails, resulting in the reduction of coal stress. The same can be inferred that, as the mining activity proceeds along the direction of the working face to the reverse fault, if the coal-bearing capacity does not exceed its strength, the coal body stress in front of the working face will increase, and the stress concentration coefficient will gradually increase; if the bearing capacity of the coal body exceeds its strength, the coal pillar between the working face and the reverse fault will fail, and the coal body will effectively lose the capacity to bear the load inflicted on it, hence lowering the stress concentration coefficient of the coal body in front of the working face.

2.2. Mechanical Calculations Associated with the Reverse Fault-Affected Mined Coal Body. Xinchun Coal Mine is located in the west of Tongzi County, Guizhou Province, with a designed production capacity of 900,000 t/a and service life of 62a. The 1503 working face is located in the southeast of the mine.

The C5 coal seam has been mined to a depth of 300–420 m using the strike longwall mining method. In the mining area of the 1503 working face, there lies the F4 reverse fault, which has a fault dip angle of 60°, length of 195 m, fault spacing of 0–6 m, and average length of 4 m. There is no other structure in the mining area of the 1503 working face; the working face layout is as illustrated in Figure 2.

To get a clearer understanding of the mechanical distribution characteristics of the reverse fault-affected mined coal body, the required calculation parameters were selected from the field geological conditions of Xinchun Coal Mine:

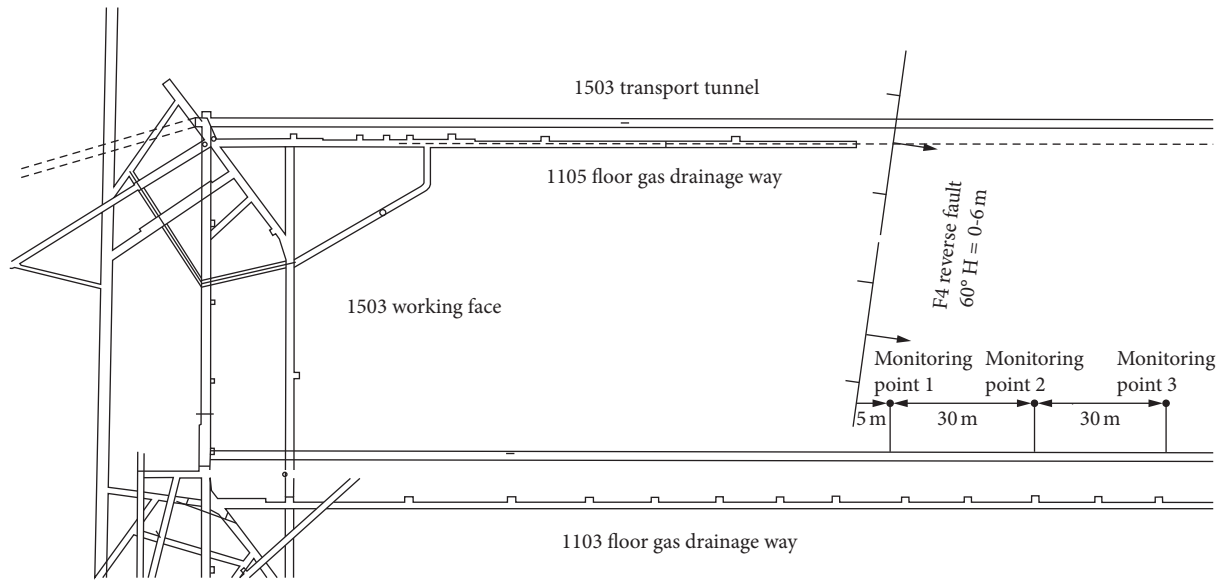


FIGURE 2: Map of 1503 working face.

vertical stress $q_x = 9.0$ MPa, horizontal stress $q_y = 13.5$ MPa, the distance between the coal seam and the roof = 9 m, and the mining height of the coal seam = 2.0 m. Relevant principles of mining science were consulted to determine the selection range of each stress zone, while a field investigation was conducted to determine specific parameters. Starting from a working face position separated by 70 m from the reverse fault, the distance parameter OA is 57 m, AB is 28 m, BC is 2 m, CD is 4 m, DF is 100 m, FG is 2 m, Hg is 28 m, K_1 is 2.3, K_2 is 0.8, and K_3 is 2.0. Substituting relevant parameters into (2), the vertical stress distribution curve of the mined coal body is calculated at various working face positions from the reverse fault, as shown in Figure 3.

When the distance between the working face and the reverse fault is 70 m, 40 m, and 10 m, respectively, there is a stress concentration area in front of the working face, and the coal body stress rises, and the vertical stress of the coal body reaches the maximum at 5 m in front of the working face. After that, the coal body stress begins to decline and gradually returns to the original stress state after exceeding the influence range of the stress increase area. By calculation, the maximum vertical stress of coal body in front of working face is 15.82 MPa and the stress concentration coefficient is 1.58 when the distance from the reverse fault is 70 m; when the distance from the reverse fault is 40 m, the maximum vertical stress of the coal body is 16.43 MPa, and the stress concentration coefficient is 1.64; when the distance from the reverse fault is 10 m, the maximum vertical stress of the coal body is 18.52 MPa, and the stress concentration coefficient is 1.85. It is found that with the decrease of the distance between the working face and the reverse fault, the stress concentration degree of the coal body in front of the working face increases, and the maximum value of the vertical stress increases.

When the distance between the working face and the reverse fault is 70 m, 40 m, and 10 m, respectively, stress concentration areas are formed in front of the respective

working faces. In these areas, the coal body stress rises and the vertical stress of the coal body reaches its maximum at 5 m in front of the working face. After that, the coal body stress begins to decline and gradually returns to the original stress state after exceeding the influence range of the stress increase area. According to the calculation, the maximum vertical stress of the coal body in front of the working face is 15.82 MPa and the stress concentration coefficient is 1.58 when the distance from the reverse fault is 70 m. When the distance from the reverse fault is 40 m, the maximum vertical stress of the coal body is 16.43 MPa, and the stress concentration coefficient is 1.64; when the distance from the reverse fault is 10 m, the maximum vertical stress of the coal body is 18.52 MPa, and the stress concentration coefficient is 1.85. It was also found that, with the decrease of the distance between the working face and the reverse fault, the stress concentration magnitude of the coal body in front of the working face increases, and the maximum value of the vertical stress increases.

3. Numerical Simulation of the Stress in the Reverse Fault-Affected Coal Body

To verify the calculation accuracy of the mechanical model with respect to the coal body stress and explore the mechanisms of how the stress concentration coefficient of the mined coal body would both increase and decrease under the influence of the reverse fault, the FLAC^{3D} numerical simulation module was used to analyze the stress variation trend of reverse fault-affected mined coal body, using which the influences on the mined coal body stress exerted by mining the hanging wall versus the footwall, as well as by reverse fault dip angle, fault throw, etc., were discussed.

3.1. Numerical Model. This study constructed the 3D numerical simulation model based on the 1503 mining face of Xinchun Coal Mine and declared the X-axis along the

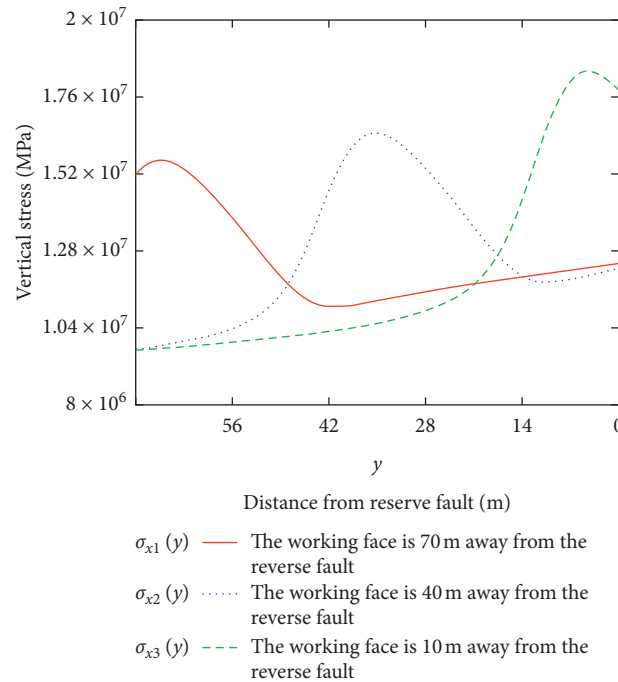


FIGURE 3: Vertical stress of coal body in different distance between working face and reverse fault.

direction of the coal seam, the Y-axis along the direction of coal seam inclination, and the Z-axis along the vertical direction. The reverse fault was designed with a dip angle of 60° and a fault throw of 4 m. The model measures 350 m, 200 m, and 103 m in length, dip length, and height, respectively. In the calculation, the mining process was simulated by excavation step by step, and the working face excavation was simulated by empty element. The reverse fault is simulated by adding 2 m-long weak bands in the middle of the upper and lower walls of the model. In the simulation, the coal-rock body model was regarded as an elastoplastic body and the Mohr–Coulomb model was selected. The mechanical parameters of coal and rock mass in 1503 working face used in the simulation process are selected according to references [18, 19], and the mechanical parameters of coal and rock mass are as shown in Table 1. Vertical movements were limited by the X and Y directions of the model and the Z-direction of the bottom plane. The upper part is a free surface, on which a vertical load is to be applied to simulate the dead weight of the overlying strata. The vertical stress is 9.0 MPa, and stress with 1.5 times of that magnitude will be applied along the horizontal direction.

3.2. Stress Variation of the Reverse Fault-Mined Coal Body

3.2.1. Variation of Hanging-Wall Mining-Inflicted Stress on the Coal Body. When the working face was 70 m, 40 m, and 10 m away from the reverse fault, the vertical stress distribution of coal body is shown in Figure 4.

When the working face is 70 m away from the reverse fault, under the shearing action of the reverse fault, the roof of the coal seam becomes wedged, the vertical stress

concentration of surrounding rock is relatively low, and the maximum vertical stress of the coal body in front of the working face is 18.2 MPa. When the working face is 40 m away from the reverse fault, the vertical stress concentration magnitude of the coal body in front of the working face increases, and the maximum vertical stress increases to 19.2 MPa. Lastly, when the working face is 10 m away from the reverse fault, the vertical stress concentration of the coal body in front of the working face further increases, and the maximum vertical stress rises to 19.8 MPa. From the statistics above, it can be concluded that, when the working face is mined toward the direction of the reverse fault, as the distance from the reverse fault decreases, the stress concentration magnitude of the coal body in front of the working face gradually increases, and the maximum of the advanced stress gradually increases.

Stress monitoring points were arranged at 65 m, 35 m, and 5 m away from the reverse fault, and the variation curve of the vertical stresses at the monitoring points was obtained as the mining activity on the working face proceeds, as shown in Figure 5.

With the advancement of the working face, the vertical stresses of the coal body at the monitoring points significantly increase. When the mining face is 110 m away from the reverse fault, the stresses captured by the three monitoring points show little difference. The monitoring point at the 65 m point is closer to the working face at this instance; hence, the greater influence from the mining activities and the highest vertical stress were recorded. The 5 m monitoring point is farthest from the working face; thus, the influence of mining activities is relatively small and the vertical stress is the least. At 70 m away from the reverse fault, the maximum vertical stress read by the monitoring point at the 65 m point

TABLE 1: Rock mechanics parameters of 1503 working face in Xinchun coal mine.

Lithology	Thickness (m)	Density (kg·m ⁻³)	Elastic modulus (GPa)	Poisson's ratio	Bulk modulus (GPa)	Shear modulus (GPa)	Cohesion (MPa)	Tensile strength (MPa)	Internal friction angle (°)
Sandstone	49	2540	17.55	0.24	14.7	8.1	10.0	11.55	26
Sandy mudstone	12	2600	15.45	0.27	10.5	7.1	1.7	2.30	30
Coal	2	1350	3.53	0.33	10.5	6.5	1.2	0.90	23
Mudstone	8	2340	4.92	0.35	9.8	7.1	0.5	1.55	39
Silty mudstone	15	2530	7.33	0.31	10.4	7.3	0.7	1.65	38
Siltstone	17	2580	10.23	0.31	13.4	7.6	1.4	1.85	37
Fault	2	2000	1.10	0.12	4.1	1.3	0.4	0.2	5

reaches 15.6 MPa. After that, the coal body at the monitoring point is mined and the stress returns to 0. When the working face advances to 40 m away from the reverse fault, the maximum vertical stress at the 35 m monitoring point reaches 16.2 MPa. Lastly, when the working face is 10 m from the reverse fault, the maximum vertical pressure at the 5 m monitoring point rises to 18.4 MPa.

Compared with the results of mechanical calculation, the numerical simulation results are identical to the conclusion of mechanical analysis. The stress concentration magnitude of the coal body in front of the working face is gradually increasing, and the maximum stress value is constantly increasing. Moreover, the stress concentration magnitude of theoretical calculation is basically consistent with the results in Figure 5, which again confirms the accuracy of theoretical analysis.

3.2.2. Variation of Footwall Mining-Inflicted Stress on the Coal Body. In order to analyze the footwall mining-inflicted stress on the coal body, when the working face was 70 m, 40 m, and 10 m away from the reverse fault, the vertical stress distribution of coal body was shown in Figure 6.

During footwall face mining, the coal body stress distribution also shows a variation trend whereby the closer the coal body gets to the reverse fault, the more concentrated the coal stress becomes. When the footwall working face is 70 m away from the reverse fault, the maximum vertical stress in front of the working face is 17.4 MPa; 40 m away, the maximum vertical stress becomes 18.9 MPa; 10 m away, and the maximum vertical stress rises to 19.0 MPa. Comparing the stress distribution in the event of hanging wall mining, it can be concluded that footwall mining incurs weaker stress concentration.

Stress monitoring points were arranged at 65 m, 35 m, and 5 m away from the reverse fault, and the variation curve of the vertical stresses at the monitoring points was obtained as the mining activity on the working face proceeds, as shown in Figure 7.

With the advancement of the working face, the stresses recorded at the monitoring points increase. When the working face is 70 m away from the reverse fault, the maximum vertical pressure at the 65 m monitoring point reaches 17.0 MPa; at 40 m away, the maximum vertical pressure at the 35 m monitoring point reaches 18.4 MPa;

10 m away, and the maximum vertical pressure at the 5 m monitoring point becomes 18.8 MPa. This shows that the stress variation trends for both the hanging wall and footwall mining cases are equivalent and that the working face positions affect the stress concentration magnitude of the coal body.

3.3. Influence of Reverse Fault Parameters on Stress Variation in Mined Coal Body

3.3.1. Influence of Reverse Fault Dip Angle on Coal Body Stress. Four reverse fault mining simulation models were established. Adjustments made for the model used throughout this experimental section were as follows. The mechanical properties of the fault plane are the same, the fault throw, the rock physical and mechanical properties are the same, and only the reverse fault dip angle has been changed to 30°, 45°, 60°, and 75°, respectively. The stress distribution characteristics of the mined coal body are as shown in Figures 8–10.

When the working face is 70 m and 40 m away from the reverse fault, the larger is the reverse fault dip angle and the smaller is the maximum advanced stress of the coal body. This is caused by the varying reverse fault dip angles, which diversify the volume of the resulting trapezoidal coal pillars between the working face and the reverse fault. Analogously, the smaller the dip angle, the larger the coal volume above the coal pillar and the higher the load. Moreover, the presence of a reverse fault structure has also diminished the effectiveness of stress transfer across the mined coal bodies, increasing the gravity load on the coal pillars as well as the stress concentration.

When the working face is 10 m away from the reverse fault, the stress on the coal body in front of the working face reaches its maximum when the dip angle of the reverse fault is 45°. Compared with the stress concentration area in front of the working face in Figure 10, part of the coal body stress concentration area does not reach its maximum at the 30° dip angle reverse fault, whereas the maximum is reached at other dip angles. This suggests that only part of the coal body can still bear the load effectively in the stress concentration area at the 30° dip angle, whereas the remaining coal body part has failed and completely lost its load-bearing capacity, hence resulting in the reduction in stress concentration

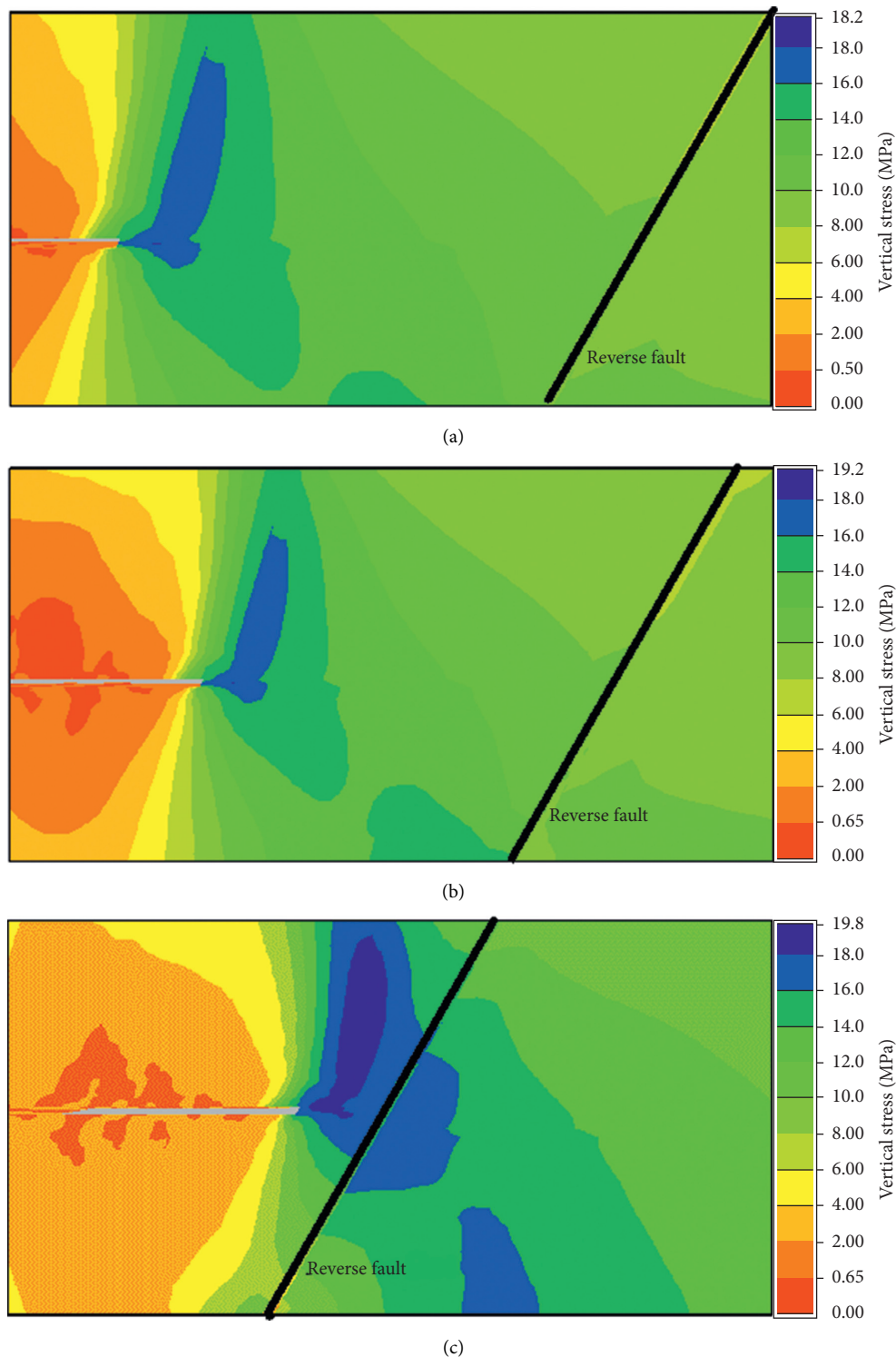


FIGURE 4: Variation of hanging-wall mining-inflicted stress on the coal body under different distance between working face and reverse fault. (a) The working face is 70 m away from the reverse fault. (b) The working face is 40 m away from the reverse fault. (c) The working face is 10 m away from the reverse fault.

magnitude. This conclusion further verifies that obtained in the theoretical analysis, which also claims the reduction in stress concentration.

Stress monitoring points were arranged at 65 m, 35 m, and 5 m away from the reverse fault, and the variation curve

of the vertical stresses at the monitoring points was obtained as the mining activity on the working face proceeds, as shown in Figure 11.

At 45°, 60°, and 75° dip angles, the stress concentration magnitudes of the coal body in front of the working face

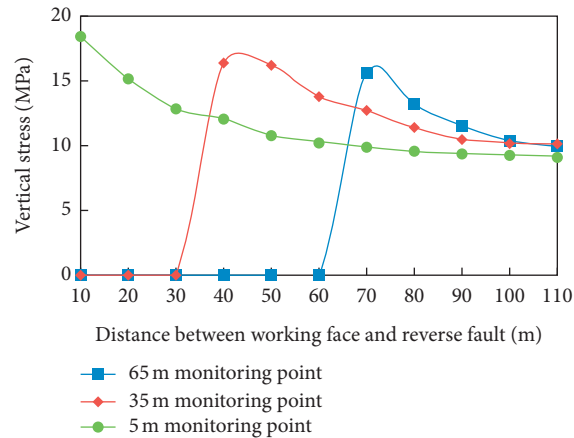


FIGURE 5: Variation curve of the vertical stresses at the monitoring points in hanging-wall mining.

gradually increase, whereas at 30° dip angle, the stress concentration magnitude of the coal body in front of the working face gradually increases first before decreasing once the distance from the reverse fault reaches 10 m. It is also worthy to note that the change in reverse fault dip angle mainly affects the stress concentration magnitude of the coal body in front of the working face, and not the stress variation trend.

When the working face is far away from the monitoring point, the vertical stress is the initial stress, and when the working face is 35 m away from the monitoring point, the vertical stress begins to rise obviously. By comparing both the two stresses, it can be seen that the value of the stress where the increase is the most significant is 1.02–1.39 times that of the initial stress, as shown in Table 2.

3.3.2. Influence of Reverse Fault Throw on Coal Body Stress. Four reverse fault mining simulation models were established. Adjustments made for the model used throughout this experimental section were as follows. The mechanical properties of the fault plane are the same, the fault dip angle, the rock physical and mechanical properties are the same, and only the reverse fault throw has been changed to 4 m, 10 m, 15 m, and 20 m, respectively. The stress distribution characteristics of the mined coal body are as shown in Figures 12–14.

When the working face is 70 m away from the reverse fault, the maximum stress of the coal body in front of the working face is between 18.2 and 18.5 MPa; at 40 m away, the maximum stress is 19.2–20.4 MPa; at 10 m away, and the maximum stress is 19.8–20.7 MPa. The coal body stress reaches its minimum when the throw is 4 m and is at its maximum when the throw is 20 m. This shows that the coal body stress increases with the fault throw.

Stress monitoring points were arranged at 65 m, 35 m, and 5 m away from the reverse fault, and the variation curves of vertical stresses at the monitoring points were obtained as the mining activity on the working face proceeds, as shown in Figure 15.

When the reverse fault throws are 4 m, 10 m, 15 m, and 20 m, the maximum vertical stress of the coal body in front

of the working face basically shows a trend of gradual increase. The change of reverse fault throw mainly affects the stress concentration degree of the coal body in front of the working face.

When the working face is far away from the monitoring point, the vertical stress is the initial stress, and when the working face is 35 m away from the monitoring point, the vertical stress begins to rise obviously. By comparing the two stresses, it can be seen that the value of the stress where the increase is the most significant is 1.04–1.31 times that of the initial stress, as shown in Table 3.

4. Field Test of the Reverse Fault-Affected Coal Body Stress

To verify the accuracy of the theoretical analysis and numerical simulation, a field test was carried out in the 1503 working face of Xinchun Coal Mine, where intrinsically safe GZY25 borehole stress sensors were used to monitor the coal body stress in front of the working face to analyze the stress variation trend of the mined coal body. GZY 25 borehole stress sensors were mainly used for monitoring the stress change of coal and rock mass, which was composed of sensor, transmitter, and junction box. At 5 m, 35 m, and 65 m from the reverse fault of 1503 transport lane, the layout of measuring points was shown in Figure 2, Φ 42 mm stress test boreholes with 10 m depth were drilled, and the stress sensors were pushed inward using the given conveyor rod accessory. The variation of borehole stress with the advancement of the working face is as shown in Figure 16.

It can be seen that the stress variation trend of the three monitoring points is the same and that the coal stress gradually increases with the decrease of the distance from the working face. When the distance separating the working face and the monitoring point is 35 m, the stress starts to increase obviously. The stress change reaches its maximum when the separation lessens to 5 m. The stress change at the 5 m monitoring point is the largest, while the stress change at the 65 m monitoring point is the smallest, indicating that the closer is the distance to the reverse fault, the higher is the

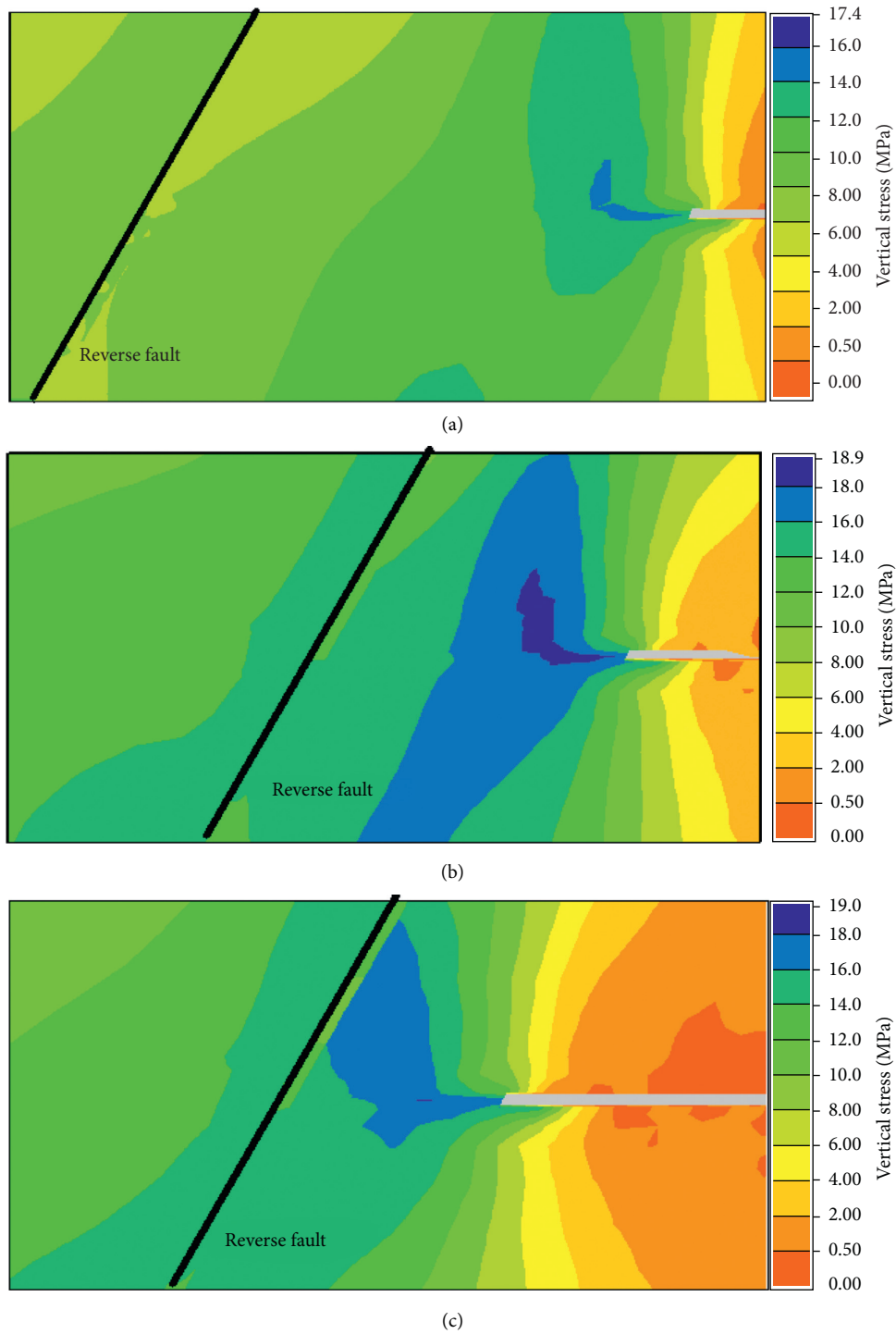


FIGURE 6: Variation of footwall mining-inflicted stress on the coal body under different distance between working face and reverse fault. (a) The working face is 70 m away from the reverse fault. (b) The working face is 40 m away from the reverse fault. (c) The working face is 10 m away from the reverse fault.

stress concentration magnitude of coal body in front of the working face. This finding conforms with the previously acquired variation trend, whereby the stress concentration magnitude of reverse fault-affected mined coal body gradually increases and is consistent with the conclusions reached in the theoretical analysis and numerical simulation.

Another coal body stress monitoring was also carried out in the F2 reverse fault area of the 1301 working face of ZuoQiuka Coal Mine in Guizhou Province. The dip angle of the F2 reverse fault was 32° and the fault distance was 6.1 m. The variation of borehole stress with the advancement of working face is as shown in Figure 17.

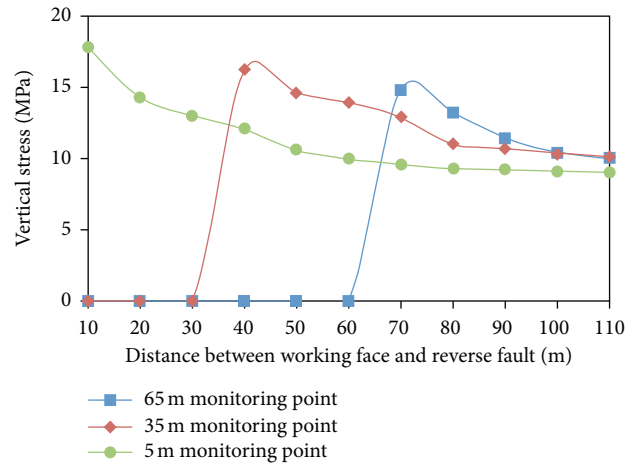
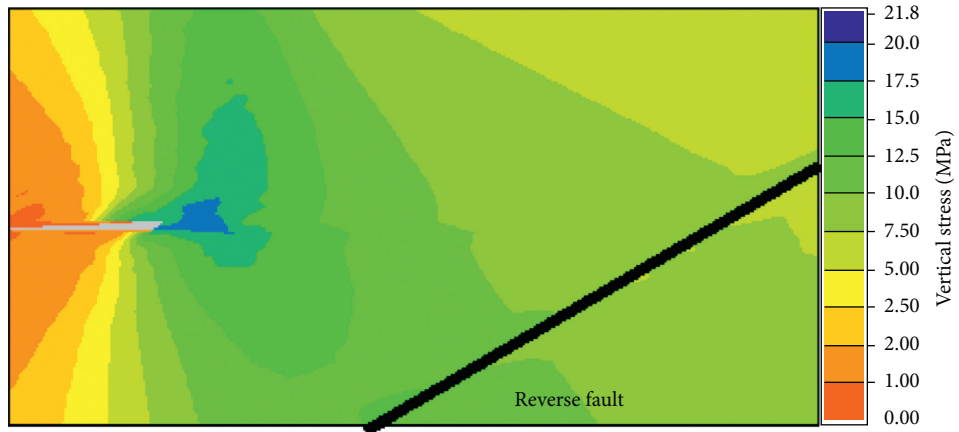
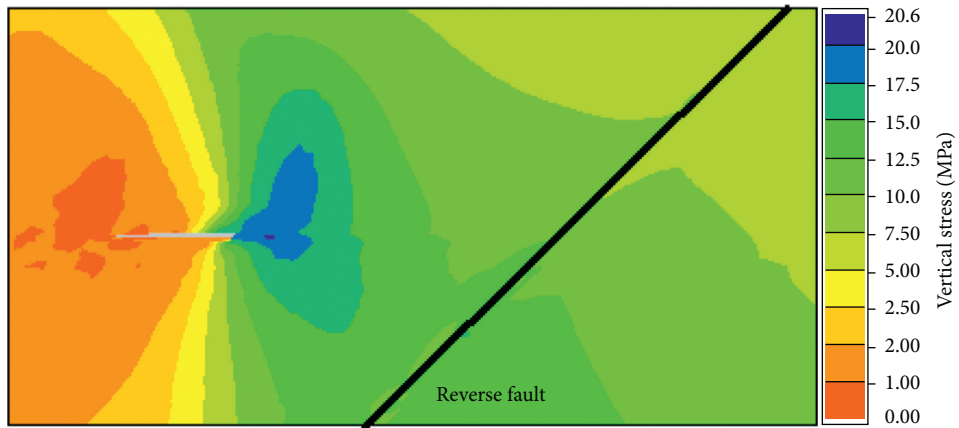


FIGURE 7: Variation curve of the vertical stresses at the monitoring points in footwall mining.



(a)



(b)

FIGURE 8: Continued.

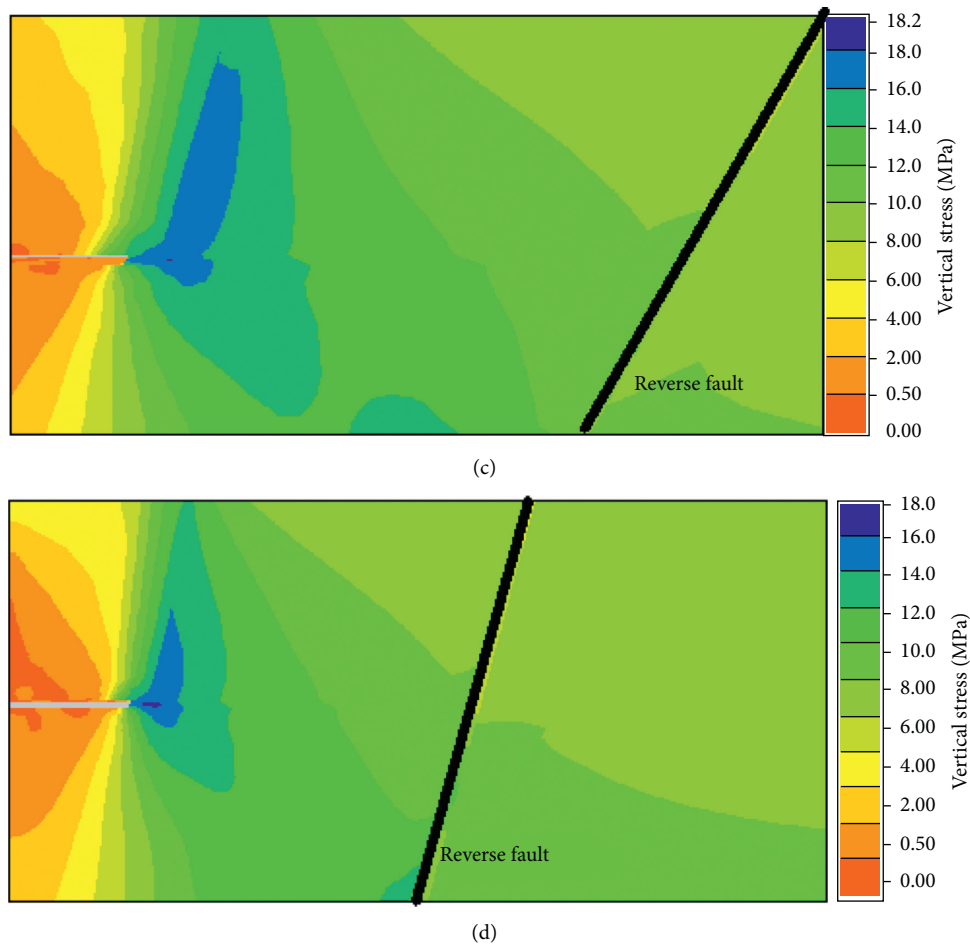


FIGURE 8: Stress distribution when the distance between working face and reverse fault is 70 m with different dip angles. (a) The dip angle of reverse fault is 30°. (b) The dip angle of reverse fault is 45°. (c) The dip angle of reverse fault is 60°. (d) The dip angle of reverse fault is 75°.

TABLE 2: Ratio of stress to initial stress when hanging wall working face is 35 m away from monitoring point.

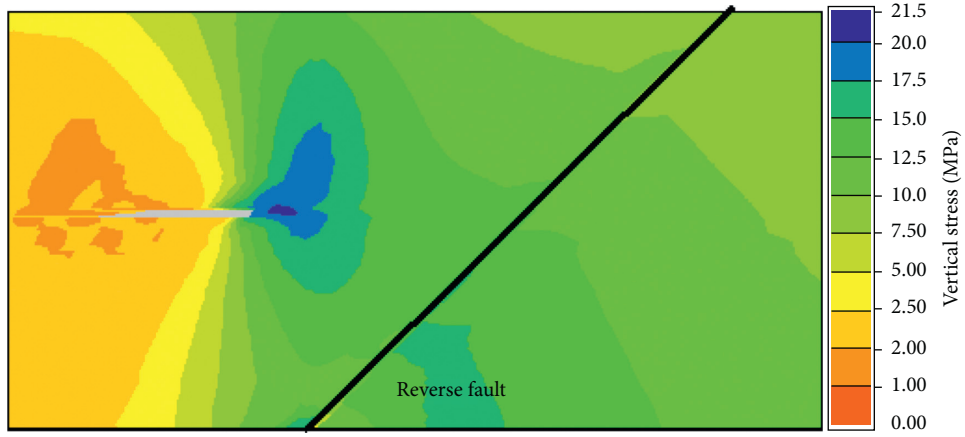
Location of monitoring points	Stress ratio of 30° reverse fault	Stress ratio of 45° reverse fault	Stress ratio of 60° reverse fault	Stress ratio of 75° reverse fault
65 m monitoring-point	1.44	1.14	1.04	1.02
35 m monitoring-point	1.32	1.33	1.27	1.23
5 m monitoring-point	1.39	1.23	1.21	1.15

TABLE 3: Ratio of stress to initial stress when working face is 35 m away from monitoring point.

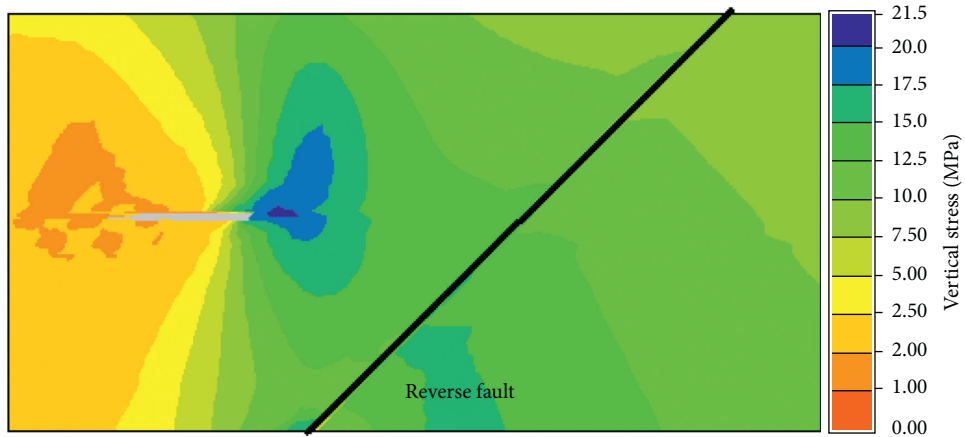
Location of monitoring points	Stress ratio of 4 m fault throw	Stress ratio of 10 m fault throw	Stress ratio of 15 m fault throw	Stress ratio of 20 m fault throw
65 m monitoring-point	1.04	1.05	1.04	1.03
35 m monitoring-point	1.27	1.20	1.29	1.31
5 m monitoring-point	1.21	1.20	1.21	1.22

It can be seen that as the distance from the working face decreases, the stresses at the three monitoring points gradually increase. However, the maximum vertical stress concentration at the monitoring point located 35 m away from the reverse fault is higher than that at the monitoring point located 5 m away, indicating that the coal body at the 5 m monitoring point failed and lost its load-bearing

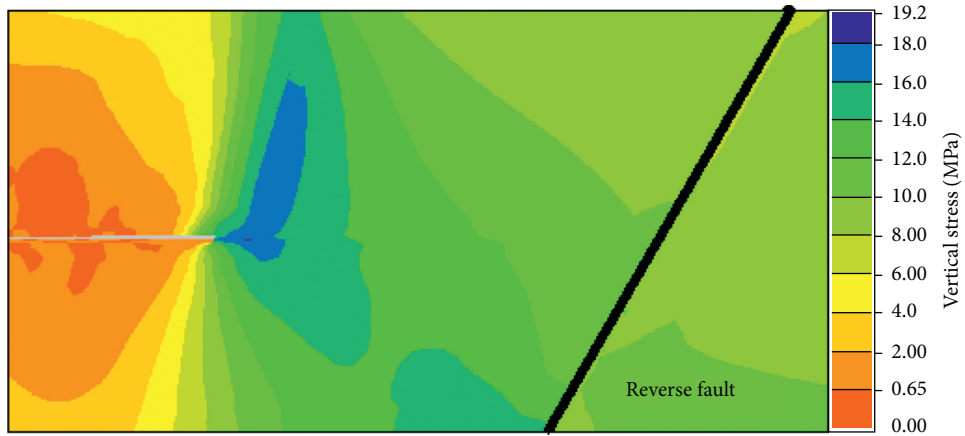
capacity, so the stress concentration magnitude decreases. It has also been verified that the stress concentration magnitude of the coal body decreases. Also, when the working face is 40 m away from the reverse fault, the vertical stress of the 5 m monitoring point increases obviously; when the 35 m monitoring point is 60 m away from the reverse fault, the vertical stress is significantly increased, indicating that when



(a)



(b)



(c)

FIGURE 9: Continued.

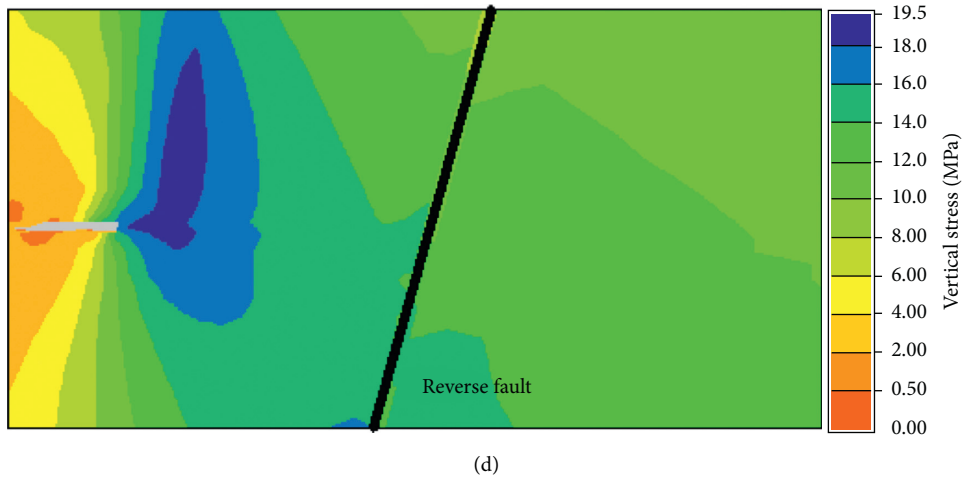


FIGURE 9: Stress distribution when the distance between working face and reverse fault is 40 m with different dip angles. (a) The dip angle of reverse fault is 30°. (b) The dip angle of reverse fault is 45°. (c) The dip angle of reverse fault is 60°. (d) The dip angle of reverse fault is 75°.

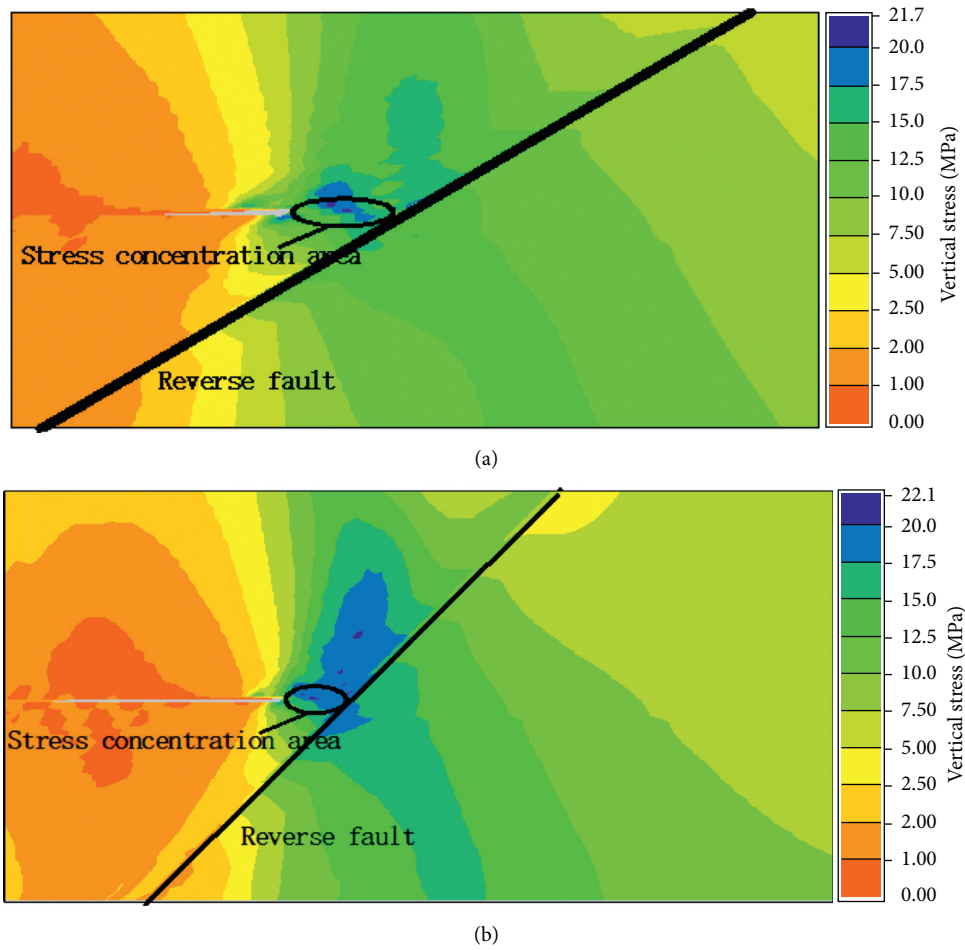


FIGURE 10: Continued.

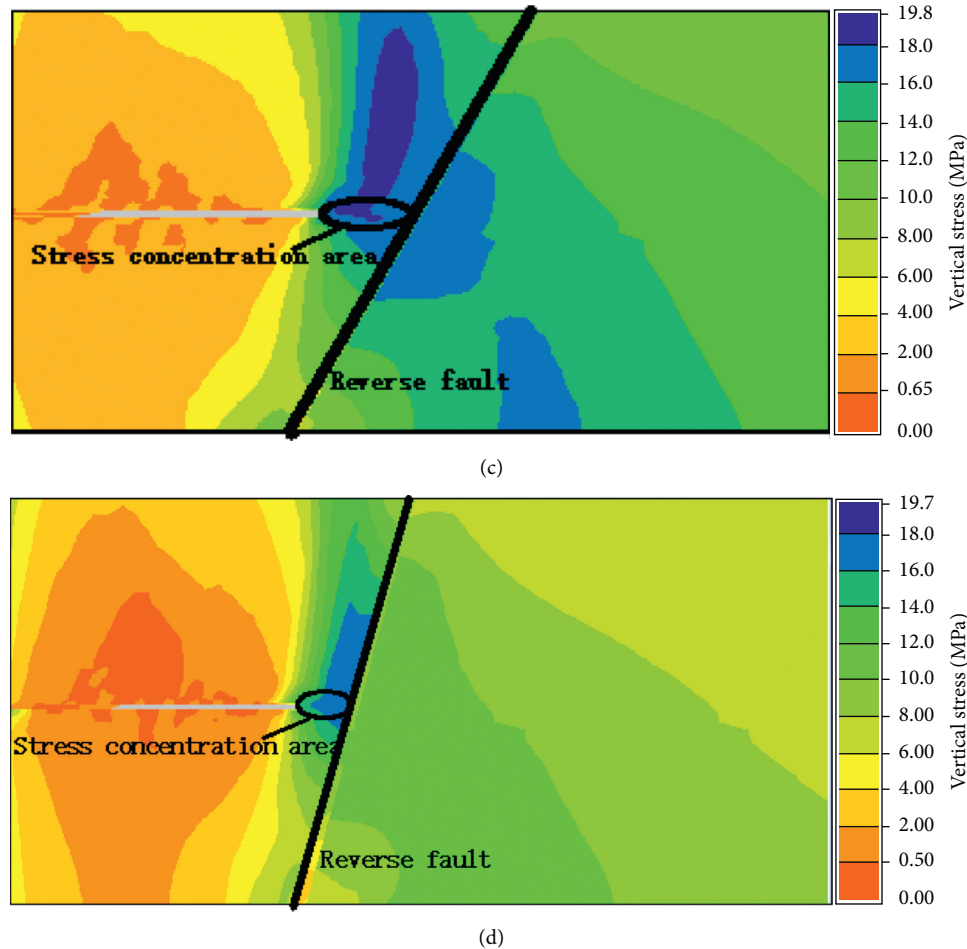


FIGURE 10: Stress distribution when the distance between working face and reverse fault is 10 m with different dip angles. (a) The dip angle of reverse fault is 30°. (b) The dip angle of reverse fault is 45°. (c) The dip angle of reverse fault is 60°. (d) The dip angle of reverse fault is 75°.

the working face is at a certain distance from the monitoring point, the mining-induced vertical stress on the coal body is significantly increased. This distance is related to several factors, such as mining speed, mining height, and reverse fault parameters.

5. Stress Variation Trend of Reverse Fault-Affected Mined Coal Body

Under the influence of mining, the coal body in the reverse fault region experienced an ongoing increase in vertical stress and an ongoing decrease in horizontal stress, until the coal body reached the point of structural failure. In the initial condition, without the influence of mining, the coal body was in the original rock tectonic stress state. With the approaching of the working face, the vertical stress of the coal body begins to rise and gradually reaches the peak pressure, before entering the pressure relief state when the coal body experiences failure, and the vertical stress decreases to the residual stress. On the other hand, when the horizontal dip stress of the coal body in front of working face is greater than that of original rock, under the influence of the inclined inlet and return air lanes of the working face, the

horizontal inclined stress gradually decreases, there is no stress concentration, and the horizontal stress decreases linearly in the mining [20]. Factors such as hanging wall and footwall mining, reverse fault dip angle, and throw mainly affect the stress concentration magnitude of coal body, not the stress variation trend on the coal body.

Therefore, based on the theoretical analysis, numerical simulation, and field testing, it can be inferred that when the reach of the mining influence coincides with the test point, the vertical stress at the test point will begin to increase, and then with the further decrease in the separation between the working face and the test point, the vertical stress begins to increase significantly. At this point, the vertical stress of the coal body can be generalized as $(1.02-1.39)\gamma \cdot H$. Finally, once the test point falls on the stress concentration area in front of the working face, the vertical stress will reach its maximum at $K \cdot \gamma \cdot H$. The horizontal stress then gradually decreases [20], and the variation of coal body stress progresses as shown in Figure 18.

Under the influence of reverse fault, the value of stress concentration coefficient K of the mined coal body is related to the distance L from the test point to the reverse fault, which mainly includes the following two situations:

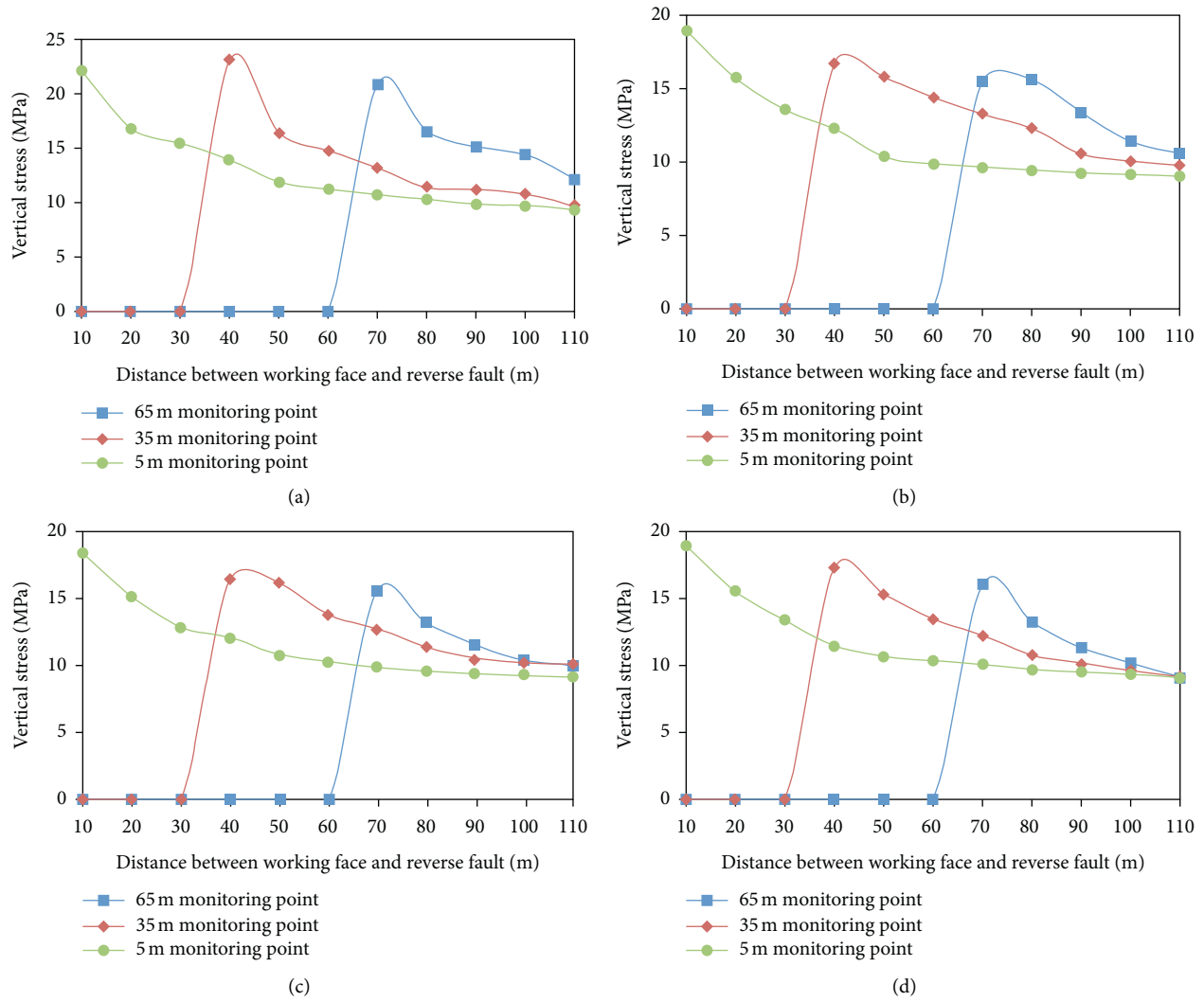


FIGURE 11: Variation curve of the vertical stresses at the monitoring points with different dip angles. (a) The dip angle of reverse fault is 30°. (b) The dip angle of reverse fault is 45°. (c) The dip angle of reverse fault is 60°. (d) The dip angle of reverse fault is 75°.

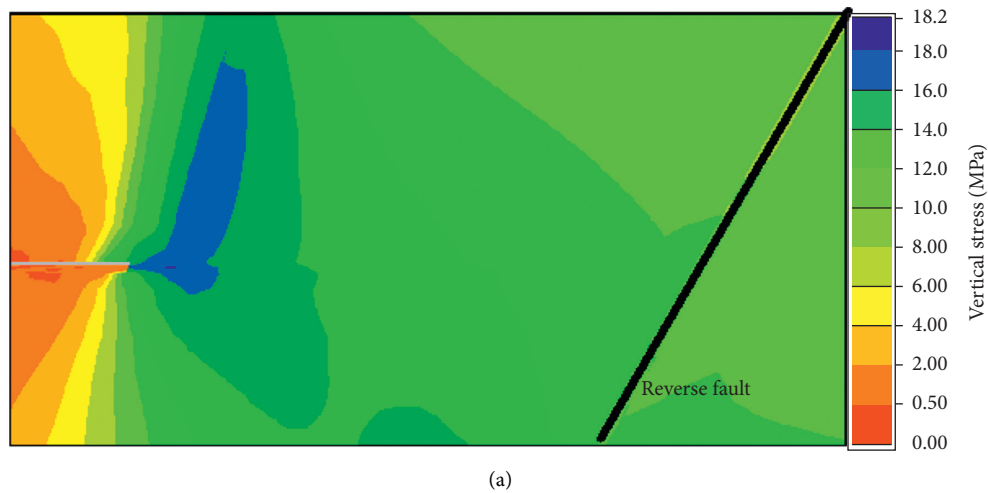


FIGURE 12: Continued.

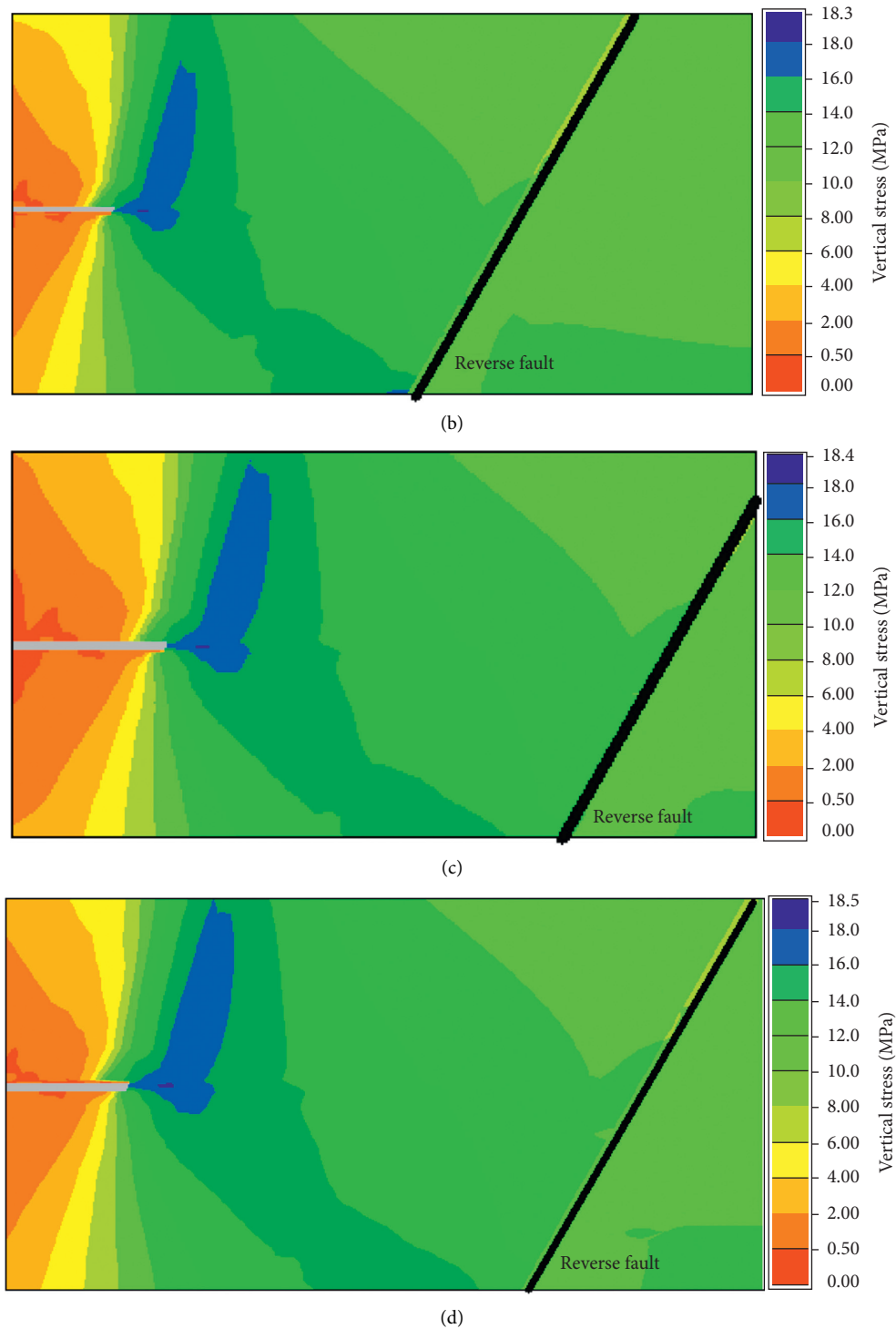
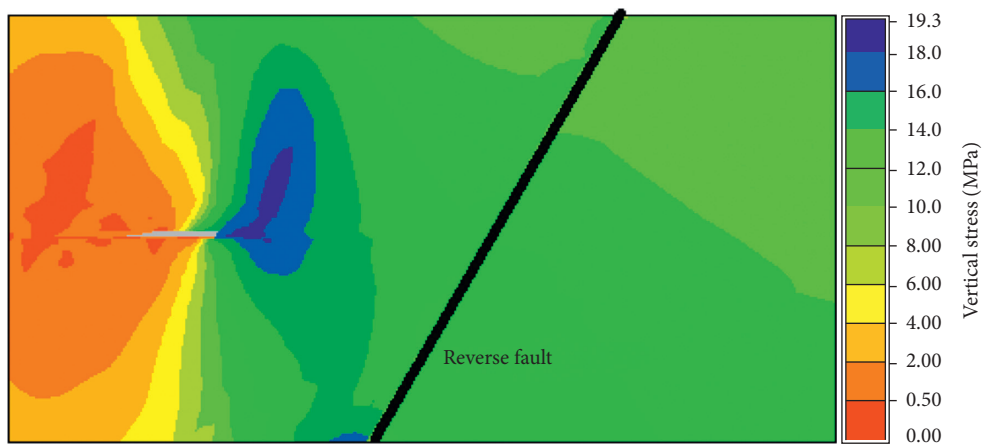


FIGURE 12: Stress distribution when the distance between working face and reverse fault is 70 m with different fault throw. (a) The throw of reverse fault is 4 m. (b) The throw of reverse fault is 10 m. (c) The throw of reverse fault is 15 m. (d) The throw of reverse fault is 20 m.

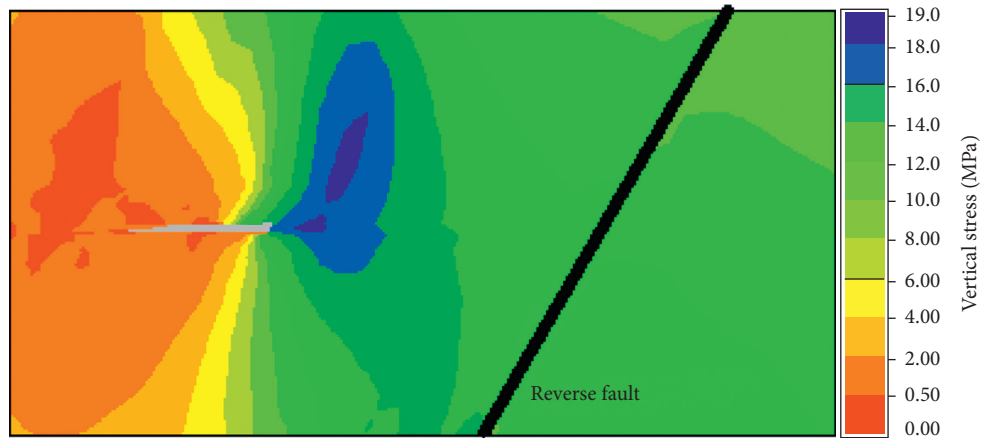
- (1) When the working face is mined along the direction facing the reverse fault, with the decrease of the distance L from the reverse fault, if the coal-bearing capacity does not exceed its strength, the coal stress in front of the working face and hence the stress concentration coefficient K will increase gradually.
- (2) When the working face is mined along the direction facing the reverse fault, with the decrease of the distance L from the reverse fault, the stress concentration magnitude of the mined coal body increases gradually at first, before decreasing, which occurs when the bearing capacity of the coal body



(a)



(b)



(c)

FIGURE 13: Continued.

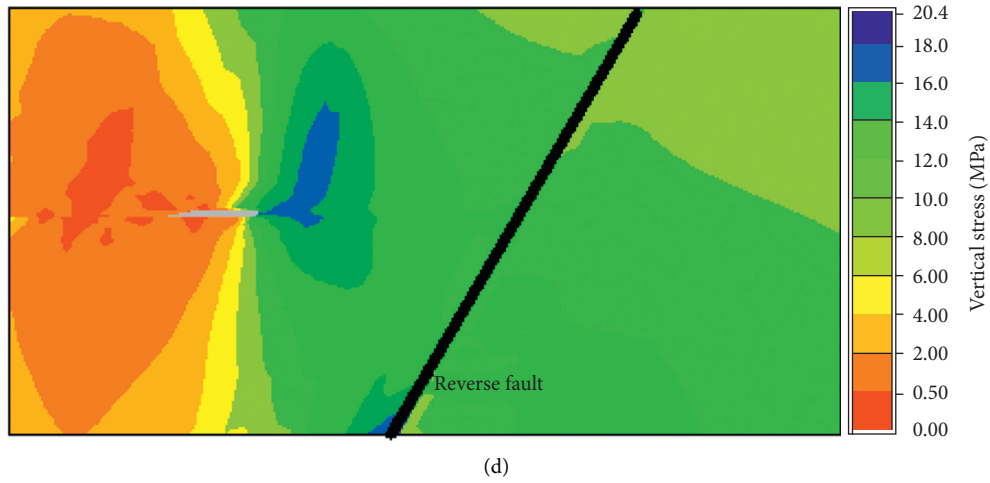


FIGURE 13: Stress distribution when the distance between working face and reverse fault is 40 m with different fault throw. (a) The throw of reverse fault is 4 m. (b) The throw of reverse fault is 10 m. (c) The throw of reverse fault is 15 m. (d) The throw of reverse fault is 20 m.

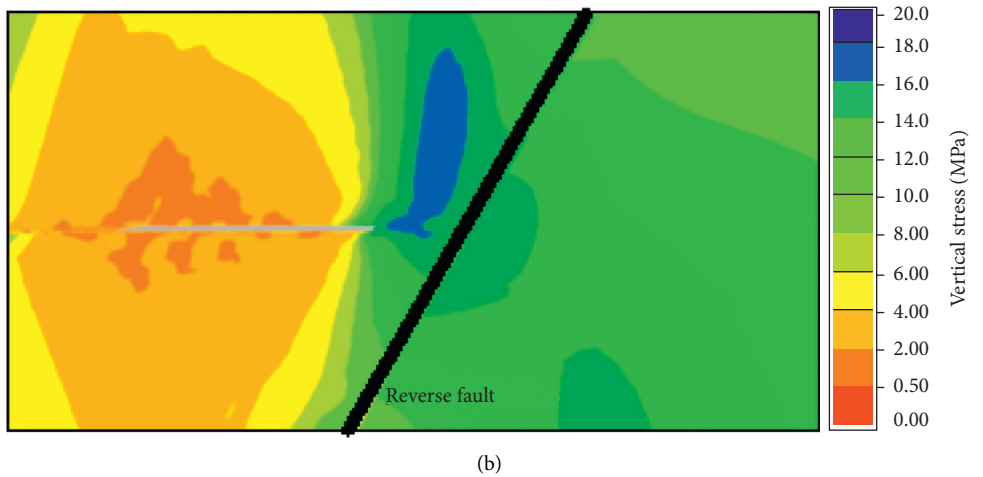
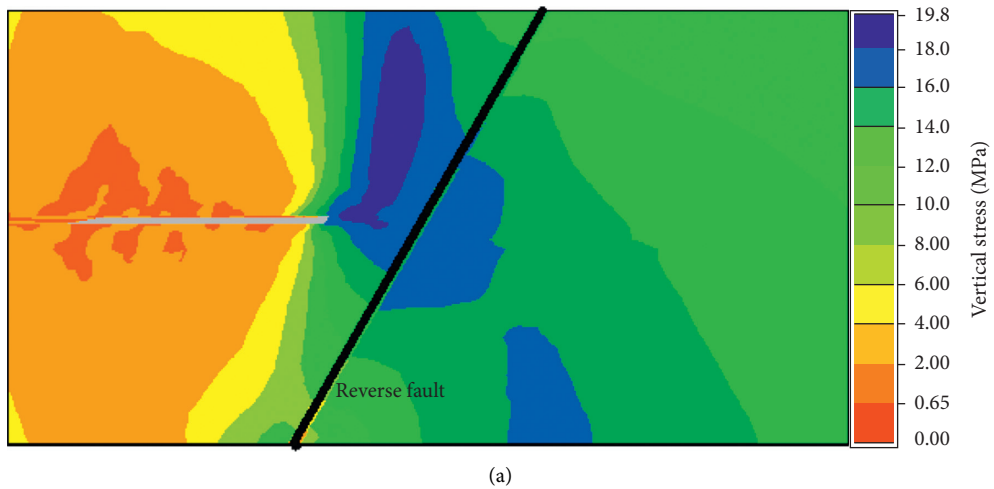


FIGURE 14: Continued.

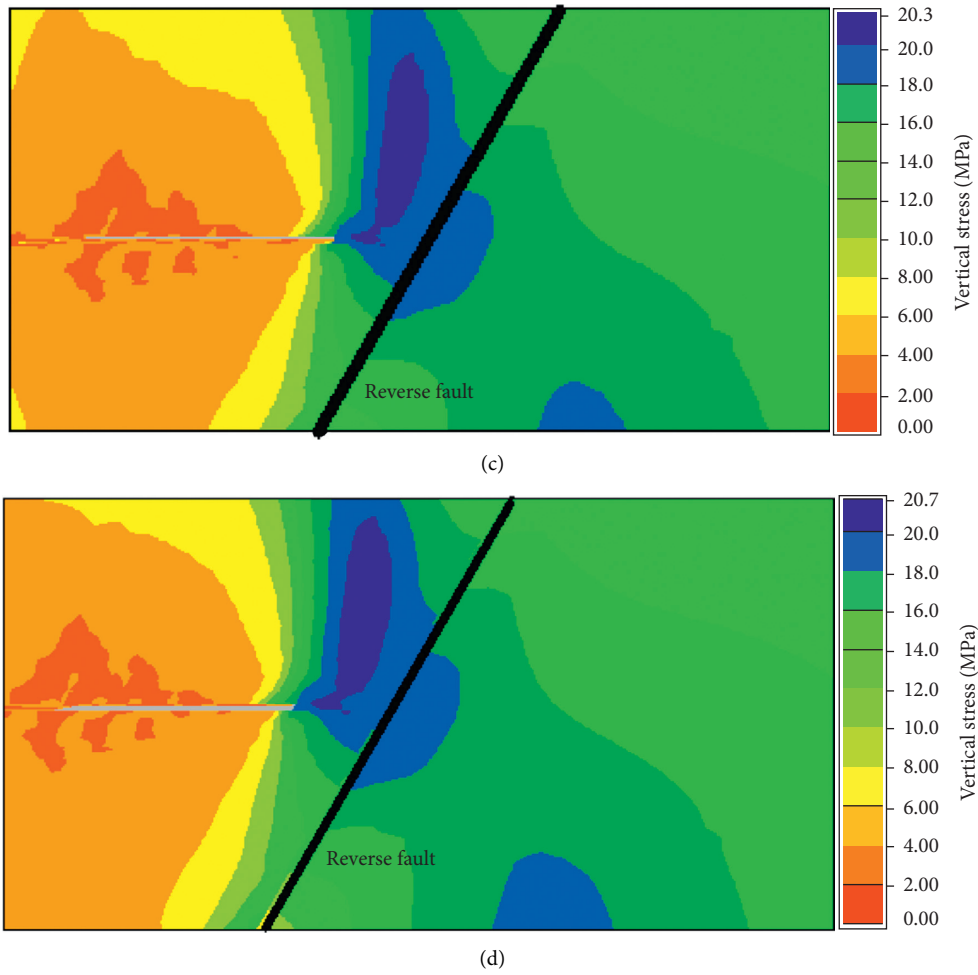


FIGURE 14: Stress distribution when the distance between working face and reverse fault is 10 m with different fault throw. (a) The throw of reverse fault is 4 m. (b) The throw of reverse fault is 10 m. (c) The throw of reverse fault is 15 m. (d) The throw of reverse fault is 20 m.

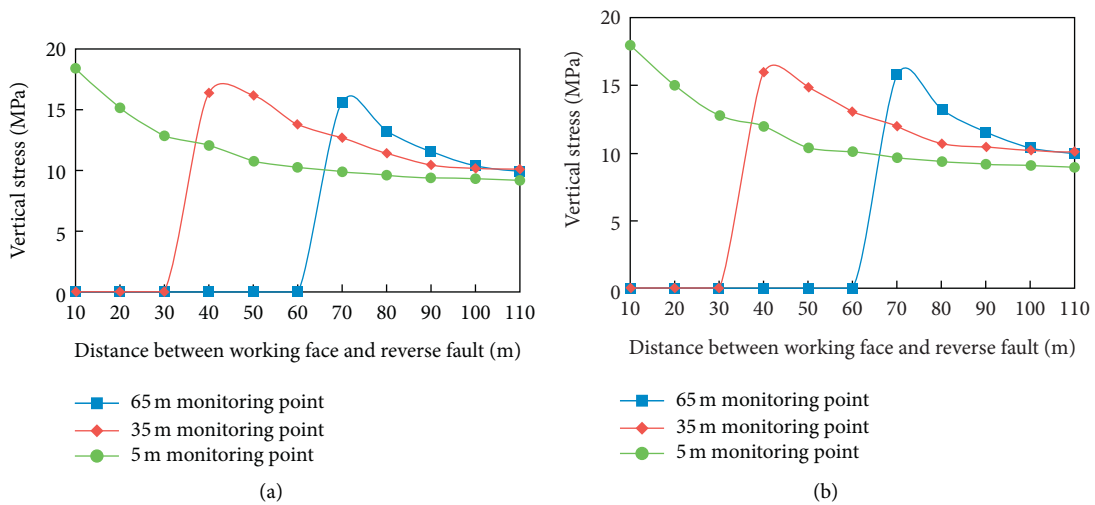


FIGURE 15: Continued.

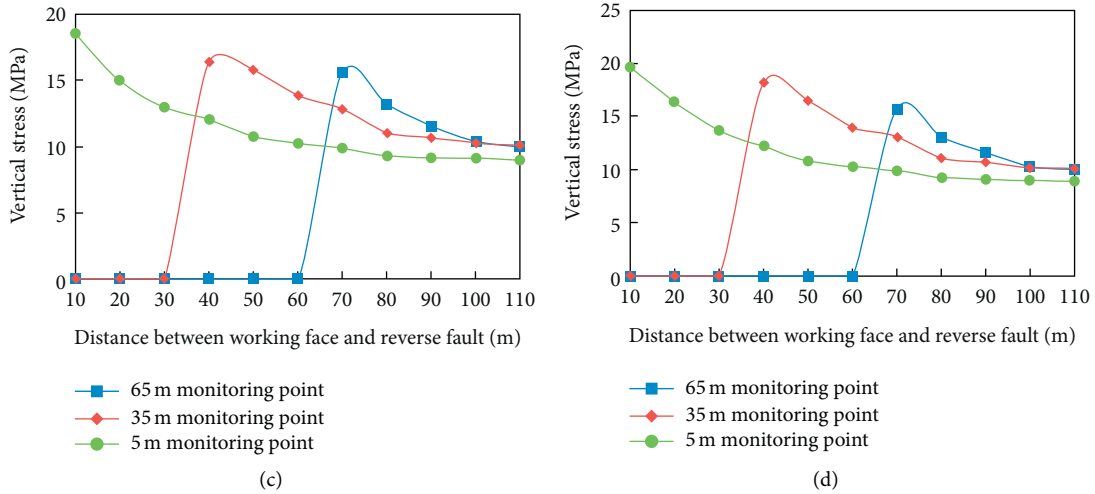


FIGURE 15: Variation curve of the vertical stresses at the monitoring points with different fault throw. (a) The throw of reverse fault is 4 m. (b) The throw of reverse fault is 10 m. (c) The throw of reverse fault is 15 m. (d) The throw of reverse fault is 20 m.

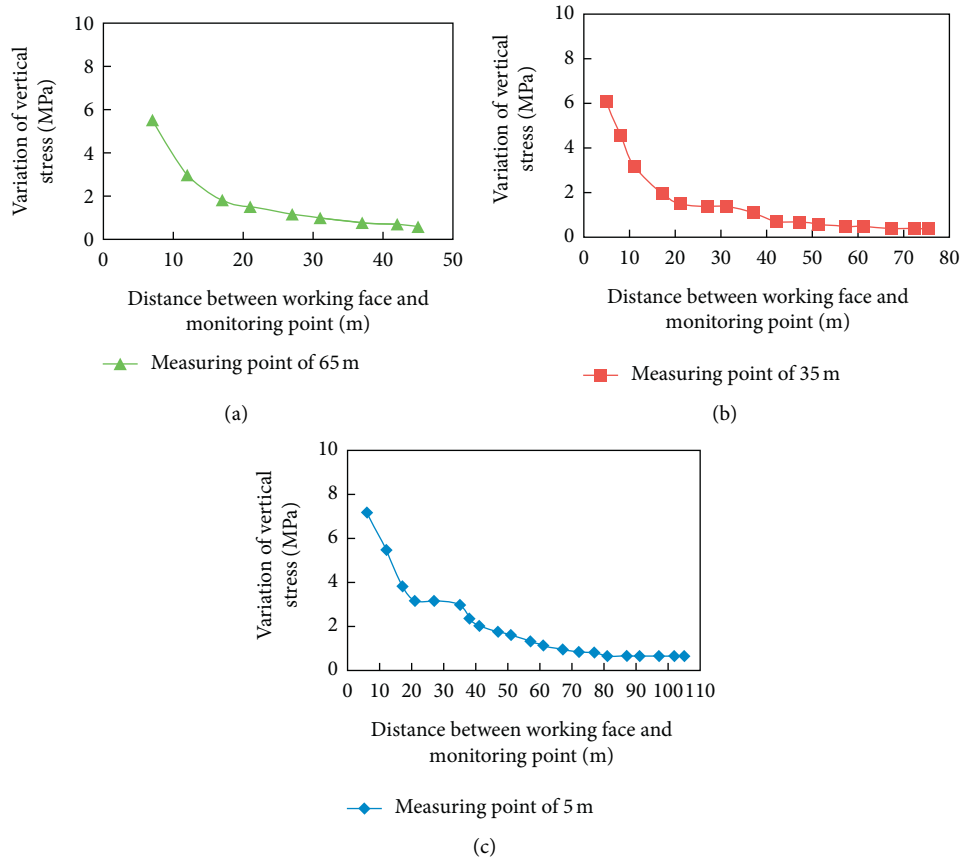


FIGURE 16: Borehole stress with working face advancing in Xinchun coal mine. (a) Change of coal stress at 65 m monitoring point. (b) Change of coal stress at 35 m monitoring point (c) Change of coal stress at 5 m monitoring point.

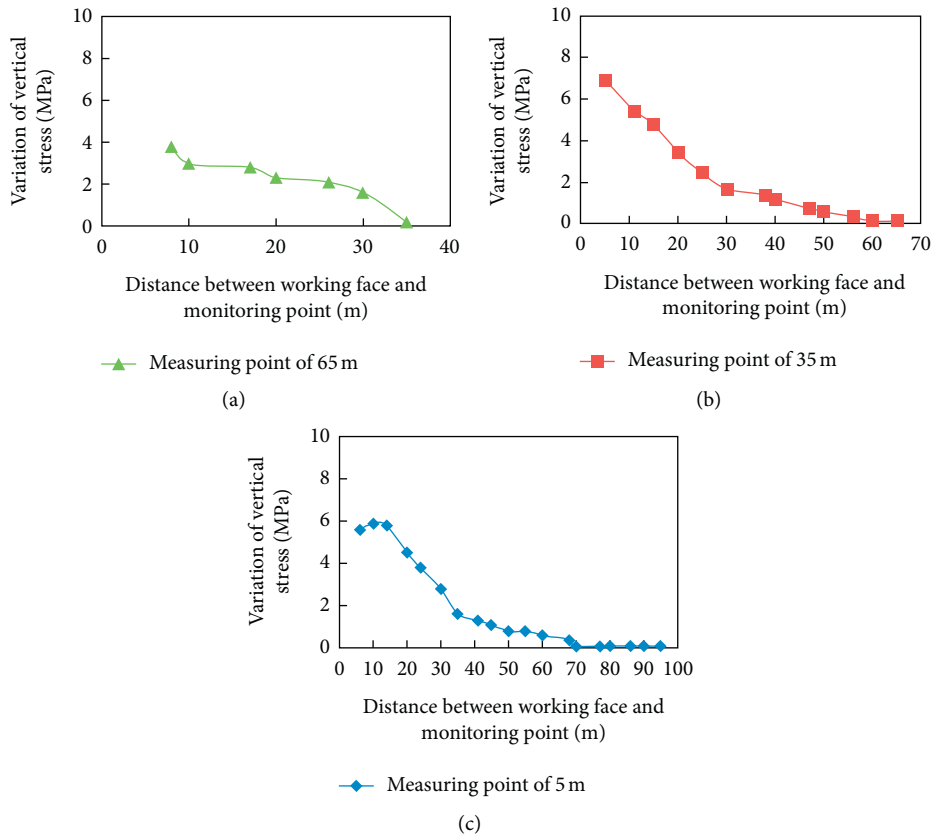


FIGURE 17: Borehole stress with working face advancing in ZuoQiuka coal mine. (a) Change of coal stress at 65 m monitoring point. (b) Change of coal stress at 35 m monitoring point (c) Change of coal stress at 5 m monitoring point.

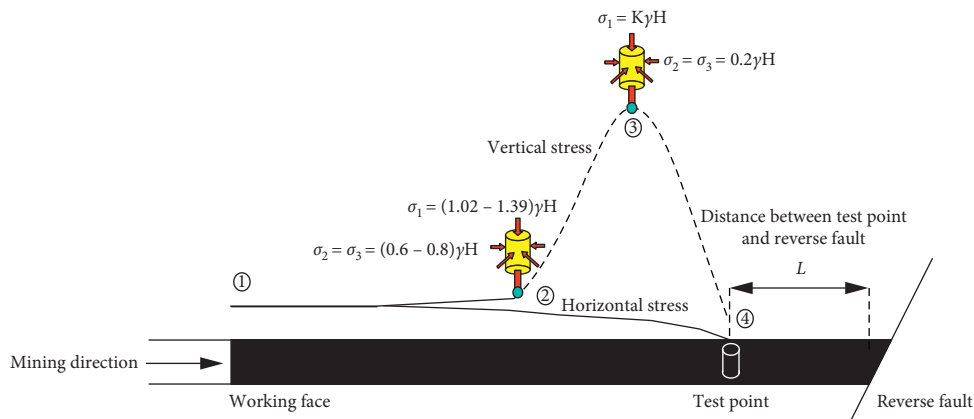


FIGURE 18: Stress change of coal in reverse fault area under dynamic influence.

exceeds its strength, causing the coal body to fail and lose its load-bearing capacity, leading to the decrease in the stress concentration coefficient K .

6. Conclusions

- (1) The mechanical analysis model of reverse fault-affected mined coal body was established, the coal stress characterization equation was derived, the coal stress distribution was calculated, and the
- (2) FLAC^{3D} was used to study the stress variation trend of the mined coal body, and the accuracy of coal body stress calculated by the mechanical model was verified. It is concluded that in case of hanging-wall

Mohr-Coulomb strength criterion was applied to analyze the stability of the coal body. It could be inferred that the closer it gets to the reverse fault, the poorer is the stability of the coal body and that the stress concentration magnitude of the mined coal body is affected by the strength of the coal body.

mining, the stress concentration of the mined coal body decreases with the increase of reverse fault dip angle and increases with the increase of reverse fault throw. Also, the stress concentration magnitude in the case of footwall mining is less than that of hanging-wall mining. The choice to mine the hanging wall or footwall and the parameters of reverse fault affect the stress concentration magnitude of the coal body. At the same time, combined with the field monitoring results of the coal body stress measured by intrinsically safe GZY25 borehole stress sensors, it has been verified that the coal body stress concentration magnitude may either increase or decrease, depending on the actual conditions.

- (3) Based on theoretical analysis, numerical simulation, and field test results, when the mining activity on the working face proceed towards the reverse fault, the vertical stress of the coal body initially demonstrates a significant rise as the distance from the reverse fault lessens. At any point during this stage, the vertical stress can be generalized as $(1.02-1.39)\gamma \cdot H$. Going into the latter stage, once the test point falls on the stress concentration area in front of the working face, the vertical stress will reach its maximum, which can be acquired by $K \cdot \gamma \cdot H$. Moreover, the stress concentration coefficient K is related to the distance L from the reverse fault, and two kinds of changes may take place. Firstly, if the coal-bearing capacity does not exceed its strength, the coal stress in front of the working face, and hence the stress concentration coefficient of the mined coal body, will increase gradually. Secondly, the stress concentration magnitude of mining coal body gradually increases first, before decreasing after the coal body bearing capacity exceeds its strength, during which the coal body experiences structural failure and loses its load-bearing capacity, ultimately resulting in the decline of the stress concentration coefficient.

Data Availability

The data used to support the findings of this study are available from the corresponding author upon request.

Conflicts of Interest

The authors declare that there are no conflicts of interest regarding the publication of this paper.

Acknowledgments

This work was supported by the National Key R&D Program of China (no. 2018YFC0807900), the Science and Technology Innovation Project of China Coal Technology and Engineering Group (no. 2018-2-MS022), and the Science and Technology Innovation Project of China Coal Technology and Engineering Group (no. 2018QN010).

References

- [1] Y. Cao, *Coal Mine Geology*, China University of Mining and Technology Press, Xuzhou, China, 2014.
- [2] X. Chen, W. Li, and X. Yan, "Analysis on rock burst danger when fully-mechanized caving coal face passed fault with deep mining," *Safety Science*, vol. 50, no. 4, pp. 645–648, 2012.
- [3] J.-F. Ritz, S. Baize, M. Ferry et al., "Surface rupture and shallow fault reactivation during the 2019 Mw 4.9 Le Teil earthquake, France," *Communications Earth & Environment*, vol. 1, no. 1, 2020.
- [4] Y. Li and R. Zhou, "Analysis of mechanical characteristics and instability law of inverse fault under the influence of mining," *Earth Sciences Research Journal*, vol. 22, no. 2, pp. 139–144, 2018.
- [5] S. Dalgiç, "Tunneling in fault zones, Tuzla tunnel, Turkey," *Tunnelling and Underground Space Technology Incorporating Trenchless Technology Research*, vol. 18, no. 5, pp. 453–465, 2003.
- [6] H. O. Safari, S. Pirasteh, B. Pradhan, and H. Amid, "Geohazards analysis of Pisa tunnel in a fractured incompetent rocks in Zagros Mountains, Iran," *Arabian Journal of Geosciences*, vol. 6, no. 4, pp. 1101–1112, 2013.
- [7] S. Husen, E. Kissling, and A. V. Deschanden, "Induced seismicity during the construction of the Gotthard Base Tunnel, Switzerland: hypocenter locations and source dimensions," *Journal of Seismology*, vol. 11, no. 1, pp. 19–28, 2013.
- [8] W. Schubert, A. Fasching, and A. Goricki, "Tunnelling in fault zones-state of the art," *Tunnelling and Underground Space Technology*, vol. 21, no. 3-4, pp. 376–377, 2006.
- [9] H. Moulouel, A. Bouchelouh, R. Bensalem et al., "The Mahelma fault: a secondary structure of the Sahel anticline?" *Arabian Journal of Geosciences*, vol. 13, no. 15, 2020.
- [10] M. Ranjbarnia, M. Zaheri, and D. Dias, "Three-dimensional finite difference analysis of shallow sprayed concrete tunnels crossing a reverse fault or a normal fault: a parametric study," *Frontiers of Structural and Civil Engineering*, vol. 14, pp. 998–1011, 2020.
- [11] M. Sabagh and A. Ghalandarzadeh, "Centrifuge experiments for shallow tunnels at active reverse fault intersection," *Frontiers of Structural and Civil Engineering*, vol. 14, pp. 731–745, 2020.
- [12] L. Zhao, X. Shen, C. Geng, and X. Hu, "Analysis and solution of abnormal fault of data storage based on NAND-flash," *Science Discovery*, vol. 8, no. 4, 2020.
- [13] Y. Fukushima and N. Ghayournajarkar, "Determination of the dipping direction of a blind reverse fault from InSAR: case study on the 2017 sefid sang earthquake, northeastern Iran," *Earth Planets and Space*, vol. 72, no. 1, p. 15, 2020.
- [14] M. Fadaee, F. Farzaneganpour, and I. Anastasopoulos, "Response of buried pipeline subjected to reverse faulting," *Soil Dynamics and Earthquake Engineering*, p. 132, 2020.
- [15] E. Wang, Q. Shao, Y. Du et al., "Genesis mechanism and distribution of structural coal on two sides of reverse fault," *Mining Safety & Environmental Protection*, vol. 37, no. 1, pp. 4–6, 2010.
- [16] M. Qian, P. Shi, and J. Xu, *Mine Pressure and Rock Strata Control*, China University of Mining and Technology Press, Xuzhou, China, 2010.
- [17] C. Liang, *Research on Failure Strain and Permeability Evolution of the Coal Ahead of Working Face and Its Application*, China University of Mining and Technology, Beijing, China, 2016.

- [18] J. Jiang, Q. Wu, and H. Qu, "Mining stress evolution and fault activation characteristics of reverse faults under hard and thick strata," *Journal of Coal Science*, vol. 36, no. 7, pp. 1067–1074, 2011.
- [19] J. Jiang, Q. Wu, and Q. Hua, "Evolutionary characteristics of mining stress near the hard-thick overburden normal faults," *Journal of Mining and Safety Engineering*, vol. 31, no. 6, pp. 881–887, 2014.
- [20] H. Xie, H. Gao, J. Liu et al., "Study on mining dynamic behavior under different mining conditions," *Journal of Coal Science*, vol. 36, no. 7, pp. 1067–1074, 2011.

Research Article

Effects of Cyclic Loading on the Pore Structure of Anthracite Coal

Dong Wang,^{1,2,3} Tie Li,¹ Zhiheng Cheng ,⁴ and Weihua Wang^{2,3}

¹State Key Laboratory of High-Efficiency Mining and Safety of Metal Mines, Ministry of Education, School of Civil and Resource Engineering, University of Science and Technology Beijing, Beijing 100083, China

²China Coal Research Institute, Beijing 100013, China

³State Key Laboratory of Coal Mining and Clean Utilization (China Coal Research Institute), Beijing 100013, China

⁴School of Safety Engineering, North China Institute of Science and Technology, Beijing 101601, China

Correspondence should be addressed to Zhiheng Cheng; an958158@163.com

Received 15 February 2021; Revised 11 April 2021; Accepted 17 April 2021; Published 29 April 2021

Academic Editor: Gong-Da Wang

Copyright © 2021 Dong Wang et al. This is an open access article distributed under the Creative Commons Attribution License, which permits unrestricted use, distribution, and reproduction in any medium, provided the original work is properly cited.

In the process of improving coalbed permeability through pulse hydraulic fracturing, the cyclic loading effect influences the characteristics of micropores in coal matrix, thus affecting the process of gas migration. Therefore, it is essential to investigate the effect of cyclic loading on the pore structure of coal. Seven groups of loading tests at different frequencies and amplitudes were conducted on anthracite coal obtained from Shanxi Province, China, using a fatigue-testing machine. Subsequently, using a PoreMaster GT-60 Mercury-intrusion apparatus, the influence of the frequency and amplitude on the structural characteristics (including mercury-injection and mercury-ejection curves, pore size distribution, porosity, and specific surface area) of pores in coal samples was analyzed. Finally, the law and mechanism of action of the loading frequency and amplitude on pores in coal samples were comprehensively analyzed. The test results showed that, in the case of maintaining the sine-wave amplitude unchanged during loading while altering the loading frequency, the overall porosity and pore volume rise at different degrees. The growth of the loading frequency presents a more significant promotive effect on the initiation and development of pores and fractures. Moreover, it drives the transformation of micropores and transition pores into mesopores and macropores, thus increasing the proportion of seepage pores. Under the condition of large sine-wave amplitude during loading, macropores and mesopores are subjected to the repeated action of the external force, thereby reducing the overall porosity. In addition, the volume of the seepage pores declines, and the number of the coalesced pores decreases. Finally, in light of these results, the implications of frequency and amplitude selection in the process of pulse hydraulic fracturing are discussed. Therefore, the results of this research will provide an important theoretical basis for the field application of pulse hydraulic fracturing technology in coal mines.

1. Introduction

Efficient extraction of coalbed methane (CBM) is important for the safe production of coal in many underground coal mines [1, 2]. Additionally, the extracted CBM can be used as energy, and the combustion of CBM can be part of the environmental protection plan of coal mine enterprises, because it can avoid the release of the greenhouse gas (CH₄) into the atmosphere [3–5]. However, the permeability of coal seams in China is generally low, which is unfavorable for the production and utilization of CBM [6, 7]. At present, hydraulic fracturing has been widely used to improve the yield of CBM reservoirs [8–10]. The technology can enhance

the permeability of coal seams by increasing the number and density of fractures, thus changing the structures of coal seams [11, 12]. In the past decades, hydraulic fracturing technology has been widely applied to coal mine production in numerous countries, including China, USA, Canada, and Australia [13, 14].

Previous research has shown that traditional hydraulic fracturing technologies employ a constant higher water pressure than the rock strength to fracture the rock [15]. Thus, to realize an ideal fracturing effect, traditional hydraulic fracturing requires high flow, high pressure, and large amounts of water. Moreover, proppants and certain chemical agents are typically used to improve the effect of

hydraulic fracturing and maintain the stability of the fracture. These proppants and chemical reagents may enter the formation water and, consequently, pollute and damage the CBM reservoirs [16–18]. In addition, high-pressure equipment required to perform hydraulic fracturing in underground coal mines should have more complex sealing requirements, which significantly increases the safety risks. Utilization of the pulse hydraulic fracturing technology has been proposed to overcome this limitation [19]. Under a low impulsive load, more secondary cracks will be generated and the surface area of coal increases to promote gas desorption. At present, this technology has been the focus of research.

During pulse hydraulic fracturing, the persistent pulse waves propagate into coal rock, and the periodically alternating stresses generated under the peak pressure and base pressure are repeatedly applied to the coal mass. Eventually, due to the influence of cyclic loads at different frequencies, the fatigue failure of pores and cracks in coal gradually becomes more obvious, thus promoting the formation of new pores and cracks. Li et al. [20] investigated the mechanism of crack propagation during pulse hydraulic fracturing by utilizing the triaxial mechanical test system and acoustic emission. Similarly, Li et al. [21] carried out field testing at Yuwu Coal Mine (Shanxi Province, China) with pulse hydraulic fracturing. The S2107 coal seam was selected as the test coal seam, showing high gas content and coal and gas outburst hazard. The pulse hydraulic fracturing technology was used in the cross-measure boreholes from the high-level roadway to the driving roadway to improve the effect of gas drainage and ensure safety during the production. The test results revealed that the amount of gas extracted from the coal seams treated with pulse hydraulic fracturing separately increases by 3.32- and 3.07-fold relative to ordinary boreholes. Wang et al. [22] analyzed the influence of the pulse pressure on the formation and propagation of cracks in coal through numerical simulation. The results showed that the radius of influence of pulse hydraulic fracturing in coal seams reaches 8 m, and the total amount of the gas extraction rises by 3.6-fold; the flow of gas extraction reaches ≤ 50 L/min. However, the above studies did not thoroughly investigate the mechanism of pulsating hydraulic slitting at the microlevel.

As a special porous medium, natural coal mass exhibits many microporous characteristics, including porosity, pore size distribution, and pore volume [23–25]. The pore characteristics of coal are closely related to the adsorption capacity of gas in coal seams and also greatly influence the dynamic characteristics of gas [26–29]. The effect of cyclic loading may influence the characteristics of micropores in coal matrix in the process of improving permeability of coal seams through pulse hydraulic fracturing. Thus, cyclic loading affects the processes of gas migration, such as gas desorption, diffusion, and seepage in coal seams. Therefore, investigating the influence of cyclic loading on the characteristics of micropores in coal may provide an important theoretical basis for analyzing the microdynamic characteristics of gas during pulse hydraulic fracturing.

Based on the above evidence, seven groups of loading tests at different frequencies and amplitudes were performed

on anthracite coal obtained from Shanxi Province, China, using a fatigue-testing machine. Afterwards, by applying a PoreMaster GT-60 Mercury-intrusion apparatus, the influence of the frequency and amplitude on the structural characteristics (e.g., mercury-injection and -ejection curves, pore size distribution, porosity, and specific surface area) of pores in coal samples was analyzed. Finally, the law and mechanism of action of the loading frequency and amplitude on pores in coal samples were comprehensively analyzed. The aim of this research study was to provide an important theoretical basis for the field application of pulse hydraulic fracturing technology in coal mines.

2. Materials and Methods

2.1. Preparation of Coal Samples. Anthracite coal obtained from Yangquan Mining Area in Shanxi Province, China, was used for the test. The location of Yangquan Mining Area is shown in Figure 1. The blocky coal samples were immediately sealed after collection from the fresh working face, packed, and sent to the laboratory.

The anisotropy of coal samples would influence the cyclic loading tests. Hence, the coal samples were crushed and processed into a briquette prior to testing and analysis for pores. The briquette is prepared mainly according to the following two steps: (1) (preparation of pulverized coal) the coal blocks were ground into fine powder particles by successively using a crusher and a grinder; afterwards, the powder particles were screened using standard sieves to attain particles of pulverized coal with pore size ranging 0.2–0.25 mm; and (2) (molding under compression) 200 g of pulverized coal and some water was loaded into a mold (diameter: 50 mm) and pressed for 20 min under the forming pressure of 100 MPa using a material testing machine with 200 t. Through this approach, coal samples were formed (the process required 10 min to load the pressure to the preset value at the loading rate of 20 kN/min).

2.2. Cyclic Loading Test. As shown in Table 1, seven groups of loading conditions were designed to investigate the influence of cyclic loading at different frequencies and amplitudes on the pore structure of anthracite coal.

During cyclic loading, a sample under loading for 20 min subjected to the forming pressure together with the mold was placed onto the fatigue-testing machine (Figure 2). According to the loading conditions in Table 1, the coal sample was loaded for 6 h, with sine waves as the loading waveform. After the loading was completed, the mold and sample were removed; furthermore, the mold was opened using a spanner to extract the final sample, whose length was measured with a Vernier caliper. Finally, after being subjected to loading, the coal particles with size ranging 1–3 mm were obtained from the sample using a knife, to be used as the test coal samples for the Mercury-intrusion test.

2.3. Determination of Pore Structure. The test was performed using the PoreMaster GT-60 Mercury-intrusion apparatus (Quantachrome Instruments, Boynton Beach, FL, USA) to

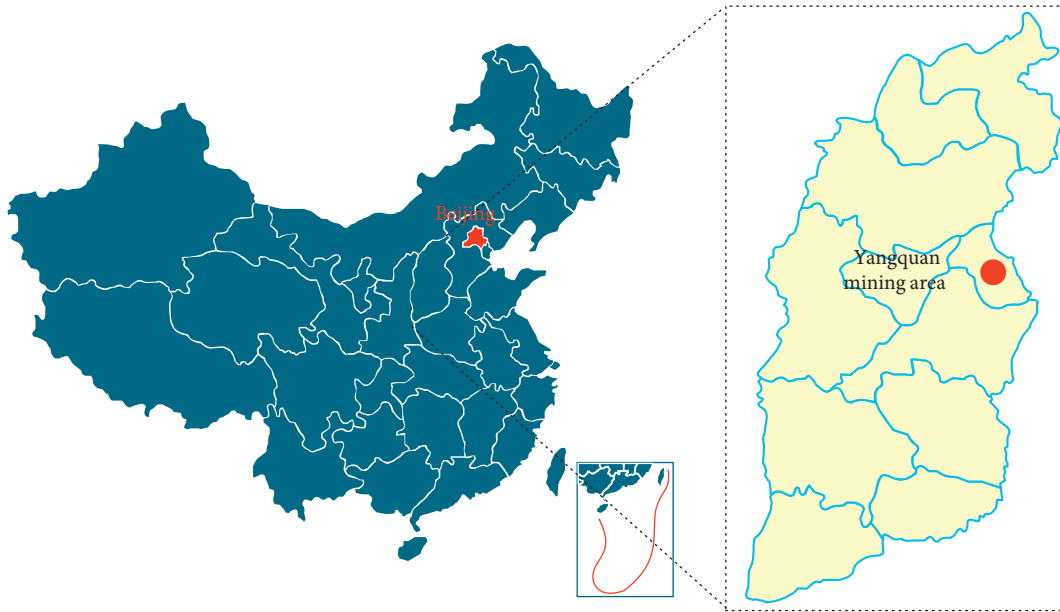


FIGURE 1: Location of Yangquan mining area.

TABLE 1: Loading conditions for the cyclic loading tests.

Group	Loading frequency (Hz)	Test condition		Loading time (h)
		Pressure amplitude during loading (MPa)		
1	10	12–18		6
2	7			
3	4			
4	7	10–20		
5	7	14–16		
6	—	15		
7	—	—		

Note. In the test groups 1–5, only the frequency or amplitude was changed; in the control group 6, the frequency or amplitude was fixed; in the blank control group 7, cyclic fatigue loading was not performed.

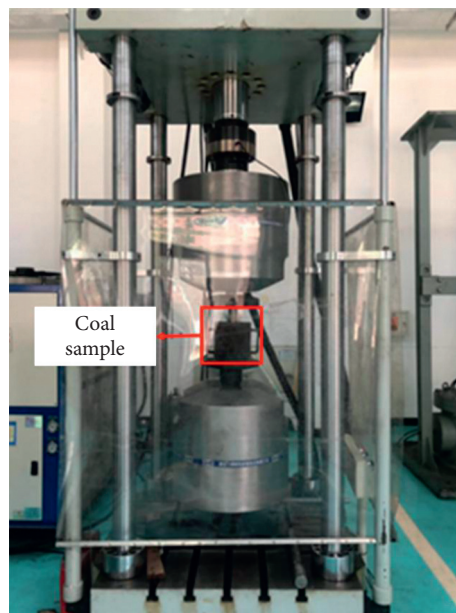


FIGURE 2: Fatigue-testing machine.

measure the volume of pores with diameter ranging 1,000–0.0035 μm (Figure 3). The apparatus is equipped with two low-pressure ports and two high-pressure ports. It is necessary to apply the low-pressure port and Mercury-injection station when measuring the volume of pores with size ranging 7–99 μm . The low-pressure examination port (under pressure of 0.2–50 psi) was used to inject Mercury with a sample tube, which measured the volume of pores with diameter ranging 1.0–4.3 μm . The high-pressure examination port (Figure 3) is utilized under pressure of 20–60,000 psi. The test data were processed using Washburn's equation [30] shown as follows:

$$p_c = \frac{2\sigma \cos \theta}{r}, \quad (1)$$

where p_c , σ , θ , and r refer to the additional pressure (MPa) of the applied liquid, surface tension (dyn/cm^2) of Mercury, wetting contact angle of Mercury, and radius (nm) of the pore throat, respectively.

Washburn's equation provides a simple relationship between the pressure and pore radius. Therefore, during the Mercury-intrusion test, it was feasible to attain the distribution of the pore radius by tracing the relationship between the amount of Mercury injected into pores and the constantly increasing pressure. Pores with different sizes show diverse degrees of resistance to Mercury; higher external pressures indicate smaller pore sizes in coal to which Mercury can enter [31]. Some other analysis parameters (e.g., specific surface area and porosity) can also be obtained by analyzing changes in the volumes of injected and ejected Mercury and pressures [32]. Of note, the pore distribution in coal samples under different loading conditions compared in this study was investigated the absence of any stress. Therefore, the influence of cyclic loading on pores can be determined to a certain extent through comparison before and after the stress-free condition.

3. Results and Discussion

3.1. Influence of Different Loading Frequencies on Pore Characteristics of Coal Mass. To investigate the influence of different loading frequencies on the pore characteristics of coal mass, tests were performed at loading frequencies of 4, 7, and 10 Hz and loading amplitude ranging 12–18 MPa (frequency magnitude that engineering applications can achieve). Moreover, the test results were compared with those attained in the control group under a steady pressure (15 MPa).

3.1.1. Mercury-Injection and Mercury-Ejection Curves. Figure 4 shows the mercury-injection and mercury-ejection curves of samples at different loading frequencies. The mercury-intrusion curves in the test groups at different loading frequencies and the control group presented a similar shape: a large growth amplitude in the low-pressure mercury-injection stage. Under the pressure of approximately 15 MPa, the curves became gentle, and they slowly rose with increasing pressure. In contrast, the mercury-



FIGURE 3: PoreMaster GT-60 Mercury-intrusion apparatus (Quantachrome Instruments).

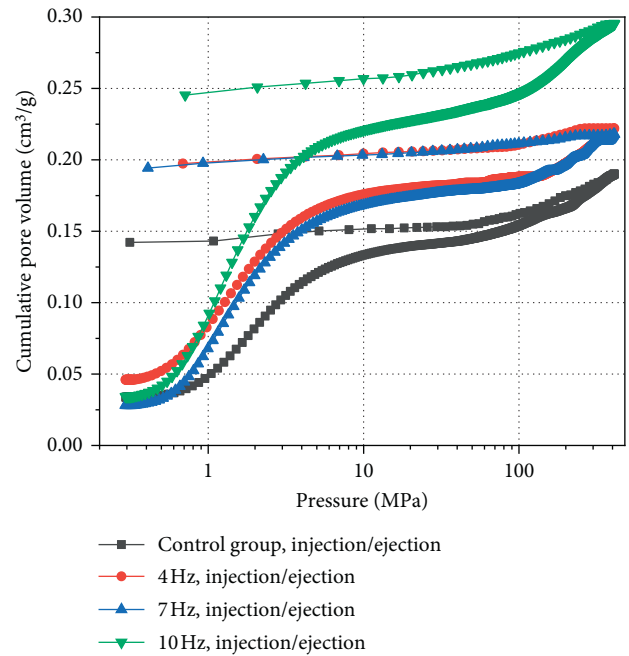


FIGURE 4: Mercury-intrusion curves of samples at different loading frequencies.

ejection curves started to separate from the injection ones under the initially high pressure, illustrating the hysteresis phenomenon. However, the final contents of Mercury injected are different, implying that the loading frequency influences the pore characteristics of coal samples to some extent. As shown in Figure 4, the highest final content of Mercury injected in the test group was shown at the loading frequency of 10 Hz, and the contents of Mercury injected in the test groups at 7 and 4 Hz differed only slightly. However, the contents of Mercury injected in the three test groups were significantly larger compared with those of the control group. It was also found that the mercury-injection and mercury-ejection curves in the two sample groups at the loading frequencies of 7 and 4 Hz were similar. This finding

indicates that, with the same amplitude, the pores in samples increase when loading sine waves with different frequencies are used. Moreover, the most remarkable influence was observed at the loading frequency of 10 Hz. In contrast, there was no great difference shown at low loading frequencies. Additionally, in terms of the difference in cumulative contents of the Mercury injected and ejected, the differences of the test groups at different loading frequencies were obviously larger than those of the control group. This result implies that when loading sine waves at different frequencies are used, the pores in samples favorably develop, and the proportion of seepage pores increases, thus optimizing the connectivity of pores.

3.1.2. Pore Size Distribution. Figure 5 shows the pore size distribution under four loading conditions, demonstrating a relatively similar overall shape to that of the control group. The pore size distribution was relatively concentrated, and the corresponding pore size ranges of two peaks were approximated; however, the peaks of the size range of the seepage pores in several test groups marginally shifted rightward; higher loading frequencies were associated with larger shift amplitudes. In other words, the peak pore volume slightly varied towards the range of macropores. The difference is that the global pore volume of the coal samples loaded with sine waves at different frequencies rose at different amplitudes, in which the pore volume of the test group at the loading frequency of 10 Hz showed the most significant growth amplitude, followed by the test groups at 7 and 4 Hz. In terms of the distribution of seepage pores and adsorption pores, the volumes of the former greatly increased, while those of the latter were similar.

3.1.3. Porosity and Percentage of Pore Volume. The division scheme of the pore size proposed by Hodot was employed in the test; pores were divided into macropores (>1,000 nm), mesopores (100–1,000 nm), transition pores (10–100 nm), and micropores (<10 nm) [33]. Micropores are space-storing gas; transition pores provide the space for gas diffusion; mesopores offer the space for slow gas flow; and macropores are space for strong flow of gas. Therefore, scholars also termed the pores with a size <100 nm (i.e., micropores and transition pores) adsorption pores, while mesopores and macropores with a size >100 nm are termed seepage pores [28, 34].

Table 2 displays the comparison data of the percentage of the pore volume and porosity under four loading conditions. In terms of the total porosity, the overall porosities of the samples loaded with sine waves at different frequencies increased slightly; higher loading frequencies were linked to higher total porosities. This indicates that the porosities of coal samples are markedly enhanced after performing cyclic loading with sine waves at different frequencies. Regarding the classification based on the pore size (Figure 6), the corresponding porosities contributed by pores of various size ranges also varied at different amplitudes. The porosities contributed by seepage pores delivered a large growth amplitude: it nearly doubled in the test group at 10 Hz, while

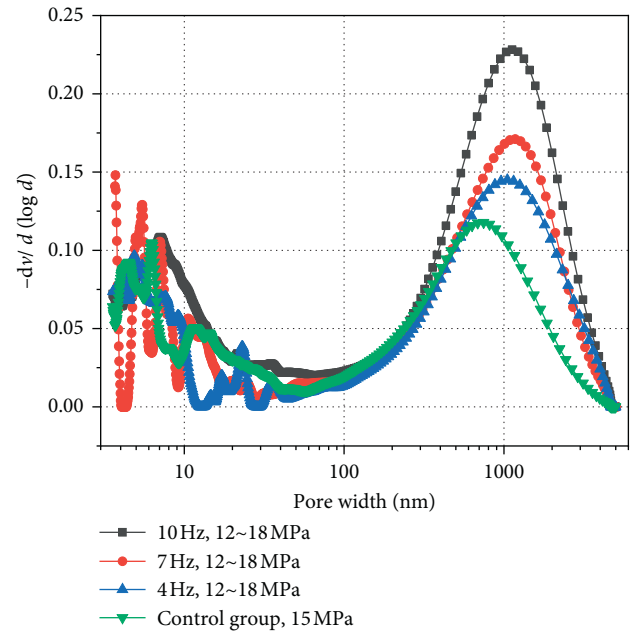


FIGURE 5: Density functions of pore volume distribution at different loading frequencies.

those in the test groups at 7 and 4 Hz increased by 3.41% and 2.04%, respectively. The porosities contributed by adsorption pores exhibited a nonsignificant increase: those in the test groups at 4 and 7 Hz hardly differed from those in the control group, and only the porosity contributed by adsorption pores in the test group at 10 Hz was slightly increased.

Table 3 shows the percentages of pore volume at different loading frequencies. The volume ratio of the adsorption pores to seepage pores in the control group was approximately 1 : 2. In contrast, the volume ratios of the adsorption pores to seepage pores in several test groups were approximately 1 : 3, and the proportion of the adsorption pores markedly decreased. This shows that loading sine waves with different frequencies can promote the expansion of pores and even fractures in coal samples. As a result, micropores and transition pores develop into mesopores and macropores, and new pores and fractures appear, thereby significantly improving the porosity of coal mass. However, the amplitude at which new pores and fractures initiate is lower than that at which pores expand. Thus, the porosity contributed by the adsorption pores nonsignificantly increases, while that contributed by seepage pores markedly rises.

3.1.4. Specific Surface Areas of Pores. The specific surface area of pores in coal mass is an important parameter for describing the pore characteristics. It is an important factor influencing the adsorption and desorption properties of gas in coal mass [5, 35, 36]. Figure 7 shows the distribution of the specific surface area of pores with the unit diameter under different loading frequencies, that is, the change in the relationship between the distribution density function $ds(d)$ for the specific surface area and the diameter d . The development trend of curves shown in Figure 8 illustrates that

TABLE 2: Percentages of the pore volume and porosities of coal mass at different loading frequencies.

Loading condition		Porosity (%)				
Frequency (Hz)	Amplitude (MPa)	Micropores (<10 nm)	Transition pores (10–100 nm)	Mesopores (100–1,000 nm)	Macropores (>1,000 nm)	Porosity (%)
4	12–18	2.42	0.69	2.06	7.55	12.71
7		2.02	1.42	5.15	5.83	14.41
10		3.15	2.11	5.88	8.68	19.81
—	15	2.15	1.60	4.40	3.18	11.32

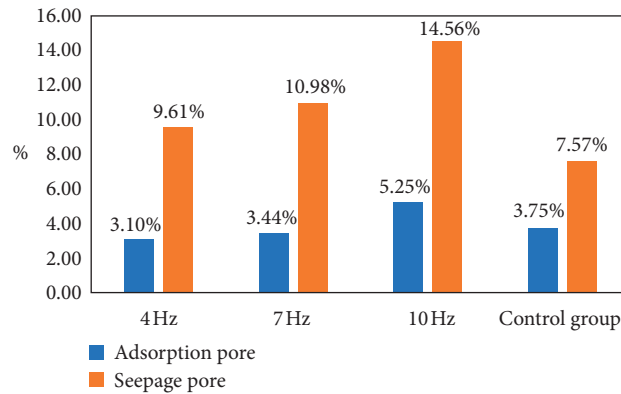


FIGURE 6: Distribution of the porosities contributed by adsorption and seepage pores at different loading frequencies.

TABLE 3: Percentages of the pore volume at different loading frequencies.

Loading condition		Percentage of the pore volume (%)					
Frequency (Hz)	Amplitude (MPa)	Micropores	Transition pores	Adsorption pores	Mesopores	Macropores	Seepage pores
4	12–18	18.31	5.41	23.72	41.57	34.72	76.28
7		14.00	9.27	23.27	39.88	36.85	76.73
10		14.91	11.76	26.67	37.20	36.13	73.33
—	15	16.70	17.15	33.85	47.66	18.49	66.15

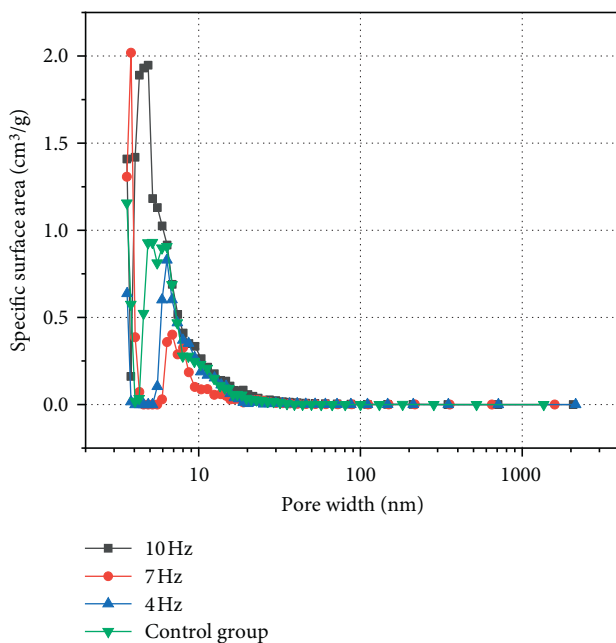


FIGURE 7: Distribution densities of the specific surface area of pores in coal mass at different loading frequencies.

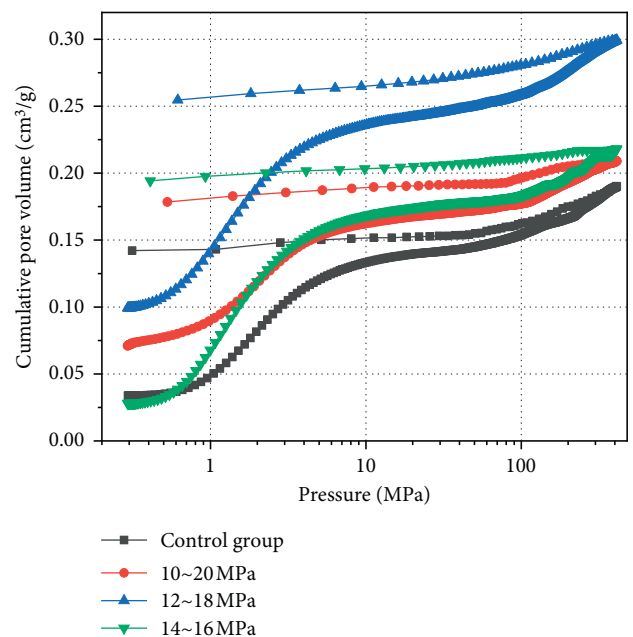


FIGURE 8: Mercury-intrusion curves of samples at different loading amplitudes.

the distribution densities of the specific surface area of all samples in the test were generally increased at first. Subsequently, they were reduced with the increasing pore size; they all reached the maximum before the pore size reached 10 nm. The peak in the test group at 10 Hz was observed at 4.57 nm, and the two peaks in the test group at 7 Hz separately appeared at 3.82 nm and 6.87 nm; the peak in the test group at 4 Hz was found at 6.37 nm, while that in the control group appeared at 6.36 nm. The growth of the distribution density shows that the growth rate of the cumulative specific surface area of pores in coal samples was gradually accelerated, and the specific surface area reached the peak at the peak of the distribution density. At the peak of the distribution density, the number of pores in coal samples with the corresponding size was the largest, or the length of pores was the largest, and the specific surface area was the largest. Based on this condition, the pores presented the strongest capacity of gas storage; in contrast, the capacity of pores for storing gas was gradually reduced.

Based on this evidence, the following conclusions can be drawn: the difference in loading frequencies influences the pore characteristics of coal samples to some extent; the pore volume generally increases significantly; although mesopores constitute the majority, followed by macropores, micropores, and transition pores, the proportions of mesopores and macropores increase, whereas those of micropores and transition pores slightly decline. This implies that the change in loading frequency exposes the coal mass to long-term fatigue loading. As a result, internal pores or fractures develop, and some micropores and transition pores are expanded and transformed into mesopores and macropores in the loading process; moreover, new pores and fractures are generated.

3.2. Influence of Different Loading Amplitudes on Pore Characteristics of Coal Mass. To investigate the influence of different loading amplitudes on the pore characteristics of coal mass, tests were carried out by separately selecting loading amplitudes (10–20, 12–18, and 14–16 MPa) and loading frequency (7 Hz). Furthermore, the results of the test were compared with those of the control group with a steady pressure (15 MPa) to analyze the influence law of the change of the loading amplitudes on the pore characteristics of coal samples.

3.2.1. Mercury-Injection and Mercury-Ejection Curves. Figure 8 shows the mercury-intrusion curves concerning the relationship between the cumulative content of Mercury injected in samples and mercury-injection and mercury-ejection pressures after loading sine waves at different amplitudes and frequency of 7 Hz. The curve in the control group under a steady pressure of 15 MPa was utilized as the reference curve. The shapes of mercury-intrusion curves in the four groups were similar. In the initial mercury-injection stage under low pressure, the mercury-injection curves abruptly rose and gently increased when the mercury-injection content reached two-thirds of the final overall content of Mercury injected. The curves slowly grew with the

increasing pressure. The change in the mercury-ejection stage was similar to that observed in the mercury-intrusion curves at different loading frequencies in the last section: hysteresis was initiated in the initial mercury-ejection stage under high pressure. The generation of hysteresis is related to the existence of “ink bottle”-shaped holes in coal. Hysteresis is caused because the Mercury inlet pressure used to completely fill such holes with Mercury is different from the Mercury withdrawal pressure utilized to completely empty Mercury. However, the final contents of Mercury injected in the four test groups markedly differed. Relative to the test groups with different loading frequencies, the final contents of Mercury injected in the test groups loaded at different amplitudes demonstrated a smaller difference. The test group with the loading amplitude of 14–16 MPa showed the highest final content of Mercury injected (approximately $0.3 \text{ cm}^3/\text{g}$), followed by the test groups (approximately $0.2 \text{ cm}^3/\text{g}$) with the loading amplitudes of 12–18 and 10–20 MPa; among these two groups, the content of Mercury injected was higher in the test group with the loading amplitude of 12–18 MPa; the final content of Mercury injected was the lowest in the control group. However, the differences between the final content of Mercury injected in the test groups with the loading amplitude of 12–18 MPa and 10–20 MPa and the control group were nonsignificant. This indicates that when the loading frequency is unchanged, while the amplitude varies, the pores in coal samples are greatly affected; also, larger amplitudes are linked to lower final pore volumes, showing a negative correlation. The most remarkable influence was noted in the test group with the loading amplitude of 14–16 MPa. In terms of the difference between the cumulative contents of Mercury injected and ejected, the differences in the test groups loaded with different amplitudes were slightly larger than those observed in the control group. This indicates that changes in the loading amplitude of sine waves lead to the development of pores in coal samples and increase the seepage pores, thereby improving the connectivity of pores.

3.2.2. Pore Size Distribution. Figure 9 shows the distribution density functions of pore volumes under four loading conditions. The four curves with a similar shape presented two peaks. The pore size ranges corresponding to the peaks were relatively similar ($d < 10 \text{ nm}$ and $d = 1,000 \text{ nm}$, respectively). However, the corresponding pore sizes of the peaks of seepage pores at 12–18 MPa and 14–16 MPa exhibited a nonsignificant rightward shift, in which the deviation value at 12–18 MPa was larger, implying that the peak pore volume slightly shifted to macropores. Moreover, the overall pore volumes of the two test groups were greatly larger than those of the control group. According to the distribution of seepage and adsorption pores, the pore volume of the former was more markedly increased, while that of the latter was less significantly increased. Nevertheless, the overall pore volume of the test group at the loading amplitude of 10–20 MPa decreased at a small amplitude relative to the control group. Among the several loading conditions, this was the only one under which the

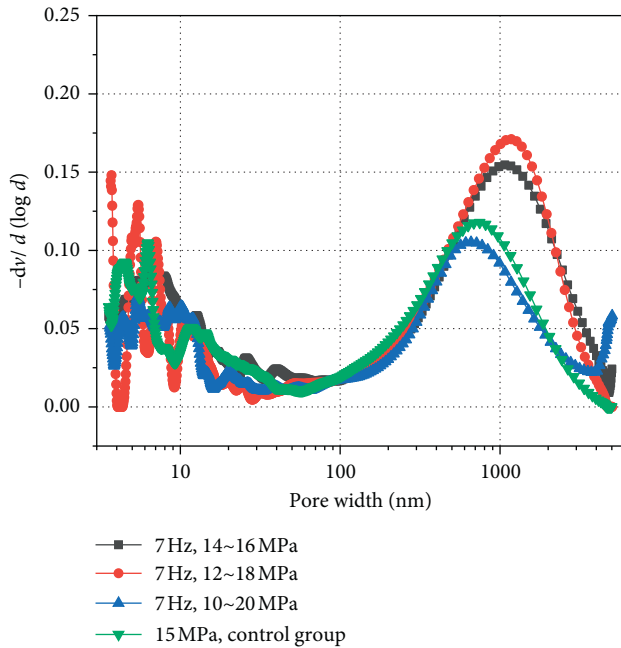


FIGURE 9: Distribution density functions of the pore volumes at different loading amplitudes.

peak distribution density of the pore volume was lower than that of the control group. This finding reveals that the loading condition of the test group possibly presents a small-amplitude inhibitory effect or nonsignificant promotive effect on the development of the pore volume of coal samples with different pore sizes.

3.2.3. Porosities and Percentages of the Pore Volume.

Table 4 lists the comparison data of the percentages of the pore volumes and porosities under four loading conditions. The test groups at amplitudes of 14–16 and 12–18 MPa exhibited the highest total porosities, which were similar (14.47% and 14.41%, respectively). Relative to the porosity (11.32%) of the control group, the test group with the largest amplitude of 10–20 MPa only showed porosity of 10.22%, which was reduced by 1%. Regarding the porosity, the loading condition of 10–20 MPa showed an inhibitory effect on the development of pores, and the pores were slightly closed. The variations in the porosities contributed by adsorption and seepage pores also differed; the porosities contributed by seepage pores at 14–16 and 12–18 MPa were markedly increased by >10%. However, the porosity contributed by seepage pores in the test group at 10–20 MPa (only 6.92%) was lower than that of the control group, and the lowest among those of the test groups, as shown in Figure 10. Moreover, the porosity contributed by adsorption pores was slightly increased only in the test group at 14–16 MPa, while those in the test groups at 10–20 (3.30%) and 12–18 MPa (3.44%) were lower than those of the control group.

Table 5 shows that the volume ratios of the adsorption pores to seepage pores in the test groups and control group approximated 1 : 2; only the volume ratio of adsorption

pores to seepage pores in the test group at 12–18 MPa approximated 1 : 3; the proportion of the adsorption pores was not markedly changed. These findings show that the change in the loading amplitude during the test exerted a non-uniform effect on promoting the formation of pores in coal samples. With the increase in loading amplitude, the seepage pores of coal showed an initially increasing trend followed by a decreasing trend, while the adsorption pores of coal showed a decreasing trend. Compared with the conventional control group (constant 15 MPa), the loading amplitude in the experimental group was the smallest (14–16 MPa), and the adsorption pores and seepage pores showed an increasing trend. The above experimental observations showed that the increase in loading amplitude can promote the expansion of existing pores or fractures, as well as the initiation of new pores and fractures. Although there was a difference in the degree of promotion of expansion and initiation, overall, the total pores in the coal sample were increased. When a loading amplitude of 10–20 MPa is used, the adsorption seepage pore porosity decreased. This showed that 10–20 MPa loading condition for the development of pore expansion inhibition and reaction, coal sample after extrusion force to change substantially, release, internal sample particles is compressed and intergranular pore, hole and the hole in the collapse of pore structure, transition into pores, holes, and microporous and transition hole by compaction, the compaction, the aperture range was lower than that of Mercury-injection experiment can measure range.

3.2.4. Specific Surface Area of Pores. Figure 11 shows the distribution of the specific surface area of pores with the unit diameter under different loading amplitudes. There is the relationship of change between the distribution density function $ds(d)$ of the specific surface area and the diameter d . According to the development trend noted in the curves, the distribution densities of the specific surface areas of all samples during the test were initially increased and subsequently decreased with the increase in pore size; they all reached the maximum before the pore size reached 10 nm. The peak in the test group at the loading amplitude of 10–20 MPa appeared at 5.18 nm, and the test group at 12–18 MPa presented two peaks at 3.82 nm and 6.87 nm; the peak in the test group at 14–16 MPa occurred at 4.31 nm, while that in the control group was found at 6.36 nm. The growth of the distribution density implies that the cumulative specific surface area of pores shows a gradually accelerated growth rate and reaches the peak at the peak of the distribution density. At the peak of the distribution density, the number of pores in samples with the corresponding size (mainly concentrated between 3.5 and 30.0 nm) was the largest, or the length of pores was the largest, and the specific surface area was the largest. Such pores demonstrated the strongest capacity for gas storage; in contrast, the capacity of pores for gas storage was gradually reduced.

According to the above evidence, the following conclusions can be drawn: the difference in the loading

TABLE 4: Percentages of the pore volume and porosities of coal mass at different loading amplitudes.

Loading condition		Porosity (%)				
Frequency (Hz)	Amplitude (MPa)	Micropores (<10 nm)	Transition pores	Mesopores	Macropores	Porosity (%)
7	10~20	1.95	1.35	3.35	3.57	10.22
	12~18	2.02	1.42	5.15	5.83	14.41
	14~16	2.51	1.77	4.97	5.22	14.47
—	15	2.15	1.60	4.40	3.18	11.32

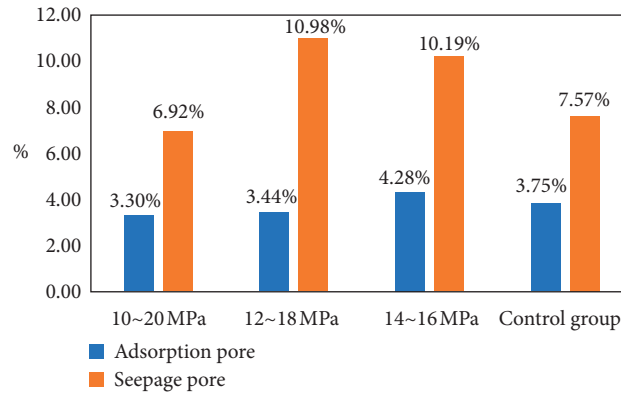


FIGURE 10: Distribution of porosities contributed by adsorption and seepage pores at different loading amplitudes.

TABLE 5: Percentages of the pore volume at different loading amplitudes.

Loading condition		Percentage of the pore volume (%)					
Frequency (Hz)	Amplitude (MPa)	Micropores (<10 nm)	Transition pores (10~100 nm)	Adsorption pores	Mesopores (100~1,000 nm)	Macropores (>1,000 nm)	Seepage pores
7 Hz	10~20	17.51	15.23	32.74	46.10	21.16	67.26
	12~18	14.00	9.27	23.27	39.88	36.85	76.73
	14~16	16.68	13.34	30.02	37.61	32.37	69.98
—	15	16.70	17.15	33.85	47.66	18.49	66.15

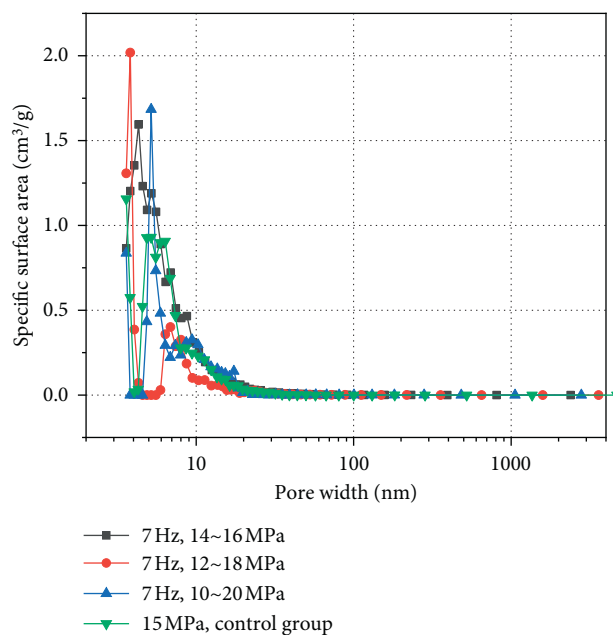


FIGURE 11: Distribution densities of the specific surface area of pores in coal mass at different loading amplitudes.

TABLE 6: Comparison of the growth amplitudes of the porosity under different loading conditions.

Frequency (Hz)	Amplitude (MPa)	Total porosity	Growth amplitude (%)	Growth amplitude of adsorption pores (%)	Growth amplitude of seepage pores (%)
—	15	11.32	—	—	—
7	10–20	10.22	−9.75	−12.00	−8.58
	12–18	14.41	27.29	−8.37	45.02
4	14–16	14.47	27.79	14.10	34.63
	12–18	12.71	12.26	−17.33	26.95
7	12–18	14.41	27.29	−8.27	45.05
10	12–18	19.81	74.99	40.00	92.34

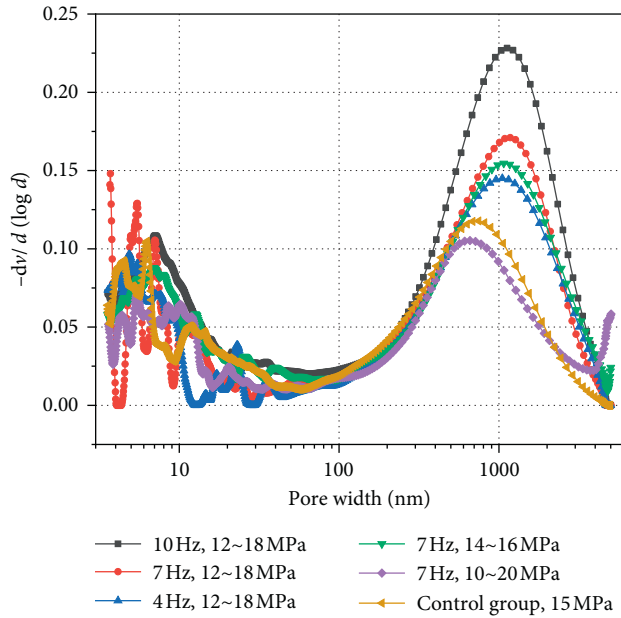


FIGURE 12: Distribution density functions of the pore volume under different loading conditions.

amplitudes influences the pore characteristics of coal sample; and the pore volume generally increases slightly. In terms of the classification based on the pore size, mesopores generally account for the majority, followed by macropores, micropores, and transition pores. Moreover, the change in loading amplitude promoted an initial increase followed by a decrease in the seepage pores of coal body, while the adsorption pores were gradually decreased. This implies that the change in amplitude plays a nonsignificant role in distinguishing the pores with different sizes. However, the porosity of the test group with the largest amplitude of 10–20 MPa decreased, and the corresponding peak of the pore volume slightly declined. These data reveal that a large loading amplitude exerts an opposite effect on the initiation and development of pores or fractures, which induces the collapse of macropores and mesopores. Furthermore, the pores were more compacted, thus leading to reduction of the porosity to lower levels than the original coal porosity or fracture occurrence degree.

4. Implications for Frequency and Amplitude Selection during Pulse Hydraulic Fracturing

According to the analysis described in Sections 3.1 and 3.2, the change in the loading frequency or loading amplitude influences the pore characteristics of coal samples. The influence was basically positive, promoting the initiation and development of pores; however, there was also negative influence noted.

Table 6 compares the effects of the change in amplitude and frequency on the porosity. Relative to the control group loaded under a steady pressure, the growth amplitude of the porosity ranged from −9.7450% to 27.7895% when changing the amplitude; lower amplitudes were linked to larger growth amplitudes. The growth amplitude of the total porosity varied between 12.2637% and 74.9861% when changing the frequency; higher frequencies were associated with larger growth amplitudes. Regarding the total porosity, the change in frequency imposed obviously greater influences than the change in amplitude.

In terms of seepage and adsorption pores, the growth amplitude of the porosity of the seepage pores in the test group with changing frequency ranged from −8.58% to 45.02%, while that of adsorption pores was between −8.37% and 14.10%; the porosity contributed by seepage pores in the test group with changing amplitude presented a growth amplitude of 26.95–92.34%, while that contributed by adsorption pores delivered a growth amplitude between −17.33% and 40.00%. This indicates that the loading frequency exerts a greater negative influence on adsorption pores; correspondingly, it exhibits a greater positive influence on seepage pores. The effects of the loading amplitude on the growth amplitudes of the porosity contributed by the two types of pores were nearly equivalent.

By comparing the distribution density functions of the pore volume under different loading conditions (Figure 12), it was found that the function curve of the pore volume in the test group at 10 Hz and 12–18 MPa was located markedly above those of the other test groups. Moreover, only the function curve of the pore volume in the test group at 7 Hz and 10–20 MPa was situated below that of the control group. The curves of the three groups at different loading amplitudes were denser than those at different loading frequencies, implying that the change in amplitude marginally

influences the pore volume, whereas the change in frequency greatly changes the pore volume of samples.

The final purpose of pulse hydraulic fracturing in underground coal mines is to increase the permeability of coal seams and further improve the amount of gas extraction. The results of this research show that the seepage pores in coal samples rose significantly in response to increasing frequency. This indicates that, in field construction, the fracturing effect can be strengthened by enhancing the frequency. However, enhancement of the frequency is associated with an increase in construction cost. Further research on this topic is warranted for the selection of the proper frequency and evaluation of the economic cost. Additionally, the results described in Section 3.2 show that the largest increment of seepage pores is observed at the amplitude of 12–18 MPa. Thus, during field construction, it is suggested to perform pulse hydraulic fracturing by selecting the amplitude within this range.

5. Conclusions

Based on the findings of the present study, the following conclusions can be drawn.

Firstly, by maintaining the loading amplitude of sine waves unchanged while changing their loading frequency, the overall porosity and the pore volume increase at different amplitudes. The increase in loading frequency exerts a more significant promotive effect on the initiation and development of pores and fractures and drives the transformation of micropores and transition pores into mesopores and macropores. The proportion of the seepage pores grows, and the change in the loading amplitude of sine waves delivers a complex influence on the pore characteristics of anthracite coal.

Secondly, when the frequency of the loaded sinusoidal wave is unchanged, the amplitude of the loaded sinusoidal wave is altered to promote change in coal seepage pores through an initial increase followed by a decrease, while the change in coal adsorption pores gradually decreases. When the loading amplitude increases, it influences the development and initiation of pores or fractures. This leads to the collapse of macropores and mesopores, and the pores become more compact.

Finally, the change in loading frequency has a greater impact on the pore characteristics of the briquette and a greater negative impact on adsorption pores than seepage pores. Amplitude of the change of adsorption and filtration could inhibit the growth of two types of pores, which is relatively close, active application in practice of changing load change coal pore properties, and if unable to meet the change of frequency and amplitude, at the same time, give priority to increasing frequency of choice to promote the initiation and development of pore, to be connected hole, and guide the internal pore gas form seepage.

Data Availability

All data, models, and code generated or used during the study are included in the manuscript.

Conflicts of Interest

The authors declare that they have no conflicts of interest to this work.

Acknowledgments

This work was supported by the National Natural Science Foundation of China (grant numbers 51674016 and 52074120), and the Fundamental Research Funds for the Central Universities (3142019005).

References

- [1] Q. Zou, H. Liu, Y. Zhang, Q. Li, J. Fu, and Q. Hu, "Rationality evaluation of production deployment of outburst-prone coal mines: a case study of Nantong coal mine in Chongqing, China," *Safety Science*, vol. 122, Article ID 104515, 2020.
- [2] H. Wang, B. Tan, Z. Shao, Y. Guo, Z. Zhang, and C. Xu, "Influence of different content of FeS₂ on spontaneous combustion characteristics of coal," *Fuel*, vol. 288, Article ID 119582, 2021.
- [3] A. Busch and Y. Gensterblum, "CBM and CO₂-ECBM related sorption processes in coal: a review," *International Journal of Coal Geology*, vol. 87, no. 2, pp. 49–71, 2011.
- [4] E. Su, Y. Liang, Q. Zou, F. Niu, and L. Li, "Analysis of effects of CO₂ injection on coalbed permeability: implications for coal seam CO₂ sequestration," *Energy & Fuels*, vol. 33, no. 7, pp. 6606–6615, 2019.
- [5] E. Su, Y. Liang, Q. Zou, M. Xu, and A. P. Sasmito, "Numerical analysis of permeability rebound and recovery during coalbed methane extraction: implications for CO₂ injection methods," *Process Safety and Environmental Protection*, vol. 149, pp. 93–104, 2021.
- [6] H. Wang, X. Fang, F. Du et al., "Three-dimensional distribution and oxidation degree analysis of coal gangue dump fire area: a case study," *Science of The Total Environment*, vol. 772, Article ID 145606, 2021.
- [7] Q. Zou and B. Lin, "Fluid-solid coupling characteristics of gas-bearing coal subjected to hydraulic slotting: an experimental investigation," *Energy & Fuels*, vol. 32, no. 2, pp. 1047–1060, 2018.
- [8] F. Du and K. Wang, "Unstable failure of gas-bearing coal-rock combination bodies: insights from physical experiments and numerical simulations," *Process Safety and Environmental Protection*, vol. 129, pp. 264–279, 2019.
- [9] A. Abdollahipour, M. Fatehi Marji, A. Yarahmadi Bafghi, and J. Gholamnejad, "DEM simulation of confining pressure effects on crack opening displacement in hydraulic fracturing," *International Journal of Mining Science and Technology*, vol. 26, no. 4, pp. 557–561, 2016.
- [10] Q. Zou, H. Liu, Z. Cheng, T. Zhang, and B. Lin, "Effect of slot inclination angle and borehole-slot ratio on mechanical property of pre-cracked coal: implications for ECBM recovery using hydraulic slotting," *Natural Resources Research*, vol. 29, no. 3, pp. 1705–1729, 2020.
- [11] Y. M. Lekontsev and P. V. Sazhin, "Directional hydraulic fracturing in difficult caving roof control and coal degassing," *Journal of Mining Science*, vol. 50, no. 5, pp. 914–917, 2014.
- [12] Q. Zou, B. Lin, C. Zheng et al., "Novel integrated techniques of drilling-slotting-separation-sealing for enhanced coal bed methane recovery in underground coal mines," *Journal of Natural Gas Science and Engineering*, vol. 26, pp. 960–973, 2015.

- [13] K. H. S. M. Sampath, M. S. A. Perera, P. G. Ranjith et al., "CH₄ CO₂ gas exchange and supercritical CO₂ based hydraulic fracturing as CBM production-accelerating techniques: a review," *Journal of CO₂ Utilization*, vol. 22, pp. 212–230, 2017.
- [14] Y. Liu, X. Wen, M. Jiang et al., "Impact of pulsation frequency and pressure amplitude on the evolution of coal pore structures during gas fracturing," *Fuel*, vol. 268, Article ID 117324, 2020.
- [15] X. Jingna, X. Jun, N. Guanhua, S. Rahman, S. Qian, and W. Hui, "Effects of pulse wave on the variation of coal pore structure in pulsating hydraulic fracturing process of coal seam," *Fuel*, vol. 264, Article ID 116906, 2020.
- [16] J. Blunski, J. Wang, and T. Ertekin, "Hydraulic fracturing mechanisms in coal: a review," *International Journal of Oil, Gas and Coal Technology*, vol. 14, no. 3, pp. 247–263, 2017.
- [17] J. Zhou, S. Tian, L. Zhou et al., "Experimental investigation on the influence of sub- and super-critical CO₂ saturation time on the permeability of fractured shale," *Energy*, vol. 191, Article ID 116574, 2020.
- [18] J. Chen, X. Li, H. Cao, and L. Huang, "Experimental investigation of the influence of pulsating hydraulic fracturing on pre-existing fractures propagation in coal," *Journal of Petroleum Science and Engineering*, vol. 189, Article ID 107040, 2020.
- [19] Q. Li, B. Lin, and C. Zhai, "The effect of pulse frequency on the fracture extension during hydraulic fracturing," *Journal of Natural Gas Science and Engineering*, vol. 21, pp. 296–303, 2014.
- [20] Q. Li, B. Lin, C. Zhai et al., "Variable frequency of pulse hydraulic fracturing for improving permeability in coal seam," *International Journal of Mining Science and Technology*, vol. 23, no. 6, pp. 847–853, 2013.
- [21] Q. Li, B. Lin, and C. Zhai, "A new technique for preventing and controlling coal and gas outburst hazard with pulse hydraulic fracturing: a case study in Yuwu Coal Mine, China," *Natural Hazards*, vol. 75, no. 3, pp. 2931–2946, 2015.
- [22] W. Wang, X. Li, B. Lin, and C. Zhai, "Pulsating hydraulic fracturing technology in low permeability coal seams," *International Journal of Mining Science and Technology*, vol. 25, no. 4, pp. 681–685, 2015.
- [23] K. Jin, Y. Cheng, Q. Liu et al., "Experimental investigation of pore structure damage in pulverized coal: implications for methane adsorption and diffusion characteristics," *Energy & Fuels*, vol. 30, no. 12, pp. 10383–10395, 2016.
- [24] F. Wang, Y. Cheng, S. Lu, K. Jin, and W. Zhao, "Influence of coalification on the pore characteristics of middle-high rank coal," *Energy & Fuels*, vol. 28, no. 9, pp. 5729–5736, 2014.
- [25] B. Nie, X. Liu, L. Yang, J. Meng, and X. Li, "Pore structure characterization of different rank coals using gas adsorption and scanning electron microscopy," *Fuel*, vol. 158, pp. 908–917, 2015.
- [26] E. Su, Y. Liang, X. Chang, Q. Zou, M. Xu, and A. P. Sasmito, "Effects of cyclic saturation of supercritical CO₂ on the pore structures and mechanical properties of bituminous coal: an experimental study," *Journal of CO₂ Utilization*, vol. 40, Article ID 101208, 2020.
- [27] E. P. Barrett, L. G. Joyner, and P. P. Halenda, "The determination of pore volume and area distributions in porous substances. I. computations from nitrogen isotherms," *Journal of the American Chemical Society*, vol. 73, no. 1, pp. 373–380, 1951.
- [28] Y. Cai, D. Liu, Z. Pan, Y. Yao, J. Li, and Y. Qiu, "Pore structure and its impact on CH₄ adsorption capacity and flow capability of bituminous and subbituminous coals from Northeast China," *Fuel*, vol. 103, pp. 258–268, 2013.
- [29] E. Su, Y. Liang, and Q. Zou, "Structures and fractal characteristics of pores in long-flame coal after cyclical supercritical CO₂ treatment," *Fuel*, vol. 286, p. 119305, 2021.
- [30] E. W. Washburn, "The dynamics of capillary flow," *Physical Review*, vol. 17, no. 3, pp. 273–283, 1921.
- [31] K. Zhang, Y. Cheng, K. Jin et al., "Effects of supercritical CO₂ fluids on pore morphology of coal: implications for CO₂ geological sequestration," *Energy & Fuels*, vol. 31, no. 5, pp. 4731–4741, 2017.
- [32] H. Jiang, Y. Cheng, and L. Yuan, "A Langmuir-like desorption model for reflecting the inhomogeneous pore structure of coal and its experimental verification," *RSC Advances*, vol. 5, no. 4, pp. 2434–2440, 2014.
- [33] B. B. Hodot, *Outburst of Coal and Coalbed Gas*, China Industry Press, Beijing, China, 1966.
- [34] E. Su, Y. Liang, L. Li, Q. Zou, and F. Niu, "Laboratory study on changes in the pore structures and gas desorption properties of intact and tectonic coals after supercritical CO₂ treatment: implications for coalbed methane recovery," *Energies*, vol. 11, no. 12, p. 3419, 2018.
- [35] X. Wang, D. Zhang, E. Su et al., "Pore structure and diffusion characteristics of intact and tectonic coals: implications for selection of CO₂ geological sequestration site," *Journal of Natural Gas Science and Engineering*, vol. 81, Article ID 103388, 2020.
- [36] J. Pan, Y. Zhao, Q. Hou, and Y. Jin, "Nanoscale pores in coal related to coal rank and deformation structures," *Transport in Porous Media*, vol. 107, no. 2, pp. 543–554, 2015.

Research Article

Experimental Study on Local Scour and Related Mechanical Effects at River-Crossing Underwater Oil and Gas Pipelines

Fan Cui ^{1,2,3} Yunfei Du ¹ Xianjie Hao ² Suping Peng ^{1,2} Zhuangzhuang Bao ¹
and Shiqi Peng ¹

¹School of Geosciences and Surveying Engineering, China University of Mining and Technology, Beijing 100083, China

²State Key Laboratory of Coal Resources and Safe Mining, China University of Mining and Technology, Beijing 100083, China

³Beijing Key Laboratory for Precise Mining of Intergrown Energy and Resources, China University of Mining and Technology, Beijing 100083, China

Correspondence should be addressed to Xianjie Hao; haoxianjie_cumtb@126.com

Received 17 December 2020; Revised 18 March 2021; Accepted 5 April 2021; Published 21 April 2021

Academic Editor: Jia Lin

Copyright © 2021 Fan Cui et al. This is an open access article distributed under the Creative Commons Attribution License, which permits unrestricted use, distribution, and reproduction in any medium, provided the original work is properly cited.

Among the various geological disasters that threaten the safe operation of long-distance oil and gas pipelines, water-damage disasters are numerous and widely developed. Especially the pipelines crossing river channels or gullies are vulnerable to scouring hazards from storms and floods. A water-damage disaster physical model was established to investigate the characteristics of the riverbed scour profile and the pipeline force when the pipeline was buried at different depths under the condition of different particle size riverbed sediment. Results indicated that the equilibrium scour depth changed in a spoon shape with the gradual increase of the embedment ratio in general. The equilibrium scour depth formed by the fine sand riverbed was the largest, about 1.5 times the pipeline diameter. When the pipeline was half exposed, the clay riverbed was more resistant to the scour of the river than the riverbed of fine sand and very fine pebbles with a larger particle size. In the riverbed of three particle sizes, fine sand was more difficult to withstand the scour of the river. The scour profile formed by the sand bed around the pipeline and the force and deformation of the pipeline were related to pipeline location and riverbed sediment type. Results of this study might be useful for the safety warning and protection measures of underwater pipeline crossing.

1. Introduction

Oil and gas pipelines play an important role in the deployment of oil and natural gas resources [1]. By the end of 2017, the total mileage of global oil and gas pipelines in service was approximately 355×10^4 km, including 296.56×10^4 km for natural gas pipelines and 58.4×10^4 km for crude oil pipelines [2]. Long-distance oil and gas pipelines inevitably have to cross rivers. Two methods are generally adopted when oil and gas pipelines traverse a river: underwater crossing and water crossing. For the former, due to the effects of riverbed evolution, riverbed scour, and water current impact, the pipeline is partially suspended or exposed and is easily damaged, which increases the risk of damage to the oil and gas pipeline at the river bottom [3]. Once the oil and gas pipeline at the bottom of the river is

damaged, it is very easy to cause dangerous situations such as leakage, poisoning, fire, or explosion. This not only is harmful to the environment, but also can cause serious economic losses and even endanger human life [4].

With the rapid development of oil and gas pipeline construction in various countries around the world, pipeline safety accidents caused by local scour of the pipeline have occurred from time to time [5]. For example, in 2011, ExxonMobil's Silvertip pipeline near Laurel was exposed and then ruptured due to riverbed erosion, causing pollution of miles of riverbanks. As a result, the municipal water supply and irrigation districts in eastern Montana were forced to suspend water from the river [6]. In 1994, the flooding of the San Jacinto River in Texas, USA, caused multiple pipelines to rupture, causing 34,500 barrels of crude oil and petroleum products to be discharged into the river and ignited [7].

Therefore, more and more scientific researchers have begun to pay attention to the problem of pipeline local scour. Mao [8], Sumer et al. [9–12], Chiew [13–15], Neelamani and Rao [16], Yang et al. [17], and Gao et al. [18] mainly studied the local scour process and mechanism of submarine pipeline by establishing physical models. Van Beek and Wind [19], Zhao et al. [20], and Liu et al. [21] used numerical simulation methods to study the flow field changes, bed surface pressure distribution, and pipeline surface pressure distribution during the local scour process of submarine pipelines. In addition, with the development of new technologies, some new equipment and methods have also been applied to the study of pipeline scouring. An et al. proposed a new type of contact image sensor (CIS) to track the development of scour pits near bridge piers [22]. Zhu et al. used a miniature camera installed in a transparent pipe to show the results of a visual experiment of three-dimensional scouring of the pipe [23]. Azamathulla and Zakaria [24] applied the artificial neural network (ANN) to pipeline scour depth estimation and verified the effectiveness of the method. In addition to that, they also studied the temporal variation of local pipeline scour depth to estimate the scour depth and proposed a regression model that can well predict the relative scour depth [25]. Najafzadeh et al. [26–29] applied the group method of data handling (GMDH) network method to predict the pipeline scour depth under wave action and compared the performance of this method with the adaptive neurofuzzy inference system (ANFIS) model, model tree (MT), and empirical formula, which verifies the superiority of the GMDH network in predicting the scour depth. Based on the above analysis, it is not difficult to find that there are many studies on long-distance oil and gas pipelines; nevertheless, most of those studies mainly focus on the prediction of scour depth and the calculation of critical suspended length. Besides, most researches are on the evolution process and scour characteristics of the seabed around submarine pipelines, and few studies are on local scour of oil and gas pipelines crossing rivers. In addition, different riverbed medium at different depth will inevitably lead to changes in the evolution process of scour.

Thus, a physical model of the local scour of oil and gas pipelines crossing rivers under water was established based on experimental conditions. Subsequently, the characteristics of riverbed scour profile and the stress and deformation of the pipeline when the pipeline was buried at different depths of the riverbed under the conditions of different particle sizes of riverbed sediment were studied. The major emphasis of the experiment is that we compared the characteristics of the scour profiles formed in the process of the pipeline being scoured by the river under the action of

the riverbed with different particle sizes and also analyzed the pressure and strain situation of the pipeline itself in this process. This study can provide theoretical guidance for the protection engineering of oil and gas pipelines crossing rivers under water and avoid serious accidents such as pipeline explosion and leakage caused by hydraulic factors.

2. Materials and Methods

2.1. Model Design

2.1.1. Model Design Principle. Local scour of oil and gas pipelines crossing rivers will cause the riverbed around the pipelines to drop, which will seriously affect the safety of operation pipelines [30, 31]. The maximum depth of riverbed descent around the pipeline is called the equilibrium scour depth. It can be used as an indicator of the intensity of local scour. As the local scour of oil and gas pipelines across rivers involves the interaction between water flow, sediment, and pipelines, the relationship between each physical quantity and the equilibrium scour depth was established through the dimensional analysis method to explore the relationship between the physical quantities and simplify the physical equations. The physical quantities related to the scouring process of oil and gas pipelines crossing rivers are shown in Table 1.

Based on the above nine physical quantities, the scour process of oil and gas pipelines crossing rivers can be expressed as

$$f(u, \rho, \mu, d_{50}, \rho_s, D, g, e, S) = 0. \quad (1)$$

Choose u as the basic variable:

$$\begin{cases} [u] = [M^0 L^1 T^{-1}], \\ [\rho] = [M^1 L^{-3} T^0], \\ [D] = [M^0 L^1 T^0]. \end{cases} \quad (2)$$

The exponential determinant of the basic dimensions of the three basic variables u , ρ , and D is

$$\begin{vmatrix} 0 & 1 & -1 \\ 1 & -3 & 0 \\ 0 & 1 & 0 \end{vmatrix} \neq 0. \quad (3)$$

Therefore, the selected basic variables are independent of each other. According to the π theorem, the other six parameters can be expressed as the dimensionless π term as follows:

TABLE 1: Main physical quantities.

Attributes	Physical quantities	Symbols	Dimensions
Water flow	Flow velocity	u	LT^{-1}
	Water density	ρ	ML^{-3}
	Kinetic viscosity	μ	$ML^{-1}\cdot T^{-1}$
Sediment	Median diameter	d_{50}	L
	Sand density	ρ_s	ML^{-3}
Pipelines	Diameter	D	L
	Gravity	g	LT^{-2}
Other	Distance between the lower wall of the pipeline and the riverbed surface in the physical model	e	L
	Scour depth	S	L

$$\left\{ \begin{array}{l} \pi_1 = \mu^{-1} \rho^1 u^1 D^1 = \frac{\rho u D}{\mu} = \text{Re}, \\ \pi_2 = d_{50} D^{-1} = \frac{d_{50}}{D}, \\ \pi_3 = \rho_s \rho^{-1} = \frac{\rho_s}{\rho}, \\ \pi_4 = (\pi_3 - 1) g^{-1} d_{50}^{-1} u_*^2 = \frac{u_*^2}{(\rho_s / \rho - 1) g d_{50}} = \theta, \\ \pi_5 = e D^{-1} = \frac{e}{D} = G, \\ \pi_6 = S D^{-1} = \frac{S}{D}, \end{array} \right. \quad (4)$$

where Re is the Reynolds number, which represents the ratio of the inertial force to the viscous force of the fluid in the process of flowing; θ is the Shields number, which reflects the ratio of the shear stress of the water flow to the river bed sediment to the underwater weight of the sand; u_*^2 represents the friction flow rate, which can be estimated using the Colebrook–White formula [32]; G is the embedment ratio, which is the ratio of the distance between the lower wall of the pipeline and the riverbed surface in the physical model (the lower wall of the pipeline is positive when it is higher than the surface of the riverbed material, and negative if it is lower than the surface of the riverbed material) and the diameter of the pipeline.

The local scour depth of the pipeline can be expressed in a unified dimensionless form, such as

$$f\left(\frac{S}{D}, \text{Re}, \frac{\rho_s}{\rho}, \frac{d_{50}}{D}, G, \theta\right) = 0, \quad (5)$$

which is

$$\frac{S}{D} = f\left(\text{Re}, \frac{\rho_s}{\rho}, \frac{d_{50}}{D}, G, \theta\right). \quad (6)$$

Refer to the actual pipeline diameter and experimental conditions to choose a pipeline diameter D of 4 cm.

2.1.2. Model Sand Selection. Seven different types of sediments were selected according to the particle size: clay, fine sand, medium sand 1, medium sand 2, coarse sand, very coarse sand, and very fine pebbles. The specific particle size distribution is shown in Figure 1 and the physical properties of sediments are shown in Table 2. In addition, the grading curves of noncohesive soils are shown in Figure 2.

2.1.3. Experimental Device. The constructed local scour test system for oil and gas pipelines crossing rivers is mainly composed of three parts: circulating water tank, pipeline model, and monitoring system. The schematic diagram of the experimental device is shown in Figure 3.

(1) Circulating Water Tank. The circulating water tank is mainly composed of a water storage tank, an experimental flume, and circulation system. The water storage tank is a rectangular parallelepiped tank with a length of 900 cm, a width of 140 cm, and a height of 100 cm. The experimental flume is a rectangular concave groove (the flume cross section is rectangular) with a length of 700 cm, a width of 60 cm, and a height of 30 cm. The side wall of the flume test area is made of transparent plexiglass, which is convenient for monitoring the scouring process and depth of sediment around the pipeline. A flat water grating is installed at the

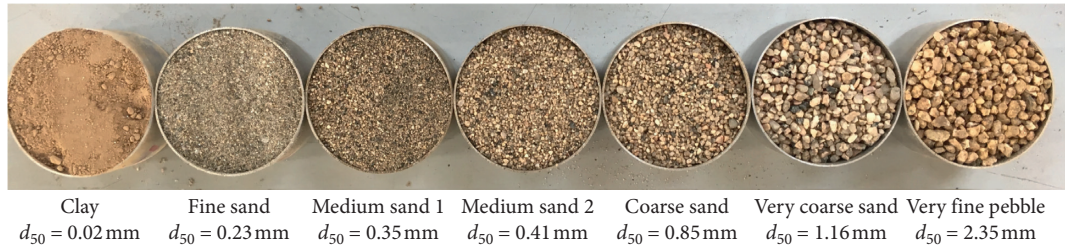


FIGURE 1: Test sediment.

TABLE 2: Physical properties of sediments.

	Clay	Fine sand	Medium sand 1	Medium sand 2	Coarse sand	Very coarse sand	Very fine pebbles
Dry density ($\text{g}\cdot\text{cm}^{-3}$)	1.40	1.37	1.34	1.29	1.22	1.30	1.23
Wet density ($\text{g}\cdot\text{cm}^{-3}$)	1.55	1.43	1.47	1.55	1.39	1.56	1.49

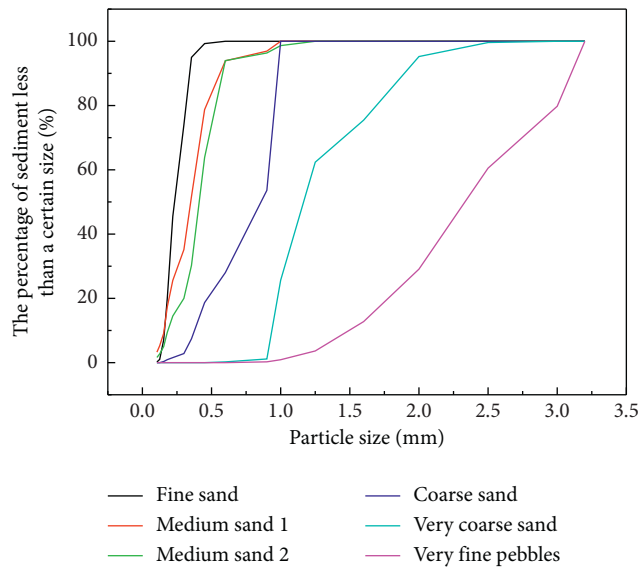


FIGURE 2: Grading curves.

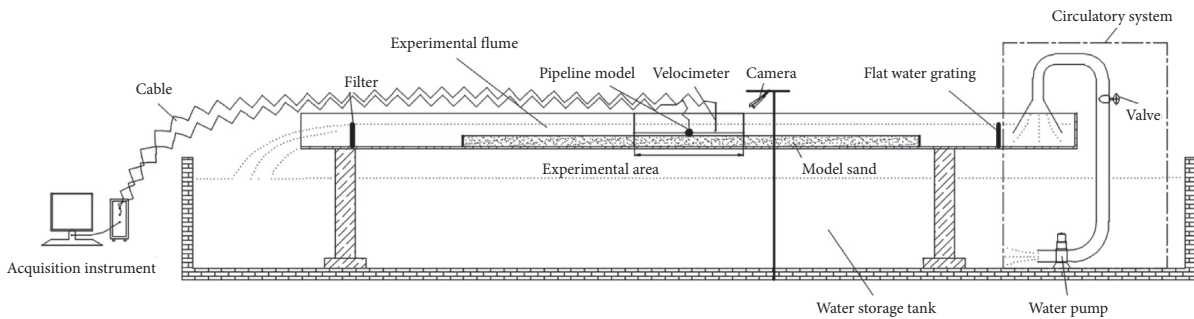


FIGURE 3: Schematic of the experiment.

water inlet port of the experimental flume to dissipate energy and reduce drag, so that the incoming flow is even and stable, and provides stable water flow conditions for the experiment. A filter screen is installed at the water outlet of the experimental flume to filter the model sand in the water flow to

prevent the model sand from causing damage to the pump. The circulation system mainly refers to the installation of a high-power water pump at the bottom of the water storage tank and the delivery of water to the experimental flume through a water delivery pipeline. After flowing through the

experimental flume and at the end, it flows into the water storage tank again to form the water circulation.

(2) *Pipeline Model.* The pipeline used in the experiment is a PVC pipeline with a diameter D of 4 cm, and the pressure sensor and strain gauge are arranged on the outer surface of the central position of the pipeline axis. The specific arrangement position is shown in Figure 4. Eight pressure sensors are evenly arranged on the left profile A to monitor the pressure in the axial center section of the pipeline. Eight strain gauges are evenly arranged on the right profile B to monitor the strain in the axial center section of the pipeline.

(3) *Monitoring System.* As shown in Figure 5, the monitoring system consists of an Acoustic Doppler Velocimetry (ADV, type: LSH10-1M), a data acquisition instrument (type: EY221), strain gauges (type: BE120-3AA), and pressure sensors (type: HCYB-16).

2.1.4. *Experimental Scheme.* Seven types of riverbed sediment were designed and tested for the model performance. The length of the mobile bed is 3 m, and the length of the approaching bed is 1 m to allow the water flow to develop fully. The sediment transport along the approaching bed will not affect the scouring process of the local riverbed sediment in the pipeline. Seven groups of tests were carried out for each type of bed sediment with embedment ratios G of -2 , -1.5 , -1 , -0.5 , 0 , 0.5 , and 1 , respectively. A total of 49 groups of experiments were conducted. Each group of experiments is carried out under live-bed condition. The schematic diagram of different embedment ratio tests is shown in Figure 6, and the test conditions of each group are shown in Table 3. Since our main concern in this experiment is the impact of riverbed particle size and pipeline depth on the riverbed scour process, it is not intended to predict the various values of riverbed scour to establish a connection with the actual project. Therefore, we ignore the influence of the sidewall effects. The experimental process is as follows:

- (1) Spread the sand evenly on the bottom of the experimental flume, and the thickness of the sand is about 10 cm. Then turn on the pump to make the water flow and turn off the pump when the sediment is fully saturated.
- (2) Paste the pressure sensor and strain gauge on the outer surface of the pipeline at the axial center position. Then glue two suction cups on both ends of the pipeline. The suction cups at both ends of the pipeline are adsorbed on the transparent plexiglass on the side wall of the test area of the sink to fix the pipeline. The relative position of the pipeline is determined according to the test group. After that, smooth the surface of the sand and keep the height at 10 cm.
- (3) Turn on the water pump again. At the same time, the camera, data acquisition instrument, and ADV were turned on to monitor the experimental process, the force and deformation of the pipeline surface, and the water flow velocity. In order to reduce the pulsation of the water flow itself and the error caused by the monitoring process, the water flow velocity under all working conditions is averaged to $V=0.4$ m/s, which is used as the water flow velocity in the experiment. The approach flow depth is 25 cm.
- (4) When the shape of the scour hole at the bottom of the pipeline remains basically unchanged and the measured data does not change more than 1 mm for three consecutive times, it is considered that the scouring has reached equilibrium and a set of tests is done. The duration of each run is not fixed until it reaches the equilibrium scour conditions. Turn off the water pump, camera, data acquisition instrument and ADV. Then reset the type of sediment and the relative position of the pipeline according to the test groups and repeat the above steps.

3. Results

3.1. *Characteristics of Equilibrium Scour Depth.* The depths of the scour holes formed when each group of scouring reaches equilibrium were analyzed. The result is shown in Figure 7. It can be seen from Figure 7 that the equilibrium scour depth changed with the gradual increase of the embedment ratio in a scoop shape in general. When the embedment ratios were -2.0 , -1.5 , and -1.0 , no scour holes were formed under the pipelines on the riverbed conditions of different particle sizes. At this time, the pipeline was buried in the riverbed and was not influenced by the river scour. When the embedment ratio was -0.5 , scouring holes began to appear under the pipeline on the conditions of riverbed with other particle sizes except for the clay riverbed. The maximum depth of the scour hole formed by the fine sand riverbed was 6 cm, which was about 1.5 times the pipeline diameter. The minimum depth of the scour hole formed by the very fine pebble riverbed was 3 cm, which was about 0.75 times the pipeline diameter.

Take $G=-0.5$ as an example to study the local scour process around the pipeline. At this embedment ratio, the pipeline is half buried and half exposed. Observation of the local scour form of the sandy riverbed below the pipeline shows that the local scour of the pipeline generally goes through four stages of scour start-up, micropore formation, scour extension, and scour equilibrium. It can be seen from Figure 8 that during the scour start-up stage (Figure 8(a)), a large-scale scour hole gradually appeared behind the pipeline, the length was about 3-4 times the pipeline diameter, and the maximum depth was about 0.5 times the pipeline diameter. At the stage of micropore formation (Figure 8(b)), the back-flow surface of the pipeline near the pipeline bottom began to spray sand and water mixture as the scouring continued. Finally, a connecting gap penetrated through the bottom of the pipeline. A large amount of water-sand mixture quickly passed through the communicating gap and covered and filled with the scour hole formed in the first stage. This phenomenon is mainly caused by the seepage force generated inside the riverbed under the action of the pressure difference on both sides of the pipeline. During the

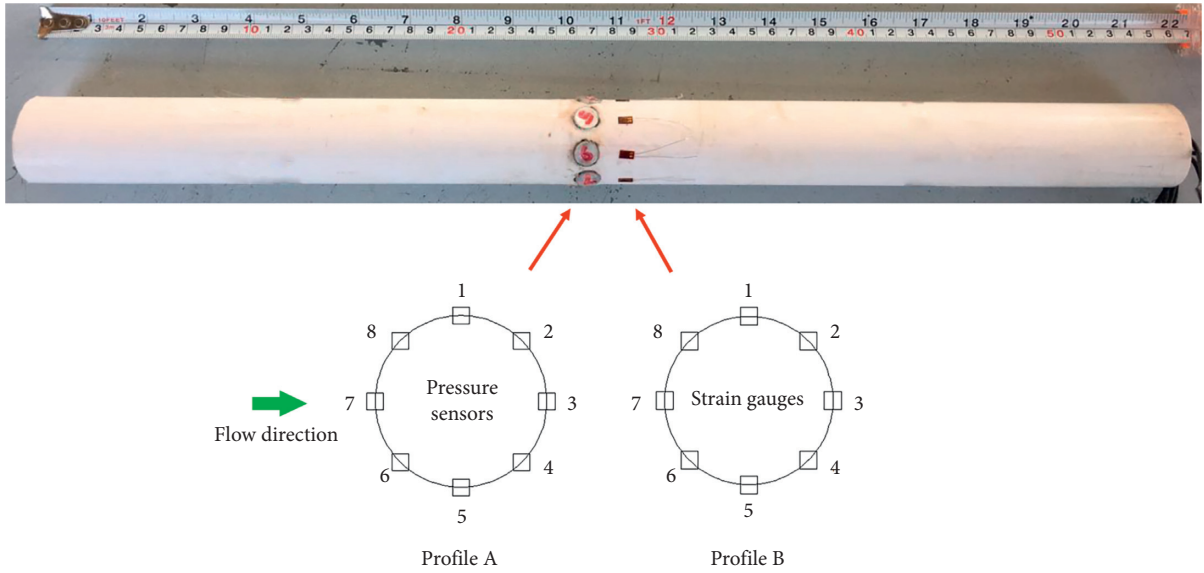


FIGURE 4: Schematic diagram of pipeline model sensor layout.

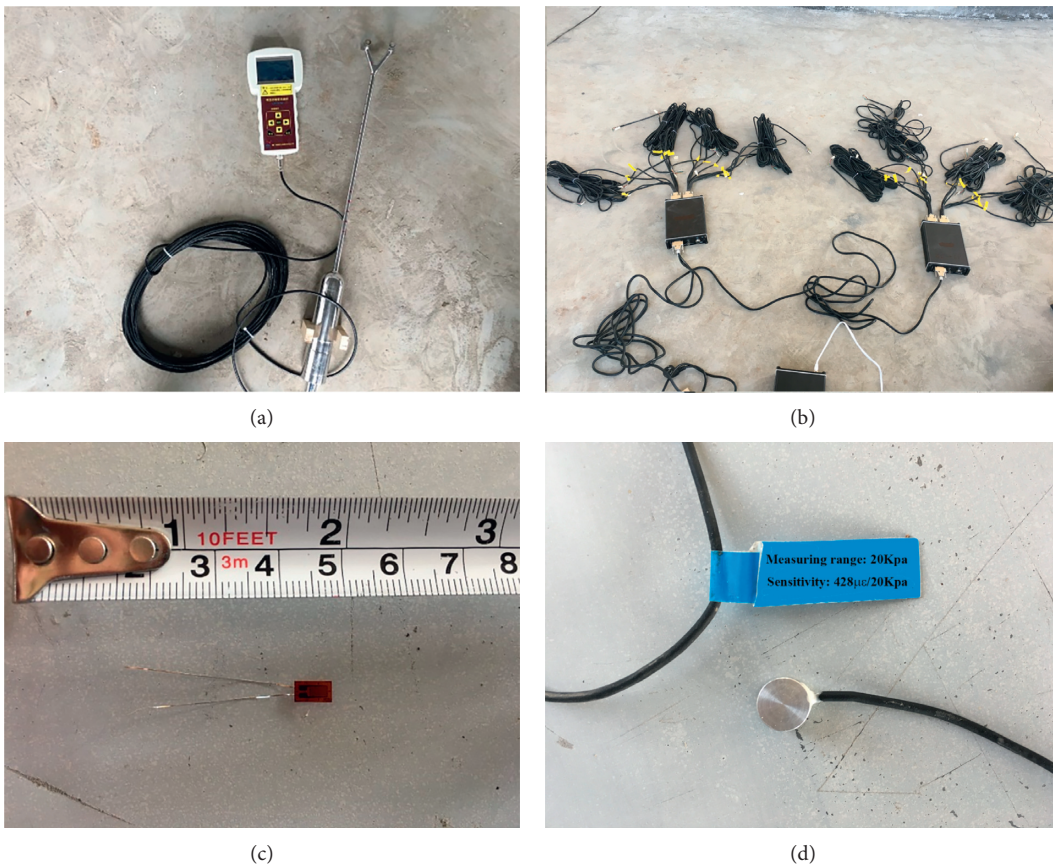


FIGURE 5: Physical image of the monitoring system: (a) acoustic Doppler velocimetry, (b) data acquisition unit, (c) strain gauge, and (d) pressure sensor.

stage of scour extension (Figure 8(c)), the connecting gap at the bottom of the pipeline gradually became deeper, and the speed of the water-sand mixture in the connecting gap

gradually slowed down. In the scour equilibrium stage (Figure 8(d)), the shape of the scouring hole at the bottom of the pipeline basically stabilized and no longer changed.

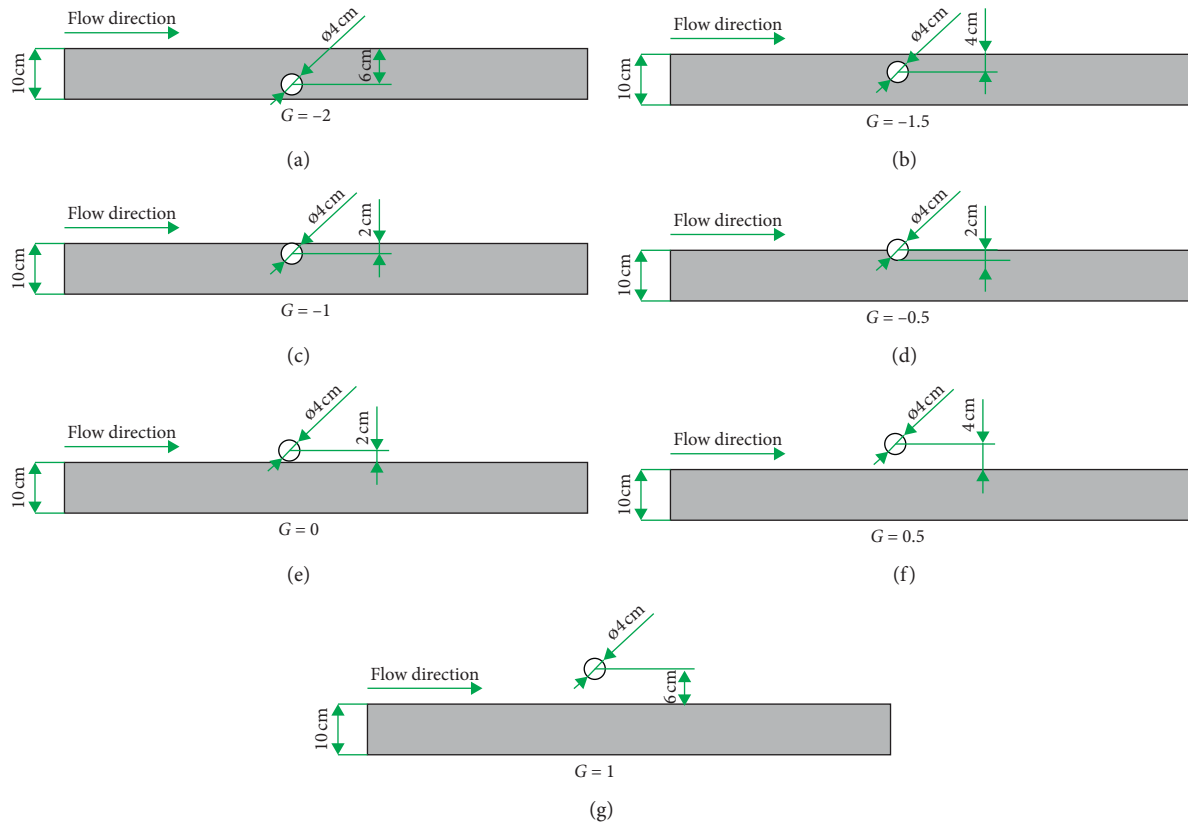


FIGURE 6: Schematic diagram of different embedment ratio tests: (a) schematic diagram of the test setup when the embedment ratio is -2 , (b) schematic diagram of the test setup when the embedment ratio is -1.5 , (c) schematic diagram of the test setup when the gap ratio is -1 , (d) schematic diagram of the test setup when the embedment ratio is -0.5 , (e) schematic diagram of the test setup when the embedment ratio is 0 , (f) schematic diagram of the test setup when the embedment ratio is 0.5 , and (g) schematic diagram of the test setup when the embedment ratio is 1 .

TABLE 3: Test conditions.

Embedment ratio (G)	Clay		Fine sand		Medium sand 1		Medium sand 2	
	Test groups	Flow velocity ($m \cdot s^{-1}$)	Test groups	Flow velocity ($m \cdot s^{-1}$)	Test groups	Flow velocity ($m \cdot s^{-1}$)	Test groups	Flow velocity ($m \cdot s^{-1}$)
-2	1-1	0.408	2-1	0.383	3-1	0.417	4-1	0.413
-1.5	1-2	0.429	2-2	0.385	3-2	0.432	4-2	0.397
-1	1-3	0.417	2-3	0.419	3-3	0.385	4-3	0.398
-0.5	1-4	0.396	2-4	0.405	3-4	0.398	4-4	0.389
0	1-5	0.394	2-5	0.408	3-5	0.411	4-5	0.387
0.5	1-6	0.423	2-6	0.391	3-6	0.413	4-6	0.397
1	1-7	0.398	2-7	0.407	3-7	0.399	4-7	0.419
Embedment ratio (G)	Coarse sand		Very coarse sand		Very fine pebble			
	Test groups	Flow velocity ($m \cdot s^{-1}$)	Test groups	Flow velocity ($m \cdot s^{-1}$)	Test groups	Flow velocity ($m \cdot s^{-1}$)		
-2	5-1	0.384	6-1	0.398	7-1	0.395		
-1.5	5-2	0.384	6-2	0.423	7-2	0.422		
-1	5-3	0.397	6-3	0.392	7-3	0.397		
-0.5	5-4	0.391	6-4	0.423	7-4	0.395		
0	5-5	0.416	6-5	0.387	7-5	0.387		
0.5	5-6	0.385	6-6	0.404	7-6	0.414		
1	5-7	0.411	6-7	0.406	7-7	0.404		

3.2. Scour Profile Characteristics. Select representative scour profiles of clay, fine sand, and very fine pebbles under different embedment ratios for analysis, and the results are shown in Figure 9.

It can be seen from Figure 9 that under the condition of the riverbed with clay particles, when G was -2 , -1.5 , and -1 ,

the pipeline was buried under the riverbed, and the bed surface was basically unchanged after the scour process. When G was -0.5 , the pipeline is semiexposed to the riverbed surface. The bed surface near the pipeline area dropped by about 1.5 cm, but no through scouring holes were formed. When G was 0 , 0.5 , and 1 respectively, the

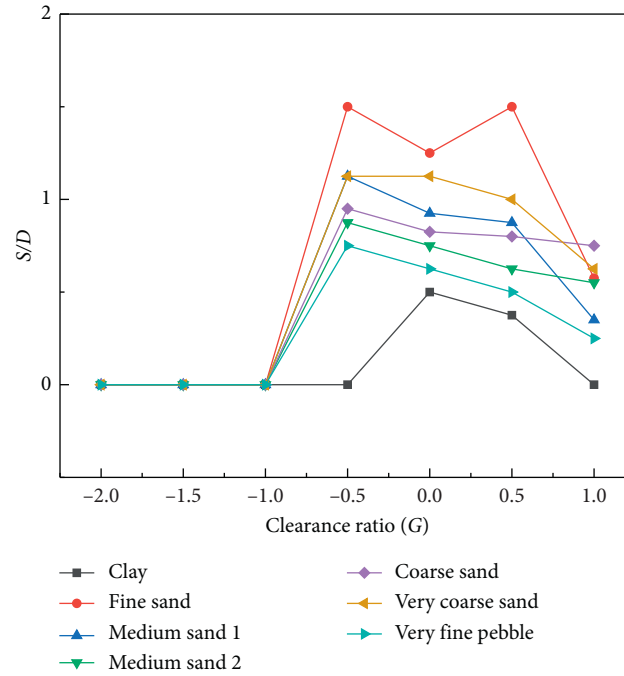


FIGURE 7: Variation of equilibrium scour depth with embedment ratio under different particle size riverbed conditions.

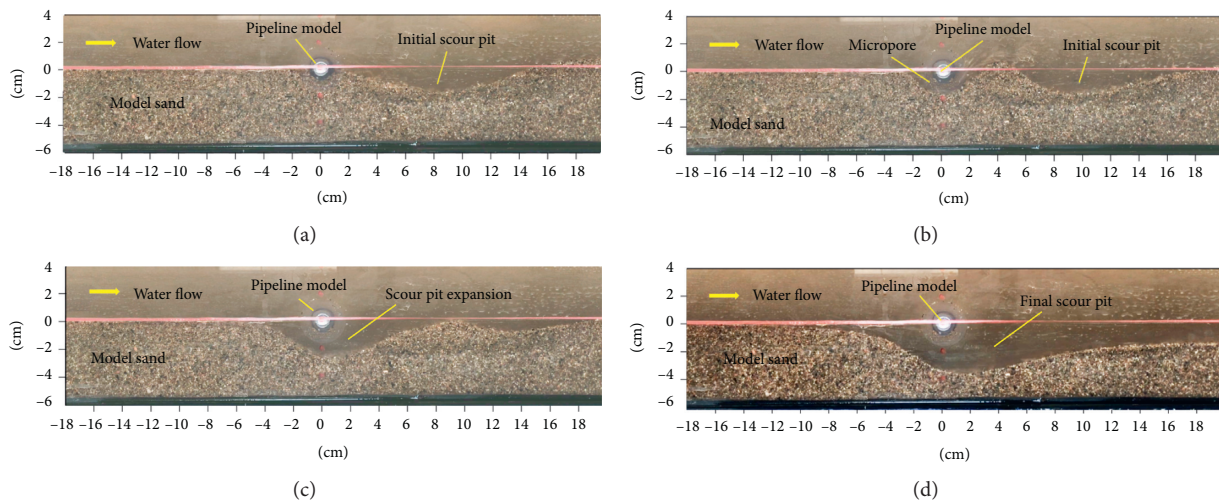


FIGURE 8: Local scour process around sandy riverbed pipelines: (a) scour start-up stage, (b) micropore formation stage, (c) scour extension stage, and (d) scour equilibrium stage.

pipeline was completely exposed above the riverbed, and a scour hole about 1.5 cm deep was formed at the bottom of the pipeline. Under the condition that the riverbed was constituted with fine sand, when G was -2 , -1.5 , and -1 respectively, the pipeline was buried under the riverbed. The entire bed surface dropped about 1 cm after scouring. When G was -0.5 , 0 , 0.5 , and 1 , the pipeline was exposed on the bed surface. After scouring, the depth of the scouring hole at the bottom of the pipeline was 4.7 cm, 4.2 cm, 3.5 cm, and 1.6 cm in sequence. The whole bed surface was lowered by about 1 cm. Under the condition that the riverbed was very fine

pebble, when G was -2 , -1.5 , and -1 respectively, the pipeline was buried under the riverbed, and the surface of the bed was basically unchanged after scouring. When G was -0.5 , 0 , 0.5 , and 1 , the pipeline was exposed on the bed surface. After scouring, the depth of the scouring hole at the bottom of the pipeline was 2.8 cm, 2.4 cm, 1.6 cm, and 0.6 cm in sequence.

3.3. Mechanical Effect of Pipeline. The profile pressure and the strain at the axial center of the pipeline were monitored

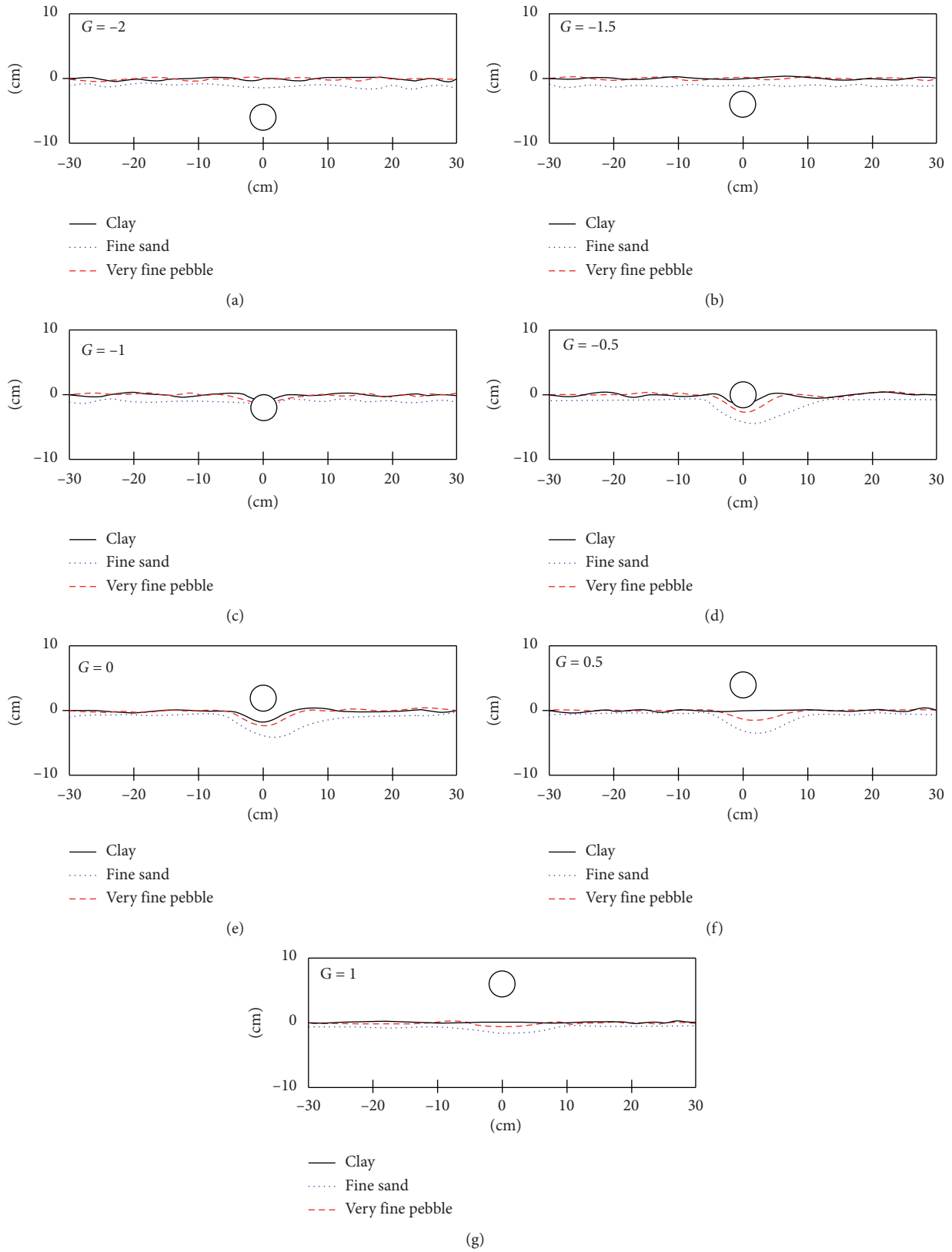


FIGURE 9: Scour profile under different embedment ratios: (a) scour profile with a embedment ratio of -2 , (b) scour profile with a embedment ratio of -1.5 , (c) scour profile with a embedment ratio of -1 , (d) scour profile with a embedment ratio of -0.5 , (e) scour profile with a embedment ratio of 0 , (f) scour profile with a embedment ratio of 0.5 , and (g) scour profile with a embedment ratio of 1 .

under different embedment ratios (buried under the bed material, half buried and half exposed, and suspended on the bed material) when the bed sediments were clay, fine sand, and very fine pebble. The results are shown in Figures 10–12, respectively. The pressure and strain in Figures 10–12 refer to the measured values when the scouring reaches an equilibrium state.

Figure 10 shows the pressure and the strain on the surface of the pipeline when G was -2 , -1.5 , and -1 (the pipeline was buried under the riverbed as a whole). It can be seen from Figure 10 that the pressure at the top of the pipeline was greater than the pressure at the bottom of the pipeline when the sediment was clay particles. And the strain at the top of the pipeline was negative, which was in the compression zone; the strain at the bottom of the pipeline was positive, and it was in the tension zone. When the sediment was fine sand and very fine pebble, the pressure at the bottom of the pipeline was larger than that at the top of the pipeline. The strain at the bottom of the pipeline was negative, which was in the compression zone, while the strain at the top of the pipeline was positive and in the tensile zone.

Figure 11 shows the pressure and strain on the surface of the pipeline when G was -0.5 (the pipeline was half buried and half exposed). It can be seen from Figure 11 that when the sediment was clay, the pressure at the top of the pipeline was larger than that at the bottom of the pipeline. The strain at the top of the pipeline was negative, which was in the compression zone, while the strain at the bottom of the pipeline was positive, which was in the tensile zone. When the sediment was fine sand or very fine pebble, the pressure on the upstream surface of the pipeline was larger than that on the downstream surface. The upstream surface of the pipeline was strained to be negative and was in the compression zone. The strain on the downstream surface of the pipeline was positive and was in the tensile zone.

Figure 12 shows the pressure and strain on the surface of the pipeline when G is 0 , 0.5 , and 1 , respectively (the pipeline is suspended on the riverbed). As Figure 12 shows, since the pipeline was suspended on the riverbed, the sediment type of the riverbed had little effect on the stress of the pipeline. Due to the impact of the water flow, the pressure on the upstream surface of the pipeline was greater than that on the downstream surface. The strain on the upstream surface was negative and in the compression zone, while the strain on the downstream surface was positive and in the tensile zone. It shows that the pipeline has a tendency to bend downstream at this time.

4. Discussion

When the embedment ratio was 0 , scour holes appeared in the clay riverbed. The depth was 2 cm, which was about half of the pipeline diameter. But it was still less than the depth of the scour hole formed by the very fine pebble riverbed when the embedment ratio was -0.5 . This is mainly due to the fact that when the noncohesive sediment starts to scour, it is mainly affected by the force of the water current (including

shear stress and lifting force) and its own effective gravity. In addition to the above two forces, the cohesive sediment is also affected by the cohesive force between particles. Cohesive sediment due to the cementation between the particles causes the clay particles to require greater water flow shear stress when starting, so when the buried depth of the pipeline is changed, the scour pits appear lagging behind the noncohesive sediment bed. After that, with the gradual increase of the embedment ratio, the equilibrium scour depth under the conditions of different particle diameters of riverbeds showed a gradual decrease in general. The reason may be that as the buried depth of the pipeline decreases, the pipeline is gradually exposed to the water flow, and the eddy effect generated by the water flowing through the pipeline gradually increases. When the pipeline is completely exposed on the riverbed, the influence of the eddy effect on the riverbed sediment gradually decreases as the gap between the pipeline and the riverbed increases.

It can be seen that when G was -2 , -1.5 , and -1 , the bed surface of the riverbed sediment with different particle sizes was basically unchanged after the scour process. It is explained that when the pipeline is buried under the riverbed, the riverbed particle size has little influence on the formation of scour holes near the pipeline. At this point, the pipeline is in a state of being less affected by the flow. When G was -0.5 , the bed surface of the clay riverbed near the pipeline area dropped by about 1.5 cm. However, no through scouring holes were formed, and scouring holes with depths of 4.7 cm and 2.8 cm appeared in both the fine sand and very fine pebble riverbeds. This shows that the clay bed is more resistant to the river erosion than the fine sand and very fine pebble riverbed with larger particle size when the pipeline is semiexposed. In these three grain-size riverbeds, fine sand is more difficult to resist the river's flushing and more likely to form a larger range of scouring holes.

When G was 0 , 0.5 , and 1 , the pipeline was completely exposed on the bed surface. At this time, a 1.5 cm deep scour hole was formed at the bottom of the pipeline in the clay riverbed. The depths of the scour holes formed by the fine sand riverbed were 4.2 cm, 3.5 cm, and 1.6 cm, respectively, and the scour holes formed by the very fine pebble riverbed were 2.4 cm, 1.6 cm, and 0.6 cm, respectively. It shows that the depth of scour hole in clay bed does not change significantly with the increase of embedment ratio when the pipeline is completely exposed to the bed. However, the depth of scour holes in fine sand and very fine pebble riverbed gradually decreases with the increase of the embedment ratio. But in general, the depth of scour holes formed by fine sand bed is greater than that of fine pebble bed.

Based on the results of Figures 10–12, it can be judged that when the pipeline is buried under the riverbed material and the sediment is clay, the pipeline has a downward bending trend, and when the sediment is fine sand or very fine pebble, the pipeline has the tendency of upward bulge. When the pipeline is half buried and half exposed and the sand is clay particles, the pipeline has a downward bending trend. When the sediment is fine sand and very fine pebbles, the pipeline tends to bend downstream.

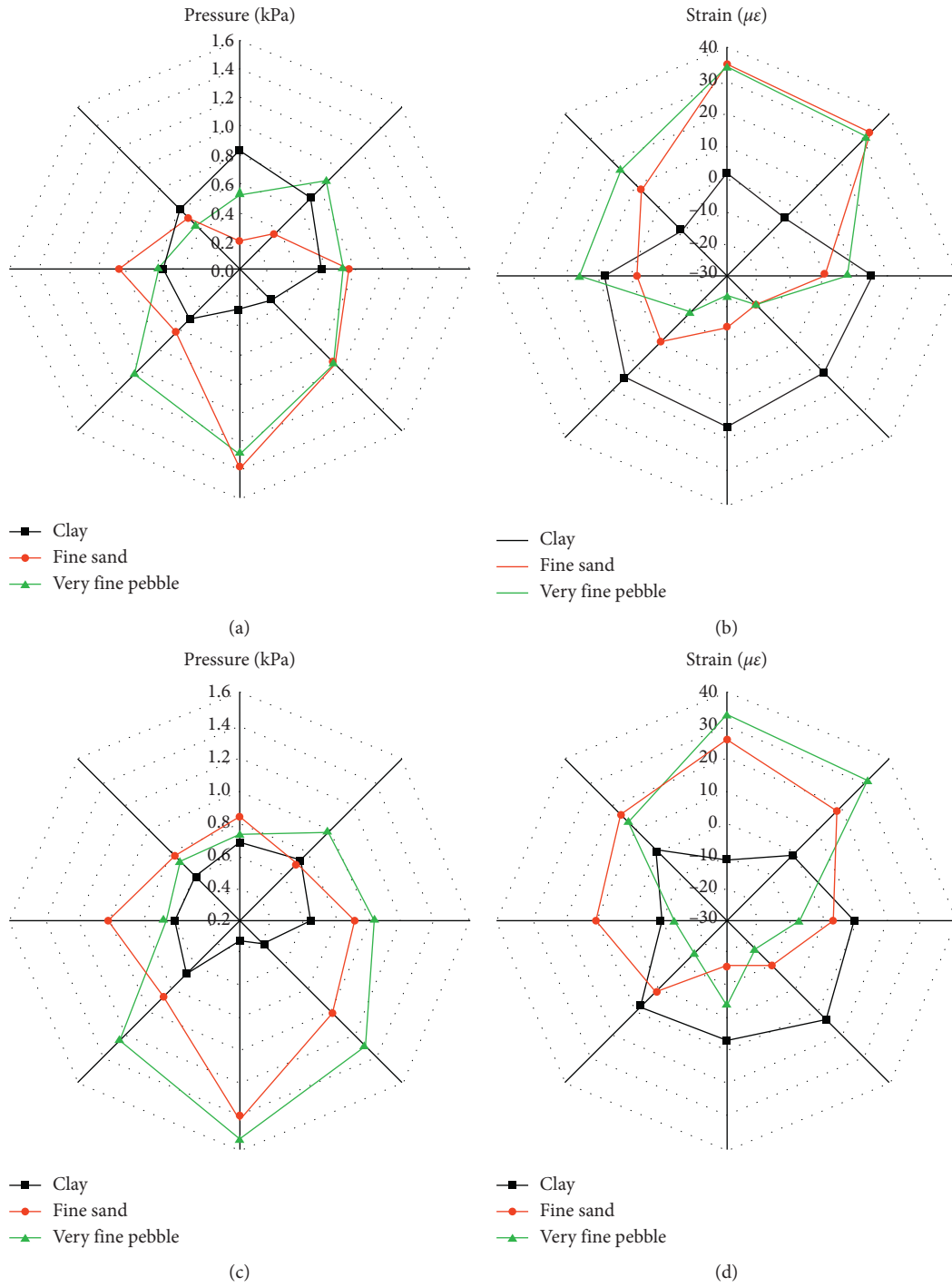


FIGURE 10: Continued.

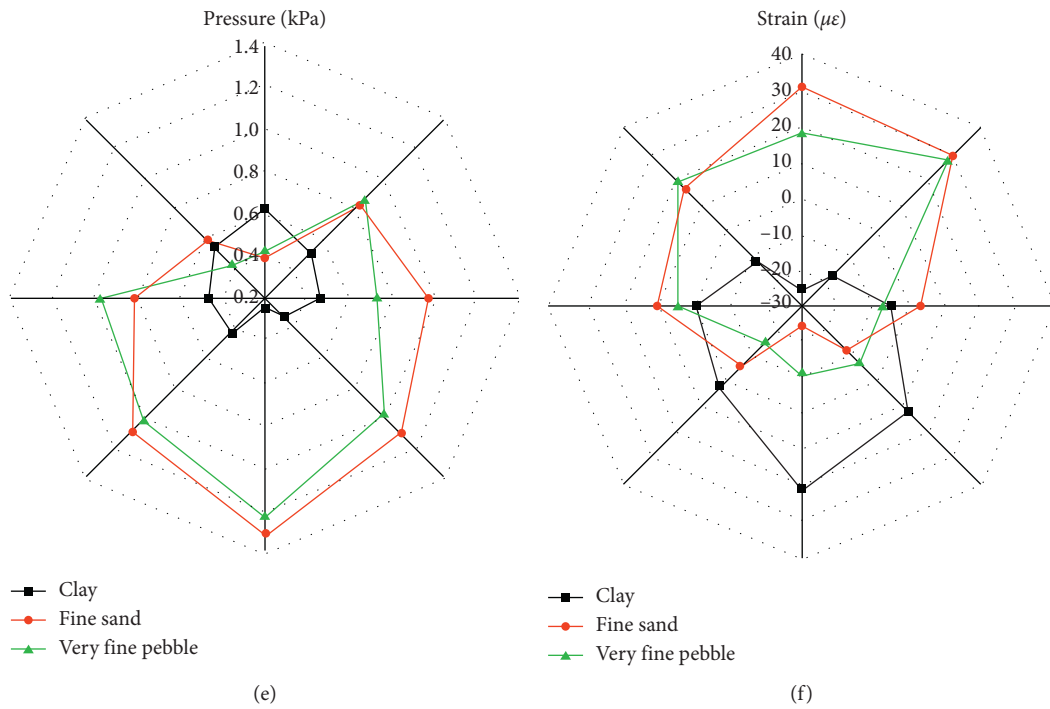


FIGURE 10: Pressure and strain on the surface of the pipeline which is buried under the riverbed: (a) pressure on the surface of the pipeline when the embedment ratio is -2 , (b) strain on the surface of the pipeline when the embedment ratio is -2 , (c) pressure on the surface of the pipeline when the embedment ratio is -1.5 , (d) strain on the surface of the pipeline when the embedment ratio is -1.5 , (e) pressure on the surface of the pipeline when the embedment ratio is -1 , and (f) strain on the surface of the pipeline when the embedment ratio is -1 .

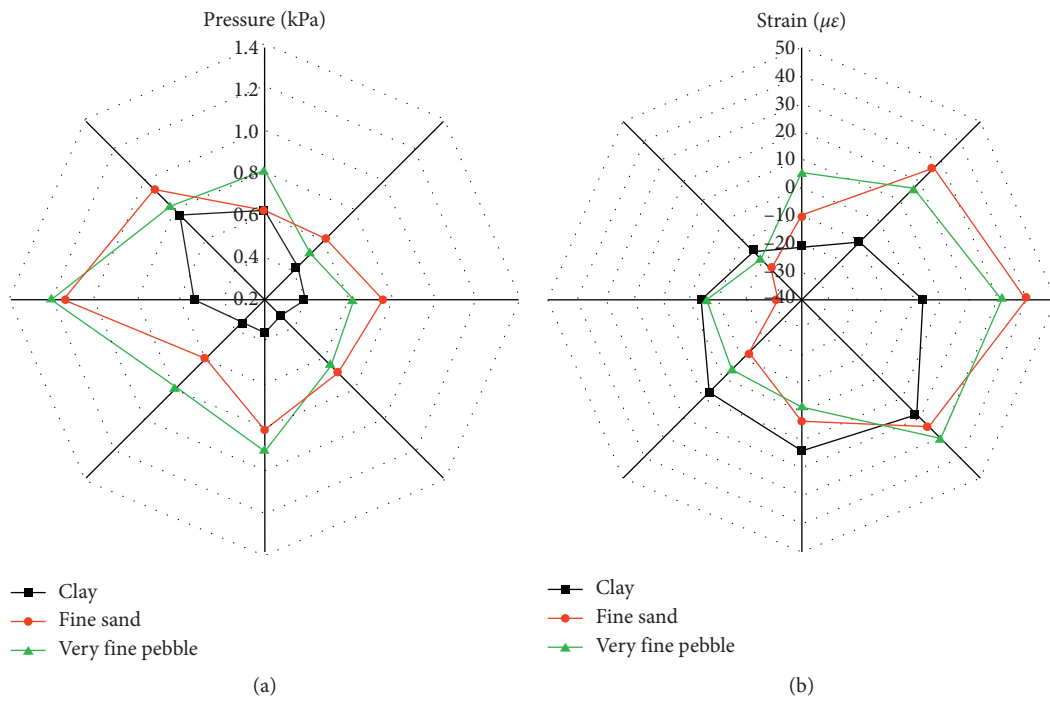


FIGURE 11: Pressure and strain on the surface of the pipeline when half of the pipeline is buried and half exposed: (a) pressure on the surface of the pipeline when the embedment ratio is -0.5 and (b) strain on the surface of the pipeline when the embedment ratio is -0.5 .

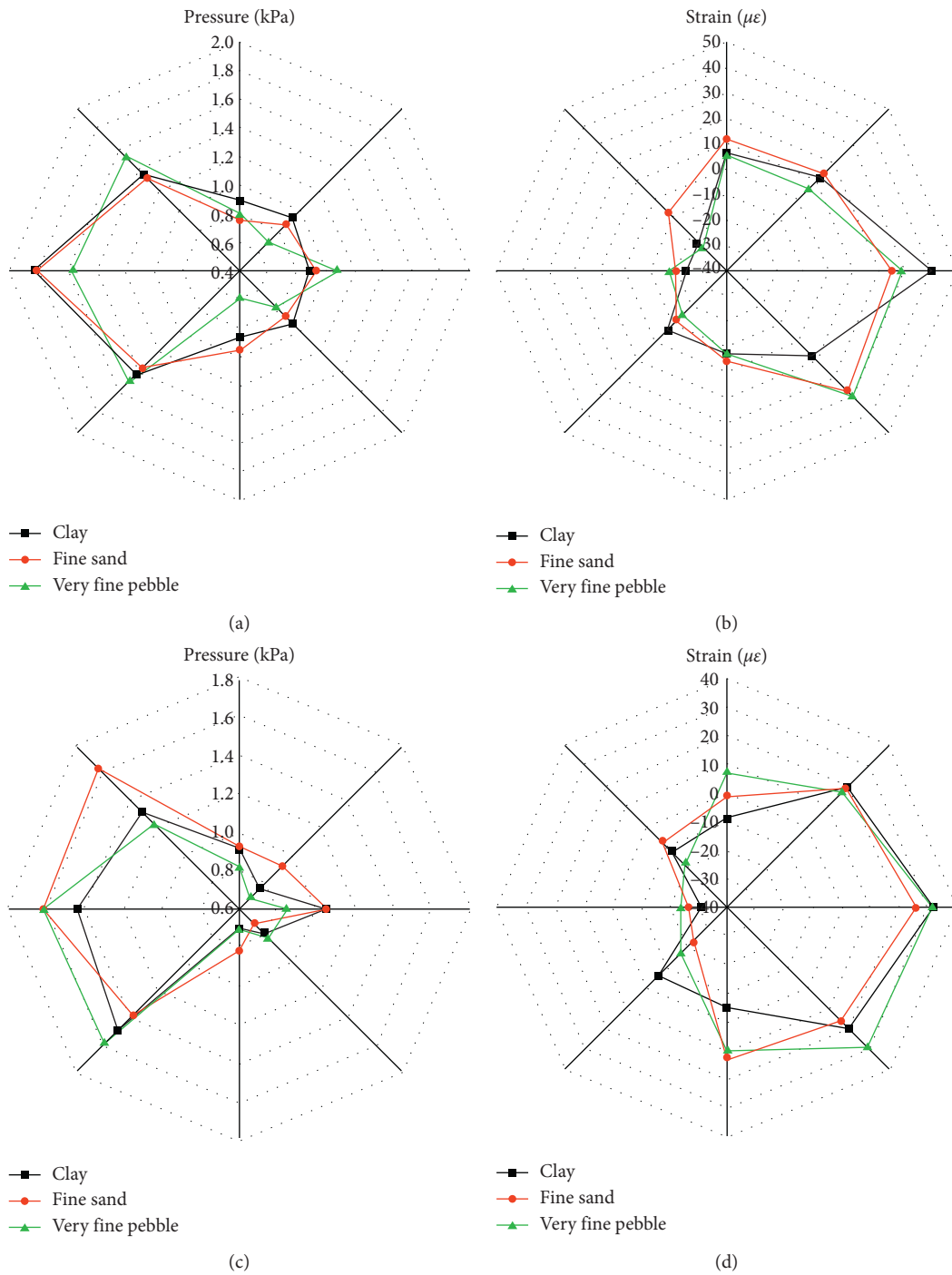


FIGURE 12: Continued.

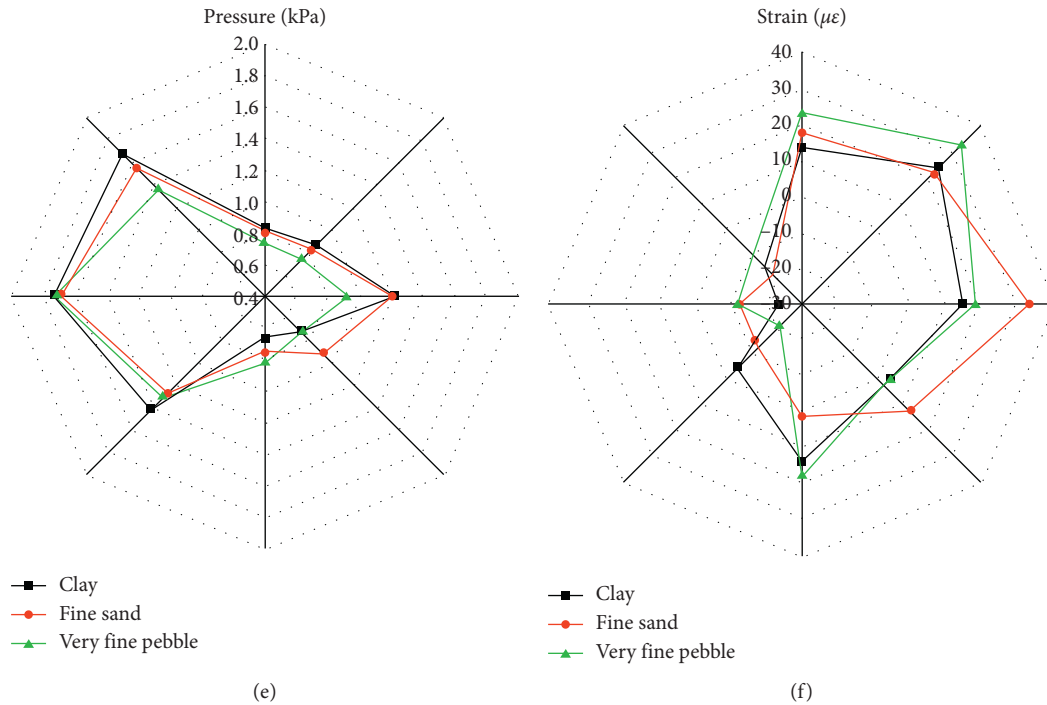


FIGURE 12: Pressure and strain on the surface of the pipeline which is suspended on the riverbed: (a) pressure on the surface of the pipeline when the embedment ratio is 0, (b) strain on the surface of the pipeline when the embedment ratio is 0, (c) pressure on the surface of the pipeline when the embedment ratio is 0.5, (d) strain on the surface of the pipeline when the embedment ratio is 0.5, (e) pressure on the surface of the pipeline when the embedment ratio is 1, and (f) strain on the surface of the pipeline when the embedment ratio is 1.

5. Conclusions

In this work, a physical model of water-damage disaster was established to test the characteristics of the riverbed scour profile and the pipeline force when the pipeline was buried at different depths under the condition of different particle size riverbed sediment. The following conclusions are obtained:

- The local scour of the pipeline generally goes through the four stages of scour start-up, micropore formation, scour expansion, and scour equilibrium. In general, the equilibrium scour depth changes in a spoon shape with the gradual increase of the embedment ratio. The equilibrium scour depth formed by fine sand riverbed is the largest, about 1.5 times of the pipeline diameter, and the clay riverbed is the smallest, about 0.5 times of pipeline diameter.
- When the pipeline is buried under the riverbed, the particle size of the riverbed has little effect on the formation of scour holes on the bed surface near the pipeline. When the pipeline is half exposed, the clay riverbed is more resistant to the erosion of the river than the riverbed of fine sand and very fine pebbles with a larger particle size. However, in the riverbed with three kinds of grain size, the fine sand riverbed is more likely to form a large range of scour holes. When the pipeline is completely exposed on the riverbed surface, the balance scour depth of the fine sand and very fine pebble riverbed will gradually decrease with the increase of the embedment ratio. But from the overall

perspective, the equilibrium scour depth of fine sand riverbed is greater than that of very fine pebble riverbed.

- When the pipeline is completely buried in the riverbed, the pipeline in the clay riverbed tends to bend downward, and the pipeline in the fine sand and very fine pebble riverbed tends to uplift upward. When half of the pipeline is under the surface of the riverbed, the clay riverbed pipeline has a downward bending trend, and the fine sand and very fine pebble riverbed pipelines have a downstream bending trend. When the pipeline is completely above the surface of the riverbed, the type of riverbed sediment has little effect on the force of the pipeline. In future studies, related numerical simulation tests will be considered to explore the factors affecting the evolution of the riverbed near the pipeline. Further designs related to prototype tests are needed and they should be compared with current research works in order to improve the existing research results.

Data Availability

The data used to support the findings of this study are available from the corresponding author upon request.

Conflicts of Interest

The authors declare no potential conflicts of interest with respect to the research, authorship, and/or publication of this article.

Acknowledgments

The project was financially supported by the Major Project of Shaanxi Coal and Chemical Industry Group Co., Ltd.: Protection and Utilization of Water Resources & Research and Demonstration of Key Technologies for Ecological Reconstruction in Northern Shaanxi Coal Mining Area (2018SMHKJ-A-J-03) and the 2030 Pilot Project of CHN ENERGY Investment Group Co., Ltd.: Research on Ecological Restoration and Protection of Coal Base in Arid Eco-fragile Region (GJNY2030XDXM-19-03.2).

References

- [1] J. Chu, L. Yang, Y. Liu et al., "Pressure pulse wave attenuation model coupling waveform distortion and viscous dissipation for blockage detection in pipeline," *Energy Science & Engineering*, vol. 8, no. 1, pp. 260–265, 2020.
- [2] H. Lu, T. Iseley, S. Behbahani, and L. Fu, "Leakage detection techniques for oil and gas pipelines: state-of-the-art," *Tunnelling and Underground Space Technology*, vol. 98, p. 103249, 2020.
- [3] Q. Yang, Q. Yang, J. Yao, Y. Zhang, and Z. Wang, "Experimental study in expansion law of scour hole of pipeline crossing mountain river," *Mountain Research*, vol. 38, no. 2, pp. 241–251, 2020.
- [4] Q. Li, X. Ban, and H. Wu, "Design of informationized operation and maintenance system for long-distance oil and gas pipelines," in *Proceedings of the 3rd International Conference on Computer Science and Application Engineering*, pp. 1–5, Sanya, China, 2019.
- [5] X. Wang and J. Shuai, "Stress analysis of pipeline floating in flood," *Engineering Mechanics*, vol. 28, no. 2, pp. 212–216, 2011.
- [6] Atkins, "Yellowstone river pipeline risk assessment and floodplain reclamation planning project," Final Report to the Yellowstone River Conservation District Council, Atkins, Epsom, UK, 2012.
- [7] S. Girgin and E. Krausmann, "Historical analysis of U.S. onshore hazardous liquid pipeline accidents triggered by natural hazards," *Journal of Loss Prevention in the Process Industries*, vol. 40, pp. 578–590, 2016.
- [8] Y. Mao, "The interaction between a pipeline and an erodible bed," *Febs Letters*, vol. 225, no. 1–2, pp. 218–222, 1987.
- [9] B. M. Sumer and J. Fredsoe, "Onset of scour below a pipeline exposed to waves," *International Journal of Offshore and Polar Engineering*, vol. 1, no. 3, pp. 189–194, 1991.
- [10] B. M. Sumer, C. Truelsen, T. Sichmann, and J. Fredsøe, "Onset of scour below pipelines and self-burial," *Coastal Engineering*, vol. 42, no. 4, pp. 313–335, 2001.
- [11] B. M. Sumer, *The Mechanics of Scour in the Marine Environment*, World Scientific Publishing Company, London, UK, 2002.
- [12] B. M. Sumer and J. Fredsøe, "Scour below pipelines in waves," *Journal of Waterway, Port, Coastal, and Ocean Engineering*, vol. 116, no. 3, pp. 307–323, 1990.
- [13] Y. M. Chiew, "Effect of spoilers on wave-induced scour at submarine pipelines," *Journal of Waterway, Port, Coastal, and Ocean Engineering*, vol. 119, no. 4, pp. 417–428, 1993.
- [14] Y. M. Chiew, "Prediction of maximum scour depth at submarine pipelines," *Journal of Hydraulic Engineering*, vol. 117, no. 4, pp. 452–466, 1991.
- [15] Y. M. Chiew, "Mechanics of local scour around submarine pipelines," *Journal of Hydraulic Engineering*, vol. 116, no. 4, pp. 515–529, 1990.
- [16] S. Neelamani and S. N. Rao, "Wave pressures and uplift forces on and scour around submarine pipeline in clayey soil," *Ocean Engineering*, vol. 30, no. 2, pp. 271–295, 2003.
- [17] B. Yang, F. P. Gao, and Y. X. Wu, "Experimental study on local scour of sandy seabed under submarine pipeline in unidirectional currents," *Engineering Mechanics*, vol. 25, no. 3, pp. 206–210, 2008.
- [18] F. Gao, X. Gu, and Q. Pu, "Experimental research on the instability process of submarine pipelines," *Chinese Journal of Geotechnical Engineering*, vol. 22, no. 3, pp. 304–308, 2000.
- [19] F. A. Van Beek and H. G. Wind, "Numerical modelling of erosion and sedimentation around offshore pipelines," *Coastal Engineering*, vol. 14, no. 2, pp. 107–128, 1990.
- [20] M. Zhao, S. Vaidya, Q. Zhang, and L. Cheng, "Local scour around two pipelines in tandem in steady current," *Coastal Engineering*, vol. 98, pp. 1–15, 2015.
- [21] Y. Liu, H. Wang, and M. Wang, "Numerical simulation analysis of local scour around submarine pipeline," *Journal of China University of Petroleum*, vol. 36, no. 6, pp. 118–122, 2012.
- [22] H. An, W. Yao, L. Cheng et al., "Detecting local scour using contact image sensors," *Journal of Hydraulic Engineering*, vol. 143, no. 4, Article ID 04016100, 2016.
- [23] Y. Zhu, L. Xie, and T. Su, "Visualization tests on scour rates below pipelines in steady currents," *Journal of Hydraulic Engineering*, vol. 145, no. 4, Article ID 04019005, 2019.
- [24] H. M. Azamathulla and N. A. Zakaria, "Prediction of scour below submerged pipeline crossing a river using ANN," *Water Science and Technology*, vol. 63, no. 10, pp. 2225–2230, 2011.
- [25] H. M. Azamathulla, M. A. M. Yusoff, and Z. A. Hasan, "Scour below submerged skewed pipeline," *Journal of Hydrology*, vol. 509, pp. 615–620, 2014.
- [26] M. Najafzadeh, G. Barani, and M. R. H. Kermani, "Estimation of pipeline scour due to waves by GMDH," *Journal of Pipeline Systems Engineering and Practice*, vol. 5, no. 3, Article ID 06014002, 2014.
- [27] M. Najafzadeh, G. Barani, and H. Azamathulla, "Prediction of pipeline scour depth in clear-water and live-bed conditions using group method of data handling," *Neural Computing and Applications*, vol. 24, no. 3–4, pp. 629–635, 2014.
- [28] M. Najafzadeh and F. Saberi-Movahed, "GMDH-GEP to predict free span expansion rates below pipelines under waves," *Marine Georesources & Geotechnology*, vol. 37, no. 3, pp. 375–392, 2019.
- [29] M. Najafzadeh and S. Sarkamaryan, "Extraction of optimal equations for evaluation of pipeline scour depth due to currents," *Proceedings of the Institution of Civil Engineers-Maritime Engineering*, vol. 171, no. 1, pp. 1–10, 2018.
- [30] W. Park, C. Yoo, D. Shin, T. Kim, and H. Lee, "A study on the risk assessment of river crossing pipeline in urban area," *Journal of the Korean Institute of Gas*, vol. 24, no. 2, pp. 22–28, 2020.
- [31] Y. Zhang, S. Zhang, and G. Li, "Seabed scour beneath an unburied pipeline under regular waves," *Marine Georesources & Geotechnology*, vol. 37, no. 10, pp. 1247–1256, 2019.
- [32] F.-P. Gao, B. Yang, Y.-X. Wu, and S.-M. Yan, "Steady current induced seabed scour around a vibrating pipeline," *Applied Ocean Research*, vol. 28, no. 5, pp. 291–298, 2006.

Research Article

Study on Change Rules of Factors Affecting Gas Loss during Coalbed Air Reverse Circulation Sampling

Demin Chen ^{1,2,3} Wei Long ¹ Yanyan Li ¹ and Rui Zhang ^{2,3}

¹School of Mechanical Engineering, Sichuan University, Chengdu 610065, China

²State Key Laboratory of Gas Disaster Monitoring and Emergency Technology, Chongqing 400037, China

³China Coal Technology and Engineering Group Chongqing Research Institute, Chongqing 400039, China

Correspondence should be addressed to Demin Chen; chendemin@stu.scu.edu.cn and Yanyan Li; yyl_scu@yeah.net

Received 8 February 2021; Revised 30 March 2021; Accepted 8 April 2021; Published 20 April 2021

Academic Editor: Jia Lin

Copyright © 2021 Demin Chen et al. This is an open access article distributed under the Creative Commons Attribution License, which permits unrestricted use, distribution, and reproduction in any medium, provided the original work is properly cited.

The gas loss in sampling is the root of coalbed gas content measurement error. The pressure and particle size have a significant impact on the gas loss. Using the self-developed coal particle pneumatic pipeline transportation experimental system, this study investigated the pressure and particle size changes in the sampling pipeline. It is found that the sampling process can be divided into four stages: no flow field stage, sample outburst stage, stable conveying stage, and tail purging stage. The extreme pressure in the sampling pipeline appears at the sample outburst stage; and the pressure in the pipeline has levelled off after sharp decrease in the stable conveying stage. It is also found that the extreme pressure increases first and then decreases with the increase of particle size. The duration of outburst stage is negatively correlated with particle size, and that of stable conveying stage is positively correlated with particle size. In addition, the results show that the loss rate of 1–3 mm particles is the smallest after the test but that particles less than 1 mm increase by about two times and particles greater than 3 mm decrease by more than three times. The study also shows that the particle size distribution of coal samples is a single peak with left skew distribution, and the gas reverse circulation sampling test does not change the location of the peak but makes it higher and sharper. The single size coal sample is more likely to collide than the mixture. This study can help to advance the understanding of impact factors on gas loss during reverse circulation sampling.

1. Introduction

Gas content has been recognized as the basic parameter of gas disaster prevention as well as coalbed methane resource development and applications [1–3]. Accurate measurement of gas content has considerable practical value and significance for productivity evaluation of coalbed methane. Regarding the accurate measurement of gas content in the coal seam, the direct methods for measurement of gas content based on air reverse circulation sampling were invented by Chinese researchers [4]. These researchers achieved stable measurement of gas content in a wide range of holes of 80 m depth with a measurement time of less than 8 h. However, the problem of large measurement error has not been resolved.

In direct methods for measurement of gas content, the gas desorption amount and residual gas content from a coal

sample are firstly measured, and then the gas loss in the sampling process is assessed. The gas loss in the sampling process has been recognized as the error source of this method [5]. Much work has been done by experts and scholars on the calculation of gas loss in the sampling process. Furthermore, some calculation models, such as the Barrer [6–8] model, Winter [9] model, Bolt [10] model, and Airey [11] model, have been developed. This gradually led to the development of a method to reverse the amount of gas loss in the sampling process by using these calculation models. However, these methods are based on the condition of fixed particle size and pressure and do not consider the influence of pressure and particle size change on gas loss during sampling.

In the process of sampling, the gas loss comes from the gas desorption and diffusion of granular coal. Gas

desorption of granular coal is the gas transfer process in porous media, and this process is affected by particle size, pressure, temperature, and other factors [12, 13]. Wang et al. [14] showed that the sensitivity of gas desorption law to particle size, temperature, pressure, moisture content, and forming pressure was pressure > temperature > particle size > moisture content > forming pressure. Qin et al. [15] proved that the desorption process of granular coal was inhibited when the desorption environment pressure was higher than the atmospheric pressure. Chen et al. [16] found that the negative pressure desorption environment significantly promoted gas desorption.

The influence of particle size on gas loss is reflected in the influence of particle size on desorption speed. The larger the particle size of the coal sample, the smaller the initial kinetic diffusion parameter, and the smaller the amount of gas desorption at the same time [17, 18]. On the other hand, the gas desorption behaviors of coal sample correlate with the surface area and depend significantly on porosity [19]. Meanwhile the coal sample with a smaller particle size has a higher specific surface area and higher pore volume [20, 21]. The specific surface area and larger pore volume can reduce the resistance of gas desorption inside the coal sample, thus increasing the gas desorption at a given time [22]. From the results of these studies, it is evident that pressure and particle size have great influence on gas desorption of coal samples. This means that the pressure and particle size have a close relation with the gas loss in the sampling process. Therefore, when calculating the amount of gas loss in the process of sampling, we need to pay attention to the changing law of pressure and particle size.

The air reverse circulation sampling technology is a method that brings the coal sample at the bottom of the hole to the surface from the central channel of the drill pipe with the help of compressed air [23]. It is currently the most commonly used sampling method in coal seam gas content measurement. The research on this sampling technology mainly focuses on the characteristics of the gas-solid flow field in the reverse circulation pipeline [23–26] and the improvement of sampling efficiency [27–29]. However, there is a lack of studies on the change rule of factors affecting gas loss in the process of sampling.

This study mainly discussed the factors affecting the gas loss during sampling rather than desorption behaviors in a closed space. Therefore, the temperature, moisture content, forming pressure, and other factors were not investigated. Instead, the change rules of pressure and particle size were experimentally studied, aiming to reveal the change rules of pressure and particle size during reverse circulation sampling and provide the basic theory for the establishment of a more accurate gas loss compensation model.

2. Materials and Methods

2.1. Experimental Setup. To study the change rules of pressure and particle size in the process of sampling, an experimental reverse circulation sampling device was designed. The experimental system included air compressor, pressure gauge, gas flowmeter, hopper, conveying pipeline,

and high-precision pressure sensors. The experimental system is shown in Figure 1.

The parameters of the main parts are outlined as follows:

- (1) Air compressor: maximum power of 110 Kw, exhaust volume of 17.1 m³/min, and exhaust pressure of 1.0 MPa.
- (2) Detecting system: a pressure gauge with range of 0–1.6 MPa was used to monitor the output pressure of the air compressor. The flowmeter was used to monitor the instantaneous flow and velocity in the pipeline. In addition, eight pressure sensors were arranged on the pipeline. The pressure sensors were installed at 0.1 m, 4 m, 8 m, 12 m, 16 m, 24 m, 65 m, and 80 m from the feed port. The sampling frequency of the pressure sensor was 2400 times in 1 s, and the accuracy level was 0.5. In addition, the concentrator and software were designed for storing measurement data.
- (3) Coal sample conveying system: the design volume of the bunker was 15 L, which can hold a coal sample of about 12 kg. The inner diameter of the pipeline was 40 mm, which was consistent with the inner diameter of the double-barreled drilling rod used in the current air counter circulation method. The total design length of the pipeline was 80 m, and a mesh bag was used to collect coal samples.
- (4) Granularity analysis system: the OCCHIO ZEPHYR ESR2 particle analyzer was used to determine the particle distribution of coal samples before and after the air reverse sampling test. This allowed easy and rapid analysis of the particle size parameters, shape parameters, and number of particles in the range of 30 μm–30 mm.

2.2. Sample Preparation. The coal samples used in this experiment were collected from No. 4 coal Seam of Xintian Colliery, which is located in Qianxi County of Guizhou Province. The location of the mine is shown in Figure 2.

The process of sample preparation is shown in Figure 3. The preparation process of coal sample was as follows. First, the cone bit and PDC (Polycrystalline Diamond Compact) bit were used to drill with the parameters of reverse circulation sampling to collect the original coal sample. With the aid of the particle analyzer, the particle size distribution of the original coal sample was measured. Moreover, the f value (consistent coefficient of coal) of the coal sample was measured in accordance with industry standards. Subsequently, the pulverizer was used to crush the lump coal of No. 4 coal seam of Xintian Colliery, and the powdered coal with various sizes was obtained after screening. Finally, according to the particle size distribution of the original coal sample, the test coal sample was obtained by mixing the powdered coal.

According to the coal sample size commonly used in gas content measurement, the original coal sample size was classified as ≤1 mm, 1–3 mm, 3–4 mm, 4–5 mm, 5–6 mm, 6–7 mm, and 7–8 mm. The particle size distribution of the

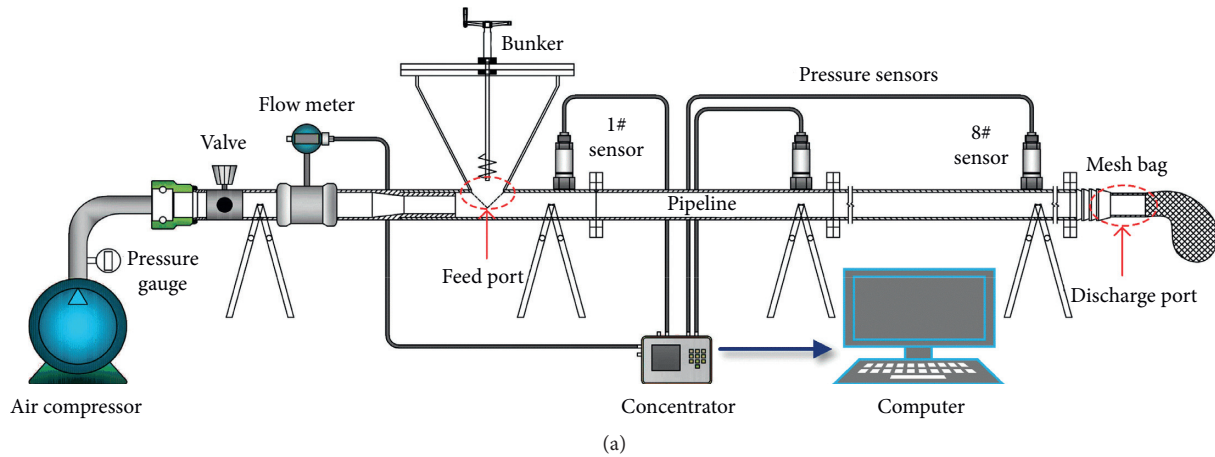


FIGURE 1: The experimental system. (a) Schematic diagram of the experimental system. (b) Physical map of the experimental system: ① Conveying pipeline. ② Particle analyzer. ③ High-speed camera. ④ Bunker. ⑤ Concentrator.

original coal sample drilled by using the cone bit and PDC bit is shown in Table 1. According to Table 1, two groups of coal samples were configured for each particle size distribution, four groups in total, of which two groups corresponding to the cone bit were numbered 1 # and 2 #, and two groups corresponding to the PDC bit were numbered 3 # and 4 #. The weights of 1 #, 2 #, 3 #, and 4 # coal samples were 12 kg. In addition, 8 kg coal samples were taken from 1–3 mm, 3–4 mm, 4–5 mm, 5–6 mm, 6–7 mm, and 7–8 mm as single particle size coal samples. The f value of No. 4 coal seam of Xintian Colliery was 0.8.

2.3. Experimental Procedure. After the equipment and the coal sample were prepared, the numbered coal samples were successively loaded into the bunker. Then, the air compressor was started. When the output pressure of the air pressure was stable at 0.6 MPa, the valve was opened. This allowed the compressed air to draw the coal sample into the pipeline and start transmission. At the same time, the

sensors collected the pressure data in the transmission pipeline. When all the coal samples had been transported, the air compressor was turned off and the coal samples in sampling mesh bag were collected. Finally, the size distributions of coal samples collected were tested by particle analyzer.

3. Results and Discussion

3.1. Pressure Variation during the Process of Sampling

3.1.1. Pressure Characteristics in the Pipe during Mixed Coal Sample Tests. The pressure change in the air reverse circulation sampling pipeline is the result of the kinetic energy transfer between gas and particles, as well as the conversion of the gas phase kinetic energy and pressure potential energy. Pressure variation in the pipeline during the tests of the mixture sample is shown in Figure 4.

The whole test process can be divided into four stages: no flow stage, sample outburst stage, stable conveying stage, and

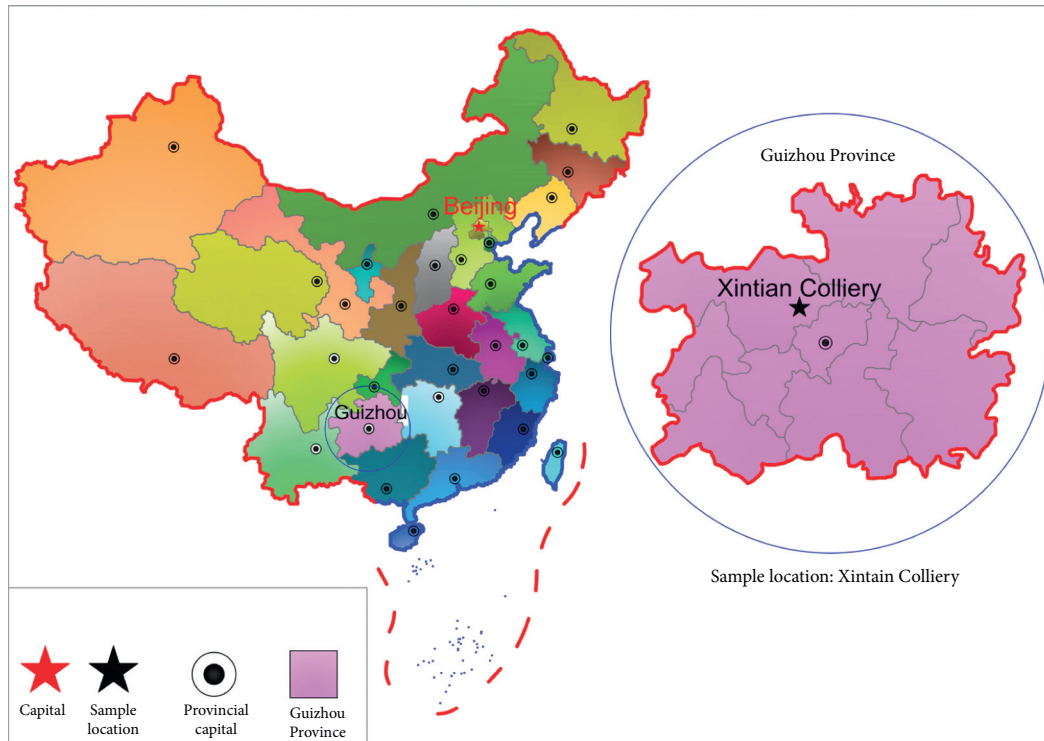


FIGURE 2: Geographical location of the coal sample.

tail purging stage. The no flow stage refers to the stage from energizing the detecting system to opening the valve. At this stage, there is no fluid in the pipeline, so the indication of the sensor is zero. The sample outburst stage refers to the completion of transportation of coal sample accumulated at the feed port. In the sample outburst stage, most of the pressure potential energy of the compressed air was rapidly converted into kinetic energy, and part of the kinetic energy was transferred to the coal sample at the feed port, so that the coal sample could achieve acceleration and move with the compressed air. Currently, the moving speed of the coal sample was less than that of the compressed air. Therefore, the movement of compressed air is the main element in the pipeline, and the pressure in the pipeline increases from atmospheric pressure to compressed air pressure. It can be seen from Figure 4 that the extreme pressure appears at the sample outburst stage. The extreme pressures of 1 # sensor were 558.84 Pa, 508.04 Pa, 509.85 Pa, and 514.30 Pa, and the maximum pressures of 8 # sensor were 76.44 Pa, 60.29 Pa, 75.14 Pa, and 78.31 Pa, respectively. This illustrates that the closer to the feed port, the higher the extreme pressure, and the closer to the discharge port, the smaller the extreme pressure. The distinction between the abscissa of point “e” and point “f” in Figure 4 represents the time difference when the extreme pressure reaches 1 # sensor and 8 # sensor and also represents the duration of sample outburst stage. The durations of sample outburst stage in the test of 1 #, 2 #, 3 #, and 4 # coal samples were 1.8 s, 0.8 s, 1.2 s, and 1.0 s, respectively.

In the stable conveying stage, coal sample enters the pipeline evenly from the feed port. The kinetic energy and

pressure potential energy of the compressed air were converted into a dynamic equilibrium. Therefore, there was relatively little pressure change in the pipeline, which is reflected in that the curve of the stable conveying stage tends to be stable after a sharp drop in Figure 4. The durations of stable conveying stage in the test of 1 #, 2 #, 3 #, and 4 # coal samples were 85.4 s, 86.2 s, 85.2 s, and 80.4 s, respectively.

In the tail purging stage, the coal sample is no longer supplied to the pipeline from the feed port, so the remaining coal sample in the pipeline is reduced. Therefore, the movement resistance of compressed air is reduced, and more pressure potential energy is converted into kinetic energy, resulting in the reduction of static pressure in the pipeline. When the particles are completely transported, the flow field returns to pure air flow, and the pressure in the pipeline returns to a lower level. It is shown in Figure 4 that the curve of the purge stage tends to be stable after the obvious decrease.

The pressure values of each measuring point in the pipeline at 35 s, 55 s, 75 s, and 95 s are shown in Figure 5. It can be seen that, in the stable conveying stage, the pressure variation trends of all measurement points are basically the same. The further from the feed port, the lower the static pressure. At the same time, the pressure loss values of the same distance are almost equal. The pressure difference between each measuring point at 35 s and 55 s is significantly higher than that at 55 s and 75 s. This means that the closer to the sample outburst stage, the higher the static pressure loss value, and much of the lost pressure potential energy is converted into the kinetic energy of compressed air and coal particles. Therefore, the moving speed of particles is still on

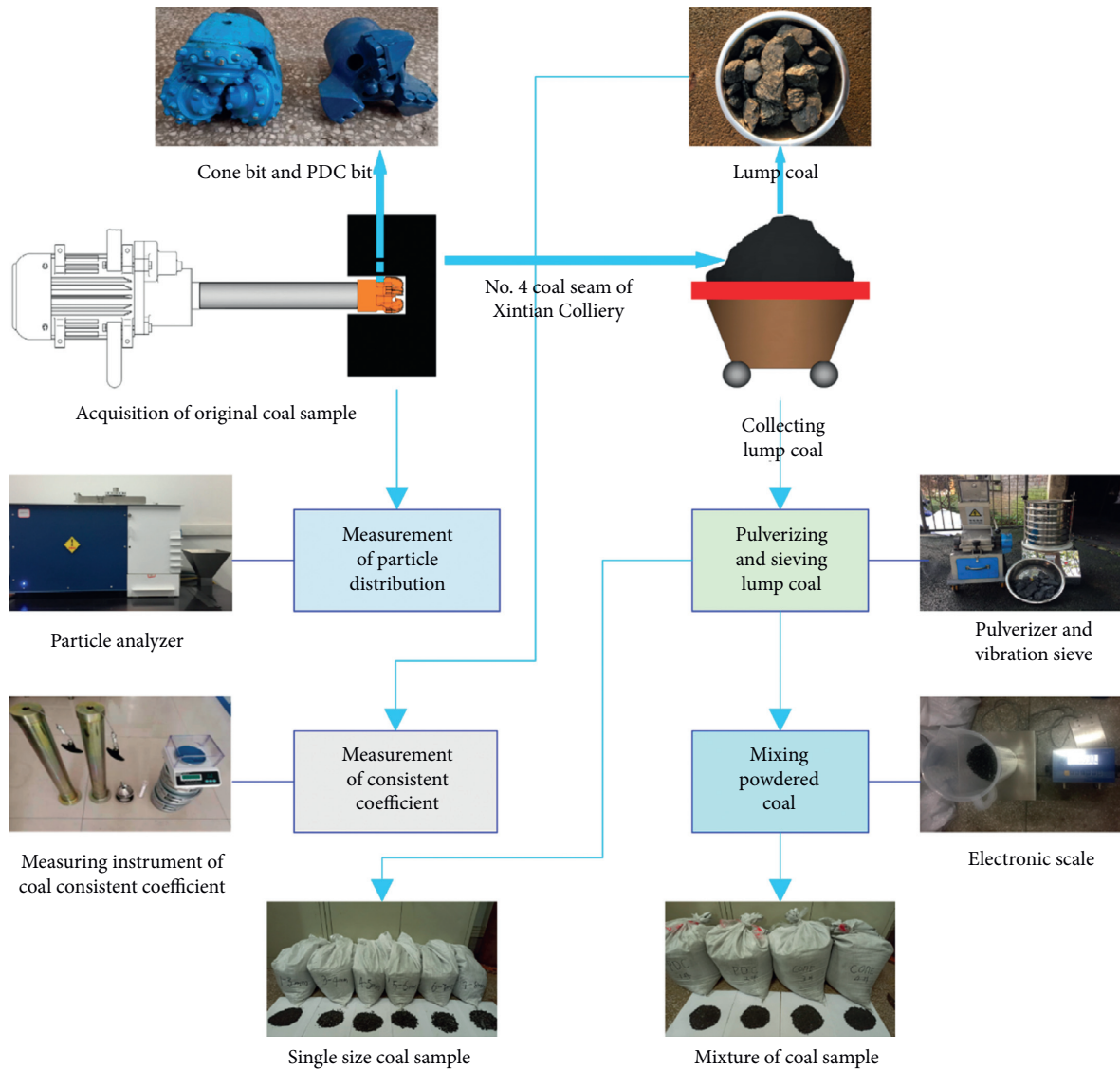


FIGURE 3: The process of coal sample preparation.

TABLE 1: Particle size distribution of the original coal sample.

Sample size	≤1 mm	1–3 mm	3–4 mm	4–5 mm	5–6 mm	6–7 mm	7–8 mm
Cone bit	34.61	35.10	8.27	9.10%	4.51%	5.45%	2.96%
PDC bit	30.87	43.29	10.10	5.61%	5.32%	1.25%	3.56%

the rise, which increases the time during which the coal sample remains in the pipeline and increases the gas loss of the coal sample.

3.1.2. Effect of Particle Size on the Pressure Characteristics in the Sampling Pipeline. Pressure variation in the pipeline during the tests of single size coal sample is shown in Figure 6. The relationship between the pressure characteristics and the particle size is shown in Figure 7. Two laws can be drawn from Figures 6 and 7: One is that the duration of outburst stage is negatively correlated with particle size, and that of stable conveying stage is positively correlated with

particle size. The other is that the extreme pressure increases first and then decreases with the increase of particle size.

In the test of 1–3 mm coal sample, the duration of sample outburst stage is 2.4 s, and that of the stable conveying stage is 20.6 s. Meanwhile, in the test of 7–8 mm coal sample, the duration of sample outburst stage is 0.8 s, which is only one-third of the 1–3 mm coal sample. The duration of stable conveying stage is 46.8 s, which is increased by 127%. This shows that the larger the coal sample size, the shorter the sample outburst stage, but the longer the duration of the stable conveying stage. In the test of 1–3 mm coal sample, the extreme pressures of 1 # and 8 # sensors are 520.53 Pa and 104.73 Pa, respectively. In the test of 6–7 mm coal sample,

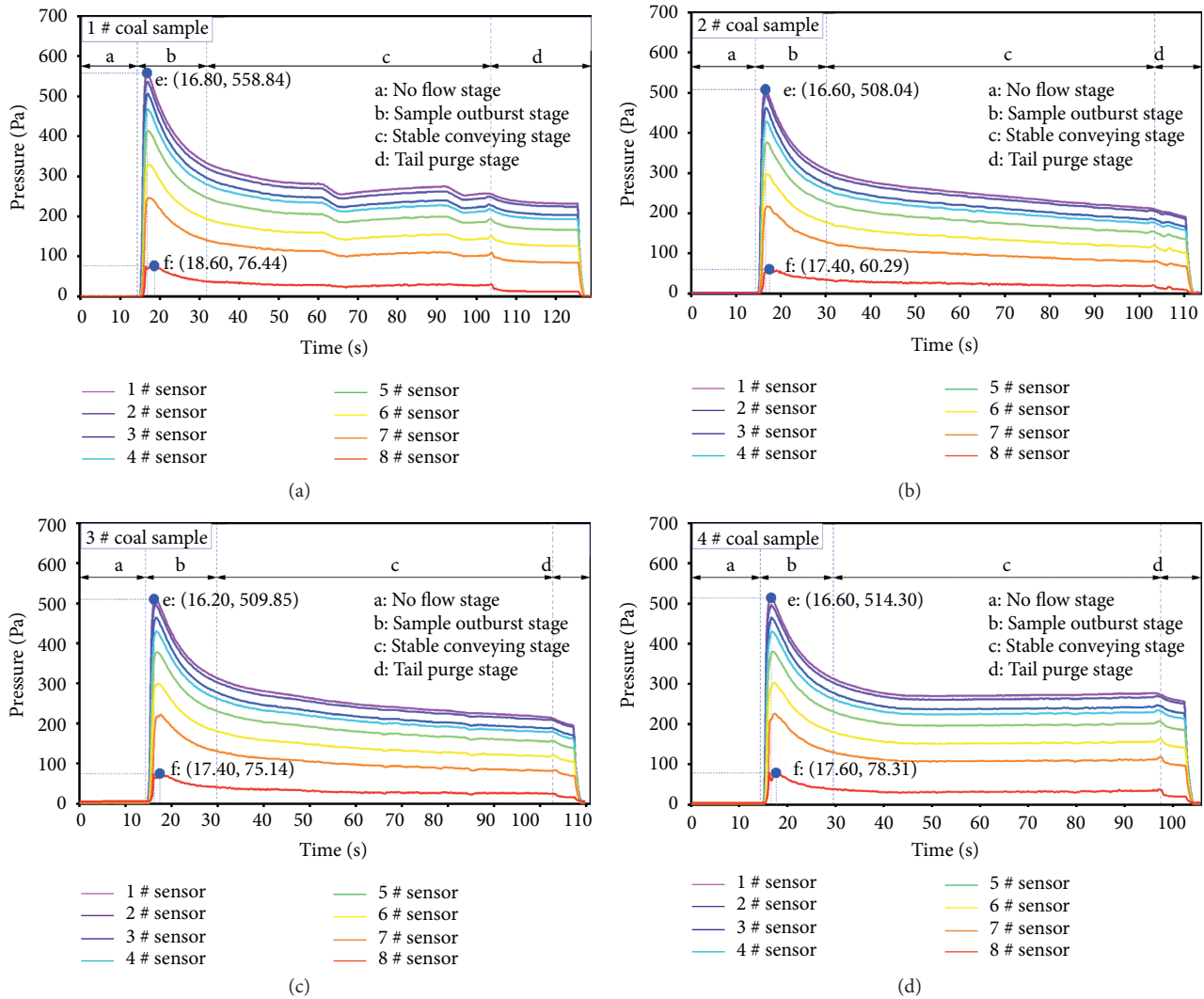


FIGURE 4: Pressure variation in the pipeline during the tests of the mixture sample. Point “e” represents the extreme pressure point of 1 # sensor, and point “f” represents the extreme pressure point of 8 # sensor.

the extreme pressures of 1# and 8 # sensors are 520.53 Pa and 104.73 Pa, which increased by 6.4% and 13.0%, respectively. However, the extreme pressures of 1# and 8 # sensors during the test of 7–8 mm coal sample are 547.78 Pa and 104.95 Pa, respectively, which are 1.1% and 12.8% lower than those of the test of 6–7 mm coal sample.

Further analysis of the results showed that if the particle size is too small, the density of small particle size sample at the feed port will be uneven, which will lengthen the duration of sample outburst stage. On the other hand, the smaller the particle size, the larger the total surface area of coal sample with the same quality and the more contact area with compressed air. As a result, more pressure potential energy of compressed air will be converted into kinetic energy of coal sample. The extreme pressure of the sample outburst stage is reduced. The movement speed of coal sample is improved, and the duration of stable conveying stage is shortened.

3.2. Particle Size Variation during the Process of Sampling

3.2.1. Particle Size Variation of the Mixed Coal Sample

The coal samples before and after the gas reverse circulation sampling tests were mixed evenly, and a certain amount of coal samples was taken from each coal sample twice. Then, the coal samples taken each time were divided into two parts: one for backup and the other for particle size distribution measurement using the particle analyzer. The particle size distribution (Feret’s minimum diameter volume distribution) after the mixed coal sample tests is shown in Table 2.

By comparing the original particle size distribution (shown in Table 1) with the particle size distribution after the tests (shown in Table 2), 30% of the original particle diameter is less than 1 mm, while more than 60% of the coal samples had a diameter less than 1 mm after the test, which is double. In addition, more than 25% of the particles of the original coal samples are larger than 3 mm, while only 7% of

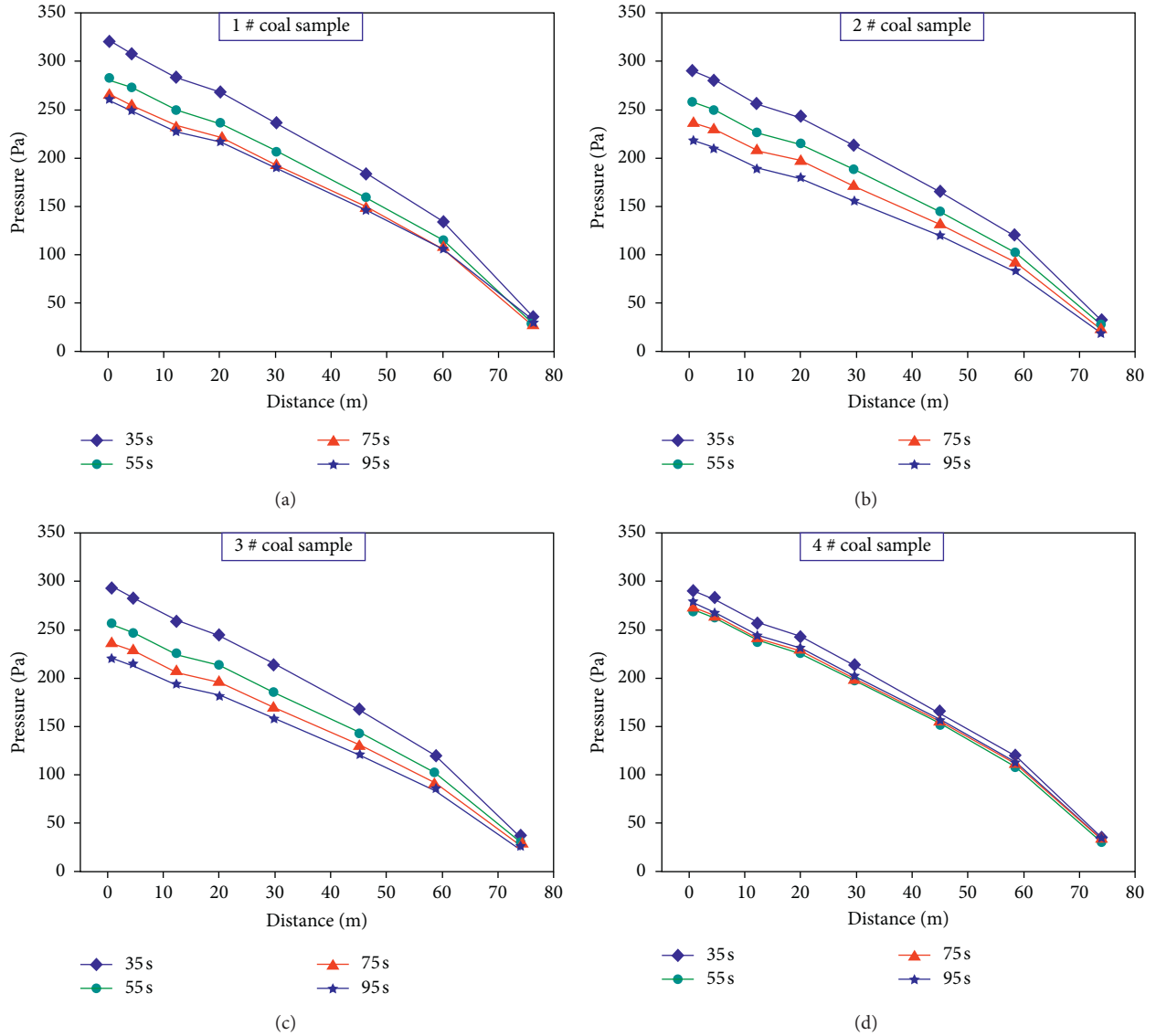


FIGURE 5: Pressure value in pipeline at different time of stable conveying stage.

the particles of the coal sample are larger than 3 mm after the test, almost 3.6 times less. This proved that the particle size changed significantly in the process of gas reverse circulation sampling due to particle-particle and particle-tube wall collision, which is mainly manifested in the sharp decrease in large particles and the obvious increase in small particles. Owing to the change in particle size, the total surface area of the coal sample increased, the gas desorption rate of the coal sample accelerated, and the gas loss increased.

According to Tables 1 and 2, coal sample particles larger than 3 mm account for a relatively small proportion. If those samples are selected to measure the gas content of coal seams, more coal samples will be obtained and more time will be spent on screening, resulting in a further increase in gas loss. Conversely, the gas loss of the coal sample particles less than 1 mm is serious. Therefore, it is suggested that a coal sample with 1–3 mm particles should be used in the actual measurement of gas content.

Figure 8 shows the distribution of particle size before and after the tests of mixed coal sample. Figure 9 shows the cumulative distribution of particle size before and after the tests of mixed coal sample. It is evident that the particle size distributions of coal samples before and after the tests are a single peak with left skew distribution. The gas reverse circulation sampling test does not change the location of the peak but makes the peak particle size distribution higher and sharper. The cumulative distribution of particle size before and after the test conforms to Rosin–Rammler distribution (R–R distribution) [30, 31], which is expressed as follows:

$$F(d) = 100 - 100 \exp \left[- \left(\frac{d}{d_0} \right)^m \right], \quad (1)$$

where $F(d)$ is the cumulative distribution; d is the particle diameter in mm; d_0 is the median diameter in mm, when $d_0 = d$, $F(d) = 63.2\%$, and therefore d_0 is the particle size

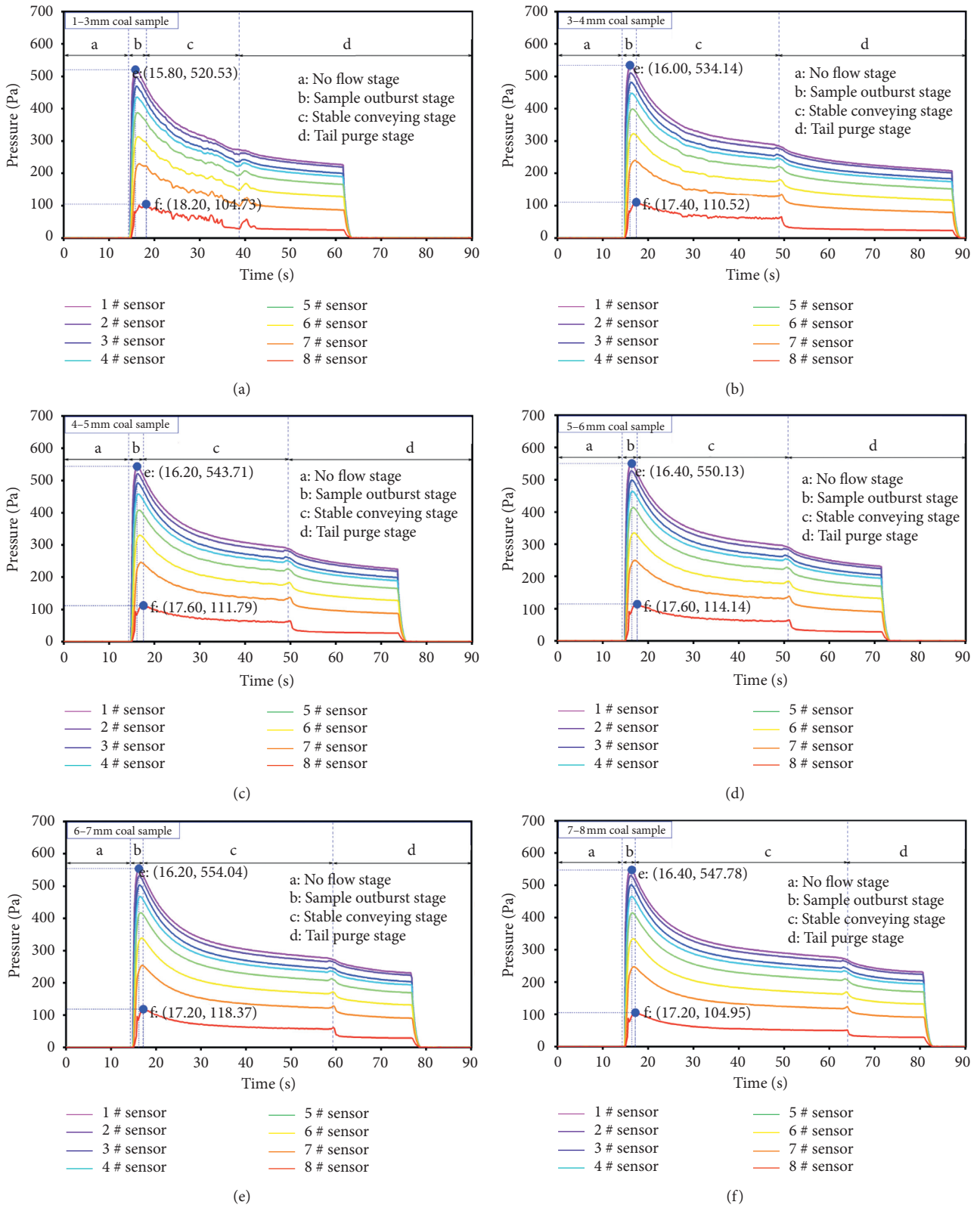


FIGURE 6: Pressure variation in the pipeline during the tests of single size coal sample. The point “e” represents the extreme pressure point of 1 # sensor, and the point “f” represents the extreme pressure point of 8 # sensor.

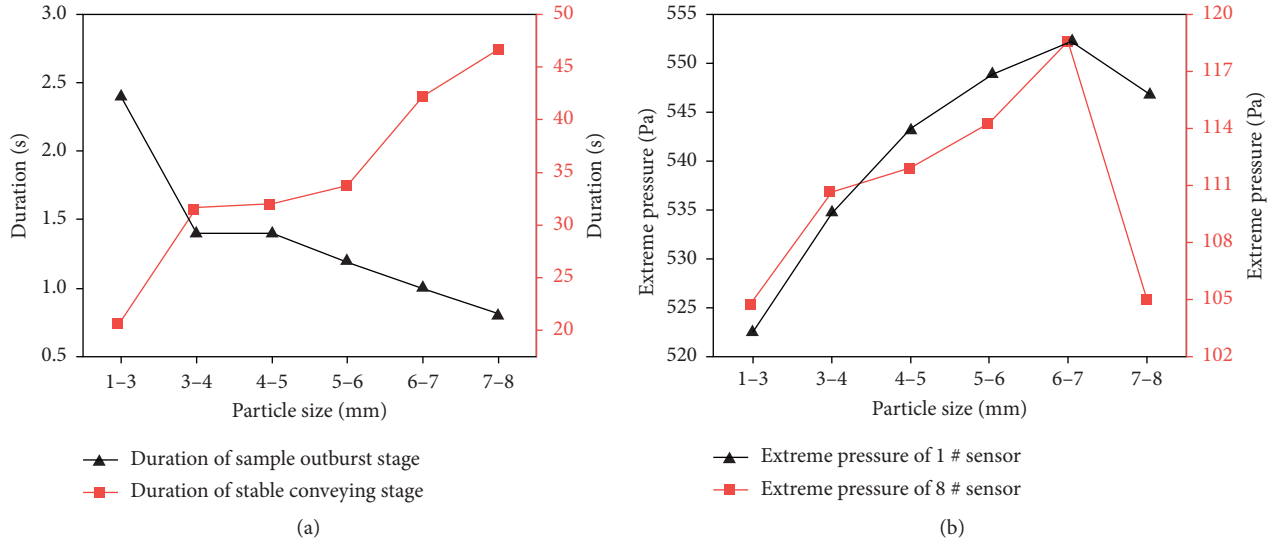


FIGURE 7: The relationship between the pressure characteristics and the particle size. (a) Duration of sample outburst stage and stable conveying stage. (b) Extreme pressure of 1 # sensor and 8 # sensor.

TABLE 2: Particle size distribution after the mixed coal sample tests.

Sample size	≤1 mm (%)	1-3 mm (%)	3-4 mm (%)	4-5 mm	5-6 mm	6-7 mm	7-8 mm
1 # coal sample	62.32	32.54	2.06	1.83%	1.24%	0	0
2 # coal sample	65.91	29.42	3.97	0.70%	0	0	0
3 # coal sample	64.74	29.41	3.61	0	2.24%	0	0
4 # coal sample	64.82	28.05	5.33	1.11%	0.69%	0	0

corresponding to $F=0.632$; and m is the parameter characterizing the particle size distribution range. After two logarithmic transformations of formula (1), the following result is obtained:

$$\ln \left\{ -\ln \left[\frac{1-F(d)}{100} \right] \right\} = m \ln d - m \ln d_0. \quad (2)$$

A straight line can be obtained by plotting $\ln\{-\ln[1-F(d)/100]\}$ on $\ln d$. The slope of the line is the uniformity index m of the R-R distribution equation, and then the characteristic particle size d_0 can be obtained according to the intercept of the line on the Y-axis. Take the derivative on both sides of formula (1) to obtain the particle size distribution density function:

$$f(d) = F(d)' = 100 \frac{m}{d_0} \left(\frac{d}{d_0} \right)^{m-1} \exp \left[-\left(\frac{d}{d_0} \right)^m \right]. \quad (3)$$

The percentage of particle volume between any two particle sizes can be calculated as follows:

$$F(d_2) - F(d_1) = \int_{d_1}^{d_2} f(d) d(d). \quad (4)$$

According to formula (2), linear regression was carried out for the cumulative particle size distribution data of the 1 # coal sample after the test, as shown in Figure 10. The linear

regression correlation coefficient $R^2=0.9971$ and the linear fitting degree is high. From the fitting results, it can be seen that the slope of the straight line is 0.95251 and the intercept is -6.53405 , and therefore the uniformity index of the R-R equation is $m=0.95251$ and the characteristic dimension is $d_0=0.9532$ mm. The same method was used to calculate the R-R fitting characteristic parameters of each coal sample before and after the test, as shown in Table 3. Hereafter, according to formula (4) and the m and d_0 values of each coal sample, it is easy to obtain the volume fraction of coal samples in any two particle size ranges.

As mentioned, m is a parameter that characterizes the range of particle size distribution. The larger the value of m , the narrower the range of particle size distribution. On the contrary, the smaller the value of m , the larger the range of particle size distribution. Meanwhile, d_0 is also a parameter to describe the characteristics of particle size distribution. The larger value of d_0 indicates that the particle is inclined to the end with larger particle size. Conversely, it tends to the end with smaller particle size. Compared with the characteristic parameters of coal particle size distribution before the tests, the characteristic parameters of coal particle size distribution after the tests have little change in the m value but the value of d_0 is generally reduced by more than two times. This reflects that, during the process of the air reverse circulation sampling test, the collision results in particle breakage, which makes the size of more than half of the coal sample particle less than 1 mm.

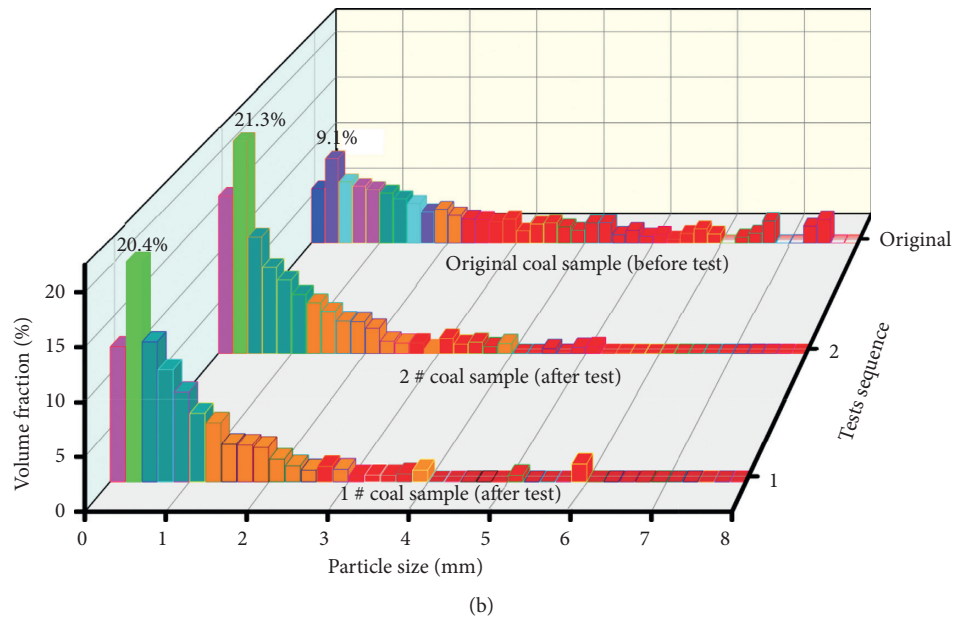
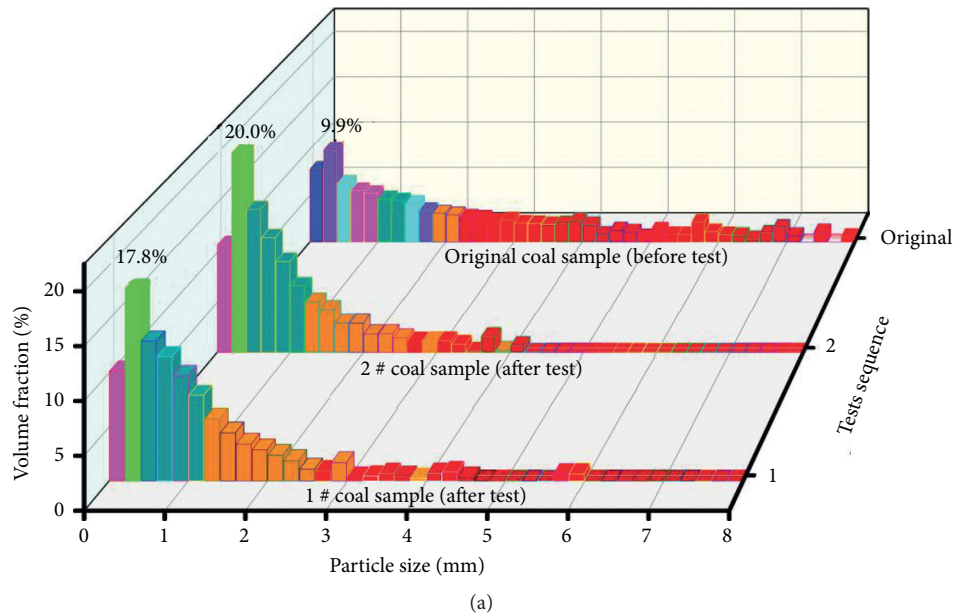


FIGURE 8: The histogram of particle size distribution before and after the tests. The volume fraction represents Feret's minimum diameter volume distribution. (a) 1 # and 2 # coal sample. (b) 3 # and 4 # coal sample.

3.2.2. Particle Size Variation of Single Size Coal Sample

Using the same method as the mixed coal sample, the gas reverse circulation sampling tests with single particle size of 1–3 mm, 3–4 mm, 4–5 mm, 5–6 mm, 6–7 mm, and 7–8 mm were conducted. The distribution of particle size after the tests is shown in Figure 11, and the cumulative distribution of particle size after the tests is shown in Figure 12, and the R–R fitting characteristic parameters of each single particle size coal sample are given in Table 4.

The results show that the particle size distribution after the test presents a single peak with left skewed distribution, and the cumulative distribution after the test conforms to the

R–R distribution. However, there is no obvious correlation between the particle size distribution and the original particle size. The fitting parameters of cumulative distribution vary widely and are not correlated with the original particle size. When comparing the particle size distribution of the mixed coal sample and the single particle, it can be seen that the number of coal samples with a particle size greater than 3 mm after the single particle size test is lower. This indicates that the impact crushing of particles in the reverse circulation sampling pipeline is a random process and the impact crushing degree of uniform single size particles is more serious than that of mixed coal samples.

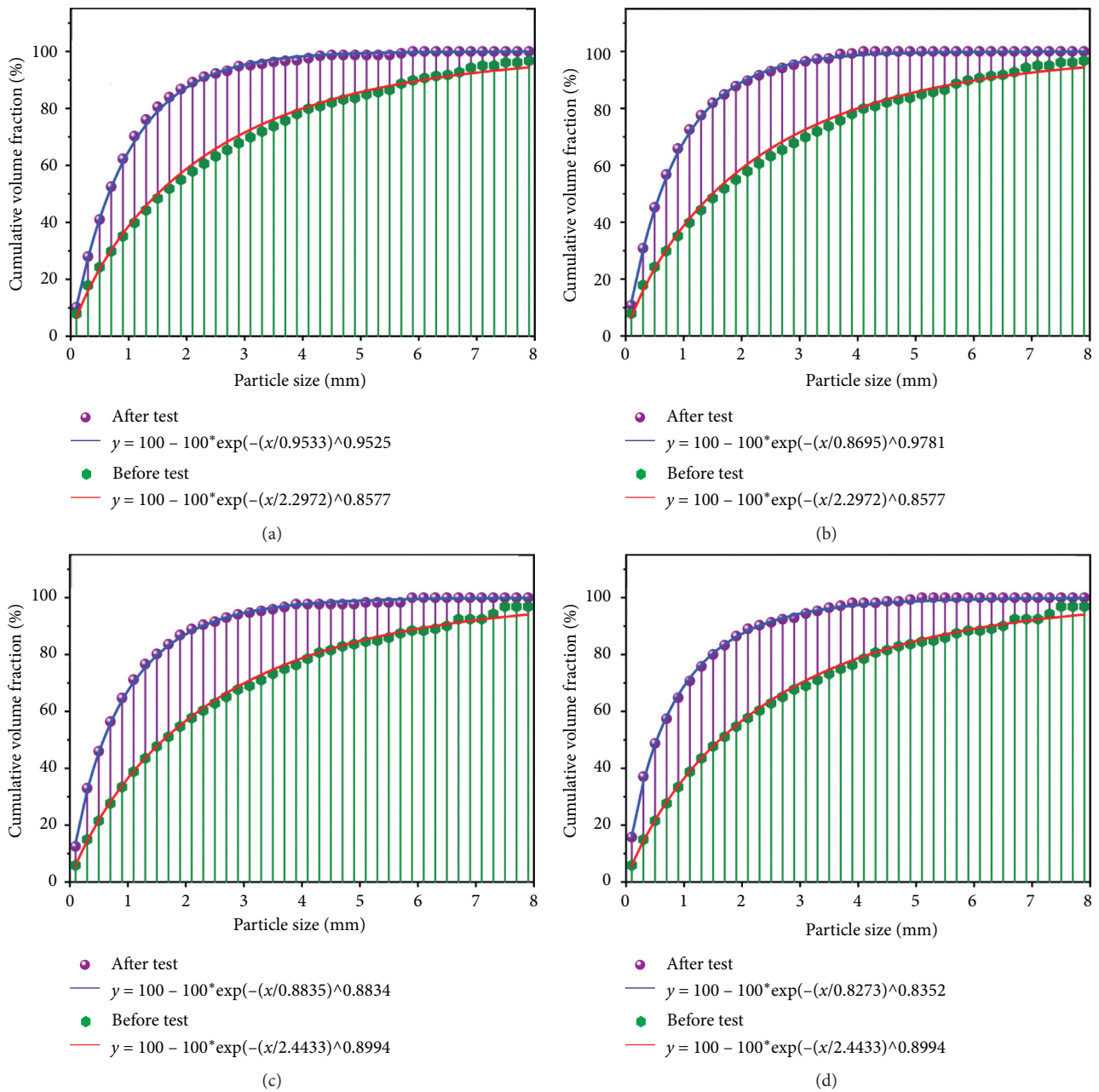


FIGURE 9: The cumulative distribution before and after the tests. (a) 1 # coal sample. (b) 2 # coal sample. (c) 3 # coal sample. (d) 4 # coal sample.

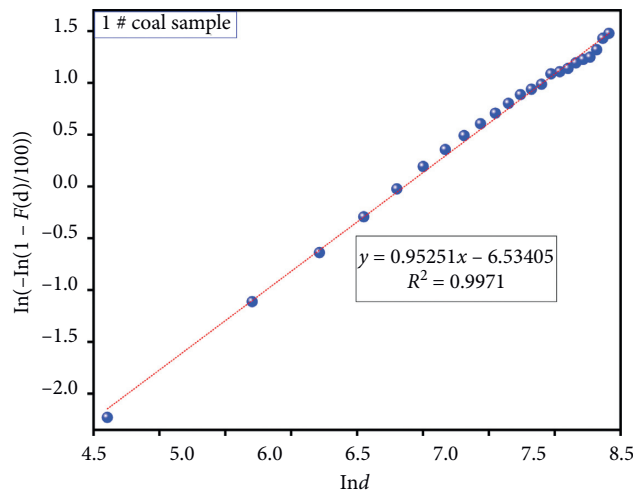


FIGURE 10: Cumulative particle size distribution and fitting results for 1 # coal sample after the test.

TABLE 3: Fitting parameters of Rosin–Rammler distribution.

Samples	Before test				After test			
	m	$m \ln d_0$	d_0	R^2	m	$m \ln d_0$	d_0	R^2
1 # coal sample	0.8577	6.6383	2.2972	0.9906	0.9525	6.5341	0.9533	0.9989
2 # coal sample	0.8577	6.6383	2.2972	0.9906	0.9781	6.6194	0.8695	0.9961
3 # coal sample	0.8994	7.0159	2.4433	0.9976	0.8834	5.9926	0.8835	0.9984
4 # coal sample	0.8994	7.0159	2.4433	0.9976	0.8352	5.6107	0.8273	0.9974

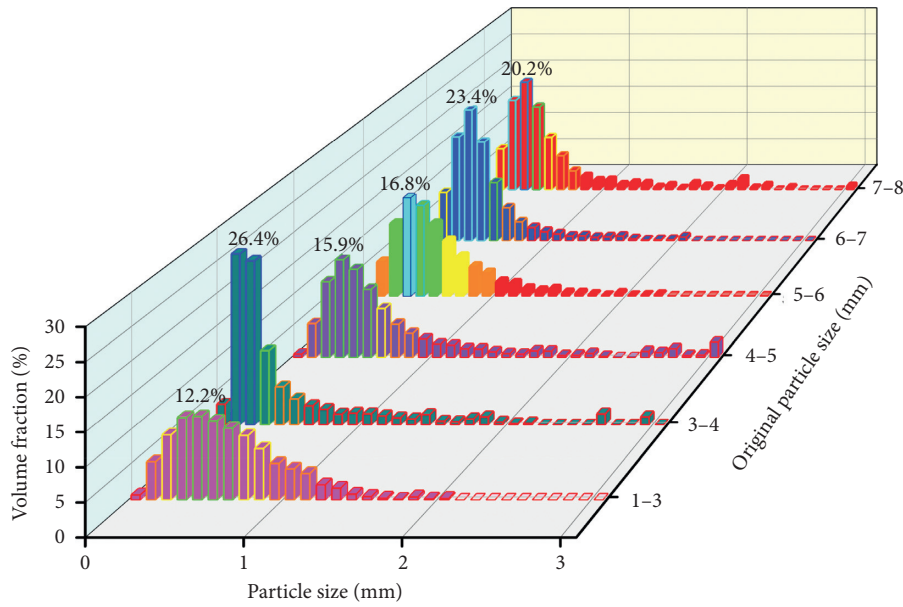


FIGURE 11: The distribution of particle size after the tests of single particle coal sample. The volume fraction represents Feret’s minimum diameter volume distribution.

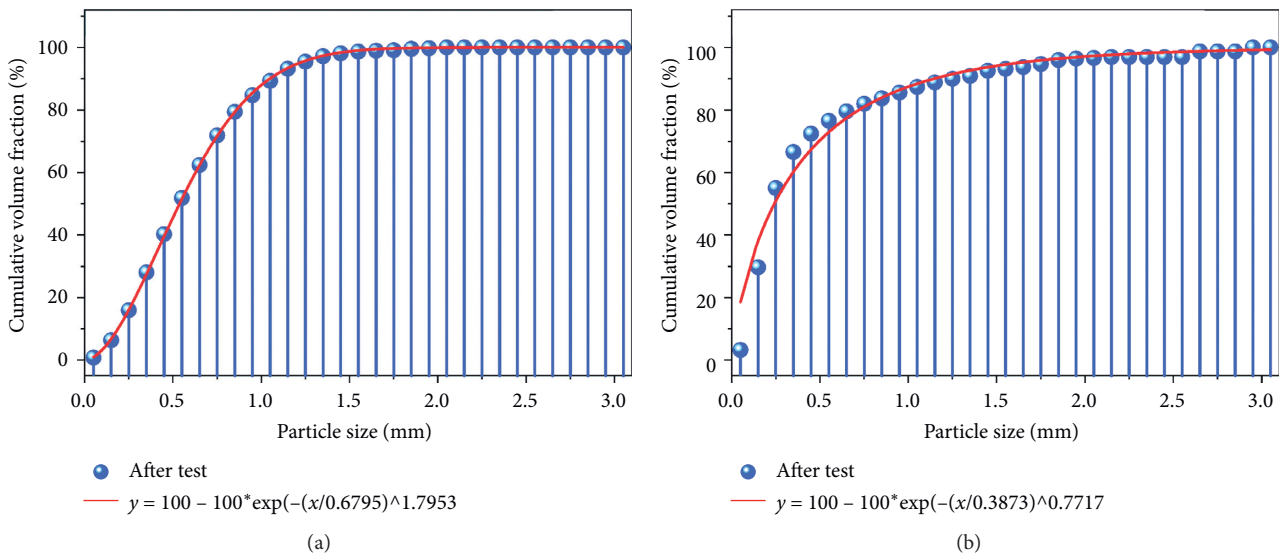


FIGURE 12: Continued.

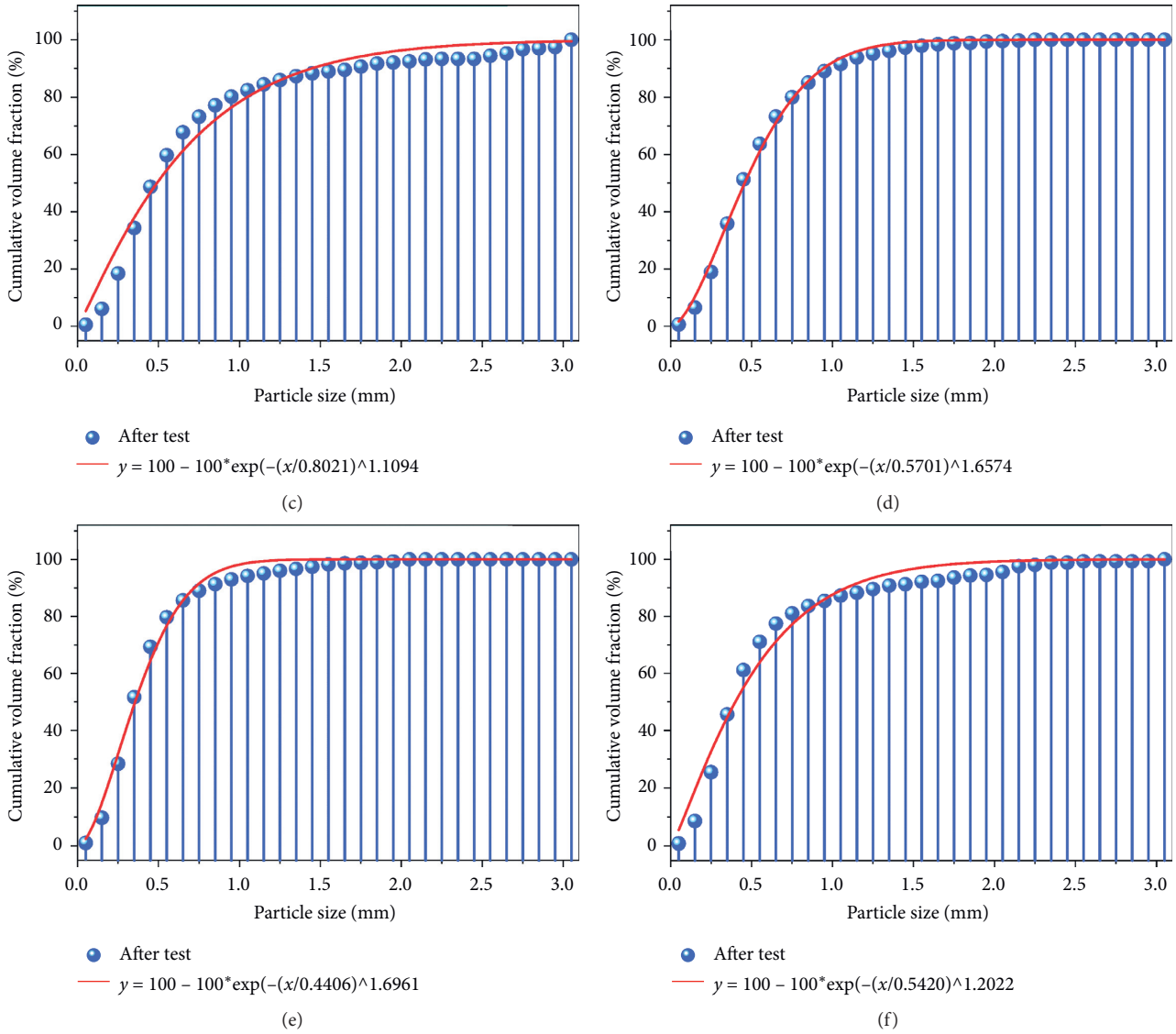


FIGURE 12: The cumulative distribution of particle size after the tests of single particle coal sample. (a) Original size: 1–3 mm. (b) Original size: 3–4 mm. (c) Original size: 4–5 mm. (d) Original size: 5–6 mm. (e) Original size: 6–7 mm. (f) Original size: 7–8 mm.

TABLE 4: Fitting parameters of Rosin–Rammler distribution.

Samples	m	After test		R^2
		$m \ln d_0$	d_0	
1–3 mm	1.7953	11.7079	0.6795	0.9998
3–4 mm	0.7717	4.5987	0.3873	0.9685
4–5 mm	1.1094	7.4188	0.8021	0.9726
5–6 mm	1.6574	10.5177	0.5701	0.9969
6–7 mm	1.6961	10.3262	0.4406	0.9905
7–8 mm	1.2022	7.5682	0.5420	0.9742

4. Conclusions

(1) In this study, change rules of pressure and coal particle size in an air reverse circulation sampling pipeline were experimentally evaluated. The results show that the sampling process could be divided into

four stages: no flow field stage, sample outburst stage, stable conveying stage, and tail purging stage. In the actual sampling process, the sample collection can be started during stable conveying stage, as the pressure in the pipeline tends to be stable in this stage. The duration of outburst stage is negatively correlated

with particle size, and that of stable conveying stage is positively correlated with particle size. The extreme pressure in the pipeline occurs in the sample outburst stage, and the extreme pressure increases first and then decreases with the increase of particle size.

- (2) The particle size changed significantly in the process of gas reverse circulation sampling due to particle-particle and particle-tube wall collision. Comparing the particle size distribution before and after the test, it is found that the proportion of 1–3 mm coal sample changes the least. Therefore, coal sample with particle size of 1–3 mm is recommended for gas content measurement.
- (3) The particle size distribution presents a left skewed distribution, and the cumulative distribution follows Rosin–Rammler distribution. After the test, the value of d_0 reduces more than 50%, which reflects that more than half of the coal sample particles are less than 1 mm in diameter due to particle breakage. Further study reveals that the impact crushing degree of uniform single size particles is more serious than that of mixed coal samples.

These results are helpful to understand the factors affecting gas loss during gas reverse circulation sampling and thus provide insights for establishing a more accurate compensation model of gas loss.

Data Availability

The data used to support the findings of this study are available from the corresponding author upon request.

Conflicts of Interest

The authors declare that there are no conflicts of interest regarding the publication of this paper.

Acknowledgments

The authors acknowledge the relevant coal mine for providing the desired coal samples for this study. This work was supported by the National Key Research and Development Plan of China (2018YFC0808001), Major National Science and Technology Project of China (2016ZX05045-006-001), and Innovation Project of Tiandi Science & Technology Co., Ltd. (2020-TD-QN014).

References

- [1] R. M. Flores, “Coalbed methane: from hazard to resource,” *International Journal of Coal Geology*, vol. 35, no. 1–4, pp. 3–26, 1998.
- [2] S. Zhi and D. Elsworth, “The role of gas desorption on gas outbursts in underground mining of coal,” *Geomechanics and Geophysics for Geo-Energy and Geo-Resources*, vol. 2, no. 3, pp. 151–171, 2016.
- [3] W. P. Diamond and S. J. Schatzel, “Measuring the gas content of coal: a review,” *International Journal of Coal Geology*, vol. 35, no. 1–4, pp. 311–331, 1998.
- [4] S. Xue and L. Yuan, “The use of coal cuttings from underground boreholes to determine gas content of coal with direct desorption method,” *International Journal of Coal Geology*, vol. 174, no. 3, pp. 1–7, 2017.
- [5] L. Wang, L.-B. Cheng, Y.-P. Cheng et al., “A new method for accurate and rapid measurement of underground coal seam gas content,” *Journal of Natural Gas Science and Engineering*, vol. 26, no. 8, pp. 1388–1398, 2015.
- [6] P. G. Sevenster, “Diffusion of gases through coal,” *Fuel*, vol. 38, no. 4, pp. 403–418, 1959.
- [7] S. P. Nandi and P. L. Walker, “Activated diffusion of methane from coals at elevated pressures,” *Fuel*, vol. 54, no. 2, pp. 81–86, 1975.
- [8] R. M. Barrer, *Diffusion in and through Solid*, Cambridge University Press, London, UK, 1951.
- [9] K. Winter and H. Janas, “Gas emission characteristics of coal and methods of determining the desorbable gas content by means of desorbometers,” in *Proceedings of the XIV International Conference of Coal Mine Safety Research*, Wollongong, Australia, August 1996.
- [10] B. A. Bolt and J. A. Innes, “Diffusion of carbon dioxide from coal,” *Fuel*, vol. 38, pp. 333–337, 1959.
- [11] E. M. Airey, “Gas emission from broken coal. an experimental and theoretical investigation,” *International Journal of Rock Mechanics and Mining Sciences & Geomechanics Abstracts*, vol. 5, no. 6, pp. 475–494, 1968.
- [12] D. Zhao, C. Zhang, H. Chen, and Z. Feng, “Experimental study on gas desorption characteristics for different coal particle sizes and adsorption pressures under the action of pressured water and superheated steam,” *Journal of Petroleum Science and Engineering*, vol. 179, no. 5, pp. 948–957, 2019.
- [13] Q. Long, Q. Hu, Z. Zhang, and T. Ren, “On factors affecting coalbed gas content measurement,” *Measurement*, vol. 121, no. 2, pp. 47–56, 2018.
- [14] F. Wang, Y. Liang, X. Li, L. Li, J. Li, and Y. Chen, “Orthogonal experimental study on multifactor conditions for gas desorption in coal,” *Advances in Civil Engineering*, vol. 2019, pp. 1–12, 2019.
- [15] Y. P. Qin, Y. J. Hao, P. Liu, and J. Wang, “Coal particle gas desorption experiment and numerical simulation in enclosed space,” *Meitan Xuebao/journal of the China Coal Society*, vol. 40, no. 1, pp. 87–92, 2015.
- [16] X. Chen, Z. Duan, L. Yang, and W. Peng, “Experiment study on diffusion features of gassy coal under negative pressure environment,” *Coal Science & Technology*, vol. 44, pp. 106–110, 2016.
- [17] W. Zhao, K. Wang, Y. Cheng, S. Liu, and L. Fan, “Evolution of gas transport pattern with the variation of coal particle size: kinetic model and experiments,” *Powder Technology*, vol. 367, pp. 336–346, 2020.
- [18] X. C. Li, Z. B. Li, T. Ren et al., “Effects of particle size and adsorption pressure on methane gas desorption and diffusion in coal,” *Arabian Journal of Geosciences*, vol. 12, no. 24, pp. 1–17, 2019.
- [19] J. E. Hilton and P. W. Cleary, “The influence of particle shape on flow modes in pneumatic conveying,” *Chemical Engineering Science*, vol. 66, no. 3, pp. 231–240, 2011.
- [20] Y. Y. Feng, W. Yang, and W. Chu, “Coalbed methane adsorption and desorption characteristics related to coal particle size,” *Chinese Physics B*, vol. 25, no. 6, pp. 1–10, 2016.
- [21] M. Yi, Y. Cheng, Z. Wang, C. Wang, B. Hu, and X. He, “Effect of particle size and adsorption equilibrium time on pore structure characterization in low pressure N₂ adsorption of

- coal: an experimental study,” *Advanced Powder Technology*, vol. 31, no. 10, pp. 4275–4281, 2020.
- [22] Y. N. Jia, Z. H. Wen, and J. P. Wei, “Experimental study on gas desorption laws of coal samples with different particle size,” *Safety in Coal Mines*, vol. 44, no. 3, pp. 1–3, 2013.
- [23] P. L. Cao, Y. W. Chen, M. M. Liu, B. Y. Chen, and J. S. Wang, “Analytical and experimental study of a reverse circulation drill bit with an annular slit,” *Advances in Mechanical Engineering*, vol. 8, no. 9, pp. 1–10, 2016.
- [24] A. Anantharaman, A. Cahyadi, K. Hadinoto, and J. W. Chew, “Impact of particle diameter, density and sphericity on minimum pickup velocity of binary mixtures in gas-solid pneumatic conveying,” *Powder Technology*, vol. 297, pp. 311–319, 2016.
- [25] J. Wei, H. Zhang, Y. Wang, Z. Wen, B. Yao, and J. Dong, “The gas-solid flow characteristics of cyclones,” *Powder Technology*, vol. 308, pp. 178–192, 2017.
- [26] S. Akhshik and M. Rajabi, “CFD-DEM modeling of cuttings transport in underbalanced drilling considering aerated mud effects and downhole conditions,” *Journal of Petroleum Science and Engineering*, vol. 160, pp. 229–246, 2018.
- [27] L. H. Zhu, Y. Huang, R. H. Wang, and J. Y. Wang, “A mathematical model of the motion of cutting particles in reverse circulation air drilling,” *Applied Mathematics and Computation*, vol. 256, pp. 192–202, 2015.
- [28] P. Cao, Y. Chen, M. Liu, and B. Chen, “Optimal design of novel drill bit to control dust in down-the-hole hammer reverse circulation drilling,” *Arabian Journal for Science and Engineering*, vol. 43, no. 3, pp. 1313–1324, 2018.
- [29] Y. Luo, J. Peng, L. Li et al., “Development of a specially designed drill bit for down-the-hole air hammer to reduce dust production in the drilling process,” *Journal of Cleaner Production*, vol. 112, pp. 1040–1048, 2016.
- [30] N. Vishnoi and S. K. Mohapatra, “Study of particle size distribution of pulverized coals in utility boilers,” *Particulate Science and Technology*, vol. 36, no. 8, pp. 999–1005, 2018.
- [31] U. Ulusoy and C. Igathinathane, “Particle size distribution modeling of milled coals by dynamic image analysis and mechanical sieving,” *Fuel Processing Technology*, vol. 143, pp. 100–109, 2016.

Research Article

A Study on the Mechanical Properties and Bursting Liability of Coal-Rock Composites with Seam Partings

Dong Xu ^{1,2} Mingshi Gao ^{1,2} Yongliang He ^{1,2} and Xin Yu ^{1,2}

¹School of Mines, Key Laboratory of Deep Coal Resource Mining, China University of Mining and Technology, Xuzhou, Jiangsu 221116, China

²The State Key Laboratory of Coal Resources and Safe Mining, China University of Mining and Technology, Xuzhou, Jiangsu 221116, China

Correspondence should be addressed to Mingshi Gao; cumt_gms@cumt.edu.cn

Received 5 March 2021; Revised 1 April 2021; Accepted 10 April 2021; Published 17 April 2021

Academic Editor: Jia Lin

Copyright © 2021 Dong Xu et al. This is an open access article distributed under the Creative Commons Attribution License, which permits unrestricted use, distribution, and reproduction in any medium, provided the original work is properly cited.

Geological tectonic movements, as well as complex and varying coal-forming conditions, have led to the formation of rock partings in most coal seams. Consequently, the coal in coal-rock composites is characterised by different mechanical properties than those of pure coal. Uniaxial compression tests were performed in this study to determine the mechanical properties and bursting liability of specimens of coal-rock composites (hereinafter referred to as “composites”) with rock partings with different dip angles θ and thicknesses D . The results showed that as θ increased, the failure mode of the composite changed from tensile and splitting failure to slip and shear failure, which was accompanied by a decrease in the brittleness of the composite and an increase in its ductility as well as a decrease in the extent of fragmentation of the coal in the composite. Additionally, as θ increased, the uniaxial compressive strength σ_u , elastic modulus E , and bursting energy index K_c of the composite decreased. The rock parting in the composite was the key area in which elastic energy accumulated. As D increased, σ_u , E , and K_c of the composite increased. In addition, as D increased, the ductility of the composite decreased, and the brittleness and extent of coal fragmentation in the composite increased. Notably, the curve for the cumulative acoustic emission (AE) counts of the composite corresponding to the stress-strain curve could be divided into four regimes: pore compaction and closure, a slowly ascending linear elastic section, prepeak steady crack propagation, and peak unsteady crack propagation. The experimental results were used to propose two technologies for controlling the stability of coal-rock composites to effectively ensure safe and efficient production at working faces.

1. Introduction

Most thick coal seams contain rock partings as a result of complex coal-forming geological conditions [1, 2]. These partings affect the stability of the working faces and roadway coal ribs in mines and can cause severe rib spalling and support system failure [3–5]. In addition, coal cutters consume more energy during cutting and cutting picks are severely worn down [6–8], significantly affecting the stoping at working faces. Moreover, sparks generated from collisions between cutting picks and rock partings are a major hazard that can trigger gas explosions in gassy coal mines [9]. Rock partings alter the stress distribution in the surrounding rock of coal seams and may produce rock bursts. Stress

perturbations induced by mining increase the risks involved in stoping operations at working faces [10]. A coal-rock composite with a seam parting consists of rocks with two lithologies. The anisotropy of the composite increases significantly with the difference between the structural plane and rock mechanical parameters. Interactions between rocks with different lithologies during the failure process produce different mechanical failure characteristics from those of pure coal and pure rock. Thus, it is important to study the mechanical properties and bursting liability of coal-rock composites.

Numerous researchers have extensively studied the mechanical properties of coal-rock composites. Yang et al. [11] studied the mechanical properties and failure modes of

coal-rock composites for various coal-rock height ratios and determined the corresponding deformation and failure patterns. Gao et al. [12] investigated the brittle failure modes of coal-rock composites under uniaxial compressive loading, analysed energy evolution patterns, and determined the failure mechanisms. Qin et al. [13] studied the energy distribution pattern in each constituent of coal-gritstone-fine sandstone composites before buckling failure and analysed the bursting failure behaviour. Song et al. [14] investigated the failure modes, deformation behaviours, and energy evolution patterns of coal-rock composites under various loading conditions. The study results provided strong support for controlling working faces and the rocks surrounding roadways. Zhang et al. [15] used uniaxial compression tests to investigate the energy evolution patterns and bursting liability of composite specimens with different rock types and produced a reasonable correction to the bursting energy index. Wang et al. [16] studied the progressive failure processes and acoustic emission (AE) characteristics of various coal-rock composites and analysed the bursting liability as well. Xie et al. [17, 18] investigated the deformation and failure patterns, as well as the energy evolution mechanisms, of coal-rock composites and proposed stability control principles for composite roofs in deep roadways. Wang et al. [19] used triaxial compression tests to investigate coal-rock composites with various height ratios and determined the stress-strain behaviours. Chen et al. [20] developed mechanical constitutive models for coal and rock-coal-rock composites to analyse the evolutionary patterns of the physical parameters of the rock-coal-rock composites during instability and loading processes. Chen et al. [21] studied the stress-strain behaviour and strength characteristics of composite rock-coal layers. Crack nucleation, propagation, and coalescence patterns in these layers at various loading rates were also investigated. Tan et al. [22] developed a “flexible-hard” combination supporting wall to control the rapid sinking of a hard roof in a roadway. Lu et al. [23] conducted a series of true triaxial tests on a layered coal-rock composite and studied the corresponding deformation and failure laws and mechanical response characteristics. In summary, the aforementioned studies on coal-rock composites have focused primarily on the mechanical properties of coal-rock, rock-coal, or rock-coal-rock composites. By contrast, few studies have been performed on the mechanical properties of coal-rock composites with partings formed from magmatic intrusions into coal seams. Therefore, studying the mechanical properties and bursting liability of coal-rock composites is important for weakening the mechanical properties of rock partings to prevent rock burst and for controlling the stability of rocks surrounding roadways.

In this study, specimens of a coal-rock composite with a rock parting (hereinafter referred to as “composites”) with different dip angles θ and thicknesses D were investigated by uniaxial compressive mechanical testing on an MTS electrohydraulic servo control test machine. The deformation and failure patterns of the composite specimens were recorded using high-speed photography and AE monitoring. The mechanical properties and bursting liability of the

composite specimens with different rock-parting characteristics were subsequently analysed. Finally, two technologies for controlling the stability of coal-rock composites were proposed. These technologies can effectively ensure safe and efficient mining at working faces.

2. Materials and Experimental Methods

2.1. Material Preparation. Experimental coal-rock samples were collected from the No. 112201 working face of a mine in Shaanxi Province. These rock samples had a sandstone lithology. All the samples were collected from intact and highly homogeneous coal-rock blocks to eliminate interference factors and ensure the reliability of the test results. Cuboidal specimens (50 mm \times 50 mm \times 100 mm) were fabricated from the coal-rock samples according to the specifications of the International Society for Rock Mechanics. The ends of each specimen were polished to ensure that the surface roughness of the ends did not exceed 0.2 mm and the non-parallelism did not exceed $\pm 0.1\%$. The specimens were divided into groups A and B. The specimens in group A had D of 20 mm and θ values of 10° , 20° , 30° , and 40° (three specimens were used for each θ). The specimens in group B had θ of 0° and D values of 10, 20, 30, and 40 mm (three specimens were used for each D). An epoxy resin adhesive was used to glue the composite specimens into standard specimens, as shown in Figures 1 and 2.

2.2. Experimental Process. Figure 3 shows the experimental testing system, which consisted primarily of a load control system, an AE monitoring system, and a high-speed digital photographic acquisition system.

An MTS-C64.106 electrohydraulic servo control system was selected as the load control system for the uniaxial compression tests. The strain control mode was used in this study. Each specimen was loaded at a rate of 0.01 mm/s until failure.

A PCI-2 AE system was used to monitor the AE activity. Four AE sensors were adhered to the surfaces of each composite specimen to collect data. The noise suppression threshold, peak definition time, hit lockout time, sampling frequency, and preamplifier gain of the AE monitoring system were set to 30 dB, 50 μ s, 300 μ s, 2 MHz, and 40 dB, respectively. The AE sensors and each composite specimen were coupled by applying Vaseline.

A GX-1/3 high-speed camera (NAC Inc, Japan) was used to acquire digital photographs to observe the loading process and record the deformation and failure patterns of the composite specimens.

3. Analysis of the Mechanical Properties of the Composite Specimens

3.1. Mechanical Properties of the Composite Specimens with Different Dip Angles (θ). In the composite specimen images, the yellow lines indicate the expansion fractures, and the pink areas indicate the coal body flakes.

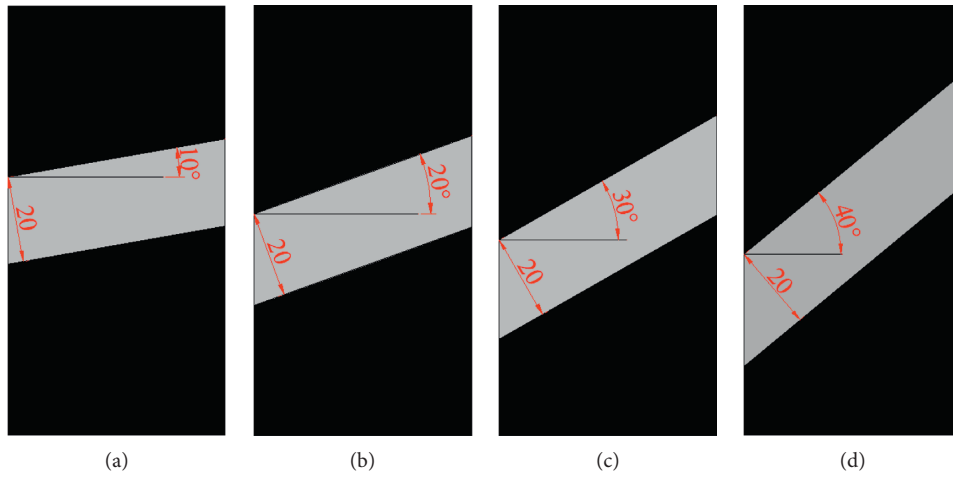


FIGURE 1: Composite specimens with different rock-parting dip angles (θ). (a) 10° . (b) 20° . (c) 30° . (d) 40° .

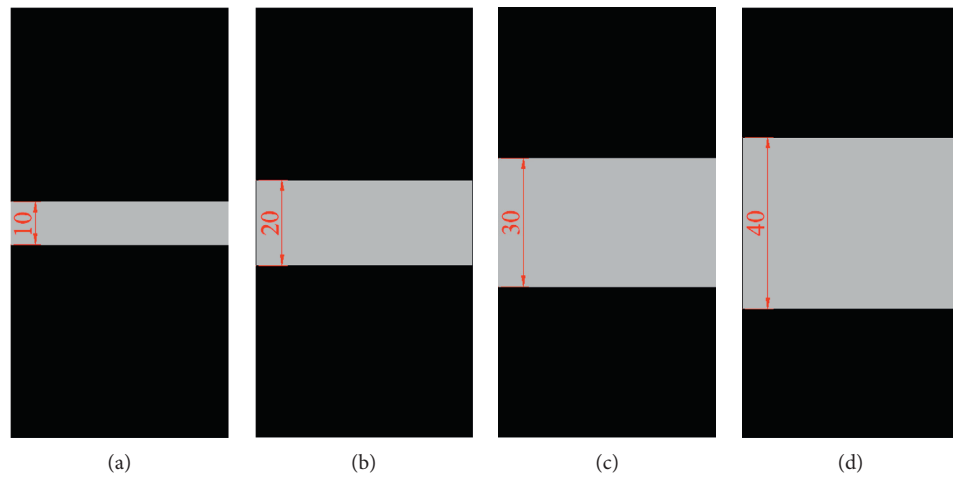


FIGURE 2: Composite specimens with different rock-parting thicknesses (D). (a) 10 mm. (b) 20 mm. (c) 30 mm. (d) 40 mm.

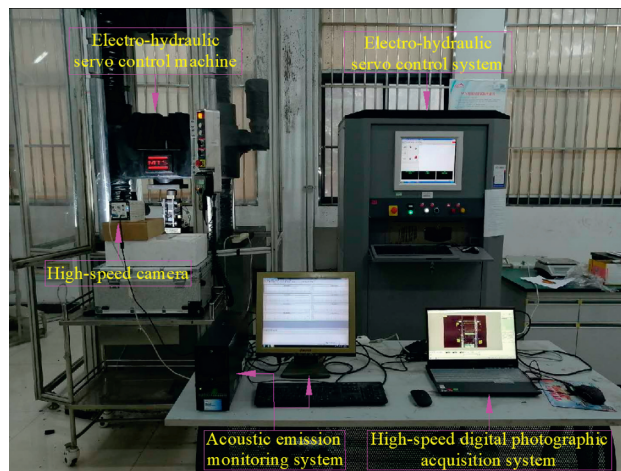


FIGURE 3: The experimental monitoring system.

The stress-strain curve of the composite could be divided into four regimes: pore compaction (OA), a linear elastic section (AB), prepeak crack development (BC), and postpeak fracture development (CD). During the pore compaction stage, the preexisting cracks and pores in the coal and the rock parting were closed, and the AE activity was weak and fluctuated slightly. The AE activity in the composite remained basically stable over the linear elastic regime. However, there was some propagation of the preexisting cracks in the composite under compressive loading, and a small quantity of coal spalled off in the form of flakes. Consequently, a few AE peaks appeared, albeit with relatively small amplitudes. During prepeak crack development, the cracks inside the composite developed steadily, accompanied by the caving of small coal blocks. A small quantity of rock powder fell off, the coal failed in local areas, there were violent fluctuations in the AE activity, and multiple AE peaks appeared. During postpeak fracture development, small coal blocks erupted accompanied by a notable cracking sound and increasing AE activity. Each steplike sudden increase observed in the cumulative AE count curve corresponded to the initiation and development of microcracks in the composite, as well as the spalling of coal in the form of flakes. The cumulative AE count curve demonstrably corresponded to the stress-strain curve and could be approximately divided into four regimes: pore compaction and closure (during which the AE count increased slightly); a slowly ascending linear elastic section (during which the AE count increased steadily overall but suddenly increased to a relatively small extent at isolated points as a result of the propagation of the preexisting cracks); prepeak steady crack propagation (during which the propagation of the preexisting cracks intensified, new cracks were initiated, the AE activity increased, and the cumulative AE count curve exhibited a large rate of increase); and peak unsteady crack propagation (during which cracks developed unsteadily, and there was a sharp increase in the cumulative AE count curve).

Increasing θ shortened the pore compaction regime of the stress-strain curve, changed the failure mode of the composite from tensile failure to slip and shear failure, and decreased the AE activity. Figure 4 shows that at $\theta = 10^\circ$, horizontally propagating cracks appeared on the surfaces of the lower coal under compressive loading, the lower coal underwent splitting and tensile failure, and the AE count was relatively high. At $\theta = 20^\circ$, horizontally propagating cracks appeared on the surfaces of the upper coal, and sudden steplike increases occurred in the cumulative AE count curve. Figure 5 shows that as the loading displacement increased, axial splitting and tensile coalescence appeared in the rock parting and the lower coal during the postpeak fracture development regime of the stress-strain curve. At $\theta = 30^\circ$, some cracks propagated into the interface between the upper coal and the rock parting, accompanied by a sudden decrease in the stress-strain curve, abnormally high AE counts, and unsteady slip failure of the composite. Figure 6 shows that over the postpeak fracture development regime of the stress-strain curve, the bearing capacity of the composite increased again, the upper coal spalled off in the

form of flakes, and there was a gradual increase in the AE count. At $\theta = 40^\circ$, the pore compaction regime of the stress-strain curve disappeared, and the linear elastic section was significantly lengthened. There were no notable sudden increases in the AE count during the pore compaction and linear elastic regimes of the stress-strain curve. This result suggests that the increase in θ prevented notable initiation and propagation of cracks in the composite and that the coal tended to undergo slip failure. AE peaks appeared over the prepeak crack development regime of the stress-strain curve because vertical splitting cracks formed in the upper coal. During the stage postpeak fracture development regime of the stress-strain curve, the interfacial cracks in the composite coalesced, and the upper coal-rock interface underwent steady slip failure, corresponding to a gradual decrease in the AE count and a slow decrease in the stress-strain curve, as shown in Figure 7.

High-speed photographs of the failure process of the composite showed that the coal failed first in the composite. This is primarily because of the large difference between the strengths of the coal and rock in the composite. The development of internal microcracks resulted in a relatively low coal strength. Consequently, under compressive loading, crack initiation and propagation occurred first in the coal, which spalled off in the form of flakes.

Figure 8 and Table 1 show that as θ increased, the uniaxial compressive strength σ_u , elastic modulus E , and bursting energy index K_e of the composite decreased. The σ_u values of the composite specimens with θ values of 20° , 30° , and 40° were 16.59%, 31.49%, and 57.93% lower, respectively, than those of the composite specimens with θ of 10° . The E values of the composite specimens with θ values of 20° , 30° , and 40° were 10.64%, 16.78%, and 31.08% lower, respectively, than those of the composite specimen with θ of 10° . The K_e values of the composite specimens with θ values of 20° , 30° , and 40° were 13.98%, 30.02%, and 37.63% lower, respectively, than those of the composite specimens with θ of 10° . This is mainly because as θ increased, the failure mode of the composite changed from splitting and tensile failure to slip and shear failure. Consequently, the composite was more prone to slip and shear failure along the coal-rock interfaces under uniaxial compressive loading. Thus, the composite σ_u decreased as θ increased. The preferential failure of the composite along the weak structural planes hindered the accumulation of elastic energy, resulting in a notable decrease in K_e . The composite became less fragmented and remained more intact as θ increased.

3.2. Mechanical Properties of Composite Specimens with Different Thicknesses (D). Similarly, the stress-strain curve of each of the composite specimens with different D values could be divided into four characteristic regimes of failure development. There was a notable correspondence between the stress-strain and cumulative AE count curves. Increasing D caused an increase in the ductility and a decrease in the brittleness of the composite.

For the composite specimen with $D = 10$ mm under uniaxial compressive loading, crack propagation occurred in

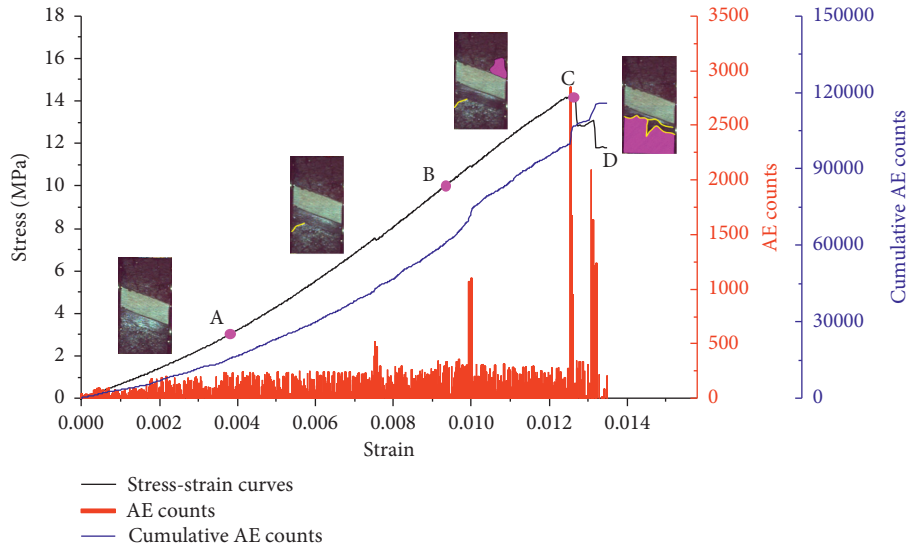


FIGURE 4: Stress-strain curve and acoustic emission monitoring curve of composite specimens with a 10° dip angle (A10-1).

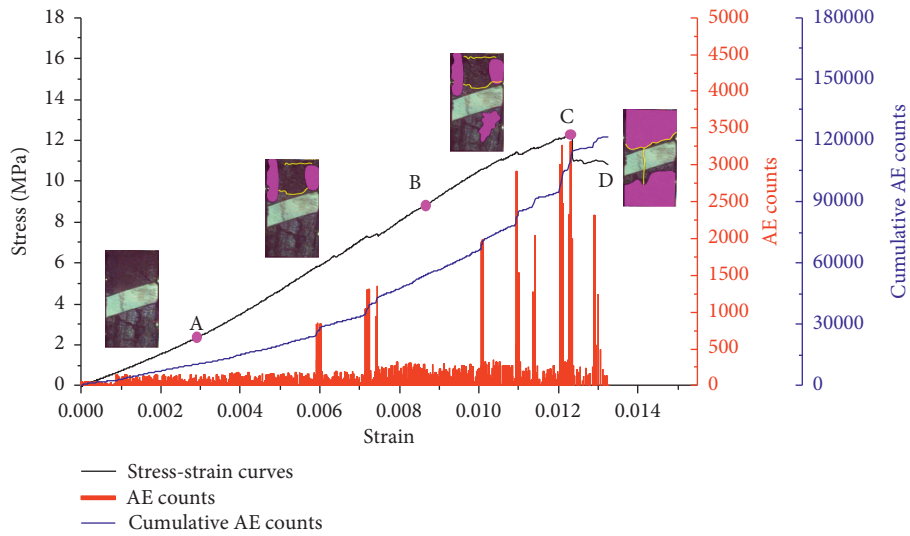


FIGURE 5: Stress-strain curve and acoustic emission monitoring curve of composite specimens with a 20° dip angle (A20-1).

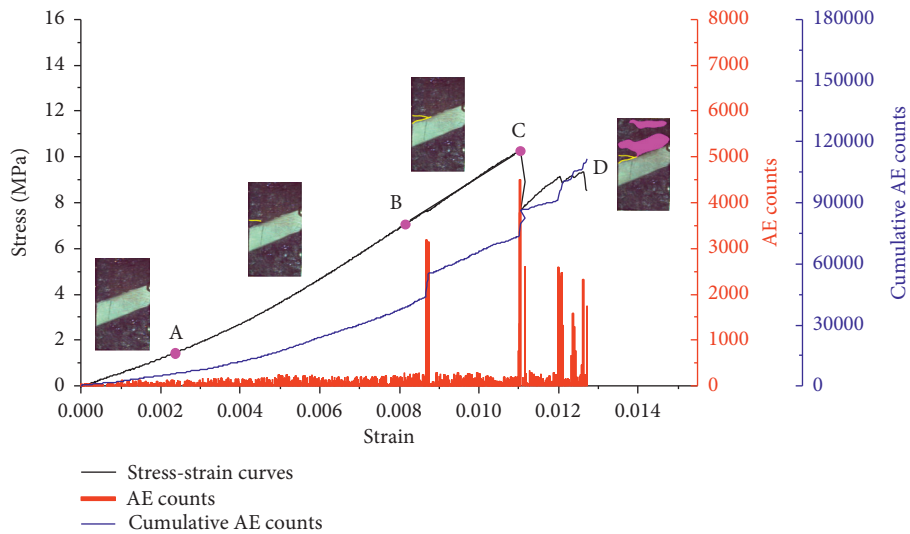


FIGURE 6: Stress-strain curve and acoustic emission monitoring curve of composite specimens with a 30° dip angle (A30-1).

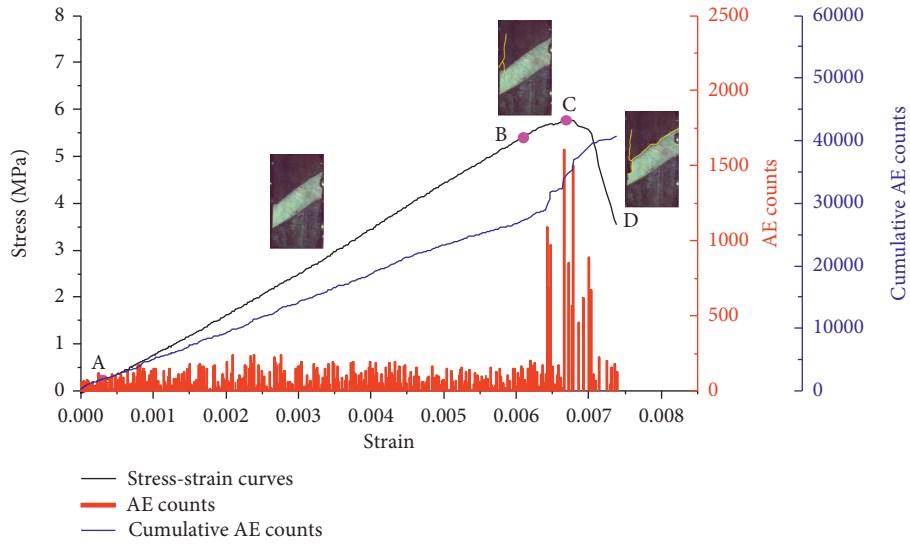


FIGURE 7: Stress-strain curve and acoustic emission monitoring curve of composite specimens with a 40° dip angle (A40-1).

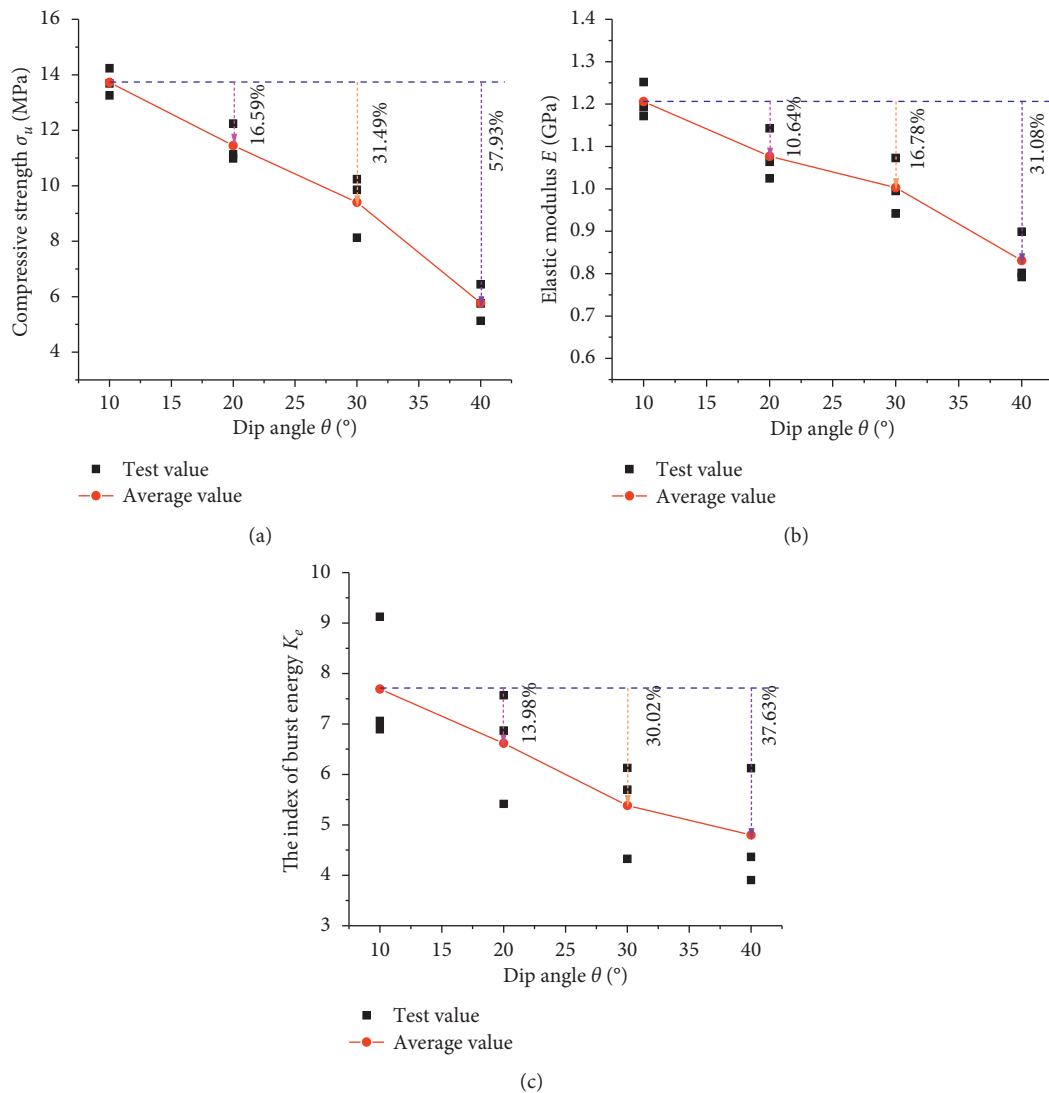


FIGURE 8: Test results of the mechanical parameters of composite specimens with different dip angles. (a) Uniaxial compressive strength. (b) Elastic modulus. (c) Bursting energy index.

TABLE 1: Mechanical parameters of composite specimens with different dip angles.

Specimen group	Uniaxial compressive strength σ_u (MPa)		Elastic modulus E (GPa)		Bursting energy index K_e	
	Tested	Average	Tested	Average	Tested	Average
A10-1	14.236		1.172		7.059	
A10-2	13.254	13.726	1.252	1.206	6.896	7.694
A10-3	13.689		1.193		9.126	
A20-1	12.240		1.064		6.870	
A20-2	11.123	11.449	1.143	1.077	7.569	6.618
A20-3	10.985		1.025		5.415	
A30-1	10.234		0.942		4.325	
A30-2	9.853	9.404	1.073	1.003	5.698	5.384
A30-3	8.126		0.995		6.129	
A40-1	5.756		0.899		6.125	
A40-2	6.443	5.775	0.792	0.831	4.365	4.799
A40-3	5.125		0.802		3.906	

the lower coal, which underwent splitting and tensile failure. The rock parting had an insignificant impact on the strength and failure of the composite, where the strength was dictated primarily by the coal strength, as shown in Figure 9. The composite specimen with $D=20$ mm was comparatively more anisotropic, and the rock parting accumulated more energy. As considerable space was vacated by crack propagation in the coal, the sudden release of the elastic energy accumulated in the rock parting at the coal-rock interfaces resulted in the violent failure of the composite and abnormally high AE counts, as shown in Figure 10. Crack propagation occurred in the upper and lower coal of composite specimen B30-1 ($D=30$ mm), accompanied by stretching and spalling, an increase in displacement, and the sudden release of the elastic energy accumulated in the rock parting, resulting in the bursting failure of the specimen, as shown in Figure 11(a). In composite specimen B30-2 ($D=30$ mm), the initiation of cracks in the rock parting did not provide conditions for the sudden release of accumulated elastic energy. Thus, the rock parting underwent static splitting and tensile coalescence failure, as shown in Figure 11(b). The composite specimen with $D=40$ mm underwent bursting failure, with notable crack propagation in the rock parting, primarily because more energy had accumulated than for the rock parting with $D=30$ mm. The considerable strain in the coal caused the rock parting to rebound and suddenly release the accumulated elastic energy, causing violent failure of the composite, as shown in Figure 12. The initiation and propagation of cracks in the composite corresponded to decreases in stress (as evidenced by the stress-strain curves) and sudden increases in the cumulative AE count (as shown by the cumulative AE count curves). Thus, the AE counts effectively reflected the internal crack propagation patterns in the composites.

Figure 13 and Table 2 show that as D increased, σ_u , E , and K_e of the composite increased. The σ_u values of the composite specimens with D values of 20, 30, and 40 mm were 13.58%, 24.62%, and 57.21% higher, respectively, than those of the composite specimens with D of 10 mm. The E values of the composite specimens with D values of 20, 30, and 40 mm in D were 10.55%, 23.06%, and 41.31% higher, respectively,

than those of the composite specimens with D of 10 mm. The K_e values of the composite specimens with D values of 20, 30, and 40 mm were 174.57%, 194.97%, and 361.68% higher, respectively, than those of the composite specimens with D of 10 mm.

As D increased, the rock parting became the main load-bearing structure, and σ_u and K_e of the composite increased, as did the risk of bursting. Under uniaxial compressive loading, the rock parting was the key structure for accumulating energy due to its relatively high strength. The relatively low coal strength enabled micro- and macrocracks to develop in the coal before the ultimate failure strength of the rock parting was reached, causing a relatively large displacement in the coal and generating a relatively large vacated space. Under these conditions, the rock parting rebounded and released the accumulated elastic energy, which precipitated the violent bursting failure of the coal. Rebounding generated a tensile stress in the rock parting and caused similar splitting and tensile failure of the surfaces. However, premature crack propagation divested the rock parting of the preconditions for accumulating energy. The corresponding composite specimens in this study were found to exhibit static failure characteristics with a considerably lower risk of bursting. The larger the composite D was, the higher the capacity of the rock parting to accumulate elastic energy was. The release of elastic energy from the rock parting increased the extent of fragmentation of the coal. The larger D was, the more fragmented the coal was.

4. Engineering Applications

The experimental results were used to formulate two technologies for controlling the stability of the surrounding rock (Figure 14). (1) Excavation causes the surrounding rock stress at the free face of a roadway to transition from a three-dimensional stress state to a two-dimensional or unidirectional stress state, thereby decreasing the rock stability. The presence of partings increases the strength anisotropy of the coal-rock composite surrounding the roadway. Under the mining-induced surrounding rock stress, the coal ribs of a roadway significantly spall off.

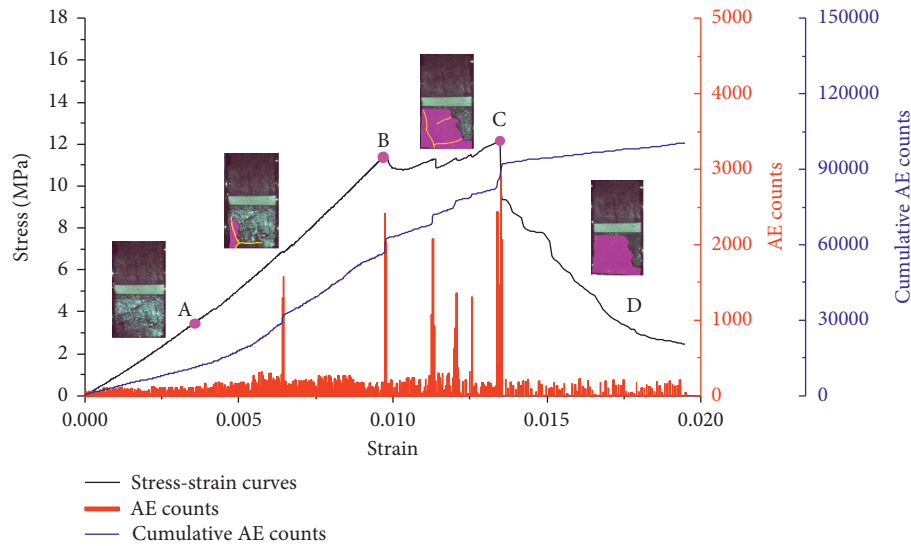


FIGURE 9: Stress-strain curve and acoustic emission monitoring curve of 10 mm-thick composite specimens (B10-1).

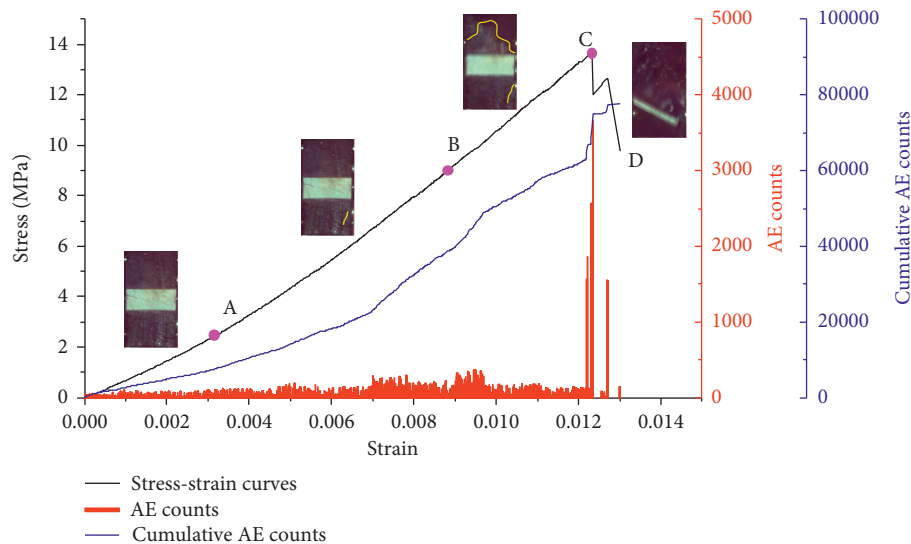
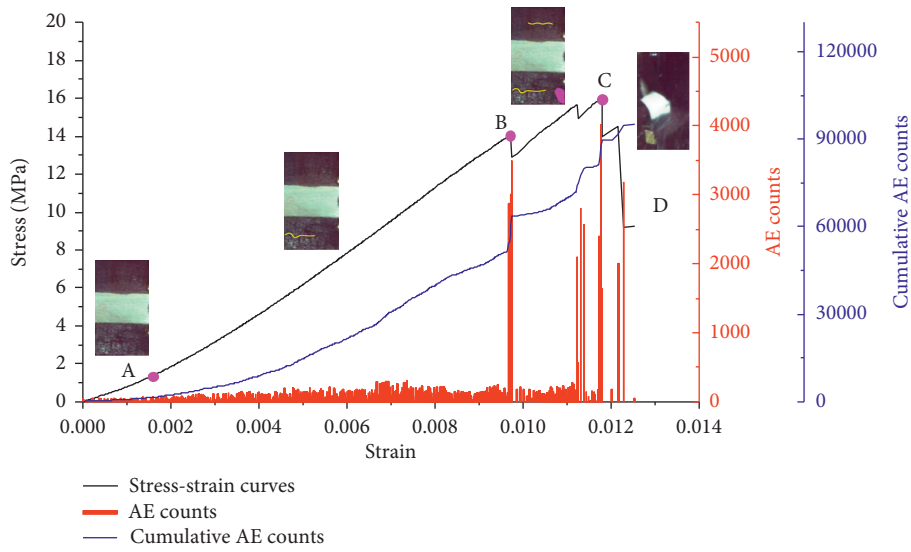


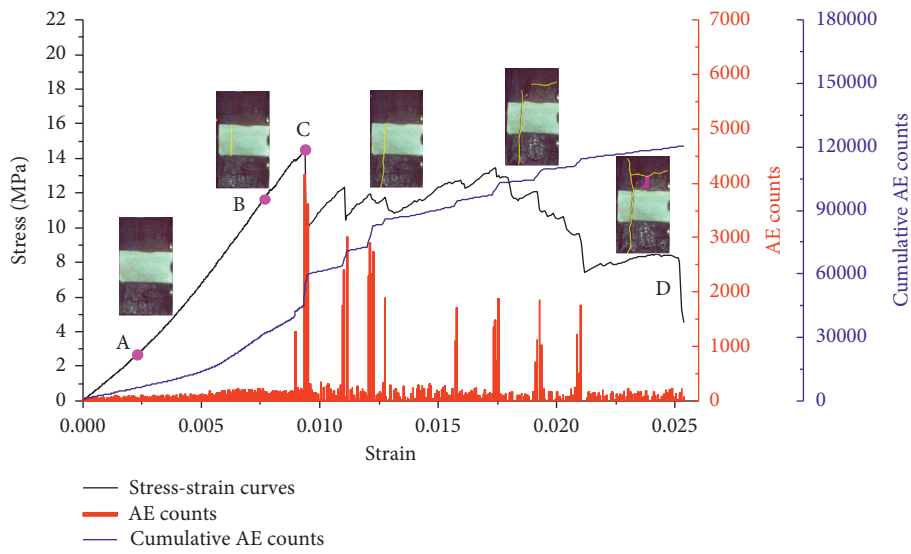
FIGURE 10: Stress-strain curve and acoustic emission monitoring curve of 20 mm-thick composite specimens (B20-1).

Consequently, an asymmetric strengthening support technology can be used to increase the strength of coal-seam support systems, reduce the difference between the strengths of the coal and rock in coal-rock composites, and maintain the stability of roadway surrounding rocks. (2) Under uniaxial compression, the initiation and propagation of microjoints and microcracks damages the coal in a coal-rock composite and thereby releases part of the accumulated elastic energy in the rock. Thus, the extent of damage sustained by the coal increases, and bursting is induced. It is necessary to reduce the extent of damage sustained by coal-rock composites, the bursting risk, and the coal cutting energy consumption. These goals can be achieved by using high-pressure fracturing to weaken and disrupt the integrity of rock partings, reduce the strength anisotropy of coal-rock composites, and decrease the risk of bursting in coal seams.

Mining is currently underway in the No. 2 coal seam of a mine in the Yushen mining area in Shaanxi. This coal seam, with an average burial depth of 370 m, is at low risk of rock burst. The No. 112201 working face of this coal seam, 350 m in length and 4,556.6 m in strike length, contains one to two partings overall but three partings in some local areas. The parting thickness is 0.6–2.0 m. The high hardness coefficient of the partings hinders excavation and makes cutting difficult. In addition, coal blocks are ejected during the cutting process, and the rocks surrounding the roadway have low stability and significantly spall off. To reduce the energy consumption of coal cutters and the dynamic manifestation at the working face, high-pressure pulsed water-jet fracturing technology was employed to reduce the strength of the partings at the working face. Figure 15 shows the partings at the working face before and after weakening.



(a)



(b)

FIGURE 11: Stress-strain curve and acoustic emission monitoring curve of 30 mm-thick composite specimens. (a) B30-1. (b) B30-2.

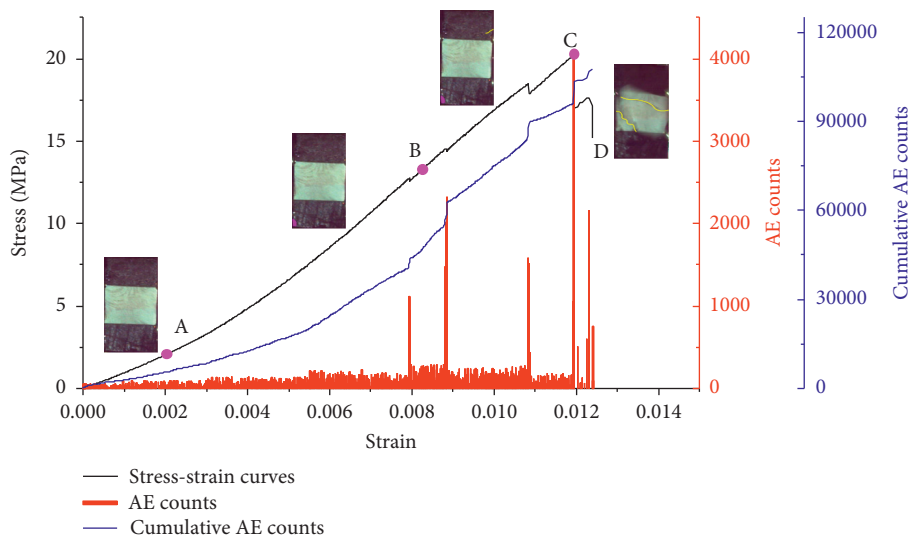


FIGURE 12: Stress-strain curve and acoustic emission monitoring curve of 40 mm-thick composite specimens.

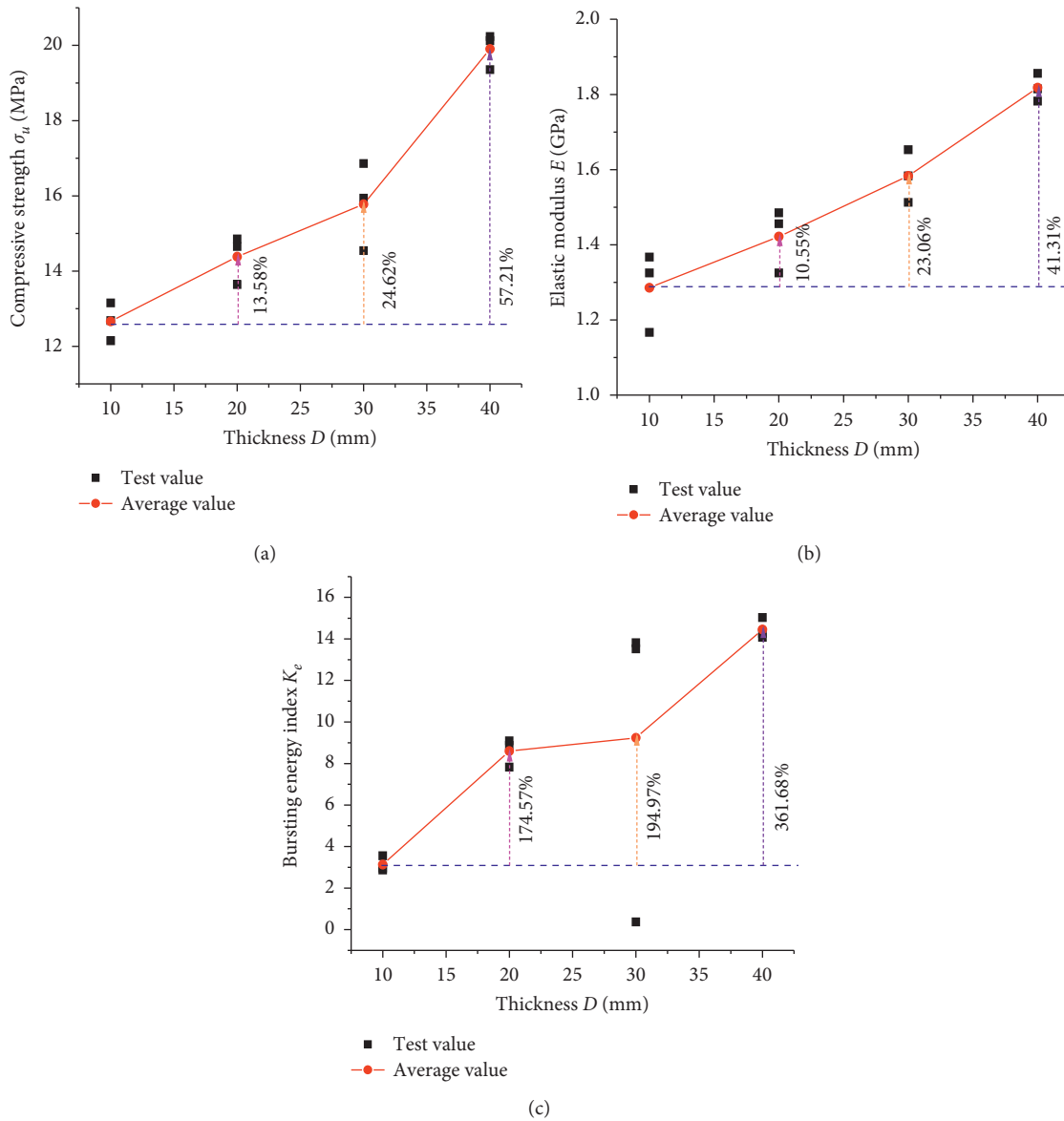


FIGURE 13: Test results of the mechanical parameters of composite specimens with different thicknesses. (a) Uniaxial compressive strength. (b) Elastic modulus. (c) Bursting energy index.

TABLE 2: Mechanical parameters of composite specimens with different thicknesses.

Specimen group	Uniaxial compressive strength σ_u (MPa)		Elastic modulus E (GPa)		Bursting energy index K_e	
	Tested	Average	Tested	Average	Tested	Average
B10-1	12.148		1.167		2.968	
B10-2	12.685	12.662	1.325	1.286	3.556	3.131
B10-3	13.154		1.367		2.869	
B20-1	13.644		1.325		9.091	
B20-2	14.851	14.382	1.485	1.422	8.873	8.597
B20-3	14.652		1.456		7.826	
B30-1	15.936		1.513		13.521	
B30-2	14.543	15.779	1.583	1.583	0.371	9.236
B30-3	16.859		1.653		13.815	
B40-1	20.237		1.782		14.071	
B40-2	20.125	19.906	1.856	1.818	15.026	14.455
B40-3	19.356		1.815		14.269	

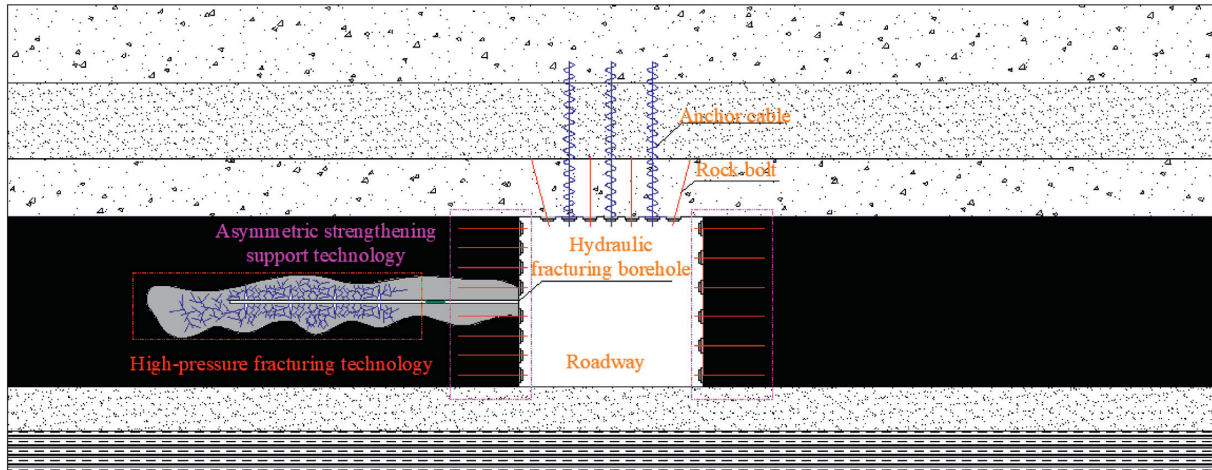


FIGURE 14: Control technology for surrounding rock.



FIGURE 15: The parting before and after fracturing at the working face. (a) Before fracturing. (b) After fracturing.

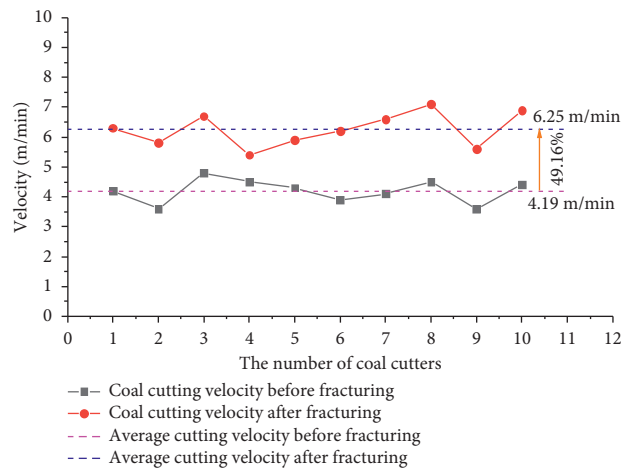


FIGURE 16: The cutting speed of the coal cutters before and after fracturing of the parting.

High-pressure pulsed prefracturing promoted crack development in the partings, reduced the parting strength, curtailed coal rib spalling and dynamic ejection of coal dust at the working face, decreased the number of cutting picks used by 36%, and increased the coal cutting speed by 49.16%,

as shown in Figure 16. The presence of the partings resulted in a poorly formed return airway at the No. 112201 working face that exhibited significant spalling, as shown in Figure 17(a). To maintain the stability of the rocks surrounding the roadway, the support parameters were adjusted

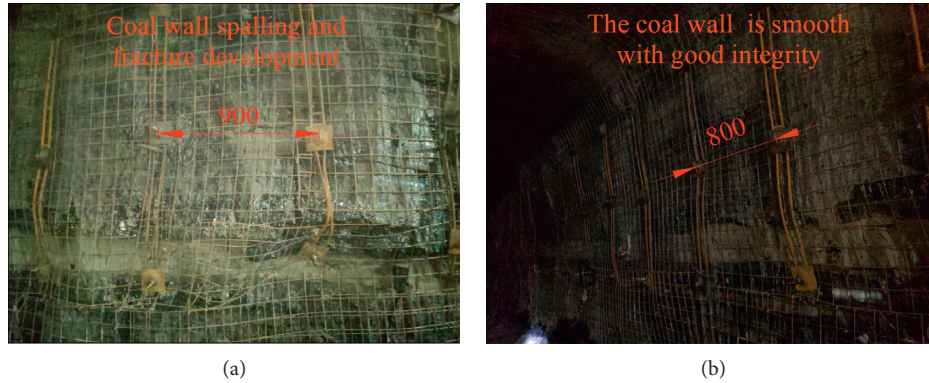


FIGURE 17: Comparison of roadway formation with different support parameters. (a) Support spacing of 900 mm \times 900 mm. (b) Support spacing of 900 mm \times 800 mm.

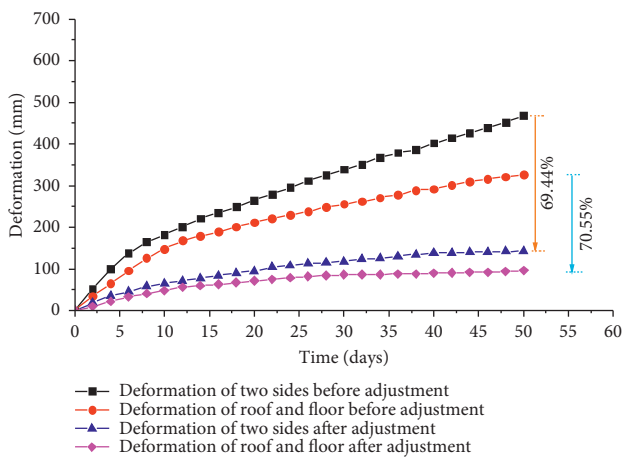


FIGURE 18: The roadway formation with different support parameters.

to increase the strength of the coal seam support system. The rock bolt spacing was changed from 900 mm \times 900 mm to 900 mm \times 800 mm. Figure 17(b) shows the performance of the roadway support system. Figure 18 shows that the adjustment notably decreased the deformation of the surrounding rocks along the two sides of the roadway and the roof and floor of the roadway by 69.44% and 70.55%, respectively, while significantly increasing the stability of the rocks surrounding the roadway.

5. Conclusions

- (1) As θ increased, the pore compaction regime of the stress-strain curve became shorter, the failure mode of the composite changed from splitting and tensile failure to slip and shear failure, the brittleness and the extent of fragmentation of the coal of the composite decreased, and its ductility increased. Additionally, as θ increased, σ_w , E , and K_e of the composite decreased. Notably, the cumulative AE count curve of the composite could be divided into four characteristic regimes corresponding to the stress-strain curve: pore compaction and closure, a slowly ascending linear elastic section, prepeak

steady crack propagation, and peak unsteady crack propagation.

- (2) The rock parting was the key area in which elastic energy accumulated. The initiation and propagation of cracks in the coal caused the rock parting to release elastic energy, which precipitated violent failure of the composite. As D increased, σ_w , E , and K_e of the composite increased. In addition, as D increased, the failure mode of the composite changed from ductile failure to brittle failure, and the extent of fragmentation of the coal increased.
- (3) The experimental results for the coal-rock composite with a seam parting were used to formulate two technologies to control the stability of the surrounding rock, namely, high-pressure fracturing technology to weaken partings at working faces and asymmetric strengthening support technology for rocks surrounding roadways. These two technologies can effectively ensure safe and efficient production at working faces.

Data Availability

Some of the data used to support the findings of this study are included within the article, and the other supporting data are available from the corresponding author upon request.

Conflicts of Interest

The authors declare that they have no known conflicts of interest or personal relationships that could appear to influence the results reported in this paper.

Acknowledgments

The authors acknowledge the financial support provided by the National Natural Science Foundation Project of China (51564044).

References

- [1] L. C. Cheng, Y. L. Qin, X. W. Li, and X. Y. Zhao, "A laboratory and numerical simulation study on compression characteristics

- of coal gangue particles with optimal size distribution based on shape statistics,” *Mathematical Problems in Engineering*, vol. 2020, Article ID 8046156, 13 pages, 2020.
- [2] M. S. Alfarzaei, Q. Niu, J. Zhao, R. M. A. Eshaq, and E. Hu, “Coal/gangue recognition using convolutional neural networks and thermal images,” *IEEE Access*, vol. 8, pp. 76780–76789, 2020.
 - [3] M. Bui, Y. Lu, W. Guo, F. Wang, and Z. Zhao, “The research on stability and supporting technology of rock in gob-side entry in thick seam with parting,” *Journal of Mining & Safety Engineering*, vol. 31, no. 6, pp. 950–956, 2014.
 - [4] R. Peng, X. R. Meng, G. M. Zhao, Y. M. Li, and J. M. Zhu, “Experimental research on the structural instability mechanism and the effect of multi-echelon support of deep roadways in a kilometre-deep well,” *PLoS One*, vol. 13, no. 2, p. 24, 2018.
 - [5] H. Y. Liu, H. S. Jia, L. Fan, and B. Han, “The Theory and Practice of Forepoling Pre-stressed system bolt in preventing the rib spalling,” in *Resources and Sustainable Development*, J. Wu, X. Lu, H. Xu, and N. Nakagoshi, Eds., Trans Tech Publications Ltd, Stafa-Zurich, Switzerland, pp. 883–887, 2013.
 - [6] K. Jiang, K. Gao, and L. Wan, “Effect of gangue distributions on cutting force and specific energy in coal cutting,” *Strojnikski Vestnik-Journal of Mechanical Engineering*, vol. 66, no. 3, pp. 203–212, 2020.
 - [7] S. F. Liu, S. F. Lu, Z. J. Wan, H. W. Zhang, and K. K. Xing, “Numerical simulation of induced cutting in deep coal,” *Royal Society Open Science*, vol. 6, no. 9, p. 12, 2019.
 - [8] D. G. Li and C. S. Liu, *Development and Experiment of Cutting Force Model on Conical Pick Cutting Rock at Different Wedge Angles*, World Scientific Publishing Co Pte Ltd, Singapore, 2016.
 - [9] L. Tian, J. Mao, and Q. Wang, “Coal and rock identification method based on the force of idler shaft in shearer’s ranging arm,” *Journal of China Coal Society*, vol. 41, no. 3, pp. 782–787, 2016.
 - [10] S. Zhu, F. Jiang, J. Liu et al., “Mechanism and monitoring and early warning technology of rock burst in the heading face of compound thick coal seam,” *Journal of China Coal Society*, vol. 45, no. 5, pp. 1659–1670, 2020.
 - [11] K. Yang, Z. Wei, X. Chi, Y. Zhang, L. Dou, and W. Liu, “Experimental research on the mechanical characteristics and the failure mechanism of coal-rock composite under uniaxial load,” *Advances in Civil Engineering*, vol. 2020, Article ID 8867809, 11 pages, 2020.
 - [12] F. Gao, H. Kang, and L. Yang, “Experimental and numerical investigations on the failure processes and mechanisms of composite coal-rock specimens,” *Scientific Reports*, vol. 10, no. 1, p. 13422, 2020.
 - [13] Z. Qin, G. B. Chen, G. H. Zhang, Q. H. Li, and T. Li, “Tests on the dynamic failure rules of coal-rock composites,” *Acta Geodynamica et Geomaterialia*, vol. 16, no. 1, pp. 39–54, 2019.
 - [14] S. Song, X. Liu, Y. Tan, D. Fan, Q. Ma, and H. Wang, “Study on failure modes and energy evolution of coal-rock combination under cyclic loading,” *Shock and Vibration*, vol. 2020, Article ID 5731721, 16 pages, 2020.
 - [15] D.-X. Zhang, W.-Y. Guo, C.-W. Zang et al., “A new burst evaluation index of coal-rock combination specimen considering rebound and damage effects of rock,” *Geomatics, Natural Hazards and Risk*, vol. 11, no. 1, pp. 984–999, 2020.
 - [16] P. Wang, H. Jia, and P. Zheng, “Sensitivity analysis of bursting liability for different coal-rock combinations based on their inhomogeneous characteristics,” *Geomatics, Natural Hazards and Risk*, vol. 11, no. 1, pp. 149–159, 2020.
 - [17] Z. Xie, N. Zhang, F. Meng, C. Han, Y. An, and R. Zhu, “Deformation field evolution and failure mechanisms of coal-rock combination based on the digital speckle correlation method,” *Energies*, vol. 12, no. 13, p. 14, 2019.
 - [18] Z. Xie, N. Zhang, Y. Yuan, G. Xu, and Q. Wei, “Study on safety control of composite roof in deep roadway based on energy balance theory,” *Sustainability*, vol. 11, no. 13, p. 18, 2019.
 - [19] T. Wang, Z. Ma, P. Gong, N. Li, and S. Cheng, “Analysis of failure characteristics and strength criterion of coal-rock combined body with different height ratios,” *Advances in Civil Engineering*, vol. 2020, Article ID 8842206, 14 pages, 2020.
 - [20] G. B. Chen, E. Y. Wang, W. C. Wang, T. Li, and G. H. Zhang, “Experimental study on the influence of lithology and rock-coal height ratio on mechanical properties and impact effect of combined body,” *Energy Sources Part A-Recovery Utilization and Environmental Effects*, vol. 24, 2019.
 - [21] S. J. Chen, D. W. Yin, N. Jiang, F. Wang, and W. J. Guo, “Simulation study on effects of loading rate on uniaxial compression failure of composite rock-coal layer,” *Geomechanics and Engineering*, vol. 17, no. 4, pp. 333–342, 2019.
 - [22] Y. L. Tan, F. H. Yu, J. G. Ning, and T. B. Zhao, “Design and construction of entry retaining wall along a gob side under hard roof stratum,” *International Journal of Rock Mechanics and Mining Sciences*, vol. 77, pp. 115–121, 2015.
 - [23] J. Lu, G. Huang, H. Gao, X. Li, D. Zhang, and G. Yin, “Mechanical properties of layered composite coal-rock subjected to true triaxial stress,” *Rock Mechanics and Rock Engineering*, vol. 53, no. 9, pp. 4117–4138, 2020.

Research Article

The Influence of Confining Stresses on Rock Fragmentation, Thrust Force, and Penetration Energy in Sandstone Indentation Tests Using Disc Cutters

Gaofeng Wang ^{1,2}, Ting Ren ³, and Gaolei Zhu ^{1,2}

¹School of Mines, China University of Mining and Technology, Xuzhou, Jiangsu 221116, China

²State Key Laboratory of Coal Resources and Safe Mining, China University of Mining and Technology, Xuzhou, Jiangsu 221116, China

³Faculty of Engineering and Information Sciences, University of Wollongong, Wollongong, NSW 2522, Australia

Correspondence should be addressed to Ting Ren; ting_ren@uow.edu.au

Received 27 January 2021; Revised 9 February 2021; Accepted 11 March 2021; Published 2 April 2021

Academic Editor: Chiara Bedon

Copyright © 2021 Gaofeng Wang et al. This is an open access article distributed under the Creative Commons Attribution License, which permits unrestricted use, distribution, and reproduction in any medium, provided the original work is properly cited.

Hard rock Tunnel Boring Machines (TBMs) engaging disc cutters as cutting tools have been employed in considerable underground coal mines to accommodate the requirement of more stone drivage as operations are going deeper. This study conducted a set of disc cutter indentation tests to explore the influence of confining stresses on rock fragmentation, thrust force, and penetration energy on sandstone, which is commonly encountered in underground coal mines. The test results show that there exists a critical confining stress, under which the maximum thrust force and penetration energy keep increasing with confining stress mounting while the maximum thrust force and penetration energy will decrease or flatten if it is surpassed. By combining with previous studies and comparing the critical confining stress values to the rock mechanical properties' values, the critical value is most likely to be of cohesion. For subsurface rock fragmentation, the Constant Cross Section (CCS) disc cutter indentation has denser cracks and their orientations are more lateral than those under the V shape one; the V shape disc cutter indentation is less sensitive to confining stresses, with no notable increase of crack number and crack reorientation with increasing confinement. Thus, the CCS disc cutter is more favorable than the V shape one from the perspective of rock fragmentation under confining stresses.

1. Introduction

Stone drivage has been in increasing demand for underground coal mines. Depletion of shallow resources forces them to go deeper. The deepest underground coal mining operation in China has been over 1500 meters beneath the ground surface, and numerous others are deeper than 1000 meters [1, 2]. With such large overburden depths, coal seams sit in high-stress regimes and hold more methane [3–7]. For that, stone roadways are needed to facilitate safe mining operations. Firstly, high ground stress deteriorates the stability of underground workings, which makes coal mains not feasible; to obtain reasonable stability, the mains need to be constructed in a more competent stone floor. Secondly, high gas content, combined with high ground stress, makes coal

seams prone to outbursts. Coal gates in outburst prone seams need to be destressed and degassed during development to eliminate risks. In many mines, destressing and degassing operations are carried out from stone roadways beneath longwall panels. Last but not least, numerous gassy mines also construct stone roadways above longwall panels to accommodate goaf gas drainage to avoid methane build-ups at longwall faces. In conclusion, stone drivage is in a great and growing demand for deep underground coal mines [8–11]. Hard rock Tunnel Boring Machines (TBMs) engaging disc cutters as rock breaking tools have been used in considerable deep underground coal mines to accommodate the requirement of stone drivage [12–14].

In the rock cutting process, thrust force applied from TBM cutting heads makes disc cutters penetrate into the

rock, as illustrated in Figure 1, and incurs rock fragmentation and penetration energy. Magnitudes of thrust force and penetration energy are indicators of cutting easiness. Rock fragmentation under a disc cutter mainly includes forming a crushed zone and incurring cracks. Crack development patterns reflect the modes of failures; radial cracks are often caused by tensile failure, while lateral cracks, that is, side chipping, indicate shear failure [15, 16]. Study of rock fragmentation, thrust force, and penetration energy under confining stresses improves understanding of TBM rock breaking in deep underground mines, which presents a prerequisite for refining cutting force prediction models and practicable feasibility study for underground coal mine TBM projects.

Disc cutter cutting force prediction is a basis for TBM cutting head design, optimization, and advance rate prediction. Numerous researchers have attempted to develop accurate cutting force prediction models. For V shape disc cutters which were adopted in the early days of TBMs, Evans, Roxborough and Philips, and Ozdemir et al. proposed their cutting force prediction models, respectively [17–20]. Along with TBMs' application in hard rock tunnelling, CCS disc cutters became more predominant than V shape ones in those cases [21]. Rostami and Ozdemir introduced new models to cover the CCS disc cutters [22]. Although researchers have been refining the cutting force prediction models, there is still no widely accepted cutting force prediction model taking due consideration of the factor of confining stresses [23, 24].

Researchers have proposed various rock-breaking mechanisms under confining stresses by disc cutters, which often conflict with each other. It means the influence of confining stresses on disc cutting is still not clear. Tarkoy and Marconi [25] proposed an unfavorable influence of high confining stresses on rock boreability by referring to field data from Star Mine tunnels driven with 1200–2000 m overburden [25]. Klein et al. [26], in contrast to Tarkoy and Marconi, argued favorable effects of high confining stresses on TBM boring based on the Field Penetration Index (FPI) data from other four TBM tunnelling projects [26]. Innaurato et al. [27] conducted laboratory disc cutter indentation tests on two hard rocks and found that thrust force increased with the confinement mounting [27]. Yin et al. [28] studied the influence of confining stresses on disc cutting rock fragmentation with up to 25 MPa confinement on marble and granite samples. The study found the existence of a critical confining stress value for the marble samples, under which the thrust force for crack initiation keeps increasing, while they decrease when the confining stress is higher than the critical value [28]. The governing factor for the critical value was however not identified in the study, and only one CCS disc cutter was adopted in the tests. Chen and Song [29] studied the confining stresses' influence on penetration energy, which is calculated by integrating the thrust force with indentation displacement. The penetration energy continuously increased with the rising of confining stresses [29]. However, only a CCS disc cutter was utilized in the tests. Conclusively, the influence of confining stresses on disc cutting is notable and not yet fully explored, the

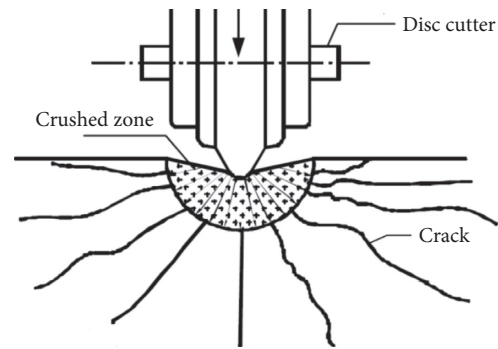


FIGURE 1: Schematic diagram of disc cutter's penetration into the rock.

mechanisms proposed by previous researcher conflict with each other. In addition, the aforementioned finding of critical confining stress needs to be further studied.

Different rocks might undergo different rock cutting mechanisms. Rocks utilized in previous studies are rarely encountered in underground coal mines. So, findings from the aforementioned studies bear questionable relevance for underground coal mine TBM operations. To remedy the shortcomings, a series of laboratory tests with bilateral confinement were conducted on sandstone, which is a commonly encountered stone in underground coal mines. In addition, both CCS and V shape disc cutters were used.

2. Test Methodology

Rock fragmentation under a disc cutter is mainly the function of thrust force. So, the cutter-rock interaction can be treated as an indentation process. This study adopts the indentation methodology to conduct the laboratory tests.

2.1. Test Equipment

2.1.1. The Cutters. The cutters used in the indentation tests are shaped as a portion of the 450 mm diameter and 30 mm width TBM cutter rings, as shown in Figures 2 and 3. For the V shape cutter, its included edge angle is 80°.

2.1.2. The Confining Box. To apply the bilateral confinement on sandstone blocks, a confining box was designed to accommodate the sandstone blocks. The sandstone block is positioned at a corner of the box, and then two steel plates are placed against the two open sides of the sandstone block. Two hydraulic flat jacks are placed between the box and steel plates to apply the confining pressure, as shown in Figure 4.

2.1.3. Penetration Platform. The indentation tests are set upon an AVERY computer-controlled electrohydraulic servo machine with a load capacity of 5000 kN, as shown in Figure 5. The confining box is placed on the bottom platen while the disc cutter is placed at the upper platen. The two flat jacks are inflated with two hydraulic hand pumps to apply confining stresses.

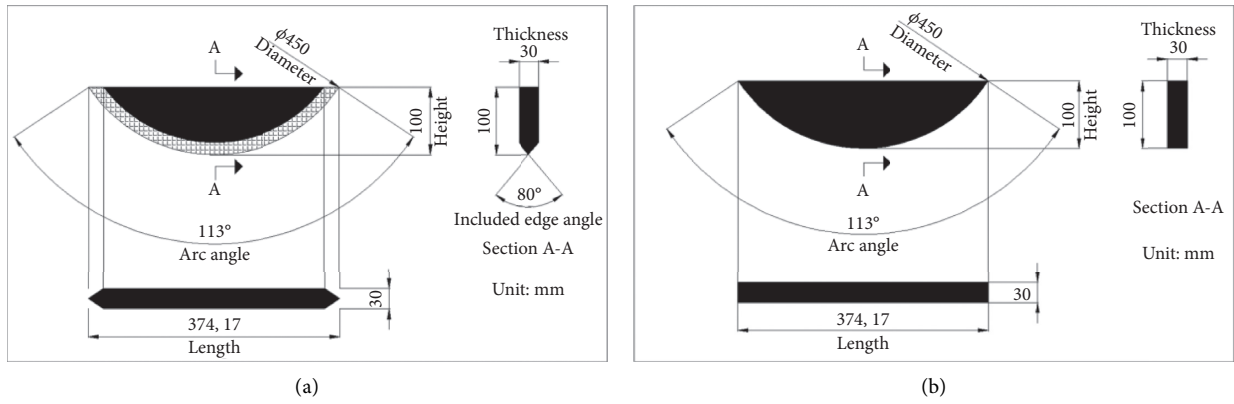


FIGURE 2: Fabricating drawings of the designed cutters: the V shape one (a) and CCS one (b).

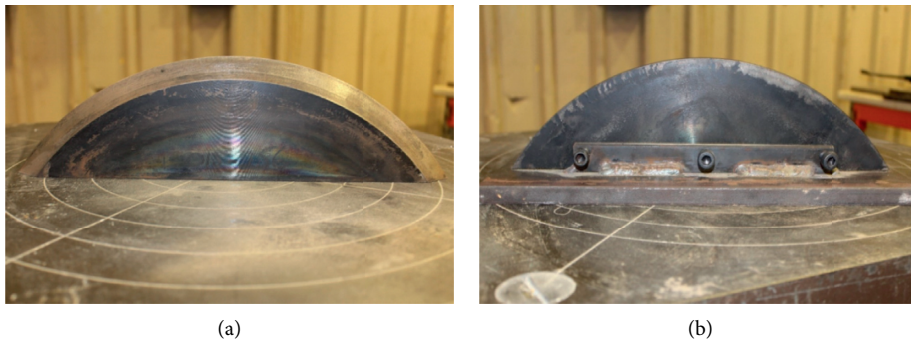


FIGURE 3: Fabricated cutters: the V shape one (a) and CCS one (b).

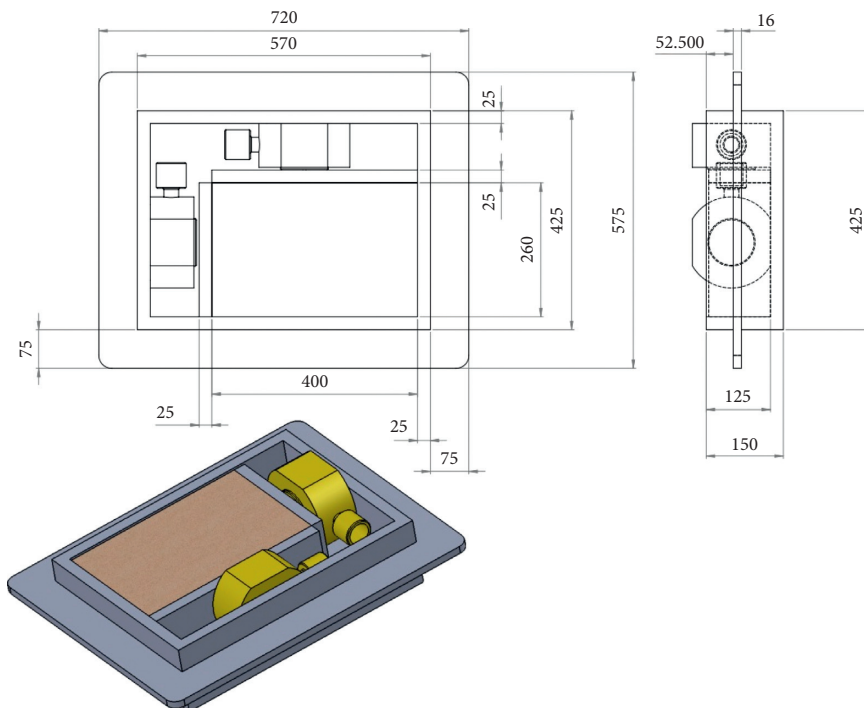


FIGURE 4: Steel box designed for applying confining stresses (all dimensions in mm).

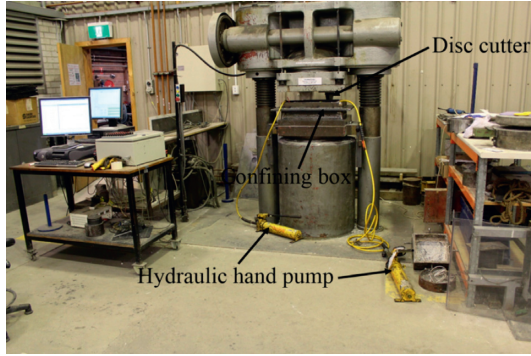


FIGURE 5: The indentation test platform.

2.2. Rock Sample Preparation. The background of this laboratory study is the application of TBMs in underground coal mines. Sandstone is the most common surrounding rock in underground coal mines. As different rock types have distinctive failure patterns under disc cutting due to the complexity of the rock properties in nature; it is hard to generalize a specific research outcome applicable for all rocks. Sandstone is chosen for this study to obtain meaningful guidelines for the application of TBMs in underground coal mines.

To ensure that the tested sandstone blocks have consistent physical and mechanical properties, all rock blocks were cut from a single large lump, from a quarry in Wollongong. They were prepared into a specified dimension of 400 mm × 260 mm × 120 mm.

The main properties of the sandstone are summarized in Table 1.

Uniaxial and triaxial tests were conducted on an Instron loading machine according to ISRM suggested methods [30]. The dimensions of all samples are 54 mm in diameter and 120 mm in height.

2.3. Testing Design and Procedure

2.3.1. Test Design. Eight rock specimens are tested: four ones under the CCS disc cutter and the other four ones under the V shape disc cutter. The variable parameters of the study are disc cutter patterns and confining stresses. Two sequential cuts are designed for each specimen on the top surface, as illustrated in Figure 6. The first cut's penetration is 6 mm and the second cut's penetration is 9 mm. Determination of each cut's position is based on reviewing of research outcome on spacing-penetration ratio. The spacing-penetration ratio is normally lower than 10 [31]. To eliminate the edge effect, the first cut's spacing to the edge is adopted as 85 mm, and the second cut's spacing to edge is adopted as 125 mm, by further adding safety factors. In addition, the spacing between the two cuts is 190 mm, which is much larger than 10 times the deeper penetration of 9 mm. Thus, the two cuts neither have edge effect nor interfere with each other.

The bilateral confining stresses are provided by inflated flat jacks, as shown in Figure 5. The confining stresses are 0, 3, 6, and 9 MPa, respectively, with the same values in two directions for the same sandstone specimen. Penetration

TABLE 1: Properties of the sandstone used in laboratory tests.

Rock properties	Property values
Specific density	2230 kg/m ³
Uniaxial compressive strength (UCS)	38.43 MPa
Brazilian tensile strength	5.29 MPa
Cohesion	6.79 MPa
Internal friction angle	47.47°
Young's modulus	48.60 GPa
Poisson's ratio	0.16

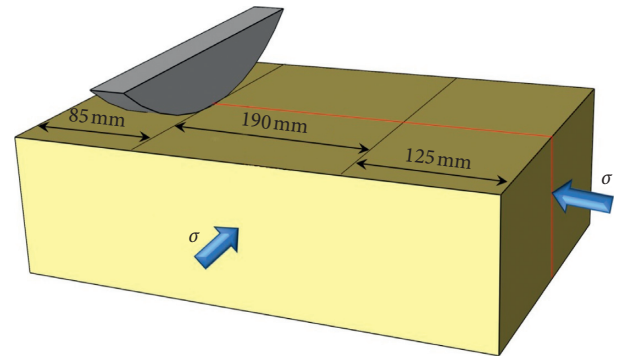


FIGURE 6: Schematic representation for the positioning of the indentation cuts.

forces of disc cutters are applied by the hydraulic servo compression machine. The vertical penetration process is controlled by displacement with the final penetration depths of 6 and 9 mm for the first and second cuts, respectively. Tested sandstone blocks are then cut to examine the sub-surface crushed zone and crack development after indentation tests.

2.3.2. Test Procedure. There are two cuts for each sample, and the testing procedure is as follows:

- (i) The sandstone specimen is put into the confining box, and the steel plates and hydraulic flat jacks are set as illustrated in Figure 4.
- (ii) The confining box is then placed onto the testing platform, as shown in Figure 5. Subsequently, the flat jacks are inflated with hydraulic hand pumps to apply designated confinement stresses onto the sandstone samples.
- (iii) The designated cutter is installed onto the hydraulic servo machine and then located to the designated positions. Penetration load is applied to the sandstone sample with displacement control, in which the penetration depth and thrust force variations are recorded.
- (iv) Once the indentation cuts are finished, the servo machine is unloaded. Sequentially, the flat jacks are deflated, and the confining box is retrieved from the test platform. The sandstone specimen is then collected from the confining box, and the confining

box will be cleaned to accommodate another specimen for being tested.

- (v) The tested specimen is diamond cut into four pieces to study the subsurface rock fragmentation under the disc cutter, as shown in Figure 7.

3. Results

3.1. Confining Stresses' Influence on Cutting Forces. The CCS disc cutter thrust cutting force evolution patterns under different confining stresses are illustrated in Figure 8. It shows that the thrust force disparities among different confining stresses are of a marginal extent with penetration lower than 3 mm. After that, thrust forces fluctuate with large amplitude up to the ultimate penetrations of 6 mm and 9 mm, and the disparities are irregular.

TBM thrust capacity is a multiplication of single cutter thrust force by the number of cutters. Thus, getting the maximum load for a single cutter is the basis for determining the thrust capacity for the TBM propelling system design. From this point of view, the influence of confining stress on maximum thrust force is of great interest. The influence identified in this study is presented in Figure 9.

Figure 9(a) shows the maximum thrust force values for the CCS disc cutter with a penetration of 6 mm. The maximum thrust force values are 249, 368, 432, and 348 kN under confining stresses of 0, 3, 6, and 9 MPa, respectively. Maximum thrust force increases with confining stresses mounting when it is lower than 6 MPa, while maximum thrust force begins to decrease from some point between 6 and 9 MPa of confinement. Figure 9(b) shows the maximum thrust force values for the CCS disc cutter with the ultimate penetration of 9 mm. It shows that the load reaches 233, 378, 480, and 483 kN under the confinement of 0, 3, 6, and 9 MPa, respectively. The correlation between confinement and maximum thrust force is similar to that of 6 mm penetration, while the maximum thrust force begins to flatten instead of decreasing from some point between 6 and 9 MPa of confinement.

The V shape disc cutter thrust force evolution patterns under different confining stresses are illustrated in Figure 10. Figure 10(a) shows the thrust force curves with penetration up to 6 mm. Thrust force disparities among different confining stresses are of the marginal extent and irregular with penetration up to 3.3 mm. Notable drops appear at 5, 5.4, and 3.3 mm afterwards for 3, 6, and 9 MPa, respectively, which present very irregular disparity patterns. Figure 10(b) shows the thrust force curves with penetration up to 9 mm. The thrust force disparities among different confining stresses are irregular but generally increase with increasing confining stresses, which is different from that of 6 mm ultimate penetration. The most notable change is the drop at 6.5 mm penetration for 0 MPa of confinement.

The influence of confining stress on maximum thrust force of V shape disc cutter is presented in Figure 11. For ultimate penetration of 6 mm, Figure 11(a) shows that the maximum thrust force reaches 132, 105, 111, and 97 kN under confining stresses of 0, 3, 6, and 9 MPa, respectively. No correlation is found between confining stress and

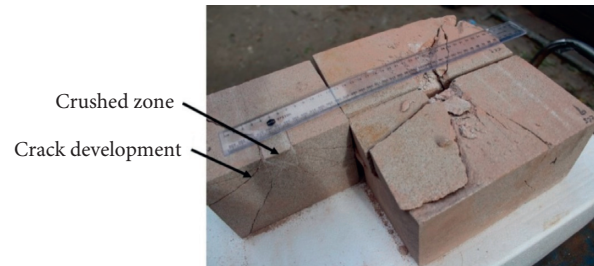


FIGURE 7: Observation of rock fragmentation.

maximum thrust force. For ultimate penetration of 9 mm, Figure 11(b) shows that maximum thrust force reaches 113, 202, 224, and 242 kN under confining stresses of 0, 3, 6, and 9 MPa, respectively, which means a positive correlation exists between confining stress and maximum thrust force. In summary, the confining stress's influence on V shape disc cutter thrust force is totally different for 6 mm penetration and 9 mm penetration, which makes it irregular and unpredictable.

3.2. Disc Cutter Pattern's Influence on Thrust Cutting Forces. Thrust cutting force evolution patterns under different disc cutters with 9 mm penetration are illustrated in Figure 12. It indicates that CCS disc cutter thrust forces are significantly higher than those of V shape disc cutter. Under 0 MPa confinement, the maximum thrust forces are 113 and 233 kN for the V shape disc cutter and the CCS disc cutter, respectively; the maximum value for the CCS disc cutter is 206.4% that of the V shape disc cutter. Under 3 MPa confinement, the maximum thrust forces are 202 and 378 kN for the V shape disc cutter and the CCS disc cutter, respectively; the maximum value for the CCS disc cutter is 187.6% that of the V shape disc cutter. Under 6 MPa confinement, the maximum thrust forces are 224 and 480 kN for the V shape disc cutter and the CCS disc cutter, respectively; the maximum thrust force for the CCS disc cutter is 214.4% that of the V shape disc cutter. Under 9 MPa confinement, the maximum thrust forces are 242 and 484 kN for the V shape disc cutter and the CCS disc cutter, respectively; the maximum thrust force for the CCS disc cutter is 200.0% that of the V shape disc cutter. Conclusively, thrust forces for the CCS disc cutter are nearly two times those of the V shape disc cutter under the given experimental setup.

3.3. Confining Stress's Influence on Crack Development. After indentation tests, the sandstone blocks were diamond cut to examine the subsurface crack development under different disc cutter patterns and confining stresses, as shown in Figures 13 and 14.

Figure 13 shows that confining stresses influence the crack number and orientation under the CCS disc cutter. Radial and lateral crack numbers increase with confinement rising. In addition, radial crack orientation turns more laterally with confining stresses increasing.

Figure 14 shows the crack development with different confining stresses under the V shape disc cutter. All cracks

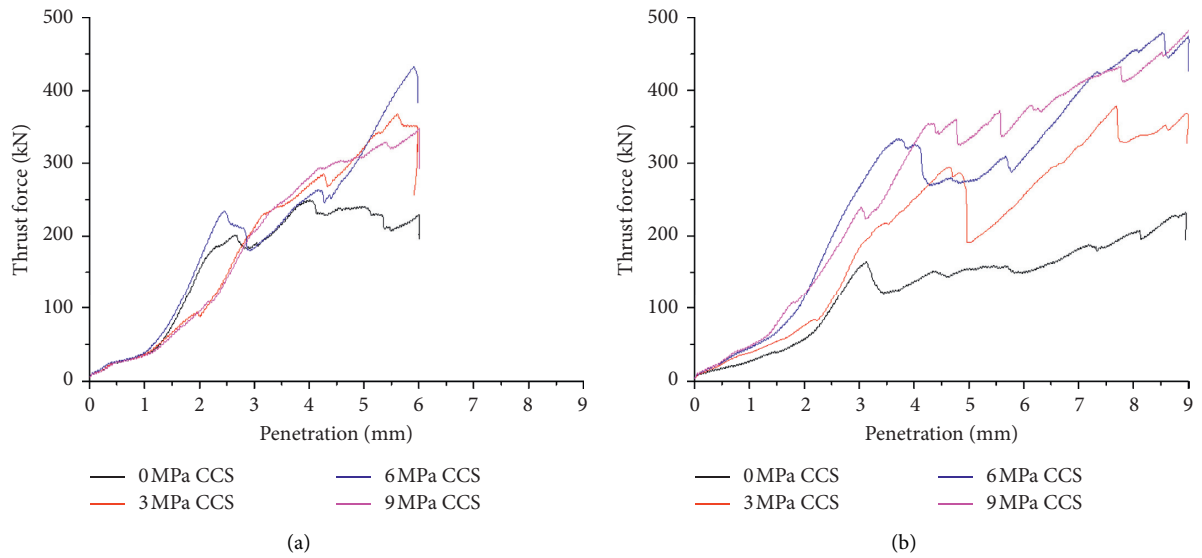


FIGURE 8: Thrust cutting force evolution patterns under the CCS disc cutter. (a) Ultimate penetration = 6 mm; (b) ultimate penetration = 9 mm.

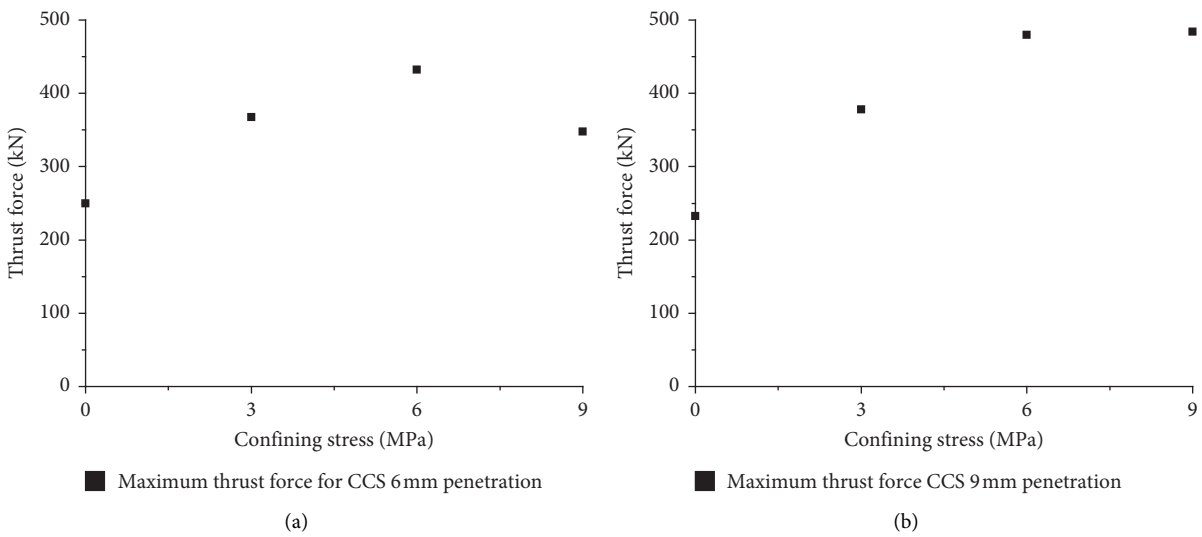


FIGURE 9: Confining stresses' influence on maximum thrust force for the CCS disc cutter. (a) Ultimate penetration = 6 mm; (b) ultimate penetration = 9 mm.

initiate from the cutter tip contact. Confining stress variation does not have a notable influence on crack development from the perspectives of crack number and orientation.

In summary, indentation under different disc cutters induces distinctive crack patterns with the same penetration and confining stresses. The CCS disc cutter indentation has denser cracks and their orientations are more lateral, which is favorable for rock cutting. The V shape disc cutter indentation is less sensitive to confining stresses, with no notable increase in crack number and crack reorientation. So, the CCS disc cutter is better for rock fragmentation.

3.4. Confining Stress's Influence on Penetration Energy. Penetration energy, which is calculated by integrating the thrust force with displacement, is an important indicator of cutting efficiency, that is, boreability. The relationship between the penetration energy and confining stress is illustrated in Figures 15 and 16.

Figure 15(a) shows the penetration energy values for 6 mm penetration for the CCS disc cutter. They are 967, 1112, 1193, and 1104 Nm under confining stresses of 0, 3, 6, and 9 MPa, respectively. Figure 15(b) shows the values for 9 mm penetration, which are 1154, 1883, 2417, and 2501 Nm under confining stresses of 0, 3, 6, and 9 MPa, respectively. It

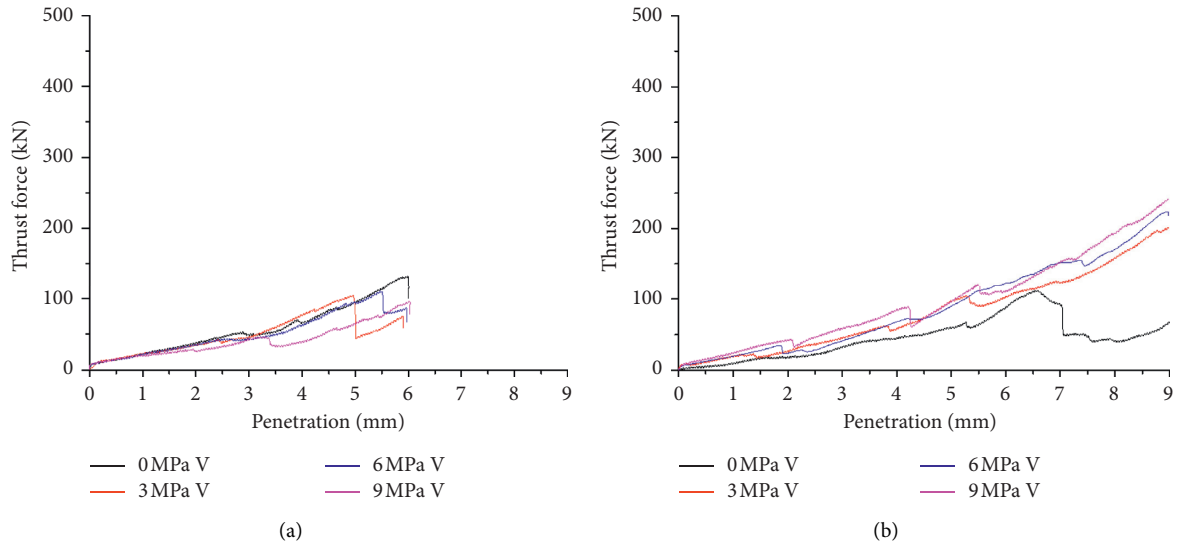


FIGURE 10: Thrust cutting force evolution patterns under the V shape disc cutter. (a) Ultimate penetration = 6 mm; (b) ultimate penetration = 9 mm.

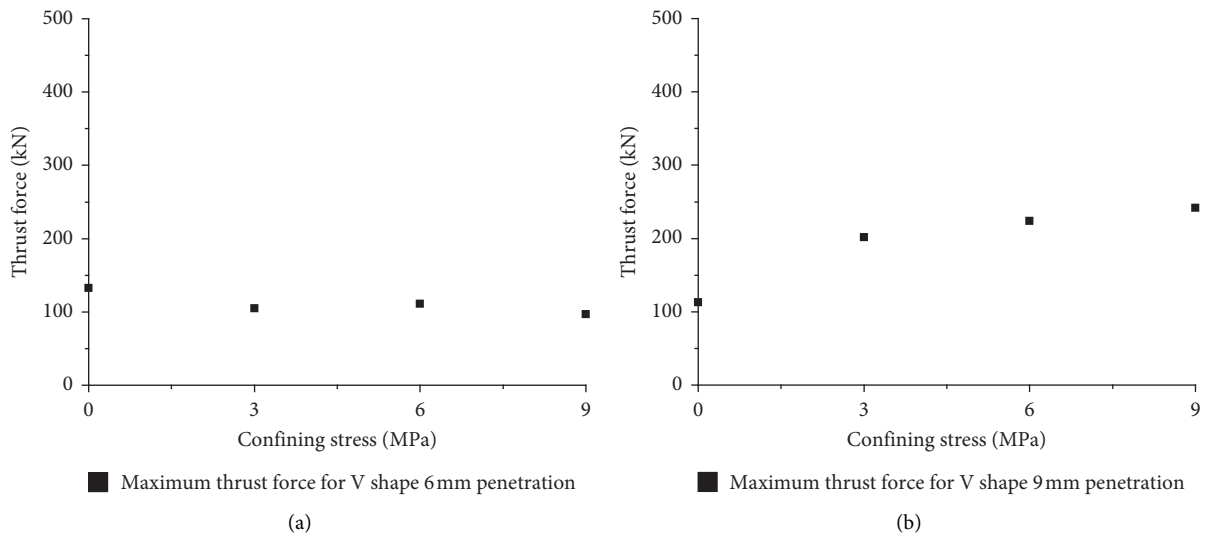


FIGURE 11: Maximum thrust force for the V shape disc cutter. (a) Ultimate penetration = 6 mm; (b) ultimate penetration = 9 mm.

is clear that when the confining stresses are no higher than 6 MPa, penetration energy increases with confining pressure mounting. While if the confinement surpasses a critical value, which is between 6 and 9 MPa, then the penetration energy will decrease or flatten with confinement increasing. It is notable that the increasing increments for 9 mm penetration are much higher than the counterparts for 6 mm penetration.

The penetration energy evolution for V shape disc cutter with the ultimate penetration of 6 mm is shown in Figure 16(a). The values are 343, 287, 305, and 243 Nm for confining stresses of 0, 3, 6, and 9 MPa, respectively. No correlation is found between confining stresses and penetration energy. The evolution pattern with the ultimate

penetration of 9 mm is shown in Figure 16(b), in which the penetration energy reaches 405, 730, 801, and 872 Nm with confining stresses of 0, 3, 6, and 9 MPa respectively; the penetration energy increases monotonically with rising confining stresses. In conclusion, the confining stress's influence on V shape disc cutter penetration energy is totally different for 6 mm penetration and 9 mm penetration, which make it irregular and unpredictable.

4. Discussion of the Indentation Tests Results

4.1. Confining Stress's Influence on Thrust Force. The highlighted feature for the CCS disc cutter cutting force evolution is the decreasing and flattening from some point between

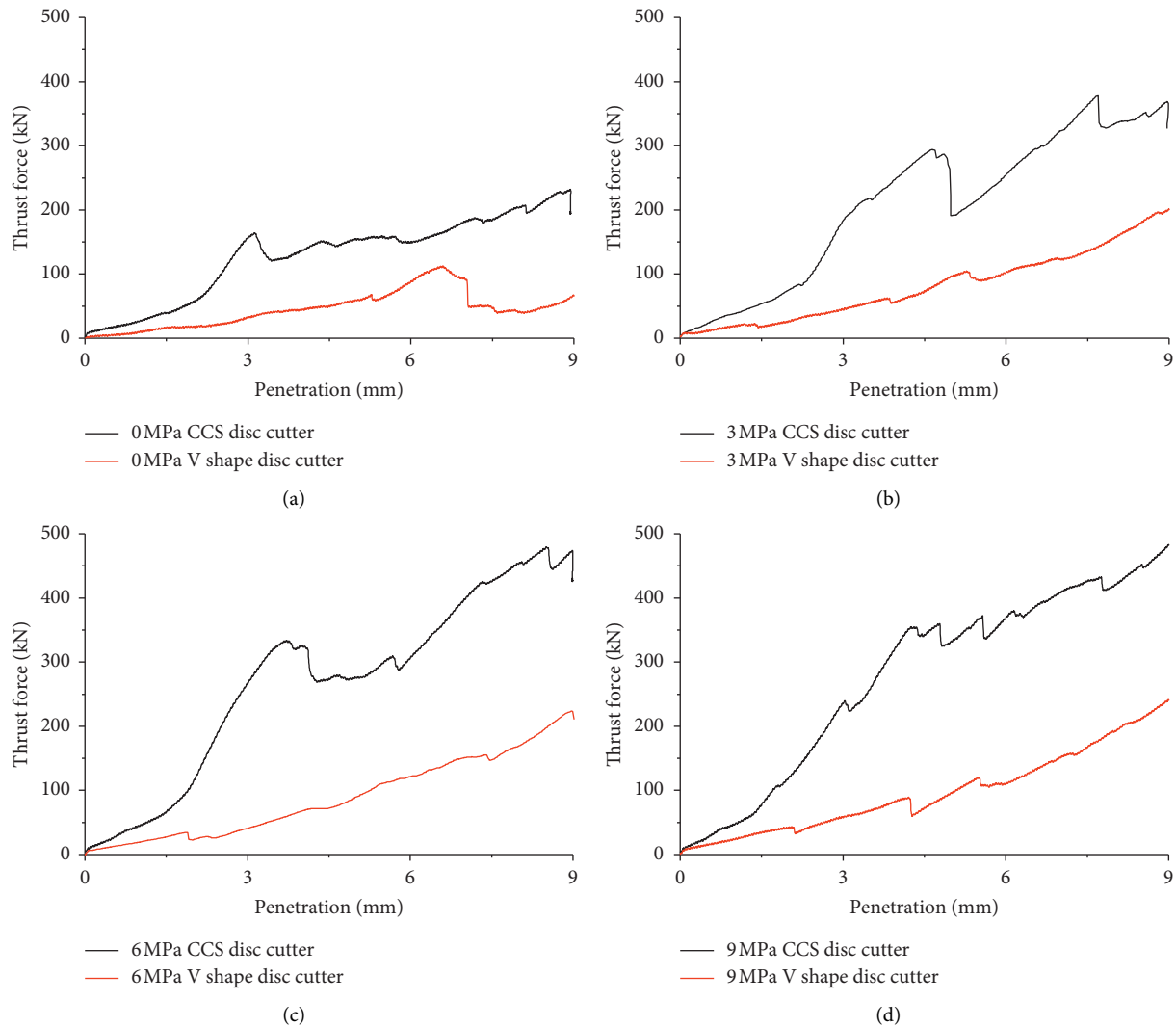


FIGURE 12: Comparison of thrust forces between CCS and V shape disc cutters. Confining stress: (a) 0 MPa; (b) 3 MPa; (c) 6 MPa; (d) 9 MPa.

6 MPa and 9 MPa confinement, as shown in Figure 9. It is in line with the findings of the experimental study of Yin et al. [28], as shown in Figure 17 [28]. In contrast, Innaurato et al. [27] found that the maximum load ever increased with the mounting pressures in their experimental study, as shown in Figure 18 [27].

Figure 17 shows that Yin et al. [28] adopted differential confining stresses in different directions, which are the minimum confining stress for one direction and the maximum confining stress for the other. For the tested marble samples, there is a critical confining stress, when the confining stresses are lower than that, the forces for crack initiation increase along with the confinement mounting; while the confining stresses are higher than that, the forces decrease or flatten with confinement mounting. However, the critical confinement phenomenon was not found on the tested granite samples [28]. Yin et al. [28] proposed that the critical confining stress level relates to the compressive strength of rock mass, while no further detailed relationship was given.

Figure 18 shows that the maximum thrust load values increase with confinement mounting up to 10 MPa, without any decreasing or flattening, for Botticino and Diorite samples [27]. By comparing the different tests, the tested rocks are of different properties. The tested sandstone's cohesion is 6.8 MPa, as shown in Table 1, which is lower than the designed maximum confinement of 9 MPa, while the tested rocks' cohesion in Innaurato's study is much higher with values of 16 and 23 MPa, as shown in Table 2, which are also higher than the designated maximum confinement of 10 MPa. For Yin's tests, Marble's cohesion is 22 MPa, and Granite's cohesion is 25 MPa, which are lower than and equal to the designed maximum confinement of 25 MPa, respectively.

The flattening and decreasing thrust patterns were not found in Innaurato et al.'s tests on Botticino and Diorite and Yin et al.'s tests on Granite because the cohesion values of the tested rocks are no lower than the maximum confining stresses. By relating cohesion values to the maximum thrust forces, it is reasonable to deduce that cohesion value is the turning point for the flattening and decreasing of thrust forces.

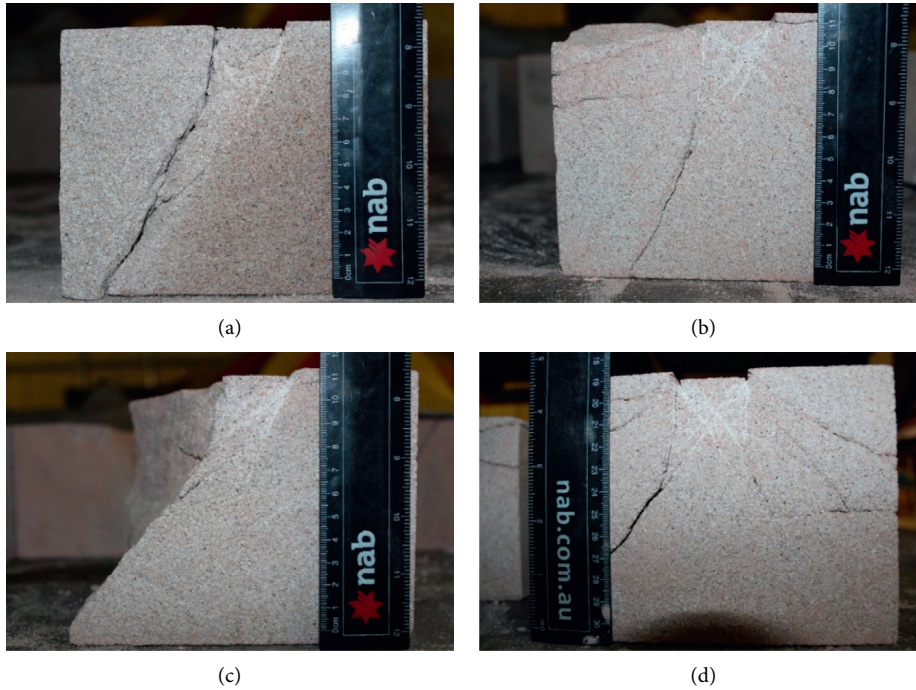


FIGURE 13: Crack development on the cross section under CCS disc cutter with 6 mm penetration. Confining stress: (a) 0 MPa; (b) 3 MPa; (c) 6 MPa; (d) 9 MPa.

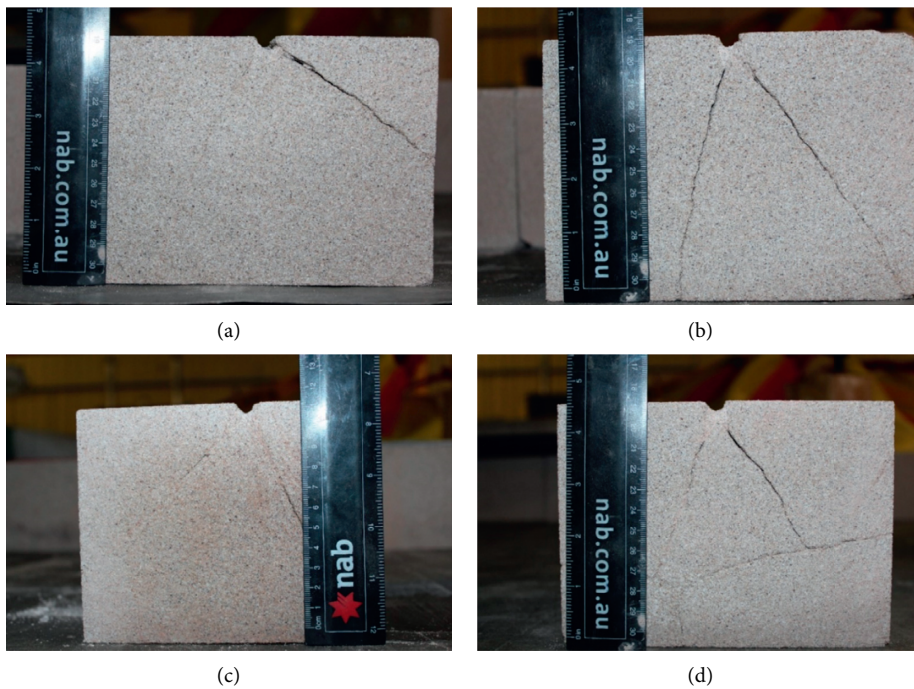


FIGURE 14: Crack development on the cross section under V shape disc cutter with 6 mm penetration. Confining stress: (a) 0 MPa; (b) 3 MPa; (c) 6 MPa; (d) 9 MPa.

4.2. *Confining Stress's Influence on Boreability.* Penetration energy and Field Penetration Index (FPI) are two indicators of boreability. This experimental study shows that, under the CCS disc cutter, decreasing and flattening of

penetration energy occurs after the confining stresses surpass a critical value, which is between 6 MPa and 9 MPa for the sandstone. By checking the rock mechanical properties, the critical value is most likely to be of cohesion, which is

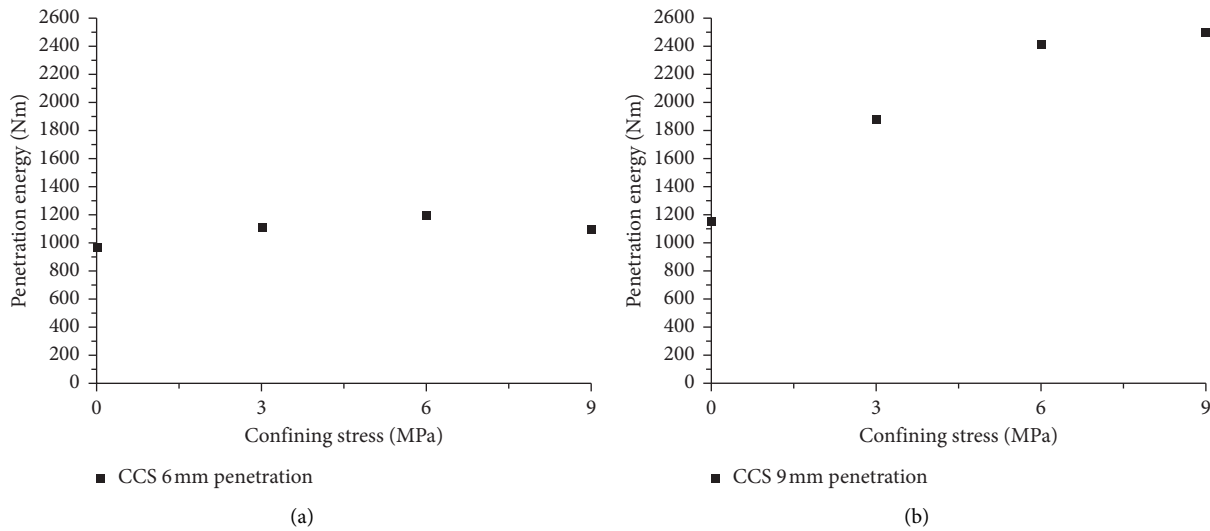


FIGURE 15: Penetration energy varies with confining stresses under the CCS disc cutter. (a) Ultimate penetration = 6 mm; (b) ultimate penetration = 9 mm.

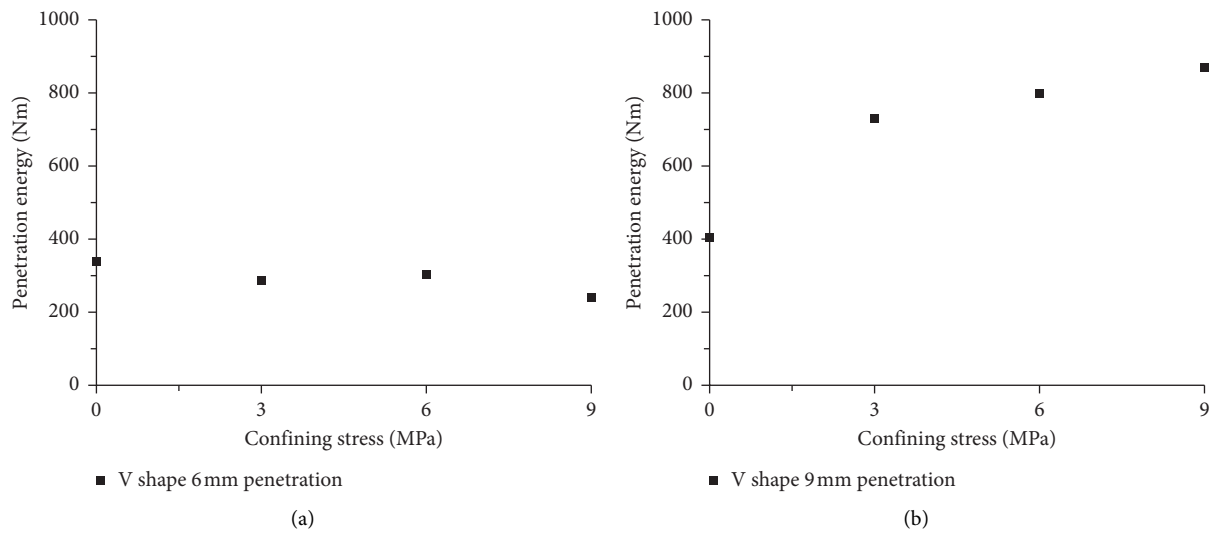


FIGURE 16: Penetration energy varies with confining stresses under V shape disc cutter. (a) Ultimate penetration = 6 mm; (b) ultimate penetration = 9 mm.

6.8 MPa for the tested rock samples. This means the boreability will increase under CCS disc cutters when the confining stresses surpass the value of cohesion.

The increasing boreability with confinement mounting is also substantiated by the field database collected and compiled by Klein et al. from the perspective of FPI, as shown in Figure 19 [26]. FPI is a normalized parameter, which is defined as the cutter loading divided by the actual penetration rate. It has been used as an important index for

boreability. The higher it is, the lower is boreability, and vice versa [32].

Figure 19 shows the correlation between FPI and the ratio of overburden pressure to UCS of rock mass. This finding indicates that, with fixed rock, higher ground pressure, that is, confining stresses, would cause lower FPI and further higher boreability. It supports the penetration energy trend between 6 MPa and 9 MPa confining pressure for the tested sandstone. The

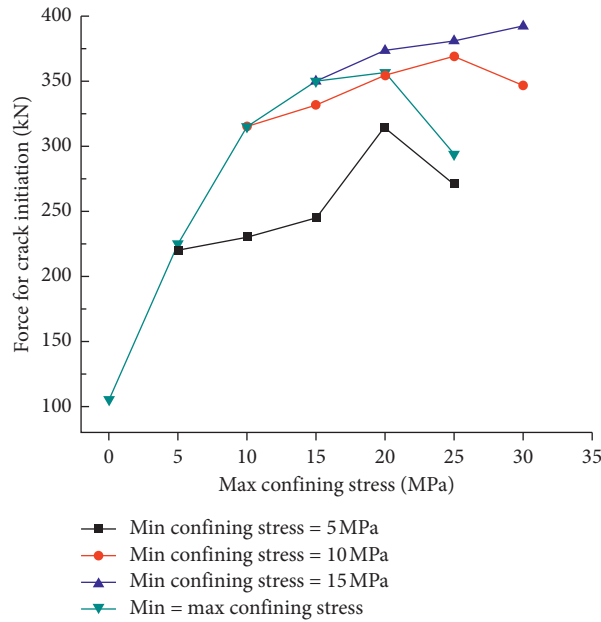


FIGURE 17: Thrust force for crack initiation with the different confining stress levels (marble samples) [28].

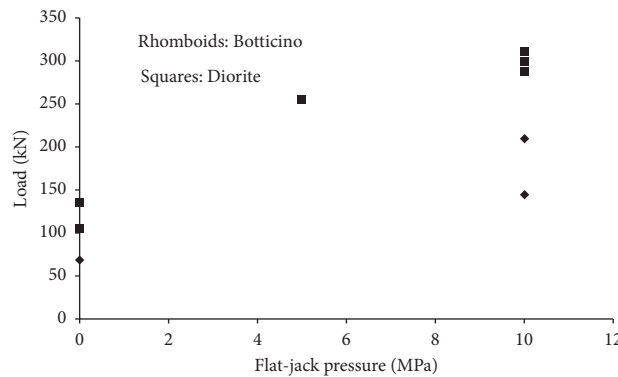


FIGURE 18: Maximum thrust load versus flat-jack confinement pressure for Botticino (rhomboids) and Diorite (squares) under the given settings [27].

TABLE 2: Physical and mechanical properties of the tested rocks adopted in Innaurato et al.’s laboratory tests and Yin et al.’s laboratory tests.

Properties	Innaurato et al.’s tests		Yin et al.,s tests	
	Botticino	Diorite	Marble	Granite
Young’s modulus (GPa)	67	30	25	23
Poisson’s ratio	0.3	0.2	0.26	0.19
Uniaxial compressive strength (MPa)	142	234	71	108
Cohesion (MPa)	16	23	22	25
Internal friction angle (°)	57	61	40	52
Tensile strength (MPa)	7.2	9.3	6.6	6.5

unfavorable influence of confinement on boreability was not found in Klein’s findings, because the collected data mainly had overburden pressure values varying between 0.2 and 0.8 times of the uniaxial compressive strength,

while cohesion value is normally 0.1 to 0.2 times the rock UCS value; the sourced projects do not have tunnelling operations falling into this lower range of ground stress regimes.

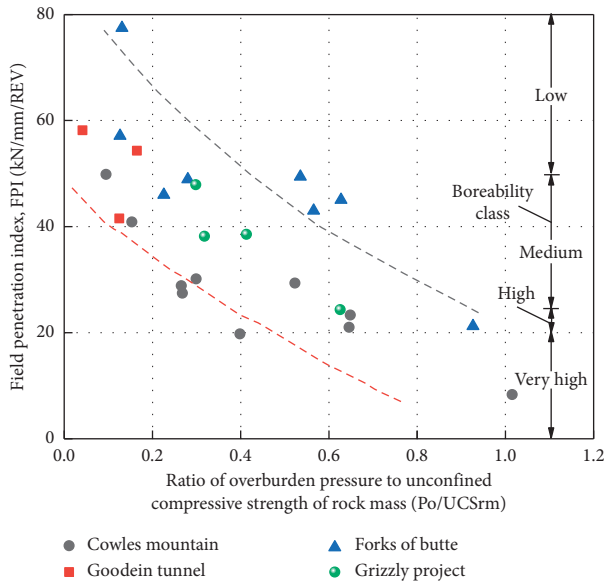


FIGURE 19: FPI correlation with the ratio of overburden pressure divided by UCS of rock mass [26].

5. Conclusions

From the perspective of subsurface rock fragmentation, the CCS disc cutter indentation has denser cracks and the crack orientations are more lateral, which is favorable for rock cutting, while the V shape disc cutter indentation is less sensitive to confining stress mounting, with no notable increase of the crack number and crack reorientation.

The existence of critical confining stress value is found for both maximum thrust force and penetration energy. When the confining stress is lower than the critical value, the maximum thrust force and penetration energy keep increasing with confining stress mounting. As the confining stress level is higher than the critical value, the maximum thrust force and penetration energy will decrease or flatten. By combining with previous studies, and comparing the critical confining stress values to the rock mechanical properties, the critical value is most likely to be of cohesion.

Finding of the critical confining stress value bears notable meaning for establishing cutting force and boreability prediction models which incorporate the confining stress factor, and even the design and optimization of cutter head layout for the TBMs employed in deep underground coal mines. However, more research efforts, including laboratory experiments, field investigation, theoretical analysis, and industrial support, are needed to build such models.

Data Availability

The data used to support the findings of this study are included within the article.

Conflicts of Interest

The authors declare that there are no conflicts of interest.

Acknowledgments

This research was sponsored by the “Fundamental Research Funds for the Central Universities (2020QN44).” Sincere appreciation goes to Alan Grant and Cameron Nelson for their efforts in setting up the experiment.

References

- [1] Q.-S. Liu, H. Xing, K. Shi, and X.-W. Liu, “Utilization of full face roadway boring machine in coal mines deeper than 1000 m and the key rock mechanics problems,” *Journal of China Coal Society*, vol. 37, no. 12, pp. 2006–2013, 2012.
- [2] Q.-S. Liu, K. Shi, and X. Huang, “Feasibility of application of TBM in construction of deep coal mine and its key scientific problems,” *Journal of Mining and Safety Engineering*, vol. 30, no. 5, pp. 633–641, 2013.
- [3] D. P. Creedy, “An introduction to geological aspects of methane occurrence and control in British deep coal mines,” *Quarterly Journal of Engineering Geology and Hydrogeology*, vol. 24, no. 2, pp. 209–220, 1991.
- [4] L. Wang and Y.-P. Cheng, “Drainage and utilization of Chinese coal mine methane with a coal-methane co-exploitation model: analysis and projections,” *Resources Policy*, vol. 37, no. 3, pp. 315–321, 2012.
- [5] M. Bauer, “High performance longwall mining in deep and methane-rich coal deposits in Germany taking into account methods and technologies for controlling the calculated gas liberation,” in *Proceedings of the International Symposium on Coal Gas Control Technology*, Huainan, China, December 2007.
- [6] H.-H. Liu, B.-Q. Lin, J.-H. Mou, and W. Yang, “Mechanical evolution mechanism of coal and gas outburst,” *Rock Mechanics and Rock Engineering*, vol. 52, no. 5, pp. 1591–1597, 2019.
- [7] C. Keles, F. Vasilikou, N. Ripepi, Z. Agioutantis, and M. Karmis, “Sensitivity analysis of reservoir conditions and gas production mechanism in deep coal seams in Buchanan County, Virginia,” *Simulation Modelling Practice and Theory*, vol. 94, pp. 31–42, 2019.
- [8] Y.-W. Liu, Q. Wang, W.-X. Chen, M.-J. Liu, and H. Mitri, “Enhanced coalbed gas drainage based on hydraulic flush from floor tunnels in coal mines,” *International Journal of Mining, Reclamation and Environment*, vol. 30, no. 1, pp. 37–47, 2016.
- [9] P. Lu, P. Li, J. Chen, C.-J. Zhang, J.-H. Xue, and T. Yu, “Gas drainage from different mine areas: optimal placement of drainage systems for deep coal seams with high gas emissions,” *International Journal of Coal Science & Technology*, vol. 2, no. 1, pp. 84–90, 2015.
- [10] H.-X. Zhou, Q.-L. Yang, Y.-P. Cheng, C.-G. Ge, and J.-X. Chen, “Methane drainage and utilization in coal mines with strong coal and gas outburst dangers: a case study in Luling mine, China,” *Journal of Natural Gas Science and Engineering*, vol. 20, pp. 357–365, 2014.
- [11] H.-F. Wang, Y.-P. Cheng, and L. Wang, “Regional gas drainage techniques in Chinese coal mines,” *Journal of China University of Mining & Technology*, vol. 22, no. 6, pp. 873–878, 2012.
- [12] Q.-S. Liu, X. Huang, Q.-M. Gong, L.-J. Du, Y.-C. Pan, and J.-P. Liu, “Application and development of hard rock TBM and its prospect in China,” *Tunnelling and Underground Space Technology*, vol. 57, pp. 33–46, 2016.

- [13] X. Huang, Q.-S. Liu, K. Shi, Y.-C. Pan, and J.-P. Liu, "Application and prospect of hard rock TBM for deep roadway construction in coal mines," *Tunnelling and Underground Space Technology*, vol. 73, pp. 105–126, 2018.
- [14] B. Tang, H. Cheng, Y.-Z. Tang et al., "Experiences of gripper TBM application in shaft coal mine: a case study in Zhangji coal mine, China," *Tunnelling and Underground Space Technology*, vol. 81, no. 1, pp. 660–668, 2018.
- [15] N. Innaurato and P. Oreste, "Theoretical study on the TBM tool-rock interaction," *Geotechnical and Geological Engineering*, vol. 29, no. 3, pp. 297–305, 2011.
- [16] J. Rostami, "Study of pressure distribution within the crushed zone in the contact area between rock and disc cutters," *International Journal of Rock Mechanics and Mining Sciences*, vol. 57, pp. 172–186, 2013.
- [17] I. Evans, "Relative efficiency of picks and discs for cutting rock," in *Proceedings of the 3rd Congress on Advances in Rock Mechanics*, pp. 1399–1405, Denver, CO, USA, September 1974.
- [18] Z.-H. Zhang, *The Research on Theory and Techniques of Service Life Management of TBM Disc Cutters*, North China Electric Power University, Beijing, China, 2008.
- [19] F. F. Roxborough and H. R. Phillips, "Rock excavation by disc cutter," *International Journal of Rock Mechanics and Mining Sciences & Geomechanics Abstracts*, vol. 12, no. 12, pp. 361–366, 1975.
- [20] L. Ozdemir, R. Miller, and F.-D. Wang, *Mechanical Tunnel Boring Prediction and Machine Design*, pp. 205–250, Research Applied to National Needs (RANN), National Science Foundation, Washington, DC, USA, 1977.
- [21] J. Roby, T. Sandell, J. Kocab, and L. Lindbergh, "Current state of disc cutter design and development directions," *Mining Engineering*, vol. 61, no. 3, pp. 26–34, 2009.
- [22] J. Rostami and L. Ozdemir, "A new model for performance prediction of hard rock TBMs," in *Proceedings of the Rapid Excavation and Tunneling Conference*, pp. 793–809, Society for Mining, Metallurgy, and Exploration, Inc. (SME), Boston, MA, USA, July 1993.
- [23] J. Li, Y.-F. Nie, K. Fu, C. Ma, J.-B. Guo, and M.-X. Xu, "Experiment and analysis of the rock breaking characteristics of disc cutter ring with small edge angle in high abrasive grounds," *Journal of the Brazilian Society of Mechanical Sciences and Engineering*, vol. 40, 2018.
- [24] D. Tumac and C. Balci, "Investigations into the cutting characteristics of CCS type disc cutters and the comparison between experimental, theoretical and empirical force estimations," *Tunnelling and Underground Space Technology*, vol. 45, no. 1, pp. 84–98, 2015.
- [25] P. J. Tarkoy and M. Marconi, "Difficult rock comminution and associated geological conditions," *International Journal of Rock Mechanics and Mining Sciences and Geomechanics Abstracts*, vol. 29, no. 4, pp. 195–207, 1992.
- [26] S. Klein, M. Schmoll, and T. Avery, "TBM performance at four hard rock tunnels in California," in *Proceedings of the Rapid Excavation and Tunneling Conference*, pp. 61–75, Society for Mining, Metallurgy and Exploration, INC, San Francisco, CA, USA, June 1995.
- [27] N. Innaurato, C. Oggeri, P. P. Oreste, and R. Vinai, "Experimental and numerical studies on rock breaking with TBM tools under high stress confinement," *Rock Mechanics and Rock Engineering*, vol. 40, no. 5, pp. 429–451, 2007.
- [28] L.-J. Yin, Q.-M. Gong, H.-S. Ma, J. Zhao, and X.-B. Zhao, "Use of indentation tests to study the influence of confining stress on rock fragmentation by a TBM cutter," *International Journal of Rock Mechanics and Mining Sciences*, vol. 72, pp. 261–276, 2014.
- [29] Y.-L. Chen and C.-P. Song, "Rock fragmentation characteristics by TBM cutting and efficiency under Bi-lateral confinement," *Applied Sciences*, vol. 8, no. 4, pp. 498–511, 2018.
- [30] R. Ulusay, *The ISRM Suggested Methods for Rock Characterization, Testing and Monitoring: 2007-2014*, Springer International Publishing, New York, NY, USA, 2015.
- [31] R. Gertsch, L. Gertsch, and J. Rostami, "Disc cutting tests in Colorado Red Granite: implications for TBM performance prediction," *International Journal of Rock Mechanics and Mining Sciences*, vol. 44, no. 2, pp. 238–246, 2007.
- [32] P. Nelson, "Factors affecting TBM penetration rates in sedimentary rocks," in *Proceedings of the 24th US Symposium on Rock Mechanics (USRMS)*, American Rock Mechanics Association, College Station, TX, USA, June 1983.

Research Article

Theoretical Analysis of Mining Induced Overburden Subsidence Boundary with the Horizontal Coal Seam Mining

Weitao Yan ^{1,2}, Junjie Chen ², Yi Tan ², Wenzhi Zhang,¹ and Liliang Cai¹

¹Henan Key Laboratory for Green and Efficient Mining & Comprehensive Utilization of Mineral Resources, Henan Polytechnic University, Jiaozuo, Henan 454003, China

²State Collaborative Innovation Center of Coal Work Safety and Clean-efficiency Utilization, Jiaozuo, Henan 454003, China

Correspondence should be addressed to Junjie Chen; chenjj@hpu.edu.cn and Yi Tan; tanyi@hpu.edu.cn

Received 3 December 2020; Revised 4 February 2021; Accepted 1 March 2021; Published 30 March 2021

Academic Editor: Zhao-hui Chong

Copyright © 2021 Weitao Yan et al. This is an open access article distributed under the Creative Commons Attribution License, which permits unrestricted use, distribution, and reproduction in any medium, provided the original work is properly cited.

The overburden subsidence induced by underground mining has caused great damage to the ecological environmental and seriously threatens the safe use of underground structures. Focusing on the overburden subsidence, this paper uses theoretical analysis method to study the overburden subsidence boundary with a horizontal coal seam mining. In this paper, the viscoelastic theory and the random medium theory are used separately to deduce and analyze the subsidence boundary of bedrock and unconsolidated stratum, which are two media with different lithology. For bedrock, the results show that the subsidence boundary of bedrock is 1/4 of the wavelength of pressure wave from the mining boundary, strata subsidence boundary expands with the increase of vertical distance between calculated strata and coal seam, and the subsidence boundary in bedrock is an upward concave curve. For unconsolidated stratum, the results show that the larger the internal friction angle, the greater the angle between subsidence boundary and horizontal line. From the bottom to the surface of the unconsolidated stratum, the internal friction angle decreases gradually and the angle between subsidence boundary and horizontal line also decreases gradually, so the subsidence boundary curve in the unconsolidated stratum is convex. Combined with the bedrock and unconsolidated stratum, it is concluded that the subsidence boundary of the whole overburden is bowl-shaped. This study is helpful to reveal the black box of rock subsidence and can provide theoretical support for the establishment of overburden subsidence prediction model and transparent mine in the later stage.

1. Introduction

After mining of underground coal resources, the initial stress in rock mass is destroyed and redistributed, which leads to the large-scale subsidence of overburden and ground surface [1–5], and seriously affects the underground pipelines, structures, water system, ecological environment, and so on. Surface subsidence is only a representation, and overburden movement is the essence. Only by understanding the movement law of overburden, can we have a clear understanding of the subsidence fundamentally. The large-scale overburden movement results in the decline of groundwater table, reduction of farmland quality, destruction of ecological environment, decline of people's living standards, etc. [6–12]. In order to mitigate those adverse effects caused by

mining subsidence, researchers have carried out a lot of work in the extraction method of subsidence information [13–15], analysis of subsidence law [16–18], revealing of subsidence mechanism [12, 19–21], establishment of subsidence prediction model [22–24], and development of mining methods with low ecological damage [25, 26]. Taking subsidence prediction as an example, scholars have proposed some subsidence prediction method, such as empirical formula method, influence function method, section function method, chart method, and other surface subsidence prediction methods [22–24, 27–30]. The content of subsidence prediction includes two aspects: the degree of subsidence and the scope of subsidence. For the prediction of surface subsidence, no matter the degree or scope of subsidence, the current research is relatively sufficient. For

the degree of subsidence of overlying strata, the prediction accuracy is relatively high. However, for the scope of subsidence of overlying strata, the study on boundary morphology of overburden subsidence is still insufficient. Therefore, it is necessary to study the subsidence boundary shape of overburden rock.

In this study, we consider bedrock and loose layer as viscoelastic medium and random medium, respectively. The theoretical analysis method was used to derive the shape of the subsidence boundary of overburden rock. Relevant research can provide knowledge support for further study of the overburden subsidence prediction methods.

2. Traditional Mining Subsidence Model

After the underground coal resources are mined out, the goaf is formed and the overburden and surface subsidence occur. When the size of the goaf is large enough, basin-like subsidence basin is formed on the surface, whereas bowl-like subsidence basin is formed on the surface. The boundary of surface subsidence basin generally refers to the outermost area of surface subsidence. According to the mining subsidence theory, because of the limitation of measuring instruments and methods, the point with subsidence of 10 mm was usually selected as the subsidence basin boundary. To define the subsidence boundary, the concept of angle of boundary was proposed in China and angle of draw was proposed in other countries, as shown in Figure 1.

- (i) Angle of boundary: when the gob reached the critical size, or nearly so, on the major section of a movement basin, the angle between the horizontal line and the line connecting the surface subsidence boundary and the gob edge at the pillar side is the angle of boundary
- (ii) Angle of draw: when the gob reached the critical size, or nearly so, on the major section of a movement

basin, the angle between the vertical line and the line connecting the surface subsidence boundary and the panel edge at the pillar side is the angle of draw

From the above definition, it can be seen that they are mutually complementary, and they have the same effect. Therefore, we are just going to analyze the angle of draw.

For the angle of draw, the larger the angle is, the larger the influence range of subsidence is. According to the theory of mining subsidence, lithology is the main factor affecting the boundary angle. The harder the strata are, the smaller the angle is and the smaller the range of strata movement is. On the contrary, the softer the lithology is, the larger the angle is and the larger the range of strata movement is.

The above two definitions assume that the movement boundary in overlying strata simply conform to the linear law. However, many experimental results show that the movement boundary in overburden does not simply conform to the linear rule. Therefore, it is necessary for us to study the boundary shape in overburden strata.

3. Theoretical Analysis

3.1. Movement Boundary Shape of Bedrock. Based on the research results of Yan (2019), the bedrock are in line with the Kelvin rheological model.

Figure 2 shows the coordinate system which is suitable for the analysis of skewed subsidence characteristics of the rock mass. Establishing the x -axis along the central axis of rock beam, the part above the pillar is positive and the part above the gob is negative. Establish the z -axis in the vertical direction, and take the downward direction as positive. The coordinate origin point O is selected just above the gob boundary. Correspondingly, the ground coordinate system XO_1W has been established on the Earth's surface.

According to the results of Yan (2019), we can derive the deflection equation of the beam:

$$W_1(x, t) = \frac{MP_z}{E_k} \frac{L_p^2}{L_k^2} (1 - e^{-kt}) e^{-(\pi/L_p)x} \left[\frac{L_k - L_p}{L_k + L_p} \sin\left(\frac{\pi}{L_p}x\right) + \cos\left(\frac{\pi}{L_p}x\right) \right] + \frac{MP_z}{E_p}, \quad x > 0, \quad (1)$$

$$W_2(x, t) = \frac{MP_z}{E_k} (1 - e^{-kt}) \left\{ e^{-(\pi/L_k)x} \left[\frac{L_k - L_p}{L_k + L_p} \sin\left(\frac{\pi}{L_k}x\right) - \cos\left(\frac{\pi}{L_k}x\right) \right] + 1 + \frac{L_p^2}{L_k^2} \right\} + \frac{MP_z}{E_p}, \quad x < 0,$$

$$L_k = L_p. \quad (2)$$

where L_p and L_k are the half wavelength of pressure wave of the coal pillar side and the gob side, respectively, M is the mining thickness, P_z is the initial stress, $P_z = \gamma H$, and E_k and E_p are the elastic modulus of the goaf side and coal pillar side, respectively.

Because MP_z/E_p is caused by the self-weight stress of overburden before mining and is not induced by mining, this item can be neglected. In addition, in order to facilitate calculation, we generally make the following approximate assumptions:

When the time tends to be infinite, the maximum subsidence value appears on the surface at a large distance from the coal pillar above the goaf:

$$\lim_{\substack{t \rightarrow \infty \\ x \rightarrow -\infty}} W(x, t) = \frac{2MP_z}{E_k} = W_{\max}, \quad (3)$$

where W_{\max} is the surface maximum subsidence value.

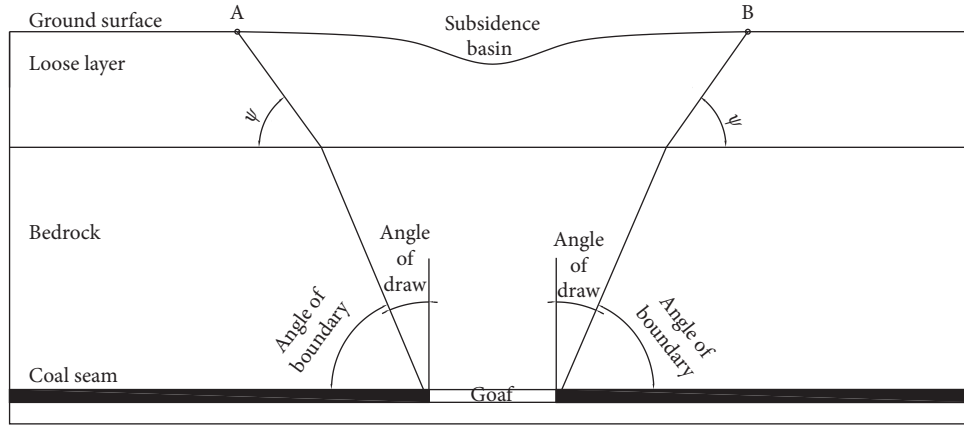


FIGURE 1: Definition of the inner boundary of overburden rock.

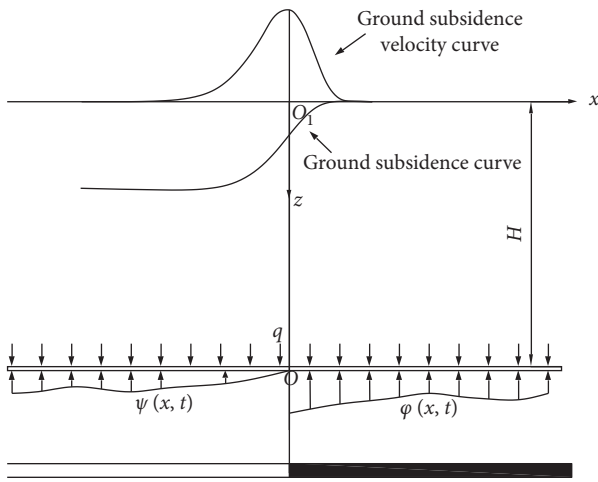


FIGURE 2: Construction of the coordinate system.

According to the above discussion, formula (1) can be simplified to

$$W_1(x, t) = \frac{W_{\max}}{2} (1 - e^{-kt}) e^{-(\pi/L)x} \cos\left(\frac{\pi}{L}x\right), \quad x > 0,$$

$$W_2(x, t) = \frac{W_{\max}}{2} (1 - e^{-kt}) \left\{ 2 - e^{(\pi/L)x} \cos(\pi/L)x \right\}, \quad x < 0. \quad (4)$$

If the mining has gone through a long time and the time tends to be infinite, the above formula can be further simplified as follows:

$$W_1(x) = \frac{W_{\max}}{2} e^{-(\pi/L)x} \cos\left(\frac{\pi}{L}x\right), \quad x > 0,$$

$$W_2(x) = \frac{W_{\max}}{2} \left\{ 2 - e^{(\pi/L)x} \cos\left(\frac{\pi}{L}x\right) \right\}, \quad x < 0. \quad (5)$$

Solving the equation $W_1(x) = 0$, we can get $x = (L/2)$. Because L represents half of the wavelength of pressure wave, the movement boundary of bedrock is 1/4 of the wavelength of pressure wave from the mining boundary.

The rock beam of the coal pillar side is compressed in normal direction of strata and pulled in parallel direction. According to the theory of rock mechanics, the relationship between compressive stress and P-wave velocity is shown in Figure 3.

The relationship between compressive stress and P-wave velocity along the vertical direction of compressive stress can be obtained by fitting:

$$v_p = (A - p)^n, \quad n \in (0, 1). \quad (6)$$

According to the general theory of coal mining subsidence, it can be seen that, in the vertical direction, the overburden subsidence of the coal pillar side and goaf side presents different changing rules:

- (1) Coal pillar side: with a certain horizontal distance from the mining boundary, the farther the vertical distance from the mining seam is, the bigger the subsidence value is, and the logarithmic growth occurs
- (2) Goaf side: with a certain horizontal distance from the mining boundary, the farther the vertical distance from the mining seam is, the smaller the subsidence value is, and it decreases logarithmically

The subsidence value of overburden rock on the coal pillar side is smaller than that on the goaf side in the same stratum.

According to the above rules, the following formulas can be used for calculating the subsidence value of overburden rock on the coal pillar side:

$$w(z) = \ln(kz), \quad (7)$$

where z is the vertical distance from the mining seam.

According to [3, 4], the supporting reaction of underlying rock mass to the rock beam is proportional to the subsidence value of rock beam. It can be described as

$$\varphi(z) = c \ln(kz), \quad (c > 0). \quad (8)$$

The compressive stress of rock strata in vertical direction is equal to the overlying gravity minus the supporting reaction:

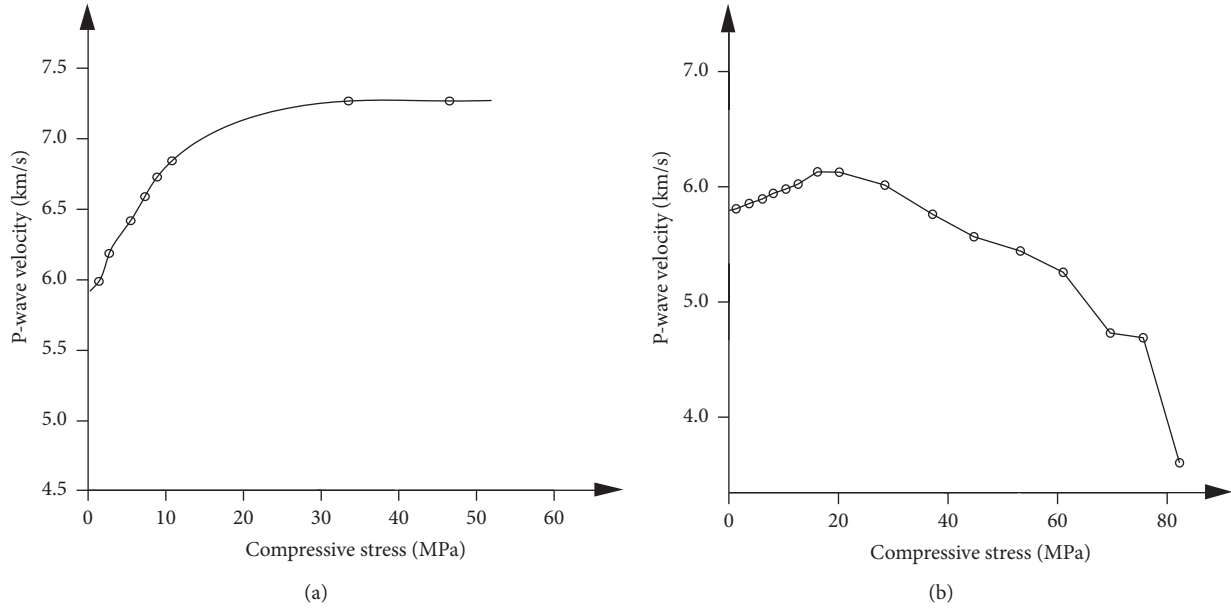


FIGURE 3: Variation curve of pressure wave velocity. (a) P-wave velocity along the direction of compressive stress. (b) P-wave velocity perpendicular to the direction of compressive stress.

$$p = P_z - \varphi(z) = \gamma(H - z) - c \ln(kz), \quad (9)$$

where p is compressive stress, P_z is overlying gravity, φ is the supporting reaction, and γ is bulk density.

Bringing formula (9) into (6), the relationship between P-wave velocity perpendicular to the direction of compressive stress and the distance from the mining coal seam can be obtained:

$$v_p = (A - \gamma H + \gamma z + c \ln(kz))^n. \quad (10)$$

According to the wave theory, we know that wavelength equals wave velocity divided by frequency. So, the relationship between the P-wave wavelength perpendicular to the compressive stress direction and the distance from it to the mining coal seam can be calculated by the following formula:

$$L = \frac{v_p}{f} = \frac{A - \gamma H + \gamma z + c \ln(kz)^n}{f}. \quad (11)$$

The relationship between the two can be illustrated by Figure 4.

It can be seen from the above that the movement boundary of strata expands with the increase of the vertical distance between the calculated strata and the mining coal seam, and the movement boundary of bedrock is concave as a whole (Figure 5).

3.2. Movement Boundary Shape of Loose Layer. Loose layer includes Quaternary and Neogene strata. It is composed of soil, sand, gravel, pebble layer, and so on. Compared with bedrock, the cohesive force between particles of the loose layer is small, and the strength of loose layer is very weak. From the knowledge of soil mechanics, we can see that the

loose layer is similar to the random medium. Therefore, when analyzing the movement boundary of the loose layer, the loose layer can be generalized as the random medium. The analysis model is as follows.

As shown in Figure 6, when the random particle A moves away and the random particle C slips toward its position. The force borne by the random particle C mainly consists of two parts: its own gravity W and the horizontal thrust T of the random particle B to it. Assuming that the angle between the movement boundary line and the horizontal plane is α , the sliding force of random particle C along the movement boundary line is $R_f = W \sin \alpha$, and the normal stress perpendicular to the movement boundary is $N = W \cos \alpha + T \sin \alpha$. The antisliding force generated by the normal stress is as follows:

$$N \tan \varphi = (W \cos \alpha + T \sin \alpha) \tan \varphi. \quad (12)$$

The total antisliding force is as follows:

$$R_o = (W \cos \alpha + T \sin \alpha) \tan \varphi + T \cos \alpha. \quad (13)$$

When $R_f = R_o$, the random particle C is in the critical sliding state. The following formula can be obtained:

$$\frac{W \sin \alpha}{(W \cos \alpha + T \sin \alpha) \tan \varphi + T \cos \alpha} = 1. \quad (14)$$

After the above formula is processed, the following formula can be obtained:

$$\tan \varphi = \frac{W - T \cot \alpha}{T + W \cot \alpha}. \quad (15)$$

According to the knowledge of soil mechanics, the deeper the loose layer is buried, the greater the compaction degree and the relative density are and the larger the internal

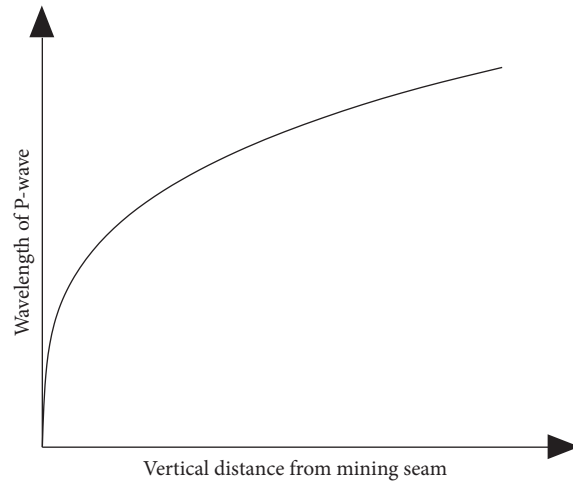


FIGURE 4: The relationship between the longitudinal wave length and the distance from it to the coal seam.

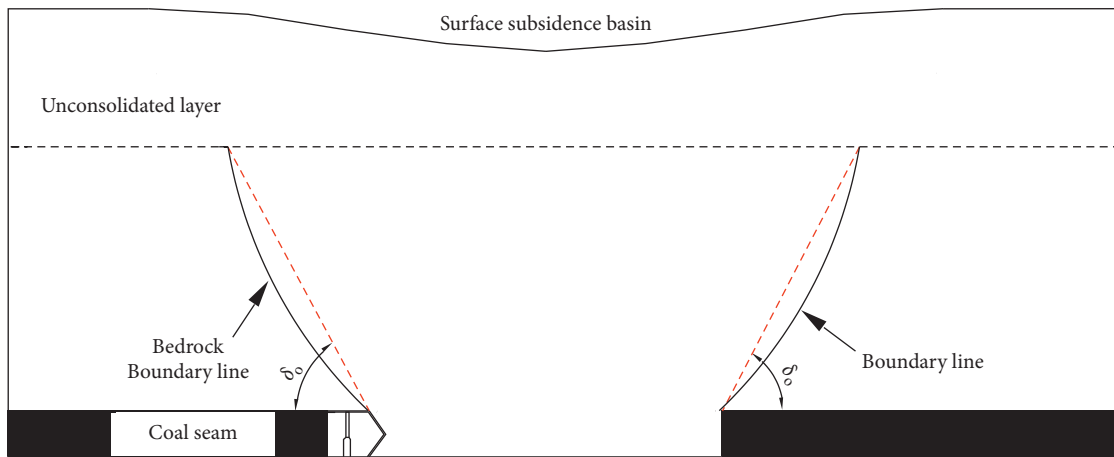


FIGURE 5: Movement boundary shape of bedrock.

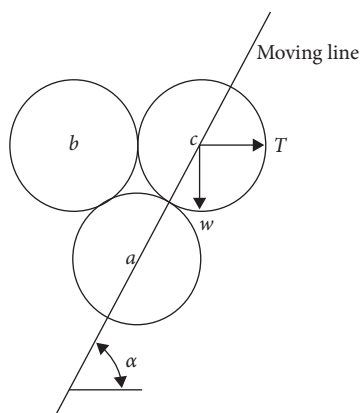


FIGURE 6: Analysis diagram of movement boundary of the loose layers.

friction angle is. Therefore, it can be concluded that, from the bottom to the surface of the loose layer, α gradually decreases, and the movement boundary line in the loose layer is

convex. The shape of movement boundary is shown in Figure 7.

3.3. *Movement Boundary Shape of Overlying Strata.* According to the above discussion, the shape of movement boundary in bedrock is convex, while that in the loose layer is convex. The combination of the two is shown in Figure 8. It can be seen from the figure that the shape of the movement boundary in the whole overburden is bowl-shaped.

3.4. *Application Scope.* This movement boundary shape of overlying strata is a theoretical analysis model. As such, the application is limited. When the movement of the strata above the gob is only affected by self-weight and overburden pressure, the movement boundary shape is high. However, when a place has a wide range of geological structure (e.g., faults and folds) or geological events (e.g., earthquakes), the movement boundary shape model is unsuitable.

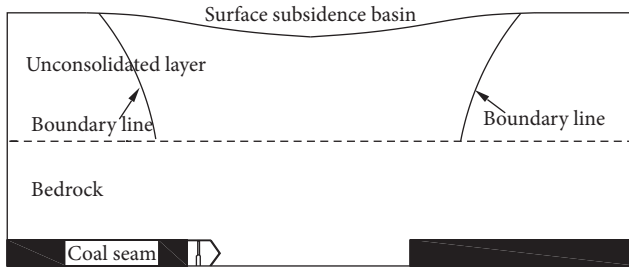


FIGURE 7: Movement boundary shape of the loose layer.

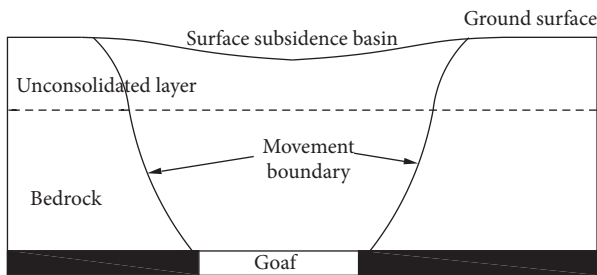


FIGURE 8: Movement boundary shape of overburden rock.

4. Conclusions

Based on the theoretical analysis, we have drawn the following conclusions.

- (1) Loose layer and bedrock constitute overlying strata together, but the lithologies of these two materials are very different. In the process of boundary morphology analysis, these two materials were treated separately. The loose layer is regarded as random medium, and the bedrock is regarded as viscoelastic medium.
- (2) The movement boundary of bedrock is $1/4$ th of the wavelength of pressure wave from the mining boundary, and the strata subsidence boundary expands with the increase of vertical distance between calculated strata and coal seam.
- (3) Based on the elastic wave theory and random medium theory, it is deduced that the shape of movement boundary in the loose layer is convex, and the shape of movement boundary in bedrock is upper concave. The shape of the movement boundary of the whole overlying strata is similar to that of a bowl.
- (4) Research results can provide theoretical support for the subsequent establishment of overlying rock subsidence prediction model and provide technical support for the protection of underground structures from the mining impacts.

Data Availability

The data used to support the findings of this study are available from the corresponding author upon request.

Conflicts of Interest

The authors declare no conflicts of interest.

Acknowledgments

This research was supported by the National Natural Science Foundation of China (Grant nos. U1810203 and 51974105), Henan Scientific and Technological Projection (Grant nos. 212102310012, 212102310414, and 202102310294), Key Scientific Research Projects of Higher Education Institutions in Henan Province (Grant no. 20A440005), Research Fund of Henan Key Laboratory for Green and Efficient Mining and Comprehensive Utilization of Mineral Resources (Henan Polytechnic University) (Grant no. KCF202004), Open Fund of State Key Laboratory of Water Resource Protection and Utilization in Coal Mining (Grant nos. WPUKFJJ2019-20 and WPUKFJJ2019-17), Fundamental Research Funds for the Universities of Henan Province (Grant no. NSFRF200314), Youth Backbone Teacher Support Program of Henan Polytechnic University (Grant no. 2019XQG-07), and Doctoral Fund Program of Henan Polytechnic University (Grant no. B2017-07). All those financial supports are gratefully acknowledged.

References

- [1] C. Chen and Z. Q. Hu, "Research advances in formation mechanism of ground crack due to coal mining subsidence in China," *Journal of China Coal Society*, vol. 43, no. 3, pp. 810–823, 2018.
- [2] X. Cui, Y. Gao, and D. Yuan, "Sudden surface collapse disasters caused by shallow partial mining in Datong coalfield, China," *Natural Hazards*, vol. 74, no. 2, pp. 911–929, 2014.
- [3] G. W. Fan, D. S. Zhang, and L. Q. Ma, "Overburden movement and fracture distribution induced by longwall mining of the shallow coal seam in the Shendong coalfield," *Journal of China University of Mining & Technology*, vol. 40, no. 2, pp. 196–201, 2011.
- [4] X. Yang, G. Wen, L. Dai, H. Sun, and X. Li, "Ground subsidence and surface cracks evolution from shallow-buried close-distance multi-seam mining: a case study in bulianta coal mine," *Rock Mechanics and Rock Engineering*, vol. 52, no. 8, pp. 2835–2852, 2019.
- [5] X. Lian, H. Hu, H. Li, and D. Hu, "Main geological and mining factors affecting ground cracks induced by underground coal mining in Shanxi Province, China," *International Journal of Coal Science & Technology*, vol. 7, no. 2, pp. 362–370, 2020.
- [6] F. G. Bell, T. R. Stacey, and D. D. Genske, "Mining subsidence and its effect on the environment: some differing examples," *Environmental Geology*, vol. 40, no. 1-2, pp. 135–152, 2000.
- [7] L. M. Fan, X. D. Ma, and R. J. Ji, "The progress of research engineering practice of water-preserved coal mining in western eco-environment frangible area," *Journal of China Coal Society*, vol. 40, no. 8, pp. 1711–1717, 2015.
- [8] S. Sinha, R. N. Bhattacharya, and R. Banerjee, "Surface iron ore mining in eastern India and local level sustainability," *Resources Policy*, vol. 32, no. 1-2, pp. 57–68, 2007.
- [9] S. Saha, S. K. Pattanayak, E. O. Sills, and A. K. Singha, "Undermining health: environmental justice and mining in India," *Health & Place*, vol. 17, no. 1, pp. 140–148, 2011.

- [10] T. Sasaoka, H. Takamoto, T. Shimada, J. Oya, A. Hamanaka, and K. Matsui, "Surface subsidence due to underground mining operation under weak geological condition in Indonesia," *Journal of Rock Mechanics and Geotechnical Engineering*, vol. 7, no. 3, pp. 337–344, 2015.
- [11] Z. Jing, J. Wang, Y. Zhu, and Y. Feng, "Effects of land subsidence resulted from coal mining on soil nutrient distributions in a loess area of China," *Journal of Cleaner Production*, vol. 177, pp. 350–361, 2018.
- [12] J. Z. Wang, J. R. Kang, and Z. Q. Chang, "The mechanism analysis on the dissymmetry of the surface subsidence basin," *Journal of China Coal Society*, vol. 24, no. 3, pp. 252–255, 1999.
- [13] H. D. Fan, L. Wang, and B. F. Wen et al., "A new model for three-dimensional Deformation extraction with single-track InSAR based on mining subsidence characteristics," *International Journal of Applied Earth Observations and Geoinformation*, vol. 94, Article ID 102223, 2021.
- [14] M. Mohammady, H. R. Pourghasemi, and M. Amiri, "Spatial modeling of susceptibility to subsidence using machine learning techniques," *Stochastic Environmental Research and Risk Assessment*, 2021.
- [15] C. Jiang, L. Wang, X. Yu, S. Chi, T. Wei, and X. Wang, "DPIM-based InSAR phase unwrapping model and a 3D mining-induced surface deformation extracting method: a case of Huainan mining area," *KSCE Journal of Civil Engineering*, vol. 25, no. 2, pp. 654–668, 2021.
- [16] J. Ju and J. Xu, "Surface stepped subsidence related to top-coal caving longwall mining of extremely thick coal seam under shallow cover," *International Journal of Rock Mechanics and Mining Sciences*, vol. 78, pp. 27–35, 2015.
- [17] Q. B. Guo, G. L. Guo, and J. F. Zha et al., "Research on the surface movement in a mountain mining area: a case study of Sujiagou mountain, China," *Environmental Earth Sciences*, vol. 75, Article ID 472, 2016.
- [18] F.-Q. Tang, "Research on mechanism of mountain landslide due to underground mining," *Journal of Coal Science and Engineering (China)*, vol. 15, no. 4, pp. 351–354, 2009.
- [19] G. W. Cheng, T. H. Yang, H. Y. Liu et al., "Characteristics of stratum movement induced by downward longwall mining activities in middle-distance multi-seam," *International Journal of Rock Mechanics and Mining Sciences*, vol. 136, Article ID 104517, 2020.
- [20] W. Yan, H. Dai, and J. Chen, "Surface crack and sand inrush disaster induced by high-strength mining: example from the Shendong coal field, China," *Geosciences Journal*, vol. 22, no. 2, pp. 347–357, 2018.
- [21] Y. Sun, J. Zuo, S. Karakus, and J. Wang, "Investigation of movement and damage of integral overburden during shallow coal seam mining," *International Journal of Rock Mechanics and Mining Sciences*, vol. 117, pp. 63–75, 2019.
- [22] W. T. Yan, J. J. Chen, and H. B. Chai, "Ground surface dynamic damage prediction model with high-strength mining in mining area," *Transactions of the Chinese Society of Agricultural Engineering*, vol. 35, no. 19, pp. 267–273, 2019.
- [23] P. S. Ramesh and N. Y. Ram, "Prediction of subsidence due to coal mining in Raniganj coalfield, West Bengal, India," *Engineering Geology*, vol. 39, pp. 103–111, 1995.
- [24] G. Ren, B. N. Whittaker, and D. J. Reddish, "Mining subsidence and displacement prediction using influence function methods for steep seams," *Mining Science and Technology*, vol. 8, no. 3, pp. 235–251, 1989.
- [25] S. Chen, D. Yin, F. Cao, Y. Liu, and K. Ren, "An overview of integrated surface subsidence-reducing technology in mining areas of China," *Natural Hazards*, vol. 81, no. 2, pp. 1129–1145, 2016.
- [26] G. L. Guo, H. Z. Li, and J. F. Zha, "An approach to protect cultivated land from subsidence and mitigate contamination from colliery gangue heaps," *Process Safety and Environmental Protection*, vol. 124, pp. 336–344, 2019.
- [27] H. Li, J. Zha, and G. Guo, "A new dynamic prediction method for surface subsidence based on numerical model parameter sensitivity," *Journal of Cleaner Production*, vol. 233, pp. 1418–1424, 2019.
- [28] Y. Luo and J. W. Cheng, "An influence function method based subsidence prediction program for longwall mining operations in inclined coal seams," *Mining Science and Technology*, vol. 19, pp. 0592–0598, 2009.
- [29] H. Y. Dai and J. Z. Wang, "Prediction model for surface movement and deformation induced by sub-critical extraction," *Journal of China Coal Society*, vol. 28, no. 6, pp. 583–587, 2003.
- [30] W. Yan, J. Chen, and Y. Yan, "A new model for predicting surface mining subsidence: the improved lognormal function model," *Geosciences Journal*, vol. 23, no. 1, pp. 165–174, 2019.

Research Article

Influencing Factors for the Instability and Collapse Mode of the Goaf Structure in a Gypsum Mine

Zhaowen Du ¹, Zhihe Liu ^{1,2}, Rui Liu,¹ Sheng Wang,¹ and Faxin Li¹

¹College of Energy and Mining Engineering, Shandong University of Science and Technology, Qingdao 266590, China

²School of Resources and Environmental Engineering, Shandong University of Technology, Zibo 255000, China

Correspondence should be addressed to Zhihe Liu; liuzhihe@sdut.edu.cn

Received 28 January 2021; Revised 7 March 2021; Accepted 18 March 2021; Published 27 March 2021

Academic Editor: Jia Lin

Copyright © 2021 Zhaowen Du et al. This is an open access article distributed under the Creative Commons Attribution License, which permits unrestricted use, distribution, and reproduction in any medium, provided the original work is properly cited.

Large-area goafs in a gypsum mine tend to collapse after 10 or more years, but the influencing factors are still unclear, and the effects of multiple factors have not been comprehensively considered. In this study, the failure mechanism and collapse mode of the room-pillar goaf structure were analyzed, and the uniaxial compressive strength tests of the pillars under different conditions were carried out in a laboratory. The influences of water, temperature, and time on the strength of the gypsum rock were considered. These three factors weakened the gypsum rock in different degrees. After 120 days of immersion, water had the greatest effect with a strength-weakening rate of 52.61%. After 20 temperature cycles, changes in temperature had little effect with a strength-weakening rate of 12.60%. After 25 years of aging, the strength-weakening rate of time was 25.13%. These results show how different factors affect the instability and collapse of the goaf structure, which are of great significance for predicting and preventing this from happening.

1. Introduction

Gypsum is an important mineral resource and widely used in various fields [1–3]. At present, gypsum is mined with the room pillar method, with multiple pillars supporting the working space and isolated pillars supporting the isolated mining unit [4–6]. The room pillar method leads to large-area goafs, which can become a major hazard [7, 8]. The instability and collapse of goafs are sudden and instantaneous [9–11]. With an obvious long-term lag effect, this makes it difficult to predict, prevent, and control the collapse behavior, which becomes a major safety issue for gypsum mines. Many researchers have studied the stability of gypsum pillars and rooms. Lu et al. [12] improved the damage evolution constitutive equation of a gypsum rock mass considering the characteristics of the surrounding rock. They found that an ore pillar should have a factor of safety greater than 1.5, and the pillar width greater than 4.3 m. Zhou et al. [13] proposed a simplified mechanical model of a gypsum column based on the given stress-strain relationship of gypsum rock, which they used to study the instability mechanism of a gypsum room-pillar system. They found that the peak pressure after

strain softening and the surrounding humidity can increase the stiffness of the support system. Xia et al. [14] established a new viscoelastic model to solve the creep failure of the mine roof by considering the rheology of a gypsum rock mass. They found that the deflection of the roof increases with time. Wang et al. [15] developed a physical model for the failure mode of a multipillar support system and found that the failure of any supporting member would cause settlement. Chen et al. [16] built a cusp catastrophe model for the support system where beams and pillars release and dissipate energy, respectively, in the plastic zone. They found that the instability of the support system is caused by uncoordinated energy release, energy dissipation, and geometric deformation. Xu et al. [17] used case studies to evaluate the pillar stability under site-specific rock mass conditions and established a correlation between the strain and aspect ratio. Jessu and Spearing [18] studied the influence of a typical fault on the stress and displacement of a goaf in a gypsum mine; they found that the loads on the roof and pillar are negatively correlated with distance from the fault. Zhang et al. [19] proposed a method to evaluate the condition of masonry pillars. Their results showed that ultrasonic stress waves can be used to monitor

the internal structure of a pillar. Zielińska and Rucka [20] conducted an experimental study on the creep of red sandstone under step loading. Xie and Gong [21] analyzed the influence of the temperature and surrounding rocks on the strength and deformation of weathered granite under freeze-thaw conditions. Shen et al. [22, 23] studied the influence of geological characteristics on overburden failure in the process of working face mining by means of restricted equilibrium and continuous numerical methods; then, they concluded that the influence characteristics of goaf stability mainly varied with different lithologies. Zhou et al. [16, 24] conducted a comprehensive evaluation of the goaf risk by combining mattering element analysis with numerical simulation; then, they obtained a relatively objective and reasonable comprehensive evaluation method.

The previous studies mainly focused on establishing a mechanical or failure evaluation model to judge or predict pillar failure according a certain influencing factor. However, the instability of a gypsum pillar is affected by many factors. In this study, the large-area goaf structure formed after many years in the Luneng Gypsum Mine was used to analyze the stress characteristics and failure modes generated by the room pillar method. The effects of water and temperature on the strength of the gypsum rock were considered. Then, the variation in strength of gypsum rock pillars at different positions and ages was tested. This paper aims to grasp the influence of different factors on the instability of the goaf structure to provide a theoretical basis for maintaining the stability of goaf, so as to promote the sustainable development of mining.

2. Theory

2.1. Mechanism of a Mining Unit. The main types of instability and collapse of the gypsum mine are as follows: (I) single-pillar instability and overlying strata stability in goaf, (II) single-pillar instability and overlying strata overall instability and collapse in goaf, (III) multiunit instability and collapse impact in goaf, (IV) group structure “domino-type” instability and collapse impact in goaf, and (V) impact form of large-area group collapse in goaf. The room pillar method is commonly used for gypsum mines; it relies on a large number of pillars to support the working space, and isolated pillars support isolated mining units. Figure 1 shows the structural model. The stability of a mining unit mainly depends on the geometric parameters of the pillars and room: the room span l and pillar side length d , as shown in Figure 2. The mechanical model of an overburdened rock beam can be used to solve for the limit span of the roof plate and analyze the stability of the mine room [25–27]. The tributary area method can be used to solve for the stress state of a pillar and analyze its stability, which in turn can be used to determine the stability of the mining unit.

2.1.1. Stability of a Mine Room. According to the classical rock beam theory of mine pressure, the initial state of the protective gypsum plate is a fixed beam at both ends. The maximum bending moment of the protective gypsum

plate is at the end of the mine room, which is given by $M_{\text{Fixed_end}} = ql^2/12$. When the cracks appear at the end of the protective gypsum plate, the entire structure becomes a simply supported beam, as shown in Figure 2. There are two failure modes for the protective gypsum plate: bending tensile failure and shear failure [16]. The maximum bending moment of the protective gypsum plate is at the middle and is given by $M_{\text{mid}} = ql^2/12$. Then, the maximum tensile stress at the middle of the protective gypsum plate is

$$\sigma_{\text{Mid}} = \frac{M_{\text{Mid}}}{W} = \frac{ql^2}{2m_0}, \quad (1)$$

where W is the interface modulus of the rock beam $W = m_0/6$ and m_0 is the thickness of the protective gypsum plate (m). When the maximum tensile stress at the middle of the protective gypsum plate is greater than the ultimate tensile strength of the gypsum rock (i.e., $\sigma_{\text{Mid}} \geq [\sigma_t]$), the protective gypsum plate is damaged by bending tension. Thus, the limit span of bending tensile failure of the protective gypsum plate can be solved as follows:

$$l_{\text{Pull}} \geq \sqrt{\frac{2m_0\sigma_t}{q}}. \quad (2)$$

When the protective gypsum plate cracks, the maximum shear force at the end is $Q_{\text{End}} = (ql/2)$.

When the maximum shear stress at the end exceeds the ultimate shear strength of the gypsum rock (i.e., $\tau_{\text{End}} \geq [\tau]$), the whole end of the room caves owing to shear failure of the protective gypsum plate. Thus, the limit span of the protective gypsum plate for shear failure can be solved as follows:

$$l_{\text{Shear}} \leq \frac{4m_{\text{Residual}}[\tau]}{3q}. \quad (3)$$

To ensure that the protective gypsum plate will not be damaged, the limit span of the room should be

$$l_0 = \min[l_{\text{Pull}}, l_{\text{Shear}}]. \quad (4)$$

Generally speaking, due to the existence of bending tension as well as the presence of fractures, the protective gypsum plate tends to fail.

2.1.2. Pillar Stability. The pillar is loaded by the overlying strata, and its stability directly determines the stability of the overlying rock in the mining unit. There are many methods to calculate pillar load, such as empirical formulas, the effective load method, and the tributary area method [28]. In this study, the tributary area method was used to calculate the effective load on a pillar, as shown in Figure 2. The pillar load is given by $Q = q(d + l)^2$. When the pillar stress exceeds the ultimate compressive strength (i.e., $\sigma_{\text{pre}} \geq \sigma_c$), the pillar is damaged and destabilized, which resulted in the overall instability and caving of the lower part of the key stratum in the mining unit. Thus, the limit size of the pillar to ensure stability can be obtained as follows:

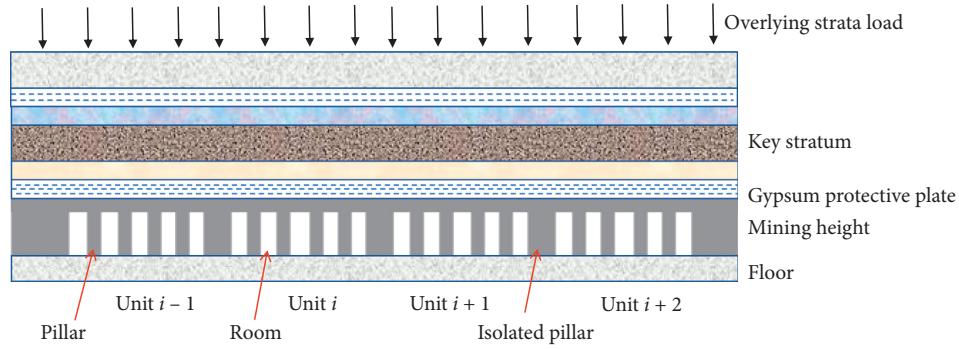


FIGURE 1: Spatial structure of overlying strata for a room-pillar gypsum mine.

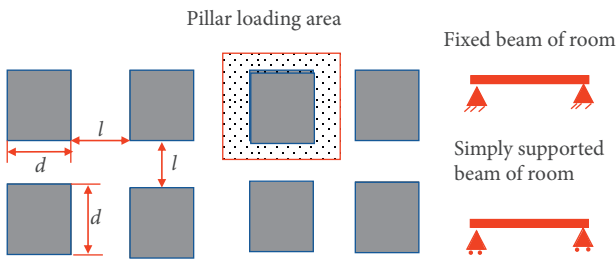


FIGURE 2: Mechanical model of a room pillar mine.

$$d_0 = \frac{l}{\sqrt{(\sigma_c/q) - 1}} \quad (5)$$

When the room is smaller than the limit span ($l \leq l_0$) and the pillar is larger than its limit size ($d \geq d_0$), the room and pillar can remain stable during the mining process. If they are not, the room and pillar will be destroyed and will destabilize the mining unit.

2.2. Modes of Instability and Collapse. At present, there are two structural collapse and instability modes in the gypsum mine goaf: room failure and pillar failure [29–33].

2.2.1. Instability Mode Induced by Room Failure. When a room is larger than the limit span (i.e., $l \geq l_0 = \min [l_{\text{Pull}}, l_{\text{Shear}}]$), it is gradually damaged by the mining process. Most rooms fail in tension. A failure arch structure forms and gradually develops upward to the bottom of the key stratum, which results in the destruction of the pillar, as shown in Figure 3. After the room and pillars in the mining unit are destroyed, the load of the critical stratum and overlying strata is transferred to an isolated pillar, resulting in stress concentration. In general, the collapse evolution process of this instability mode is relatively slow. Although the mining unit will collapse, if the key stratum remains stable, a serious accident will not occur. For actual sites, the geometric parameters are generally far less than the limit span of the mine room. However, a large amount of on-site accidents in available data shows that even if the mine room is far smaller than the limit span, the protective gypsum plate is gradually weathered and collapsed under the influence of various

factors such as water, temperature, and mining disturbances, as shown in Figure 4.

2.2.2. Overall Unit Instability Mode Induced by Pillar Failure. When a pillar is less than the stability limit size (i.e., $d \leq d_0 = l / (\sqrt{(\sigma_c/q) - 1})$), it may suddenly fail and destabilize during the mining process. This results in the overall collapse of the protective gypsum plate and the soft rock strata above up to the upper key stratum, as shown in Figure 5. After the pillar and room are destroyed, the load of the key stratum and overlying strata is transferred to an isolated pillar, which results in a stress concentration. The instability and collapse mode develop rapidly, and it can be induced by an impact. The state of a gypsum mine goaf is complex, and a pillar is affected by water, mining disturbances, and other factors. The accident data of on-site disasters prove that even large pillars have a high risk of later failure and instability, which is why current pillars are far greater than the size that leads to ultimate failure, as shown in Figure 6.

Therefore, the collapse mode of goaf can be changed by adjusting the thickness of roof protection and the unit size of goaf, such as increasing the thickness of roof protection and decreasing the unit size.

3. Experimental Study on the Influencing Factors for the Instability and Collapse of the Room Pillar Structure

The room pillar method has formed stable and large-area goafs in the gypsum mine. Over time, a collapse may occur; this indicates a long time lag resulting from the combined effects of many external factors. This part takes the Luneng Gypsum Mine as a case to study the weakening effects of water, temperature, and age on gypsum rock.

3.1. Methodology. At the same pillar location of the gypsum mine, the original gypsum rock were obtained and transported to the laboratory. Through rock coring equipment, the original rock is processed into a standard rock mechanics test specimen: cylindrical ($\Phi 100 \times 50$ mm). Then, the second screening and wave velocity test are carried out on the specimens, and the specimens with no obvious joint cracks

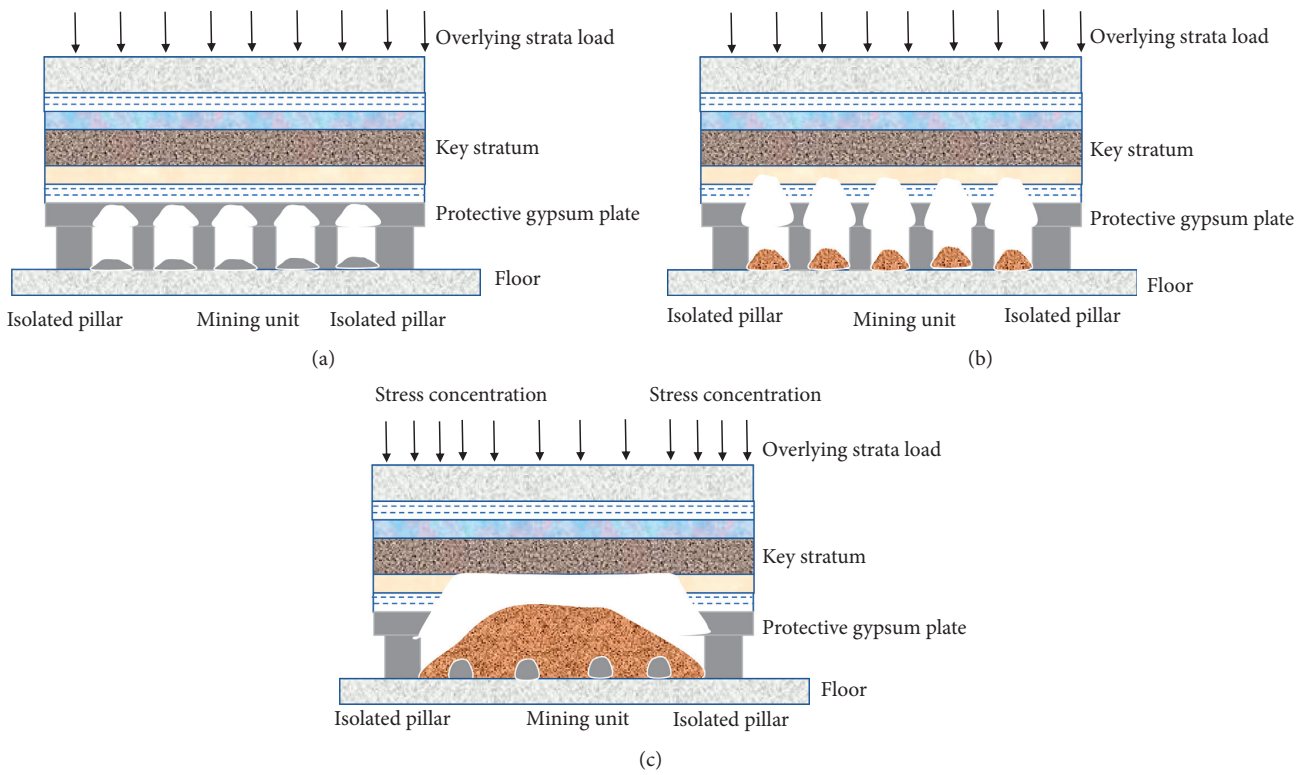


FIGURE 3: Progressive failure mode of a mining unit induced by room failure: (a) cracking and caving of the protective gypsum plate, (b) upward development of the arch structure, and (c) overall failure of the room pillar structure with stable suspension of the key stratum.



FIGURE 4: Weathering damage of a gypsum mine room.

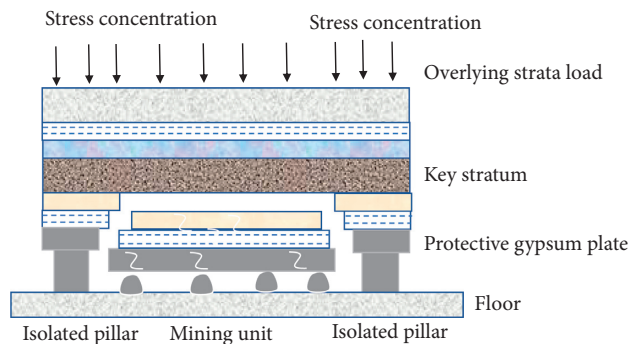


FIGURE 5: Overall instability mode induced by pillar failure.



FIGURE 6: Weathering damage of gypsum mine pillars.

on the surface and little difference in wave velocity are selected as the final specimens of this test.

3.1.1. Experimental Design and Process of Water Effects. Gypsum mines are susceptible to water, and some accidents have shown that water contributes to goafs' instability and collapse. The presence and amount of water affect the mechanical properties of gypsum rock [34–38]. In this study, the uniaxial compressive strength of gypsum rock was used as the evaluation parameter, and the strength-weakening rate was taken to quantify the effect of water on gypsum rock. The natural water content of gypsum rock is 2.17%. Gypsum rock specimens were immersed in water for different amounts of time (1–120 days). The uniaxial compressive strength of the gypsum rock was then measured, and the strength-weakening rate was determined. Figure 7 shows the experimental process.

3.1.2. Experimental Design and Process of Temperature Effects. Through an analysis of collapse accidents of gypsum mine goafs, it is shown that the collapse accidents of the goafs mostly occur in spring and winter, especially for loose goafs. This indicates that changes in temperature due to seasons may have a weakening effect. Therefore, the strength-weakening effect of temperature cycles on gypsum rock was considered [39–41]. Specimens were placed in different temperature environments to simulate the four seasons. Figure 8 shows the specific experimental process, which is detailed as follows:

(1) Spring: specimens were placed in a refrigerator at a set temperature of 4°C

(2) Summer: specimens were placed in an incubator at a set temperature of 30°C

(3) Autumn: specimens were placed in a refrigerator at a set temperature of 4°C

(4) Winter: specimens were placed in a refrigerator at a set temperature of -10°C

Each stage was 4 h, and a cycle comprised all four stages. During the experiment, the gypsum specimens were sealed with the film to ensure that the moisture content remained stable and to eliminate the influence of water. After each cycle, the wave velocity of the specimen was tested. The uniaxial compressive strength was tested after the specimen was kept for 24 h at room temperature. Specimens were subjected to up to 20 cycles, which represented 20 years.

Each stage was 4 h, and a cycle contains all four stages. During the experiment, the gypsum specimens were film-sealed to ensure that the moisture content remained stable and to eliminate the influence of water. After the end of each cycle, the wave velocity of the specimen was tested. The uniaxial compressive strength of the specimen was tested after being stored for 24 h at room temperature. Specimens were subjected to up to 20 cycles, which represented 20 years.

3.1.3. Experimental Design and Process of Time Effects. The goafs of a gypsum mine created by the room pillar method often remain intact for several years or even decades before collapse. Under long-term stress, the stability and lag collapse of a gypsum mine goaf depend to a large extent on the ultimate support capacity of the gypsum ore pillars over time [42–47]. The uniaxial compressive strength test was



FIGURE 7: Water immersion test of gypsum rock specimens.



FIGURE 8: Experiments on the influence of the cycle temperature.

carried out on the large-area goaf specimens of the Luneng Gypsum Mine. The strength-weakening rate was taken as the key parameter to evaluate the effect of age.

When a room in a gypsum mine is exhausted, the resulting goaf should be sealed. A goaf has no water or power supply. Over time, the conditions in the goaf become complex and changeable, and the risk to workers entering the goaf is high. This led to many difficulties with taking specimens. With the help of on-site engineers and technicians, a simple and portable sampling equipment was designed that comprises an electric drill, battery, and coring sleeve.

To ensure personnel safety, gypsum rock pillars were mainly sampled from the relatively stable II-1 gypsum stratum. Three to five pillars with good integrity were selected to specimen different ages. The coring position was 1.0–1.5 m from the bottom of the gypsum pillar. The coring depth was 2.5–3.5 m on both sides of the pillar at a 45° syncline. The boreholes on both sides crossed in the middle to ensure that the entire transverse range of the pillar was drilled. The cores were arranged in order after being taken out and processed into standard rock specimens for laboratory tests. The coring process is shown in Figure 9.

3.2. Results

3.2.1. Experimental Results of Water Effects. The saturated water content of the gypsum rock was 10.05%. It reaches saturation within 48 h. The wave velocity of the specimens under different immersion times was measured. After reaching the saturation state, the wave velocity fluctuated in the range of 2100–2300 m/s. Throughout the immersion period, the

specimens showed no obvious disintegration. However, in later stages of immersion (>90 days), the surface and edges of the specimens showed obvious exfoliation and slagging. Figure 10 shows the uniaxial compressive stress-strain curves of the gypsum rock specimens with different immersion times. As the immersion time increased, the compression of the specimen increases significantly; the uniaxial compressive strength decreases clearly, and the strain corresponding to the peak strength increases clearly. The compressive strength of the specimens showed obvious small fluctuations before reaching the peak strength.

The strength-weakening rate for the uniaxial compressive strength of gypsum rock is given by

$$\eta_{\text{Water}} = \frac{\sigma_c - \sigma_{\text{Water}}}{\sigma_c} \times 100\%, \quad (6)$$

where σ_c is the natural compressive strength of the gypsum rock (MPa) and σ_{Water} is the compressive strength of the gypsum rock with different immersion times (MPa).

Figure 11 indicates the variation in the uniaxial compressive strength and strength-weakening rate of gypsum rock specimens with different immersion times. As the immersion time increased, the uniaxial compressive strength and strength-weakening rate decreased and increased, respectively. Each showed a rapid change, followed by a slow change and then a stable state. Water had a greater effect on the strength initially and less at later stages. The maximum strength-weakening rate was 52.61% at an immersion time of 120 days. For mining areas that are greatly affected by water, water should be considered as a key factor leading to the destruction of pillars and delayed collapse of a goaf, and targeted prevention and control measures should be taken.

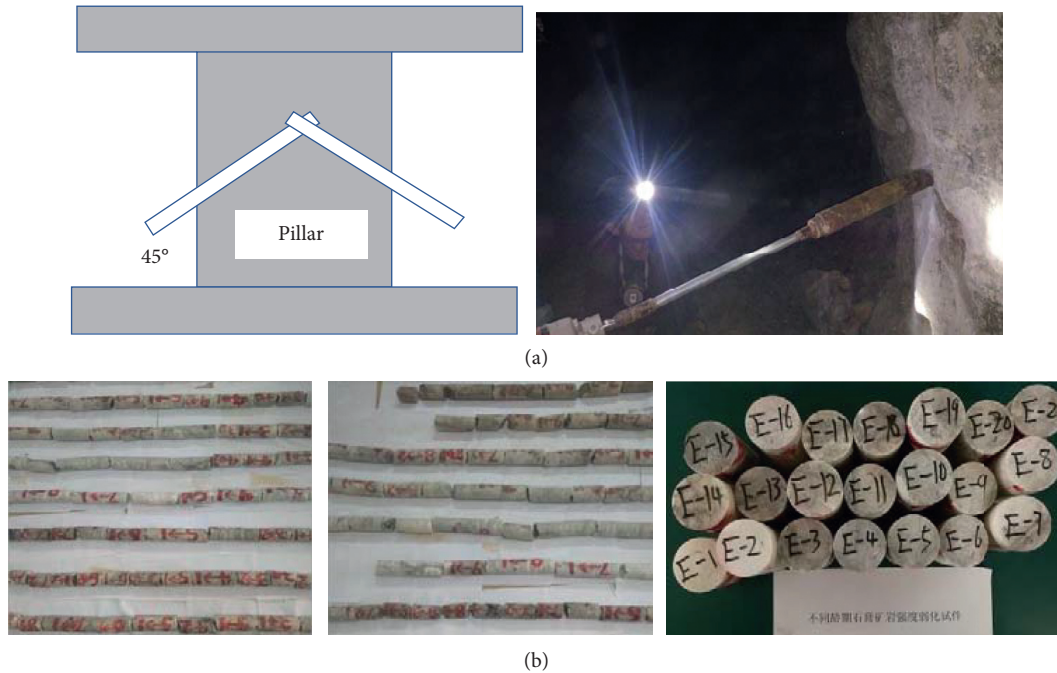


FIGURE 9: In situ sampling and process. (a) Sampling method in the goaf. (b) Sorting and processing of cores.

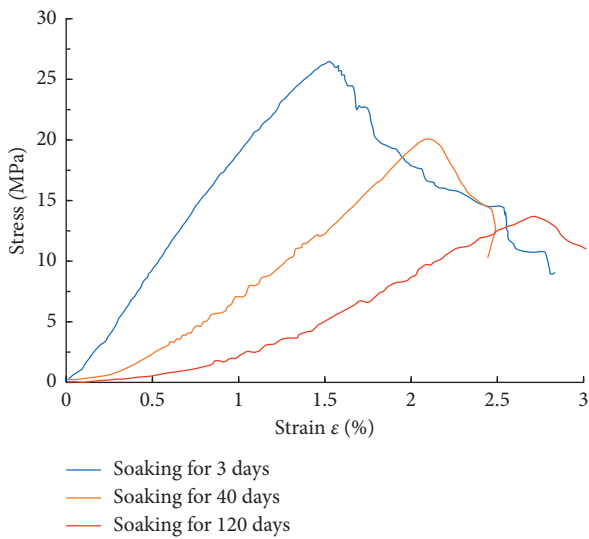


FIGURE 10: Uniaxial compressive stress-strain curve of gypsum rock at different soaking times.

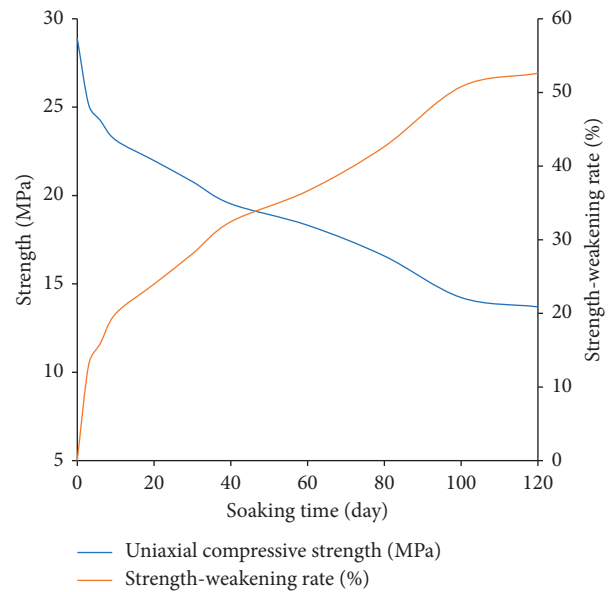


FIGURE 11: Strength and strength-weakening rate of gypsum at different soaking times.

3.2.2. Experimental Results of Temperature Effects.

Figure 12 shows the various values of wave velocity of the gypsum rock specimen with the number of temperature cycles. In different states, the wave velocity value of the test specimen shows that the velocity value is not constant. Instead of a steady increase or decrease, the results show a fluctuating change, but the overall trend is downward. The wave velocity changes for the first three cycles are not obvious. After 3–10 cycles, the wave velocity decreased by 500–900 m/s but there is a certain fluctuation. After 10 cycles, the wave velocity tended to stabilize, although it still

showed some fluctuation. As the number of temperature cycles increased, the wave velocity initially remained stable before rapidly declining and then stabilizing again. The variation range was more than 35%.

Figure 13 shows the uniaxial compressive stress-strain curves of the gypsum rock specimens with different amounts of temperature cycles. With the number of temperature cycles, the compressive stress of the specimens increases clearly. This indicates that the internal microstructure of the

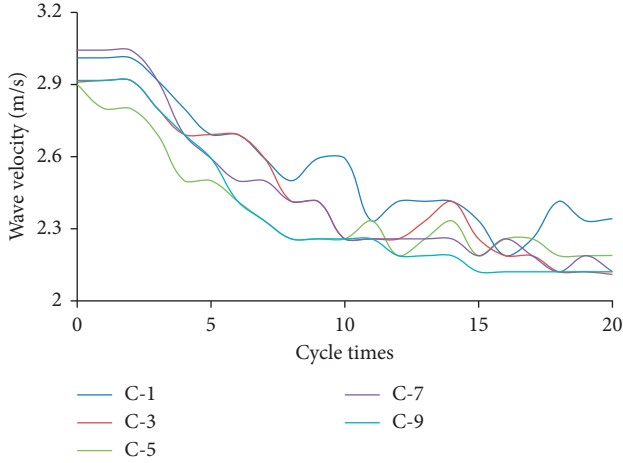


FIGURE 12: Wave velocity curves of specimens with different temperature cycles.

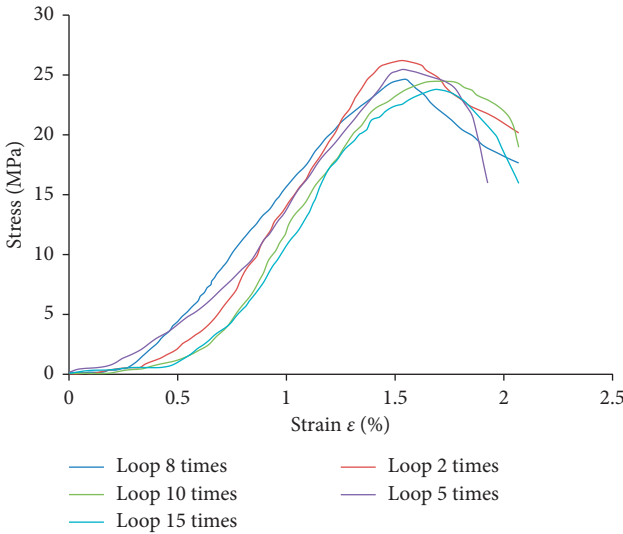


FIGURE 13: Uniaxial compressive stress-strain curves at different temperature cycles.

gypsum ore and rock was expanded and extended by the action of temperature cycling. After more than 10 temperature cycles, the uniaxial compressive stress-strain curve showed obvious fluctuations. As the number of temperature cycles increased, the strength decreased overall, but the range of the decrease was small. The uniaxial compressive strength was 24.53 MPa after 15 cycles.

The strength-weakening rate for the uniaxial compressive strength of gypsum rock subjected to temperature cycles is given by

$$\eta_{Tem} = \frac{\sigma_c - \sigma_{Tem}}{\sigma_c} \times 100\%, \quad (7)$$

where σ_{Tem} is the compressive strength of the gypsum rock with different temperature cycles (MPa).

Figure 14 shows the variations in the uniaxial compressive strength and strength-weakening rate of gypsum rock specimens with different temperature cycles. As the number of

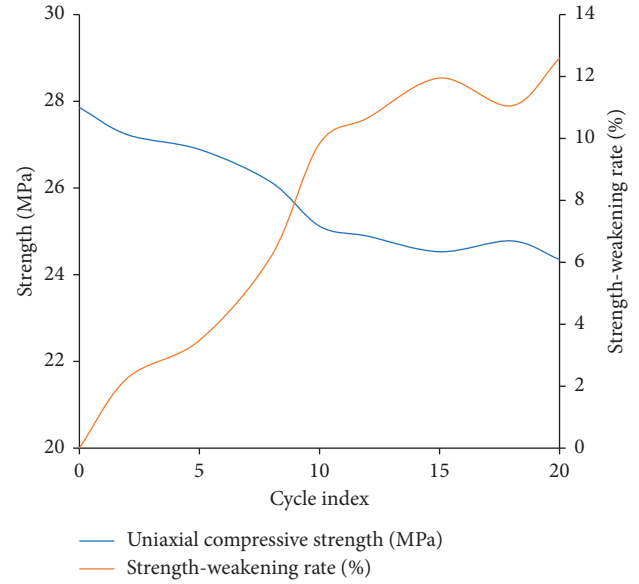


FIGURE 14: Uniaxial compressive strength and strength-weakening curves with different temperature cycles.

temperature cycles increased, the uniaxial compressive strength decreased, and the strength-weakening rate increased. After 20 cycles, the maximum strength-weakening rate was 12.60%, which is relatively low. This indicates that temperature cycles do not have an obvious effect on the strength of gypsum rock, so they do not significantly affect the lag collapse of gypsum mine goafs. Apart from the lax sealing of some mining areas, gypsum mine goafs are generally sealed quite well. Thus, a goaf can be regarded as a closed space with constant temperature and humidity. Temperature cycles should have a relatively small strength-weakening effect on the gypsum rock. Therefore, the seasonal temperature change can be considered an influencing factor for the lagging collapse of goafs in unsealed gypsum mines.

3.2.3. Experimental Results of Time Effects. The gypsum pillars in the goaf were 4–6 m wide. To study the strength-weakening rate at different pillar depths, the cores at depths of 0.5, 1.5, and 2.5 m were processed into standard specimens. To standardize the specimens, the precision of the depth had to be within 0.2 m. The uniaxial compressive strength was tested in a laboratory. To eliminate the error, the average peak strength of several specimens was taken as the final strength for different ages and pillar depths. Figure 15 shows the variation in the peak strength.

The following characteristics and laws were obtained:

- (1) With increasing pillar depth, the uniaxial compressive strength gradually increased, and the strain corresponding to the peak strength gradually decreased. This trend became more obvious with increasing age. The gypsum rock was stronger and close to the pillar surface (0.5 m depth) than deep within the pillar (2.5 m depth) with increasing age.

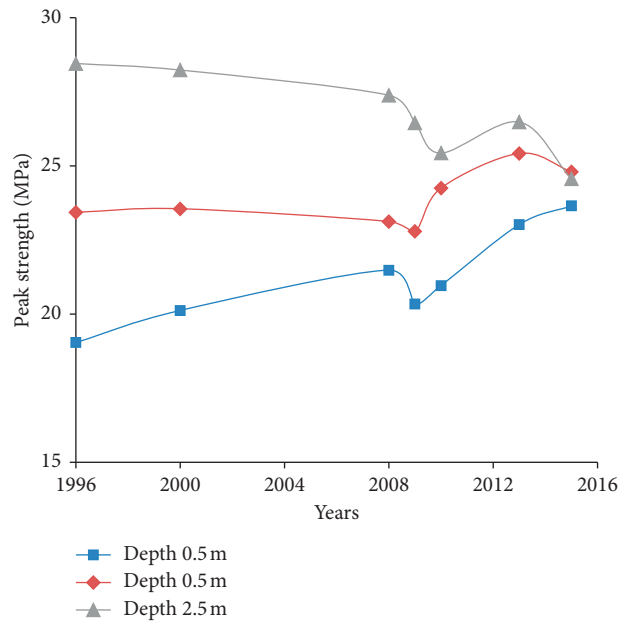


FIGURE 15: Variation in the peak strength of gypsum rocks at different ages and depths.



(a)



(b)

FIGURE 16: On-site photos of mine pillars in the goaf. (a) 1996. (b) 2015.

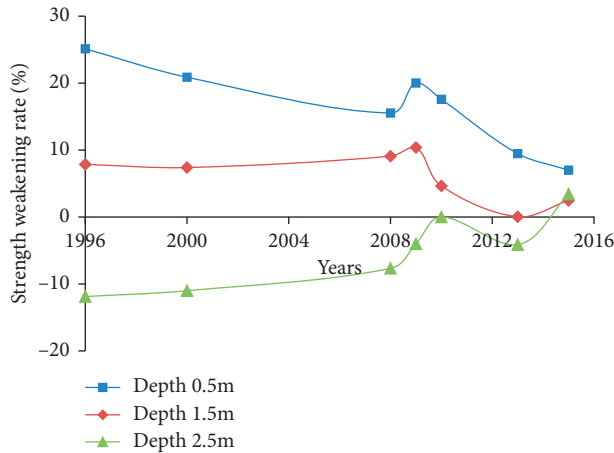


FIGURE 17: Strength-weakening rate of gypsum rock at different ages.

- (2) The strength of the gypsum rock greatly differed at pillar depths of 1.5 and 2.5 m with increasing age. The difference gradually increased with age (e.g., before 2015). However, the strength showed little difference at the pillar depths of 1.5 and 2.5 m for younger pillars (e.g., after 2015).

These can be explained as follows:

- (1) With increasing age, the influences of water, temperature, disturbances, and weathering on the pillar surface increased, and joints and fissures in the gypsum rock developed. Phenomena such as breakage, expansion, and spalling were observed on-site, as shown in Figure 16. When the cores were taken, the gypsum rock had low integrity near the pillar surface, and few cores had a length greater than 10 cm. These reasons led to the increased compaction and decreased strength of the gypsum rock near the pillar surface, which only increased with age.
- (2) Under the long-term stress of overlying strata, the gypsum rock deep in the pillar will creep continuously. Before failure and instability occur, the continuous creep will increase the compaction and strength of the gypsum rock. Meanwhile, weathering of the gypsum rock near the pillar surface will reduce the effective support area of the pillar and increase the peak stress deep within the pillar. During coring, some pillars showed obvious obstructions to drilling. The increased stress gradually increased the compaction and strength of the gypsum rock (i.e., plastic hardening). These reasons explain the increased strength of the gypsum rock deep within the pillar with increasing age.
- (3) New goafs had little time for weathering and creep, which explains the little change in strength for these samples.

The weakening rate for the uniaxial compressive strength of gypsum rock at different ages is given by

$$\eta_{\text{Tem}} = \frac{\sigma_t - \sigma_c}{\sigma_c} \times 100\%, \quad (8)$$

where σ_t is the compressive strength of gypsum rock (MPa).

Figure 17 shows the variation in the strength-weakening rate of gypsum rock specimens with different ages and depths. Near the pillar surface (depth of less than 1.5 m), the strength-weakening rate increased with age. Deep within the pillar, the strength-weakening rate showed the opposite trend. The maximum strength-weakening rate was 25.13% (1996), which is relatively low. This is the main reason for the long-term stability of well-sealed goafs, which may not collapse for several years or even decades.

4. Conclusions

- (1) Two conditions must be satisfied to ensure the stability of the room pillar structure: the pillar is larger than the limit size, and the room is less than the limit span. If these conditions are not met, rock collapse and instability will occur due to pillar or room failure. Pillar failure has a large effect on instability and collapse.
- (2) Water has a significant influence on the strength of gypsum rock. The strength-weakening rate of specimens was 52.61% after immersion in water for 120 days. This indicates that water penetration or flooding can easily destabilize a large-area goaf.
- (3) The temperature cycles indicated little effect on the strength of gypsum rock. However, changes in temperature often affect the relative humidity. Therefore, it is a major factor for pillar failure in unsealed goafs.
- (4) The gypsum rock near the pillar surface is gradually weathered over time, and it loses its bearing capacity. The supporting pressure is transferred deep within the pillar, so the effective support capacity gradually decreases over time.

Data Availability

The data used to support the findings of this study are available from the corresponding author upon request.

Conflicts of Interest

The authors declare that there are no conflicts of interest regarding the publication of this paper.

Authors' Contributions

Z.W.D. performed the data analysis and wrote this paper. Z.H.L. helped to perform the experiments and revised this manuscript. L.B.Z., F.X.L., and S.W. guided the data analysis method and supervised the experiments.

Acknowledgments

This study was supported by the Shandong Provincial Natural Science Fund (ZR2018ZC0740).

References

- [1] Y. X. Guo, P. Wang, and G. R. Feng, "Experimental study on diffusion process of sulfate ion in cemented gangue backfill material," *Advances in Civil Engineering*, vol. 2020, Article ID 5846397, , 2020.
- [2] C. Ju, Y. S. Liu, Z. Y. Yu, and Y. Z. Yang, "Cement-lime-fly ash bound macadam pavement base material with enhanced early-age strength and suppressed drying shrinkage via incorporation of slag and gypsum," *Advances in Civil Engineering*, vol. 2019, Article ID 8198021, , 2019.
- [3] S. Ma, P. Bao, and N. Jiang, "Experimental study of gypsum-concrete dense-column composite boards with external thermal insulation systems," *Applied Sciences*, vol. 10, no. 6, p. 1976, 2020.
- [4] K. Kubicka, U. Pawlak, and U. Radoń, "Influence of the thermal insulation type and thickness on the structure mechanical response under fire conditions," *Applied Sciences*, vol. 9, no. 13, p. 2606, 2019.
- [5] N. Zhou, H. Yan, S. Jiang, Q. Sun, and S. Ouyang, "Stability analysis of surrounding rock in paste backfill recovery of residual room pillars," *Sustainability*, vol. 11, no. 2, p. 478, 2019.
- [6] B. Chen, S. C. Zhang, and Y. Y. Li, "Physical simulation study of crack propagation and instability information discrimination of rock-like materials with fault," *Arabian Journal of Geosciences*, vol. 966, 2020.
- [7] S. Wei, C. Wang, Y. Yang, and M. Wang, "Physical and mechanical properties of gypsum-like rock materials," *Advances in Civil Engineering*, vol. 2020, pp. 1–17, 2020.
- [8] J. Huang, C. Tian, L. Xing, Z. Bian, and X. Miao, "Green and sustainable mining: underground coal mine fully mechanized solid dense stowing-mining method," *Sustainability*, vol. 9, no. 8, p. 1418, 2017.
- [9] T. J. Zhang, M. K. Pang, and X. F. Zhang, "Determining the seepage stability of fractured coal rock in the karst collapse pillar," *Advances in Civil Engineering*, vol. 2020, Article ID 1909564, , 2020.
- [10] S. Chen, Z. Du, Z. Zhang, H. Zhang, Z. Xia, and F. Feng, "Effects of chloride on the early mechanical properties and microstructure of gangue-cemented paste backfill," *Construction and Building Materials*, vol. 235, Article ID 117504, 2020.
- [11] T. J. Tan, Z. Yang, F. Chang, and H. Zhao, "Prediction of the first weighting from the working face roof in a coal mine based on a GA-BP neural network," *Applied Sciences*, vol. 9, no. 19, p. 4159, 2019.
- [12] R. Lu, F. S. Ma, J. Zhao et al., "Monitoring and analysis of stress and deformation features of boundary part of backfill in metal mine," *Sustainability*, vol. 10, no. 22, p. 733, 2020.
- [13] Y. Zhou, M. Li, X. Xu, X. Li, Y. Ma, and Z. Ma, "Research on catastrophic pillar instability in room and pillar gypsum mining," *Sustainability*, vol. 10, no. 10, p. 3773, 2018.
- [14] K. Xia, C. Chen, and Y. Zhou, "Catastrophe instability mechanism of the pillar-roof system in gypsum mines due to the influence of relative humidity," *International Journal of Geomechanics*, vol. 19, no. 4, Article ID 6019004, 2019.
- [15] J.-A. Wang, D. Z. Li, and X. C. Shang, "Creep failure of roof stratum above mined-out area," *Rock Mechanics and Rock Engineering*, vol. 45, no. 4, pp. 533–546, 2012.
- [16] L. Chen, Z. Zhou, C. Zang, L. Zeng, and Y. Zhao, "Failure pattern of large-scale goaf collapse and a controlled roof caving method used in gypsum mine," *Geomechanics and Engineering*, vol. 18, no. 4, pp. 449–457, 2019.
- [17] X. Xu, Y. Zhou, and S. Pang, "Analysis of catastrophic instability of plastic supporting system in old goaf of gypsum mine," *Chinese Journal of Rock Mechanics and Engineering*, vol. 37, no. 11, pp. 2548–2555, 2018.
- [18] K. V. Jessu and A. J. S. Spearing, "Direct strain evaluation method for laboratory-based pillar performance," *Journal of Rock Mechanics and Geotechnical Engineering*, vol. 11, no. 4, pp. 860–866, 2019.
- [19] C. Zhang, X. Yang, G. Ren, B. Ke, and Z. Song, "Instability of gypsum mining goaf under the influence of typical faults," *IEEE Access*, vol. 7, pp. 88635–88642, 2019.
- [20] M. Zielińska and M. Rucka, "Non-destructive assessment of masonry pillars using ultrasonic tomography," *Materials*, vol. 11, no. 12, p. 2543, 2018.
- [21] W. J. Xie and C. Gong, "Experimental study on creep characteristics of red sandstone under step loading," *Journal of Safety Science and Technology*, vol. 13, no. 6, pp. 34–39, 2017.
- [22] B. Shen, B. Poulsen, X. Luo, J. Qin, R. Thiruvenkatachari, and Y. Duan, "Remediation and monitoring of abandoned mines," *International Journal of Mining Science and Technology*, vol. 27, no. 5, pp. 803–811, 2017.
- [23] B. Pouthors, M. Khanal, and A. M. Rao, "Mine overburden dump failure: a case study," *Geotechnical and Geological Engineering*, vol. 32, no. 2, pp. 297–309, 2014.
- [24] Z. Zhou, H. Zang, W. Cao, X. Du, Lu Chen, and C. Ke, "Risk assessment for the cascading failure of underground pillar sections considering interaction between pillars," *International Journal of Rock Mechanics and Mining Sciences*, vol. 124, 2019.
- [25] J. M. Li and G. Y. Li, "The strength and deformation characteristics of saturated weathered granite under freezing and thawing conditions," *Journal of Glaciology and Geocryology*, vol. 42, no. 2, pp. 1–9, 2020.
- [26] Z. Du, S. Chen, J. Ma, Z. Guo, and D. Yin, "Gob-side entry retaining involving bag filling material for support wall construction," *Sustainability*, vol. 12, no. 16, p. 6353, 2020.
- [27] S. Chen, Z. Du, Z. Zhang, D. Yin, F. Feng, and J. Ma, "Effects of red mud additions on gangue-cemented paste backfill properties," *Powder Technology*, vol. 367, pp. 833–840, 2020.
- [28] Y. Yu, S.-E. Chen, K.-Z. Deng, and H.-D. Fan, "Long-term stability evaluation and pillar design criterion for room-and-pillar mines," *Energies*, vol. 10, no. 10, p. 1644, 2017.
- [29] J. A. Wang, D. Z. Li, and H. T. Ma, "Study of rheological mechanical model of pillar-roof system in mined-out area," *Chinese Journal of Rock Mechanics and Engineering*, vol. 29, no. 3, pp. 577–582, 2010.
- [30] Y. Zhang, S. Cao, L. Lan, R. Gao, and H. Yan, "Analysis of development pattern of a water-flowing fissure zone in shortwall block mining," *Energies*, vol. 10, no. 5, p. 734, 2017.
- [31] X. Shao, X. Li, L. Wang et al., "Study on the pressure-bearing law of backfilling material based on three-stage strip backfilling mining," *Energies*, vol. 13, no. 1, p. 211, 2020.
- [32] W. Cao, X. Wang, P. Li, D. Zhang, C. Sun, and D. Qin, "Wide strip backfill mining for surface subsidence control and its application in critical mining conditions of a coal mine," *Sustainability*, vol. 10, no. 3, p. 700, 2018.
- [33] G. Song and S. Yang, "Probability and reliability analysis of pillar stability in South Africa," *International Journal of Mining Science and Technology*, vol. 28, no. 4, pp. 715–719, 2018.
- [34] O. Vardar, F. Tahmasebinia, C. Zhang, I. Canbulat, and S. Saydam, "A review of uncontrolled pillar failures," *Procedia Engineering*, vol. 191, pp. 631–637, 2017.

- [35] Z.-H. Xu, G.-L. Feng, Q.-C. Sun, G.-D. Zhang, and Y.-M. He, "A modified model for predicting the strength of drying-wetting cycled sandstone based on the P-wave velocity," *Sustainability*, vol. 12, no. 14, p. 5655, 2020.
- [36] W. Guan, D. Zhang, and Y. Wen, "Influence of curing humidity on the compressive strength of gypsum-cemented similar materials," *Advances in Materials Science and Engineering*, vol. 2016, Article ID 7062624, , 2016.
- [37] S. Mohammadhossein and J. Vitton Stanley, "Laboratory study of gypsum dissolution rates for an abandoned underground mine," *Rock Mechanics and Rock Engineering*, vol. 52, no. 7, pp. 2053–2066, 2019.
- [38] S. Mohammadhossein and J. Vitton Stanley, "Analysis of drying and saturating natural gypsum specimens for mechanical testing," *Journal of Rock Mechanics and Geotechnical Engineering*, vol. 11, no. 2, pp. 219–227, 2019.
- [39] Z. Du, S. Chen, S. Wang, R. Liu, D. Yao, and H. S. Mitri, "Influence of binder types and temperatures on the mechanical properties and microstructure of cemented paste backfill," *Advances in Civil Engineering*, vol. 2021, Article ID 6652176, 10 pages, 2021.
- [40] F. Krause, B. Renner, F. Coppens, J. Dewanckele, and M. Schwotzer, "Reactivity of gypsum-based materials subjected to thermal load: investigation of reaction mechanisms," *Materials*, vol. 13, no. 6, p. 1427, 2020.
- [41] T. Meng, Y. Hu, R. Fang, Q. Fu, and W. Yu, "Weakening mechanisms of gypsum interlayers from Yunying salt cavern subjected to a coupled thermo-hydro-chemical environment," *Journal of Natural Gas Science and Engineering*, vol. 30, pp. 77–89, 2016.
- [42] S. Chen, D. Zhang, T. Shang, and T. Meng, "Experimental study of the microstructural evolution of glauberite and its weakening mechanism under the effect of thermal-hydrological-chemical coupling," *Processes*, vol. 6, no. 8, p. 99, 2018.
- [43] A. Christophe, H. Françoise, and S. Claudia, "The aging of gypsum in underground mines," *Engineering Geology*, vol. 74, pp. 183–196, 2004.
- [44] Z. Peter, D. Heather, and S. Daniel, "Influence of longwall mining on the stability of gas wells in chain pillars," *International Journal of Mining Science and Technology*, vol. 30, no. 1, pp. 3–9, 2020.
- [45] C. Riccardo, R. Nova, and O. Gianmarco, "Evaluation and remediation of an abandoned gypsum mine," *Journal of Geotechnical and Geoenvironmental Engineering*, vol. 136, no. 4, pp. 629–639, 2010.
- [46] H. Sylke, A. Viktoria, and R. Franz, "Hydrogeology in gypsum karst as base for geotechnical long term prognosis in mining plants," *Grundwasser*, vol. 19, no. 1, pp. 39–49, 2014.
- [47] W. Ge, M. Chen, Y. Jin et al., "Analysis of the external pressure on casings induced by salt-gypsum creep in build-up sections for horizontal wells," *Rock Mechanics and Rock Engineering*, vol. 44, no. 6, pp. 711–723, 2011.

Research Article

Coupling Technology of Deep-Hole Presplitting Blasting and Hydraulic Fracturing Enhance Permeability Technology in Low-Permeability and Gas Outburst Coal Seam: A Case Study in the No. 8 Mine of Pingdingshan, China

Wei Wang,^{1,2,3} Yanzhao Wei,⁴ Minggong Guo ,⁵ and Yanzhi Li⁵

¹School of Emergency Management, Henan Polytechnic University, Jiaozuo 454000, Henan, China

²State Key Laboratory Cultivation Base for Gas Geology and Gas Control, Henan Polytechnic University, Jiaozuo 454000, Henan, China

³The Collaborative Innovation Center of Coal Safety Production of Henan, Henan Polytechnic University, Jiaozuo 454000, Henan, China

⁴College of Safety Science and Engineering, Henan Polytechnic University, Jiaozuo 454000, Henan, China

⁵The No. 8 Mine of Pingdingshan Tianan Coal Mining Co., LTD, Pingdingshan 467000, Henan, China

Correspondence should be addressed to Minggong Guo; gmg666@163.com

Received 12 January 2021; Revised 23 February 2021; Accepted 14 March 2021; Published 23 March 2021

Academic Editor: Gong-Da Wang

Copyright © 2021 Wei Wang et al. This is an open access article distributed under the Creative Commons Attribution License, which permits unrestricted use, distribution, and reproduction in any medium, provided the original work is properly cited.

The current study aims to analyze the principles of integrated technology of explosion to tackle the problems of coal seam high gas content and pressure, developed faults, complex structure, low coal seam permeability, and high outburst risk. Based on this, we found through numerical simulation that as the inclination of the coal seam increases, the risk of coal and gas outburst increases during the tunneling process. Therefore, it is necessary to take measures to reduce the risk of coal and gas outburst. We conducted field engineering experiments. Our results show that the synergistic antireflection technology of hydraulic fracturing and deep-hole presplitting blasting has a significant antireflection effect in low-permeability coal seams. After implementing this technology, the distribution of coal moisture content was relatively uniform and improved the influence range of direction and tendency. Following 52 days of extraction, the average extraction concentration was 2.9 times that of the coal seam gas extraction concentration under the original technology. The average scalar volume of single hole gas extraction was increased by 7.7 times. Through field tests, the purpose of pressure relief and permeability enhancement in low-permeability coal seams was achieved. Moreover, the effect of gas drainage and treatment in low-permeability coal seams was improved, and the applicability, effectiveness, and safety of underground hydraulic fracturing and antireflection technology in low-permeability coal seams were verified. The new technique is promising for preventing and controlling gas hazards in the future.

1. Introduction

Gas is the main factor restricting coal mining safety. Coal-gas outburst is a complex dynamic phenomenon in underground coal mines, which has occurred frequently over the past 150 years. The coal-gas outburst process includes four stages: outburst occurrence, rapid development, deceleration development, and outburst termination [1]. The coal mines enter the stage of deep mining in China [2]. The

prevention of coal and gas outbursts is facing unprecedented challenges with an average mining depth of 650 m and rapid extension to the deep at a rate of 10~25 m per year and the increase of coal seam mining depth [3]. Most of the dynamic disasters occurred in areas deeper than 700 m [4]. Currently, the main tools to enhance coal seam permeability and strengthen gas drainage mainly include hydraulic fracturing, hydraulic punching, hydraulic slitting, loose blasting, and deep-hole presplitting blasting.

Recently, many scholars have conducted extensive and in-depth research on deep-hole presplitting blasting, the mechanism of hydraulic fracturing technology, and field applications and achieved promising results. They used numerical simulation, analyzed the expansion law of coal blasting lines, and determined the spacing of drainage holes. The coal body firmness coefficient and coal seam gas pressure positively affect the penetration enhancement of coal seam deep-hole blasting. Moreover, high ground stress severely inhibits the coal seam blasting cracks and studies the coal seam's plot coefficient $f < 1$ and the impact of time on the antireflection effect [5, 6]. To study the influence of the distance from a control hole to a blasting hole on fractures' evolution laws, finite element software LS-DYNA is used to perform presplitting blasting of the deep hole for different distance coal. It is concluded that, under the effect of tensile stress superposition from stress wave and free surface reflection effect, 3 m blasting hole around the control hole can form 10 to 13 main cracks [7].

The permeability improvement method uses presplitting and blasting technology and multiple boreholes to improve the permeability of the soft coal seam, which is achieved by optimizing the in-seam distribution of generated fractures through multiple control boreholes. The permeability improved by presplitting and blasting with deep boreholes is 2.5 times higher than the original coal seam [8]. Previous study reports the mechanism of deep-hole presplitting blasting, which strengthened gas drainage in coal seams with low permeability. Hydraulic fracturing technology is widely used in the development of low-permeability oil and gas fields [9, 10].

In 1965, the Fushun Branch of the Central Coal Research Institute introduced the technology for the coal seam penetration enhancement. Coal seam pulsating hydraulic fracturing pressure can provide relief and increase the permeability enhancement technology based on ordinary hydraulic fracturing and pulse water injection technology [11, 12]. Hydraulic fracturing has a significant effect and mechanism for improving coal and rock permeability and enhancing gas drainage capacity [13]. The coal seam pulse hydraulic fracturing technology was studied and compared with general methods of hydraulic fracturing, the results of industrial experiments show that pulse hydraulic fracturing generates a better effect of pressure relieving and permeability improving [14]. Permeability improvement technology of directional hydraulic penetration by guided groove was described and studied in detail, and they found that the efficiency of gas drainage has been significantly improved [15]. Variable frequency, a new pattern of pulse hydraulic fracturing, is presented for improving permeability in coal seam, and they found that it is better to select the sequence of low frequency at first and then high frequency. Which hydraulic fracturing for the bottom-draining roadway was investigated [16]. They develop the fractal calculation models of the fracture robustness and the filtration coefficient of fracturing fluid under hydraulic fracturing [17]. The evolution laws of permeability and gas pressure during hydraulic fracturing in the underground gas drainage were studied and several influence factors were analyzed by accomplishing a series of simulations. Gas drainage can effectively be enhanced when the hydraulic fracturing induced damage zone is a breakthrough at the drainage hole. After the coal seam is effectively fractured, the gas

flux has a decline-incline-decline tendency with increasing drainage time. The breakthrough time of the damage zone increases linearly with coal seam elastic modulus, increases exponentially with vertical stress and borehole spacing, and decreases exponentially with injecting pressure [18]. When the fracturing time increases, the coal seam's porosity gradually increases and finally reaches a fixed value [19].

Recently, to solve the problems of a long time and high cost of gas drainage for common coal seam antireflection measures, numerous studies report the coupled antireflection technology of hydraulic and blasting and found that the coupling technology has better coal seam permeability compared with the original technology. The coupling technology greatly improved in recent years. For the gas drainage effect of a coal seam with high gas content and low permeability, hydraulic-controlled blasting of a deep hole was conducted to provide pressure relief and increase a coal seam's permeability. Moreover, they found that the technology can connect boreholes through fractures, effectively discharge coal seam gas and release gas pressure, significantly improve the coal seam's permeability, and reduce gas drainage time [20]. Hydraulic fracturing and deep-hole presplitting blasting synergistic antireflection technology improve the permeability of coal seams more efficiently than the hydraulic fracturing technology, deep-hole presplitting blasting antireflection technology, and ordinary drainage technology [21]. The increasing water content of coal can significantly reduce the risk of gas outbursts. The technology of promoting coal seam infusion by blasting has been proposed to increase the water injection volume. The blasting promotes equilibrium distribution in the stress field and generates new fractures, promoting the water injection [22]. In an attempt to increase the permeability and high-gas coal seams and improve gas utilization and drainage efficiency, a previous study proposed the hydraulic fracturing deep-hole presplitting blasting composite antipermeability technology and analyzed the hydraulic fracturing deep-hole presplitting [23]. The blasting cracking mechanism of the composite antireflection of split blasting was established, as well as the equation of the stress intensity factor of the crack and the equation of the secondary crack propagation radius under detonation gas [24].

To solve the problems of coal seam gas content, high gas pressure, developed faults, complex structure, poor coal seam permeability, and high outburst risk in the 8th Mine of Pingdingshan Coal Mining Group, the method of combining theoretical analysis and field engineering tests were used for coupling technology of deep-hole presplitting blasting and hydraulic fracturing.

2. Numerical Simulation of the Influence of Coal Seam Dip Angle Change on Outburst Hazard of Coal Heading Head

2.1. Working Face Profile. The buried depth of 15–15060 face working in the 8th Mine of Pingdingshan Coal Mining Group is 580~636 m, the coal seam thickness is relatively stable, the coal thickness is usually 2.9~3.8 m with an average of 3.3 m, the coal seam inclination is 10~18°, the average is 12°, and the coal seam is semibright-type coking coal. The

lower part is the 16th coal, the thickness of the coal seam is 1.5 to 2.3 m, the average thickness is 1.9 m, and the interlayer spacing is 7.9 m. The 15th coal seam's direct roof is dark gray thick layered sandy mudstone with clear bedding, and the basic top is light gray medium-fine-grained sandstone. The coal seam's direct bottom is mudstone, containing plant root fossils, which is easy to expand when exposed to water, and the basic bottom is a thin layer gray shape sandy mudstone. The gas pressure is 1.89 MPa, and the gas content is 13.7 m³/t. It is classified according to the outburst hazard level and belongs to the outburst hazard working face.

2.2. Model Building. During underground coal road excavation, the excavation work destroys the original equilibrium state of the surrounding coal and rock, resulting in a stress concentration area, and the roadway wall area near the heading head also has a significant numerical displacement; therefore, the heading head is often more prone to outburst accidents. The stress concentration area is generated during the roadway excavation process. It is easy to understand the possibility of outburst hazards around coal roadways under different coal seam inclination angles and study the effect of coal seam inclination on outburst accidents by a comparative analysis of the maximum stress and the area of the stress concentration area under different coal seam inclination angles. The FLAC3D simulation software is used to establish a numerical simulation model of coal and rock layers during tunneling in underground coal mines. Based on the different inclination angles of coal seams, a total of 6 models have been established. The inclination angles of coal seams are 0°, 5°, 10°, 15°, 20°, and 25°. The size of the model is 80 m × 80 m × 80 m, and it is divided into three layers. The upper layer is the coal seam's top rock layer, the middle layer is the coal seam, and the lower layer is the bottom rock layer of the coal seam. The coal seam is 3.3 m thick, and the roadway is dug in the middle of the coal seam. The roadway is 5 m wide, and the middle part of the roadway is 2.2 m high. The top surface is directly excavated to the rock layer. The stress boundary is set on the top surface of the rock layer at the top of the model, and the displacement boundary is set on the remaining 5 surfaces of the model, as shown in Figure 1.

According to the measured in situ stress value of the mine, the model's in situ stress is set to 20 MP, and the mechanical parameters of coal and rock are shown in Table 1.

For simulation, the length of the model is 80 m, and the roadway is driven 40 m in the coal seam. Among them, the first 25 meters are located at the edge of the model and exhibit a boundary effect, which is not suitable for detailed analysis. Therefore, rapid excavation is adopted, and only 3 calculations were performed. The next 15 meters are in the middle of the model, with a high grid density and high accuracy. The calculation was performed after every one meter of excavation.

2.3. Influence of Coal Seam Dip Angle Change on Outburst Danger of Driving Head. The stress cloud diagram on the section of the heading head is drawn through the software, and a three-dimensional stress diagram is constructed, as shown in Figures 2 and 3.

We found that the stress distribution of the head section shows a distribution law of double peaks and deep valleys during

stress map analyses. The possible reason is that the coal in the tunnel is excavated and removed, the stress value in this area is 0, and it forms a deep valley on the three-dimensional stress map. Observing the coal seams on both sides of the driving roadway, when the distance from the driving roadway increases, the coal seam stress gradually increases and reaches a maximum value at a certain distance from the driving roadway. Two towering peaks are formed on the three-dimensional stress map because the tunneling destroys the coal seam's original stress balance, causing the stress around the roadway to accumulate gradually. When the distance from the excavation roadway exceeds the stress peak position, the coal seam stress gradually decreases until it reaches a stable value. This is because the coal seams that are far away from the roadway are less affected by the roadway. Observing the rock formation area around the roadway, it can be found that, except for the area close to the excavation roadway due to the influence of tunneling, the stress value of the rock formation is maintained in a relatively stable area, which appears as a plain on the three-dimensional stress map. The possible reason is that the rock layer is harder, and the stress state is not easily affected by roadway driving.

We found that the stress distribution of the head section shows a distribution law of double peaks and deep valleys by analyzing the stress diagram. As the coal in the tunnel is excavated and removed, the stress value in this area is 0, forming a deep valley on the three-dimensional stress map. Observing the coal seams on both sides of the driving roadway, with different coal seam inclination angles, the stress distribution of the head section still shows similar distribution characteristics, indicating a state of double peaks with deep valleys, rotating around the driving roadway, and the double peaks are often in the coal seam. These findings indicate that no matter how the inclination angle of the coal seam changes, the outburst around the roadway still mainly occurs in the coal seam, and the outburst of the rock layer around the roadway is less dangerous.

The increase of the inclination of the coal seam can progressively improve the maximum stress on the section of the heading head from -2.9865×10^7 to -3.1265×10^7 , with an increase of about 4.7%. For every 1° increase in the average coal seam inclination, the maximum stress value increased by 0.16%. Therefore, considering the maximum stress, when the inclination of the coal seam increases, the danger of outbursts around the roadway will also be increased.

2.4. Conclusions Reached through FLAC3D Simulation

- (1) No matter how the inclination angle of the coal seam changes, the outburst hazard around the roadway mainly occurs in the coal seam during the driving process of the coal roadway, and the outburst in the rock layer is less dangerous.
- (2) When the inclination of the coal seam increases, the probability of outburst around the heading head will also be increased.
- (3) When the coal seam's inclination angle increases, the areas with a higher probability of outbursts around the roadway will gradually gather in the coal seam above the roadway.

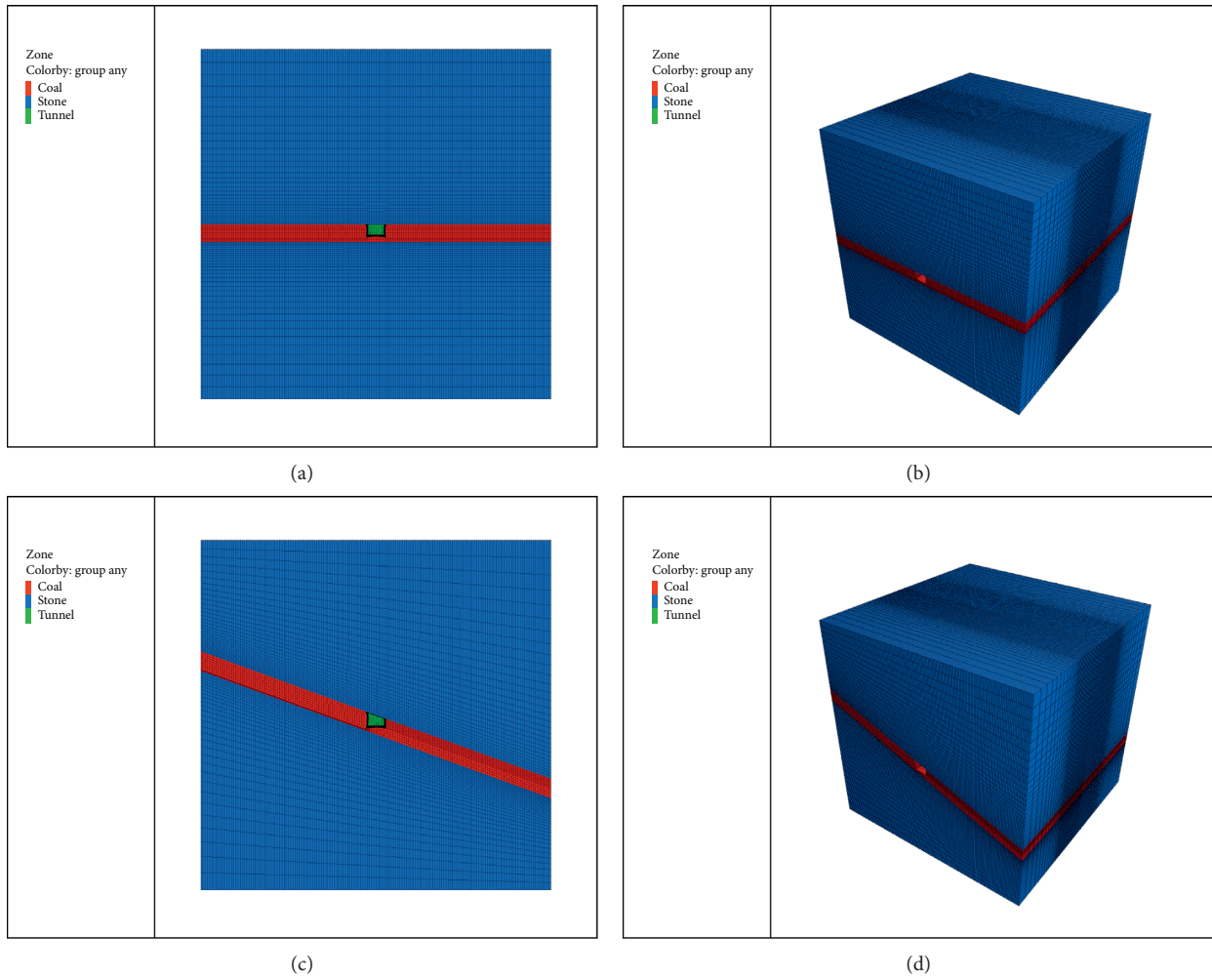


FIGURE 1: Example diagram of numerical simulation model of coal road driving with 0° and 20° dip angle coal seams.

TABLE 1: Mechanical parameters of coal and rock formations.

Classification	Elastic modulus (GPa)	Poisson's ratio	Internal friction angle (°)	Cohesion (MPa)	Density (kg/m ³)
Coal	2	0.35	20	0.3	1350
Rock	10	0.3	25	2	2500

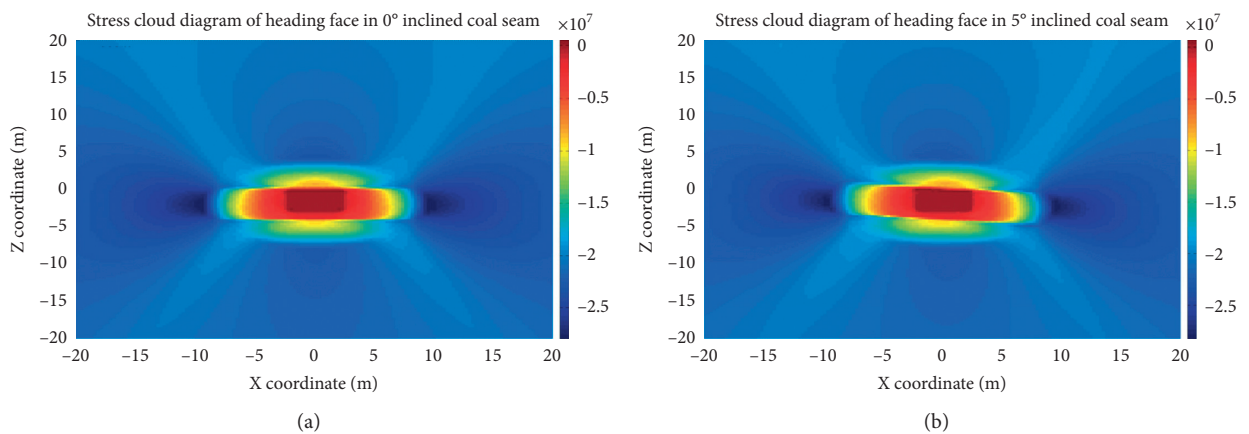


FIGURE 2: Continued.

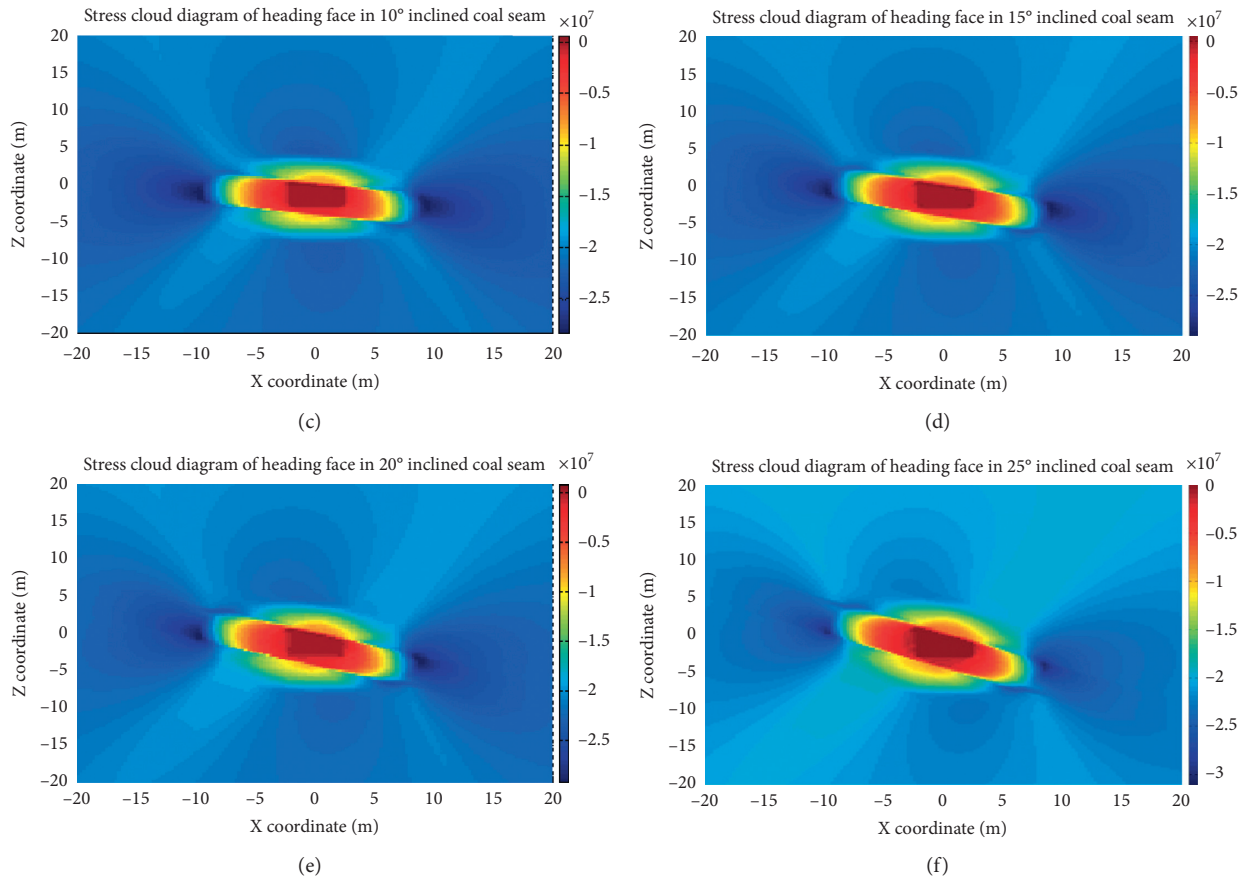


FIGURE 2: Plane cloud diagram of the section stress of the roadway heading head under each coal seam dip.

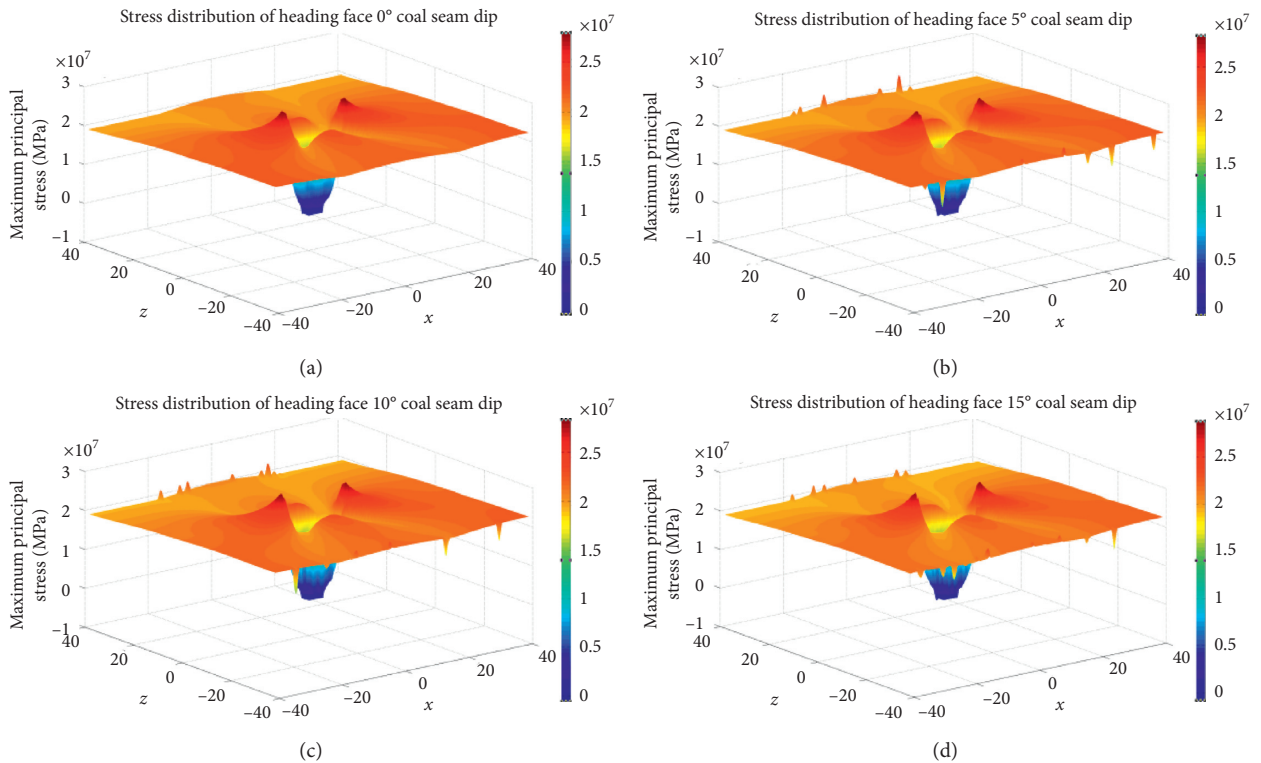


FIGURE 3: Continued.

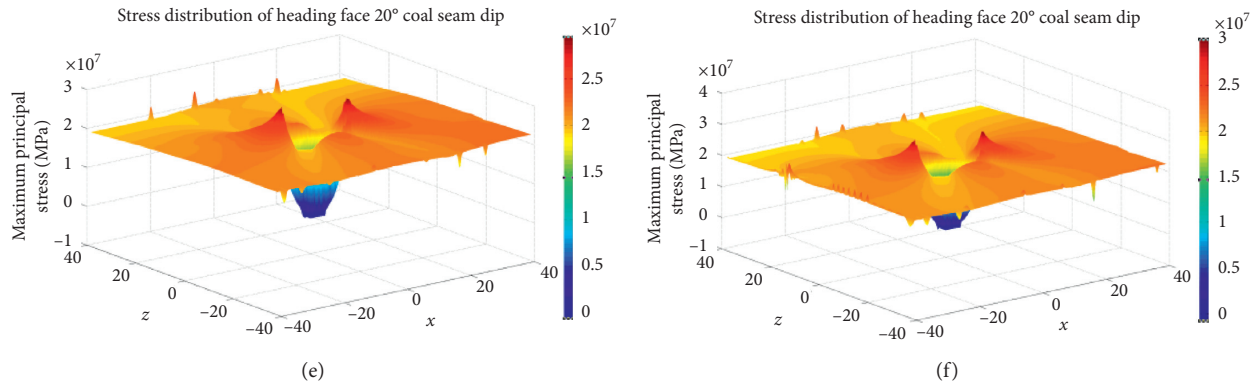


FIGURE 3: Three-dimensional diagram of the section stress of the roadway heading head under each coal seam dip.

From the above conclusions, it is established that, during coal roadway excavation, the roadway's outburst danger mainly occurs in the coal seam. Therefore, in these positions, gas outburst enhancement and elimination technology must be adopted to ensure coal mine production safety. These technologies include hydraulic enhancement, mining protective layer, loose blasting, and deep-hole presplitting blasting. These drainage technologies have long drainage cycles in outburst coal seams with low air permeability and a small impact area, increasing the time and cost of safe investment in the mining. Because the coal seam has a certain inclination angle, numerical simulation can show that as the inclination angle increases, the risk of coal seam outburst also increases. Not only is the No. 8 Mine of Pingdingshan Coal Mining buried deep but also it has a certain inclination angle, and the effect of conventional gas penetration enhancement measures is average. Therefore, it is necessary to adopt a more effective method to increase the permeability of coal seam gas.

This paper uses the blast-injection integrated antireflection technology for research. The blasting and injection integrated antireflection technology can directly perform hydraulic fracturing after deep-hole presplitting blasting to achieve the comprehensive purpose of strengthening gas drainage at the working face and improve coal seam permeability.

3. Field Engineering Test of Blast-Injection Integrated Antireflection Technology

The test site is located in the bottom extraction roadway of 15–15160 machine road in the No. 8 Mine of Pingdingshan Coal Mining Group Co., Ltd. The pressure holding hole and the blasting-injection hole are arranged, and the distance between the two holes is 100 m. As shown in Figure 4, the pressure-holding hole is arranged at an elevation angle of 58° at the bottom of the suction roadway of 15–15060 machine roadway, which is perpendicular to the middle line of the roadway side. As shown in Figure 5, the opening position of the blasting hole is located at the lower side of the roadway at an elevation angle of 74° , passing through the center of the roadway, and the drill hole passes through the 15th coal seam's 0.5 m roof.

As shown in Figure 6, we constructed 10 drilling holes in each of the four horizontal and vertical directions around the pressure-holding hole, for a total of 40 observation holes. The distances between the bottom of the 10 observation holes in each direction and the pressure-holding hole are 3 m, 6 m, 9 m, 12 m, 15 m, 18 m, 21 m, 25 m, 30 m, and 35 m, respectively. The drilling of No. 20–No. 40 is perpendicular to the direction of the roadway. As shown in Figure 7, the drill moves to a fixed position when constructing a fracturing hole and changes the drilling angle to construct Nos. 21–40 holes.

As shown in Figure 8, the blast hole is constructed with 8 observation holes in each of the four horizontal and vertical directions, for a total of 32 observation holes. The distances between the 8 observation holes in each direction and the bottom of the blast hole are 3, 6, 9, 12, 15, 18, 21, and 25 m, respectively. The 41–56 holes are drilled parallel to the direction of the roadway. As shown in Figure 9, the 57–72 holes are drilled perpendicular to the direction of the roadway and arranged in two rows, the single number row is outside the roadway, the double number row is inside the roadway, and the two split holes are 0.5 m away from the blast hole.

4. Test Effect Analysis

4.1. Comparison of Blast-Injection Integrated Antireflection Technology and Conventional Hydraulic Fracturing Influence Radius. We take the upper, middle, and lower coal samples of the observation hole of the pressure holding hole and the blast-injection hole to measure the water content, as shown in Figure 10, and draw the relationship between the water content and the distance.

It can be seen from Figures 10(a) and 10(b) that, without blasting, the water content of the observation hole around the pressure holding hole is unevenly distributed, and the direction of the observation hole is within the range of $-18\text{ m}\sim 15\text{ m}$, and the inclined observation hole is within the range of $-21\text{ m}\sim 18\text{ m}$. The coal sample moisture content curve fluctuates abruptly, indicating that, during the fracturing process, the water body is not evenly distributed along with the trend or along the strike, and it is difficult to

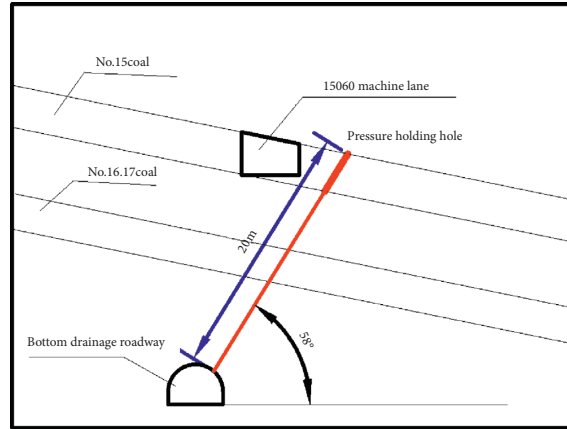


FIGURE 4: Sectional view of pressure holding hole.

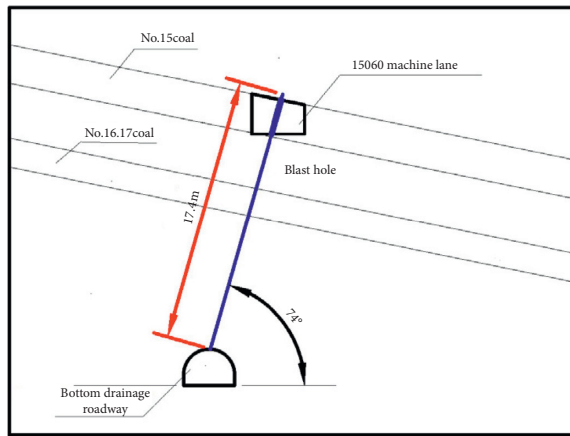


FIGURE 5: Sectional view of pressure blast hole.

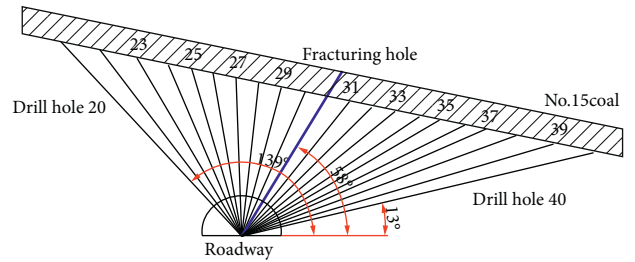


FIGURE 7: Sectional view of the observation hole number of the pressure holding hole.

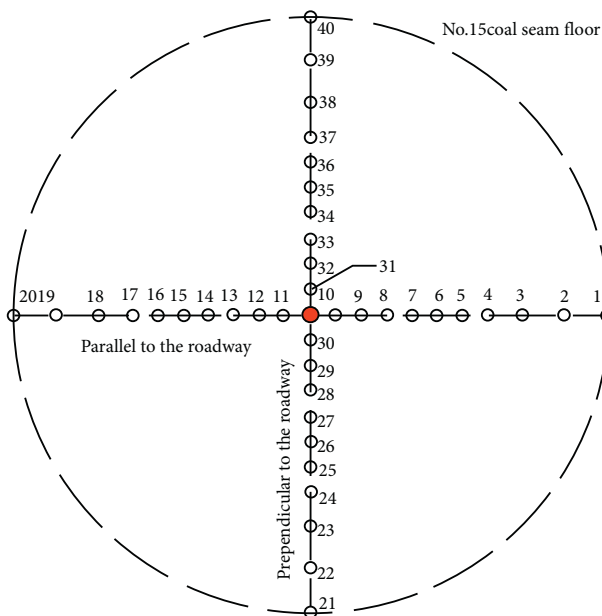


FIGURE 6: Schematic diagram of the observation hole number of the pressure holding hole.

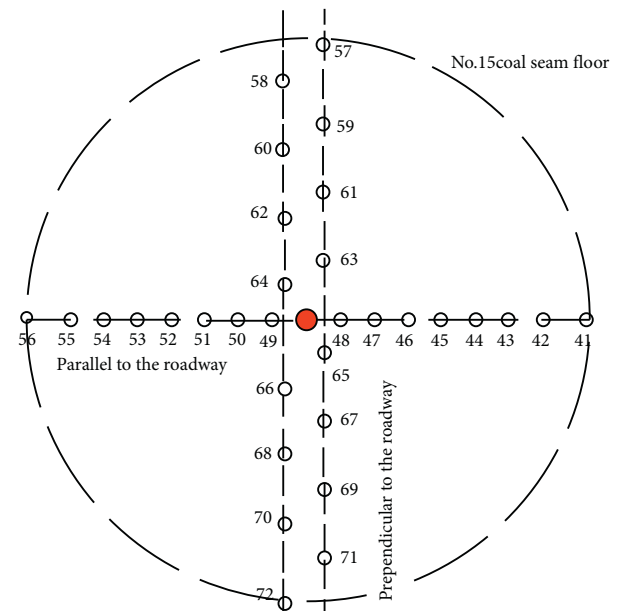


FIGURE 8: Schematic diagram of blast observation hole number.

determine the fracturing water's whereabouts. The coal body contains water at different sampling positions in the same observation hole and has a big difference in the rate. Generally, the lower coal sample has high water content, and the middle and upper parts have low water content.

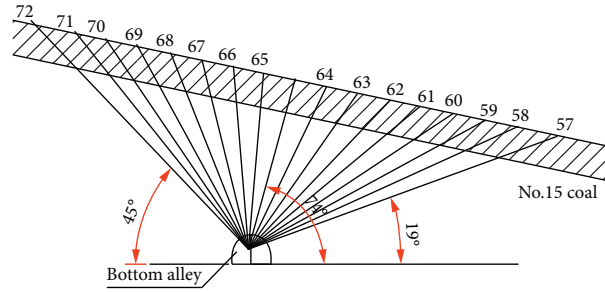


FIGURE 9: Sectional view of blast observation hole number.

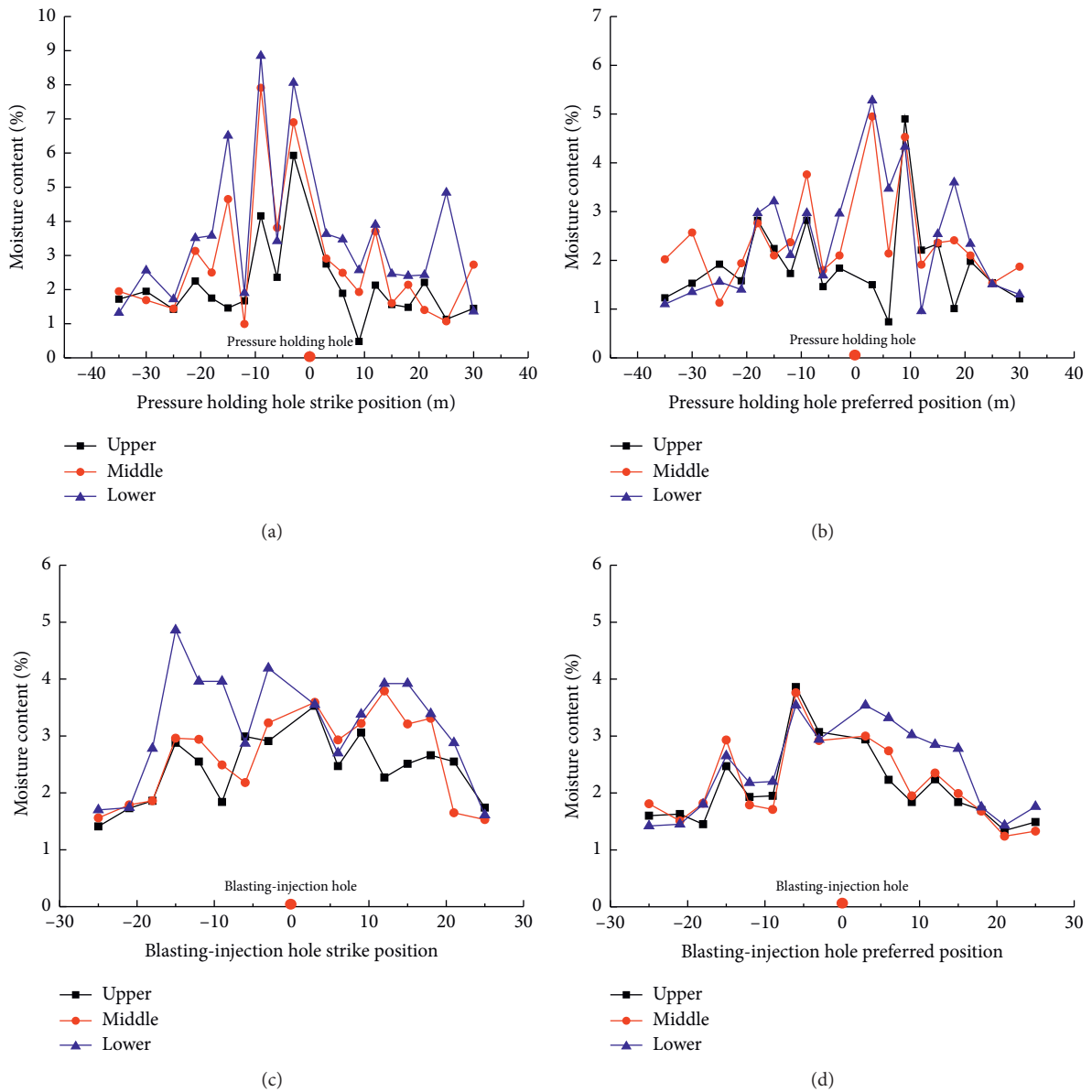


FIGURE 10: Water cut curve at different positions around the fracturing hole.

It can be seen from Figures 10(c) and 10(d) that, after blasting, the water content curve of the coal body around the blasting hole is significantly smoother than the pressure

holding hole. At different sampling positions of the same observation hole, the water content of the middle and upper coal bodies is higher, indicating good consistency. Except

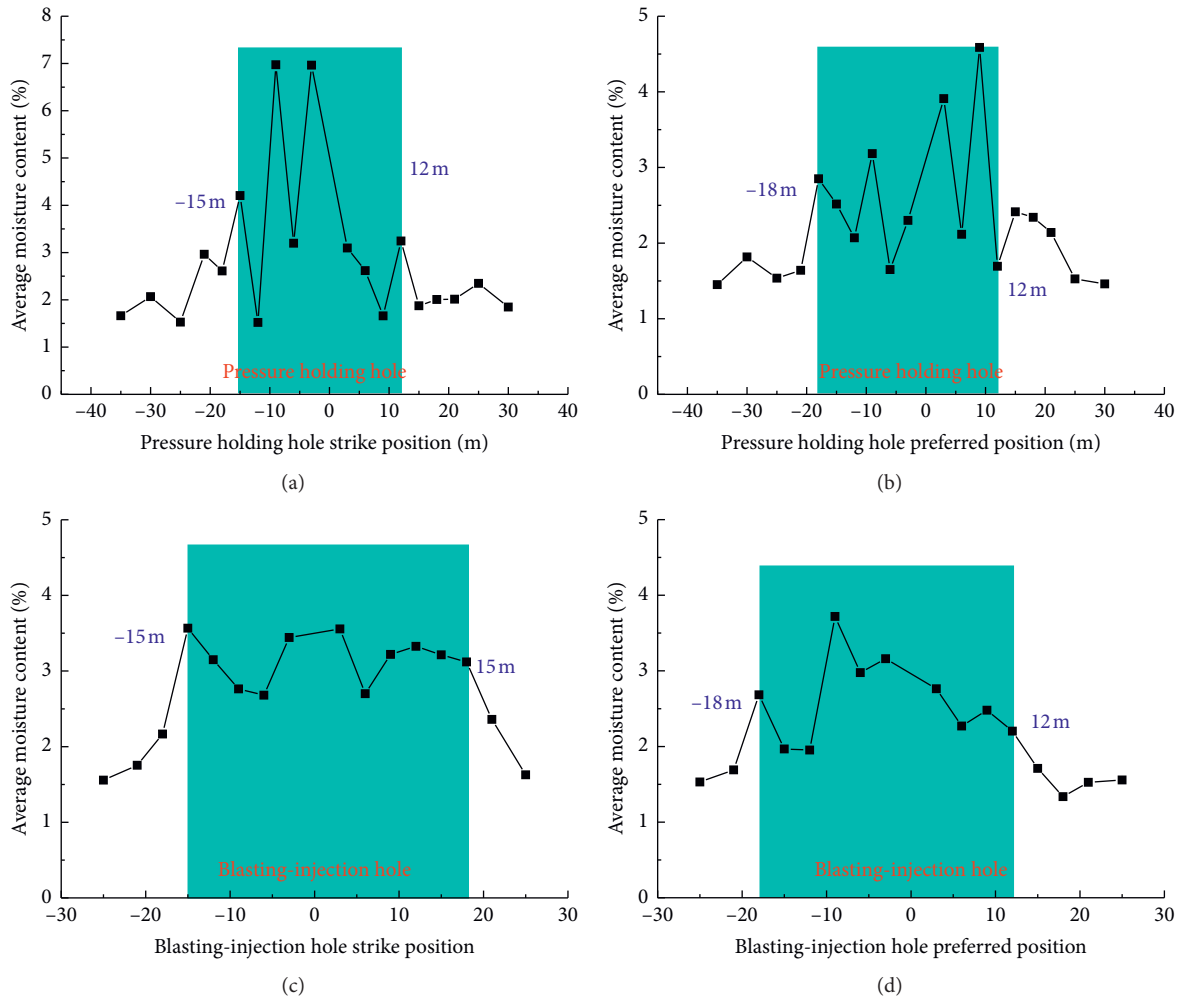


FIGURE 11: Relationship between test location and average moisture content.

that the water content of the lower coal body is generally higher with a range of $-18\text{m}\sim-6\text{m}$, the water contents of the upper, middle, and lower coal bodies are not much different in other test areas.

To determine the effective radius of the influence of the two fracturing methods, the relationship between the position of the observation hole and the average water content is plotted in Figure 11.

The pressure-holding hole direction and the water content tendency are unevenly distributed, as shown in Figures 11(a) and 11(b). After going to -15m and 12m , the water content begins to decrease and gradually stabilizes. After the tendency to -18m and 12m , the water content gradually decreases and progressively stabilizes. In Figures 11(c) and 11(d), after blast hole strikes -15m and 15m , the moisture content gradually decreases and reaches the minimum value in the test range and tends to the area outside -18m and 12m , and the moisture content begins to decrease and achieves stability.

4.2. Comparison of Gas Drainage Effect between Blast-Injection Integrated Antireflection Technology and Conventional

Hydraulic Fracturing. After 52 days of on-site monitoring, the blast-injection integrated antireflection technology was compared with the original unfractured coal seam gas drainage data in the same drainage time to investigate the drainage effect before and after fracturing. We plot the gas concentration, average flow, and cumulative scalar into a curve.

It can be seen from Figures 12–14 that, after 52 days of drilling, the average concentration of gas in the blasting and fracturing area is 66.3%, and the maximum concentration of a single group is 82%. The average concentration is the same as that of coal seam gas extraction under the original technology, 2.9 times the concentration. The average gas scalar of a single drill hole is $0.024\text{m}^3\cdot\text{min}^{-1}$, and the maximum is $0.0031\text{m}^3\cdot\text{min}^{-1}$, which is an average increase of 7.7 times. For 52 days' draining, the blast-injection integrated synergistic antireflection technology is adopted. The scalar amount of gas drainage is 14003m^3 , but when conventional hydraulic fracturing is used for gas drainage, the scalar amount of drainage is only 2310m^3 , which increases nearly 6 times.

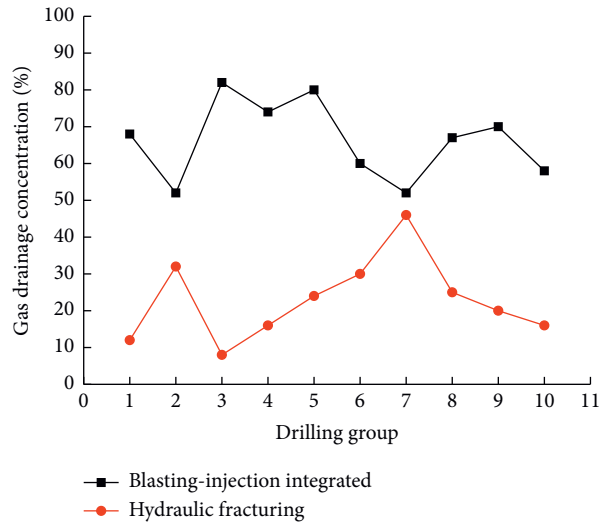


FIGURE 12: Comparison curve of gas drainage concentration before and after blasting-injection integrated antireflection technology.

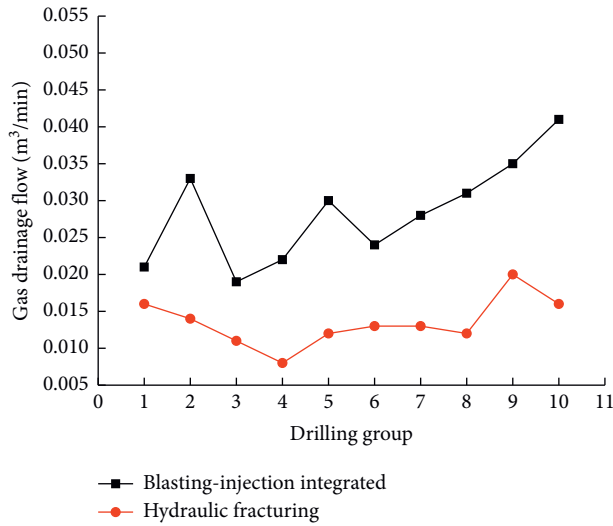


FIGURE 13: Comparison curve of gas drainage flow before and after blasting-injection integrated antireflection technology.

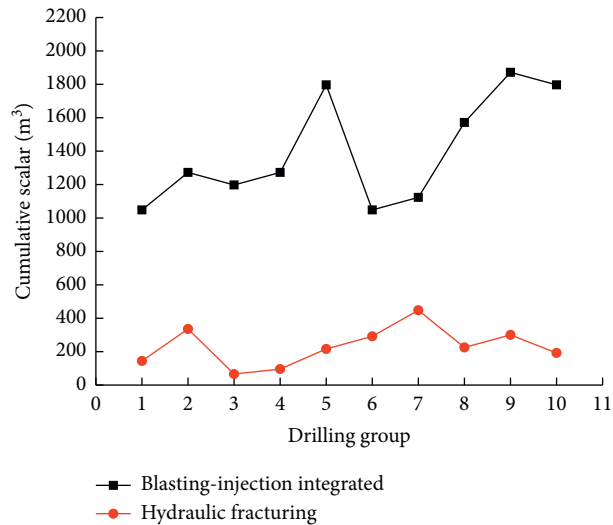


FIGURE 14: Comparison curve of cumulative scalar volume of gas drainage before and after blasting-injection integrated antireflection technology.

5. Conclusion

We draw the following conclusions after analyzing the principle of blast-injection integrated antireflection technology and applying it in the No. 8 Coal Mine of Pingdingshan Coal Mine and comparing the effect of conventional hydraulic fracturing.

- (1) Through numerical simulation, we found that it is established that, during coal roadway excavation, the roadway's outburst danger mainly occurs in the coal seam.
- (2) The water content in coal bodies is severely rough near conventional fracturing and the peak and valley of water content alternately appear; however, blast-injection integrated technology is adopted to distribute water evenly around the fracturing hole. The blast-injection integrated technology has larger area of influence on the strike compared to conventional fracturing.
- (3) After implementing blast-injection integrated technology, the gas drainage effect of outburst coal seams has low permeability. After 52 days of drainage, the average drainage concentration is 2.9 times that of the coal seam gas drainage concentration under the original technology. The average scalar was increased by 7.7 times.
- (4) Through field tests, the purpose of pressure relief and permeability enhancement in low-permeability coal seams was achieved. Moreover, the effect of gas drainage and treatment in low-permeability coal seams was improved, and the applicability, effectiveness, and safety of underground hydraulic fracturing and antireflection technology in low-permeability coal seams were verified.

This paper has conducted an in-depth analysis of the integrated technology of explosive injection and has achieved promising results. However, the experimental research is mainly conducted in the Ping coal mine area, and it still needs to be extended to other different mining areas to improve the construction technology. Different solidity coefficients of coal samples were studied separately to deal with different degrees of metamorphism, resulting in certain limitations in the experiment.

Data Availability

The data used to support the findings of this study are available from the corresponding author upon request.

Conflicts of Interest

The authors declare that there are no conflicts of interest regarding the publication of this paper.

Acknowledgments

This work was supported by the Key Science Research Project in Universities of Henan (19B620001 and

20A620004) and Key Science and Technology Program of Henan Province (202102310221).





References

- [1] F. Du, K. Wang, X. Zhang, C. Xin, L. Shu, and G. Wang, "Experimental study of coal-gas outburst: insights from coal-rock structure, gas pressure and adsorptivity," *Natural Resources Research*, vol. 29, no. 4, pp. 2481–2493, 2020.
- [2] H. Lan, D. K. Chen, and D. B. Mao, "Current status of deep mining and disaster prevention in China," *Coal Science and Technology*, vol. 44, no. 1, pp. 39–46, 2016.
- [3] M. C. He, H. Xie, P. S. Pneg, and Y. D. Jiang, "Study on rock mechanics in deep mininng engineering," *Chinese Journal of Rock Mechanics and Engineering*, vol. 16, pp. 2803–2813, 2005.
- [4] K. Wang and F. Du, "Coal-gas compound dynamic disasters in China: a review," *Process Safety and Environmental Protection*, vol. 133, pp. 1–17, 2020.
- [5] A. G. Su, *Numerical Simulation on the Propagation Law of Pre-splitting Blasting Lines in Low Permeability Coal seams*, Liaoning Technical University, Fuxin, China, 2013.
- [6] B. Y. Zhao and H. D. Wang, "Feasibility of deep-hole blasting technology for outburst prevention and permeability enhancement in high-gas-content coal seams with low-permeability subjected to high geo-stresses," *Explosion and Shock Waves*, vol. 34, no. 2, pp. 145–152, 2014.
- [7] C. Lv, J. Liu, and L. J. Guo, "Evolution laws of cracks under different hole pitch in deep hole pre-splitting blasting," *Safety in Coal Mines*, vol. 47, no. 11, pp. 65–68, 2016.
- [8] C. G. Huang, Y. B. Zhang, J. F. He, Y. Luo, and Z. G. Sun, "Permeability improvements of an outburst-prone coal seam by means of presplitting and blasting with multiple deep boreholes," *Energy Science & Engineering*, vol. 7, no. 5, pp. 2223–2236, 2019.
- [9] S. Xiao, Z. Ge, L. Cheng, Z. Zhou, and J. Chen, "Gas migration mechanism and enrichment law under hydraulic fracturing in soft coal seams: a case study in songzao coalfield," *Energy Sources Part A Recovery Utilization and Environmental Effects*, pp. 1–15, 2019.
- [10] J. Liu, Z. G. Liu, K. Gao, and W. Zhou, "Application of deep hole pre-splitting blasting to gas drainage at deep well and low permeability coal seam," *Journal of Safety Science and Technology*, vol. 10, no. 5, pp. 148–153, 2014.
- [11] Y. L. Li, Y. Liu, C. Wang, and Q. X. Wang, "Research and application of deep hole pre-splitting blasting technology for permeability enhancement in high gas and low permeability coal seam," *Journal of Safety Science and Technology*, vol. 16, no. 9, pp. 71–76, 2020.
- [12] Z. W. Li, C. Zhai, Q. Bi, and Y. Y. Wen, "Pressure relief and permeability-increasing technology based on high pressure pulsating hydraulic fracturing and its application," *Journal of Mining & Safety Engineering*, vol. 28, no. 3, pp. 452–455, 2011.
- [13] Z. Yuan and Y. Shao, "Numerical modeling on hydraulic fracturing in coal-rock mass for enhancing gas drainage," *Advances in Civil Engineering*, vol. 2018, no. 8, 16 pages, Article ID 1485672, 2018.
- [14] C. Zhai, X. Z. Li, and G. Q. Li, "Research and application of coal seam pulse hydraulic fracturing technology," *Journal of China Coal Society*, vol. 36, no. 12, pp. 1996–2001, 2011.
- [15] Y. F. Wang and Y. Z. Li, "Technology and application of directional hydraulic penetration permeability improvement by guided groove," *Journal of China Coal Society*, vol. 37, no. 8, pp. 1326–1331, 2012.

- [16] L. Quangui, L. Baiquan, Z. Cheng et al., "Variable frequency of pulse hydraulic fracturing for improving permeability in coal seam," *International Journal of Mining Ence and Technology*, vol. 23, no. 6, pp. 847–853, 2013.
- [17] F. Cai and Z. Z. Liu, "Simulation and experimental research on upward cross-seams hydraulic fracturing in deep and low-permeability coal seam," *Journal of China Coal Society*, vol. 41, no. 1, pp. 113–119, 2016.
- [18] X. Zhang, S. Zhang, Y. Yang, P. Zhang, and G. Wei, "Numerical simulation by hydraulic fracturing engineering based on fractal theory of fracture extending in the coal seam," *Journal of Natural Gas Geoscience*, vol. 1, no. 4, pp. 319–325, 2016.
- [19] X. D. Zhao and J. P. Tang, "Establishment and numerical simulation of fluid-solid coupling model of coal seam under hydraulic fracturing," *Mining Safety & Environmental Protection*, vol. 47, no. 5, pp. 18–22, 2020.
- [20] Q. Ye, Z. Jia, and C. Zheng, "Study on hydraulic-controlled blasting technology for pressure relief and permeability improvement in a deep hole," *Journal of Petroleum Science and Engineering*, vol. 159, p. 433, 2017.
- [21] Y. T. Chen, J. T. Qin, and W. B. Xie, "Application study on hydraulic fracturing and deep hole pre-splitting blasting joint permeability improvement technology," *Safety in Coal Mines*, vol. 49, no. 8, pp. 141–144+148, 2018.
- [22] W. Yang, H. Wang, Q. Zhuo et al., "Mechanism of water inhibiting gas outburst and the field experiment of coal seam infusion promoted by blasting," *Fuel*, vol. 251, pp. 383–393, 2019.
- [23] M. H. Lin, *Research on Outburst Prevention Mechanism and Technology of Integrated Blasting Injection in Working Face*, China University of Mining and Technology, Xuzhou, China, 2020.
- [24] X. H. Gao and M. Y. Wang, "Study on hydraulic fracturing-deep hole pre-splitting blasting composite permeability enhancement technology," *Coal Science and Technology*, vol. 48, no. 7, pp. 318–324, 2020.

Research Article

Influence of Deformation and Instability of Borehole on Gas Extraction in Deep Mining Soft Coal Seam

Xue-Bo Zhang ^{1,2,3,4}, Shuai-Shuai Shen,³ Xiao-Jun Feng ^{4,5}, Yang Ming ^{1,2,3}
and Jia-jia Liu ^{1,2,3}

¹State Collaborative Innovation Center of Coal Work Safety and Clean-Efficiency Utilization, Jiaozuo, Henan 454003, China

²State Key Laboratory Cultivation Base for Gas Geology and Gas Control, Jiaozuo, Henan 454003, China

³College of Safety Science and Engineering, Henan Polytechnic University, Jiaozuo, Henan 454003, China

⁴Henan Shenhuo Group Co., Ltd., Yongcheng 476600, China

⁵School of Safety Engineering, China University of Mining and Technology, Xuzhou 221116, China

Correspondence should be addressed to Xiao-Jun Feng; xiaojun.feng@cumt.edu.cn

Received 26 November 2020; Revised 5 February 2021; Accepted 23 February 2021; Published 8 March 2021

Academic Editor: Jia Lin

Copyright © 2021 Xue-Bo Zhang et al. This is an open access article distributed under the Creative Commons Attribution License, which permits unrestricted use, distribution, and reproduction in any medium, provided the original work is properly cited.

To study the effects of the three deformation instability modes of gas drainage borehole on gas drainage, the deformation instability mechanism of soft coal seams is analyzed, three deformation instability modes are proposed for soft coal seams, namely, complete holes, collapse holes, and plug holes, and a solid-fluid coupling model incorporating dynamic change of borehole suction pressure is established. The results of the study show the following. (1) When there is no borehole deformation (i.e., complete borehole), the suction pressure loss of drainage system in the borehole is very small, whose effect on gas drainage can be neglected. (2) In case of borehole collapse, the suction pressure loss is big at the collapse segment, and the total suction pressure loss of the drainage system in the borehole is bigger than that in the complete hole. However, it is smaller than the suction pressure of the drainage system and exerts limited effect on gas drainage. As the borehole collapse deteriorates, the effective drainage section of the borehole becomes smaller, while the suction pressure loss in the borehole increases continuously; thus, the gas drainage effect continuously worsens. (3) In case of plug hole, a continuous medium forms between the plug segment coal body and the surrounding coal seam, the plug segment drainage pressure turns into coal-bed gas pressure, and effective drainage length of the borehole shortens, seriously affecting the gas drainage effect. The study carries important theoretical guiding significance for improving gas drainage effect and effectively preventing gas disasters.

1. Introduction

Deeply mined soft coal seams are characterized by high stress, low mechanical strength, high gas content and desorption velocity, great coal seam thickness variation, etc. During extraction drilling construction on soft coal seam, dynamic problems such as spit-out, drilling tool sticking, and jamming often bother, causing large-scale hole collapse and formation of drilling cave [1], which severely restrict drilling depth; after the accomplishment of hole drilling, influenced by poor tamper resistance capacity of coal mass, the hole wall may deform, fall, or even collapse under crustal stress; moreover, with

extraction going on, soft coal mass may creep and cause hole diameter to shrink or even to clog, which may block gas discharge and flow channel [2–4], and severely impact on gas extraction efficiency. Deformation, instability, collapse, etc. of borehole can all be attributed to dynamic instability caused by redistribution of stress field and flow field of gas-bearing coal around the borehole [5], i.e., instability failure of borehole wall. The study on the effect of deformation instability of gas drainage borehole on high-stress soft coal seam means important theoretical guiding significance for solving the problem of high-stress soft coal seam in borehole instability and collapse and for effectively improving gas drainage effect.

Many scholars both at home and abroad have studied the deformation and instability disciplines of coal rocks around the extraction boreholes [6–20]. Tezuka and Niitsuma [6] proposed some borehole stability models and conducted theoretical analysis on the stability of borehole wall based on such models. Wang et al. [7] established the mechanical model of drilling hole instability and researched the destruction modes and instability characteristics of borehole bottom and coal mass nearby borehole wall. Shengqi et al. [8, 9] studied the influence of fracture dip angle on the mechanical properties of sandstone under uniaxial compression by using sandstone with pore fractures as research object and studied the crack growth characteristics and its influence on the stress strain curve of sandstone with combined defects of single fracture, double fracture, and circular holes using acoustic emission and digital photography. Cheng et al. [10] analyzed the instability and deformation mechanisms of boreholes on soft outburst coal seams under coal mines and pointed out the main roots for the frequent occurrence of destruction and instability, hole collapse, and difficulty in hole formation in the weak hole wall structure after fracturing drilling in coal seam construction. Yao et al. [11] adopted Kastner formula and utilized numerical simulation method to research the variation disciplines of stress field, displacement field, and plastic failure area of borehole. Hao et al. [12] established the viscoelastic-plastic softening model of coal mass around borehole, conducted the comparative analysis on the pressure relief effects of boreholes in soft and hard coal seams, and researched the variation discipline of borehole diameter. Predecessors have not yet studied the effect of borehole deformation, instability, and collapse on distribution law of suction pressure of the drainage system as well as drainage volume.

The results show that many achievements have been made on borehole instability, but the effect of borehole deformation instability collapse on the distribution of negative pressure and pumping capacity has not been studied. Targeting at the practical problem of easy deformation and instability of gas drainage borehole in high-stress loose coal seams, this paper aims to analyze the mechanism of borehole deformation and instability, put forward the model of borehole deformation and instability, and establish a solid-fluid coupling model considering the dynamic change of borehole negative pressure to analyze the effect of different borehole instability modes on gas drainage. The study carries important theoretical guiding significance for optimizing arrangement of gas drainage borehole, improving gas drainage effect, and effectively preventing gas disasters.

2. Study on Mechanism and Mode of Deformation Instability of Gas Drainage Borehole

2.1. Mechanism of Deformation Instability of Gas Drainage Borehole. There are natural factors and engineering factors causing deformation instability of borehole. Fundamentally

speaking, instability failure of borehole means that of coal-rock mass around the borehole, which is a mechanical instability process. The essence is instability failure caused by inability of coal-rock mass strength to withstand the applied stress; in other words, ground stress is the root cause of borehole instability. Deformation failure of the surrounding coal-rock mass follows the formation of gas drainage boreholes, which mainly includes the two stages: formation of plastic zone and rupture zone and borehole collapse.

- (1) As shown in Figure 1(a), the borehole results in elastic zone, plastic zone, and rupture zone from the outside to the inside, the coal body strength in the rupture zone is significantly lower than the virgin rock stress, and the pressure relief zone caused by the drilling construction is mainly concentrated within the rupture zone.
- (2) With the continuous extension of time, the deformation of the coal body in the rupture zone and plastic zone further increases, while the coal body strength in the two zones further lowers. When the cohesive force and friction between the coal blocks cannot resist deformation pressure and weight of the internal coal-rock mass, the broken coal body around the borehole will fall and collapse into the borehole. The deformation resistance of the compacted coal body in the collapse zone continuously grows until it can balance the deformation pressure transmitted by the rupture zone when new balance of forces emerges and coal body in each zone maintains relative stability. The final distribution of the deformation instability in each area is shown in Figure 1(b). The fracture surface is in irregular shape after instability collapse of the borehole. The fracture surface size has close relation to load stress, coal body strength, and expansion coefficient of collapsed coal body and time.

2.2. Mode of Deformation Instability of Gas Drainage Borehole. The effect of borehole gas drainage mainly concerns suction pressure of the drainage system, borehole diameter, and permeability of the surrounding coal body. Previous studies found that borehole deformation instability exerts little effect on permeability of surrounding coal body, and the main influencing factor is borehole diameter, i.e., the size of effective flow cross-sectional area of the gas. Therefore, this paper classifies borehole deformation instability modes based on bore diameter after borehole instability. Considering that both borehole shrinkage and hole collapse will occur in gas drainage borehole of deeply mined soft coal seams, this paper classifies deformation instability of gas drainage borehole into complete borehole, collapse hole, and plug hole as shown in Figure 2.

The complete hole means the borehole wall is intact. At this time, there is no deformation of borehole which remains in a quasicircular shape. The collapse hole means the wall surface around the borehole has fallen and collapsed, the fallen coal dust is accumulated on the wall surface below the

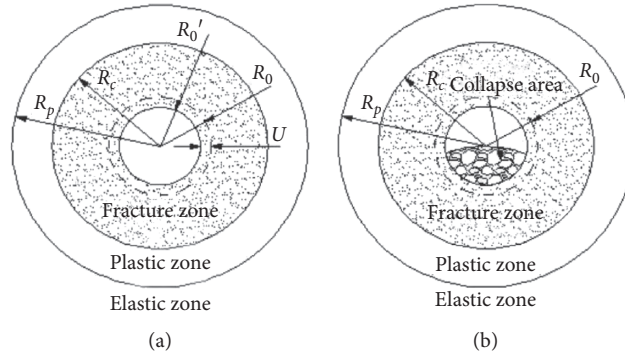


FIGURE 1: Sketch map of unstable deformation area of coal seam around borehole. (a) Before the borehole collapses. (b) After the borehole collapses. R_0 , borehole radius before instability; R_c , radius of fracture zone; R_p , radius of plastic zone; R_0' , borehole radius after instability; U , radial deformation of coal body.

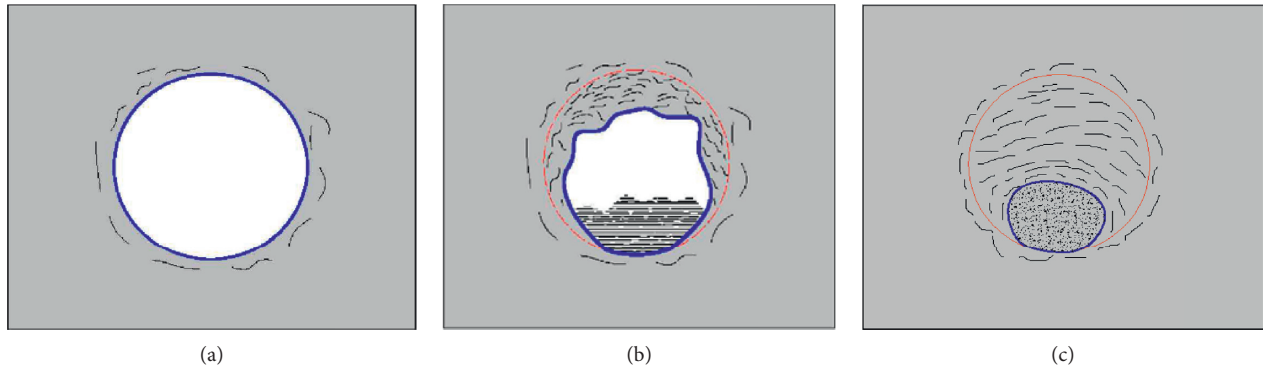


FIGURE 2: Scheme of borehole deformation and instability. (a) Complete hole. (b) Collapse hole. (c) Blocked hole.

hole, making the effective cross-sectional area of circulation in the hole smaller, local drainage resistance increased, and the drainage flow decreased. The plug hole means the borehole wall surface undergoes sharp collapse, and the collapsed coal dust completely blocks the gas flow passage, making it extremely difficult to extract the gas. Next, gas operation under the three modes of deformation instability of gas drainage borehole is numerically simulated to analyze the effect of borehole instability.

3. Establishment of Theoretical Model for Borehole Gas Drainage

3.1. Basic Hypothesis. The following basic hypotheses are introduced to establish the solid-fluid coupling model describing the gas drainage process: (1) the coal seam is an isotropic elastic medium; (2) the gas coal seam is in saturated single-phase adsorption state; (3) the gas flow in the coal seam is isothermal flow that follows the modified Darcy's law; (4) the adsorption and desorption of gas follow Langmuir equation; (5) deformation of the gas-bearing coal seam is a small deformation.

3.2. Coal Seam Deformation Control Equation. If we view coal-rock mass as a linear body, considering the pore pressure in the coal seam and the expansion stress generated by gas adsorption, the stress equilibrium equation can be obtained according to Terzaghi's effective stress principle:

$$\sigma'_{ij,j} + (np\delta_{ij})_{,j} + \left(\frac{2a\rho_s RT \ln(1+bp)}{3V_m} \delta_{ij} \right)_{,j} + F_i = 0, \quad (1)$$

where n is the porosity of the coal seam; δ_{ij} is a Kronecker symbol; R is the molar gas constant, $J/(\text{mol}\cdot\text{K})$; T is the absolute temperature, K ; a is the limit adsorption of coal-rock mass, m^3/kg ; b is the adsorption constant, MPa^{-1} ; ρ_s is the apparent density of coal-rock mass, kg/m^3 ; p is the gas pressure, MPa ; V_m is the molar volume, m^3/mol ; and F_i is the volume force tensor, N/m^3 .

Geometric equation can be established according to the Cauchy equation as

$$\varepsilon_{ij} = \frac{1}{2}(u_{i,j} + u_{j,i}), \quad (2)$$

where R_{ij} is the strain tensor of gas-bearing coal and u_i is the displacement component, m .

According to the basic hypothesis for the model construction, the coal body follows the generalized Hooke's law in the elastic deformation stage, i.e.,

$$\sigma'_{ij} = \lambda \delta_{ij} \varepsilon_v + 2G \varepsilon_{ij}, \quad (3)$$

where λ is the Lamé constant; ε_v is the volumetric strain; and G is the shear modulus.

The deformation control equation of the solid-fluid coupling model for gas-bearing coal body can be obtained by integration of formulas (1)~(3):

$$(\lambda + G)u_{j,ji} + Gu_{i,jj} + np_{,i} + \left(\frac{2a\rho_s RT \ln(1+bp)}{3V_m} \right)_{,i} + F_i = 0. \quad (4)$$

3.3. Dynamic Model of Coal Seam Porosity and Permeability. In view of the coal body deformation caused by gas pressure, the calculation formula of porosity in the elastic phase of gas-bearing coal rock considering coal body deformation can be obtained according to the definition of porosity n :

$$n = 1 - \frac{(1 - n_0)}{1 + \varepsilon_v} \left(1 - \frac{\Delta p}{k_s} \right), \quad (5)$$

where k_s is the bulk modulus of the coal body, MPa; Δp is the change of the gas pressure; ε_v is the volume strain; and n_0 is the initial porosity of the coal seam.

With full consideration to the deformation of gas coal rock, gas pressure change of pore, and the effect of pore volume change on permeability, the permeability calculation formula can be obtained using Kozeny-Carman equation:

$$k = \frac{k_0}{1 + \varepsilon_v} \left[1 + \frac{\varepsilon_v + \Delta p(1 - n_0)/k_s}{n_0} \right]^3, \quad (6)$$

where k is the coal seam permeability, m^2 , and k_0 is the initial permeability of coal seam, m^2 .

3.4. Coal Seam Gas Migration Control Equation. By combining the modified Darcy's law (Klinkenberg effect incorporated), the gas content equation, the continuity equation, and the gas state equation, the coal-bed gas migration control equation incorporating seepage and adsorption gas analysis can be obtained.

$$2 \left[n + \frac{p(1-n)}{k_s} + \frac{abp_0}{(1+bp)^2} \right] \frac{\partial p}{\partial t} - \nabla \left[\frac{k}{\mu} \left(1 + \frac{m}{p} \right) \nabla p^2 \right] + 2(1-n)p \frac{\partial \varepsilon_v}{\partial t} = 0, \quad (7)$$

where μ is the dynamic viscosity coefficient of gas, Pa·s, and m is the Klinkenberg factor.

3.5. Suction Pressure Loss Calculation Model for Gas Drainage Borehole. As gas discharges along the borehole, gas flow in the hole is a variable mass flow. Since pressure loss in the

variable mass flow can only be calculated after obtaining experimental coefficients, the gas flow in the borehole is simplified as pipeline constant mass flow to facilitate calculation. That is, the borehole is divided into several segments as shown in Figure 3. The suction pressure loss in the borehole is obtained via piecewise calculation of suction pressure of the drainage system from the aperture to the hole bottom, as shown in formula (8). In suction pressure loss calculation of each segment, average flow rate is used to replace the actual one, so that suction pressure loss along the borehole can be calculated using formula (9).

$$p_i = p_d + \sum_{n=0}^{i-1} \Delta p_n, \quad (i = 1, 2, \dots, n), \quad (8)$$

$$\Delta p_n = \lambda_d \frac{\Delta l}{d} \frac{\rho_a v_n^2}{2}, \quad (9)$$

where p_d is the suction pressure of the drainage system at the aperture, MPa; p_i is the average suction pressure of the drainage system in the i th section of the borehole, MPa; Δp_n is the suction pressure loss in the n th segment of the borehole, MPa; Δl is the borehole length, m; d is the borehole diameter, m; v_n is the average flow rate for the i th segment of the borehole, m/s; ρ_a is the gas density, kg/m^3 ; and λ_d is the drag coefficient along the course.

To calculate the resistance loss in borehole, flow state of the fluid is first judged by Reynolds number Re . Drag coefficient along the course is $\lambda_d = 64/Re$ for laminar flow, while that of turbulent flow can be calculated based on the empirical formula proposed by Arisuri:

$$\lambda_d = 0.11 \left(\frac{k_s}{d} + \frac{68}{Re} \right)^{0.25}. \quad (10)$$

The local energy loss caused by the deformation and instability of borehole is expressed as a function of flow kinetic energy factor, and the local resistance coefficient is determined according to the calculation method of corresponding local resistance coefficient of underground tunnel.

4. Effect of Deformation Instability of Gas Drainage Borehole in Deep Mining of Soft Coal Seams

4.1. Engineering Background and Establishment of Physical Model. The simulated mine is located in the eastern part of the Pingdingshan mining area. The designed production capacity of the mine is 3 million tons per year, and the mineable coal seams in the mine consist of three groups of 4 layers, that is, Ding, Wu, and Ji. The vertical shaft is used for multilevel up and down to develop the whole mine field. The JI₁₅-21030 working face is the first mining face in Ji No.1 mining area, which is located in the Middle East wing of Ji No.1 mining area. The average mining strike length of the working face is 1420 m, the average inclined width is 152 m, the average coal thickness is 5.0 m, the buried depth is 860 m~1020 m, and the original gas pressure of coal seam is 1.6 MPa. The coal-bed bedding gas drainage borehole and

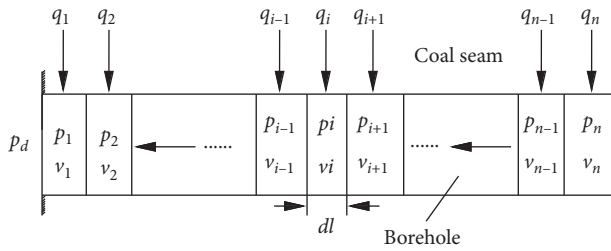


FIGURE 3: Schematic diagram of the calculation of negative pressure in a borehole.

the floor laneway through the layer gas drainage borehole are used in the working face.

Simulation study in this paper is achieved via secondary development of COMSOL Multiphysics. The research object is coal-bed bedding gas drainage borehole process. The established physical model according to the actual condition of working face as shown in Figure 4 is a three-dimensional model of $100\text{ m} \times 20\text{ m} \times 5\text{ m}$. The bedding gas borehole locates in the center of the coal seam with a thickness of 5 m. The gas drainage borehole is 80 m long (hole sealing is 20 m) and 0.094 m in diameter. The simulation parameters are shown in Table 1.

4.2. Initial Conditions and Boundary Conditions. As regards initial conditions, there is an initial gas pressure of 1.6 MPa inside the coal seam, the suction pressure of the drainage system is 14 kPa at the aperture, and the initial stress state is a result of stress distribution after the open-off cut.

Regarding boundary conditions, gas only flows in the coal seam, the open face has a given atmospheric pressure of 0.1 MPa, and the rest of surfaces are with zero-flux, non-ventilated boundary. The surrounding of the model is constrained in the form of roller support (displacement in the direction of the restraint normal line), with fixed constraint for the lower part and freedom for the upper part. The upper part bears rock mass with stress at 27.0 MPa. Meanwhile, the model has self-weight load.

The boundary of suction pressure of the drainage system at the hole wall is a dynamic function boundary. Every 2 m borehole is set as an infinitesimal calculation segment. The suction pressure of a segment is obtained by piecewise calculation of suction pressure loss from the aperture to the hole bottom. The calculation model adopts the theoretical model of borehole suction pressure loss established in the paper. The hole wall flow required for the model calculation is obtained by coupling calculation of coal seam gas migration model.

For calculation scheme, simulation of the effect of deformation instability of gas drainage borehole on gas migration law, suction pressure distribution, etc., is carried out in the three following schemes: (1) there is no borehole deformation, i.e., a complete hole; (2) collapsed hole occurs in the rear 40 m, with the section reduced to half of the original; (3) plug hole occurs in the rear 40 m, i.e., rear borehole blockage.

4.3. Numerical Simulation Results

4.3.1. Effect of Deformation Instability of Gas Drainage Borehole on Gas Distribution in Peripheral Coal Seam. When there is no borehole deformation (i.e., complete hole), collapsed hole, or plug hole, the gas pressure distribution in the coal seam is shown in Figures 5~7 for different drainage time.

The following can be seen from Figures 5~7. (1) Under the effect of gas drainage borehole, coal-bed gas forms an elliptical pressure relief zone around the borehole; the extension of the drainage time makes the coal-bed gas pressure around the gas drainage borehole decrease continuously and results in constantly increasing pressure relief zone, though the increasing rate gradually decreases and eventually stabilizes. (2) Collapsed hole at 40 m below the hole bottom exerts little effect on coal-bed gas pressure distribution around the borehole. Compared with coal-bed gas pressure distribution of complete hole, gas pressure distribution in case of collapsed hole differs only at the collapsed hole segment, while coal-bed gas pressure distribution at other locations is basically the same as that of complete borehole. (3) Plug hole leads to the change of coal seam permeability near the plug hole segment; that is, the permeability becomes better. This causes great difference in coal-bed gas pressure distribution compared to that of complete hole. In this way, the pressure relief zone in the coal seam in front of the plug segment enlarges, and the drainage pressure in the plug segment becomes positive. The drainage pressure closer to the hole bottom is larger, until it becomes the original gas pressure.

4.3.2. Effect of Deformation Instability of Gas Drainage Borehole on Suction Pressure Distribution of the Drainage System. When there is no borehole deformation (i.e., complete hole), collapsed hole, or plug hole, the extraction negative pressure distribution of the drainage system is shown in Figures 8~10 for different drainage time.

The following can be seen from Figures 8~10. (1) Drainage pressure in the borehole gradually decreases with the increasing distance from the aperture, and the decrease range shows a reducing trend. The suction pressure loss of the drainage system is small for complete borehole. As the drainage time increases, the borehole suction pressure loss gradually decreases due to continuous decay of drainage flow. On the 1st day of drainage, suction pressure loss of 80 m borehole is 22.9 Pa. The figure is only 8.0 Pa on the 30th day of drainage. (2) In case of borehole collapse, the decreased borehole section at the collapse segment renders the suction pressure loss of the segment larger, while the suction pressure loss is small for complete segment. The extension of the drainage time makes the drainage flow decay and results in smaller suction pressure loss. After one day of drainage, the suction pressure loss of the first 40 m complete segment is 27.2 Pa. The figure is 70.8 Pa for the latter 40 m collapse segment. Thus, the 80 m borehole loses 98.0 Pa. After one month of drainage, the suction pressure loss of the first 40 m complete segment is 9.5 Pa. The figure is 25.3 Pa for the latter

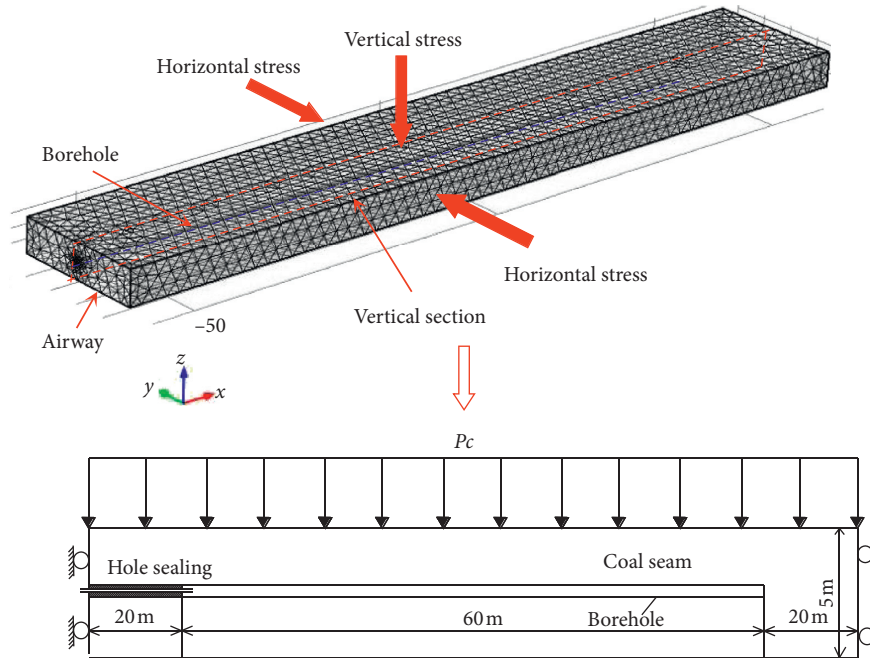


FIGURE 4: Map of three-dimensional geometrical modeling.

TABLE 1: Simulation parameters.

Parameter	Value	Unit
Maximum amount of adsorbed gas per unit mass of coal	28.84	m ³ /t
Adsorption constant of coal	0.49	MPa ⁻¹
Gas density under the standard condition	0.717	kg/m ³
Standard atmospheric pressure	0.1	MPa
Initial porosity of coal seam	0.064	—
Initial permeability of coal seam	0.0227	mD
Moisture of coal	0.014	—
Coal ash	0.127	—
Coal density	1380	kg/m ³
Crustal stress	27.0	MPa
Poisson's ratio of coal	0.339	—
Modulus of elasticity of coal body	2863	MPa
Dynamic viscosity of gas	1.08 × 10 ⁻⁵	Pa·s
Radius of borehole	0.047	m
Initial gas pressure of coal seam	1.6	MPa
Extraction negative pressure	14	kPa

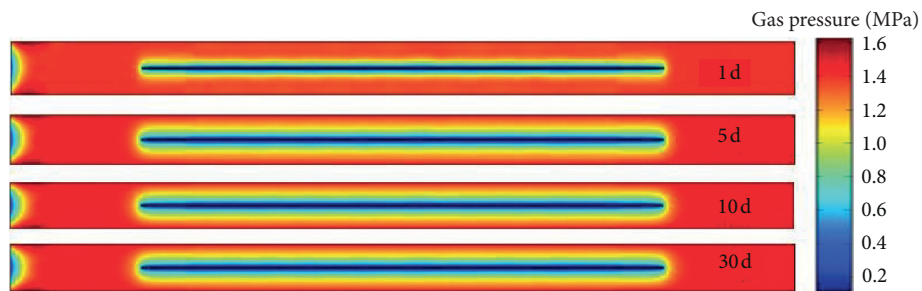


FIGURE 5: The gas pressure distribution of complete hole in the coal seam.

40 m collapse segment. Thus, the 80 m borehole loses 34.8 Pa, which is very small. As the borehole collapse gradually aggravates, the effective drainage section of the borehole

becomes smaller, and the suction pressure loss within the borehole increases, leading to deterioration in gas drainage effect. (3) The drainage pressure changes little for the

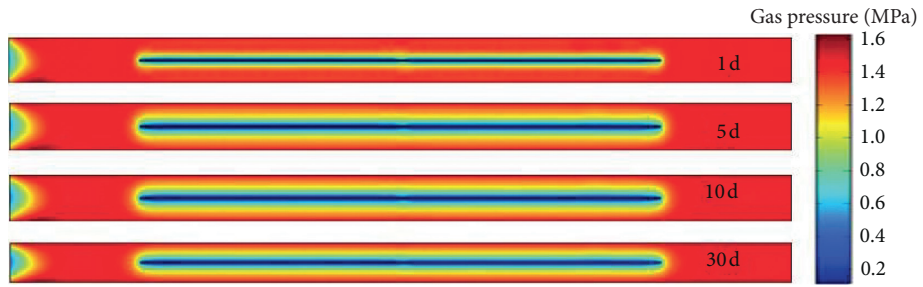


FIGURE 6: The gas pressure distribution of collapsed hole in the coal seam.

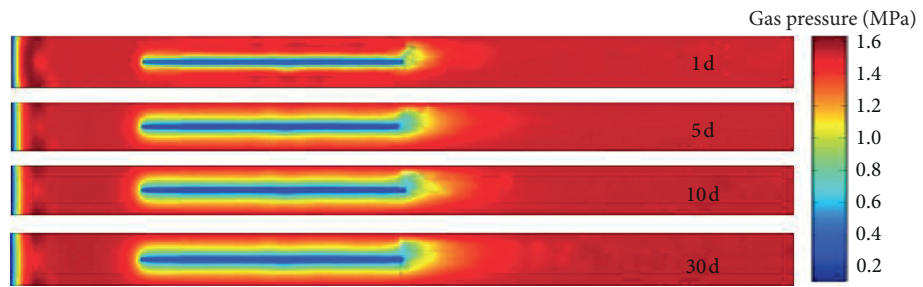


FIGURE 7: The gas pressure distribution of plug hole in the coal seam.

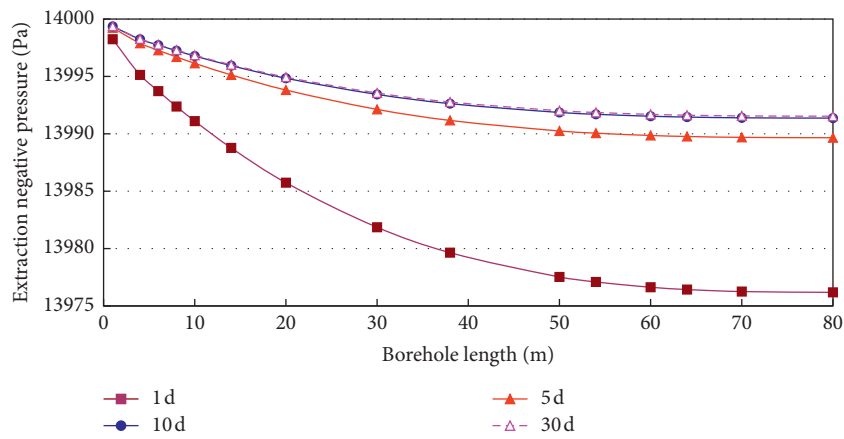


FIGURE 8: The gas extraction negative pressure distribution of complete hole.

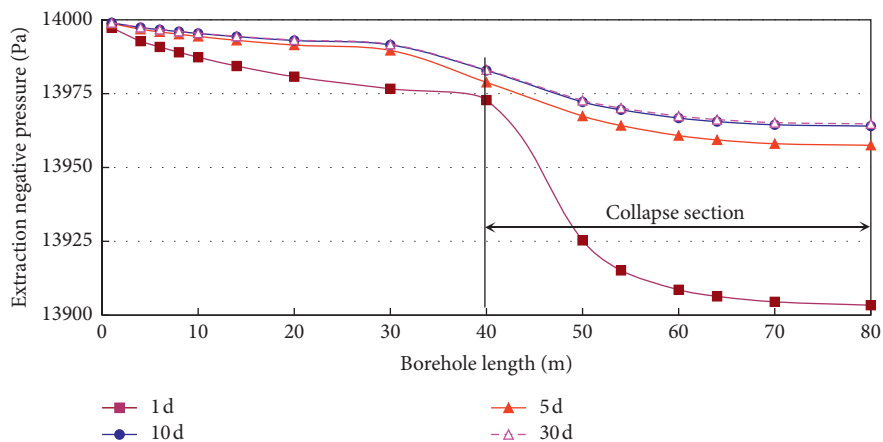


FIGURE 9: The gas extraction negative pressure distribution of collapsed hole.

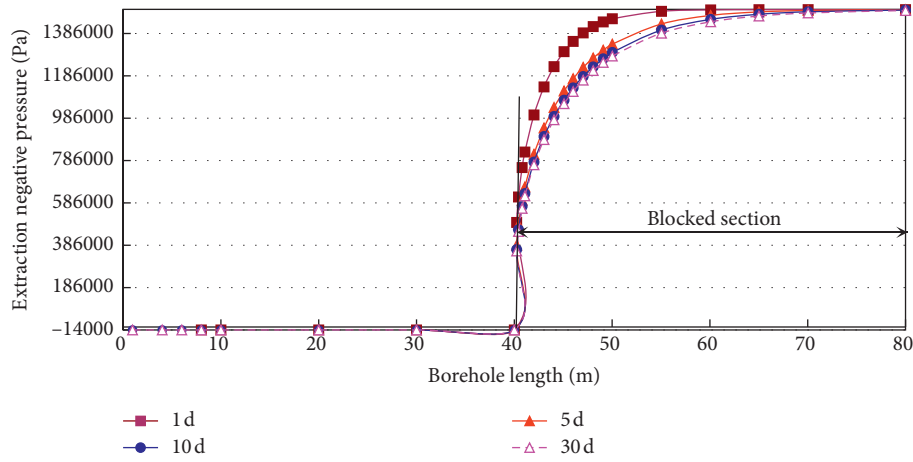


FIGURE 10: The gas extraction pressure distribution of plug hole.

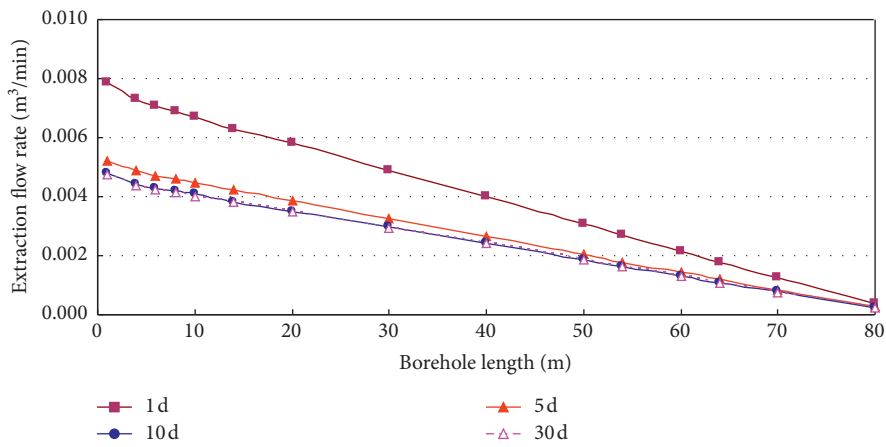


FIGURE 11: The drainage flow distribution of complete hole along the borehole length.

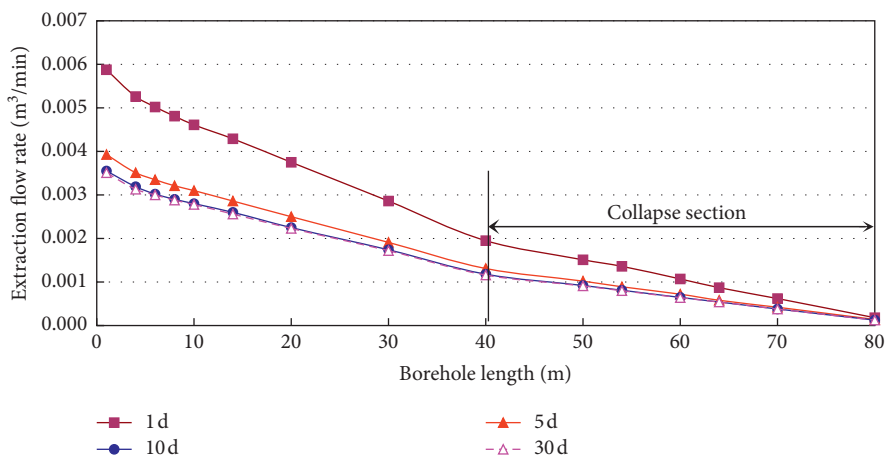


FIGURE 12: The drainage flow distribution of collapsed hole along the borehole length.

complete segment and remains negative, while the drainage pressure of the plug segment becomes positive, and that closer to the borehole bottom is closer to the original gas pressure.

4.3.3. *Effect of Deformation Instability of Gas Drainage Borehole on Gas Drainage Effect.* When there is no borehole deformation (i.e., complete hole), collapsed hole, or plug

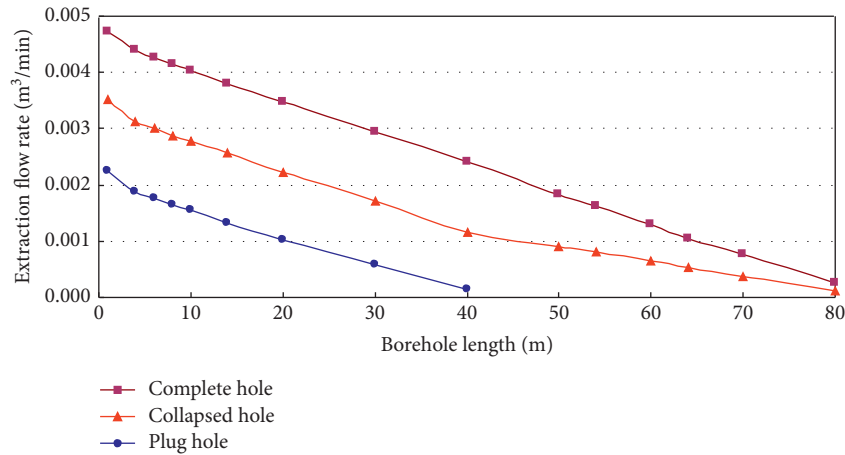


FIGURE 13: The drainage flow distribution of borehole along the borehole length for 30 days after extraction.

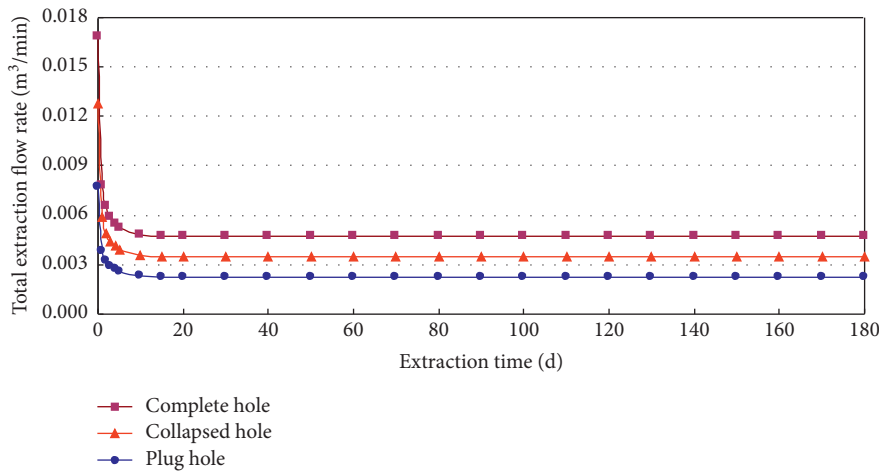


FIGURE 14: The total flow change of complete hole, collapsed hole, and plug hole.

hole, the drainage flow distribution of the borehole is shown in Figures 11 and 12 for different drainage time.

It can be seen from Figure 11 that the borehole drainage flow is roughly in linear distribution along the hole length. The drainage flow is smaller if the borehole is farther from the aperture. The borehole drainage flow decreases with the increasing drainage time but stabilizes finally.

It can be seen from Figure 12 that drainage flow decreases with the extension of drainage time and then stabilizes in case of borehole collapse. The drainage flow still decreases as the distance from the aperture increases, but the drainage flow is no longer in linear distribution along the hole length but with slight turning point at the junction between the collapse segment and the normal segment. Compared with the decreasing extent of complete segment drainage flow along the hole length, that of collapse segment is slower. However, compared with the complete hole, the latter has decreased total drainage flow, which means that gas drainage effect will be worse in case of hole collapse.

When there is no borehole deformation (i.e., complete hole), collapsed hole, or plug hole, the borehole drainage flow distribution along the hole length and its total flow

change after one month of drainage are shown in Figures 13 and 14.

It can be easily seen from Figures 13 and 14 that the drainage effect is ideal for complete hole but worse for borehole collapse, which renders borehole aperture smaller. In case of borehole plug, the drainage effect is poorer, owing to the reduced effective drainage length.

4.4. Suction Pressure Distribution of the Drainage System in the Field Test. The bunch of pipes method can be used to test the negative pressure at different depth in the borehole in the field. As shown in Figure 15, we put a group of copper tubes of different length into the borehole, record the position of each copper tube, and measure negative pressure at different depth of hole with U-type mercury column meter.

The gas extraction negative pressure distribution of bedding borehole for 1 day after extraction was measured by bunch of pipes method in the JI₁₅-21030 working face. The test results are shown in Figure 16.

As can be known from Figure 16, the suction pressure loss is small within 40 m from the borehole, it suddenly

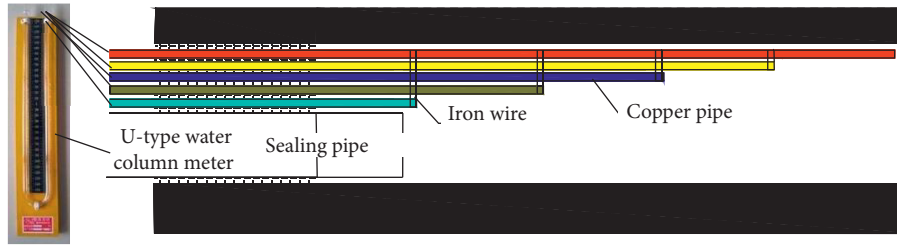


FIGURE 15: Schematic diagram about using bunch of pipes method to test negative pressure distribution.

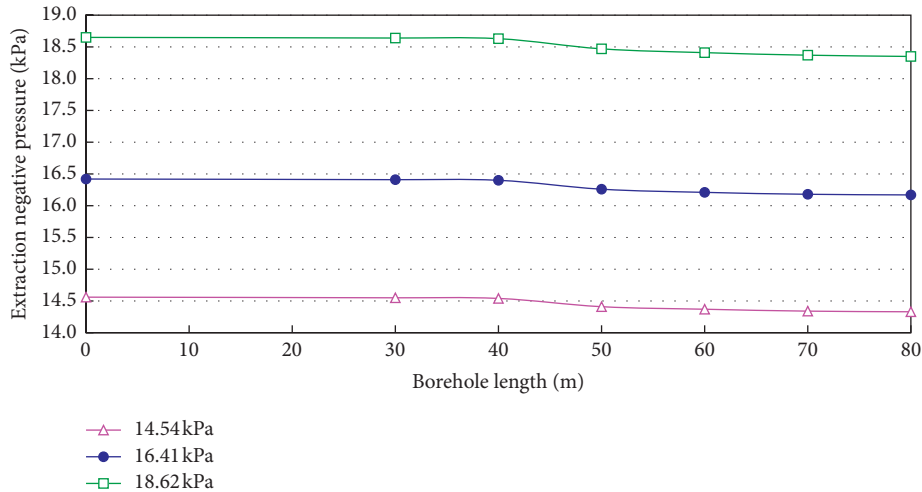


FIGURE 16: The gas extraction negative pressure distribution of borehole along the borehole length for 1 day after extraction.

increases 40 m away from the hole, and it is even bigger within 40 m from the bottom, which is consistent with the suction pressure distribution law in case of collapse at the bottom. It can be inferred from the magnitude of suction pressure loss that great collapse occurs in the rear 40 m of the borehole, i.e., a serious hole collapse. In this case, the smaller effective gas circulation area in the borehole leads to greater suction pressure loss.

5. Conclusion

- (1) The deformation instability mechanism of soft coal seams is analyzed, and three deformation instability modes are proposed for soft coal seams, namely, complete holes, collapse holes, and plug holes. A solid-fluid coupling model incorporating dynamic change of borehole suction pressure is established. The effects of the three deformation instability modes of gas drainage borehole on gas drainage are analyzed.
- (2) Collapsed hole at the hole bottom exerts little effect on coal-bed gas drainage. In case of borehole collapse, the suction pressure loss is big at the collapse segment, and the total suction pressure loss of the drainage system in the borehole is bigger than that in the complete hole. However, it is smaller than the suction pressure of the drainage system and exerts limited effect on gas drainage. As the borehole collapse deteriorates, the effective drainage section of the

borehole becomes smaller, while the suction pressure loss in the borehole increases continuously; thus, the gas drainage effect continuously worsens. Compared with coal-bed gas pressure distribution of complete hole, gas pressure distribution in case of collapsed hole differs only at the collapsed hole segment.

- (3) Borehole plugging at the hole bottom exerts big effect on coal-bed gas drainage. In case of plug hole, a continuous medium forms between the plug segment coal body and the surrounding coal seam, the plug segment drainage pressure turns into coal-bed gas pressure, and effective drainage length of the borehole shortens, seriously affecting the gas drainage effect. Borehole plugging has a great influence on gas pressure distribution in coal seam, and it cannot play the role of drainage and pressure relief in the section of borehole plugging. The research results can be used to monitor the instability region and the degree of borehole instability.

Data Availability

The data used to support the findings of this study are available from the corresponding author upon request.

Conflicts of Interest

The authors declare that they have no conflicts of interest.

Acknowledgments

This study was supported by the National Key Research and Development Program of China (2018YFC0808103), the National Natural Science Foundation of China (grants nos. 51734007, 51704099, and 52074106), the Program for Innovative Research Team in University of Ministry of Education of China (grant no. IRT_16R22), the Key R&D and Promotion Projects in Henan Province (grant no. 212102310105), and the Doctoral Fund of Henan Polytechnic University (grant no. B2019-56).

References

- [1] Y. Sun, Y. L. Wang, X. S. Di, and X. F. Wang, "Analysis on reasons of drilling difficulty in soft and outburst coal seam," *Journal of China Coal Society*, vol. 37, no. 1, pp. 117–121, 2012.
- [2] L. Chun, *Study on Mechanism and Controlling of Borehole Collapse in Soft Coal Seam*, China University of Mining and Technology, Xuzhou, China, 2014.
- [3] L. Yuan, "Strategic thinking of simultaneous exploitation of coal and gas in deep mining," *Journal of China Coal Society*, vol. 41, no. 1, pp. 1–6, 2016.
- [4] H. Zhao, M. Chen, Y. Li, and W. Zhang, "Discrete element model for coal wellbore stability," *International Journal of Rock Mechanics and Mining Sciences*, vol. 54, pp. 43–46, 2012.
- [5] T. Zhang, *Study on Nonlinear Mechanical Mechanism of Mining Instability of Gas Rich Coal and Rock Mass*, Xi'an University of Science and Technology, Xi'an, China, 2009.
- [6] K. Tezuka and H. Niitsuma, "Stress estimated using micro seismic clusters and its relationship to the fracture system of the Hijiori hot dry rock reservoir," *Engineering Geology*, vol. 56, no. 1-2, pp. 47–62, 2000.
- [7] Z. Wang, Y. Liang, and H. Jin, "Analysis of mechanics conditions for instability of outburst-preventing borehole," *Journal of Mining & Safety Engineering*, vol. 25, no. 4, pp. 444–448, 2008.
- [8] Y. Shengqi, J. Hongwen, and X. Tao, "Mechanical behavior and failure analysis of brittle sandstone specimens containing combined flaws under uniaxial compression," *Journal of Central South University*, vol. 21, no. 5, pp. 2059–2073, 2014.
- [9] S. Yang, X. Liu, and Y. Li, "Experimental analysis of mechanical behavior of sandstone containing hole and fissure under uniaxial compression," *Chinese Journal of Rock Mechanics and Engineering*, vol. 31, no. 2, pp. 3539–3546, 2012.
- [10] Z. Cheng, Q. Li, S. Chen, G. H. Ni, and W. Yang, "Analysis on borehole instability and control method of pore forming of hydraulic fracturing in soft coal seam," *Journal of China Coal Society*, vol. 39, no. 9, pp. 1431–1436, 2012.
- [11] X. Yao, G. Cheng, and B. Shi, "Analysis on gas extraction drilling instability and control method of pore forming in deep surrounding rock with weak structure," *Journal of China Coal Society*, vol. 35, no. 12, pp. 2073–2081, 2010.
- [12] F. C. Hao, G.-H. Zhi, and L.-J. Sun, "Stress distribution and movement law around drainage borehole when considering rheological property," *Journal of Mining & Safety Engineering*, vol. 30, no. 3, pp. 449–455, 2013.
- [13] S. Wang, D. Mao, and Y. Ren, "Parameter optimization of drilling holes for pressure relief," *Coal Mining Technology*, vol. 15, no. 5, pp. 14–17, 2010.
- [14] X. Feng and Q. Zhang, "The effect of backfilling materials on the deformation of coal and rock strata containing multiple goaf: a numerical study," *Minerals*, vol. 8, no. 6, p. 224, 2018.
- [15] X. Feng, Q. Zhang, E. Wang, M. Ali, Z. Dong, and G. Zhang, "3D modeling of the influence of a splay fault on controlling the propagation of nonlinear stress waves induced by blast loading," *Soil Dynamics and Earthquake Engineering*, vol. 138, Article ID 106335.
- [16] W. Zhao, K. Wang, R. Zhang, H. Dong, Z. Lou, and F. An, "Influence of combination forms of intact sub-layer and tectonically deformed sub-layer of coal on the gas drainage performance of boreholes: a numerical study," *International Journal of Coal Science & Technology*, vol. 7, no. 4, pp. 1–10, 2020.
- [17] X.-B. Zhang, W.-Y. Wang, and M. Yang, "Study on deformation and destabilization characteristics and modes of drainage borehole," *Energy Sources, Part A: Recovery, Utilization, and Environmental Effects*, vol. 42, no. 19, pp. 2448–2459, 2019.
- [18] X. Zhang, W. Wang, M. Yang, H.-H. Cai, J. Liu, and S. Shen, "Study on mechanical failure and permeability characteristics of porous gas-bearing coal under triaxial stress," *Shock and Vibration*, vol. 2020, Article ID 8838966, 10 pages, 2020.
- [19] X. Wu, Y. Peng, J. Xu, Q. Yan, W. Nie, and T. Zhang, "Experimental study on evolution law for particle breakage during coal and gas outburst," *International Journal of Coal Science & Technology*, vol. 7, no. 1, pp. 97–106, 2020.
- [20] C. Wu, C. Yuan, G. Wen, L. Han, and H. Liu, "A dynamic evaluation technique for assessing gas output from coal seams during commingling production within a coal bed methane well: a case study from the Qinshui Basin," *International Journal of Coal Science & Technology*, vol. 7, no. 1, pp. 122–132, 2020.

Research Article

Three-Dimensional, Real-Time, and Intelligent Data Acquisition of Large Deformation in Deep Tunnels

Yue-Mao Zhao ¹, Yong Han ¹, Yong-Yuan Kou ², Lin Li ³ and Jiu-Hua Du ³

¹Key Laboratory of Ministry of Education on Safe Mining of Deep Metal Mines, Northeastern University, Shenyang, 110819, China

²Jinchuan Group Co., Ltd., Jinchang 737100, China

³ZhongKuang Gold Industry Stock Co., Ltd., Yantai 265400, China

Correspondence should be addressed to Yue-Mao Zhao; 1510456@stu.neu.edu.cn

Received 14 December 2020; Revised 25 December 2020; Accepted 31 December 2020; Published 15 January 2021

Academic Editor: Gong-Da Wang

Copyright © 2021 Yue-Mao Zhao et al. This is an open access article distributed under the Creative Commons Attribution License, which permits unrestricted use, distribution, and reproduction in any medium, provided the original work is properly cited.

Potential disasters of large deformation pose serious threats to deep underground projects such as tunnels and mines. Engineering with large deformation is typically characterized by high stress, complex engineering geology, strong disturbance, and squeezing deformation, posing a great challenge to the design of an effective and accurate monitoring system. To address this problem, it is necessary to grasp the three-dimensional features of deformation and establish integrated monitoring of a support system. Monitoring equipment should be selected to obtain joint, stress, deformation, cracking process, and other information, and this information can be fed back to the warning and control module. The scheme of the monitoring system presented here was successfully applied to a deep metal mine. This intelligent monitoring system ensures safety during the construction and operation of the tunnel under complex surrounding rock conditions, allows the use of field monitoring data to guide construction and design, and provides a reference for future construction and project monitoring.

1. Introduction

With the rapid development of the world economy, easily accessible resources have been nearly exhausted and resource exploitation requires deep excavation. Deep engineering is also required for many road and rail tunnels that cut through huge mountains and are buried thousands of meters deep. The engineering environment is significantly different for deep and shallow engineering, and deep projects present unique engineering problems with poorly understood mechanisms [1–3]. In exploitation and utilization of underground resources, outburst-rockburst, large deformation, and other disasters are the threats of deep mining [4]. Under the influence of mining disturbance, the coupling effect of high ground stress, high gas pressure, and low permeability is stronger [5].

Tunnels under the conditions of high geostress, excavation disturbance, and weak engineering geology may encounter problems such as collapse, spalling, and large extrusion deformation [6]. This study focused on large

deformation during the construction period of deep underground engineering. Large deformation refers to the support system of surrounding rock displacement in the radial direction after tunnel excavation under high ground pressure. Large deformation occurs when the displacement of the squeezing deformation exceeds the conventional deformation of the surrounding rock [7].

Given the unique challenges of deep underground engineering, monitoring is typically performed in real time and using systematic features that can be used to assess squeezing during the construction and service periods [8]. The formation mechanism of large deformation remains a complex problem, as reflected in the lack of systematic studies of advanced monitoring of internal fractures of surrounding rock and the lack of three-dimensional (3D) sensing technology of deformation in squeezing tunnel [9, 10]. Because underground projects may face various potential disaster threats, a monitoring system with an intelligent early warning function is required [11, 12].

With the development of the information age, the development and popularization of sensors, intelligent total station, the Internet, and other technologies has improved engineering monitoring and allow real-time synchronization of monitoring data and monitoring terminals [13–15]. Online synchronization and real-time monitoring are the basis of the Internet of Things [16]. To investigate the large deformation formation mechanism, real-time and systematic data were acquired. Setting up an early warning and evaluation module needs further collection of data and the establishment of an intelligent security monitoring system.

2. Technical Challenges Facing Jinchuan Mine Monitoring System

The Jinchuan mine is an extremely large metal mine in China, with deep tunnel large deformation [17]. The tunnels there often traverse complex engineering geological environments, such as fractured hard rock, weak rock, and other materials. The geological structure and mineralization process have created unique unfavorable tunneling conditions making these areas extremely unstable [18]. There is high geostress in a tunnel, especially horizontal tectonic stress. During tunneling, a bolt-net-shotcrete support system is usually adopted, and after the implementation of support, rapid squeezing deformation of the tunnel can occur [19, 20].

As shown in Figure 1, there is obvious squeezing deformation on both sides of the tunnel, which tends to tear apart the metal mesh and the shotcrete. The left-sidewall of the tunnel cracked out, with a displacement of about 300 mm. The shotcrete on the right side also crumbled and fell, with extrusion of the metal mesh. The use of a fixed point for surface monitoring is vulnerable to damage, limiting the acquisition of continuous data. If a surface failure occurs, the extent and depth of internal cracking are unknown. Thus, the construction of a three-dimensional, real-time, and intelligent monitoring system is required to reveal the interaction mechanism between support and surrounding rock mass.

The large deformation of the tunnel in the Jinchuan mine has a large impact range, with annual repair costs as high as hundreds of millions of yuan [17]. This mine transport roadway has been in service for more than five years and there are often problems with large deformation. After several repairs, the deformation often converges and the rheology continues for a period, exhibiting significant accumulation. At intervals of 10 m along the tunnel axis, the convergence value of the section was roughly calculated for deformation of about 0.6 m–1.3 m. The calculations are shown in Figure 2. Given the magnitude of this problem, it is urgent to explore the mechanism of large deformation to find a reasonable control technique.

To ensure tunnel safety, there has been extensive monitoring in this mine since 1970, with monitoring techniques including surface settlement, measurement of ground pressure, observation of convergence deformation, and observation of displacement in the surrounding rock [18]. Monitoring equipment [19–21] adopted in the tunnel



FIGURE 1: Large area of extrusion cracking on the sidewall of the deep tunnel.

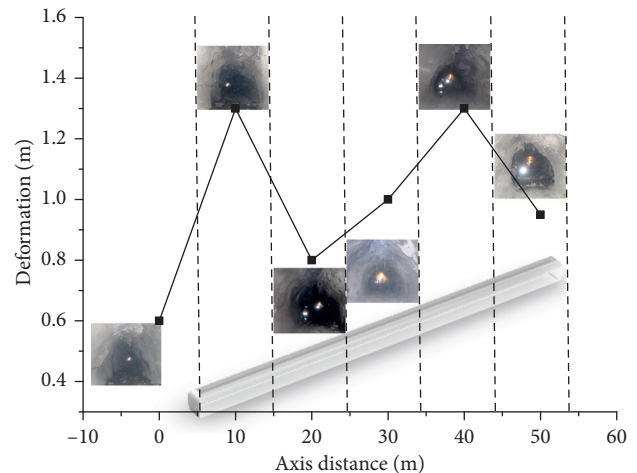


FIGURE 2: Convergence deformation along the axis section of the tunnel.

includes (1) steel ruler, convergence gauge, laser rangefinder, and other tools to monitor surface convergence deformation; (2) extensometer, multipoint displacement gauges, acoustic emission, and other devices to monitor the internal cracking and deformation of deep surrounding rock; (3) fiber Bragg grating (FBG) information fusion to measure the deformation of surrounding rock. Although much information has been acquired, these monitoring systems cannot acquire and process data in real time and cannot intelligently select useful information for decision-making.

3. Monitoring System

3.1. Design of Monitoring System. An intelligent monitoring system was designed to monitor the process of large deformation. The system consists of several modules for monitoring, data storage and transmission, warning, and control. Each module obtains, stores, and analyzes data for its design objectives. As shown in Figure 3(a), the three

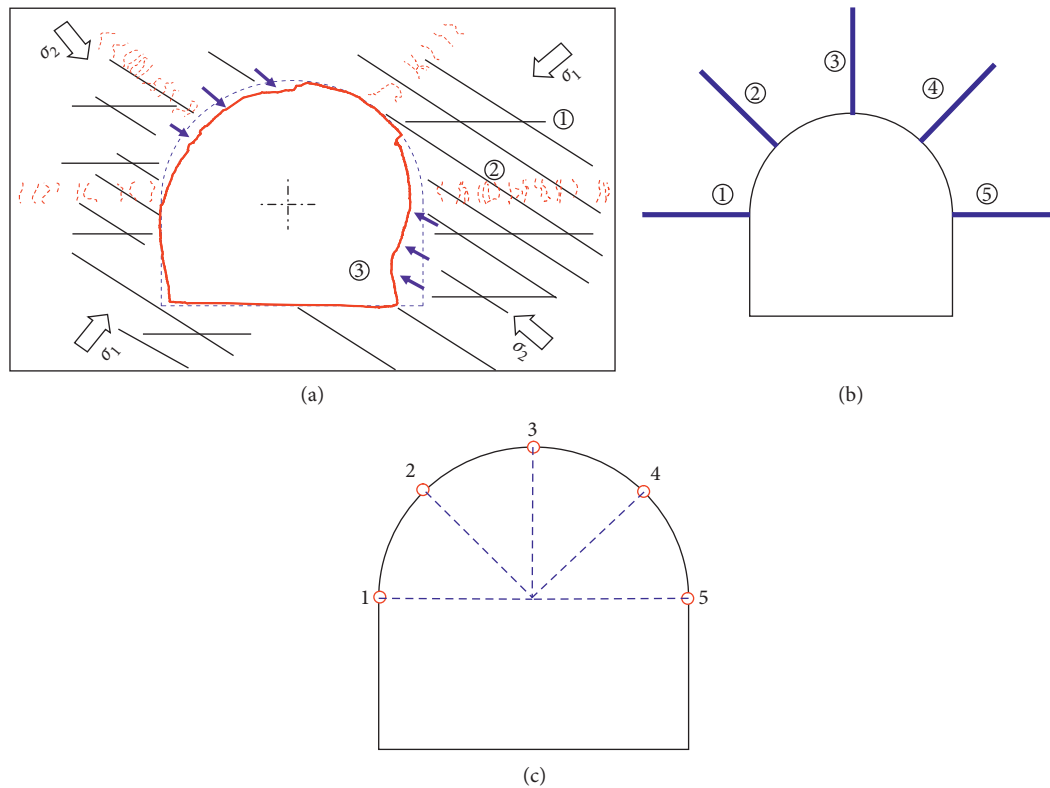


FIGURE 3: Basic principle of large deformation measurement in the tunnel. (a) Major aspects of large deformation, (b) boreholes to measure information in the surrounding rock, and (c) monitoring points on the tunnel surface.

major aspects of large deformation are characteristics of engineering geology, internal cracking of surrounding rocks, and surface deformation. As shown in Figure 3(b), a borehole is usually adopted to measure the interior of the surrounding rock in fine detail, with a measurement accuracy of millimeters. The cracking depth and degree can be determined by observing the cracking evolution process in the surrounding rock with a borehole camera. As shown in Figure 3(c), the tunnel surface can be measured by a laser point cloud, with a measurement accuracy of millimeters.

During large deformation, the surface and interior of the surrounding rock will show some mechanical behaviors, requiring comprehensive observation. As shown in Figure 4, the basic data of rock mechanics, joints, and water should be obtained first. Next, the setting of the monitoring system should consider characteristics of the deformation and cracking occurring inside and on the surface of the tunnel and obtain the stress, strain, pressure, and displacement data. The displacement variables can be obtained by non-contact 3D laser scanning. For evolution observation of the degree and depth of rock cracking, the internal cracking of the surrounding rock can be observed by digital borehole televiewer. In addition, the stress-strain data of internal deformation of rock mass-support can be comprehensively obtained by bolt stress gauge, multipoint displacement gauge, pressure cell, and hollow inclusion stress gauge.

As shown in Figure 5, applying the Internet of Things and cloud computing techniques, an intelligent monitoring system can acquire sensor data; transmit, store, and process

these data; and send early warnings. Effective transmission is essential to the real-time application of an intelligent monitoring system. In this design, the wired transmission is adopted to ensure the timeliness and reliability of transmission. The network system consists of data cables, optical cables, data acquisition modules, a switch, a gateway, and other transmission terminal equipment. Multivariate data exists as big data in a cloud platform and can be directly used for disaster warning and control measures.

Using the control platform shown in Figure 6, all the monitoring data can be collected in real time from the sensor equipment, with both automatic and manual acquisition functions. A manual acquisition can be used to collect data for monitoring specific sections as needed with manual control of collection frequency and time. Automatic collection requires the setting of frequency and period for periodic data collection. In addition to the real-time display of monitored data, the control platform allows query, analysis, statistics, graphical display, and other functions. When the warning module reaches a set level of danger, the software platform will make a sound and show a pop-up dialog box, send messages, and automatically increase the cross section of the monitoring frequency. Reasonable control measures from the control module are also suggested.

The study of monitoring data is needed to study the mechanism of large deformation disaster, design control measures, and evaluate control techniques. The support of the network, big data, Internet of Things, and artificial

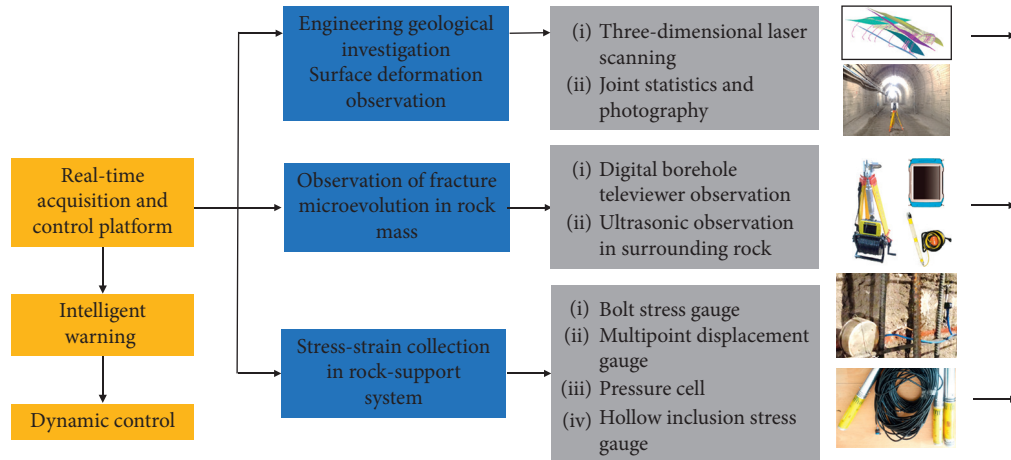


FIGURE 4: Intelligent monitoring system for large deformation.

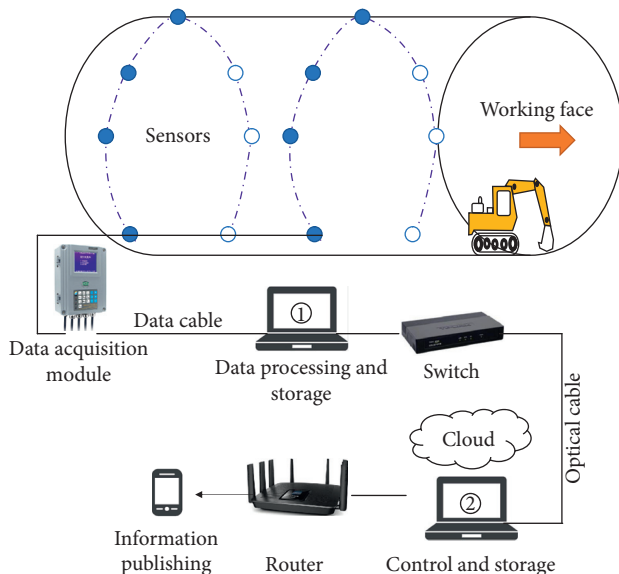


FIGURE 5: Transmission network of the intelligent monitoring system.

intelligence technologies will then be used to further analyze the large deformation disaster mechanism.

3.2. Surface Information Acquisition. Engineering geological survey can determine the geological factors that affect tunnel safety. Preparatory work includes the acquisition of preliminary geological data, tunnel design parameters, and construction data. As shown in Figure 7, site survey to obtain engineering geological information related to tunnel excavation includes working face reconnaissance, joint set statistics, photography, and other data acquisition before each construction cycle. After determining the geological conditions, it is necessary to evaluate the influence and scale of appropriate engineering according to the structure and operation requirements of the tunnel as the basis for ensuring building stability and use.

For surface information acquisition, a three-dimensional (3D) laser scanning system, High-Definition Surveying (HDS), can be used. HDS uses laser ranging to continuously and closely record the three-dimensional coordinates, reflectivity, and texture information of the surface of a target. This system captures data as a point cloud to generate a real three-dimensional record of the space of interest. As shown in Figure 8, this provides point cloud data of engineering surface during construction. The 3D laser scanning equipment consists of a target, scanner, leveling base, bracket, and other components. Field operations require control network establishment, field scanning, and recording measurement. As shown in Figure 9, a single acquisition can obtain tens of meters of high-precision data that can be spliced together to provide data for the whole tunnel along the axis. Using specialized software, 2D or 3D graph, line drawing, point cloud graph, 3D model, and ASCII coordinate data can be output.

After the application of a set of algorithms and data processing methods [10] and sufficient data acquisition, the project profile changes can be obtained. Additionally, the displacement data for key positions can be extracted to obtain a curve of continuous engineering deformation, as shown in Figure 10. Large deformation disaster is characterized by convergence deformation reaching 0.4 m, with serious damage to the support system during excavation. During the service period after lining construction, the deformation rate is slow, but cracking and deformation of the lining must still be monitored.

3.3. Internal Cracking Process of Surrounding Rocks. To assess the failure mechanism of the surrounding rock, a digital borehole televiewer was used to continuously observe the crack. The cracking evolution process at a single location can be sensed by continuous borehole photography. As shown in Figure 11, continuous borehole video is obtained by passing a borehole camera through the borehole and conversion of the video data in the acquisition instrument. Two important indexes are used to assess the evolution of cracking in the surrounding rock [22, 23]: (1) the depth of the maximum cracking area and (2) the degree of cracking in this area.

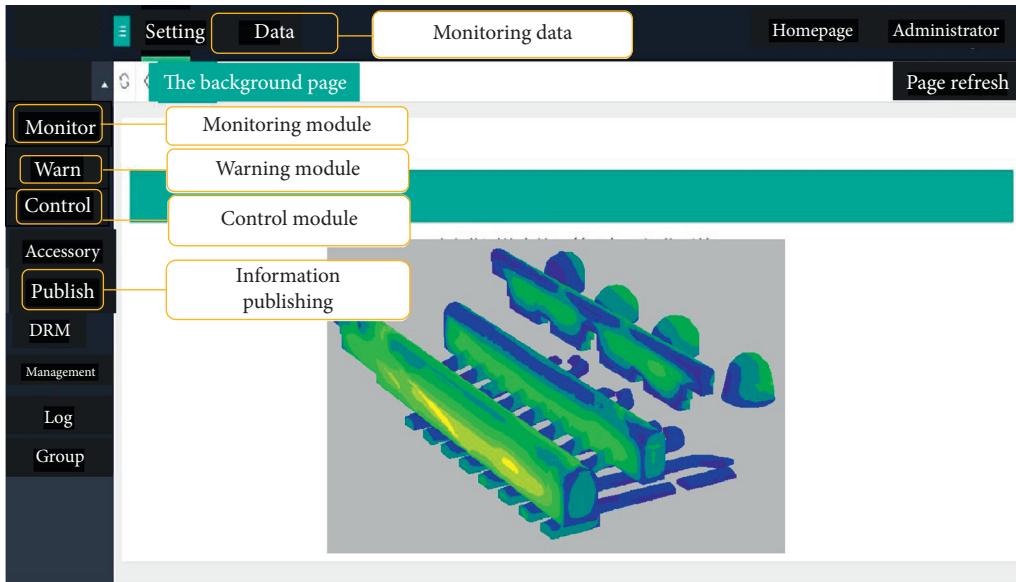


FIGURE 6: Control platform.

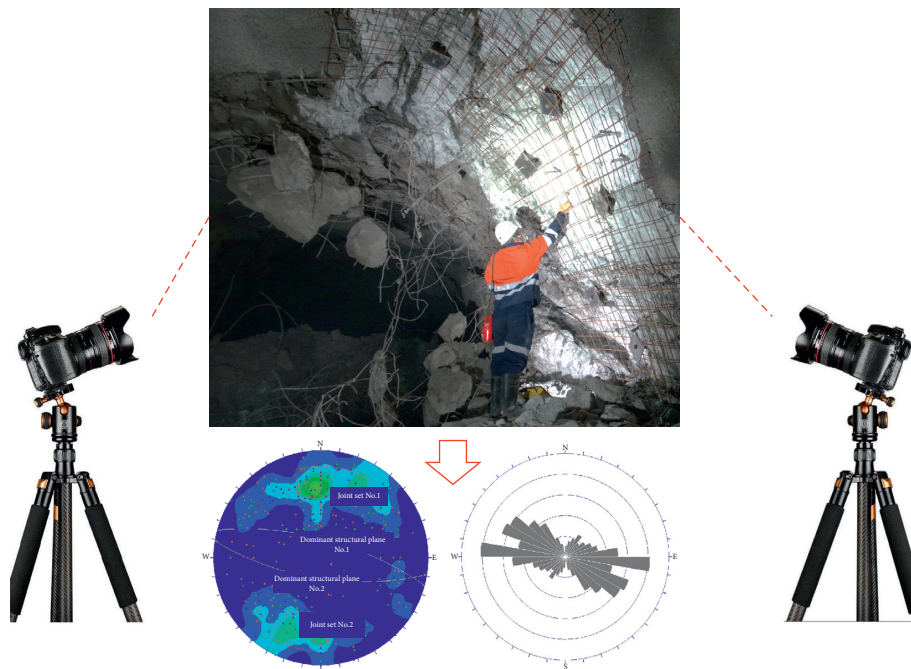


FIGURE 7: Site reconnaissance of engineering geology.

In the surrounding rock mass, fractures develop in many areas over time. As shown in Figure 12, over almost eight months, the crack width increased from the original 7.2 mm (position ① in Figure 8) to 8.4–84 mm (position ② in Figure 8, almost 6 months later) and 9.4 mm (position ③ in Figure 8, almost 8 months later). In addition, the development of cracks can be accompanied by the initiation of new cracks, which can interlace with old cracks to further degrade the surrounding rock quality.

As shown in Figure 13(a), due to geological conditions, extremely poor rock mass integrity can decrease the stability of a geological borehole, resulting in hole collapse. Even after

hole formation, hole collapse may occur due to low stability, excavation disturbance, or blasting vibration (Figure 13(b)). Future work should include the development of in situ geological borehole protection technology to facilitate the study of the adverse geological rock mass.

3.4. Acquisition of Stress-Strain Data in Surrounding Rocks. High-frequency acquisition of internal stress and strain of the rock mass and support system includes bolt stress gauge, multipoint displacement gauges (extensometers), pressure cells, concrete strain gauges (vibrating wire), hollow

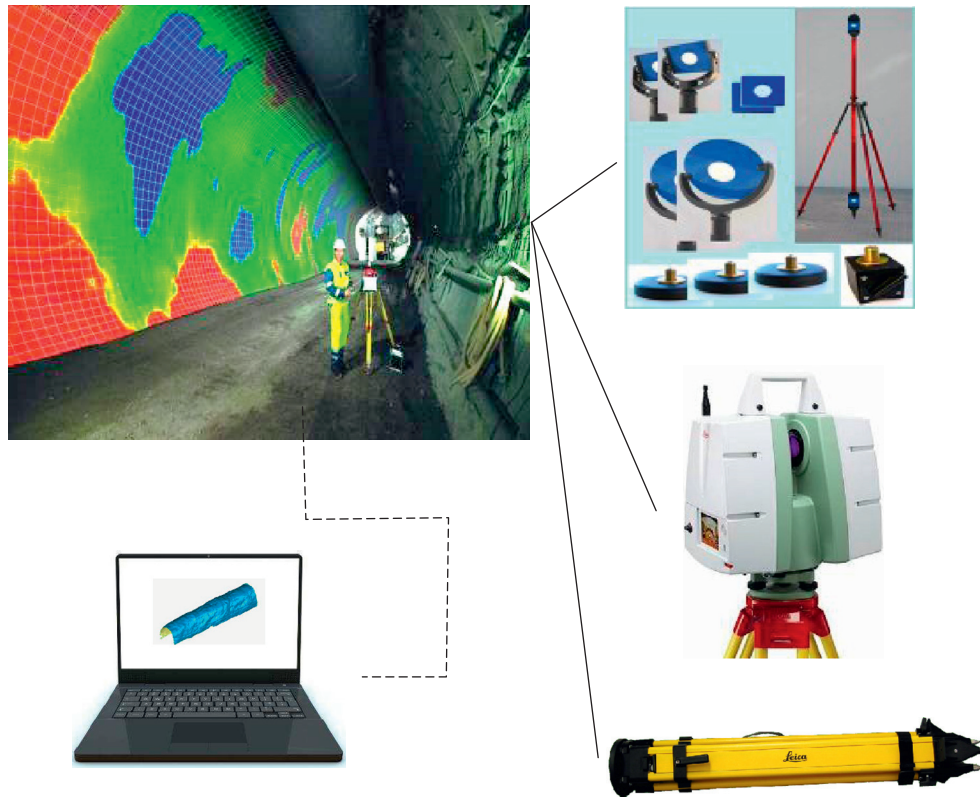


FIGURE 8: Operation of 3D laser scanning equipment.

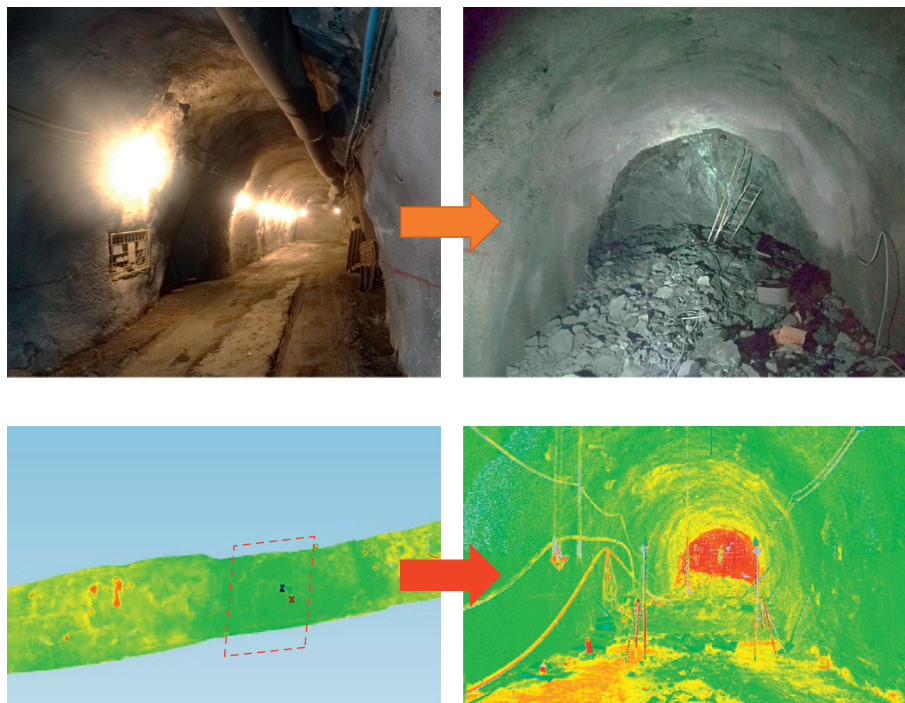


FIGURE 9: Comparison of the data obtained by real scene photos and 3D laser scanning equipment.

inclusion stress gauges, and other sensing elements. As shown in Table 1, these components are connected as a sensing system. The bolt stress gauge and pressure cell can obtain the mechanical characteristics of both the rock mass

and the support system. The data link field operation is shown in Figure 14(a). Sensors are wired to the acquisition module (Figure 14(b)), and the data can be automatically collected by computer control.



FIGURE 10: Convergence deformation curve of the tunnel for a typical cross section [10].

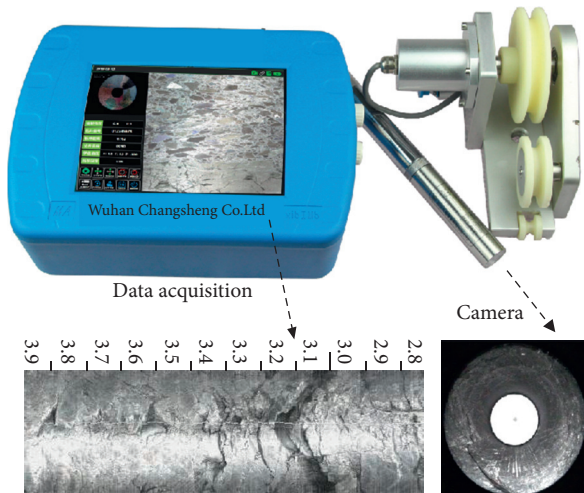


FIGURE 11: Application of drilling camera equipment.

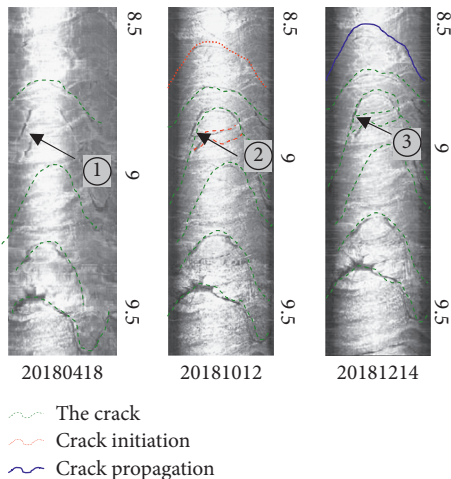


FIGURE 12: Continuous observation of cracking process.

Typical data are shown in Figure 15 and constitute a multivariate information system. In multipoint displacement gauge data shown in Figure 15(a), the displacement curve of each measuring point at 3 m, 10 m, and 20 m increased with time. The deformation of the deep measuring point was greater than that of the shallow measuring point in surrounding rocks, and the maximum depth of displacement in the surrounding rock reached 20 m. As shown in Figures 15(c) and 15(d), the stress curves also increased with time and showed a good correlation with the displacement curve data. The pressure cell data in Figure 15(b) also showed significant changes.

4. Warning and Control of Large Deformation

4.1. Basic Principles of Early Warning. When a rock mass is overdeformed, there is an increased risk of structural failure such as collapse, large deformation, and surrounding rock instability, which will increase safety risk. With the large deformation of deep tunnel surrounding rock, surrounding rock points can be displaced to the surface, leading to the failure of tunnel structure, including serious deformation of the support structure, lining cracking, and other functional failures. Therefore, it is necessary to construct an early warning system that can detect the initiation of large deformation. Early warning evaluates changes in the surrounding rock mass, the support system, and deformation, described in detail below. As shown in Figure 16, focusing on the interior of the surrounding rock can help identify early signs of the start of large deformation.

- (1) Early warning of surrounding rock: as shown in formula (1), a warning is triggered when the cracking depth of surrounding rock (D) is greater than or equal to the length of reinforcement ($L_{support}$). This indicates insufficient control ability of the existing reinforcement (rock bolt or grouting) to the surrounding rock and the possibility that the surrounding rock mass will gradually experience large deformation after excavation under high stress environment. This warning would be based on data from borehole cameras, multipoint displacement gauges, and support design parameters:

$$D \geq L_{support} \tag{1}$$

- (2) Early warning of support system: the time-dependent characteristic of large deformation is also reflected in the gradual failure of the support structure. As shown in formula (2), a warning is triggered when the monitoring data of support ($M_{support}$) are greater than or equal to the reasonable index (I_R). This indicates that the existing support system is near the critical value for breaking. The concrete can fail when the bolt stress exceeds the yield point, the lining pressure exceeds the reasonable value, and the concrete stress exceeds the reasonable value. The reasonable index can refer to an engineering design guide and relevant literature. These data can be

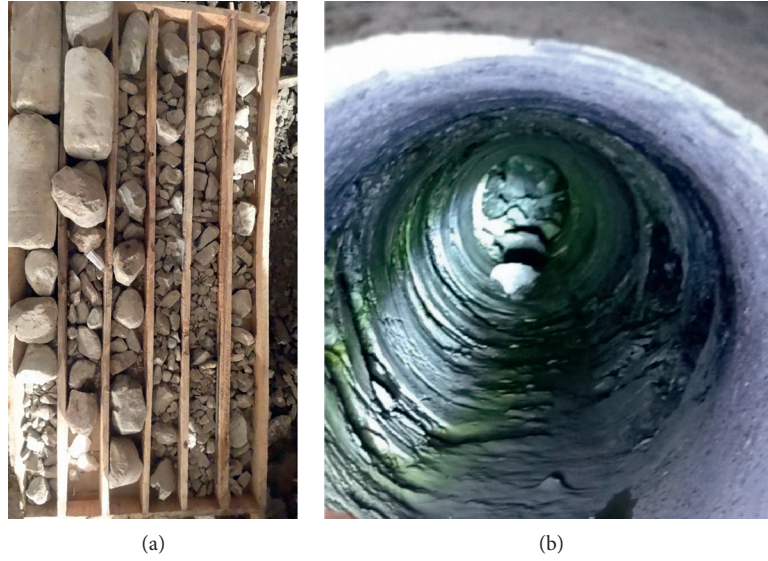


FIGURE 13: Collapse of borehole. (a) Broken core and (b) caving of borehole.

TABLE 1: Multiple sensing elements of rock mass-support system.

Name	The main parameters	Target
Multipoint displacement gauge	Number, range, sensitivity	Displacement of rock mass at different depths
Bolt (reinforcement) stress gauge	Range, sensitivity	Variation of stress
Pressure cell	Range, sensitivity	Change of pressure between shotcrete and lining
Hollow inclusion stress gauge	Range, sensitivity	Change of stress in the rock mass



FIGURE 14: Data connection of field equipment. (a) Data link field operation and (b) data acquisition module.

obtained from the bolt stress gauge, pressure cell, and steel bar gauge:

$$M_{\text{support}} \geq I_R, \quad (2)$$

- (3) Early warning of deformation: if the size of the tunnel section cannot meet the design requirements, early remedial action may be required. As shown in formula (3), this criterion is based on the relationship between the convergence deformation (C_f), the limit of section size (L_0) used in the tunnel, and the initial section size (L_i) after excavation. When the on-site monitoring data of displacement reach this condition, the convergence

deformation is too large, and the existing support cannot effectively control the surrounding rock and meet its use function. Thus, it is necessary to carry out engineering reinforcement and treatment:

$$C_f \geq L_i - L_0. \quad (3)$$

4.2. *Dynamic Control of Large Deformation.* The early warning module can guide dynamic regulation, as shown in Figure 17, by optimizing the parameters of the excavation process, support system, and support timing. This requires the use of monitoring data to calculate the analysis parameters.

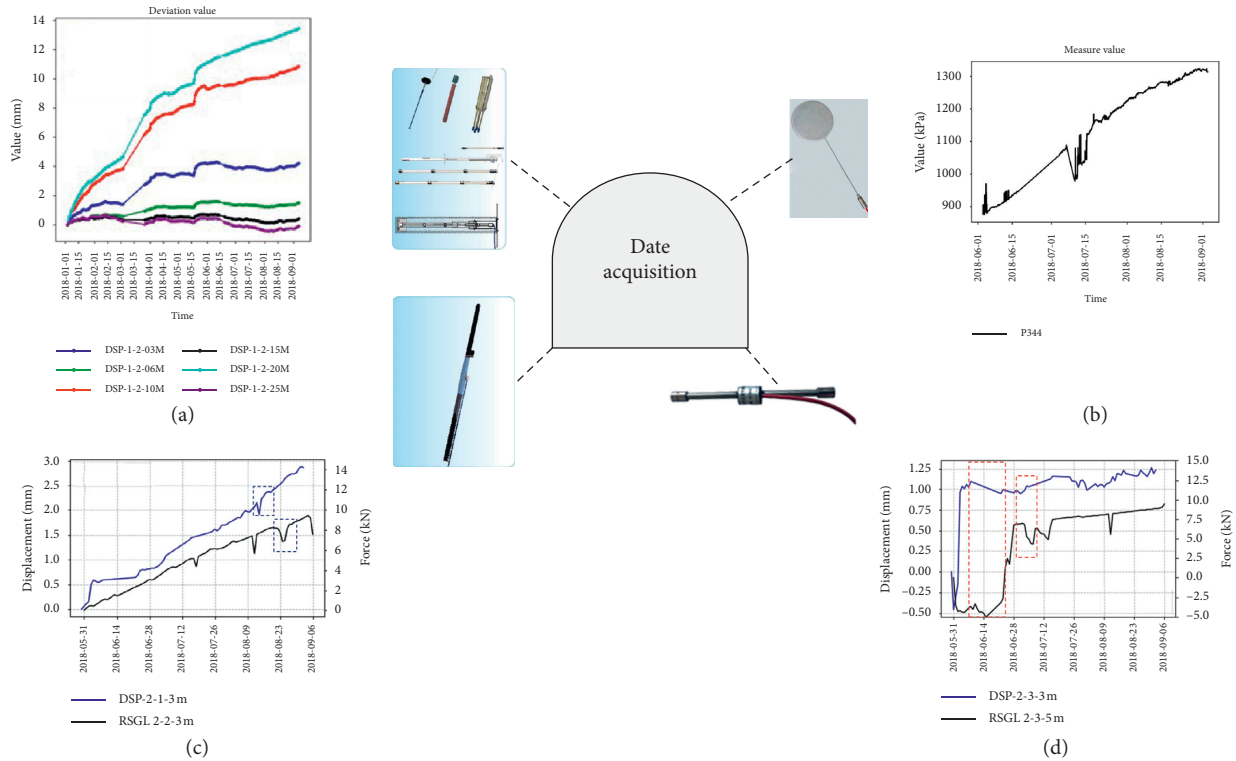


FIGURE 15: Multivariate data collection [10]. (a) Multipoint displacement gauge. (b) Pressure cell. (c) Bolt stress gauge. (d) Reinforcement stress gauge.

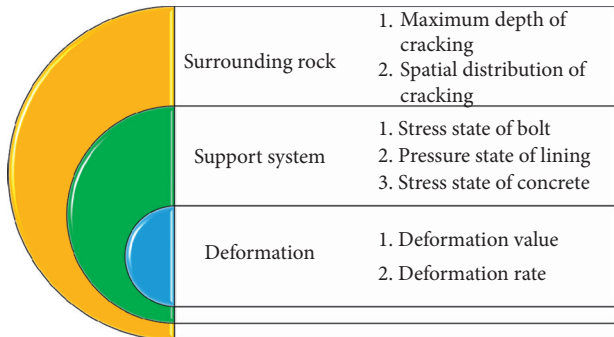


FIGURE 16: Multiple forms of warning information.

The specific parameters of the excavation process are the step size and step sequence, and these construction parameters can be optimized based on the monitoring data of surrounding rock. Parameters of the support system mainly include the bolt-mesh-shotcrete system parameters (length and spacing of rock bolt, thickness of shotcrete layer, and metal mesh measurements), grouting parameters (length and spacing), and lining parameters (thickness and strength). Support timing describes the sequence of the support system and the time to construct.

5. Discussion

Using the above-described monitoring data, the nonuniformity of shallow and deep cracks in the surrounding rock mass and the progressiveness of the aging displacement

change can be observed. Excavation of the tunnel under high geostress induces cracking in a certain range around the tunnel, and stress redistribution may promote the gradual deepening of cracking. In this process, the gradual cracking of surrounding rock decreases its bearing capacity and shows the characteristics of aging deformation, as shown in Figure 18. Some locations, such as the bottom corner of the wall, exhibit large deformation (displacement far exceeds the overall deformation capacity of the bolt), but where a bolt has not failed, it may be because the bolt is parallel to the structural plane and moves with the surrounding rock. The mechanism of large deformation can be further studied by means of model tests or numerical simulation.

Different control measures can be selected based on the indexes of the evolution of cracking in the surrounding rock, considering the depth of the cracking area affected by excavation and the cracking degree of the surrounding rock. Monitoring the change of these two indexes can guide support design and evaluation. According to previous studies [22, 24], support parameters such as reasonable support depth and support timing will affect the development of internal cracks in surrounding rocks. As shown in Figure 19, the deformation coordination function of the first layer of the bolt-mesh-shotcrete system can be reasonably utilized to allow adjustment of the surrounding rock. The second layer of the support system, including bolt-mesh-shotcrete and grouting, can effectively strengthen the surrounding rock and restrain the development of cracking in surrounding rock for the control of large deformation.

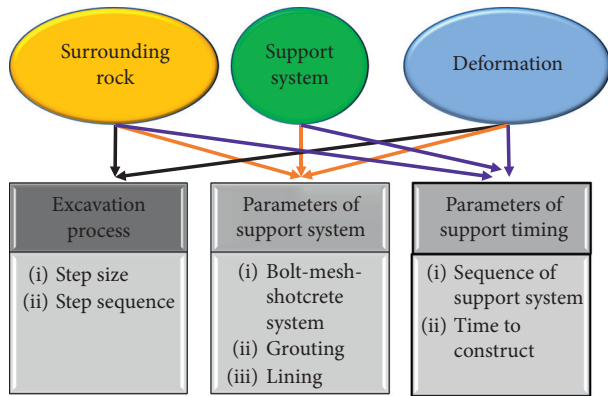


FIGURE 17: Monitoring information used to assess the risk of large deformation.

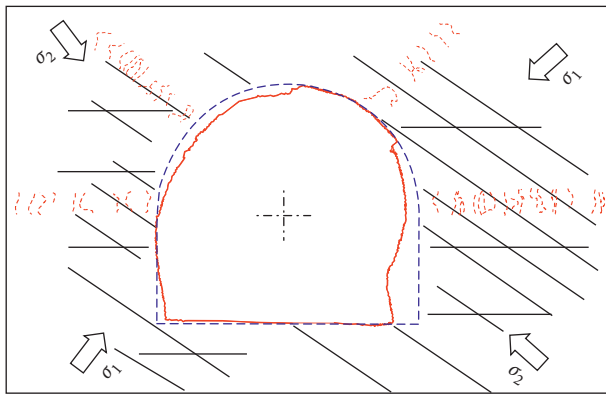


FIGURE 18: Preliminary mechanism of large deformation.

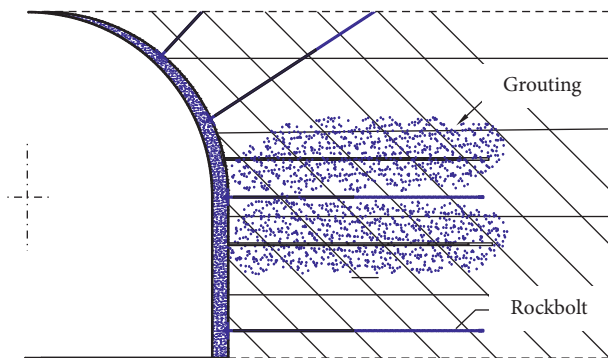


FIGURE 19: Schematic diagram of the support system.

Overall, to control large deformation, it is essential to predict large deformation and implement reasonable prevention and control measures. Prevention of large deformation requires comprehensive preparation at the design stage and the collection and use of geological monitoring data.

6. Conclusion

This work describes how to obtain real-time and three-dimensional information in a fractured hard rock tunnel to limit the risk of the development of large deformation. The

collected information can guide engineering design and construction, provide early warning, and suggest effective control measures. The main conclusions of this work are summarized below.

- (1) The use of a 3D, real-time monitoring system can capture the essence of a large deformation disaster. Evolution of large deformation can be analyzed by monitoring the deformation of surrounding rock, the dynamic process of rock cracking, and the pressure and internal stress of the surrounding support structure. Automatic data collection, real-time data transmission, and efficient data storage enable visual real-time display of the mechanical state of the surrounding rock and tunnel structure.
- (2) A real-time warning and control module can be constructed to intelligently analyze data. The use of a three-dimensional monitoring system can detect the start of large deformation of surrounding rock, enabling the implementation of reasonable control measures. Based on tunnel service requirements, real-time monitoring data can be utilized for early warnings. Based on the warning information, data analysis can be carried out to propose the most appropriate control measures.
- (3) The internal cracking of the surrounding rock is the fundamental cause of large deformation and cracking gradually expands to the interior. Observing the space-time relationship between support and large deformation should guide the strengthening of the support system. More attention should focus on the early restraint effect of rock bolt on the surrounding rock cracking, and rock bolt length should be extended when the cracking depth is insufficient.

Data Availability

The data used to support the findings of this study are available from the corresponding author upon request.

Conflicts of Interest

The authors declare that they have no conflicts of interest.

Acknowledgments

The authors gratefully acknowledge the financial support from the National Natural Science Foundation of China (no. 51621006) and National Key Research and Development Program of China (no. 2016YFC0600707). For their help, the authors also thank Professor Quan Jiang, Associate Professor Shuai Xu, Dr. Lei-Bo Song, and Dr. Jie Liu from the Shaoxing University, and Dr. Shan Zhong from the Institute of Rock and Soil Mechanics, Chinese Academy of Sciences.

References

- [1] N. Barton, R. Lien, and J. Lunde, "Engineering classification of rock masses for the design of tunnel support," *Rock Mechanics*

- Felsmechanik Macanique des Roches*, vol. 6, no. 4, pp. 189–236, 1974.
- [2] Z. T. Bieniawski, *Engineering Rock Mass Classifications*, Wiley, New York, NY, USA, 1989.
 - [3] G. Barla, “Squeezing rocks in tunnels,” *ISRM News Journal*, vol. 2, no. 3-4, pp. 44–49, 1995.
 - [4] K. Wang and F. Du, “Coal-gas compound dynamic disasters in China: a review,” *Process Safety and Environmental Protection*, vol. 133, pp. 1–17, 2020.
 - [5] F. Du and K. Wang, “Unstable failure of gas-bearing coal-rock combination bodies: insights from physical experiments and numerical simulations,” *Process Safety and Environmental Protection*, vol. 129, pp. 264–279, 2019.
 - [6] Ö. Aydan, T. Akagi, and T. Kawamoto, “The squeezing potential of rocks around tunnels; Theory and prediction,” *Rock Mechanics and Rock Engineering*, vol. 26, no. 2, pp. 137–163, 1993.
 - [7] R. D. Dwivedi, M. Singh, M. N. Viladkar, and R. K. Goel, “Prediction of tunnel deformation in squeezing grounds,” *Engineering Geology*, vol. 161, pp. 55–64, 2013.
 - [8] M. K. Panda, S. Mohanty, B. M. P. Pingua, and A. K. Mishra, “Engineering geological and geotechnical investigations along the head race tunnel in teesta stage-III hydroelectric project, India,” *Engineering Geology*, vol. 181, pp. 297–308, 2014.
 - [9] W. Yu, W. Wang, X. Chen, and S. Du, “Field investigations of high stress soft surrounding rocks and deformation control,” *Journal of Rock Mechanics and Geotechnical Engineering*, vol. 7, no. 4, pp. 421–433, 2015.
 - [10] Q. Jiang, S. Zhong, P.-Z. Pan, Y. Shi, H. Guo, and Y. Kou, “Observe the temporal evolution of deep tunnel’s 3D deformation by 3D laser scanning in the jinchuan no. 2 mine,” *Tunnelling and Underground Space Technology*, vol. 97, p. 103237, 2020.
 - [11] F. Ariznavarreta-Fernández, C. González-Palacio, A. Menéndez-Díaz, and C. Ordoñez, “Measurement system with angular encoders for continuous monitoring of tunnel convergence,” *Tunnelling and Underground Space Technology*, vol. 56, no. Jun, pp. 176–185, 2016.
 - [12] S. Mahdevari, S. R. Torabi, and M. Monjezi, “Application of artificial intelligence algorithms in predicting tunnel convergence to avoid TBM jamming phenomenon,” *International Journal of Rock Mechanics and Mining Sciences*, vol. 55, pp. 33–44, 2012.
 - [13] P. Egger, “Design and construction aspects of deep tunnels (with particular emphasis on strain softening rocks),” *Tunnelling and Underground Space Technology*, vol. 15, no. 4, pp. 403–408, 2000.
 - [14] J. G. Zhou, H. L. Xiao, and W. W. Jiang, “Automatic subway tunnel displacement monitoring using robotic total station,” *Measurement*, vol. 151, Article ID 107251, 2019.
 - [15] H. Song and P. H. Zhu, “Monitoring of tunnel excavation based on the fiber Bragg grating sensing technology,” *Measurement*, vol. 169, Article ID 108334, 2020.
 - [16] H. P. Xie, “Research review of the state key research development program of China: deep rock mechanics and mining theory,” *Journal of China Coal Society*, vol. 44, no. 5, pp. 1283–1305, 2019, in Chinese.
 - [17] M. Cai and H. Peng, “Advance of in-situ stress measurement in China,” *Journal of Rock Mechanics and Geotechnical Engineering*, vol. 3, no. 4, pp. 373–384, 2011.
 - [18] M. F. Cai, L. Qiao, C. Li, B. Yu, and S. Wang, “Results of in situ stress measurements and their application to mining design at five Chinese metal mines,” *International Journal of Rock Mechanics and Mining Sciences*, vol. 37, pp. 509–515, 2000.
 - [19] R.-H. Cao, P. Cao, and H. Lin, “A kind of control technology for squeezing failure in deep roadways: a case study,” *Geomatics, Natural Hazards and Risk*, vol. 8, no. 2, pp. 1715–1729, 2017.
 - [20] X. L. Feng, F. S. Ma, and H. J. Zhao, “Deformation, failure and analysis of convergence monitoring of rock mass in deep high-stress and swelling roadway,” *Journal of Engineering Geology*, vol. 26, pp. 716–723, 2018, in Chinese.
 - [21] Q. Jiang, X. T. Feng, S. J. Li, G. S. SU, and Y. X. Xiao, “Cracking-restraint design method for large underground caverns with hard rock under high geostress condition and its practical application,” *China Journal of Rock Mechanics and Engineering*, vol. 38, no. 6, pp. 1081–1101, 2019, in Chinese.
 - [22] Y. Zhang, X. T. Feng, X. X. Zhang, Z. F. Wang, M. Sharifzadeh, and C. X. Yang, “A novel application of strain energy for fracturing process analysis of hard rock under true triaxial compression,” *Rock Mechanics and Rock Engineering*, vol. 52, no. 2, pp. 1–16, 2019.
 - [23] T. Chen, X.-T. Feng, G. Cui, Y. Tan, and Z. Pan, “Experimental study of permeability change of organic-rich gas shales under high effective stress,” *Journal of Natural Gas Science and Engineering*, vol. 64, pp. 1–14, 2019.
 - [24] X. T. Feng, X. J. Hao, Q. Jiang, S. J. Li, and J. A. Hudson, “Rock cracking indices for improved tunnel support design: a case study for columnar jointed rock masses,” *Rock Mechanics and Rock Engineering*, vol. 49, pp. 2115–2130, 2016.